



**Development of a Multi-port DC-DC Converter  
For a Magnetically-Coupled Residential  
Micro-grid**

**Mohammad Jafari**

M.E. (Electrical Engineering), B.E. (Electrical Engineering)

**School of Electrical, Mechanical and Mechatronic Systems  
University of Technology Sydney, Australia**

**A thesis submitted to the University of Technology Sydney  
for the Degree of Doctor of Philosophy**

**August 2017**

## **CERTIFICATE OF AUTHORSHIP/ORIGINALITY**

I certify that the work in this thesis has not previously been submitted for a degree nor has it been submitted as part of requirements for a degree except as part of the collaborative doctoral degree and/or fully acknowledged within the text.

I also certify that the thesis has been written by me. Any help that I have received in my research work and the preparation of the thesis itself has been acknowledged. In addition, I certify that all information sources and literature used are indicated in the thesis.

This research is supported by an Australian Government Research Training Program Scholarship.

The research also is partially supported by Commonwealth Scientific and Industrial Research Organisation (CSIRO) under the CSIRO's postgraduate scholarship program.

Signature of Student: Mohammad Jafari

Date: 20/08/2017

## **ACKNOWLEDGEMENTS**

First of all, I would like to express my sincere appreciation and gratitude to my supervisor, Professor Jianguo Zhu, for his invaluable guidance, support and consistent encouragement throughout my study at UTS. His extensive knowledge and creative thinking has been a source of inspiration for me throughout the entire research project. I am also thankful to Dr. Greg Hunter, Dr. Li Li, and Dr. Ha Pham for their useful suggestions and support as co-supervisors of the project.

Also, I would like to thank Dr. Glenn Platt, the external co-supervisor, from the Commonwealth Scientific and Industrial Research Organisation (CSIRO) for his useful suggestions, kind support and encouragement.

Importantly, my appreciation goes towards my parents for their consistent support and encouragement. Their consistent support and practical experience sharing have been important and helpful during my life.

At last, with my deepest love, I would like to thank my wife, Zahra, for her love and understanding. This thesis would not have been possible without her encouragement and extensive support. I also should thank my children, Anahid and Avash, for the moments of happiness they brought to us.

## TABLE OF CONTENTS

CERTIFICATE OF AUTHORSHIP/ORIGINALITY .....	i
ACKNOWLEDGEMENTS .....	ii
LIST OF SYMBOLS .....	viii
LIST OF ABBREVIATIONS .....	xiii
LIST OF FIGURES.....	xvi
ABSTRACT.....	xxv
CHAPTER 1 .....	1
INTRODUCTION .....	1
1.1 Background.....	1
1.2 Distributed Generation and Micro-grids .....	2
1.3 Residential Consumers of Renewable Energies.....	3
1.4 Hybrid Renewable Energy Systems.....	5
1.5 Residential Micro-grids, Challenges and Solutions .....	6
1.6 Research Framework .....	7
1.7 Objectives and Contributions of the Research .....	10
1.8 Outline of the Thesis .....	12
References.....	15
CHAPTER 2 .....	17
LITERATURE REVIEW .....	17
2.1 Introduction.....	17
2.2 Renewable Energy Resources for Residential Consumers .....	17
2.2.1 Solar energy .....	18
2.2.2 Wind energy.....	18
2.2.3 Micro combined heat and power.....	19
2.2.4 Fuel cell generator.....	19
2.2.5 Bioenergy .....	20
2.2.6 Geothermal.....	20
2.2.7 Hydro .....	20
2.2.8 Energy storage .....	21
2.3 Hybrid Renewable Energy System .....	21
2.4 Residential Micro-grids .....	22
2.5 Multi-port Dc-dc Converters in Small Scale Residential Micro-grids.....	22

---

2.6 Multi-port Converter in Islanded Micro-grids .....	24
2.6.1 Roadway lighting and traffic lights.....	24
2.6.2 Remote monitoring, research and communication sites.....	25
2.6.3 Fuel cell and solar supplied electric vehicles .....	26
2.7 Review of the Multi-port Dc-dc Converter Topologies .....	27
2.7.1 Classification of multi-port converters.....	28
2.7.2 Topologies based on synthesizing voltage and current source cells .....	30
2.7.3 Topologies based on time sharing concept .....	33
2.7.4 Topologies based on flux additivity .....	35
2.8 Multi-input, Multi-output Converters .....	38
2.9 Discussion .....	40
2.10 Summary .....	41
References.....	42
CHAPTER 3 .....	50
DESIGN AND DEVELOPMENT OF A MICRO-GRID FOR HOUSEHOLD APPLICATIONS.....	50
3.1 Introduction.....	50
3.2 Selection of the Micro-grid Topology .....	50
3.3 Selection of DC-DC Converter Topology for PV Port .....	52
3.4 Selection of DC-DC Converter Topology for Battery .....	54
3.5 Basics of Operation in Steady State.....	54
3.6 Modular Design as An Option for Off-grid Consumers .....	55
3.7 Comparison of full Bridge, Half Bridge, Current-Fed Half Bridge and Inter-leaved Current-fed DC-DC Converters.....	56
3.7.1 Performance analysis of the topologies .....	56
3.8 Overall Evaluation of the Topologies .....	69
3.9 Design and Experimental Development of Micro-grid.....	70
3.9.1 Design of TAB converter .....	71
3.9.2 Bi-directional buck-boost converter.....	72
3.9.3 Inter-leaved current-fed boost converter .....	74
3.9.4 Sensor and protection board.....	76
3.9.5 Driver board .....	78
3.9.6 Control and interface board.....	80
3.10 Experimental Development.....	80
3.11 Digital Signal Processing (DSP) Board .....	82
3.12 Summary of Chapter .....	83

References.....	84
CHAPTER 4 .....	89
DESIGN AND DEVELOPMENT OF MULTI-WINDING MAGNETIC LINK .....	89
4.1 Introduction.....	89
4.2 Application of Magnetic Link.....	90
4.3 Equivalent Model of the Magnetic Link .....	92
4.4 Design of High Frequency Magnetic Link .....	95
4.4.1 Selection of magnetic material.....	97
4.5 Design of Magnetic Link Geometry using RNM.....	103
4.6 Loss Analysis of the Magnetic Link .....	110
4.7 Core Loss Analysis .....	110
4.8 Conduction Loss Analysis .....	114
4.8.1 Harmonic based analysis of the winding currents.....	116
4.8.2 Calculation of ac resistance.....	121
4.9 Calculation of Maximum Copper loss .....	124
4.10 Loss Analysis under Phase Shift and Duty Ratio Variation .....	127
4.11 Thermal Analysis of the Magnetic Link .....	130
4.12 Experimental Validation of Design.....	134
4.12.1 Core loss measurement .....	136
4.12.2 Copper loss measurement .....	139
4.13 Validation of Temperature Rise Analysis.....	142
4.14 Measurement of Inductive and Resistive Elements .....	143
4.15 Summary of the Chapter .....	153
References.....	154
CHAPTER 5 .....	161
STEADY STATE OPERATION ANALYSIS AND CONTROL OF CONVERTERS IN MICRO-GRID .....	161
5.1 Introduction.....	161
5.2 Control Strategy of the Proposed Micro-grid.....	162
5.3 DC-DC Converters in the Proposed Micro-grid .....	165
5.4 Analysis of the TAB Converter .....	167
5.4.1 Analysis of power flow in the DAB converter.....	170
5.4.2 Currents in the DAB converter .....	175
5.4.3 Steady state analysis of the TAB converter .....	177
5.4.4 Analysis of soft switching operation in the TAB converter.....	178
5.4.5 Small signal modelling of the TAB converter .....	183

---

5.4.6	Design of closed loop control for TAB converter.....	186
5.4.7	Simulation of TAB converter.....	188
5.4.8	Experimental waveforms.....	189
5.4.9	Simulation of dynamic response of TAB converter.....	190
5.4.10	Experimental test of TAB converter dynamic response.....	190
5.5	Analysis of Bi-directional Buck-boost Converter.....	194
5.5.1	Steady state operation analysis.....	196
5.5.2	Small signal model of bi-directional buck-boost converter.....	197
5.5.3	Design of controller.....	209
5.5.4	Simulation of bi-directional buck-boost converter.....	212
5.5.5	Experimental measurements.....	213
5.6	Analysis of Interleaved Current-fed Boost Converter.....	216
5.6.1	Analysis of maximum power point tracking.....	217
5.6.2	Steady state operation analysis of current-fed boost converter.....	221
5.6.3	Control strategy of the current-fed converter.....	223
5.6.4	Design of MPPT controller.....	224
5.6.5	Simulation of the PV port operation in steady state.....	227
5.6.6	Experimental test results.....	228
5.7	Analysis of Single Phase Bi-directional Inverter.....	229
5.7.1	Control strategy of the single phase bi-directional inverter.....	230
5.7.2	Simulation and experimental tests of single phase bi-directional inverter.....	233
CHAPTER 6	.....	241
SYSTEM CONTROL AND ENERGY MANAGEMENT	.....	241
6.1	Introduction.....	241
6.2	Energy Management in Residential Households.....	242
6.2.1	Smart energy homes.....	242
6.2.2	Demand side management (DSM).....	243
6.3	Residential Load Profile.....	246
6.4	Power Analysis of the Proposed Micro-grid.....	248
6.5	Structure of the Proposed Micro-grid.....	252
6.6	Energy Management Unit (EMU).....	254
6.6.1	Review of pre-processing unit operation.....	255
6.6.2	Structure of fuzzy logic controller.....	257
6.8	Mode Transistion Unit.....	270
6.9	Validity Test of the Fuzzy Based Energy Management Unit.....	271

6.9.1 First energy management scenario (a sunny day with flexible grid energy transfer) .....	277
6.9.2 Analysis of the EMU operation in second energy management scenario.....	284
6.9.3 Analysis of EMU operation in the third energy management scenario (Off-grid operation) .....	287
6.10 Summary of Chapter .....	293
References.....	294
CHAPTER 7 .....	299
CONCLUSION AND FUTURE WORK .....	299
7.1 Conclusion .....	299
7.2 Recommendations for Future Work.....	301
APPENDIX A:.....	302
PUBLICATIONS BASED ON THE THESIS WORK .....	302

**LIST OF SYMBOLS**

$A_i$	Seated area of $i$ th component
$h_{\max}$	Height of the highest component
$P_{ij}$	Transferred power from port $i$ to $j$
$P_i$	Power of port $i$
$\eta_k$	Efficiency factor
$\lambda_s$	Failure rate of a converter block
$\lambda_j$	Component failure rate per million hours
$\lambda_b$	Base failure rate of component
$\pi_i$	Failure rate modification factor
LT	Life time of component
RF	Reliability factor
$R(\text{ripple})$	Current ripple factor
$X_i(\text{norm})$	Normalized value of the parameter
$\delta_i$	Weighting factor of $i$ -th parameter
$I_Q(\text{rms})$	$\text{rms}$ current in each IGBT switch Q
$I_{fc}(\text{rated})$	Nominal current of the fuel cell port
$P_{Q-\text{loss}}$	Maximum power loss on the switch
$\Delta L$	Inductor current ripple
$D$	Duty cycle
$T_s$	Switching period
$L_C$	Critical inductance
r	Ripple ratio
$v_i$	Voltage of winding $i$

$i_i$	Current of winding $i$
$R_{W_i}$	Resistance of $i$ -th winding
$\lambda_{ij}$	Flux linkage from winding $j$ on winding $i$
$L_{ij}$	Mutual inductance between windings $i$ and $j$
$L_m$	Magnetizing inductance,
$R_m$	Core loss equivalent resistance
$R_w$	Winding resistances
$Q_{ijk}$	3D magnetic element
$R_{ijk}$	Reluctance of the 3D element
$F_{ijk}$	Equivalent MMF in 3D element
$\Phi$	Magnetic flow
$V_i$	Volume of 3D element
$L_{eq}$	Equivalent inductance
$B$	Flux density
$H$	Field intensity
$L_{11}, L_{22}, L_{33}$	Winding self-inductances
$L_{23}, L_{12}, L_{13}$	Leakage inductances
$\mu_r$	Permeability of magnetic core
$N_S$	Number of turns of winding
$Y'$	Central node linked conductance
$Y$	Source linked conductance
$\tilde{V}$	Central node voltage
$\tilde{F}$	Source voltage matrices
$W_S$	Stored energy in a 3D element
$\mu$	Magnetic permeability
$P_v$	Magnetic loss density

$f$	Frequency
$B_{sq}$	Maximum flux density
$\Omega$	Zero voltage angle
$H$	Magnetic field intensity
$P_{Cu,n}$	Copper loss due to n-th harmonic of current
$R_{ac,n}$	AC resistance due to n-th harmonic of current
$I_n$	Peak value of n-th harmonic of current
$R_{dc}$	Dc resistance of wire
$F_{r,n}$	Ratio of ac to dc resistance
$\eta_{str}$	Porosity factor of Litz wire
$\gamma_n$	Round conductor penetration ratio
$P_f$	Packing factor of Litz wire
$r_s$	Strand radius of Litz wire
$r_b$	Bundle radius of Litz wire
$R_{ins}$	Thermal resistance of insulation layer
$R_{con}$	Convection thermal resistance
$h_{rad}$	Radiative heat transfer coefficient
$P_w$	Total heat loss in the winding
$l_x$	Fraction of the length of a turn in the respective direction x
$L_n$	Length of a turn of winding
$J$	Current density
$\varepsilon$	Emissivity of the surface
$T_s$	Surface temperature
$T_a$	Ambient temperature
$\sigma$	Stefan-Boltzmann's constant
$\alpha_n$	Phase shift angle
$\beta_n$	Phase shift angle

---

$\varphi_{ij}$	Phase shift angle of port $i$ to $j$
$\psi_n$	Phase shift angle
$v_{ij}$	Dispatch factor
$L_{ij}$	Leakage inductance between winding $i$ and $j$
$V_i$	DC voltage of port $i$
$V_i$	AC voltage of winding $i$ of the magnetic link
$V_{bus}$	DC bus voltage
$\varphi_B$	Boundary phase shift angle
$g^{jk}$	Gyrator gain in small signal modelling of TAB converter
$G_{ij}$	Transfer function of input $i$ to output $j$
$Z_{Chd}$	Battery impedance during the charge
$Z_{Dsg}$	Battery impedance during the discharge
$Z_{fc}$	Fuel cell equivalent impedance
$R_{mpp}$	PV panel resistance at maximum power point
$\tilde{E}_{PV\_24h}(k)$	Predicted 24h-ahead energy generated by PV at the $k$ -th sample
$\tilde{P}_{PV\_24h}(t)$	The forecasted 24 hours-ahead power profile of PV
$t_0$	Prediction starting time
$\tilde{E}_{LD\_24h}(k)$	Predicted energy demand of the load at the $k$ -th sampling time
$T_L$	Moving Long time frame
$C_{GD}(n)$	Cost of energy received from or transferred to the grid at the $n$ -th sampling time
$C_{FC}(n)$	Fuel cell energy cost
$E_{BT\_24h}^{CHD}$	Energy received by battery in charging mode
$E_{BT\_24h}^{DCH}$	Energy supplied by the battery in discharging mode
$E_{BT\_24h}^{SEL}$	Energy sold to the grid

$E_{BT\_24h}^{BUY}$  Energy supplied by the grid

## **LIST OF ABBREVIATIONS**

A/D	Analogue to Digital Converter
AEMO	Australian Energy Market Operator
BCD	Binary-Coded Decimal
CCM	Continuous Conduction Mode
CCS	Code Composer Studio
CFBC	Current-Fed Boost Converter
CFFB	Current Fed Full Bridge
CFHB	Current-Fed Half Bridge
CHP	Combined Heat and Power
DAB	Dual Active Bridge
DG	Distribution Generation
DSM	Demand Side Management
EMU	Energy Management Unit
EVs	Electric Vehicles
FB	Full Bridge
FCBB	Forward Conducting Bidirectional Blocking
FEA	Finite Element Analysis
FEM	Finite Element Method
FBEMU	Fuzzy Based Energy Management Unit
GEVIC	Green Energy and Vehicle Innovations Centre
GUI	Graphic User Interface
HAM	Home Area Network
HB	Half Bridge
INC	Incremental Conductance
LGEC	Load and Grid Energy Control

MAB	Multi-Active Bridge
$\mu$ CHP	micro-Combined Heat and Power
MIMO	Multi-Input Multi-Output
MISO	Multi-Input Single-Output
MPC	Multi-Port Converters
MPP	Maximum Power Point
MPPT	Maximum Power Point Tracking
MSE	Modified Steinmetz Equation
MTBF	Mean Time Between Failures
MTU	Mode Transition Unit
MWT	Multi-Winding Transformer
NSE	Natural Steinmetz Extension
OSE	Original Steinmetz Equation
PCB	Printed Circuit Board
PCC	Point of Common Coupling
PCSC	Pulsating Current Source Cell
PEM	Proton Exchange Membrane
PI	Proportional-Integral
PL	Positive Large
PS	Positive Small
PLL	Phase-Locked-Loop
PV	Photo Voltaic
PVSC	Pulsating Voltage Source Cell
PWM	Pulse Width Modulation
RES	Residential
RNM	Reluctance Network Model
SIMO	Single-Input Multi-Output

SOC	State Of Charge
SOH	State Of Hydrogen
STD	State Transition Diagram
TAB	Triple Active Bridge
USB	Universal Serial Bus
WAN	Wide Area Network
WCSE	Waveform-Coefficient Steinmetz Equation
ZE	Zero
ZOH	Zero-Order-Hold
ZVS	Zero Voltage Switching

## LIST OF FIGURES

Fig.1.1 Major sectors of electrical energy consumers in the world (a) in 1973 and (b) in 2010 [1.3].	4
Fig.1.2 Major sectors of electrical energy consumers in Australia in (a)- 1973 and (b)- 2010 [1.3].	4
Fig.1.3 Number of solar PV installed annually in Australia over the last few years [1.1].	5
Fig.1.4 The size of installed solar systems in Australia over the last few years [1.1].	5
Fig.1.5 Structure of a micro-grid, (a) without the magnetic link, and (b) with the magnetic link	9
Fig.1.6 Structure of the thesis	13
Fig.2.1 Structure of a large scale residential smart grid.	23
Fig.2.2 Structure of a small scale residential micro-grid using multi-port converter	24
Fig.2.3 Application of multi-port converter in roadway lighting system.	25
Fig.2.4. Small scale micro-grid employed in a remote monitoring station [2.54]	26
Fig.2.5 Application of multi-port converter in electric vehicle drive system	27
Fig.2.6. Classification of multi-port converters based on their operation principal.	30
Fig.2.7 Basic input cells, (a) PVSC, (b) PCSC, (c) series connection of buck-PCSC, and (d) parallel connection of boost PVSC [2.63],[2.65].	31
Fig.2.8 Multi-port topologies derived from synthesizing buck type PVSC and SEPIC converter (a) buck converter in series with output and (b) buck converter in parallel with the output [2.63].	31
Fig.2.9 MPC topologies using isolated PVSC and PCSC, (a) isolated PVSCs and PCSCs, (b) and (c) series connected isolated cells and (d) partially isolated topology [2.64]	32
Fig.2.10 Isolated single primary winding MPC topologies based on (a) fly back, and (b) full-bridge [2.66]	32
Fig.2.11 PVSC topologies, (a) input cell, (b) bi-directional cell, (c) output cell (d) partially isolated multi-port buck-boost bi-directional converter and (e) non-isolated three-port buck-boost hybrid converter with one bidirectional port [2.65].	33
Fig.2.12 MISO topologies using time sharing concept, (a) buck-boost [2.67], (b) buck topologies [2.68], (c) isolated fly-back topology [2.69], and (d) MISO bidirectional topology [2.70].	34
Fig.2.13 Multi-port dc-dc converter topologies based on flux additivity in a magnetic link, (a) different dc to ac converter cells, (b) three port converter based on H-bridge cells in inputs and output [2.73], (c) topology using boost-half bridge as inputs and half bridge as output [2.74], and (d) topology using boost-half bridge and half bridge as inputs and half bridge as output [2.75].	36
Fig.2.14 MISO topologies with common DC-link and magnetic couple [2.77]	37
Fig.2.15 The general topology of MPC with a combination of dc bus and magnetic coupling [2.77]	37

Fig.2.16 MIMO converter topologies, (a) non-isolated with common inductor [2.78], (b) topology based on buck-boost topology [2.79], (c) topology using multi-winding transformer,[2.80], (d) topology using single primary winding transformer [2.67], and (e) non-isolated single-input multi-output topology [2.81].	39
Fig.3.1 The average of maximum power consumed by a residential house occupied by a four person family in NSW is 1.3 kW in summer and 1.7 kW in winter [3.5].	51
Fig.3.2 Structure of proposed multi-active bridge phase shift converter.	53
Fig.3.3 Simulation circuit of DAB converter using PSIM	57
Fig.3.4 The simulated dc-ac converter cells, (a) half bridge, (b) full bridge, (c) current-fed half bridge and (d) current-fed full bridge.	57
Fig.3.5 Simulated wave forms of transformer primary voltage $v_1$ , transformer secondary voltage $v_2$ , current transferred from source one $I_{dc1}$ , current received by source two $I_{dc2}$ , and the power loss of one single switch $P_{sw1}$ in the cases (a) full bridge converter and (b) inter-leaved current-fed full bridge converter	59
Fig.3.6 Simulated wave forms of transformer primary voltage $v_1$ , transformer secondary voltage $v_2$ , current transferred from source one $I_{dc1}$ , current received by source two $I_{dc2}$ , and the power loss of one single switch $P_{sw1}$ in the case of (a) half bridge converter and (b) current-fed half bridge converter.	60
Fig.3.7 Start-up current of the cell topologies, (a) current-fed half bridge, (b) current-fed full bridge, and (c) full bridge.	61
Fig.3.8 Comparison of total cost for FB, HB, CFFB and CFHB topologies	62
Fig.3.9 The power transfer efficiency versus phase shift angle.	64
Fig.3.10 Comparison of switching power loss of FB, HB, CFHB and CFFB topologies	64
Fig.3.11 The relation between failure rate and life time for components of a circuit	65
Fig.3.12 The percentage of current ripple for all conversion cells	68
Fig.3.13 Power transfer range of all topologies versus phase shift angle	69
Fig.3.14 Fuel cell port and H-bridge unit	71
Fig.3.15 Schematic of conventional bi-directional buck-boost converter during, (a) buck operation and (b) boost operation modes	72
Fig.3.16 The inductor maximum and minimum current versus inductance for $V_{bus2}=100$ V and $V_{bat}=18-24$ V	74
Fig.3.17 Schematic of inter-leaved current-fed boost converter	74
Fig.3.18 Voltage and current measurement signal-conditioning and fault detection circuits	77
Fig.3.19 Input to output characteristics of current sensor LTS 25 NP [3.36].	78
Fig.3.20 Schematic of driver board using VLA567-01R driver integrated circuit [3.38]	79
Fig.3.21 Flowchart of short circuit protection process [3.38]	80
Fig.3.22 The designed and developed PCBs for the proposed micro-grid, (a) H-bridge board, (b) buck-boost converter, (c) sensor and protection board, and (d) control and interface board.	81
Fig.3.23 Experimentally developed micro-grid	82

Fig.3.24 The C2000 experimenter kit [3.39].	82
Fig.4.1 Comparison of two renewable energy systems, (a)-without, and (b)-with the common magnetic link	91
Fig.4.2 Structure of proposed renewable energy system	91
Fig.4.3 Toroidal core transformer including $n$ windings.	92
Fig.4.4 The equivalent electrical model of three windings transformer	95
Fig.4.5 The flowchart of the main stages of multi-winding magnetic link design.	97
Fig.4.6 The characteristics of Ferrite 3F3, (a) temperature dependency of saturation flux density, (b) loss density, (C) initial permeability, and (d) dependency of complex permeability to the frequency [4.12], [4.25].	99
Fig.4.7 Comparison of characteristics of different soft magnetic materials, (a) relative permeability versus saturation flux density, and (b) core loss versus saturation flux density [4.26].	102
Fig.4.8 B-H curve of selected amorphous material (260SA1) for frequency of 1 kHz [4.27].	102
Fig.4.9 The design flow chart of the magnetic link using MATLAB	104
Fig.4.10 A sample of 3D reluctance element	105
Fig.4.11 (a) the self-inductance of winding one for two cases of fixed and stretchable layer selection, (b) self-inductance of winding one for various external distances.	109
Fig.4.12 The waveforms of voltage and magnetic induction for $\Omega=\pi/3$ .	113
Fig.4.13 (a) T-model and, (b) $\Delta$ -model representation of the three winding magnetic link.	117
Fig.4.14 The $\Delta$ -model equivalent circuit of three winding magnetic link.	117
Fig.4.15 Voltage and current wave forms related to current $i_1$ in winding one.	118
Fig.4.16 Fundamental phasor diagram of the three port converter	119
Fig.4.17 Ac resistance factor as a function of wire diameter for: (a) different number of winding layers, and (b) various harmonics of the current in windings of the magnetic link.	125
Fig.4.18 Calculated value of ac resistance $R_{ac}$ , copper loss and harmonic amplitudes of the three windings of the magnetic link for maximum conduction loss condition. (a) winding one, (b) winding two and (c) winding three.	126
Fig.4.19 Conduction loss of the windings one and three for zero voltage angle, $\Omega=0$ to $3\pi/4$ and phase shift angle, $\varphi_{31}=0$ to $\pi/2$ .	127
Fig.4.20 Trends of the windings current in the magnetic link versus phase shift angle.	128
Fig.4.21 Copper loss of the magnetic link for different values of $\varphi_{21}$ and $\varphi_{31}$	129
Fig.4.22 Changes in the amplitudes of harmonics of the windings current and THD versus phase shift angle, $\varphi_{31}$ (a) current $i_1$ , (b) current $i_2$ (c) current $i_3$ and (d) THD of $i_1$ , $i_2$ and $i_3$ .	129
Fig.4.23 Conduction loss of the magnetic link for zero voltage angle $\Omega=0$ to $3\pi/4$ and phase shift angle $\varphi_{31}=0$ to $\pi/2$ , (a) winding one W1, (b) winding two W2, (c) winding three W3, and (d) entire magnetic link.	130
Fig.4.24 Equivalent thermal circuit of the magnetic link	131
Fig.4.25 Experimental test platform	135

Fig.4.26 (a) development set of toroidal core, (b) developed magnetic link, and (c) dimension of magnetic core.....	135
Fig.4.27 (a) measured hysteresis loops the magnetic core and (b) measured core loss of <i>Metglas 2605SAI</i> for 10, 30 and 50 kHz excitation currents. ....	137
Fig.4.28 Comparison of calculated and experimentally measured core loss using OSE, IGSE and WcSE calculation methods, exciting voltages are applied to port three ( $\Omega=0$ to $\pi$ , $V_3=90$ V) and port one ( $D=1$ , $V_1=300$ V) and phase shift $\beta=\pi/3$ , (a) specific core loss, and (b) normalized specific core loss to OSE method.....	138
Fig.4.29 Structure of proposed residential micro-grid.....	139
Fig.4.30 Experimental wave forms of the voltages and currents in the windings for $\varphi_{21}=\varphi_{31}=\pi/2$ , (a) $\Omega=3\pi/4$ and (b) $\Omega=\pi/4$ . ....	140
Fig.4.31 Harmonic spectrum of the current in the windings for maximum loss condition (a) winding one, (b) winding two and (c) winding three .....	140
Fig.4.32 Calculated and measured values of resistances of windings one, two and three for different harmonics.....	141
Fig.4.33 Comparison of calculated and experimentally measured conduction loss for (a)-Zero voltage angle, $\Omega$ varies from 0 to $\pi/2$ and two cases of phase shift angles, $\varphi_{31}=0$ and $\varphi_{31}=\pi/2$ , (b)-Phase shift angle, $\varphi_{31}$ varies from 0 to $\pi/2$ and two cases of zero voltage angle, $\Omega= \pi/10$ and $\Omega= 3\pi/4$ .....	141
Fig.4.34 Thermal image of the magnetic link under three different load conditions, (a) power transfers from W2 and W3 to W1, (b) power transfers from W2 and W3 to W1 and (c), power transfers from W3 to W1.....	142
Fig.4.35 The measured and calculated temperature rise of the winding, $T_w$ and magnetic core, $T_c$ for winding one of the magnetic link.....	143
Fig.4.36 Experimental tests of multi-winding transformer, (a) secondary open circuit test, (b) primary open circuit test, (c) differentially coupled test, and (d) cumulatively coupled test. ....	145
Fig.4.37 Experimental measured parameters of the winding one, (a) inductive elements, (b) resistive elements and, (c) inductive elements and resulting error. ....	147
Fig.4.38 The equivalent circuit of MWT under (a) inductive load, (b) short circuit and (c) capacitive load test conditions.....	148
Fig.4.39 Frequency response of winding one to three of MWT for cases, (a) inductive load, (b) short circuit and (c) capacitive load conditions (solid line is simulation and dashed line is experimental results).....	150
Fig.4.40 Simulation results of magnetic link modeling using PSIM, (a) short circuit condition, (b) capacitive load and (c) inductive load.....	151
Fig.4.41 Experimental test results for (a) short circuit condition, (b) capacitive load and (c) inductive load conditions, CH1: secondary voltage, CH2: primary voltage, CH3: primary current. ....	152
Fig.5.1 The control levels of the proposed micro-grid.....	162
Fig.5.2 The schematic of control circuits of proposed micro-grid.....	163
Fig.5.3 Generation of single fault-signal using comparators and diodes .....	165

Fig.5.4 Dc-Dc converters including TAB converter, bidirectional buck-boost converter and interleaved current-fed boost converter, (a) electrical schematic, and (b) experimentally developed system.....	166
Fig.5.5 Structure of multi-active bridge phase shift converter, (a) actual circuit and (b) simplified model.....	168
Fig.5.6 Simplified model of multi-active bridge phase shift converter, (a) T-equivalent model, (b) applying super-position rule considering two sources only, (c) simplified T-model, and (d) simplified equivalent $\Delta$ -model.....	169
Fig.5.7 Simplified model of multi-active bridge phase shift converter .....	170
Fig.5.8 DAB converter schematic, (a) circuit topology and (b) Equivalent circuit .....	171
Fig.5.9 (a) The power transferred versus phase shift using two analytical methods and (b) relative error between two analytical methods versus phase shift ratio for different voltage ratios ( $d$ ).....	172
Fig.5.10 (a) power flow in DAB converter in the second operation mode using two approaches and (b) the resultant error in the case of using fundamental component approach for power flow calculation .....	174
Fig.5.11 (a) power flow range versus phase shift ratio for two methods in operation mode three and (b) resultant error in the case of using fundamental component approach for different values of duty cycles $D_1$ and $D_2$ .....	175
Fig.5.12 Changes of converter currents versus $d$ , $D$ and $\varphi$ for, (a) Mode one, (b) Mode two, (c) Mode three and (d) Changes in phase shift angle versus voltage conversion ratio for constant power flow .....	176
Fig.5.13 Structure of TAB converter as a part of proposed micro-grid.....	177
Fig.5.14 The $\Delta$ -model equivalent circuit of the TAB converter [5.16].....	178
Fig.5.15 Steady state operating waveforms of TAB converter with and without duty cycle control considering soft-switching and hard switching conditions .....	182
Fig.5.16 The small signal model of TAB converter [5.7].....	185
Fig.5.18 The Bode diagram of closed loop control of TAB converter .....	188
Fig.5.19 The simulated waveforms of the TAB converter for two different cases (a) $D=1$ , $\varphi_{31} = \pi/3$ and $\varphi_{21} = \pi/5$ , and (b) $D=0.8$ , $\varphi_{31} = \pi/5$ and $\varphi_{21} = \pi/3$ .....	191
Fig.5.20 The experimentally measured waveforms of the TAB converter for two different cases .....	193
Fig.5.21 Simulation results of the TAB converter operation under load variation, (a) fuel cell is supplying a constant power and battery follows the load variations, and (b) fuel cell follows the load variation and battery operates as a compensator.....	193
Fig.5.22 Experimental test of the TAB converter dynamic response .....	194
Fig.5.23 Topology of the bidirectional buck-boost converter.....	195
Fig.5.24 Operation areas of bi-directional buck-boost converter .....	196
Fig.5.25 The wave-forms of voltage and current in bi-directional converter [5.22].....	197
Fig.5.26 (a) Equivalent model of lead acid battery and (b) equivalent high frequency model .	198

Fig.5.27 Frequency response of a lead-acid battery.....	199
Fig.5.28 Output characteristics of a PEM fuel cell, (a) output voltage versus current and (b) output power versus current .....	200
Fig.5.29 Equivalent model of PEM fuel cell for (a) steady state and (b) high frequency analysis .....	201
Fig.5.30 Data sheet of a commercial fuel cell stack [5.28].....	202
Fig.5.31 Frequency response of fuel cell for small signal analysis.....	202
Fig.5.32 Bidirectional buck-boost converter.....	203
Fig.5.33 The equivalent model of bidirectional buck-boost converter .....	204
Fig.5.34 Bode diagram of open-loop transfer functions of (a) inductor current and (b) capacitor voltage .....	208
Fig.5.35 The double loop control diagram of bidirectional buck-boost converter .....	209
Fig.5.36 Bode plots of closed loop discretized transfer functions of (a) inner current loop (b) outer voltage loop .....	212
Fig.5.37 Simulated waveforms of the buck-boost bidirectional converter operating in (a)-boost or charging mode, (b)-boundary between buck and boost and (c)-buck modes.....	214
Fig.5.38 Experimental waveforms of the buck-boost bidirectional converter operating in (a) boost or charging mode, (b) boundary between buck and boost and (c) buck modes.....	215
Fig.5.39 The step response of buck-boost converter from boost to buck mode for a limited time .....	216
Fig.5.40 The output voltage-current characteristics of a PV panel for various (a)- solar irradiation and (b)- temperature levels [5.34].....	218
Fig.5.41 The output voltage-current characteristics of a PV panel for various (a)-solar irradiation and (b)-temperature levels [5.34]. .....	218
Fig.5.42 The slope of incremental conductance on P-V characteristics of solar panel.....	219
Fig.5.43 Flowchart of variable step MPPT process .....	221
Fig.5.44 The hardware implementation of MPPT in the proposed micro-grid.....	222
Fig.5.45 The equivalent circuit of current fed dc-dc converter cascaded by H-bridge dc-ac converter .....	222
Fig.5.46 The equivalent circuit of PV panel for dual loop voltage control analysis.....	223
Fig.5.47 The equivalent circuit of buck-boost converter for PV dual loop control analysis ....	224
Fig.5.48 The dual loop control diagram of the PV voltage and inductor current .....	225
Fig.5.49 The Bode plots of closed loop control, (a) PV voltage control loop, and (b) inductor current loop.....	227
Fig.5.50 Simulated waveforms of current-fed boost converter.....	228
Fig.5.51 Experimentally measured waveforms of current-fed boost converter.....	229
Fig.5.52 Schematic of inverter as a part of proposed micro-grid.....	230
Fig.5.53 The control scheme of bidirectional inverter.....	231

Fig.5.54 Simulation and experimental waveforms of the bidirectional inverter.....	233
Fig.6.1 The effects of DSM on the shape of load profile.....	244
Fig.6.2 Architecture of DSM in residential micro-grid [6.16].....	245
Fig.6.3 Electrical schematic of the proposed residential micro-grid.....	249
Fig.6.4 Modelling of the proposed micro-grid for power flow and energy management analysis. .....	249
(a) detailed model, and (b) simplified model.....	249
Fig.6.5 Schematic of a multi-input multi-output energy hub.....	252
Fig.6.6 Structure of the proposed micro-grid including system level and device level controllers .....	253
Fig.6.7 (a) Comparison of measured and estimated load power demand for 24h-ahead, and (b) relative error between measured and estimated values.....	257
Fig.6.8. Structure of the proposed fuzzy logic control.....	258
Fig.6.9 24-h ahead forecasted power of (a) PV generation, (b) load demand and (c) the difference between PV and load demand .....	260
Fig.6.10 Membership function of long-term fuzzy controller, (a) $\Delta SOC(n)$ (b), $\Delta SOH(n)$ (c), $SOH(n)$ (d), $\tilde{E}_{BT\_T_L}$ (e), $\tilde{E}_{FC\_T_L}$ and (f) $SOC(n)$ .....	264
Fig.6.11. Distribution of battery capacity including real-time and desired levels of SOC for.. (a) $\Delta SOC > 0$ and (b) $\Delta SOC < 0$ .....	266
Fig.6.12 Membership function of short-term fuzzy controller (a) $\Delta SOC(n)$ (b), $\Delta SOH(n)$ (c), $SOH(n)$ (d), $\tilde{E}_{BT\_T_L}$ (e), $\tilde{E}_{FC\_T_L}$ and (f) $SOH(n)$ .....	268
Fig.6.13 Flowchart of mode transition unit (MTU) operation.....	272
Fig.6.14 State transition diagram of mode transition unit in (a) grid connected and (b) islanded operation modes.....	273
Fig.6.15 The experimental test set up of the proposed grid for energy management tests .....	273
Fig.6.16 Schematic of the EMU hardware signals and connections.....	275
Fig.6.17 Profiles of the PV power generation, load power demand, energy cost and SOC/SOH levels for the first energy management scenario .....	280
Fig.6.18 Profiles of the difference between PV power generation and load power demand, grid power, fuel cell power and the battery power for the first scenario .....	281
Fig.6.19 Energy analysis of the proposed micro-grid for the first energy management scenario .....	283
Fig.6.20 Energy cost analysis of the proposed micro-grid for the first energy management scenario.....	283
Fig.6.21 Profiles of the PV power generation, load power demand, energy cost and SOC/SOH levels for the second energy management scenario.....	285
Fig.6.22 Profiles of the difference between PV power generation and load power demand, grid power, fuel cell power and the battery power for the second scenario.....	286

Fig.6.23 Profiles of the PV power generation, load power demand and SOC/SOH levels for the third energy management scenario ..... 288

Fig.6.24 Profiles of the difference between PV power generation and load power demand, grid power, fuel cell power and the battery power for the third scenario ..... 289

Fig.6.25 Energy distribution analysis of the proposed micro-grid for the third energy management scenario ..... 291

Fig.6.26 Energy cost analysis of the proposed micro-grid for the third energy management scenario ..... 291

Fig.6.27 Comparison of energy costs of proposed residential load for three cases, grid-supplied only, grid-connected with renewable sources and off-grid with renewable sources . 292

## LIST OF TABLES

TABLE 2.1 Comparison of Characteristics of Different Topologies .....	41
TABLE 3.1 Estimated Sizes of FB, HB, CFHB and CFFB Topologies.....	63
TABLE 3.2 Value of Failure Rate and Life Time For Three Main Components of Topologies	66
TABLE 3.3 Comparison of Reliability Factor for Four Topologies.....	67
TABLE 3.4 Complexity Factors of The Topologies.....	67
TABLE 3.5 Normalized Parameters of Three Topologies.....	70
TABLE 3.6 Weighting Factors For Evaluation .....	70
TABLE 3.7 The Final Results of Evaluation of The Topologies .....	70
TABLE 3.8 Specifications of The Fuel Cell Port .....	71
TABLE 3.9 Electrical Characteristics of The PV Port .....	75
TABLE 4.1 Main Properties of the MnZn and NiZn Ferrites [4.12].....	98
TABLE 4.2 Main Properties of Permalloy [4.12].....	100
TABLE 4.3 Main Properties of the Amorphous Materials [4.12] .....	101
TABLE 4.4 Main Properties of the Nano-Crystalline Material [4.24] .....	101
TABLE 4.5 Physical Dimension and Characteristics of Magnetic Tapes [27].....	103
TABLE 4.6 Electrical Parameters of the Magnetic Link.....	111
TABLE 4.7 Parameters of the Design and Experimental Tests.....	111
TABLE 4.8 Magnetic and Loss Analysis Parameters of the Magnetic Link.....	112
TABLE 4.9 Coefficients of Steinmetz Equation.....	114
TABLE 4.10 Equations of Model Parameters for Different Test Procedures .....	146
TABLE 5.1 Circuit Parameters of the TAB Converter During Simulation .....	189
TABLE 5.2 Characteristics of Various Types of Batteries for Renewable Energy Applications .....	199
TABLE 5.3 Parameters of the Bidirectional Buck-Boost Converter .....	208
TABLE 5.4 Comparison of Different Continuous to Discrete Time Transforms.....	208
TABLE 5.5 The PV Port Parameters for Small Signal Analysis .....	226
TABLE 6.1 Rules of Long-term Fuzzy Controller for Estimation (a)-Fuel Cell SOH and (b)- Battery SOC.....	264
TABLE 6.2 Rules of Short-term Fuzzy Controller.....	267
TABLE 6.3 Grid-connected Operation Modes .....	269
TABLE 6.4 Off-grid Operation Modes.....	270

## ABSTRACT

Over the last century, the global average air temperature at the earth surface has been raised for about  $0.74^{\circ}\text{C}$ , which has generated serious concerns all around the world about the global warming and consequent environmental problems. The electricity generation as one of the major contributors to the environmental pollutions should undergo a fundamental change towards the clean energy sources. In the residential sector, one of the major electricity users, the demand for renewable energy sources is increasing significantly.

This thesis presents an effort to develop a residential micro-grid, including multiple renewable energy sources, energy storage, and local loads with multiport power electronic converters capable of bidirectional power flow and intelligent algorithms for power converter and micro-grid controls. A topology of multi-port converter using a high frequency magnetic link is proposed for residential micro-grid applications. Using the magnetic link in the proposed multi-port converter can reduce the complexity and size of the entire micro-grid effectively.

The micro-grid is designed to supply a 4.5 kW residential load from combined energy sources of a PV array, a fuel cell stack, and a battery bank. It is controlled by a Texas instrument DSP (C2000/TMS320F28335) at the device level and a PC system as the energy management unit (EMU) at the system level. A single phase bidirectional inverter is designed to link the proposed micro-grid to the main grid. The inverter is controlled by a second DSP at the device level and by the EMU at the system level.

The proposed micro-grid is able to operate in different operation modes based on the power flow directions and energy management scenarios. The EMU defines the appropriate operation mode of the system based on the short-term and long-term predictions of PV generation, and load demand by changing the power flow directions between the sources, energy storage unit, and loads.

Due to the importance of the magnetic link in the micro-grid performance and complexity of design of high-frequency multi-winding magnetic components, a major part of the research is focused on the design, development and experimental test of the magnetic link. The geometry of the magnetic link including the dimensions of magnetic core and windings are designed through numerical analysis by using the reluctance

network model (RNM). The core loss and copper loss analysis of the magnetic link are carried out accurately considering the non-sinusoidal effect of voltage and current waveforms. The designed component is then evaluated for the thermal limits by using the thermal electric model. The last part of this stage is the prototyping, experimental tests, and measurement of the component parameters and performance.

The second part of the research is mainly focused on the design and analysis of the converters as the device level analysis of proposed micro-grid. It contains the analysis of the three dc-dc converters in the steady and transient states, discussion on the modulation technique of each converter, power flow control techniques, small signal modelling, and closed loop control design. The converter steady state waveforms are simulated and the soft-switching operation range is discussed. The converter waveforms are experimentally measured and compared with the numerical simulation results.

The third part of the research is dedicated to the system level control of the micro-grid and energy management analysis. In this section, the main operation modes of the system are defined for both grid-connected and isolated operation conditions according to the power flow directions in the system. An energy management strategy is proposed considering both the short- and long-term energy forecasts and the real-time operational data of the system. The proposed strategy is implemented in an energy management unit using MATLAB/GUI and is used to control the system operation modes considering different control objectives and scenarios.

## CHAPTER 1

# INTRODUCTION

### 1.1 Background

Over the past century, the average global air temperature at the earth surface has been raised for about 0.74 °C, which has generated serious concerns about the global warming and consequent environmental problems. Some studies suggested that this is mainly caused by the excessive use of various fossil fuels, such as oil and coal. Fossil fuels have been traditionally used as the main energy source for industries, transportation, and human daily life (almost all aspects of human civilisation). The excessive gas emission generated by the use fossil fuels causes the greenhouse effects which lead to the earth atmosphere temperature rise and this has increased the emission of greenhouse gases. On the other hand, because of the limited fossil fuel reserves, it is more and more difficult to meet the increasing industrial, commercial and residential energy demands. Therefore, the demand for environment friendly sustainable energy sources, such as wind, solar, hydro, tidal, biomass, and geothermal energy, has increased significantly over the past decades.

The electricity generation as one of the major contributors to environmental pollution should undergo a fundamental change towards clean energy sources. In the residential sector, one of the major electricity users, renewable energy systems, such as solar, wind, and micro-combined heat and power ( $\mu$ CHP), are widely used and growing rapidly. In Australia, the share of renewable energies in electricity in 2014 was 13.47 %, which is enough for supplying approximately 4.5 million average households [1.1]. The annual installed capacity of solar photovoltaic (PV) in the residential and commercial sectors has increased from 20 MW in 2008 to 1000 MW in 2015 [1.1]. This can effectively reduce the electricity bill of the households and contributes significantly towards the reduction of greenhouse gas emission. This research is an effort to design and development a residential based renewable energy system including multiple energy

sources and energy storage due to the importance of the residential sector in future smart grids.

## **1.2 Distributed Generation and Micro-grids**

Although various distributed generation (DG) systems based on renewable energy, such as solar and wind, sources have been used for many years, it is still a serious challenge to integrate them into the conventional distribution networks since these renewable energy sources are intermittent, resulting in poor power quality. This problem can be effectively solved by adopting the concept of smart micro-grids, which integrate closely the renewable power generation, energy storage, and consumption through intelligent communication and control strategies. When there is rich renewable source and the load demand is low, the excessive electricity generated can be stored in the energy storage unit, and released when there is a need. On the other hand, when there is a need, the micro-grid can also exchange electricity with the main grid. To implement this, power electronic converters capable of bidirectional power flows and four quadrant operation are required. Special control strategies, embedded in the power converter controllers and micro-grid control centre, should be developed to control the power quality and maintain steady voltage and frequency in the islanded and grid connected modes. This new development of micro-grids has initiated a wide range of new technologies in electricity generation, distribution and consumption.

In general, in a micro-grid various types of consumers such as residential, commercial and industrial buildings can be connected to the common ac or dc bus. The micro-grid should be designed to operate in both grid connected and isolated modes and be able to avoid any instability problems when changing from one mode to the other. It is also expected that the designed micro-grid will provide sufficient generation capacity to supply at least a portion of the load in the isolated mode. The micro-grid should be linked to the utility system via an electrical point known as point of common coupling (PCC). In the grid connected mode, the renewable sources should contribute to the majority of the load demand within the micro-grid and the difference should be provided by the utility. The bidirectional grids are the only feasible solution for integrating the distributed energy generators into the utility system. The conventional utility grids, which have been used to transfer electrical energy from the central power stations to the residential or industrial loads over the past decades, need to be changed

by the new concept of smart grid technologies. The development of such bidirectional power distribution networks needs advanced control methods and communication systems from which emerges the concept of smart grids. Therefore, the electric power industries are required to cope with the new concepts in all areas of generation, transmission and distribution to incorporate the renewable sources into the future power market efficiently.

### **1.3 Residential Consumers of Renewable Energies**

Residential consumers as an important portion of electricity consumers are changing from passive energy users to active small scale energy producers. The future smart-grid networks should be able to provide an opportunity for residential, commercial and industrial customers to supply electricity generated from the surrounding renewable energy sources to the power grids. Fig.1.1 compares the details of the major consumers of electrical energy in 1973 and 2010 according to the IEA/OECD report in 2015 [1.2]. According to the report on the quality of electrical energy consumption in the world, residential sectors have consumed almost 32% of produced electricity in the world in 2010. As shown in the figure, much of the growth in electricity consumption since 1973 has taken place in the residential and commercial, and public services sectors and their combined shares increased from 46.5 % in 1973 to 62 % in 2010. The electricity market share in the residential sector has increased substantially with an average annual growth rate of 9.4% between 1960 to 1973 and a slower rate of 2.7% from 1973 to 2010 [1.2]. The demand for electrical energy by residential consumers in the OECD countries has also been increasing over the past decades. Figure 1.2 illustrates the share of main electricity consumers in Australia in 1973 and 2010 according to the IEA/OECD report in 2015 [1.2]. As shown in the figure, the share of the residential section in electrical energy consumption has been about 30% in 2010. The above information indicates that any improvement in residential renewable energy technologies has significant effects on energy sustainability and reduction of environmental pollution. Therefore, the research on design, analysis and control of residential renewable energy systems and residential smart micro-grids has attracted so much interest over the past decade.

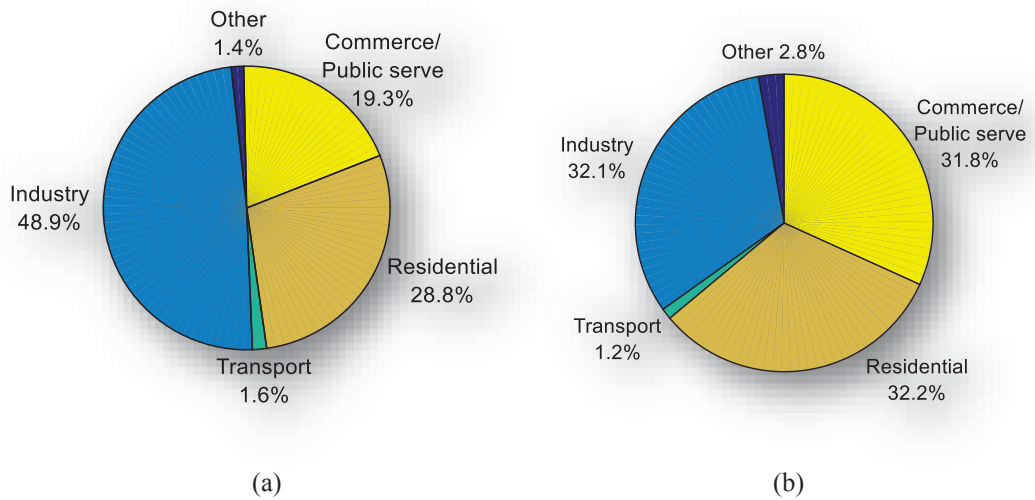


**Fig.1.1 Major sectors of electrical energy consumers in the world (a) in 1973 and (b) in 2010 [1.3].**

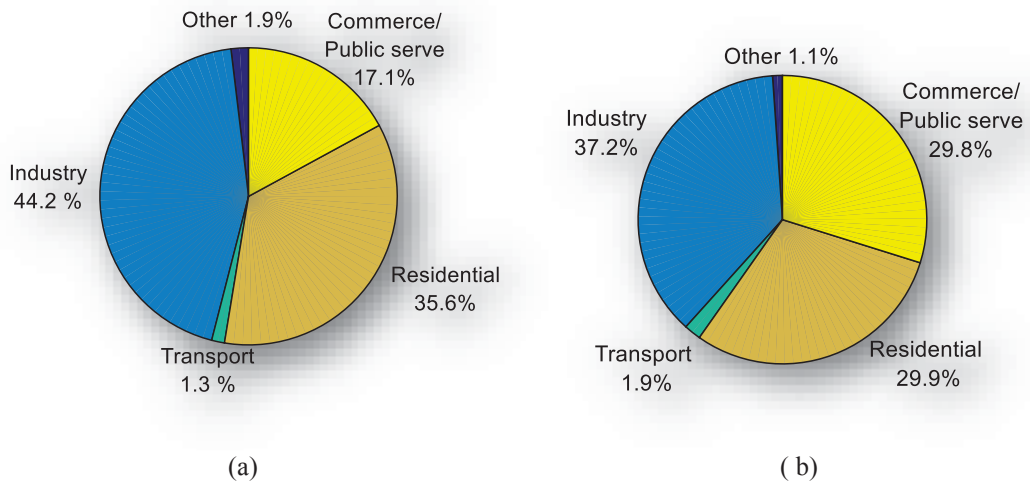


**Fig.1.2 Major sectors of electrical energy consumers in Australia in (a)- 1973 and (b)- 2010 [1.3].**

In Australia, solar PV systems continue to be very popular in the residential sector and about 1.5 million Australian homes are now using solar panels. The proportion of solar energy users is about 18 % and in some urban areas reaches over 50 % [1.3]. The annual number of solar PV systems installed in the residential sector has increased significantly over the last few years as presented in Fig.1.3 [1.1]. The nominal power of installed systems increased from 1 kW in 2007 to about 5 kW in 2014 as illustrated in Fig.1.4 and it is expected to increase to 5.3 kW by the end of 2015 [1.1].

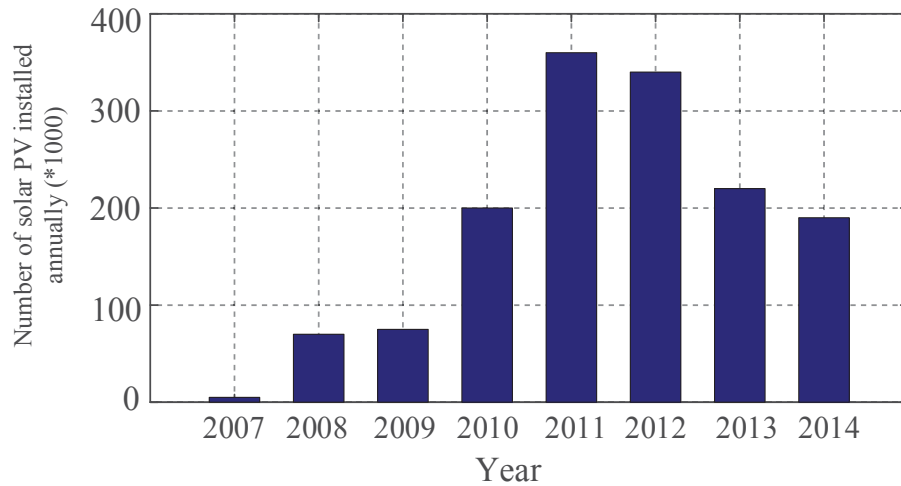


Fig.1.3 Number of solar PV installed annually in Australia over the last few years [1.1].

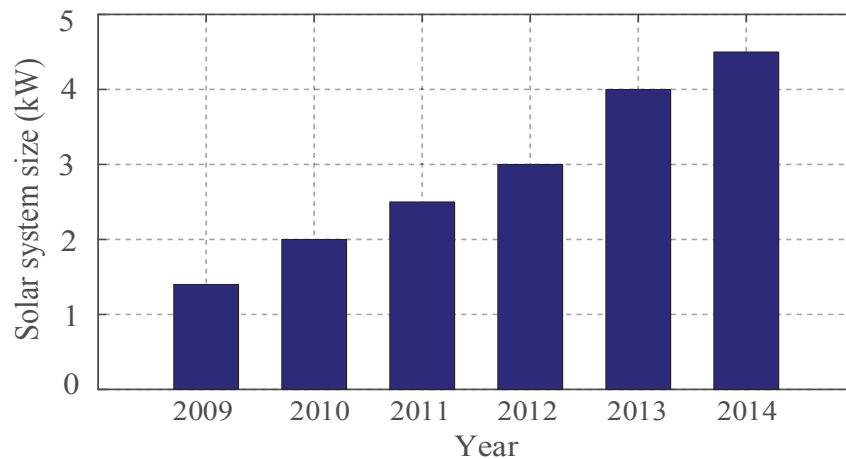


Fig.1.4 The size of installed solar systems in Australia over the last few years [1.1].

#### 1.4 Hybrid Renewable Energy Systems

A hybrid renewable energy system combines the energies of several renewable sources along with energy storage devices to overcome the intermittent nature of renewable energy sources. A widely used hybrid system includes wind and solar energy sources providing a more reliable source due to their complementary nature. It may need an energy storage device such as battery to save the energy for the times that none of the sources are available. The storage device can be used to smooth the transition from one source to another and balance the energy transfer in the case of using sources with low dynamic response such as fuel cells. Another advantage of using energy storage in the hybrid system is that the size of primary sources only needs to be defined according to the average power consumed by the load, not necessarily to the peak

power. This prevents oversizing of the main renewable sources and is economically beneficial. Over the last few years, the demand for combined multiple energy sources has grown significantly, especially for off-grid applications, while the residential consumers in urban areas prefer to use only one renewable energy source (commonly PV) along with the grid and are rarely interested in using hybrid systems. On the other hand, the cost of grid energy in some cases is less than renewables considering the running cost and capital cost of a hybrid system. Another advantage of hybridization is achieving more reliable energy supplies by utilizing complementary patterns of energy generation from different sources. According to this, the hybrid energy systems are more interested by the off grid consumers due to their tendency to generate more reliable energy and utilizing all energy generation options. Many householders in urban areas have found their reliable energy source with a grid connected line and a hybrid system is not of interest to them. The off-grid consumers can be categorized into the residential and non-residential consumers. The residential consumers mostly are farmers living far from the grid network and the non-residential consumers of hybrid systems are mainly small size commercial and industrial systems designed for research, communicating or monitoring services situated in remote areas. Other applications are in road lighting and traffic lights as will be discussed in chapter two. To combine the sources and storage devices with different voltage levels to a common electrical bus, each source or storage device should be connected to a voltage conversion block to adapt its voltage to the bus level. This increases the size, cost and efficiency of the hybrid system. The alternative solution is using a multi-port converter to combine all conversion blocks in a unique system. Many multi-port converter topologies and their control methods for integration of renewable energies have been reported recently. A review on some of these topologies is provided in chapter two of the thesis.

### **1.5 Residential Micro-grids, Challenges and Solutions**

Consumption of electrical energy in the residential sector has been growing during the last decades and it is expected to continue with a higher rate in the future due to the increasing demand for using electrical appliances. Electrification of household systems such as for heating and cooking has been increasing significantly during the past years. Energy management of households has attracted lots of research interest due to their major contribution in overall world energy consumption. The demand side energy management methods have been proposed by researchers to optimize the energy

consumption in the residential sector. The concept of smart homes and smart cities is expanding to a wide range of areas such as smart environment, smart economy, smart mobility and smart living. The smart energy homes are employing energy management techniques to save the household energy bills with less influence on convenience and healthiness of the occupants. Research on design and development of household energy management systems as an important infrastructure of future smart grids has been attractive for researchers. The household renewable energy system can be considered as a micro-grid which includes all elements of generation, distribution and consumption. It can be connected to the utility grid to feed energy back to the grid or receive it on demand. Currently residential distribution networks are facing major challenges with the large penetration of renewable energy resources such as photovoltaic systems, electric vehicles and  $\mu$ CHP units into the grid due to their less predictable generation and consumption. Residential smart grid provides a bidirectional power flow path and communication network to utilize the renewable sources, manage their extracted energy efficiently and decrease the waste of energy in households. Research on residential renewable energy systems mainly is focused on the energy management methods and there is not much research on infrastructures that are required for implementation of those methods. Therefore, there is a need for research on different topologies of residential micro-grids, control strategies, energy management, and energy balance techniques. This research is an effort to bridge this gap and study analysis and technical issues of design and implementation of a residential micro-grid.

## **1.6 Research Framework**

The common structure of a residential micro-grid includes several voltage conversion blocks to adapt the output voltage of each individual source, storage or load to the common intermediate electrical ac or dc bus. To control the entire micro-grid system a communication bus is required to link the micro-grid control centre to an individual controller of each converter. Fig.1.5 (a) shows an example of a residential micro-grid including multiple voltage conversion blocks and a common electrical dc bus. The main drawback of such a micro-grid structure is its control complexity even if each converter has a simple structure and control method. A multi-port converter as a single power processing unit is an alternative for the multi-conversion based micro-grid. This can effectively reduce the total size and cost of the micro-grid system and individual controllers can be compacted into a centralized control unit. Due to this many

attempts have been made to explore new topologies of multi-port converter topologies for hybrid renewable energy systems and micro-grid applications [1.4]-[1.12]. A review on the most common topologies of multi-port converters is provided in chapter two of the thesis, their main features such as practical range of power, maximum number of ports, bidirectional power flow capability, isolation and safety features, efficiency and flexibility are reviewed briefly. Although many multi-port converter topologies have been introduced over the last few years for integration of renewable energies, few of them are applicable to the residential applications due to their characteristics and features.

A topology of a multi-port converter using a high frequency magnetic link is proposed in this research for residential micro-grid applications. Using a magnetic link in the proposed multi-port converter reduces the complexity and size of the entire micro-grid effectively. Fig.1.5 (a) presents the structure of a multi-conversion based residential micro-grid. Comparing this structure with the one presented in Fig.1.5(b) shows that employing the magnetic link can reduce the number of voltage conversion blocks, consequently resulting in increased system efficiency and reduced system size and cost.

The red dashed lines in both Figs.1.5 (a) and (b) show that the power flow path from the PV array to the battery can be reduced effectively by using the magnetic link. According to their application in integration of renewable energy sources, high frequency magnetic links have attracted significant attentions. They can effectively reduce the number of conversion stages in micro-grids and improve the conversion efficiency with the help of modern soft magnetic materials and low power loss solid state switching devices [1.13]-[1.16].

The magnetic link is quite similar to the conventional multi-winding high frequency transformers except that it provides bidirectional paths for magnetic fluxes and power flows between different ports. It also provides galvanic isolation and possibility of bidirectional power flows between the converter ports [1.17]-[1.20]. Research on magnetic links mainly focused on their design, characterization, numerical modelling and optimization.

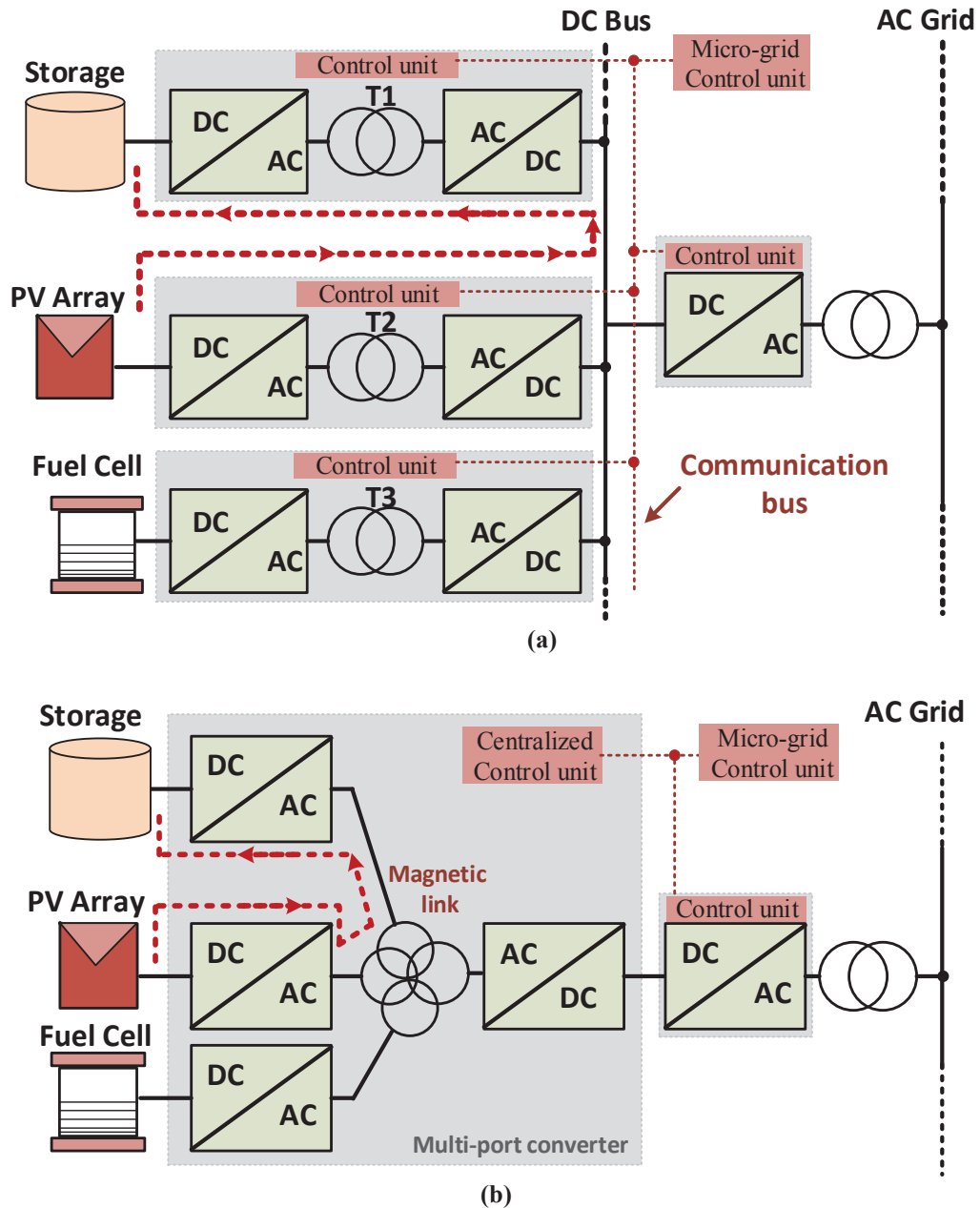


Fig.1.5 Structure of a micro-grid, (a) without the magnetic link, and (b) with the magnetic link

This research is mainly focused on design, analysis and implementation of a magnetically coupled micro-grid for residential users. It provides a detailed study on all stages of design, simulation, development and experimental tests. The proposed system is designed to operate in different modes and energy management scenarios. An energy management unit (EMU) is designed to effectively control the power flow direction between the sources, storage device and the load. The research contents can be classified mainly into three areas according to the research materials and study levels.

The first area of the research is focused on the design of micro-grid dc-dc converters including triple active bridge (TAB) converter, bi-directional buck-boost converter and

current-fed boost converter. The first step of design is to define the specifications and parameters of each converter and to select appropriate components such as switching device, high speed drives and magnetic components. The majority of work in this stage focused on the design and development of the magnetic link due to the employing of a multi-winding high frequency transformer as a common magnetic bus. It includes study on various magnetic materials for selection of appropriate core material, numerical design of magnetic core, prototyping and experimental test.

The second part of the research is mainly focused on the steady state operation analysis of the micro-grid, dynamic and transient analysis, modulation techniques, energy balance, and power flow control techniques. The waveforms of the converters are studied in the steady state operation and the soft-switching operation range are discussed. The small signal model of each converter is derived analytically and the closed loop control loops are designed.

The third part of the research is focused on system level study and energy management analysis. In this section, the micro-grid system is modelled as an energy hub considering all input energy sources, storage devices and loads. The main operation modes of the system are defined for both grid-connected and isolated operation conditions according to the power flow directions in the system. An energy management strategy is proposed considering short-term and long-term energy forecasts and real-time system information. The proposed strategy is realized through an energy management unit and is used to control the systems operation modes considering three different control objectives and scenarios.

### **1.7 Objectives and Contributions of the Research**

The future energy systems should be more smart, reliable, efficient and flexible to respond to the rapid growth of consumer demands. Residential consumers as one of the important parts of future energy users need proper infrastructures to adapt with the smart grid concepts. Due to the importance of household users, in future electrical users research on residential renewable energy systems and residential micro-grids have been attractive for research over the past decade. Energy efficiency as an important factor of smart grids has been the main subject of research in household renewable energy systems and micro-grids. A majority of research works have focused on effective energy management methods and demand side control of residential loads. On the other

hand, there are lots of research on design and development of different topologies of multi-port dc-dc converters as a part of hybrid renewable energy systems. Nevertheless, not many researches can be found that provides a detailed study on both fields and links them together. This research combines multiple converters in a single conversion unit using a magnetic link to form a compact medium power micro-grid. The proposed micro-grid can be used in a residential load as an experimental platform for applying various energy management methods. This research is an effort to perform the design and analysis of the system in both device and system levels and to link them together to make a complete view on the main issues of a practical residential micro-grid. The micro-grid topology by using magnetic link is able to provide higher level of efficiency, reliability and flexibility as important factors of future smart grids. Research on design of the proposed micro-grid is carried out in component level, system level and energy management methods. At the component level, this research is mainly focused on the design and development of the high frequency magnetic link as the main component of the designed micro-grid and TAB converter. Due to the complexity of design of multi-winding high frequency magnetic components the main part of the research at this stage is focused on the design, development and experimental test of the magnetic link. The contributions of the research in this part can be listed as:

- (1) Numerical design of the toroidal core for high frequency magnetic link using reluctance network model (RNM),
- (2) Accurate core loss analysis of the magnetic link according to the waveforms of voltages and currents in the windings,
- (3) Accurate copper loss analysis of the magnetic link taking into account the amplitude, duty ratio and phase shifts of the wave forms of the windings,
- (4) Accurate analysis of high frequency skin and proximity effects in the loss evaluation, and
- (5) Thermal analysis of the designed component and experimental measurement of the component temperature considering radiation and convection effects.

The second part of the research is focused on the design and development of micro-grid topology. The proposed micro-grid includes a TAB dc-dc converter, a current-fed boost converter and a bidirectional buck-boost converter. The main contributions of the research in this section include:

- (1) Steady state analysis and simulation of converters for different operation modes,
- (2) Small signal modelling, frequency response analysis and closed loop control design of the converters and micro-grid system, and
- (3) Analysis of modulation technique, soft-switching operation range, switching losses and conversion efficiency.

The third part of the research is focused on the energy management strategy including different operation modes and energy management scenarios. The main contribution of the research in this stage can be listed as:

- (1) Design of an effective energy management strategy considering long term and short term predictions, and
- (2) Analysis of stored, transferred and consumed energy of the micro-grid for three different operation scenarios.

### **1.8 Outline of the Thesis**

This research is focused on the optimal design of a magnetically coupled micro-grid for residential applications. The main goal of the research is to design a smart, high efficiency, flexible and reliable micro-grid for residential consumers of future smart grids. The thesis contains six chapters as illustrated in Fig.1.6.

Chapters one, two and three provide an introduction on the work and review on the residential micro-grids and multi-port converter topologies respectively. Chapters four, five and six are the main chapters of the thesis which provide a detailed analysis on design of magnetic link, dc-dc converters and energy management method. Each chapter starts with theoretical analysis, simulation and experimental results and can be read independently or in combination with the previous chapters. The conclusions and future work recommendations are presented in chapter seven. More details on the contents of each chapter is provided in the following sections.

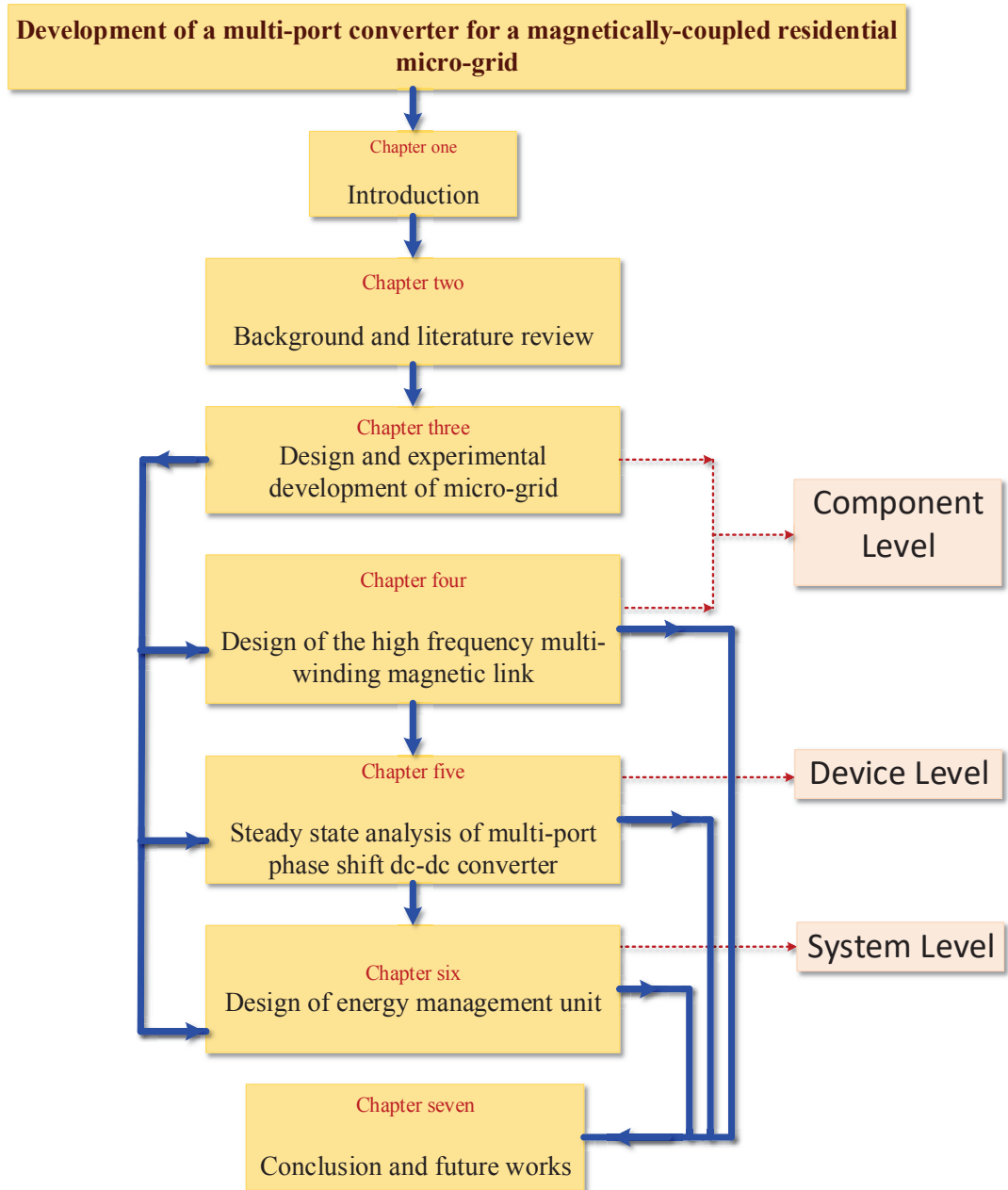


**Fig.1.6 Structure of the thesis**

**Chapter two:** This chapter includes an introduction on the residential consumers and residential smart grids and recent research trends in the field. A brief review on the renewable energy sources with application in households is provided. The concept of smart micro-grids, residential micro-grids and household renewable energy systems are discussed. A complete review on the different topologies of multi-port converters and their advantages and drawbacks is provided. The topology of the proposed micro-grid and the multi-port dc-dc converter is introduced at the end of the chapter.

**Chapter three:** This chapter provides a detailed study on the design and experimental development of dc-dc converters and magnetic based micro-grid. It includes the details of converter design including the selection of appropriate components and experimental design of sensor and protection circuits, switching drive circuits and printed circuit boards (PCBs).

**Chapter four:** This chapter is focused on the design of a high frequency multi-winding transformer as a common magnetic link for integration of renewable energy sources and power transfer between the ports in the form of magnetic flux. This includes design of magnetic link based on the required specifications of the proposed micro-grid. It starts with selection of magnetic materials based on their characteristics, geometrical design of windings and the magnetic core, accurate prediction of core and copper losses and thermal analysis of the designed component.

**Chapter five:** The main objective of this part is the design and analysis of a high efficiency, reliable and flexible micro-grid. This chapter is mainly focused on the analysis and design of control of the TAB converter, bi-directional buck-boost converter and current-fed boost converter. The dc-dc TAB converter as the main component of the proposed micro-grid is designed to efficiently couple renewable energy sources to the energy storage device, load and grid. A detailed study on topology of proposed converter, switching techniques, steady state and transient operation modes, small signal model and control methods is provided in this section. The soft-switching operation conditions and various operation modes are analysed and the converter losses and overall efficiency are evaluated.

**Chapter six:** This chapter studies the energy management strategy of the micro-grid and selection of appropriate operation modes according to the desired objectives. The designed strategy operates based on the real time information of the energy generation and consumption, short term and long term predictions. Therefore, it is able to efficiently manage the total energy of the system to avoid the waste of energy through the proposed micro-grid.

**Chapter seven:** This chapter includes a conclusion on the overall research and the main contributions of thesis. It also includes some recommendations for future works and ideas for continuing the research. A list of publications related to the research is illustrated at the end of the chapter.

## References

- [1.1] Clean-Energy-Australia-Report-2014, [www.cleanenergycouncil.org.au/reports](http://www.cleanenergycouncil.org.au/reports).
- [1.2] Key World Energy Statistics 2015, <http://www.iea.org/publications>.
- [1.3] Medium term renewable energy market-Report 2015, <http://www.iea.org/bookshop>
- [1.4] M. H. Taghvaei, M. A. M. Radzi, S. M. Moosavain, H. Hizam, and M. Hamiruce Marhaban, "A current and future study on non-isolated DC-DC converters for photovoltaic applications," *Renewable and Sustainable Energy Reviews*, vol. 17, pp. 216–227, 2013.
- [1.5] Y. C. Liu and Y. M. Chen, "A systematic approach to synthesizing multiple-input dc–dc converter," *IEEE Trans. Power Electronics*, vol. 24, no. 1, pp. 116–127, Jan. 2007.
- [1.6] Y. Li, X. Ruan, D. Yang, F. Liu, and C. K. Tse, "Synthesis of multipleinput dc/dc converters," *IEEE Trans. Power Electronics*, vol. 25, no. 9, pp. 2372–2385, September 2010.
- [1.7] H. Tao, A. Kotsopoulos, J. L. Duarte, and M. A. M. Hendrix, "Family of multiport bidirectional DC–DC converters," *IEE proc. Electric Power Applications*, Vol.153 ,Issue: 3, pp.451-458, 2006
- [1.8] A. Kwasinski, "Identification of feasible topologies for multiple-input DC-DC converters," *IEEE Trans. Power Electronics*, vol.24, no.3, pp. 856–861, March 2009.
- [1.9] H. Wu, J. Zhang, Y. Xing, "A Family of Multi-Port Buck-Boost Converters Based on DC-Link-Inductors (DLIs)," *IEEE Trans. Power Electronics*. vol. 30, no. 2, pp. 735-746, Feb. 2015.
- [1.10] Y. M. Chen and Y. C. Liu, "Development of multi-port converters for hybrid wind-photovoltaic power system," in proc. *10th IEEE Int. Conference on Electrical and Electronic Technology Region*, Vol.2, pp.804-808, 2001.
- [1.11] Y. M. Chen, Y.C.Liu, S.C. Hung, and C. S Cheng "Multi-input inverter for grid-connected hybrid PV/wind power system," *IEEE Trans. Power Electronics*, vol.22, Issue.3, pp.1070-1077, 2007.
- [1.12] A. Nami, F. Zare, A. Ghosh, F. Blaabjerg, "Multi-output DC-DC converters based on diode-clamped converters configuration: topology and control strategy," *IET Power Electronics*, vol.3, issue 2, pp .197-208, 2010.
- [1.13] Y. M. Chen, Y. C. Liu, and T. F. Wu, "Multi-input dc–dc converter based on the multi-winding transformer for renewable energy applications," *IEEE Trans. Industry Applications*, vol. 38, no. 4, pp. 1096–1104, July/August 2002
- [1.14] M. R. Islam, G. Lei, Y. Guo and J. Zhu, "Optimal Design of High-Frequency Magnetic Links for Power Converters Used in Grid-Connected Renewable Energy Systems," *IEEE Trans. Magnetics*, vol. 50, no. 11, pp. 1-4, Nov. 2014
- [1.15] H. Tao, A. Kotsopoulos, J. L. Duarte and M. A. M. Hendrix, "Transformer-Coupled Multiport ZVS Bidirectional DC–DC Converter With Wide Input Range," *IEEE Trans. Power Electronics*, vol. 23, no. 2, pp. 771-781, March 2008.
- [1.16] H. Tao, A. Kotsopoulos, J. L. Duarte, and M. A. M. Hendrix, "Family of multiport bidirectional DC-DC converters," *IEE Proc. Electric Power Applications*, vol. 153, no. 3, pp. 451-458, May 2006.
- [1.17] Y. Chen, X. Liu, Y. Cui, J. Zou and S. Yang, "A Multi-Winding Transformer Cell-to-Cell Active Equalization Method for Lithium-Ion Batteries With Reduced Number of Driving Circuits," *IEEE Trans. Power Electronics*., vol. 31, no. 7, pp. 4916-4929, July 2016.

- [1.18] H. Tao, J. L. Duarte, M. A. M. Hendrix, “Three-port triple-half bridge bidirectional converter with zero voltage switching,” *IEEE Trans. Power Electronics*, vol. 23, no.2, pp 782–792, March 2008.
- [1.19] J. Zhang, H. Wu, X. Qin and Y.Xing, “PWM Plus Secondary-Side Phase-Shift Controlled Soft-Switching Full-Bridge Three-Port Converter for Renewable Power Systems,” *IEEE Trans. Power Electronics*, vol. 62, no. 11, pp. 7061-7072, Nov. 2015.
- [1.20] C. Zhao, S.D.Round, and J.W.Kolar, “An isolated three-port bidirectional DC–DC converter with decoupled power flow management,” *IEEE Trans. Power Electronics*, vol. 23, no. 5, pp. 2443–2453, Sep. 2008.

## CHAPTER 2

# LITERATURE REVIEW

### 2.1 Introduction

Power electronic converters are required to integrate multiple renewable energy sources along with the battery to supply the loads. Compact, reliable and high efficiency converters are necessary for future renewable energy systems to adapt with the new smart grid concepts. Multi-port converter based renewable energy systems have been an attractive research topic over the last decade due to their superior characteristics compared with the conventional multi-conversion, dc-bus-linked topologies. Many topologies of multi-port converter are proposed in the literatures, covering a wide range of performances and applications. Each topology has its own advantages and disadvantages, depending on the particular application. The main evaluation factors are the isolation between the different ports, range of processing power, power flow flexibility, maximum number of inputs and outputs that can be handled practically, safety, reliability, and system size, etc. To design an appropriate topology of multi-port converter for the proposed residential micro-grid, a review on specifications of both micro-grid and multi-port converter topologies is required. This chapter starts with a review on renewable energy sources with residential applications. The main topologies of multi-port dc-dc converters proposed in the literatures are reviewed briefly and their characteristics are highlighted. Finally, the topology of micro-grid proposed in this research is designed taking into account the requirements of the residential load and specifications of the converter topologies.

### 2.2 Renewable Energy Resources for Residential Consumers

Renewable energies are gaining popularity due to their low CO<sub>2</sub> emission levels, availability and high operation efficiencies [2.1]. They have been widely used to supply residential loads and household appliances [2.2]. A lot of research effort is being put into the development and improvement of residential renewable energy systems and

micro-grids. Following energy resources are some of the widely developed clean generation systems, with special attention paid to residential applications.

### **2.2.1 Solar energy**

Solar energy as a truly renewable source can be directly converted into electricity by using photovoltaic (PV) systems. The output power of PV system ranges from a few watts to megawatt power stations [2.3]. They have found a wide range of applications from portable low power device such as roadside emergency telephones, remote area research and communication sites and remote sensing to satellites, space crafts and off-grid house power although they have high initial installation cost which is expected to reduce considerably in the coming years. PV systems are very promising in the renewable energy generation market, particularly for powering residential buildings although their produced electricity depends on the amount of sun light energy [2.4], [2-5]. Generally large energy storage like batteries are used to store the captured electrical energy for the time that the sun is not shining and PV energy is not available. The battery can be used as a backup energy source to level the power transients in the system [2-6].

### **2.2.2 Wind energy**

Wind energy as a clean, renewable, and widely distributed source, has a very high potential amount around the world. The small scale wind turbines are used to supply electricity in rural areas where the power grid is not accessible [2-7]. On the other hand the large scale wind farms are used to generate electricity for utility grids. The wind turbines are used to convert the kinetic wind energy into electricity ranging from a few hundred watts for residential applications to a few megawatts for wind farms. The small wind turbines have been used for household applications in combination with batteries over the last decades [2-8]. However, the availability of wind energy heavily depends on the weather conditions and output power control is not easy due to large inertia of the wind turbine blades [2-9]. Therefore, it requires a battery as back up energy source particularly in stand-alone operation mode.

### **2.2.3 Micro combined heat and power**

Cogeneration is already well established in industry, but for small scale private use. The large scale combined heat and power (CHP) systems produce the required heat by utilizing the wasted heat of electrical generation system to obtain higher energy conversion efficiency. Micro-CHP systems work in the opposite way. In this small scale systems heat is the main generation and electricity is a by-product. The operation principle of micro-CHP systems is similar to boilers and the electricity generation capacity is added to the basic heating system. To produce the required heat either gas or LPG can be used as the main input source. Micro-CHP systems can be replaced with existing hot water boilers at single homes and apartments [2.10], [2.11]. Due to the fluctuating of power demand they need to be used along with the heat storage [2.12]. The micro-CHPs have higher efficiency and lower CO<sub>2</sub> emission compared with the conventional coal-burning power plants [2.13].

### **2.2.4 Fuel cell generator**

Fuel cells are devices that combine hydrogen fuel and oxygen to generate electricity via an electrochemical process producing some water and heat as reaction outcomes. They have the potential to revolutionize power generation as an environmentally friendly energy conversion technology. They can be used in a wide range of applications as small as cell phones to large scale power generators [2.14], [2.15]. The proton exchange membrane (PEM) fuel cells are able to provide a high density output power to small and medium power residential loads [2.16]-[2-18]. The main drawback of fuel cells is their slow dynamic response due to the slow fuel supply regulation and hydration control. This causes a long time-constant against the fast load transients. Therefore, they need a fast and high energy density storage device such as batteries or super capacitors to be connected in parallel for dynamic compensation [2.16]. The application of fuel cells for electricity and heat generation for home applications is generating interest although its use has been limited because of cost considerations. Increasing research on their structure, materials and process opened up the possibility of cost reduction in the future [2.19]. In summary, considering their power availability and system dynamics, their generated power is not ideal for immediate use and needs to be conditioned using a storage mechanism. In this case the system performance and functionality will improve in both stand-alone and grid-connected modes.

### **2.2.5 Bioenergy**

Bioenergy as a general term covers a wide range of electricity generation techniques from a variety of organic materials including fossil fuels, plant residues, wood and agricultural crops and residues, human and animal fats or wastes [2.20]. The conversion process will produce a solid, liquid or gaseous fuel resulting from thermal, physical or chemical reactions. Bioenergy can be used in various applications from heating and transport fuel to power generation and is one of the feasible electricity generation technologies for residential application especially in rural areas [2.21],[2.22]. A large number of commercial technologies are available for conversion processes and utilization of the end-products. Therefore different types of bioenergy technologies exhibit considerable variation in physical and chemical characteristics which influence their use as fuels.

### **2.2.6 Geothermal**

The heat emitted from within the earth, usually in the form of steam or hot water can be used as a geothermal energy source. The geothermal heat results from formation of the earth by gravitational collapse or the radioactive decay of various isotopes [2.23]. The resultant heat then can be used for heating water for domestic use in residential or industrial applications (50 - 150°C) or for generating electricity (150°C+) depending on the temperature [2.24]-[2.26]. The geothermal energy is an inexhaustible energy source as the earth's crust is continuously emitting heat towards its surface while the temperature of the earth centre has reduced only about 2% over the past 4 billion years.

### **2.2.7 Hydro**

Extracting electrical energy from water falling from a higher to a lower altitude is known as hydro-power generation [2.27]. In this method the falling water is made to pass through a water turbine as energy conversion device to convert the energy of water into mechanical energy. The resultant energy then is converted into electrical energy by using a generator. In some cases the hydropower is extracted from river currents by placing a water turbine directly in the direction of water flow [2.28]. The generated power ranges from tens of Watts to hundreds of Megawatts. The small scale hydro-power systems as a mature power generation technology have been used by residential consumers in rural areas for decades [2.29].

### **2.2.8 Energy storage**

In household consumers it is possible to use small scale energy storage systems which can be used to improve grid performance especially in peak demand hours. Energy storage is necessary for standalone hybrid renewable energy systems to have continuous and reliable power supply with desired power quality [2.30]-[2.33]. Batteries are the most common energy storage devices for small scale RES applications. To improve the grid performance, using small storage devices is more efficient than costly and huge energy storage systems in large scale. Using batteries along with other available energy sources improves the reliability and performance of electrical energy for households [2.34].

### **2.3 Hybrid Renewable Energy System**

Due to the intermittent nature of most renewable energy resources such as wind, solar and ocean wave, combinations of two or more of these relevant power generation technologies along with an energy storage system can improve the RES performance. For example, wind and solar energy resources in a given area are somewhat complementary on a daily basis and their integration improves the system performance and energy reliability significantly. Combination of two or more renewable energy sources and/or storage devices forms a hybrid energy system. In general, a hybrid system converts all types of energies into one form (typically electricity) and/or stores the energy into some forms (chemical, compressed air, thermal, mechanical flywheel, etc.), and the aggregated output is used to supply a variety of loads. It is obvious that hybridization of energies can improve the reliability and stability of the entire energy system and may result in higher conversion efficiency and/or improved performance [2.35]-[2.37]. For instance, a fuel cell micro-turbine hybrid energy system with combined cycle can better utilize the energy available in the fuel cell to achieve a significantly higher efficiency than either source alone can possibly achieve. The response of a residential RES including a slow dynamic renewable source such as wind or fuel cell can be enhanced by adding a storage device with faster dynamic response such as super capacitor, battery bank or flywheel to meet different types of loads from slow to fast transients [2.38], [2.39]. The most usual combination of renewable resources is to use solar panels along with wind turbines due to their complementary generation patterns [2.40]. Another benefit of using hybrid energies is the reduction in

size of the energy storage device because of the supply diversity. In the case of using a hybrid wind/solar energy system the reduction in battery capacity is more considerable.

## **2.4 Residential Micro-grids**

The residential micro-grids and their structure are widely studied in the literature [2.41]-[2.44]. The micro-grid structure mainly depends on the range of power, available renewable sources, type of common electrical bus (ac or dc voltage) and type of end users. According to the range of power the residential micro-grid can be classified into small scale (0.5-10 kW), medium scale (10-100 kW) and large scale (>100 kW). In general, the nominal power of a medium scale residential micro-grid designed for a single house is less than 10 kW while in the large scale micro-grids this can increase to a few hundred kilowatts and the micro-grid changes to mini-grid. Fig.2.1 presents the structure of a large scale residential mini-grid connected to the utility system. As can be seen each residential user utilizes two or more renewable energy sources to form a small or medium scale micro-grid and these are linked to a common electrical bus to configure a mini-grid. The communication network links the local controllers of each residential or commercial micro-grid to the mini-grid control centre. Each local controller receives control and information data such as energy transfer conditions, weather forecasts and projection of renewable energy generation in the next short and long time intervals.

This research mainly focuses on the small scale micro-grid and local controller operation. The structure of the small scale residential micro-grid and the role of the multi-port converter as the main component of the micro-grid which facilitate faster control and energy management are studied in the following sections.

## **2.5 Multi-port Dc-dc Converters in Small Scale Residential Micro-grids**

The multiport converters are emerging as an alternative for multi-conversion systems in small generation systems, where there is often more than one input source [2.45]-[2-47]. In multi-port converters separate power processing units are combined into a single unit. In general, a multiport converter is used to integrate multiple power sources and storage devices. It steps up or down the voltage of sources or changes their voltage types to link them to a common energy bus.

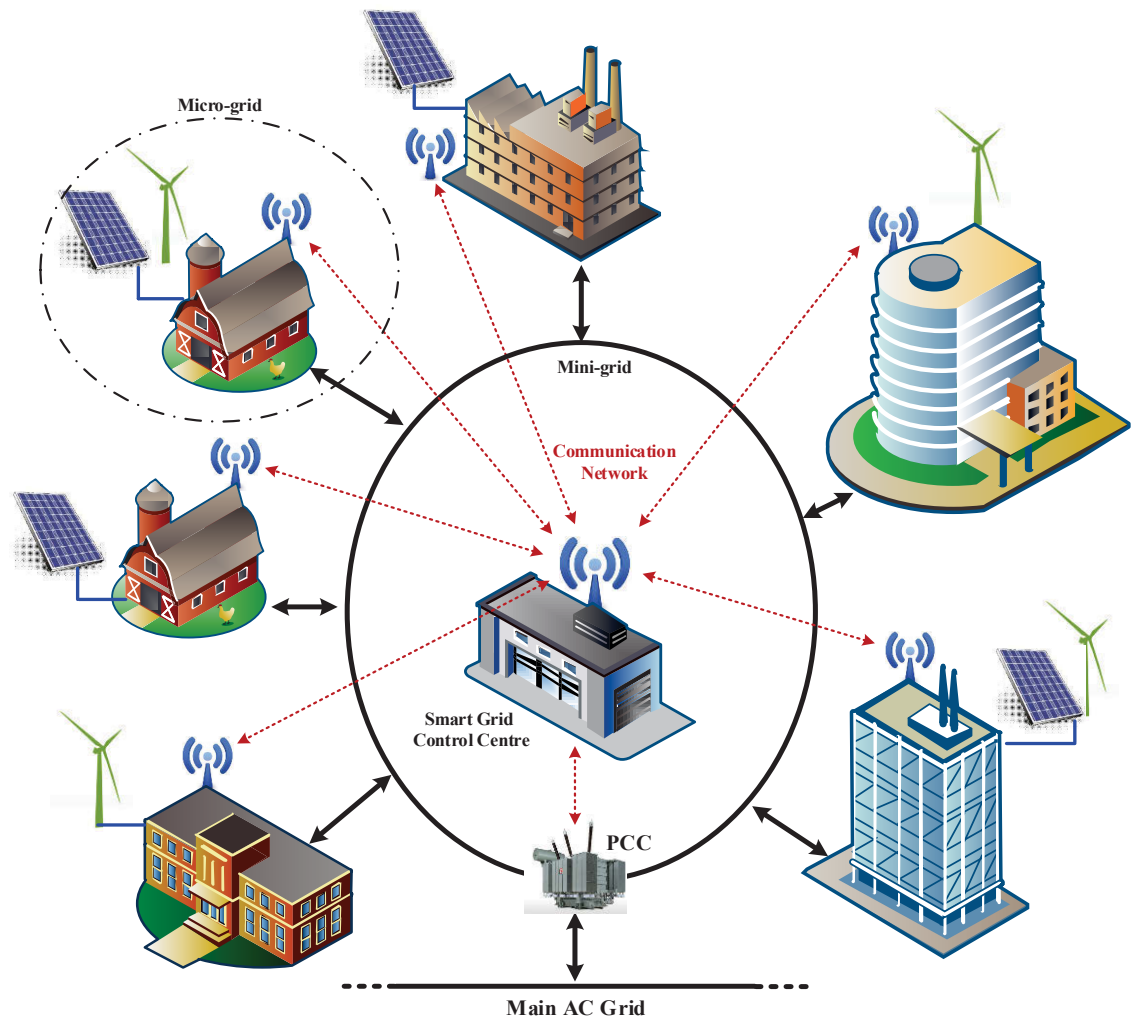
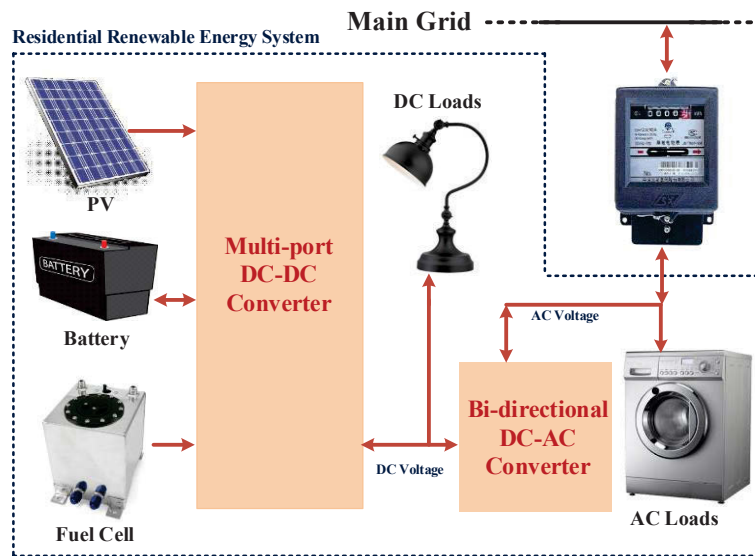


Fig.2.1 Structure of a large scale residential smart grid

It also manages the power flow direction between sources, load and storage. Fig.2.2 illustrates an example of a small scale residential micro-grid for domestic application. The multi-port converter is used to manage the power flow between the fuel cell generator, PV panel, battery and inverter or load. The system is able to operate in both grid-connected and islanded modes.

A bi-directional dc-ac converter operates as an inverter (dc to ac) mode to transfer the surplus energy from micro-grid to the main grid and in rectifier mode (ac to dc) from the main grid to the micro grid. Battery is used to compensate the slow dynamic of fuel cell against load transients and stores the energy. The fuel cell can be used as a back-up energy source and operates only in case of system black out or off-grid operation. It can be replaced by a wind turbine generator especially in off-grid applications.



**Fig.2.2 Structure of a small scale residential micro-grid using multi-port converter**

In case of off-grid applications the micro-grid structure is almost similar to Fig.2.2 and the only difference is that a back-up energy source such as fuel cell or diesel generator is employed in off grid systems to improve the reliability of the system due to the absence of grid energy and there is no need for a bidirectional meter. A dump load may be required to avoid overcharge of the battery although it can be replaced by a house water heating system to prevent wasting electrical energy.

## 2.6 Multi-port Converter in Islanded Micro-grids

Multi-port converters have found a large number of applications in both off-grid and grid connected renewable energy systems due to their advantages. This section provides a review of some applications of multi-port converters in off-grid renewable energy systems.

### 2.6.1 Roadway lighting and traffic lights

Recently a considerable attention has been made on roadway renewable energy systems [2.48]-[2.50]. The wind turbines and solar panels along with the batteries are linked through the multi-port converter to form a small scale micro-grid for supplying the roadway lighting or traffic lights. The structure of the proposed system is shown in Fig.2.3.

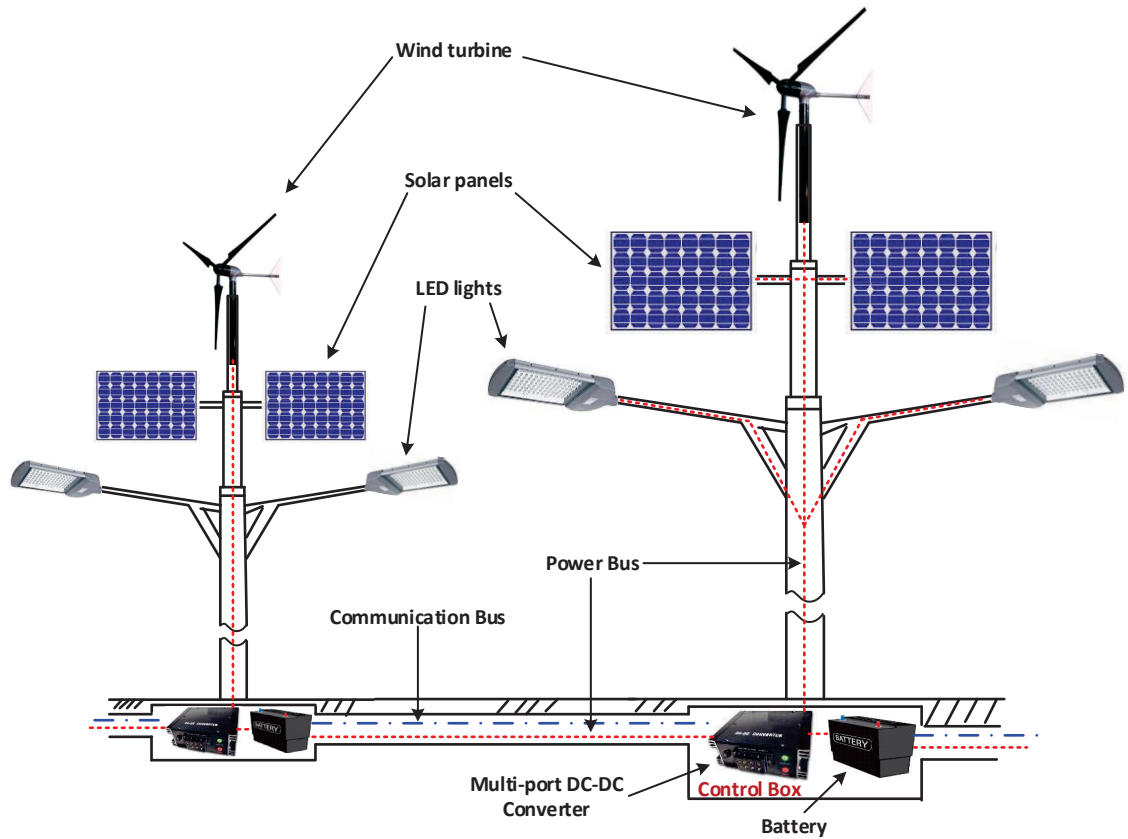


**Fig.2.3 Application of multi-port converter in roadway lighting system**

As can be seen the multi-port converter is used similar to the residential systems and the main difference is in the range of rated power for wind turbine and solar panel. Each tower has an installed PV panel and small power wind turbine, the highly energy efficient LED lights, control unit, multi-port converter, and battery as energy storage. The lighting towers can be linked together via a communication network and energy transfer bus. In this case the energy storage can be used in the form of a centralized battery bank which minimizes the maintenance cost although it decreases the system efficiency. The energy transfer bus can be linked to the utility grid in the case of grid connected operation mode.

### **2.6.2 Remote monitoring, research and communication sites**

As another application, the multi-port converter can be used in RES to supply small to medium power range monitoring, data recorders, and communication sites in remote areas [2.51]-[2.53]. Due to their limited access to the main grid these stations need a reliable and stable supply of energy.



**Fig.2.4. Small scale micro-grid employed in a remote monitoring station [2.54]**

Therefore it is preferable to use a combination of solar and wind energies along with long life, low maintenance batteries to improve reliability and efficiency of their supply system. An example of such a small scale micro-grid is presented in Fig.2.4 [2.54].

### **2.6.3 Fuel cell and solar supplied electric vehicles**

Due to the environmental problems of the fossil fuel based automobiles and rapid depletion of the earth's petroleum resources different types of electric vehicles (EVs) have been designed and developed. The drive system in most EVs includes a battery with high energy storage capability, a super-capacitor with high power capability and a renewable energy source like a fuel cell and power electronic drive of the electrical motor [2.55]-[2.58].

A dc-dc converter should be used for each component to transfer the energy to/from the common dc bus. Due to the automotive constraints, the power converter structure has to be reliable, lightweight, small volume, with high efficiency, low electromagnetic interference and low current/voltage ripple.

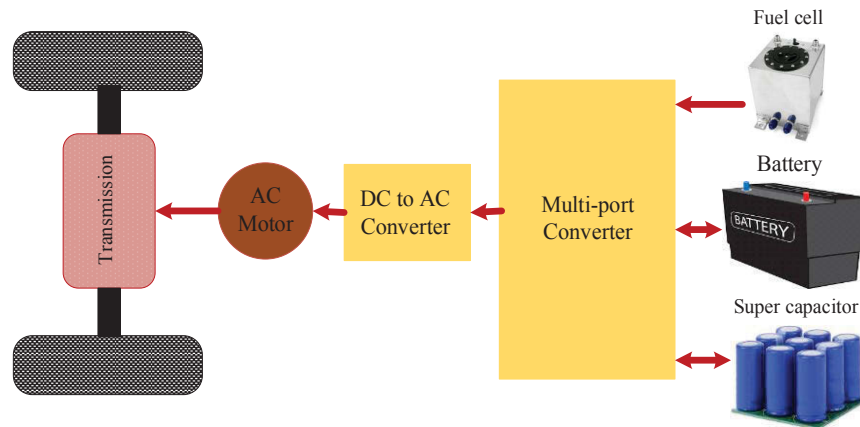


**Fig.2.5 Application of multi-port converter in electric vehicle drive system**

Using a multi-port converter can effectively combine the multiple conversion blocks into a single unit as illustrated in Fig.2.5. Therefore, the volume, cost and mass of the drive system is decreased significantly and more flexibility and faster control is achieved [2.58].

## 2.7 Review of the Multi-port Dc-dc Converter Topologies

Since the middle of the 20th century, a great amount of research has been done and a large number of technical papers and books have been published in the field of power electronics. The continuous invention of new power electronic components and improvement of their quality have enabled power electronic systems to handle higher and higher power in lower volume. As the switching devices gradually become smaller in size, they are able to operate more efficiently in comparison with the bulky gas filled tubes. During recent years, many different converter topologies were proposed and studied due to the wide spread use of power electronic switching devices. The rapid increase in world consumption of electrical energy and the ever growing environmental problems caused by the intensive use of fossil fuels increased attention to renewable energy resources. A lot of research has been conducted on conversion of renewable energies into electricity to make electrical energy more reliable and environmental friendly. Recently, a combination of various renewable energy sources and energy storage units, such as wind turbines, fuel cells, photovoltaic (PV) panels, batteries and ultra-capacitors have attracted extensive research interests. Future power grids will require integrating various energy sources of different voltage and power levels. The diversity of renewable energy resources and their intermittent nature are the main

reasons for integration of these resources into a micro-grid as a unique and more reliable supply. Dc-dc converters are an effective means for changing characteristics of the sources to meet the load requirements. Multi-port dc-dc converters are designed to integrate several energy resources to manage the extracted energy and supply the loads. Most of the proposed multi-port topologies in the literature are focused on multi-input dc-dc converters integrating renewable energy resources [2.59]-[2.62]. Various literatures have reviewed and/or analyzed multi-port converter topologies, but they are mostly limited to the circuits with the same switching scheme or similar characteristics [2.63]-[2.66]. It would be much more desirable if a clear classification and comparison of all types of topologies were provided. This section provides a classification, technical review and comparison of the main characteristics of various topologies of multi-port dc-dc converters and their feasibility of application in a residential micro-grid. The review includes the basics of operation, electrical structure, practical features, applications, advantages and disadvantages of each topology or group of topologies from the beginning to the state of the art.

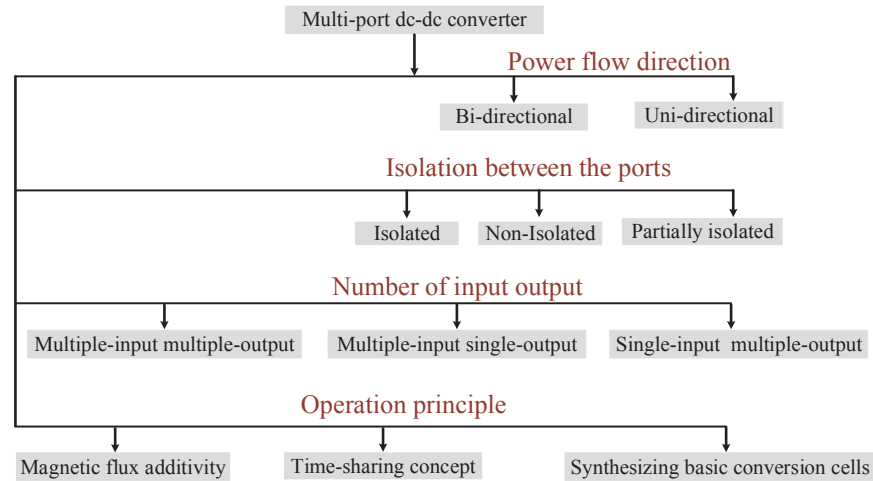
### **2.7.1 Classification of multi-port converters**

The major indicators that are used in this research to classify the topologies are principle of operation, isolation between the ports, power flow flexibility, quantity of input and output ports, range of power and feasibility of application in residential micro-grids. A majority of recently published papers on classifications of multi-port topologies have focused only on a particular group of topologies with the same operation principle and/or have provided a limited review on the other topologies. In [2.63], a systematic approach to synthesize multiple-input dc-dc converters is presented although the proposed topologies are limited to non-isolated ones based on six basic converter topologies. Several basic rules for generating multiple-input converter topologies using basic converter cells are proposed in [2.64]. A group of isolated multi-port bidirectional dc-dc converter topologies based on a combination of dc-link (dc-bus) and magnetic coupling are reviewed in [2.65]. In [2.66], the analysis in [2.65] is extended to isolated multi-input converters using a single primary winding transformer. The proposed topologies are more suitable for input sources with the same characteristics, e.g. a set of solar panels, and are suitable only for low power applications.

This research reviews different topologies of multi-port dc-dc converters and classifies them according to their principals of operation, power flow direction, quantity of connected ports and feasibility of application in residential PV systems. The systematic approaches for synthesizing multi-port topologies, proposed in the literatures are reviewed and some resultant topologies are presented.

In general, there are three basic methods in integrating various energy sources to supply the loads. The simplest methods include series, parallel or hybrid connection of several basic converter cells [2.67], [2.68]. Each cell usually includes an input source, one or more switching devices and passive components to form a constant current or voltage source. The series or parallel connected cells are usually linked to a common voltage bus including a shared energy storage component. The shared component can be an inductor, capacitor or a transformer. The next group of topologies operates on the basis of a time sharing concept to integrate renewable energy resources [2.69], [2.70]. The basis of operation in this group is quite similar to the previous one. The difference is that the cells are simply composed of input source in series with a controllable switch and only one cell will be able to transfer energy to the common bus at any time instance. Therefore, each input source is connected to the common bus and shared storage component for a fraction of the switching time period. The third group of topologies integrates the input energy sources in the form of electromagnetic flux using a high frequency multi-winding transformer [2.71] - [2.77]. The dc voltages of all input sources are chopped into high frequency ac square wave voltages of the same frequency and are applied to the windings of the high frequency transformer. The transformer steps up or down the input voltages, and provides a magnetic isolation among the ports. The power flow among the converter ports can be controlled by the phase shifts between the square-wave voltages applied to the transformer windings.

Another important feature of a multi-port topology is its options for power flow direction. According to their power flow direction, topologies can be classified into unidirectional and bi-directional. Further, each of the above groups according to the number of input and output ports can be categorized as multi-input single-output (MISO), single-input multi-output (SIMO), and multi-input multi-output (MIMO) dc-dc converters. The last factor is isolation between the converter ports.



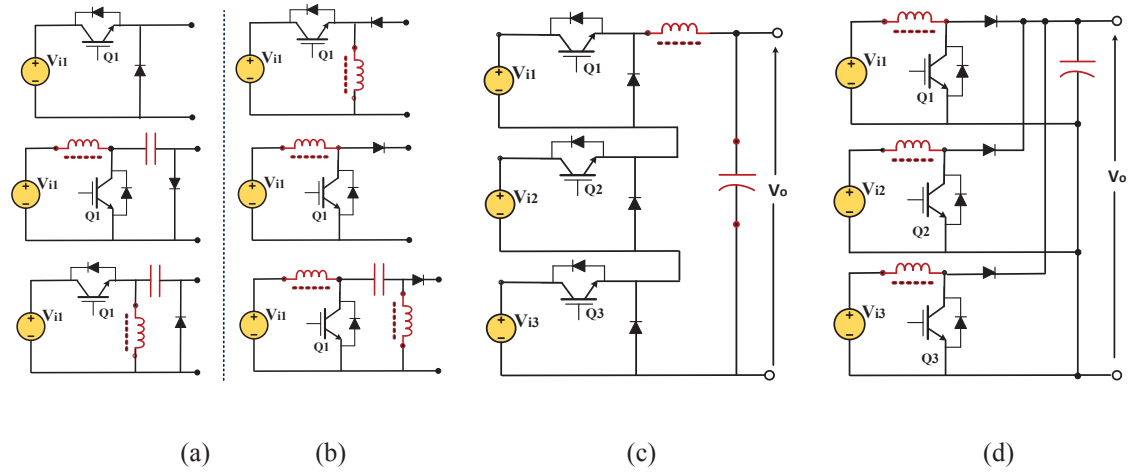
**Fig.2.6. Classification of multi-port converters based on their operation principal**

Fig.2.6 shows the classification of converters on the basis of operation principal, power flow direction, number of input and output ports and isolation between the ports.

### 2.7.2 Topologies based on synthesizing voltage and current source cells

To date, a lot of switching topologies have been proposed and studied in the literature for multi-port dc-dc converters. The proposed methods are mostly focused on MISO converters due to the recent interest on integrating renewable resources to supply the loads. As already mentioned, there are three basic methods of interfacing input sources in MISO converters. The first method includes series or parallel connection of several input cells to the common bus. Each input cell includes an input source, which can be a PV panel and one or more switching devices and/or passive components linked on the basis of buck, boost, buck-boost, Cuk, SEPIC and Zeta converter topologies [2.63]-[2.65]. The input cells are connected to a common voltage or current bus including an energy storage component, such as an inductor, capacitor or transformer.

In [2.63], a systematic approach is proposed to design MPCs using pulsating voltage source cell (PVSC) and pulsating current source cell (PCSC) extracted from the basic topologies as presented in Fig.2.7 (a). The extracted cells can be connected in series or parallel to form a multi-port topology. Hybrid topologies can also be achieved by inserting PVSCs in series or PCSC in parallel with the inductor or capacitor of basic converters such as buck, boost and SEPIC [2.63]-[2.65]. As can be seen in Fig.2.7(c), buck type PVSCs are connected in series, and in Fig.2.7 (d) boost type PCSCs are connected in parallel to form a multi-port topology.



**Fig.2.7 Basic input cells, (a) PVSC, (b) PCSC, (c) series connection of buck-PCSC, and (d) parallel connection of boost PVSC [2.63],[2.65].**

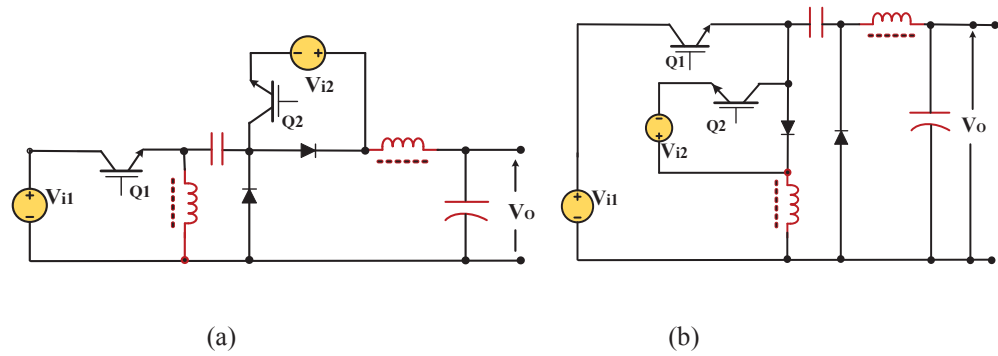


**Fig.2.8 Multi-port topologies derived from synthesizing buck type PVSC and SEPIC converter (a) buck converter in series with output and (b) buck converter in parallel with the output [2.63].**

This method can be used to boost the output voltage of photovoltaic panels and integrate their output energies into the common dc bus. Fig.2.8 shows two hybrid topologies derived from synthesizing buck type PVSC and SEPIC converter, where buck converter is connected in series or parallel with output [2.63]. A set of basic rules for generating topologies using isolated PVSC and PCSC are suggested in [2.64] and some isolated cells and resultant topologies are presented in Fig.2.9.

In [2.66], an attempt was made to isolate the source cells and the load of the topologies in [2.63] using a single primary winding high frequency transformer based on fly back, full bridge and push pull topologies. The single primary winding reduces the leakage inductance, power loss and voltage stress on switching components. The output of series or parallel connection of PVSCs was applied to a fly back, half bridge and full bridge as illustrated in Fig.2.10.

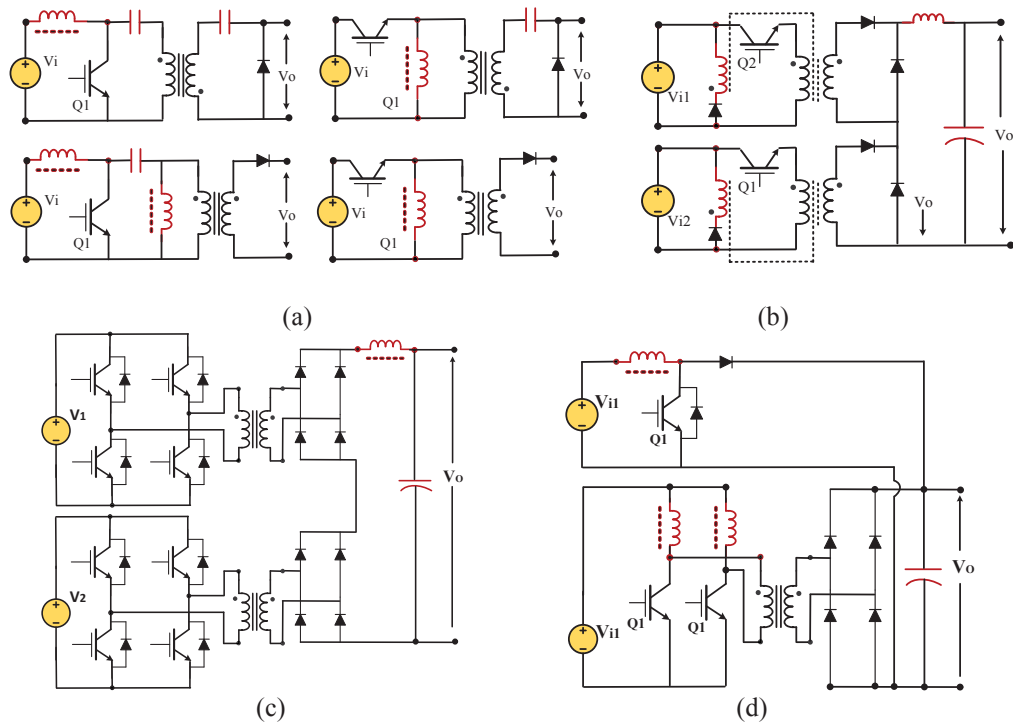


**Fig.2.9 MPC topologies using isolated PVSC and PCSC, (a) isolated PVSCs and PCSCs, (b) and (c) series connected isolated cells and (d) partially isolated topology [2.64]**

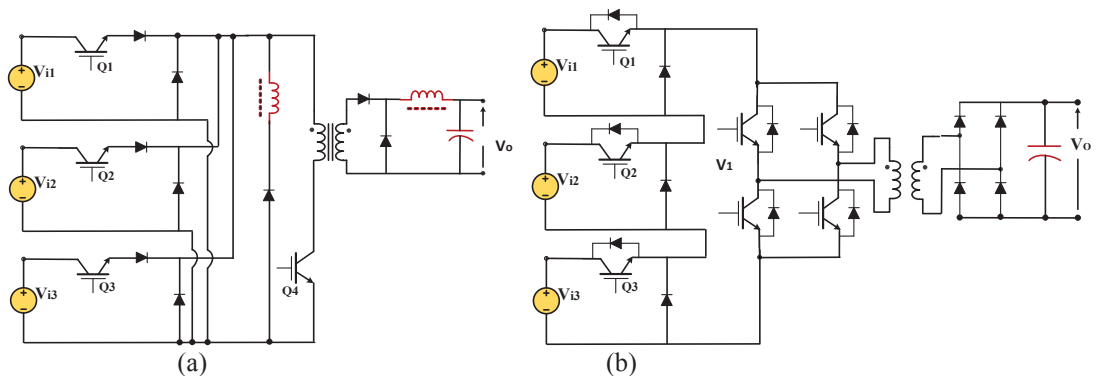


**Fig.2.10 Isolated single primary winding MPC topologies based on (a) fly back, and (b) full-bridge [2.66]**

A systematic method for derivation of a family of multi-port topologies, including multi-input, multi-output and bidirectional dc-dc converters based on a common dc bus is proposed in [2.65]. The proposed topologies are synthesized using input type, output type, and bidirectional type PVSCs. The cells are designed to step up or down the voltages of the sources to match their voltage with the common dc link. The proposed topologies are non-isolated and partially isolated based on the buck-boost topology.

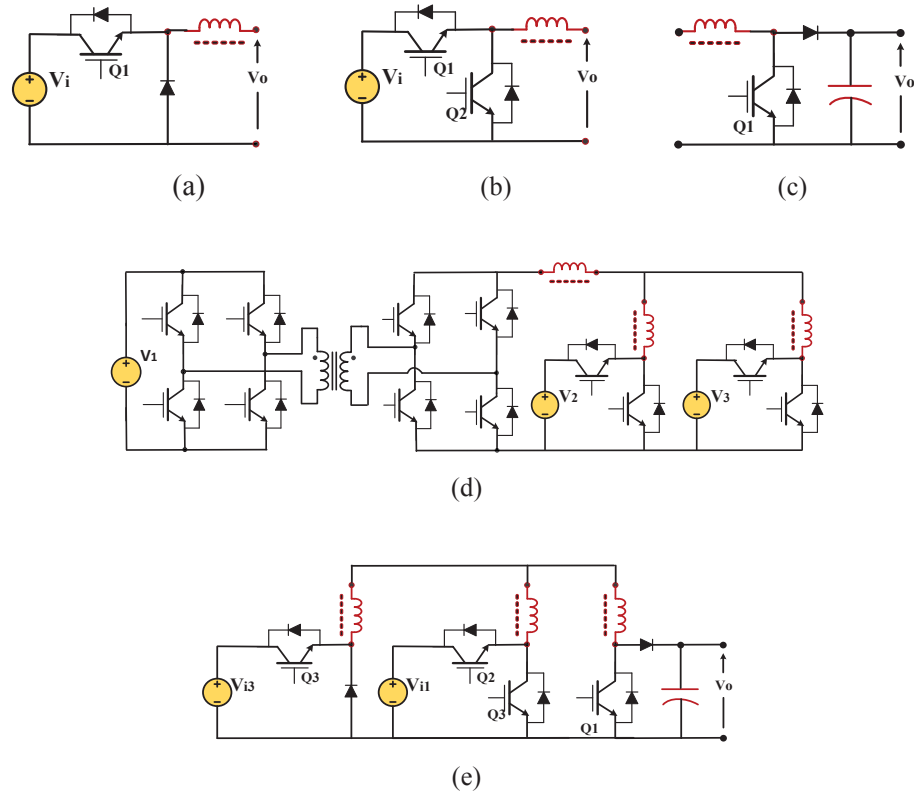


**Fig.2.11 PVSC topologies, (a) input cell, (b) bi-directional cell, (c) output cell (d) partially isolated multi-port buck-boost bi-directional converter and (e) non-isolated three-port buck-boost hybrid converter with one bidirectional port [2.65].**

Fig.2.11 shows some of the proposed cells and derived topologies. As can be seen, although the resulting topologies are simple in structure, the converter cells are linked through inductors, which increase the size and cost of converter.

### 2.7.3 Topologies based on time sharing concept

The second group of multi-port dc-dc converters operates on the basis of time sharing concept. Time sharing topologies are the simplest form of integrating multiple input sources so far. Their structure is based on the parallel connection of several PVSCs including only source and switch. In these topologies only one source can transfer energy to the load at a time. Therefore, a time-multiplexing scheme should be designed for switching process. An energy storage element such as an inductor, capacitor or transformer interfaces the input sources and links them to the output. The topologies operating in boost mode based on the time sharing concept can be used in photovoltaic systems. They can boost and integrate the output of several PV panels. A lot of multi-port topologies based on this technique have been proposed in the literature.

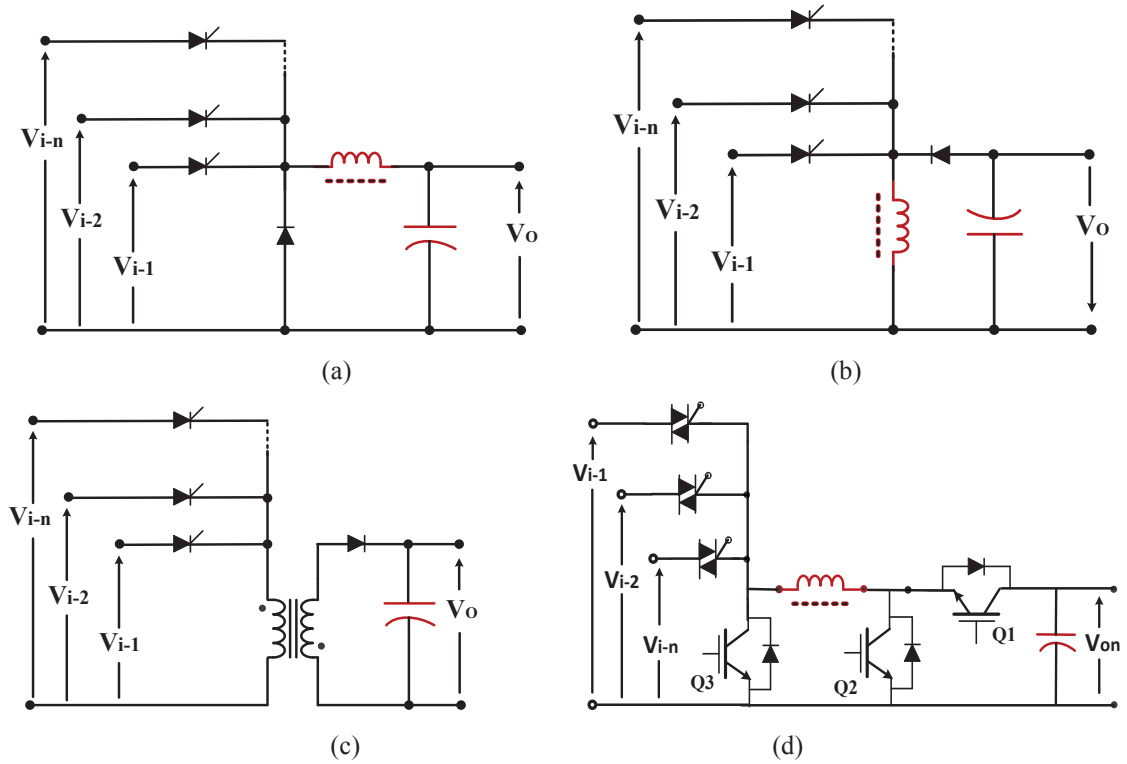


**Fig.2.12 MISO topologies using time sharing concept, (a) buck-boost [2.67], (b) buck topologies [2.68], (c) isolated fly-back topology [2.69], and (d) MISO bidirectional topology [2.70].**

In [2.67],[2.68], new topologies were proposed based on the basic topologies of boost, buck and buck-boost converters as illustrated in Fig.2.12 (a) and (b). A MISO converter topology based on buck converter is presented in Fig.2.12 (a) and a buck-boost topology in Fig.2.12 (b). The circuits are able to interface sources of different voltage and power characteristics with the minimum number of components. The input sources are interfaced through forward conducting bidirectional blocking (FCBB) switches. Although these structures are simple, they do not provide isolation among all inputs and outputs. Bidirectional power flow is only possible by using another converter connected from the output back to the input and the output voltage is in negative polarity. The converter can be used for integrating sources such as primary batteries, fuel cells and solar cells. The topology presented in Fig.2.12(c) is an isolated version of the topology in [2.67] based on fly back converter [2.69]. Using a transformer in this topology not only increases the conversion voltage ratio, which makes it suitable for low voltage sources, but also provides the isolation between the inputs and outputs, which enables the use of a non-inverted output. A MISO topology which can operate in all modes of buck, boost, and buck- boost and provide positive output voltage with bidirectional power flow was proposed in [2.70]. All inputs share a common inductor such that all input currents can be monitored using a current sensor for inductor current.

Fig.2.12(d) shows the electrical structure of this converter. It can be used in electrical vehicles and grid connected hybrid renewable energy systems.

#### **2.7.4 Topologies based on flux additivity**

The third group of topologies employs a multi-winding high frequency transformer as a magnetic bus to integrate the energy of input sources in the form of magnetic flux. The designed transformer provides a magnetic isolation between converter ports and helps the designers to step up or down the voltages of ports by adjusting the turns ratio of the transformer [2.71]-[2.76]. This however will become difficult when the number of windings increases (normally more than four windings). In general, four basic cells can be used to generate high frequency ac waveforms from dc sources and apply them to the transformer windings. The dc to ac converter cells are known as full-bridge, half-bridge, boost-half bridge and push-pull bidirectional as presented in Fig.2.13 (a). Some of the topologies based on this technique are presented in Fig.2.13 (b) to (d). The topology presented in Fig.2.13 (b) uses three H-bridge dc-ac converters to generate high frequency square wave ac signals for the transformer windings [2.73]. In this topology bi-directional power flow is possible between the ports by selection of one port as reference and leading or lagging phase shifts of the other two ports. This topology is suitable for integration of input sources with different voltage levels by adjusting the turns ratio of transformer windings [2.71]-[2.73]. Soft switching operation is possible especially in the case of small changes in dc voltages. To limit the current ripple of the dc sources and boost the voltage of the source, boost-half bridge dc-ac converter cells can be used. The topology illustrated in Fig.2.13(c) is used to link the battery and fuel cell as inputs to supply the load [2.74]. Using this topology can reduce the current ripple on the battery and fuel cell and can also boost the source voltages which reduce the number of turns of transformer winding [2.74]. Fig.2.13 (d) shows another topology that uses a boost-half bridge cell to realize a current fed port for battery storage and a half bridge cell for fuel cell. In this structure by changing the duty cycle of boost-half bridge switches the voltage variation on one port can be achieved [2.75]. The soft switching operating range can be extended and conduction loss and stress on switches can be reduced.

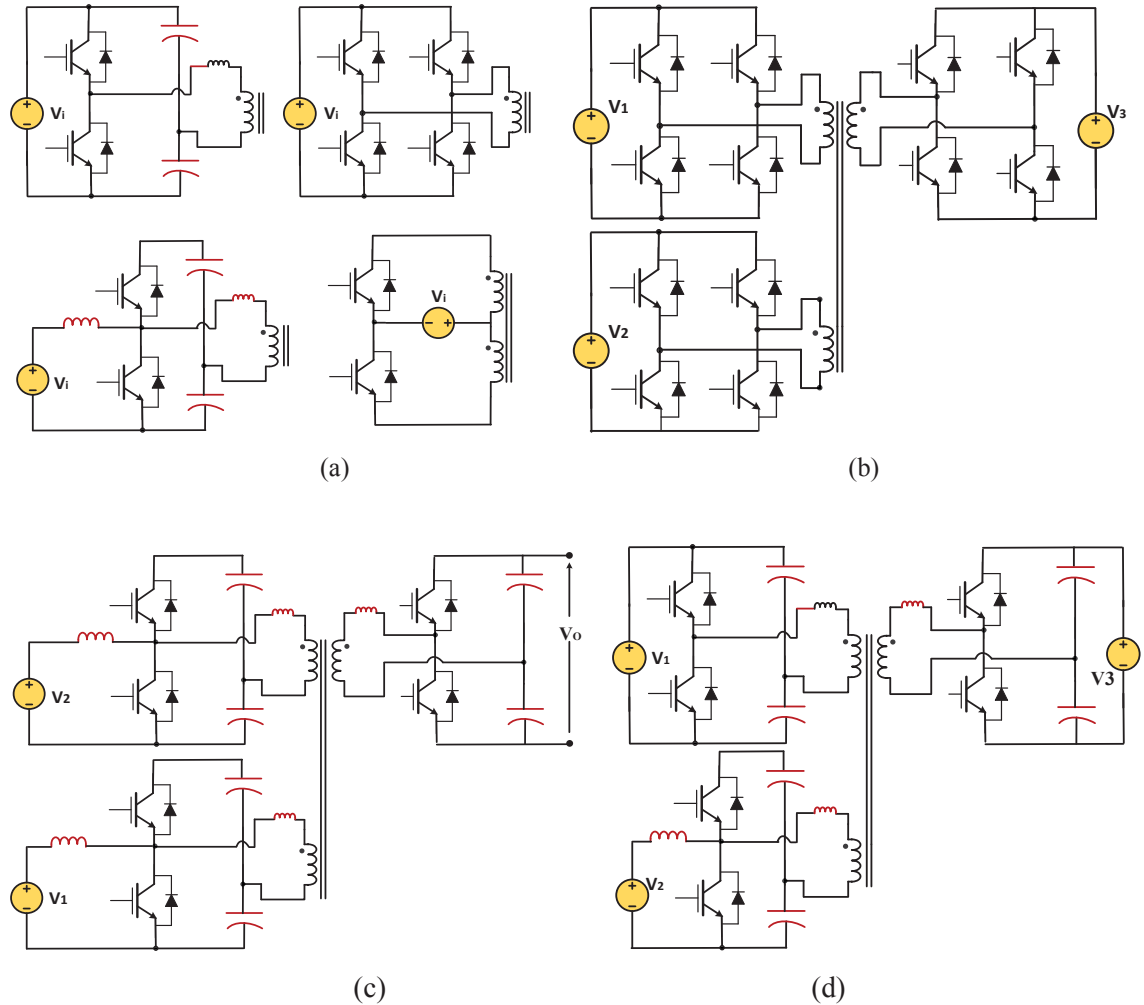


**Fig.2.13 Multi-port dc-dc converter topologies based on flux additivity in a magnetic link, (a) different dc to ac converter cells, (b) three port converter based on H-bridge cells in inputs and output [2.73], (c) topology using boost-half bridge as inputs and half bridge as output [2.74], and (d) topology using boost-half bridge and half bridge as inputs and half bridge as output [2.75].**

A family of multiport bidirectional dc-dc converters was derived from a general topology based on a combination of common dc bus and magnetic coupling in [2.77]. The dc bus usually consists of a common storage component, e.g. a capacitor which will be charged by a series or parallel connection of several source cells. However, the dc bus cannot handle a wide range of sources. To avoid large buck/boost ratios, voltage levels of input sources should be selected close to each other [2.77]. On the other hand in the case of using dc bus, there is no isolation between the sources.

In Fig.2.14 a simple dc-dc converter is presented using two boost-half-bridge cells in parallel connected to a common dc bus to supply the load. As can be seen in this topology the number of switching device is reduced and it is suitable for integrating low voltage sources to supply high voltage loads [2.77].

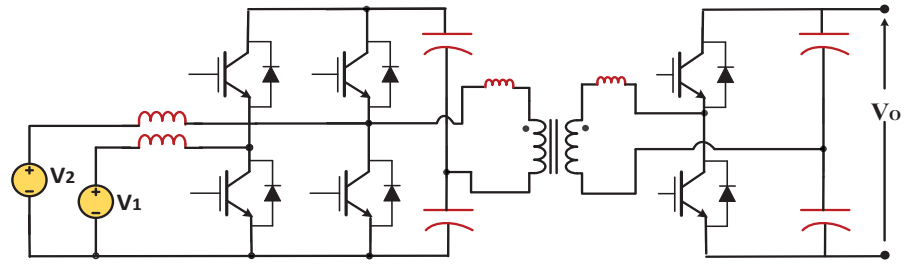


Fig.2.14 MISO topologies with common DC-link and magnetic couple [2.77]

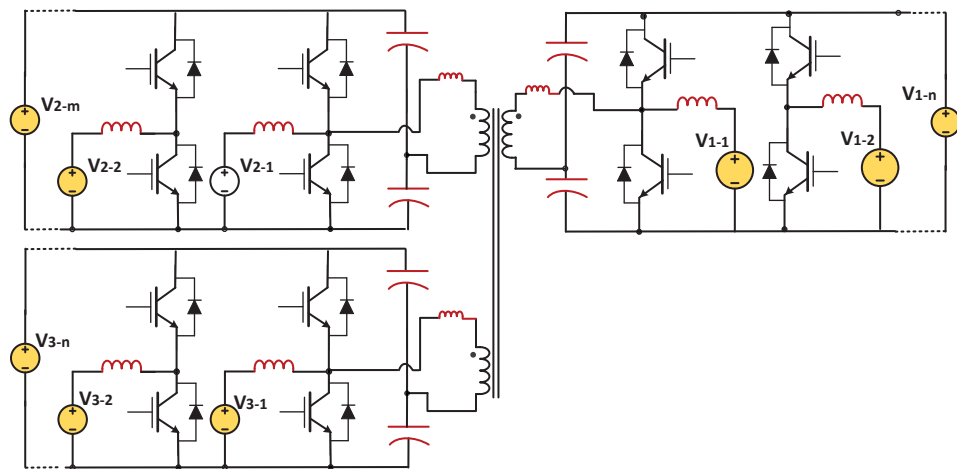


Fig.2.15 The general topology of MPC with a combination of dc bus and magnetic coupling [2.77]

The voltage levels of the connected sources should be within a close range. All three ports of this topology are bidirectional and the number of input sources and paralleled boost-half bridge branches is extendable.

Fig.2.15 shows the most complete topology of a combination of dc bus and flux additivity proposed in [2.77]. As illustrated in the figure, the topology includes several dc buses and a multi-winding high frequency transformer. Each dc bus contains several bidirectional buck/boost-half bridge cells linking the input sources to the two common capacitors. An extra source should be directly connected to the dc bus to form a half bridge structure along with the capacitors. The capacitors at each dc bus act as both half bridge and dc bus capacitors. The sources with close voltage levels can be connected in parallel to the same dc buses while the sources with different voltage levels should be connected to the separate dc buses [2.77]. This topology is the most general isolated multi-port dc-dc converter topology which can be used in relatively high power ranges up to 10 kW considering the transformer limitations. The main drawback with this

method is the effect of leakage inductance and complexity in calculation and design of multi-winding transformers especially when the number of windings increases. There are several other MISO dc-dc converter topologies proposed in the literature, but most of them are extended or optimized versions of the presented circuits.

## **2.8 Multi-input, Multi-output Converters**

Multi-input multi-output (MIMO) dc-dc converters are able to integrate multiple input sources to supply multiple loads. The MIMO converter topologies proposed in the literatures can be classified as isolated and non-isolated circuits. A single inductor MIMO converter is introduced in [2.78]. The proposed topology is shown in Fig.2.16-(a). Although it is simple, the contribution of each source in supplying the loads reduces when the number of inputs and outputs increases. Therefore the proposed topology is suitable for low power applications. Another non-isolated MIMO topology based on the buck-boost topology with a matrix structure on the basis of a power sharing concept is proposed in [2.79]. As shown in Fig.2.16 (b), the proposed topology becomes complex and difficult to be realized experimentally when the number of inputs and outputs is extended. Several isolated topologies using high frequency multi-winding transformers are reported in the literature.

An isolated topology was proposed in [2.80] which employed a multi winding transformer with separate winding for each input or output as is shown in Fig.2.16(c). The structure is similar to the multiple fly-back converters in parallel except that the transformers of all converters are combined on one core.

The main drawback of this structure is that increasing the number of windings on the transformer raises the leakage inductance and consequently switching losses. On the other hand, the transformer core should be suitably large in this circuit which would result in large volume and complex design.

Another version of MIMO converter topology similar to the one proposed in [2.80] was suggested using a single-primary multiple-secondary transformer as shown in Fig.2.16 (d) [2.67]. It is based on the fly-back topology, and each input source can be connected to the primary winding for a short time based on a time sharing concept. This topology is not bi-directional inherently although for bidirectional power flow an output such as battery can be connected back to the inputs.

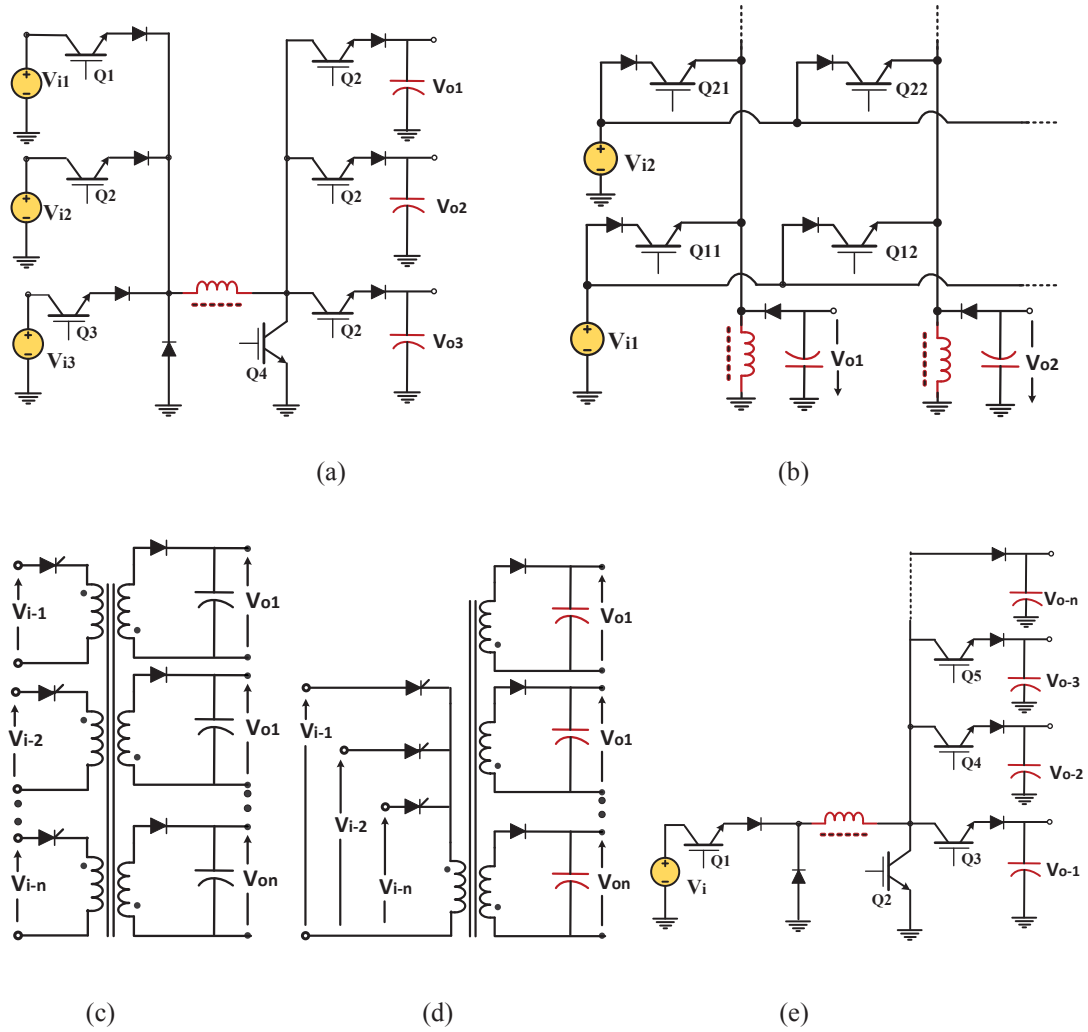


**Fig.2.16 MIMO converter topologies, (a) non-isolated with common inductor [2.78], (b) topology based on buck-boost topology [2.79], (c) topology using multi-winding transformer,[2.80], (d) topology using single primary winding transformer [2.67], and (e) non-isolated single-input multi-output topology [2.81].**

In general, the main disadvantage of time sharing technique is the limitation in capacity of energy storage components, which limits the converter power. Therefore, this group of converters is suitable for low power applications (usually less than 1 kW). Another disadvantage of this technique is reduction of connection time for each source as the number of input sources increase. This reduces the effective contribution of each source in supplying power to the output and increases the harmonics of input currents. Finally, there is no isolation between the input and output ports.

Single-input multi-output (SIMO) dc-dc converters are used to supply several loads with different voltage levels using a single input source. The conventional topology of isolated SIMO converter has been widely developed using single-primary multiple-secondary high frequency transformer. Fly-back and Forward topologies have been the

usual topologies of this group for many years. Recently, some non-isolated SIMO converters are proposed in the literature [2.81], [2.82] which are not reviewed in this section due to their limited application in renewable energy systems. Fig.2.16 (e) shows one of these non-isolated topologies.

## **2.9 Discussion**

The main characteristics of the topologies discussed in the previous sections are illustrated in Table 2.1. As can be seen, the bi-directional power flow capability is possible in topologies operating on the basis of magnetic flux additivity. This group of topologies shares a common magnetic bus to transfer the energy between the ports. They are able to operate in the medium power range, and can be connected in parallel to supply high power systems. They also provide isolation between the ports due to the use of a multi-winding transformer. These converters usually use H-bridge or half bridge switches to produce a high frequency square wave and this will increase the number of switching devices and consequently control complexity. The isolation between the ports can increase the system safety and balance the different voltage levels of input sources. Despite their advantages, design of multi-winding transformers is complex and they need complex control techniques.

The topologies based on the common magnetic bus are isolated inherently although it is also possible for the other two groups of multi-port converter topologies. Generally, isolation of low power converters is not preferred as it will increase the cost. Another important factor in comparison of different topologies is the number of active switches which will impact on the converter efficiency, cost, and complexity. The topologies operate using a magnetic bus have the highest number of switching devices as they need to convert the input dc voltage to a high frequency square wave ac voltage before applying it to the transformer. The dc to ac conversion cell can be H-bridge, half bridge and boost half bridge which requires several switching devices and driving circuits which increases the cost, size and complexity of topologies. In the other two groups of topologies usually one switch is allocated to each input conversion cell which reduces the cost, size and complexity. There are a large number of topologies that are not considered in this chapter while they are either insignificant technically or operate more or less on the same principles as those that have been discussed.

**TABLE 2.1 Comparison of Characteristics of Different Topologies**

Topology Characteristics	Time sharing concept	Magnetic flux additivity	Synthesizing Cells
Power flow direction	Uni-direction	Bi-direction	Uni-direction
Range of handling power	Low (P<1kW)	Medium (P<10kW)	Low (P<1kW)
Control Complexity	Low	Medium	Low
Isolation between the ports	No	Yes	No
Isolation between input and output ports	Possible	Yes	Possible
Number of switching device for each port	Low	High	Medium
Safety and reliability	Low	Medium	Low
Total cost of converter	Low	High	Low

## 2.10 Summary

A review on the basic concepts of the micro-grid is presented in this chapter. It started with a quick introduction on renewable energy sources with application in residential renewable systems, the concept of hybridization of energy resources and residential micro-grids. Due to the importance of the multi-port dc-dc converter as the main part of the proposed micro-grid, a major part of the chapter is allocated to the review of different proposed topologies of multi-port dc-dc converters. The topologies are classified in three groups based on the operation principle and the characteristics of each group including positive and negative points and practical issues are highlighted. The study in this chapter provides useful information required for design and development of the multi-port converter and micro-grid structure.

**References**

- [2.1] B. K. Bose, "Global Warming: Energy, Environmental Pollution, and the Impact of Power Electronics," *IEEE Ind. Electronics Magazine*, vol. 4, no. 1, pp. 6-17, March 2010.
- [2.2] M. Liserre, T. Sauter and J. Y. Hung, "Future Energy Systems: Integrating Renewable Energy Sources into the Smart Power Grid Through Industrial Electronics," *IEEE Ind. Electronics Magazine*, vol. 4, no. 1, pp. 18-37, March 2010.
- [2.3] P. Vithayasrichareon and I. F. MacGill, "Valuing large-scale solar photovoltaics in future electricity generation portfolios and its implications for energy and climate policies," *IET Renewable Power Generation*, vol. 10, no. 1, pp. 79-87, 1 2016.
- [2.4] IRENA: 'Solar photovoltaics' (International Renewable Energy Agency (IRENA),(2012)
- [2.5] A. Audenaert, L. De Boeck, S. De Cleyn, S. Lizin, and J-F. Adam, "An economic evaluation of Photovoltaic Grid Connected Systems (PVGCS) in flanders for companies: A generic model," *Renewable. Energy*, vol. 35, pp. 2674–2682, 2010.
- [2.6] M. Sechilariu, B. Wang and F. Locment, "Building Integrated Photovoltaic System With Energy Storage and Smart Grid Communication," *IEEE Tran. on Industrial Electronics*, vol. 60, no. 4, pp. 1607-1618, April 2013.
- [2.7] J. L. Acosta, K. Combe, S. Ž Djokic and I. Hernando-Gil, "Performance Assessment of Micro and Small-Scale Wind Turbines in Urban Areas," *IEEE Systems Journal*, vol. 6, no. 1, pp. 152-163, March 2012.
- [2.8] A. M. Gee, F. V. P. Robinson and R. W. Dunn, "Analysis of Battery Lifetime Extension in a Small-Scale Wind-Energy System Using Supercapacitors," *IEEE Trans. Energy Conversion*, vol. 28, no. 1, pp. 24-33, March 2013.
- [2.9] Y. S. Park, S. M. Jang, J. H. Choi, J. Y. Choi and D. J. You, "Characteristic Analysis on Axial Flux Permanent Magnet Synchronous Generator Considering Wind Turbine Characteristics According to Wind Speed for Small-Scale Power Application," *IEEE Tran. Magnetics*, vol. 48, no. 11, pp. 2937-2940, Nov. 2012.

- [2.10] M. Houwing, R. R. Negenborn and B. De Schutter, "Demand Response With Micro-CHP Systems," *Proceedings of the IEEE*, vol. 99, no. 1, pp. 200-213, Jan. 2011.
- [2.11] B. Jiang and Y. Fei, "Smart Home in Smart Microgrid: A Cost-Effective Energy Ecosystem With Intelligent Hierarchical Agents," *IEEE Trans. Smart Grid*, vol. 6, no. 1, pp. 3-13, Jan. 2015.
- [2.12] G. K. H. Larsen, N. D. van Foreest and J. M. A. Scherpen, "Distributed MPC Applied to a Network of Households With Micro-CHP and Heat Storage," *IEEE Trans. Smart Grid*, vol. 5, no. 4, pp. 2106-2114, July 2014.
- [2.13] A. D. Hawkes and M. A. Leach, "Cost-effective operating strategy for residential micro-combined heat and power," *Energy*, vol. 32, no. 5, pp. 711–723, May 2007.
- [2.14] M. A. Laughton, "Fuel cells," *Power Engineering Journal*, vol. 16, no. 1, pp. 37-47, Feb. 2002.
- [2.15] B. Cook, "Introduction to fuel cells and hydrogen technology," *Engineering Science and Education Journal*, vol. 11, no. 6, pp. 205-216, Dec 2002.
- [2.16] M. Uzunoglu and M. S. Alam, "Dynamic modeling, design, and simulation of a combined PEM fuel cell and ultra-capacitor system for stand-alone residential applications," *IEEE Trans. Energy Conversion*, vol. 21, no. 3, pp. 767-775, Sept. 2006.
- [2.17] M. Tanrioven and M. S. Alam, "Modeling, Control, and Power Quality Evaluation of a PEM Fuel Cell-Based Power Supply System for Residential Use," *IEEE Trans. Industry Applications*, vol. 42, no. 6, pp. 1582-1589, Nov.-dec. 2006.
- [2.18] S. K. Mazumder, R. K. Burra, R. Huang, M. Tahir and K. Acharya, "A Universal Grid-Connected Fuel-Cell Inverter for Residential Application," *IEEE Trans. Industrial Electronics*, vol. 57, no. 10, pp. 3431-3447, Oct. 2010.
- [2.19] A. Taleb, E. Kjeang and E. Maine, "Cost analysis for durable proton exchange membrane in PEM fuel cells," in proc. *Technology Management for Emerging Technologies conference, PICMET '12*, Vancouver, BC, 2012, pp. 2943-2950.
- [2.20] D. H. Maunder, K. A. Brown and K. M. Richards, "Generating electricity from biomass and waste," *Power Engineering Journal*, vol. 9, no. 4, pp. 188-196, Aug. 1995.

- [2.21] Yuan Li and Mei Song, "Analysis of the use of China's rural biomass energy and countermeasures," in proc. *2nd Int. Conference on Artificial Intelligence, Management Science and Electronic Commerce*, Deng Leng, 2011, pp. 6139-6141.
- [2.22] R. Namuli and P. Pillay, "Maximisation of revenue from biomass waste to energy conversion systems on rural farms," in proc. *IEEE Power and Energy Society General Meeting*, San Diego, CA, 2012, pp. 1-5.
- [2.23] Michael Brower, "Geothermal Energy," *Cool Energy: Renewable Solutions to Environmental Problems*, 1, MIT Press, 1992, pp.127-154
- [2.24] C. R. DeNardin *et al.*, "Underground geothermal energy to reduce the residential electricity consumption," in proc. *3rd Renewable Power Generation Conference Naples*, 2014, pp. 1-6.
- [2.25] F. Casella, "Modeling, Simulation, control, and optimization of a geothermal power plant," *IEEE Trans. Energy Conversion*, vol. 19, no. 1, pp. 170-178, March 2004.
- [2.26] T. J. Hammons and A. Gunnarsson, "Geothermal sustainability in Europe and worldwide," in proc. *43rd Int. Universities Power Engineering Conference*, Padova, 2008, pp. 1-10.
- [2.27] V. Smil, "Renewable Energy Flows," *Power Density: A Key to Understanding Energy Sources and Users*, 1, MIT Press, 2015, pp.320-325
- [2.28] M. Andreica, S. Bacha, D. Roze, I. Exteberria-Otadui and I. Munteanu, "Micro-hydro water current turbine control for grid connected or islanding operation," in proc. *IEEE Power Electronics Specialists Conference*, Rhodes, 2008, pp. 957-962.
- [2.29] A. Desai, I. Mukhopadhyay and A. Ray, "Theoretical analysis of a Pico-hydro power system for energy generation in rural or isolated area," in proc. *IEEE PES Asia-Pacific Power and Energy Engineering Conference*, Hong Kong, 2014, pp. 1-4.
- [2.30] J. M. Carrasco *et al.*, "Power-Electronic Systems for the Grid Integration of Renewable Energy Sources: A Survey," *IEEE Trans. on Industrial Electronics*, vol. 53, no. 4, pp. 1002-1016, June 2006.
- [2.31] J. P. Barton and D. G. Infield, "Energy storage and its use with intermittent renewable energy," *IEEE Trans. Energy Conversion*, vol. 19, no. 2, pp. 441-448, June 2004.

- [2.32] A. Khaligh and Z. Li, "Battery, Ultracapacitor, Fuel Cell, and Hybrid Energy Storage Systems for Electric, Hybrid Electric, Fuel Cell, and Plug-In Hybrid Electric Vehicles: State of the Art," *IEEE Trans. Vehicular Technology*, vol. 59, no. 6, pp. 2806-2814, July 2010.
- [2.33] M. S. Whittingham, "History, Evolution, and Future Status of Energy Storage," *Proceedings of the IEEE*, vol. 100, no. Special Centennial Issue, pp. 1518-1534, May 13 2012.
- [2.34] R. Atia and N. Yamada, "Sizing and Analysis of Renewable Energy and Battery Systems in Residential Microgrids," *IEEE Trans. Smart Grid*, vol. 7, no. 3, pp. 1204-1213, May 2016.
- [2.35] N. R. Tummuru, M. K. Mishra and S. Srinivas, "Dynamic Energy Management of Renewable Grid Integrated Hybrid Energy Storage System," *IEEE Trans. Industrial Electronics*, vol. 62, no. 12, pp. 7728-7737, Dec. 2015.
- [2.36] M. Trifkovic, M. Sheikhzadeh, K. Nigim and P. Daoutidis, "Modeling and Control of a Renewable Hybrid Energy System With Hydrogen Storage," *IEEE Trans. Control Systems Technology*, vol. 22, no. 1, pp. 169-179, Jan. 2014.
- [2.37] P. Li, R. Dargaville, F. Liu, J. Xia and Y. D. Song, "Data-Based Statistical Property Analyzing and Storage Sizing for Hybrid Renewable Energy Systems," *IEEE Trans. Industrial Electronics*, vol. 62, no. 11, pp. 6996-7008, Nov. 2015.
- [2.38] L. Wang and H. Li, "Maximum Fuel Economy-Oriented Power Management Design for a Fuel Cell Vehicle Using Battery and Ultracapacitor," *IEEE Trans. Industry Applications*, vol. 46, no. 3, pp. 1011-1020, May-june 2010.
- [2.39] H. Tao, J. L. Duarte and M. A. M. Hendrix, "Three-Port Triple-Half-Bridge Bidirectional Converter With Zero-Voltage Switching," *IEEE Trans. Power Electronics*, vol. 23, no. 2, pp. 782-792, March 2008.
- [2.40] H. M. Al-Masri and M. Ehsani, "Feasibility Investigation of a Hybrid On-Grid Wind Photovoltaic Retrofitting System," *IEEE Trans. Industry Applications*, vol. 52, no. 3, pp. 1979-1988, May-June 2016.
- [2.41] M. Tasdighi, H. Ghasemi and A. Rahimi-Kian, "Residential Microgrid Scheduling Based on Smart Meters Data and Temperature Dependent Thermal Load Modeling," *IEEE Trans. Smart Grid*, vol. 5, no. 1, pp. 349-357, Jan. 2014.
- [2.42] A. Anvari-Moghaddam, H. Monsef and A. Rahimi-Kian, "Optimal Smart Home Energy Management Considering Energy Saving and a Comfortable Lifestyle," *IEEE Trans. Smart Grid*, vol. 6, no. 1, pp. 324-332, Jan. 2015.

- [2.43] X. Chen, T. Wei, and S. Hu, "Uncertainty-aware household appliance scheduling considering dynamic electricity pricing in smart home," *IEEE Trans. Smart Grid*, vol. 4, no. 2, pp. 932–941, Jun. 2013.
- [2.44] M. Tushar, C. Assi, M. Maier, and M. Uddin, "Smart microgrids: Optimal joint scheduling for electric vehicles and home appliances," *IEEE Trans. Smart Grid*, vol. 5, no. 1, pp. 239–250, Jan. 2014.
- [2.45] K. Itoh, M. Ishigaki, N. Yanagizawa, S. Tomura and T. Umeno, "Analysis and Design of a Multiport Converter Using a Magnetic Coupling Inductor Technique," in *IEEE Trans. Industry Applications*, vol. 51, no. 2, pp. 1713-1721, March-April 2015.
- [2.46] J. Zeng, W. Qiao, L. Qu and Y. Jiao, "An Isolated Multiport DC–DC Converter for Simultaneous Power Management of Multiple Different Renewable Energy Sources," *IEEE Journal of Emerging and Selected Topics in Power Electronics*, vol. 2, no. 1, pp. 70-78, March 2014.
- [2.47] H. Tao, A. Kotsopoulos, J. L. Duarte and M. A. M. Hendrix, "Family of multiport bidirectional DC-DC converters," *IEE Proceedings - Electric Power Applications*, vol. 153, no. 3, pp. 451-458, 1 May 2006.
- [2.48] W. Qiao, A. Sharma, J. L. Hudgins, E. G. Jones and L. Rilett, "Wind/solar hybrid generation-based roadway micro-grids," in proc. *IEEE Power and Energy Society General Meeting*, San Diego, CA, 2011, pp. 1-7.
- [2.49] Yanping Jiao and W. Qiao, "A hierarchical power management strategy for multiple single-phase roadway microgrids," in proc. *IEEE Power & Energy Society General Meeting*, Vancouver, BC, 2013, pp. 1-5.
- [2.50] The ODOT Solar Highway. [Online]. Available: [http://www.oregon.gov/ODOT/HWY/OIPP/Pages/inn\\_solarhighway.aspx](http://www.oregon.gov/ODOT/HWY/OIPP/Pages/inn_solarhighway.aspx)
- [2.51] U. D. Deep, B. R. Petersen and J. Meng, "A Smart Microcontroller-Based Iridium Satellite-Communication Architecture for a Remote Renewable Energy Source," *IEEE Trans. Power Delivery*, vol. 24, no. 4, pp. 1869-1875, Oct. 2009.
- [2.52] Powering remote surveillance, border patrol, Homeland Security, monitoring and control, and communications. Available at: <https://www.sunwize.com/application-item/security-surveillance/>
- [2.53] Mohamad.A.A, Shabani.B, "Sustainable Power Supply Solutions for Off-Grid Base Stations," *Energies* **2015**, 8(10), 10904-10941;
- [2.54] [www.wholesalesolar.com](http://www.wholesalesolar.com)

- [2.55] F. Yi and W. Cai, "Modeling, Control, and Seamless Transition of the Bidirectional Battery-Driven Switched Reluctance Motor/Generator Drive Based on Integrated Multiport Power Converter for Electric Vehicle Applications," *IEEE Trans. Power Electronics*, vol. 31, no. 10, pp. 7099-7111, Oct. 2016.
- [2.56] Y. J. Lee, A. Khaligh and A. Emadi, "Advanced Integrated Bidirectional AC/DC and DC/DC Converter for Plug-In Hybrid Electric Vehicles," *IEEE Trans. Vehicular Technology*, vol. 58, no. 8, pp. 3970-3980, Oct. 2009.
- [2.57] A. Khaligh and Z. Li, "Battery, Ultracapacitor, Fuel Cell, and Hybrid Energy Storage Systems for Electric, Hybrid Electric, Fuel Cell, and Plug-In Hybrid Electric Vehicles: State of the Art," *IEEE Trans. on Vehicular Technology*, vol. 59, no. 6, pp. 2806-2814, July 2010.
- [2.58] C. Zhao, S. D. Round and J. W. Kolar, "An Isolated Three-Port Bidirectional DC-DC Converter With Decoupled Power Flow Management," *IEEE Trans. Power Electronics*, vol. 23, no. 5, pp. 2443-2453, Sept. 2008.
- [2.59] Y. M. Chen, Y. C. Liu, and S. H. Lin, "Double-input PWM DC/DC converter for high-/low-voltage sources," *IEEE Trans. Industrial Electronics*, vol. 53, no. 5, pp. October 2006.
- [2.60] J.L. Duarte, et al., "Three-port bidirectional converter for hybrid fuel cell systems," *IEEE Trans. Power Electronics*, vol. 22, no. pp.480–487, 2007
- [2.61] H. Tao, et al., "Multi-input bidirectional DC-DC converter combining DC link and magnetic coupling for fuel cell systems," in Proc. *Fortieth IAS Annual Meeting and Industry applications Conference*, 2005, vol.3, pp. 2021–2028.
- [2.62] H. Wu, K. Sun, R. Chen, H. Hu, and Y. Xing, "Full-bridge three-port converters with wide input voltage range for renewable power systems," *IEEE Trans. Power Electronics*, vol. 27, no. 9, pp. 3965–3974, September 2012.
- [2.63] Y. C. Liu and Y. M. Chen, "A systematic approach to synthesizing multiple-input dc–dc converter," *IEEE Trans. Power Electronics*, vol. 24, no. 1, pp. 116–127, Jan. 2007.
- [2.64] Y. Li, X. Ruan, D. Yang, F. Liu, and C. K. Tse, "Synthesis of multiple input dc/dc converters," *IEEE Trans. Power Electronics*, vol. 25, no. 9, pp. 2372–2385, September 2010.
- [2.65] H. Wu, J. Zhang and Y. Xing, "A Family of Multiport Buck–Boost Converters Based on DC-Link-Inductors (DLIs) ," *IEEE Trans. Power Electronics*, vol. 30, no. 2, pp. 735-746, Feb. 2015.

- [2.66] Q. Wang, J. Zhang, X. Ruan, and K. Jin, "Isolated single primary winding multiple-input converters," *IEEE Trans. Power Electronics*, vol. 26, no. 12, December 2011.
- [2.67] N. D. Benavides and P. L. Chapman, "Power budgeting of a multiple-input buck-boost converter," *IEEE Trans. Power Electronics*, vol. 20, no. 6, pp. 1303–1309, November 2005.
- [2.68] B. G. Dobbs, P. L. Chapman, "A multiple-input DC-DC converter topology," *IEEE Trans. Power Electronics*, vol. 1, no. 1, March 2003.
- [2.69] N. Benavides and P. L. Chapman, "Object-oriented modeling of a multiple-input multiple-output fly-back converter in Dymola," in Proc. *IEEE Workshop Computers Power Electronics*, pp. 156–160, 2004
- [2.70] A. Khaligh, J. Cao, and Y. J. Lee, "A multiple-input DC-DC converter topology," *IEEE Trans. Power Electronics*, vol. 24, no. 3, March 2009.
- [2.71] Y. M. Chen, Y. C. Liu, and T. F. Wu, "Multi-input dc-dc converter based on the multi-winding transformer for renewable energy applications," *IEEE Trans. Industry Applications*, vol. 38, no. 4, pp. 1096–1104, July/August 2002.
- [2.72] M. Michon, J. L. Duarte, M. Hendrix, and M. G. Simoes, "A three port bi-directional converter for hybrid fuel cell systems," in Proc. *IEEE Power Electronics Conference (PESC)*, Aachen, Germany, pp 4736–4742, June 2004.
- [2.73] H. Tao, A. Kotsopoulos, J. L. Duarte, and M. A. M. Hendrix, "A soft-switched three port bi-directional converter for fuel cell and supercapacitor applications," in Proc. *IEEE Power Electronics Specialist Conference (PESC)*, Recife, Brazil, pp 2487–2493, June 2005.
- [2.74] D. Liu and H. Li, "A ZVS Bi-Directional DC-DC Converter for Multiple Energy Storage Elements," *IEEE Trans. Power Electronics*, vol. 21, no. 5, pp. 1513–1517, Sept. 2006.
- [2.75] H. Tao, J. L. Duarte, M. A. M. Hendrix, "Three-port triple-half bridge bidirectional converter with zero voltage switching," *IEEE Trans. Power Electronics*, vol. 23, no.2, pp 782–792, March 2008.
- [2.76] H. Tao, A. Kotsopoulos, J. L. Duarte, and M. A. M. Hendrix, "Triple-half bridge bidirectional converter controlled by phase shift and PWM," in Proc. *IEEE Applied Power Electronics Conference and Exposition (APEC)*, USA, March 2006.

- [2.77] H. Tao, A. Kotsopoulos, J. L. Duarte, and M. A. M. Hendrix, "Family of multiport bidirectional DC–DC converters," *IEE proceedings of Electric Power Applications*, Vol.153 ,Issue: 3, pp.451-458, 2006
- [2.78] H. Behjati, A. Davoudi, "A multi-port dc-dc converter with independent outputs for vehicular applications," in proc. *IEEE Conference on Vehicle Power and Propulsion*, pp.1-5, 2011
- [2.79] M. Jafari, G. Hunter, J. G. Zhu, "A new topology of multi-input multi-output Buck-Boost DC-DC converter for microgrid applications," in Proc. *IEEE Power and Energy Conference (PECON2012)*, pp.286-291, 2-5 Dec 2012.
- [2.80] H. Matsuo, T. Shigemizo, F. Kurokawa, and N. Watanabe, "Characteristics of the multiple-input dc-dc converter," in Proc. *24<sup>th</sup> annual IEEE PESC'93*, pp. 115–120, 1993.
- [2.81] W. H. Ki, D. Ma, "Single-inductor multiple-output switching converters," in Proc. *32nd IEEE Annual Power Electronics Spec. Conf.*, vol. 1, pp. 226–231, 2001.
- [2.82] A. Nami, F. Zare, A. Ghosh, F. Blaabjerg, "Multi-output DC-DC converters based on diode-clamped converters configuration: topology and control strategy," *IET Power Electron*, vol.3, issue 2, pp .197-208, 2010.

## CHAPTER 3

# DESIGN AND DEVELOPMENT OF A MICRO-GRID FOR HOUSEHOLD APPLICATIONS

### 3.1 Introduction

This chapter reviews the main stages of design and development of the micro-grid for household applications. At first, the design specifications of the residential micro-grid are defined and an appropriate topology of micro-grid is selected according to the design requirements. The proposed topology contains three dc-dc converters including a triple active bridge (TAB) dc-dc converter to link the photovoltaic (PV), fuel cell and load, a bi-directional buck-boost converter charge and discharge the battery and an interleaved current-fed boost converter to increase the PV output voltage level and maintain maximum power point tracking (MPPT). The TAB converter is the heart of the micro-grid and includes a three-winding high frequency transformer as a common magnetic link. It also contains three dc-ac conversion cells to change the input dc voltages to high frequency ac waveforms and apply them to the transformer windings. In this chapter, a study is carried out on the widely used dc-ac conversion cells known as H-bridge, half bridge and current-fed boost half bridge to select the appropriate one for them TAB converter. The bi-directional buck-boost and inter-leaved current-fed converter topologies are analysed in the next stage and their design methodology is discussed. The last stage of this chapter is allocated to design and experimental development of the micro-grid including the converters.

### 3.2 Selection of the Micro-grid Topology

The first step in design and development of a residential micro-grid is selection of an appropriate topology for the micro-grid. The conventional topology for micro-grids is based on the multi-conversion structure. In this structure each renewable energy source is connected to a common ac or dc bus through a voltage conversion unit to adapt its voltage level to the common bus. As a majority of renewable energy sources generate dc voltage as output, to link them to the common electrical bus, a dc-dc converter is required in the case of using a dc bus or a dc-ac converter (inverter) in the case of using ac bus.

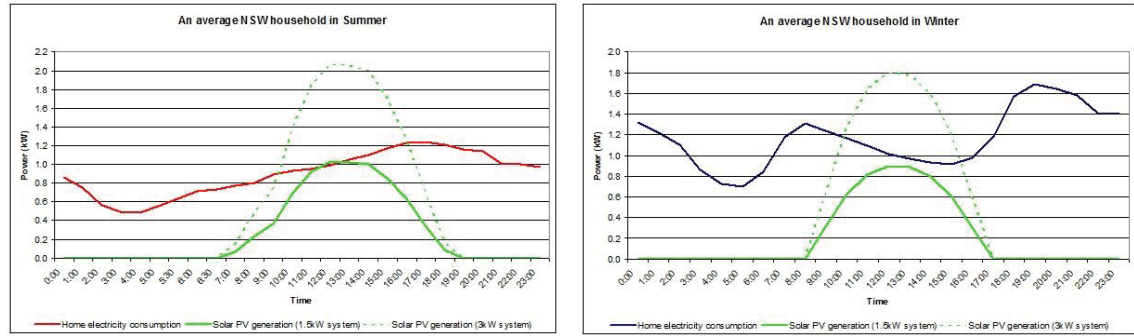


**Fig.3.1** The average of maximum power consumed by a residential house occupied by a four person family in NSW is 1.3 kW in summer and 1.7 kW in winter [3.5].

Generally, a boost converter may be required to increase the voltage level of renewable sources due to the small level of output voltage in most of the micro-grid elements such as PV, fuel cell and battery. To select the dc-dc converter for each voltage source the main parameters that need to be considered are voltage, current and power ratings of the load and the source. A large number of research articles have been published on optimal sizing of the elements in renewable energy systems according to the amount of available energy, load profile, energy management scenario, flexibility and reliability [3.1]-[3.4]. In this research, the power ratings of elements in the proposed micro-grid are defined according to the average of maximum power consumed by the residential house as discussion on the optimal sizing of the renewable energy system is outside of the scope of this thesis. As can be seen in Fig.3.1, the average maximum power consumed by a residential house occupied by a four person family in NSW is about 1.7 kW according to the data provided by the Australian Energy Market Operator (AEMO) [3.5]. Therefore, the proposed micro-grid in this research is designed to supply a 4.5 kW residential load which covers a wide range of residential users. Due to the range of power (as presented in Chapter 2, Table 2.1) the multi-port converter topology using a high frequency transformer is selected as the main dc-dc converter in the micro-grid topology. Other parameters such as safety and reliability, control flexibility, converter size and efficiency have been taken into account.

A TAB topology as reviewed in section 2.8 was selected as the main dc-dc converter in the proposed micro grid to integrate the PV, fuel cell, battery and load together as a micro-grid. It will be shown in the next chapters that the TAB phase-shift dc-dc converter provides the required specifications and is an appropriate choice for the proposed application. The multi-winding transformer is used as a high frequency

magnetic link to transfer the power between the sources, load and battery in the form of magnetic flux. The structure of the proposed micro-grid is presented in Fig.3.2. The power flow direction can be easily controlled by leading or lagging of the phase shift angles between the high frequency square-waves generated by H-bridge units. On the other hand, the amount of transferred power is easily controlled by the value of phase shift angles and/or duty ratios.

### **3.3 Selection of DC-DC Converter Topology for PV Port**

To select an appropriate topology of dc-dc converter for PV port several technical issues should be taken into account. Due to the intermittent nature of irradiation level and temperature, the maximum power extracted from a PV port is variable and depends on climatological conditions. Therefore, the PV operation point needs to be adjusted on the maximum power point (MPP) at any time instant. According to this the dc-dc converter topology selected for the PV port should be able to track the MPP of the PV panel. On the other hand, the range of output voltage of PV panel is small (generally between 5-40V) and needs to be boosted before applying to the H-bridge unit of TAB converter. The selected topology also should generate minimum current ripple on the PV ports to avoid the effects of current ripple on the maximum power point tracking (MPPT) process. High current ripple deteriorates the MPPT performance and the PV panel efficiency [3.6]-[3.8]. The boost dc-dc converters have been conventionally used to step up the PV output voltage and utilize MPPT [3.9], [3.10]. Implementing a current control loop for the converter can effectively reduce the ripples on the PV current which provides higher MPPT performance [3.11]. On the other hand, using a multi-winding magnetic link isolates the PV port from other ports. Recently a current-fed dc-ac converter is proposed in the literature that combines two current-fed dc-dc boost converters and H-bridge dc-ac converter to reduce the size and the cost of PV-linked converters [3.6],[3.12]. The proposed topology is promising for high power PV-linked converters. However, start-up circuits are required to control the converter at the starting time as duty cycle in this topology can never be less than 50 % [3.6]. According to the required specifications, a current-fed boost converter (CFBC) topology is selected for PV port as can be seen in Fig.3.2. More details on the steady state operation of the converter, control technique and the waveforms will be provided in the following chapters.

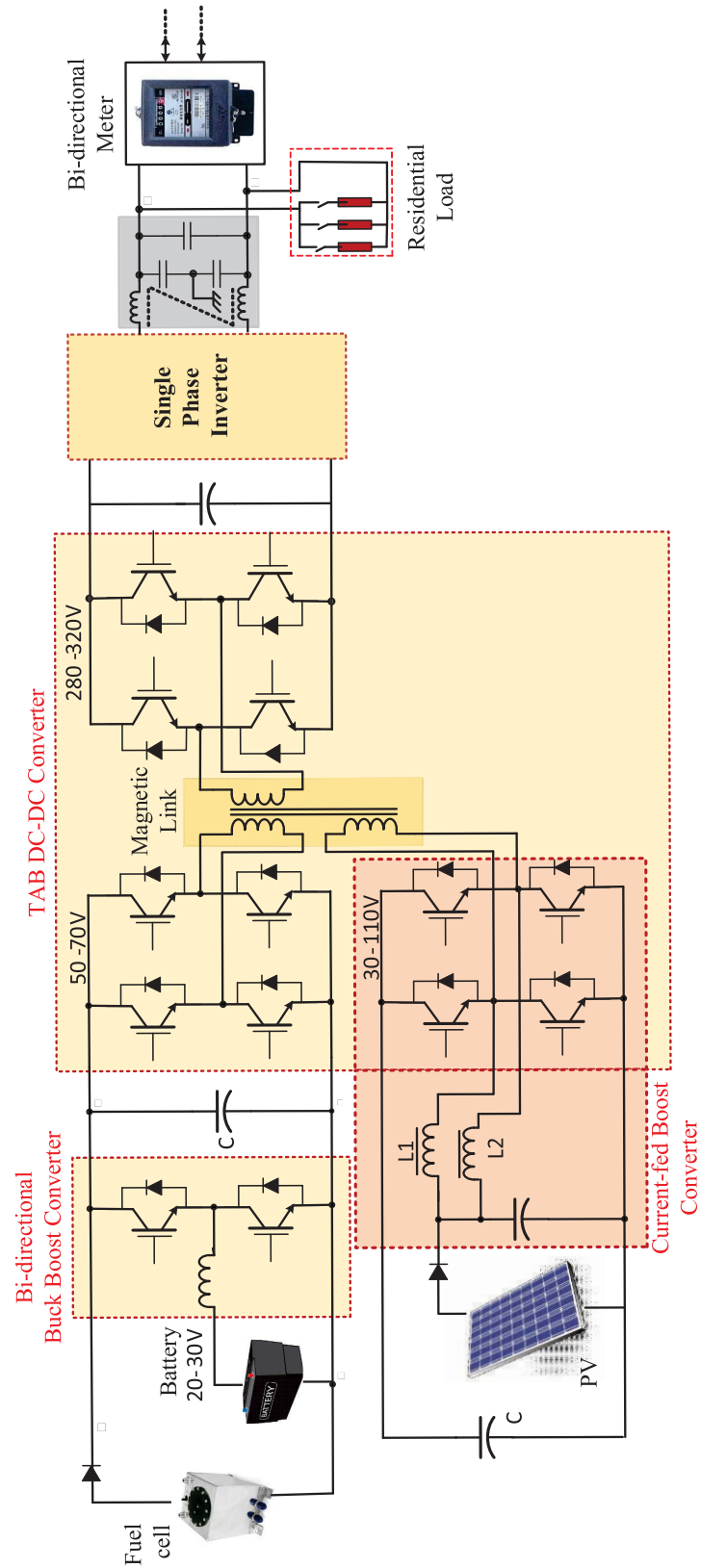


Fig.3.2 Structure of proposed multi-active bridge phase shift converter.

### 3.4 Selection of DC-DC Converter Topology for Battery

Batteries as the main energy storage device in the proposed micro-grid should be able to be charged and discharged on demand. Bi-directional buck-boost dc-dc converters have been widely used to charge and discharge the batteries in renewable energy systems [3.13]-[3.15]. In this research a bi-directional buck-boost converter is used to link the battery to the micro-grid as illustrated in Fig.3.2. It is used to boost the battery voltage (20-30 V) to the bus voltage level (50-70 V) and also controls the charge and discharge currents of the battery. The converter is connected in parallel to the fuel cell bus to balance the voltage of the bus due to the slow dynamic response of a fuel cell. Therefore, the battery port remains in stand-by condition during the fuel cell operation. On the other hand, the battery can be used to supply the load and send energy to the grid by discharging into the fuel cell bus when the bi-directional converter is operating in boost mode. It can be charged by fuel cell, PV or grid when converter is operating in buck mode.

### 3.5 Basics of Operation in Steady State

As can be seen in Fig.2.18, the proposed micro-grid includes a TAB phase shift dc-dc converter, a buck-boost bi-directional converter, a double current-fed boost converter and a grid-connected single phase inverter. The proposed system is designed to supply a 4.5 kW residential load by combining the energy of a PV array, fuel cell stack and the battery bank. It is controlled by a Texas instrument DSP (C2000/TMS320F28335) at device level and a PC system as energy management unit (EMU) at the system level. The EMU communicates with the regional distribution network control centre via internet (either cable or wireless) to manage the system energy based on the short-term and long-term plans. The phase shift converter includes three H-bridge units to generate a high frequency square-wave voltage from a dc source and apply it to the corresponding winding of the magnetic link. To control the power flow, ports two and three are shifted for a leading or lagging phase angle to send or receive power to the port one as the reference port. To extract the maximum power from PV array, a duty cycle control is applied to the port three. Port one is a bi-directional port that transfers power from renewable sources or battery to the inverter and further to the load and grid. It also is used in the reverse direction to transfer the power from the grid to the battery (using port two and four simultaneously). A 40-60 V, dc bus links port two to the fuel

cell stack and to the battery via bi-directional buck-boost converter to charge the battery in the buck and discharge it in the boost mode. The fuel cell stack can be used as energy back up source and PV is considered as the preferred source to supply the load and possibly the grid. The battery bank is used as energy storage device and also balances the voltage of dc bus due to the low dynamic response of fuel cell. It can be charged by any one of the fuel cell, PV or grid. The magnetic link presented as multi-winding transformer (MWT) provides isolation and flexibility in the direction of power flow between the ports. It facilitates the operation of the system in different modes according to the direction of power flow. The operation mode of the micro-grid is controlled according to the long-term and short-term predictions of PV generation and load demand, for different energy management scenarios in both grid connected and islanding modes. Details of the system operation modes will be reported on in the future chapters. The leakage inductances of the windings are used as energy transfer components in the phase shift converter [3.16]-[3.19]. This requires the magnetic link to be designed for certain values of inductances according to the desired operating phase shift at the required power throughput. On the other hand, design of multi-winding magnetic structures for certain values of inductances is difficult. Using external bulk inductors in series with the transformer windings is suggested although it increases the size and cost of the converter [3.18]-[3.20]. Using external inductances can be avoided in case of small values of required leakage inductances by including desired values in the design process. In this paper, the magnetic link is optimally designed for certain values of inductances.

### **3.6 Modular Design as An Option for Off-grid Consumers**

The main point related to off-grid consumers is their wide range of demanded power changing from less than 1 kW to 20 kW and even more. This feature prevents designers from designing a unique system with a particular range of power for them. Therefore, a renewable energy system with modular converters is a feasible solution for this group of consumers. The modular structure is applicable to a wide range of users with different demands. It also provides other features, such as higher reliability and efficiency, flexibility and power quality. It has been seen that the efficiency of power electronic systems normally decreases in light and full load conditions and it improves under the medium load conditions [3.21]. On the other hand, the normal load profile of residential consumers shows that these consumers most of the time (70 – 80 % of daily hours) are

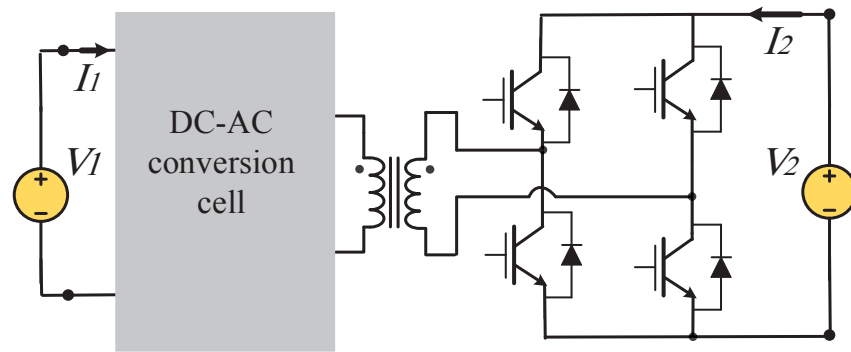
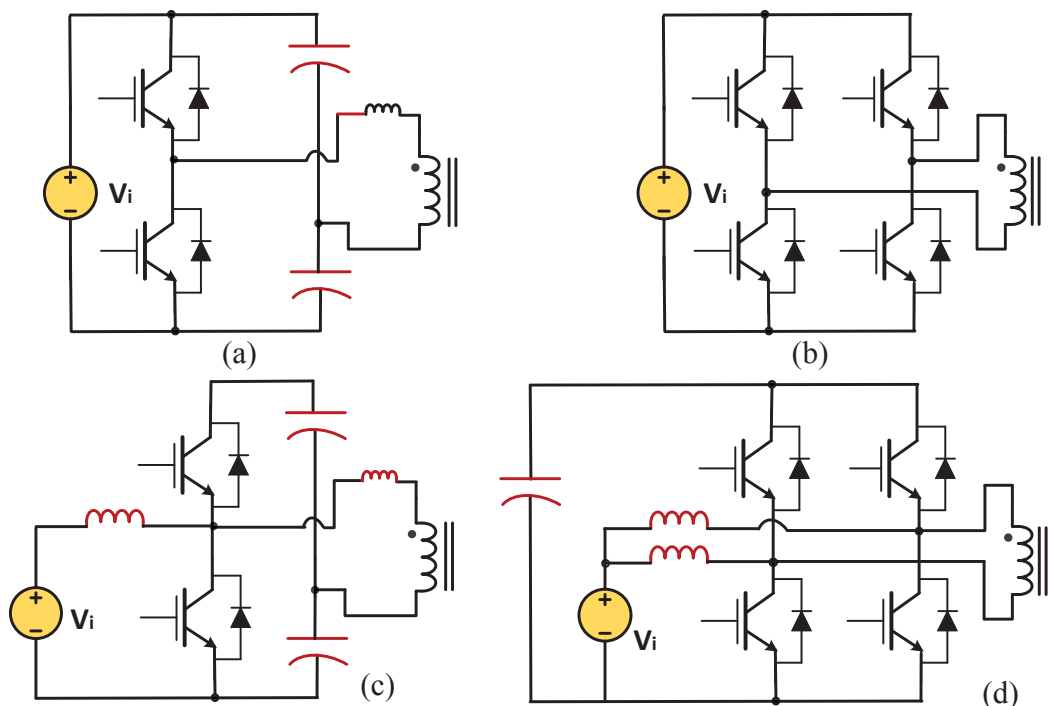
operating under the light or full load conditions. The modular structure can improve the converter efficiency both under the light and full load conditions [3.22], [3.23]. This improvement is based on management of the number of active and de-active modules according to the load conditions. The system can be designed so that all active modules operate at medium load with the highest possible efficiency when the overall load is considerably high. Under light load conditions, the number of active modules can be reduced by control unit which causes a moderate load and high efficiency operation for active modules. It also provides better marketing, maintenance and service capabilities for manufacturing companies. An elementary study was made on the possibility of modular design of the system which is not discussed in the thesis. The advantages of modular design for off-grid residential users are studied and the characteristics of modular and singular converters are compared [3.24].

### **3.7 Comparison of full Bridge, Half Bridge, Current-Fed Half Bridge and Inter-leaved Current-fed DC-DC Converters**

Phase shift converters are one of the best candidates for micro-grid applications as they are able to provide a controllable bi-directional power flow among the source, storage and loads [3.16]-[3.20]. The basic phase shift converter including two bi-directional ports is called a dual active bridge (DAB) converter. The topology can be extended to TAB and even multi-active bridge (MAB). As discussed in Chapter Two, section 2.9.4, the topologies of full bridge (FB), half bridge (HB), current-fed half bridge (CFHB), and current fed full bridge (CFFB) can be used as a dc-ac conversion cell in phase shift converters [3.25]. To select the appropriate converter for each port of the multi-port dc-dc converter, an accurate analysis of the conversion cells and comparison of their features is required. The next section provides a brief review of the main characteristics of the conversion cells.

#### **3.7.1 Performance analysis of the topologies**

Selection of an appropriate high frequency dc-ac conversion cell for the multi-port converter requires a detailed study on both characteristics of renewable source and performance of the conversion cell. Therefore a qualitative and quantitative performance analysis of the conversion cells is required at this stage of research.

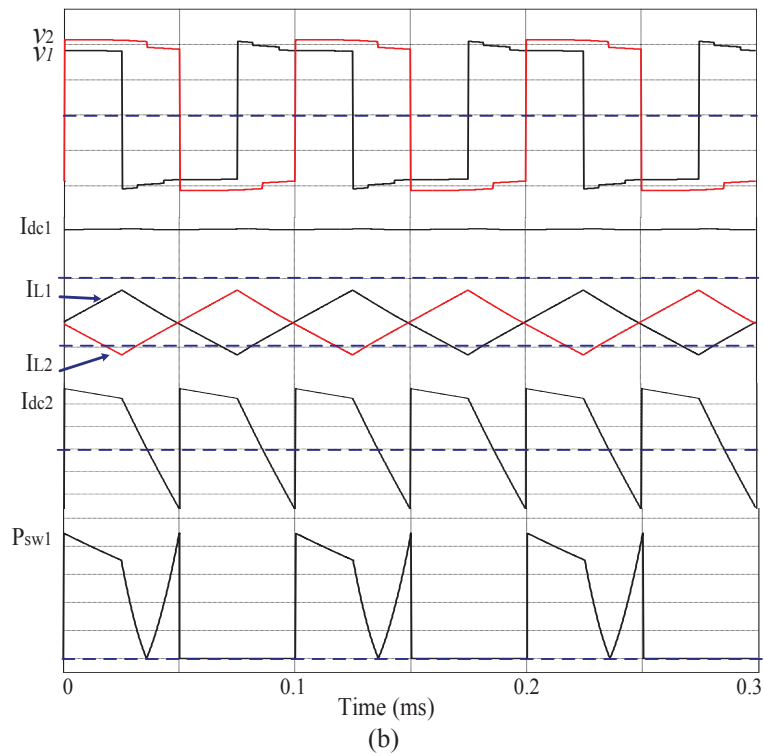
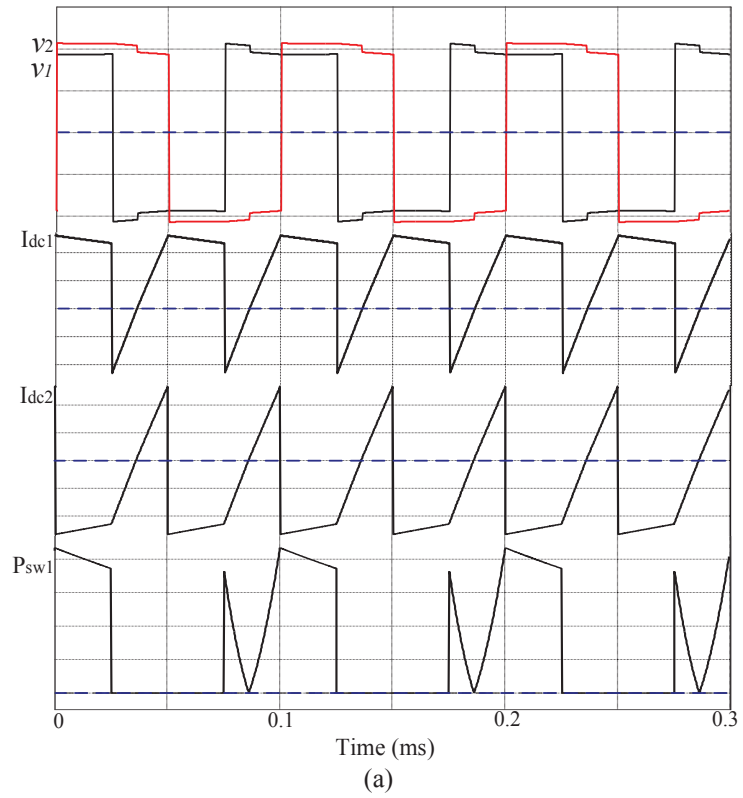

**Fig.3.3 Simulation circuit of DAB converter using PSIM**

**Fig.3.4 The simulated dc-ac converter cells, (a) half bridge, (b) full bridge, (c) current-fed half bridge and (d) current-fed full bridge.**

To study the main electrical characteristics of the cells, a DAB converter with a high frequency dc-ac conversion cell at one side and a full bridge port at the other side as presented in Fig.3.3 is simulated. The left hand side cell is selected to be one of FB, HB, CFHB or CFFB cells (presented in Fig.3.4) at each simulation step. The voltages  $V_1$  and  $V_2$  and transferred power from  $P_1$  to  $P_2$ , presented as  $P_{12}$ , are kept constant during all tests. The simulation test condition is  $V_1=V_2=100$  V,  $P_{12}=70$ W and transformer parameters are  $N_1=N_2=10$ ,  $L_1=L'_2=0.01$   $\mu$ H,  $L_m=50$  mH,  $r_{L1}=r_{L2}=0.01$   $\Omega$ ,  $R_m=50$   $\Omega$  and the switching device had real parameters.

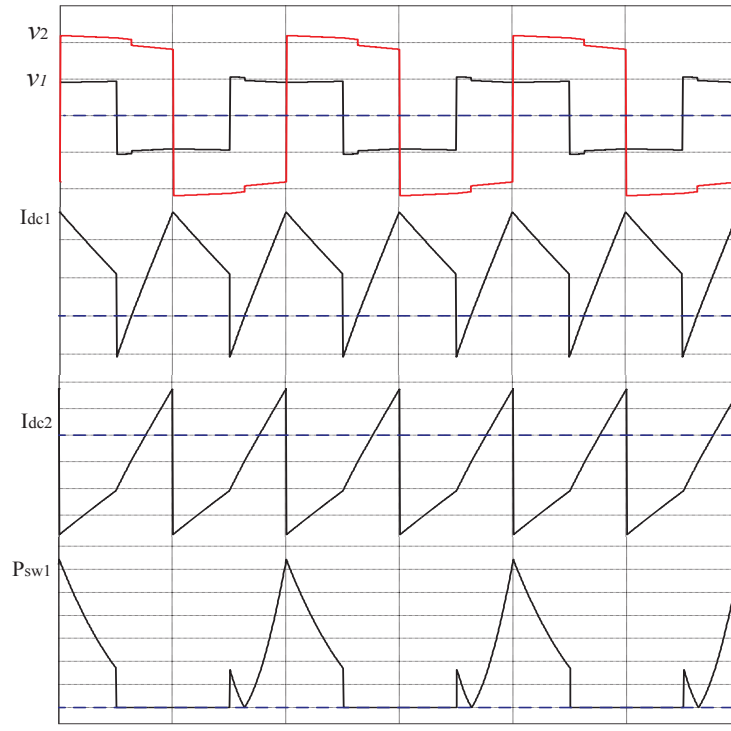
Fig.3.5(a) shows the simulated wave forms of transformer primary voltage,  $v_1$ , transformer secondary voltage,  $v_2$ , the current transferred from source one to source two,  $I_{dc1}$ , the current received by source two,  $I_{dc2}$ , and the power loss of one single switch,  $P_{sw1}$ , in the case of using the FB topology. Fig.3.5 (b) presents the same parameters for the inter-leaved CFFB topology. As can be seen, in this case the current in input source,  $I_{DC1}$ , is almost a constant dc with small ripples due to the use of interleaved inductors in the input and the complementary switching pattern. Fig.3.6 (a) shows the waveforms of the HB converter under the same input and load conditions. The amplitude of input current for the same transferred power is doubled compared with the FB as the amplitude of voltage on the primary of transformer is half due to the using two capacitors in series as voltage divider. In case of using the CFHB, the input current changes to the triangle form which reduces the current ripple although the percentage of ripple still is much more than the CFFB topology.

The recorded presented simulation results are used to evaluate characteristics of the topologies, such as efficiency, switching loss and current ripple factor. The simulation results are also used to compare the switching stress and the transients on the output power at the start time. As an example, the start-up current of the converter for three cases of using the CFHB, CFFB and FB are presented in Fig.3.7. It can be seen that under the same load and input conditions, the CFFB and CFHB topologies present a large overshoot in the output current and consequently output voltage. This is due to the use of inductors at the primary source  $V_1$  which operates as a current source. The overshoot is considerable due to the operation of converter in open loop mode and using a current control loop can reduce it considerably as can be seen in Chapter 5. Another solution to avoid such a problem is to use a soft start technique at the starting time which limits the start-up current of the converter by gradually increasing the duty cycle.

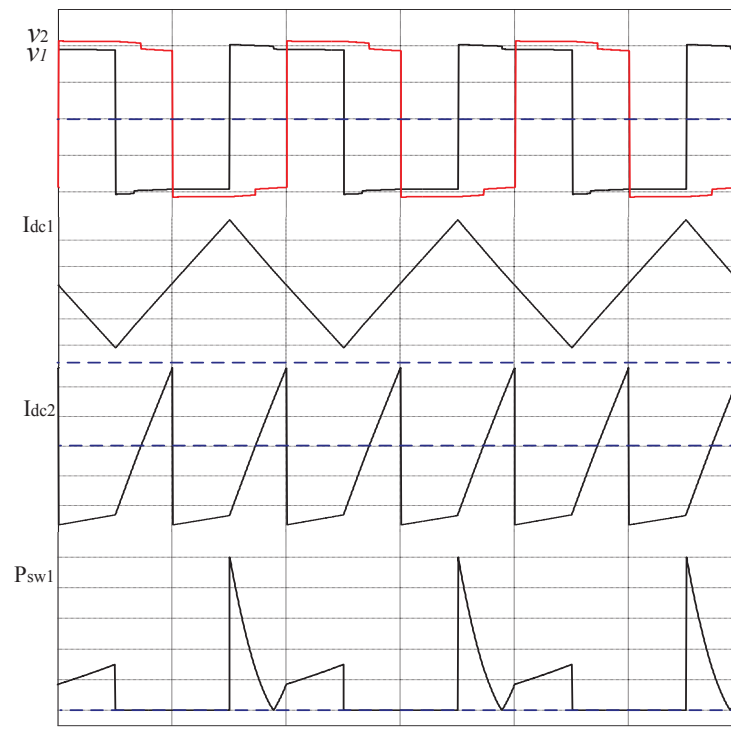
To study the characteristics of the topologies, other factors, such as cost, size of the circuit, efficiency, power flow range, reliability, switching loss, current ripple and control complexity, are also considered as the evaluation factors. The evaluation factors are normalized and integrated applying some weighting factors to find the final factor for each topology. More details on the evaluation method are provided in the next section.



**Fig.3.5 Simulated wave forms of transformer primary voltage  $v_1$ , transformer secondary voltage  $v_2$ , current transferred from source one  $I_{dc1}$ , current received by source two  $I_{dc2}$ , and the power loss of one single switch  $P_{sw1}$  in the cases (a) full bridge converter and (b) inter-leaved current-fed full bridge converter.**

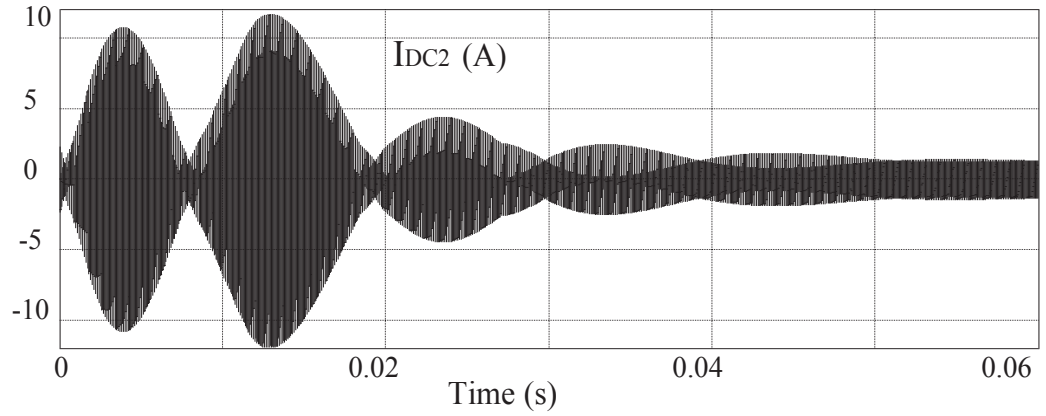


(a)

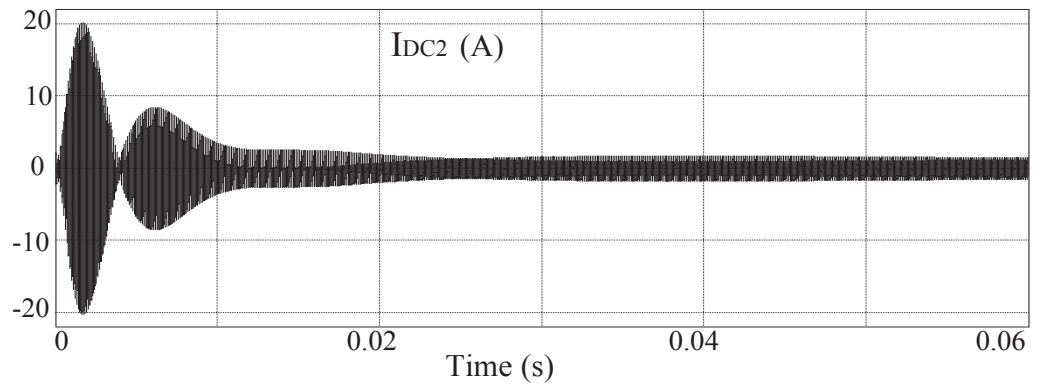


(b)

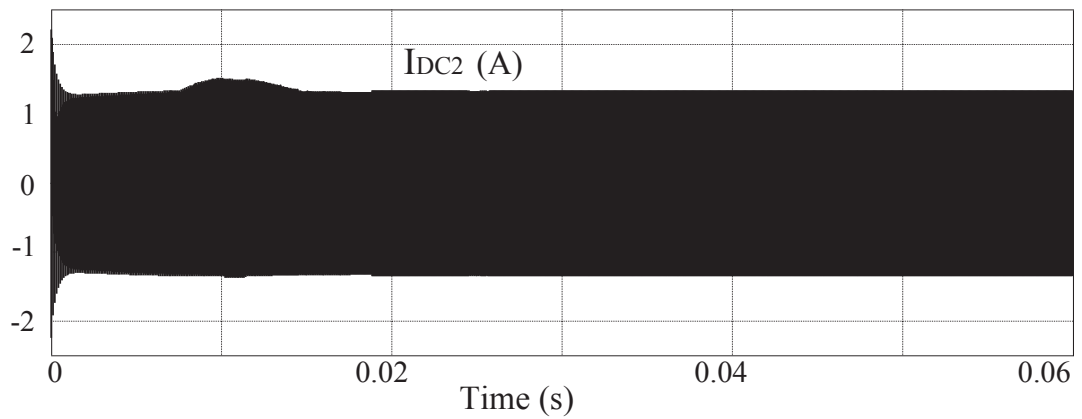
**Fig.3.6 Simulated wave forms of transformer primary voltage  $v_1$ , transformer secondary voltage  $v_2$ , current transferred from source one  $I_{dc1}$ , current received by source two  $I_{dc2}$ , and the power loss of one single switch  $P_{sw1}$  in the case of (a) half bridge converter and (b) current-fed half bridge converter.**



(a)



(b)



(c)

**Fig.3.7 Start-up current of the cell topologies, (a) current-fed half bridge, (b) current-fed full bridge, and (c) full bridge.**

The selected cells are replaced in the simulated circuit, and the waveforms of the voltage, current, transferred power and switching power loss are recorded for each cell.

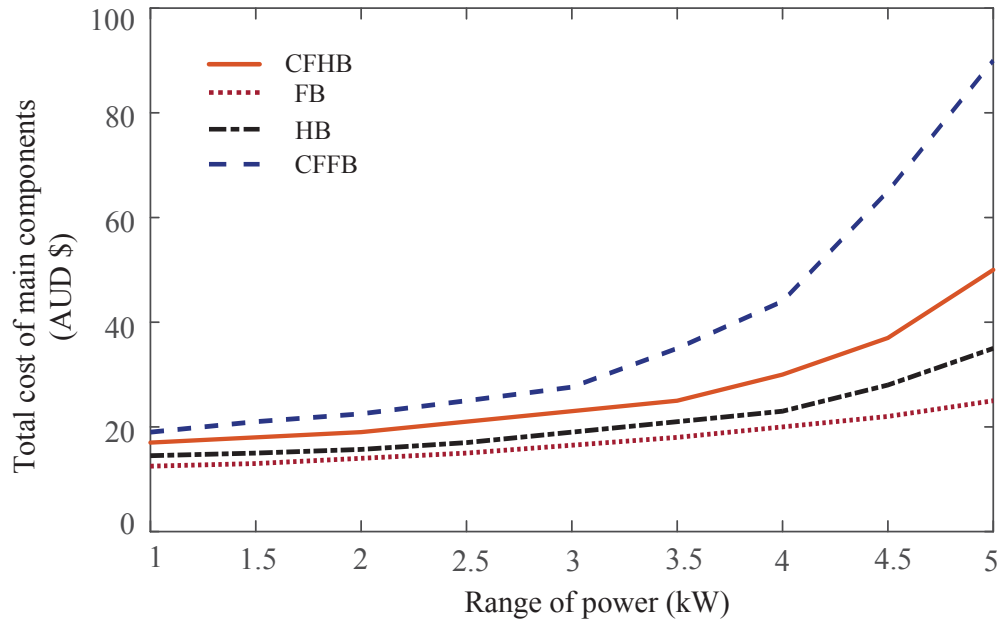


**Fig.3.8 Comparison of total cost for FB, HB, CFFB and CFHB topologies**

#### *A. Cost of topologies*

The cost of the topologies was evaluated on the basis of the number of main components and their average price in the market.

The main components of the topologies, such as switching device, diode, capacitor, inductor and transformer, have been taken into account. The total cost of the topologies is calculated for the power ranges from 1kW to 5kW using the average prices for the main components as presented in Fig.3.8. It can be seen that the total cost for the CFFB topology is the highest and for FB topology is the lowest for all ranges of rated power. Therefore, the normalized cost factors for FB, HB, CFHB and CFFB topologies can be estimated as 1, 0.86, 0.72 and 0.61 respectively where the higher value of the cost factor is allocated to the lowest cost.

#### *B. Size of topologies*

To evaluate the occupied size of each topology, the average size of included components is calculated by

$$A_k = 1.2 \left( \sum_{i=1}^{N_k} A_i \right) h_{\max} \quad (3.1)$$

where  $A_i$  is the seated area of  $i$ -th component on PCB and  $h_{\max}$  the height of the highest component. A 20% additional area is considered as spare area among the components. Table 3.1 shows the estimated size of each topology for different ranges of rated power. It was seen that the estimated size of the FB topology is less than others because it includes no capacitor and no inductor, while the HB topology needs two capacitors and in the CFHB an inductor should be added to the capacitors. The highest size belongs to the CFFB topology with two inductors and four switching devices.

**TABLE 3.1 Estimated Sizes of FB, HB, CFHB and CFFB Topologies**

Power range	1 kW	2 kW	3 kW	5 kW
Topology				
FB	112 cm <sup>3</sup>	144 cm <sup>3</sup>	144 cm <sup>3</sup>	150 cm <sup>3</sup>
HB	146 cm <sup>3</sup>	146 cm <sup>3</sup>	156 cm <sup>3</sup>	164 cm <sup>3</sup>
CFHB	180 cm <sup>3</sup>	180 cm <sup>3</sup>	216 cm <sup>3</sup>	224 cm <sup>3</sup>
CFFB	210 cm <sup>3</sup>	220 cm <sup>3</sup>	250 cm <sup>3</sup>	280 cm <sup>3</sup>

### C. Power transfer ratio

Power transfer ratio shows the efficiency of power transferred from source  $V_1$  to  $V_2$  for phase shift angle ranges between 0 to  $\pi/2$ . To evaluate this factor the power extracted from  $V_1$  to  $V_2$ , known as  $P_{12}$ , is measured in the simulated circuit. The efficiency factor was defined as the ratio of transferred power ( $P_{12}$ ) to the input power ( $P_1$ ) for each topology as the following

$$\eta_k = 100 \frac{P_{12}}{P_1} \quad (3.2)$$

The simulation results are shown in Fig.3.9. It can be seen that at the lower phase shift angles the efficiency of power transfer decreases in all types of topologies and the highest efficiency can be achieved around the phase shift angles of 30-60 degrees. The efficiency of HB, FB, and CFHB is higher than CFFB especially with low phase shift angles.

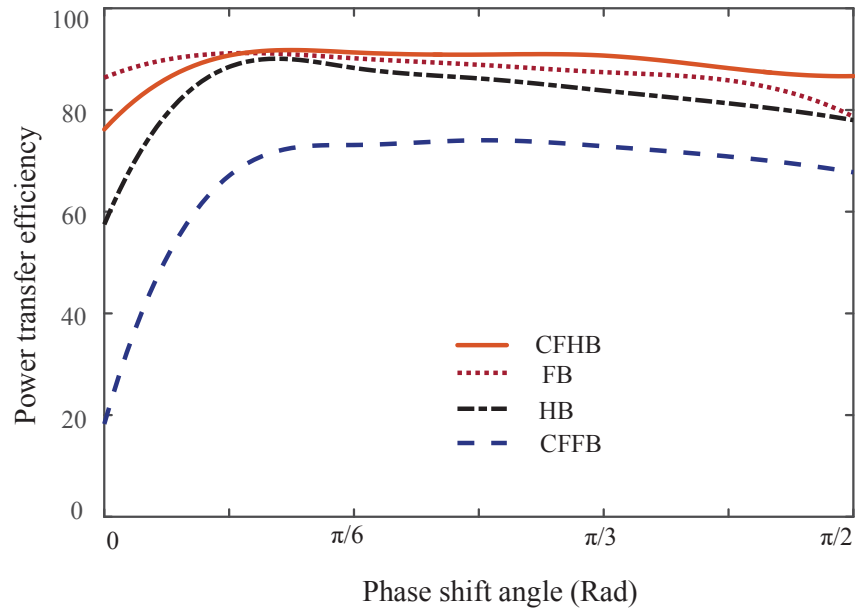


Fig.3.9 The power transfer efficiency versus phase shift angle.

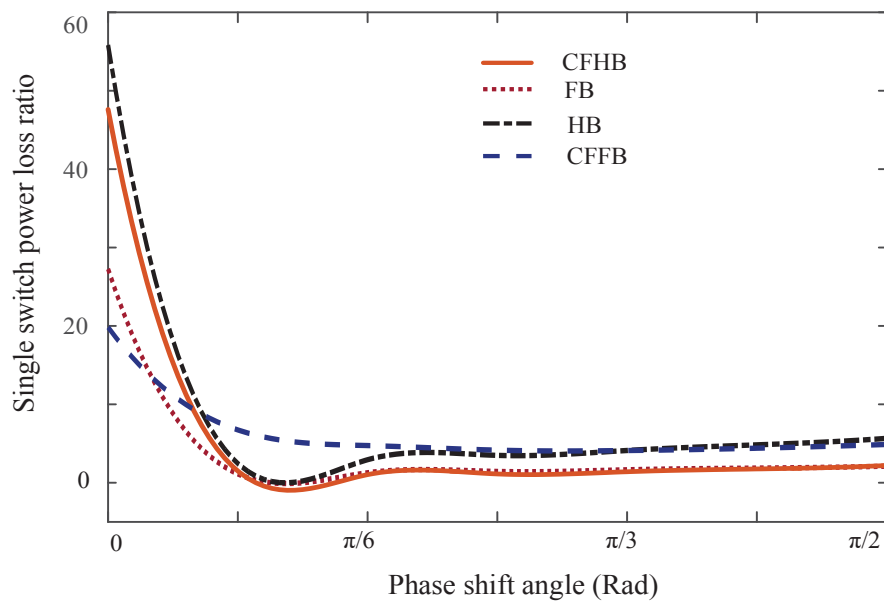


Fig.3.10 Comparison of switching power loss of FB, HB, CFHB and CFFB topologies

#### D. Single switch power loss ratio

The switching loss is another indicator to study the performance of the topologies. The simulated circuit of DAB converter employing real characteristic switching device was used to measure the loss. Single switching power loss ratio was defined as ratio of loss in one switch to input power. It was measured for all topologies under the same load conditions using simulated circuit. It was seen that the switching loss of HB and CFHB are higher than that of other topologies at lower phase shift angles (Less than  $\pi/12$ ). Increasing phase shift angle raises the loss on the switching device although HB

and CFFB topologies present higher loss compared with others as can be seen in Fig.3.10.

### *E. Reliability assessment*

The reliability of the topologies is an important factor to evaluate the conversion cells especially for converters with off-grid applications [3.26]-[3.28]. There are two main factors related to reliability known as failure rate and life time of the topology. The failure rate is defined as the number of failures during a specific test time of components [3.28] and it is used to calculate the mean time between failures (MTBF). On the other hand, the life time is an expected average time maintaining the required performance before the wear-out. Fig.3.11 shows the relation between failure rate and life time of components. In general, the reliability assessment of the converter depends on the reliability of each main block of the converter and the reliability of each block depends on failure rate of its included components.

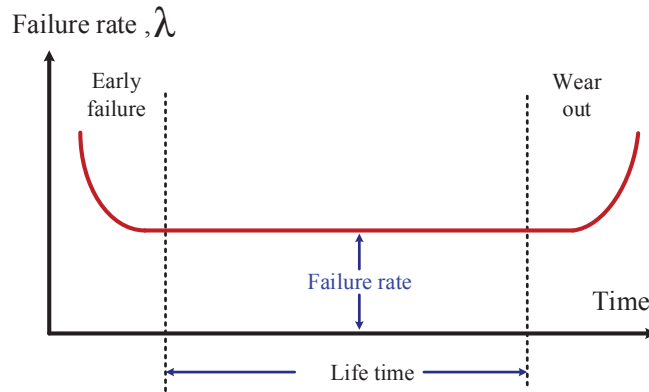


**Fig.3.11 The relation between failure rate and life time for components of a circuit**

To evaluate the reliability of each topology, the MTBF and LT of the topology needs to be calculated. The MTBF for each conversion cell is defined as the inverse of its failure rate as the following

$$MTBF = \frac{1}{\lambda_s} \quad (3.3)$$

where  $\lambda_s$  is defined as the sum of failure rates of all included components, or

$$\lambda_s = \sum_{j=1}^m \lambda_j \quad (3.4)$$

and  $\lambda_j$  is the component failure rate per million hours. The failure rate of components can be defined for a period of one million hours according to the military hand book of MIL-HDBK-217 and is calculated by

$$\lambda_j = \lambda_b \prod_{k=1}^n \pi_i \quad (3.5)$$

where  $\lambda_b$  is the base failure rate of component and  $\pi_i$  the  $i$ -th modification factor which modifies the base failure rate according to the environmental and operational conditions which affects the reliability of the component. The life time of each topology is equal to the life time of the component with minimum life time compared with other components and is defined as

$$LT = \text{Min}(LT_{IGBT}, LT_{Capacitor}, LT_{Inductor}) \quad (3.6)$$

Therefore, to define the failure rate of each topology, the failure rate and life time of the main components of the topologies in temperature (70 C°) are evaluated as presented in Table 3.2. The reliability factor of each topology can be defined as the normalized MTBF and LT as the following

$$R.F = \frac{MTBF}{MTBF(\text{max})} \times \frac{LT}{LT(\text{max})} \quad (3.7)$$

In (3.7), the MTBF (max) and LT (max) are the maximum values of these parameters among the topologies. The results of reliability comparison are shown in Table 3.3. As shown, the FB topology provides the best reliability as it does not have any installed capacitor.

**TABLE 3.2 Value of Failure Rate and Life Time For Three Main Components of Topologies**

Component	IGBT	Capacitor	Inductor
Failure Rate (/1000000 hours)	0.241	1.071	0.012
Life time (hour)	458,000	125,000	2,153,000

**TABLE 3.3 Comparison of Reliability Factor for Four Topologies**

Topology Parameter	FB	HB	CFHB	CFFB
MTBF	1,037,344	381,097	379,362	648,200
Life time (hour)	458,000	125,000	125,000	260,000
Reliability Factor (R.F)	1.00	0.74	0.62	0.84

### F. Complexity assessment

To compare the complexity of the topologies, some indicators such as number of switching devices, number of driving signals, number voltage balance circuits and number of parameters that need to be controlled (voltage or current) are considered. The reason that the number of switching device is considered as a complexity indicator is that each switching device means a gate drive signal and drive circuits which increases the complexity of the converter. The complexity factors of the topologies are compared in Table 3.4 and the topology with less complexity obtains higher grade.

**TABLE 3.4 Complexity Factors of The Topologies**

Complexity element Topology	Number of switching devices	Number of controllable parameters	Number of driving signals	Number of required voltage balance circuits	Complexity factor
FB	4	1	2	1	1
HB	2	2	2	2	0.8
CFHB	2	3	2	2	0.7
CFFB	4	2	2	1	0.9

### G. Current ripple factor

The next parameter that is used as a performance indicator is the ripples of current supplied by the voltage source. The simulated DAB circuit was used to measure this parameter. The current ripple factor is defined as

$$R(\text{ripple})\% = 100 \cdot \sqrt{\frac{I_{rms}^2}{I_{av}^2} - 1} \quad (3.8)$$

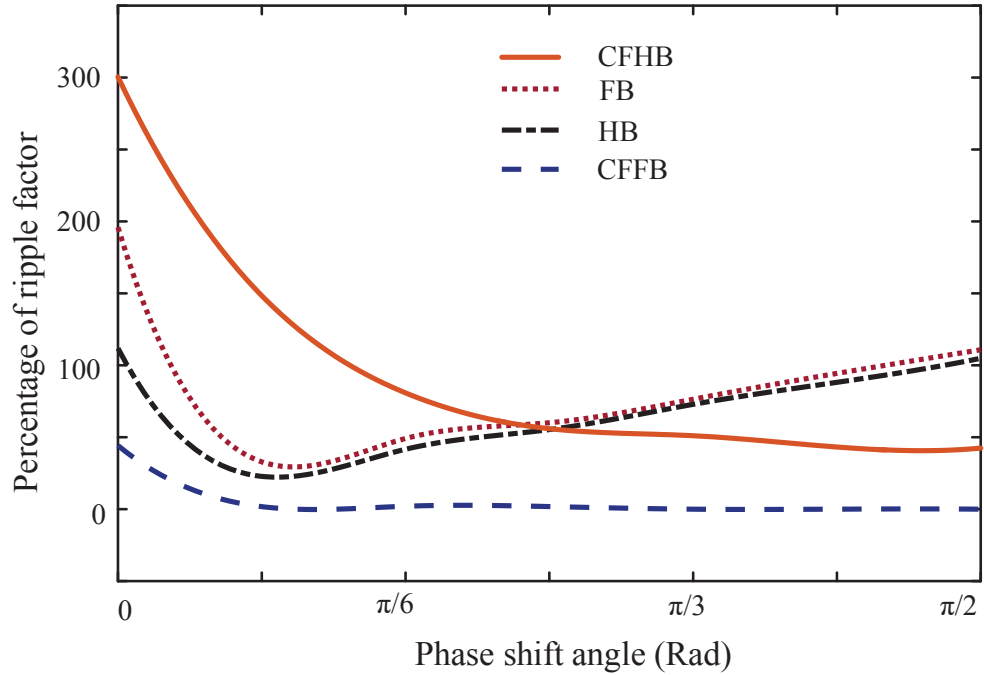


**Fig.3.12** The percentage of current ripple for all conversion cells

The current ripple factors of the topologies are calculated for different phase shift angles.

As shown in Fig.3.12, the value of current ripple in all topologies decreases as the phase shift angle increases. The value of the current ripple for the CFHB topology is higher than others for phase shift angles less than  $\pi/4$  while the FB and HB topologies present higher ripples for higher phase shift angles. The CFFB topology presents the lowest current ripples throughout the entire range of phase shift angle.

#### **H.** Power transfer range

The last factor of performance evaluation is the power transfer range. The simulated circuit is used to measure the transferred power for all topologies of conversion cells under the same load and input conditions. The transferred power from port one to port two for all topologies are measured and normalized as presented in Fig.3.13.

It can be seen that the CFFB topology provides the maximum power transfer ratio compared with other converter cells.

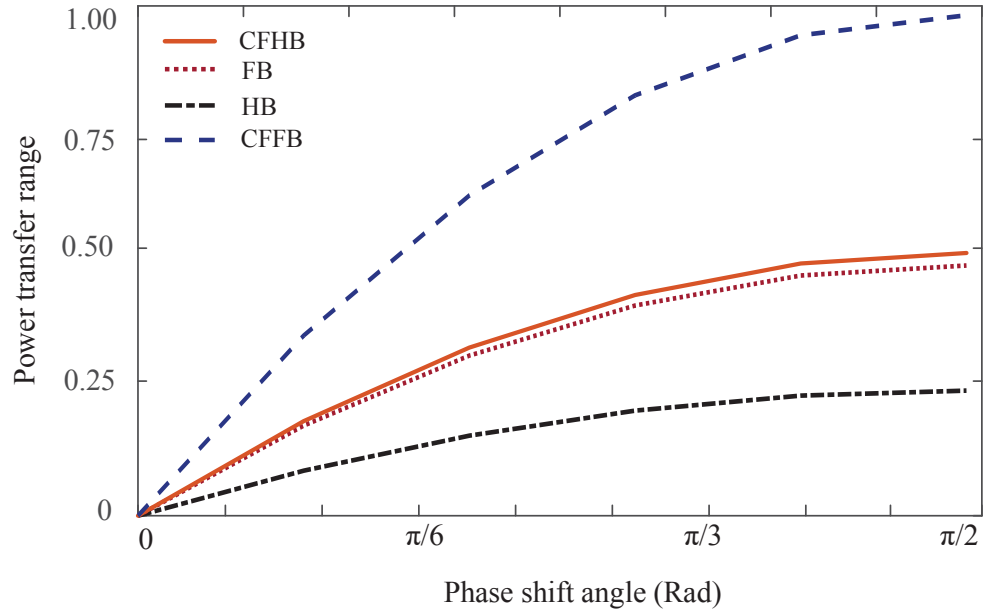


Fig.3.13 Power transfer range of all topologies versus phase shift angle

### 3.8 Overall Evaluation of the Topologies

It is possible to assess the overall performances of the topologies, using the evaluated factors under the same input and output conditions. To do the assessment, the evaluated factors should be normalized as the first step and then added together with appropriate weighting factors. The normalization equation is based on the difference between maximum and minimum values of the parameters as the following

$$X_i(norm) = \frac{X - X_{min}}{X_{max} - X_{min}}, \quad 0 \leq X_i(norm) \leq 1 \quad (3.9)$$

where  $X_i(norm)$ ,  $X_{max}$ ,  $X_{min}$ , and  $X$  are the normalized, maximum, minimum and actual value of the parameters, respectively. A weighting factor for each parameter should be defined to apply the importance of the parameter in the entire converter topology and summation of all weighting factors should be equal to one, or

$$\sum_{i=1}^n \delta_i = 1 \quad (3.10)$$

where  $(\delta_i)$  is the  $i$ -th weighting factor. The overall evaluation factor,  $K$  for each of the topologies can be calculated by summing up all effective factors multiplied by their weighting factor as

$$K = \sum_{i=1}^n [\delta_i X_i(\text{norm})] \quad (3.11)$$

Table 3.5 shows the normalized parameters of the topologies as indicators to compare their performances. Table 3.6 shows the selected weighting factors for evaluation of quality of three topologies. The final results are shown in Table 3.7. As can be seen, the overall evaluation factor for the FB, HB, CFHB and CFFB topologies are 0.93, 0.79, 0.74, and 0.79, respectively. This means that the full bridge topology presents the best performance for our application taking into account the size, reliability, cost, current ripples, and switching loss as effective factors.

### 3.9 Design and Experimental Development of Micro-grid

In this section, the design and experimental development of the micro-grid is discussed, including the design and methodology of the dc-dc converters, measurement and protection circuits, and experimental development.

**TABLE 3.5 Normalized Parameters of Three Topologies**

Topologies	FB	HB	CFHB	CFFB
Evaluation parameters				
Cost	1.00	0.86	0.72	0.61
Size	1.00	0.80	0.70	0.60
Reliability	1.00	0.74	0.62	0.84
Control complexity	1.00	0.80	0.70	0.90
Current ripple	0.50	0.50	0.80	1.00
Switching loss	0.80	1.00	0.80	1.00
Efficiency	0.95	0.90	1.00	0.80
Power transfer range	0.80	0.60	0.80	1.00

**TABLE 3.6 Weighting Factors For Evaluation**

Evaluation parameters	Cost	Reliability	Efficiency	Switching loss	Current ripple	Size	Control complexity	Power transfer range
Weighting factor	0.27	0.23	0.10	0.08	0.05	0.10	0.05	0.12

**TABLE 3.7 The Final Results of Evaluation of The Topologies**

Topology	FB	HB	CFHB	CFFB
Result	0.93	0.79	0.74	0.79

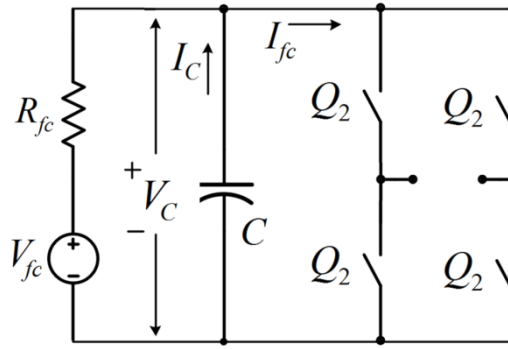


Fig.3.14 Fuel cell port and H-bridge unit

### 3.9.1 Design of TAB converter

As presented in Fig.3.2, the TAB converter includes three H-bridge dc-ac cells. To design the converter, it is required to define the voltage and current ratings of the H-bridge units. The voltage and current rating of the switching device and components of the low-pass filter are calculated as defined using nominal power of converter port, nominal range of voltage on the dc bus, desired efficiency and the acceptable range of current ripple derived from dc source. The design methodology presented here is based on simple approximations of the voltage and current waveforms and provides enough accuracy for our application although there is possibility for a more accurate design considering optimal operation conditions and maximum possible efficiency [3.29]. Fig.3.14 presents the fuel cell port including H-bridge switches Q1-Q4 and capacitor C as a low pass filter. According to the nominal power of the micro-grid and the TAB converter specifications and variation ranges, parameters of the fuel cell port are presented in Table 3.8.

TABLE 3.8 Specifications of The Fuel Cell Port

$V_{fc}(Max)$	$V_{fc}(rated)$	$V_{fc}(Min)$	$P_{rated}(kVA)$	$\eta$	$\Delta I_{ripple}$
70 V	60 V	50 V	2.5 kVA	$\approx 90\%$	200 mA

The *rms* current in each IGBT switch,  $I_Q(rms)$ , should be evaluated using the nominal current of the fuel cell port,  $I_{fc}(rated)$  as

$$I_{fc}(rated) = \frac{P_{rated}}{V_{fc}} = \frac{2500}{50} = 50 A \Rightarrow I_Q(rms) = 50 / 2 = 25 A \quad (3.12)$$

The maximum power loss on each switch considering the desired efficiency of the H-bridge cell can be determined as

$$P_{Q-loss} \approx \frac{P_{rated}(1-\eta)}{4} = \frac{2500(1-0.9)}{4} \approx 60W \quad (3.13)$$

### 3.9.2 Bi-directional buck-boost converter

The bi-directional buck-boost converter should be designed to operate in the boundary between the conventional continuous-conduction mode (CCM) and discontinuous-conduction mode (DCM), which can be achieved through applying a complementary gating control [3.30]. Therefore, the inductor current should change between negative and positive values. The converter is able to continuously change from buck operation mode to the boost mode by changing the duty ratio of  $Q_1$  and  $Q_2$ . In conventional buck-boost converters only  $Q_1$  and  $D_2$  are actively contributing during buck mode and  $Q_2$  and  $D_1$  are active in boost mode and the converter operates in CCM in both operation modes as presented in Fig.3.15.

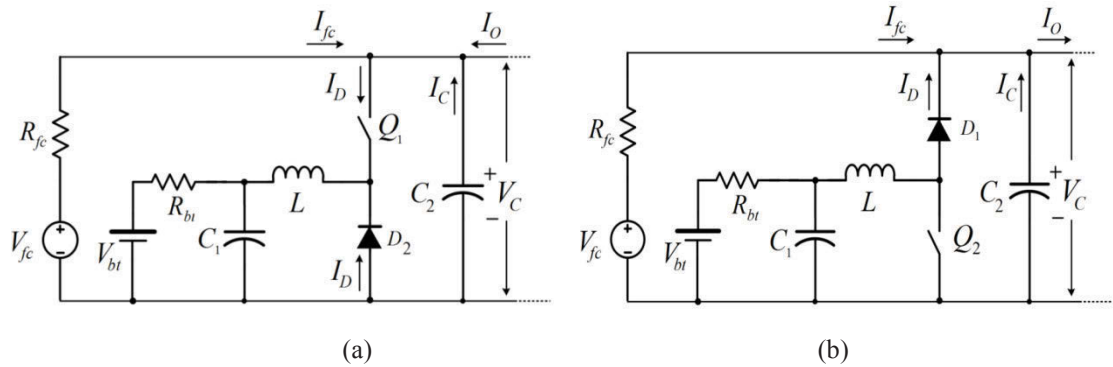


**Fig.3.15 Schematic of conventional bi-directional buck-boost converter during, (a) buck operation and (b) boost operation modes**

In the complementary gating control,  $Q_1$ ,  $Q_2$  and their anti-parallel diodes  $D_1$  and  $D_2$  are used during a complete cycle. More details on the steady state operation of the converter are provided in Chapter Five. The main component in the converter is the inductor which has a significant effect on the converter operation modes and performance. The average value of inductor current can be found by

$$I_{L\_avg} = \frac{P_{bat}}{V_{bus2}} \quad (3.14)$$

where  $I_{L\_avg}$  is the inductor average current and  $P_{bat}$  the nominal power of battery port. Considering  $I_{L\_max}$  and  $I_{L\_min}$  as the maximum and minimum values of inductor current, the inductor current ripple  $\Delta I_L$  in buck mode can be defined as

$$\Delta I_L = \frac{1}{2} \frac{V_{bus2} - V_{bat}}{L} D T_s \quad (3.15)$$

where  $D = V_{bat}/V_{bus2}$  is the duty cycle of  $Q_1$  and  $T_s$  the switching period. The maximum and minimum value of inductor current can be found by

$$I_{L\_max} = I_{L\_avg} + \Delta I_L, \quad I_{L\_min} = I_{L\_avg} - \Delta I_L \quad (3.16)$$

The *rms* value of inductor current can be determined by

$$I_{L\_rms} = \sqrt{(I_{L\_avg})^2 + \frac{(\Delta I_L)^2}{3}} \quad (3.17)$$

To guarantee the soft-switching operation of the converter, the inductor current should always swing between a negative and positive value and never enter the CCM operation area [3.30]. The condition can be applied as  $\Delta I_L < I_{L\_avg}$  and  $L < L_C$ . The critical inductance  $L_C$  can be determined by

$$L_C = \frac{1}{2} \frac{(V_{bus2} - V_{bat})}{P_{bat}} \frac{V_{bat}^2}{V_{bus2}} T_s \quad (3.18)$$

On the other hand reducing inductance increases the current ripple and  $I_{L\_max}$  and  $I_{L\_min}$  are a function of inductance. Therefore, the minimum value of inductance is limited by the current rating of selected IGBT switch. The maximum and minimum values of inductor current for a wide range of inductance from less than critical inductance  $L_C$  to more than it is presented in Fig.3.16. It can be seen that the appropriate range of inductance is 8-13  $\mu\text{H}$  considering 70 A as the IGBT current rating. The effect of variation on bus voltage on the inductance range is not considerable. Selection of IGBT switches is carried out based on the maximum and *rms* currents and the blocking voltage during switching which is equal to  $V_{bus2}$ .

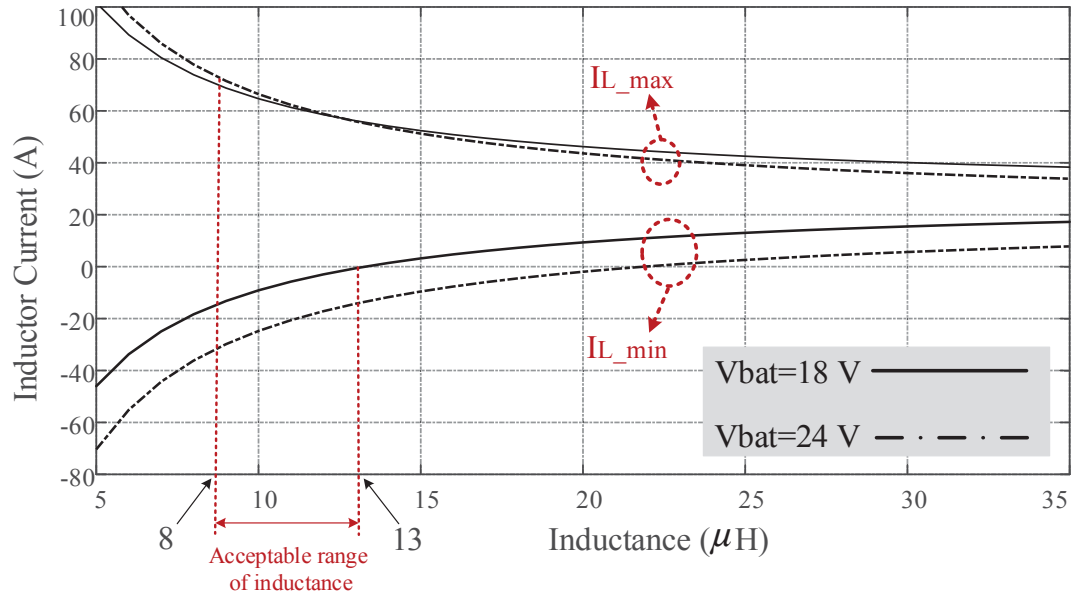


**Fig.3.16** The inductor maximum and minimum current versus inductance for  $V_{bus2}=100\text{ V}$  and  $V_{bat}=18\text{-}24\text{ V}$

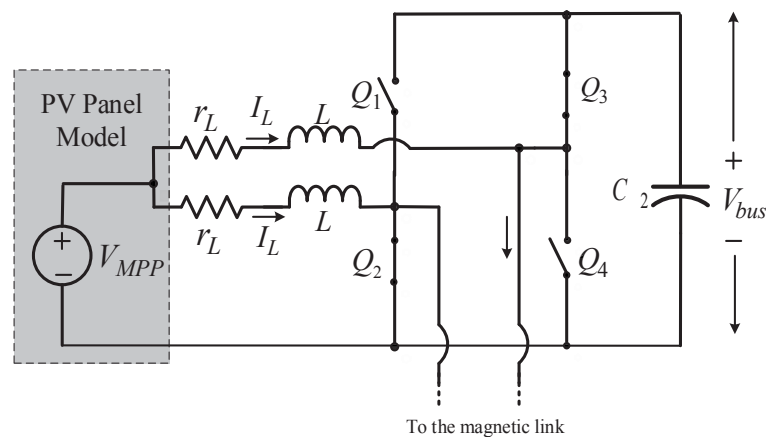


**Fig.3.17** Schematic of inter-leaved current-fed boost converter

### 3.9.3 Inter-leaved current-fed boost converter

The inter-leaved current-fed boost converter is designed to link the PV to Bus 3 of the TAB converter. The inter-leaved topology reduces the current ripple on the PV port which is an important factor on the dc-dc converter performance and stability of operation point on the maximum power point [3.31]-[3.33]. The converter should be designed to operate in CCM for the whole operation range to minimize the ripples on current derived from the PV panel. As presented in Fig.3.17 the converter contains two inter-leaved boost converters which are activated in a complementary pattern. It is assumed that in steady state operation both converters are operating independently and do not make any considerable effect on each other although they are connected to a

similar input source and output bus. According to this assumption, the design process is carried out for a single boost converter due to the similarity of their components and operation principles.

To design the converter the variation range of input voltage and output voltage should be considered. The output voltage of PV panels does not change in a wide range due to the irradiation level and temperature and the main effect is on the output current [3.34]. On the other hand, the voltage on Bus 3 should be almost constant although a limited variation range should be considered. Table 3.9 illustrates the information required for the interleaved current-fed boost converter design.

**TABLE 3.9 Electrical Characteristics of The PV Port**

$V_{PV}(\min)$	$V_{PV}(\max)$	$V_{PV}(\text{Nom})$	$V_{bus}(\min)$	$V_{bus}(\max)$	$V_{bus}(\text{Nom})$	$I_{PV}$
25 V	35 V	30 V	100 V	120 V	110 V	10-40 A
$V_d(\text{on})$	$V_{CE}(\text{on})$	<i>Ripple ratio</i>	$V_{\text{ripple @ battery}}$	$V_{\text{ripple @ bus}}$	$I_{bus}$	$f_s$
0.5 V	1.6 V	0.4	200 mV	500 mV	5-20 A	20 kHz

To determine the value of inductance, the worst operation case for the converter should be considered. The duty cycle of switch can be determined by

$$D = \frac{V_{bus} - V_{bat} + V_D}{V_{bus} - V_{SW} + V_D} \quad (3.19)$$

Considering the ripple ratio  $r = 0.4$ , and the minimum bus current as  $I_{bus\_min} = 5A$  then the minimum inductance that guarantees operation of converter in CCM can be determined by

$$L = \frac{V_{bus} + V_D - V_{SW}}{I_{bus} r f_{SW}} D(1 - D)^2 \quad (3.20)$$

The average value of current transferred to the dc bus and capacitor can be determined by

$$I_{bus}(\text{Avg}) = I_{PV}(1 - D) \quad (3.21)$$

### 3.9.4 Sensor and protection board

The voltages of Bus 1 linked to the inverter, Bus 2 linked to the fuel cell, Bus 3 linked to the PV and battery are required to control the micro-grid. They are also used to evaluate the transferred power and energy between the micro-grid ports. Furthermore the voltages of the ports are required to be monitored during the normal operation of system and should be sent to the over and under voltage protection circuits to prevent the system damage due to the voltage faults. Therefore, a sensor and protection board including voltage and current measurement sensors, signal conditioning and protection circuits is designed. More details on the measurement and protection circuit design for the proposed micro-grid are presented in the following sections.

#### *A. Voltage measurement*

To measure the voltage of the converter ports a closed loop (compensated) current transducer Hall effect voltage sensor LEM is selected. The selected sensor provides excellent accuracy and dynamic response. It presents very good linearity, low thermal drift and high immunity to external interference and can be used both in ac and dc measurements [3.35]. The output of sensor is a current proportional to the measured voltage passing through the series connection of external resistors R9 and VR6 as illustrated in Fig.3.18. The resultant voltage is proportional to the measured voltage, which is filtered out and amplified to the required level and is used for the following applications:

- (1) They are sent to a window comparator to be compared with high and low voltage references and which generates over-voltage and under-voltage fault signals. The fault signal is sent to the logic circuit on the control and interface board and further to the DSP for appropriate reaction.
- (2) The amplified signals should be sent to the control and interface board and further to the DSP as input to the closed loop PI controller.
- (3) The measured voltage and current signals are also transferred to the A/D converter, multiplexer and further to the PC through RS232 communication port. The transferred data is used by energy management unit to calculate and record the energy transferred between the ports.

- (4) The measured voltage and current of the PV are used as an input to the MPPT unit. The resulting MPPT reference signal then is sent to the DSP through control and interface board. On the other hand the battery voltage and current signals are used to evaluate the state of charge (SOC) of battery as an important factor for energy management process.

As can be seen in Fig.3.2, the energy management unit is implemented in a PC. The MPPT process is performed by PC through a MATLAB M-file and the signals of the measured voltage and current of PV panel are used as the input to the MPPT unit.

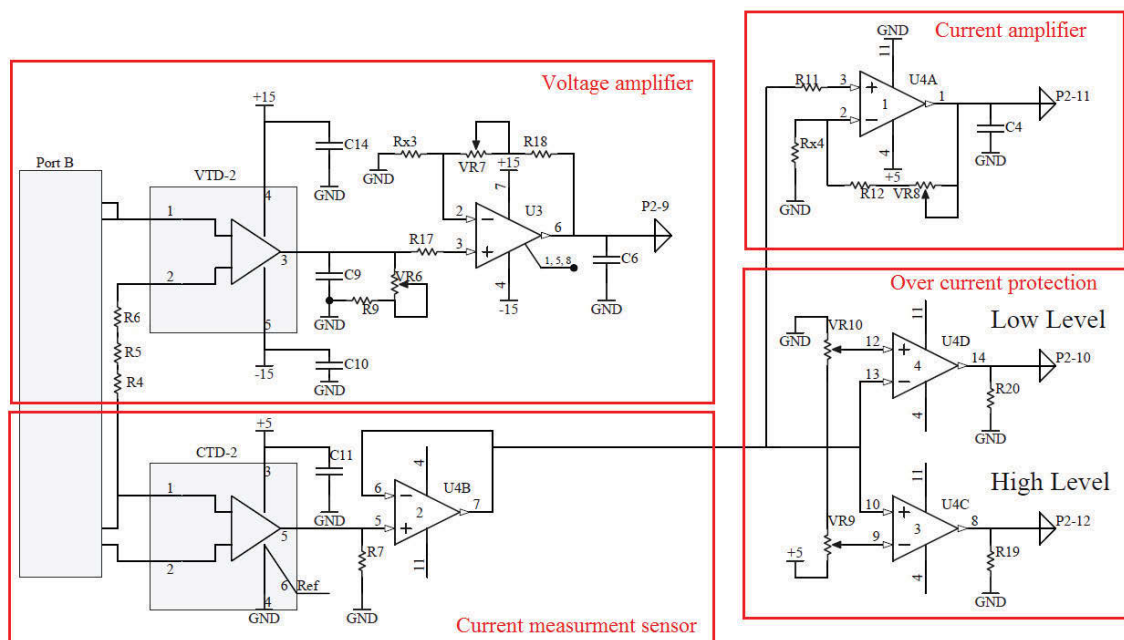


**Fig.3.18 Voltage and current measurement signal-conditioning and fault detection circuits**

As presented in the figure, resistors R4, R5 and R6 are used to drop the voltage to the voltage sensor level and the proportional compensation factor can be considered in the software due to the linear behaviour of the sensor.

### B. Current measurement

To measure the dc current of each converter port closed loop Hall Effect current sensors LTS 25NP made by LEM are used. The sensor has a compact format which facilitates its PCB mounting. It also provides excellent precision, good linearity and low temperature drift and can be used for both ac and dc measurements.

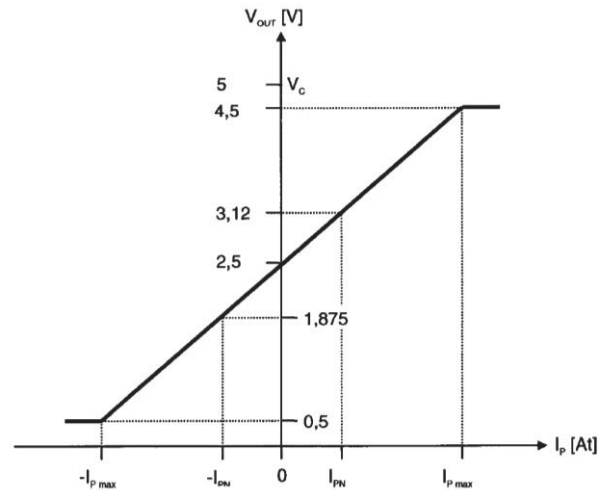


Fig.3.19 Input to output characteristics of current sensor LTS 25 NP [3.36].

The output of the sensor is a voltage proportional to the measured current changes between 0.5 for  $-I_p(max)$  to +4.5 V for  $+I_p(max)$  as presented in Fig.3.19 [3.36]. Therefore for zero current the output voltage is equal to +2.5 V. The output voltage of current sensor is buffered and sent to a current amplifier to change the appropriate variation range, as can be seen in Fig.3.18. It also is used to be compared with high and low references through a window comparator to detect the over current in both positive and negative directions.

The reason for this is that the current sensor generates a positive voltage for both current directions to match the output level to specific interfaces, such as the A/D converter of DSPs or microprocessors [3.37]. The outputs of overcurrent protection circuits of all ports are changed to the logic level and sent to the AND gate in the control and interface board. The resultant signal then is sent to the DSP as over current fault signal.

### 3.9.5 Driver board

A driver board is designed to drive the IGBTs of each leg of H-bridge cell and bi-directional converter. The drive signals are applied to the switching device through a hybrid integrated circuit, VLA567-01R made by Powerex as presented in Fig.3.20 [3.38]. The hybrid circuit is able to drive n-channel IGBT modules. It contains an internal isolated dc-dc converter which facilitates the gate drive process. It also has a built in short circuit protection circuit which provides gate lockout to maintain reverse bias for a predetermined time,  $T_{trip}$  after the detection of the short circuit [3.38].

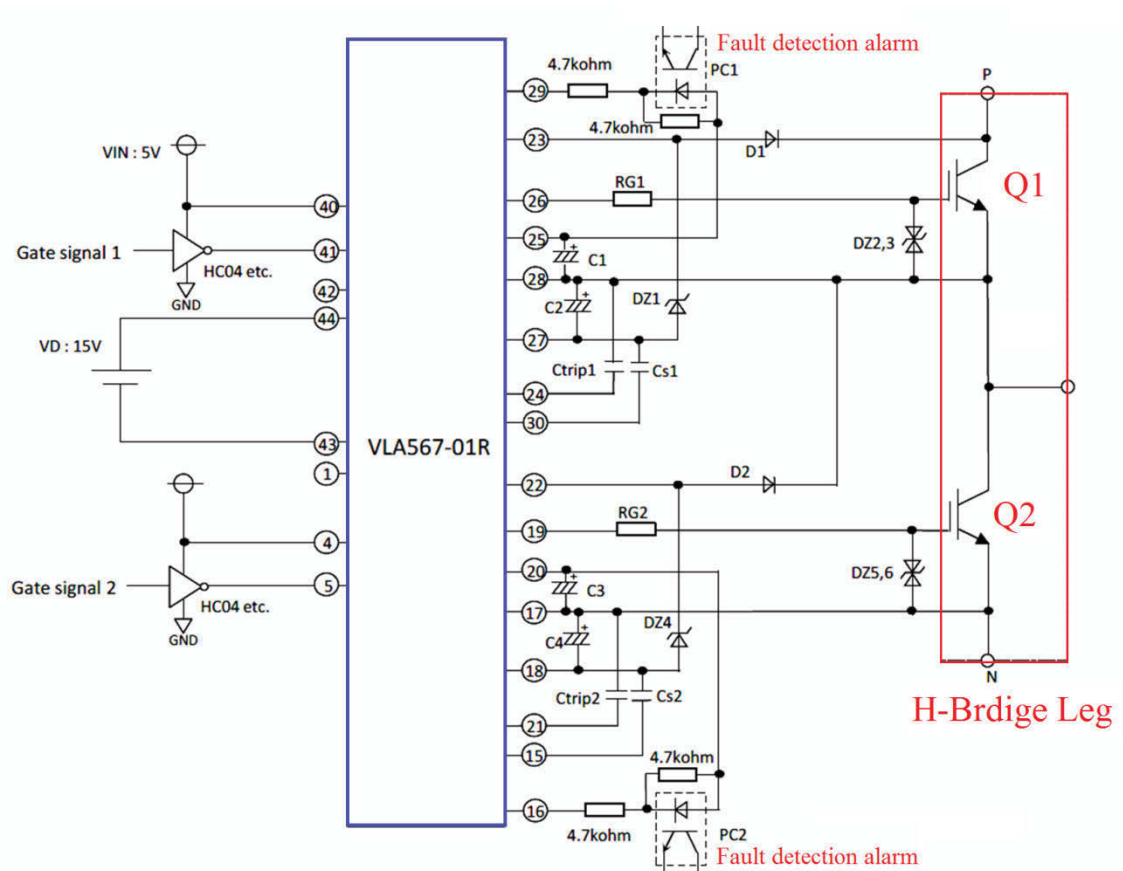
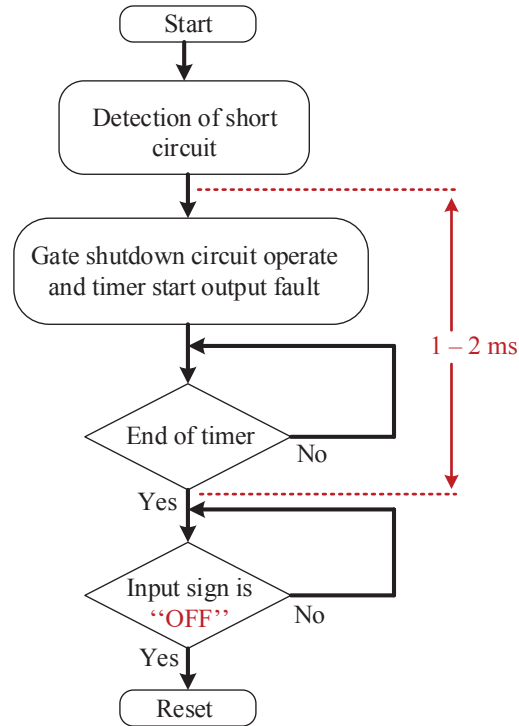


Fig.3.20 Schematic of driver board using VLA567-01R driver integrated circuit [3.38].

Other advantages of using the integrated circuit are electrical isolation voltage equal to 2500 V (*rms*) and CMOS Compatibility. The built-in short circuit detection compares the collector-emitter voltage of the switch during ON state  $V_{CE(ON)}$ , with a predefined voltage  $V_{CE(ref)}$ . During the normal operation of switch in ON state it is expected that  $V_{CE(ON)} < V_{CE(ref)}$ . In case of short circuit during ON state,  $V_{CE(ON)}$  increases due to the over current and  $V_{CE(ON)} > V_{CE(ref)}$ . This condition is recognized as short circuit by hybrid IC and reduces the gate voltage immediately. It also generates a short circuit fault signal which can be sent to the DSP as the main PWM signal generator to stop the gate signals. The protection circuit will reset after a minimum predefined shutdown time an OFF input signal is applied. Fig.3.21 presents the flowchart of short circuit detection process in hybrid integrated circuit. There is a small delay at the beginning time that IGBT is going to be turned on when gate signal is ON and  $V_{CE} > V_{CE(ref)}$  and this may be recognized as short circuit condition. To avoid this problem a short time  $T_{trip}$  is set so that the IGBT can be fully turned on before detection of a short circuit condition.



**Fig.3.21 Flowchart of short circuit protection process [3.38]**

The  $T_{\text{trip}}$  can be adjusted by a capacitor connected to pins 17 and 21 for Q1 as well as 28 and 24 for Q2 as presented in Fig.3.20. The opto-isolators PC1 and PC2 are activated by pins 16 and 29 to transfer the short circuit fault signal to the DSP.

### 3.9.6 Control and interface board

A control and interface board is designed to link the EMU, DSP and driver board. It contains the signal conditioning circuits to change the analogue protection signals such as over voltage, under voltage and over current to digital signals compatible with DSP I/O ports. It also buffers the PWM gate-drive signals and transfers them to the driver boards. It provides a data communication line with EMU through RS232 data transfer port.

### 3.10 Experimental Development

The proposed micro-grid is developed experimentally in the labs of Green Energy and Vehicle Innovations Centre (GEVIC), University of Technology Sydney. The PCBs are designed using Altium-designer-V9 and fabricated in the GEVIC workshop, as presented in Fig.3.22. The structure of developed prototype is presented in Fig.3.23.

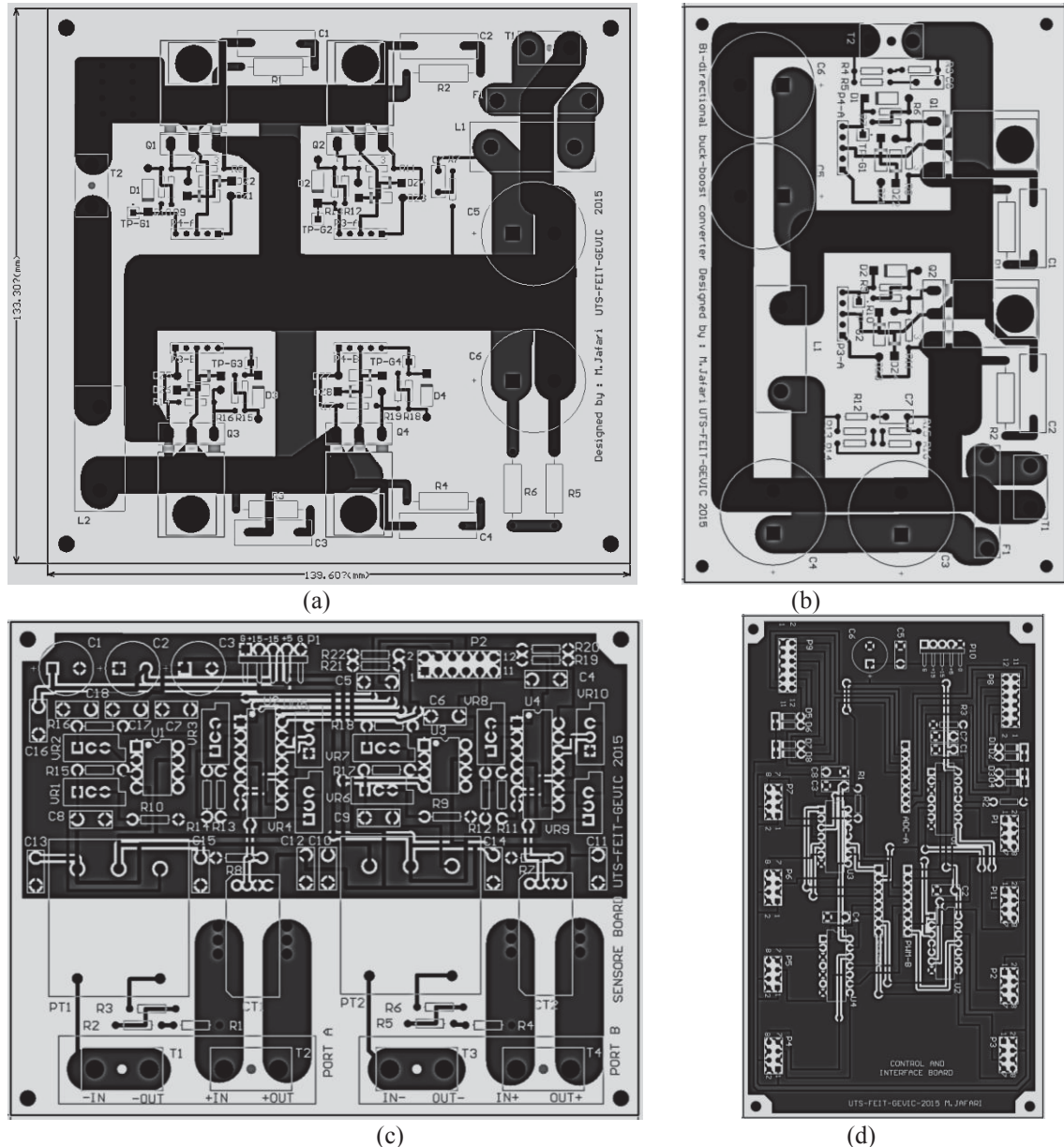


Fig.3.22 The designed and developed PCBs for the proposed micro-grid, (a) H-bridge board, (b) buck-boost converter, (c) sensor and protection board, and (d) control and interface board.

As can be seen, the developed prototype includes three H-bridge cells and multi-winding transformer to form TAB phase shift converter, a bi-directional buck-boost converter, two sensor and protection boards, a control and interface board and a C2000 DSP experimenter kit.

Each H-bridge cell contains two vertically plugged in driver boards and each driver board is designed to drive two IGBTs of an H-bridge leg. The IGBT switches are mounted on the heat sink using insulator pads.

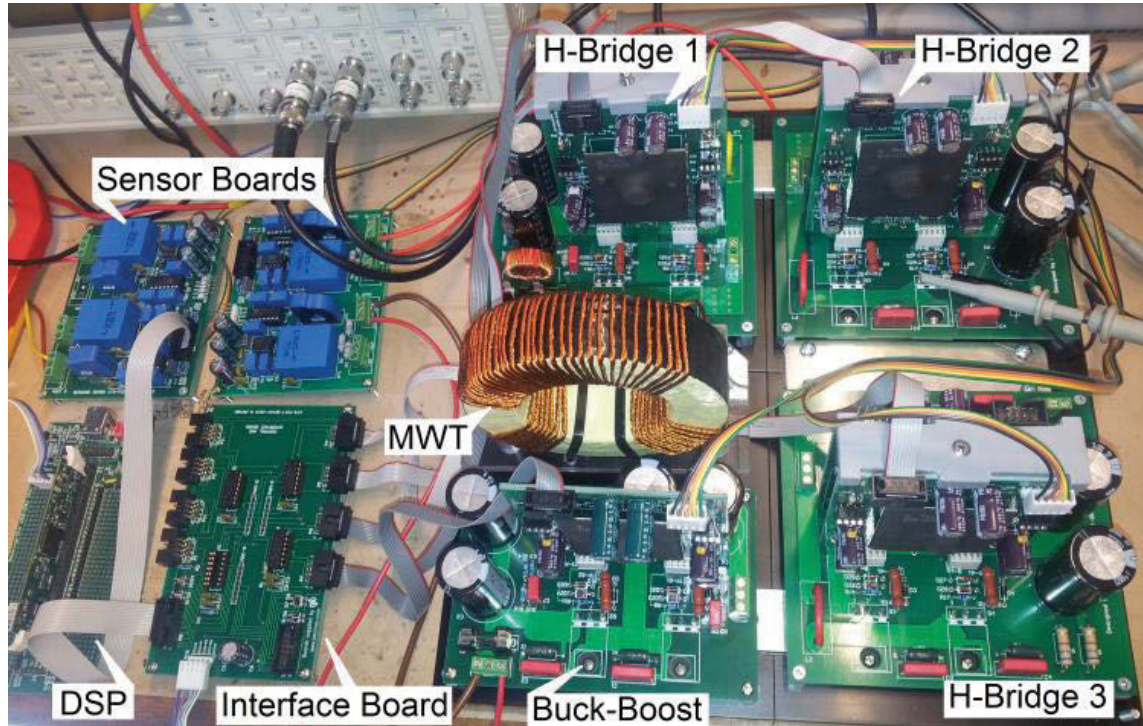


Fig.3.23 Experimentally developed micro-grid

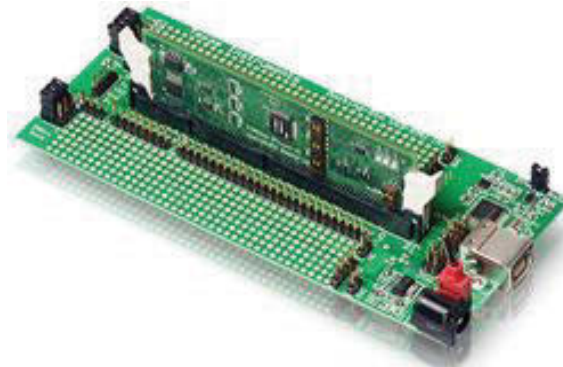


Fig.3.24 The C2000 experimenter kit [3.39].

### 3.11 Digital Signal Processing (DSP) Board

A C2000 experimenter kit is used to realize the device level controller and generate PWM signals for dc-dc converters. The kit provides a hardware prototyping platform for real-time control with C2000 DSP family [3.39]. It can be used as a very useful tool to control the power electronic converters, motor drives, digital power supplies. The experimenter kit employed in this research utilises MS320F28335 DSP made by Texas Instruments (TI) as the main processor. The processor features a 150 MIPS processing core with floating point support, 512 KB integrated flash, 18 PWM channels with high resolution capability and 12-bit 12.5 MSPS ADC [3.39]. The kit includes an isolated XDS100 JTAG emulator for connection to the PC via USB. It facilitates real time in-

system programming and debugging. For development, programming and debugging with C2000 experimenter kit a version of code composer studio (CCS) should be used. Fig.3.24 shows a photo of the C2000 experimenter kit.

### **3.12 Summary of Chapter**

A review on the design and experimental development of proposed micro-grid was presented in this chapter. Four types of dc-ac conversion cells were introduced for use in the TAB converter. Their characteristics are evaluated and compared. The H-bridge cell finally was selected taking into account the efficiency, current ripple, power transfer range, switching loss, control complexity, size, cost, and reliability as the main indicators. The selected topologies of dc-dc converters were studied and the design process was discussed in brief. The last section of the chapter was allocated to the experimental setup design and prototyping of the proposed micro-grid including measurement and protection circuits.

## References

- [3.1] R. Atia and N. Yamada, "Sizing and Analysis of Renewable Energy and Battery Systems in Residential Microgrids," *IEEE Trans. Smart Grid*, vol. 7, no. 3, pp. 1204-1213, May 2016.
- [3.2] M. Jafari, G. Platt, Z. Malekjamshidi and J. G. Zhu, "Technical issues of sizing Lead-Acid batteries for application in residential renewable energy systems," in proc. *4th Int. Conf. Electric Power and Energy Conversion Systems (EPECS)*, Sharjah, 2015, pp. 1-6.
- [3.3] W. D. Kellogg, M. H. Nehrir, G. Venkataramanan and V. Gerez, "Generation unit sizing and cost analysis for stand-alone wind, photovoltaic, and hybrid wind/PV systems," *IEEE Trans. Energy Conversion*, vol. 13, no. 1, pp. 70-75, Mar 1998.
- [3.4] X. Zhu; J. Yan; N. Lu, "A Graphical Performance-based Energy Storage Capacity Sizing Method for High Solar Penetration Residential Feeders," *IEEE Trans. Smart Grid* , vol.PP, no.99, pp.1-1
- [3.5] The Australian Energy Market Operator (AEMO), Website:  
<http://www.aemo.com.au/>
- [3.6] Y. Shi, R. Li, Y. Xue and H. Li, "High-Frequency-Link-Based Grid-Tied PV System With Small DC-Link Capacitor and Low-Frequency Ripple-Free Maximum Power Point Tracking," *IEEE Trans. Power Electronics*, vol. 31, no. 1, pp. 328-339, Jan. 2016.
- [3.7] N. Femia, G. Petrone, G. Spagnuolo, and M. Vitelli, "A technique for improving P&O MPPT performances of double-stage grid-connected photovoltaic systems," *IEEE Trans. Ind. Electron.*, vol. 56, no. 11, pp. 4473–4482, Nov. 2009.
- [3.8] S. Jiang, D. Cao, Y. Li and F. Z. Peng, "Grid-connected boost-half bridge photovoltaic microinverter system using repetitive current control and maximum power point tracking," *IEEE Trans. Power Electron.*, vol. 27, no. 11, pp. 4711–4722, Nov. 2012.

- [3.9] M. W. Ahmad, N. Agarwal and S. Anand, "Online Monitoring Technique for Aluminum Electrolytic Capacitor in Solar PV-Based DC System," *IEEE Trans. Industrial Electronics*, vol. 63, no. 11, pp. 7059-7066, Nov. 2016.
- [3.10] G. R. Chandra Mouli; J. Schijffelen; P. Bauer; M. Zeman, "Design and Comparison of a 10kW Interleaved Boost Converter for PV Application Using Si and SiC Devices," *IEEE Journal of Emerging and Selected Topics in Power Electronics* , vol. PP, no.99, pp.1-1,2016.
- [3.11] X. Liu, H. Li, and Z. Wang, "A fuel cell power conditioning system with low-frequency ripple-free input current using a control-oriented power pulsation decoupling strategy," *IEEE Trans. Power Electron.*, vol. 29, no. 1, pp. 159–169, Jan. 2014.
- [3.12] Z. Wang and H. Li, "An integrated three-port bidirectional dc-dc converter for PV application on a dc distribution system," *IEEE Trans. Power Electron.*, vol. 28, no. 10, pp. 4612–4624, Oct. 2013.
- [3.13] B. Mangu, S. Akshatha, D. Suryanarayana and B. G. Fernandes, "Grid-Connected PV-Wind-Battery-Based Multi-Input Transformer-Coupled Bidirectional DC-DC Converter for Household Applications," *IEEE Journal of Emerging and Selected Topics in Power Electronics*, vol. 4, no. 3, pp. 1086-1095, Sept. 2016.
- [3.14] H. Wu, P. Xu, H. Hu, Z. Zhou and Y. Xing, "Multiport Converters Based on Integration of Full-Bridge and Bidirectional DC–DC Topologies for Renewable Generation Systems," *IEEE Trans. Industrial Electronics*, vol. 61, no. 2, pp. 856-869, Feb. 2014.
- [3.15] M. A. Khan, A. Ahmed, I. Husain, Y. Sozer and M. Badawy, "Performance Analysis of Bidirectional DC–DC Converters for Electric Vehicles," *IEEE Trans. Industry Applications*, vol. 51, no. 4, pp. 3442-3452, July-Aug. 2015.
- [3.16] Junjun Zhang; Hongfei Wu; Xiaoqing Qin; Yan Xing, "PWM Plus Secondary-Side Phase-Shift Controlled Soft-Switching Full-Bridge Three-Port Converter for Renewable Power Systems," *IEEE Trans. Ind. Electron*, vol.62, no.11, pp.7061-7072, Nov. 2015

- [3.17] Yuxiang Shi; Rui Li; Yaosuo Xue; Hui Li, “Optimized Operation of Current-Fed Dual Active Bridge DC–DC Converter for PV Applications,” *IEEE Trans. Ind. Electronics*, vol.62, no.11, pp.6986-6995, Nov. 2015
- [3.18] M. Ishigaki, K. Ito, S. Tomura, T. Umeno, “A new isolated multi-port converter using interleaving and magnetic coupling inductor technologies,” in proc *Twenty-Eighth Annual IEEE Applied Power Electronics Conference and Exposition (APEC)*, pp. 1068 – 1074, 17-21 March 2013
- [3.19] Chuanhong Zhao; Kolar, J.W., “A novel three-phase three-port UPS employing a single high-frequency isolation transformer,” in Proc. *Power Electronics Specialists Conference, PESC*. vol.6, no., pp.4135-4141 Vol.6, 20-25 June 2004
- [3.20] H. Tao, J. L. Duarte, M. A. M. Hendrix, “Three-port triple-half bridge bidirectional converter with zero voltage switching,” *IEEE Trans. Power Electronics*, vol. 23, no.2, pp 782–792, March 2008.
- [3.21] H. Cha, R. Ding, Q. Tang, and F. Z. Peng, “Design and development of high-power dc–dc converter for metro vehicle system,” *IEEE Trans. Ind. Appl.*, vol. 44, no. 6, 2008.
- [3.22] L. Zhang, K. Sun, Y. Xing, L. I. Feng, and H. Ge, “A modular grid-connected photovoltaic generation system based on dc bus,” *IEEE Trans. Power Electron.*, vol. 26, no. 2, 2011.
- [3.23] R. Karki, R. Billinton, “Reliability/cost implications of PV and wind energy utilization in small isolated power systems,” *IEEE Trans. Energy Conv.*, vol. 16, no. 4, pp. 368–373, 2001.
- [3.24] M. Jafari, Z. Malekjamshidi, M. R. Islam and J. Zhu, “Comparison of singular and modular structures of multiport converters for residential applications in smart grids,” in proc. *IEEE Innovative Smart Grid Technologies - Asia (ISGT ASIA)*, Kuala Lumpur, 2014, pp. 606-611.
- [3.25] H. Tao, A. Kotsopoulos, J. L. Duarte, and M. A. M. Hendrix, “Family of multiport bidirectional DC–DC converters,” in proc. *Electric Power Applications*, Vol.153 ,Issue: 3, pp.451-458, 2006

- [3.26] H. Jiang, L. F. Rodrguezy, S. Bellz, D. Kortenkampx, and F. Capristan, “Prediction of reliability of environmental control and life support systems,” *J. Spacecr. Rock.*, vol. 48, no. 2, pp. 336–345, Mar. 2011.
- [3.27] V. S. Dhople, A. Davoudi, A. D. Dom´inguez-Garc´ia, P. L. Chapman, “A unified approach to reliability assessment of multiphase dc–dc converters in photovoltaic energy conversion systems,” *IEEE Trans. Power Electron.*, vol. 27, no. 2, 2012
- [3.28] F. H. Aghdam and M. Abapour, “Reliability and Cost Analysis of Multistage Boost Converters Connected to PV Panels,” *IEEE Journal of Photovoltaics*, vol. 6, no. 4, pp. 981-989, July 2016.
- [3.29] C. Zhao, S. D. Round and J. W. Kolar, “An Isolated Three-Port Bidirectional DC-DC Converter With Decoupled Power Flow Management,” *IEEE Trans. Power Electronics*, vol. 23, no. 5, pp. 2443-2453, Sept. 2008.
- [3.30] J. Zhang, J. S. Lai, R. Y. Kim and W. Yu, “High-Power Density Design of a Soft-Switching High-Power Bidirectional dc–dc Converter,” *IEEE Trans. Power Electronics*, vol. 22, no. 4, pp. 1145-1153, July 2007.
- [3.31] Y. Shi, R. Li, Y. Xue and H. Li, “High-Frequency-Link-Based Grid-Tied PV System With Small DC-Link Capacitor and Low-Frequency Ripple-Free Maximum Power Point Tracking,” *IEEE Trans. Power Electronics*, vol. 31, no. 1, pp. 328-339, Jan. 2016.
- [3.32] Y. Shi, R. Li, Y. Xue and H. Li, “Optimized Operation of Current-Fed Dual Active Bridge DC–DC Converter for PV Applications,” *IEEE Trans. Industrial Electronics*, vol. 62, no. 11, pp. 6986-6995, Nov. 2015.
- [3.33] Y. Shi, L. Liu, H. Li and Y. Xue, “A single-phase grid-connected PV converter with minimal DC-link capacitor and low-frequency ripple-free maximum power point tracking,” *IEEE Energy Conversion Congress and Exposition*, Denver, CO, 2013, pp. 2385-2390.
- [3.34] Roberto Francisco, Coelho Denizar Cruz,” Martins An Optimized Maximum Power Point Tracking Method Based on PV Surface Temperature Measurement,” 10.5772/51167, 2012
- [3.35] LEM Voltage transducer datasheet,

- [www.lem.com/docs/products/lv\\_25-p\\_sp5.pdf](http://www.lem.com/docs/products/lv_25-p_sp5.pdf)
- [3.36] LEM Current transducer/ LTS 25NP datasheet,  
[www.lem.com/docs/products/lts%2025-np.pdf](http://www.lem.com/docs/products/lts%2025-np.pdf)
- [3.37] LEM Current and Voltage Transducers for Industrial Applications,  
<http://www.europowercomponents.com/media>
- [3.38] VLA567-01R Driver datasheet, [www.pwr.com/pwr/docs/VLA567-01R.pdf](http://www.pwr.com/pwr/docs/VLA567-01R.pdf)
- [3.39] TMS320F28335 Experimenter Kit datasheet,  
<http://www.ti.com/tool/tmdsdock28335>

## CHAPTER 4

# DESIGN AND DEVELOPMENT OF MULTI-WINDING MAGNETIC LINK

### 4.1 Introduction

High frequency magnetic links have attracted significant attention due to their application in the integration of renewable energy resources into the grid. Improvements of smart micro-grid technologies have increased demands for more reliable and flexible converters and control techniques. The high frequency magnetic link can reduce effectively the number of conversion stages in micro-grids and improve the conversion efficiency with the help of modern soft magnetic materials and low power loss solid state switching devices [4.1]-[4.4]. The magnetic link is quite similar to the conventional multi-winding high frequency transformer except that it provides bidirectional paths for magnetic fluxes and power flows between different ports. It is known as a feasible replacement for traditional electrical ac and dc buses in smart micro grids for integrating renewable energies. Their application as a common magnetic bus in multi-port converters makes it possible to simplify the integration of power sources of different voltage levels using different turns ratios [4.5]-[4.7]. They also provide galvanic isolation and the possibility of simultaneous and bidirectional power flow between the converter ports [4.8], [4.9]. Research on design, characterization and modelling of magnetic links has attracted considerable interests in recent years due to their increasing applications [4.10], [4.11].

In this chapter, a review on different stages of design, prototyping and experimental test of multi-winding transformer is provided due to its importance in operation and efficiency of the entire renewable energy system. A major part of this research is focused on design and development of the magnetic link. In the first step of design, the specifications of the magnetic link, such as voltage, power and magnetic core material, and turns ratio of windings, are defined according to the design requirement and application. The magnetic link geometry is designed for certain values of parameters

using reluctance network method (RNM). The designed component is then evaluated for equal core and copper losses to maintain the maximum efficiency taking into account limitations of temperature rise. The resultant structure is modified iteratively to achieve the optimal core and winding geometries. The core loss is accurately evaluated based on the modified Steinmetz equation for non-sinusoidal and variable duty ratio wave forms [4.12], [4.13]. The conduction loss analysis is based on the harmonic content of non-sinusoidal currents considering skin and proximity effects. The temperature rise of the component is evaluated using a dynamic thermal electric model considering the effects of duty ratio variation of wave forms on heat source points. To validate the proposed design procedure, a prototype of the magnetic link has been fabricated using amorphous magnetic materials. The open circuit, differentially and cumulatively coupled tests are conducted on the prototype to characterize the magnetic link and to measure the inductive and resistive elements. The core loss, copper loss and temperature rise are measured experimentally, and compared with the predefined specifications to validate the design and modelling procedures.

#### **4.2 Application of Magnetic Link**

The hybrid renewable energy systems are gaining popularity in sustainable energy generation systems where a multi-port interface is necessary to link the energy storage, renewable sources, load and grid. Multi-winding magnetic links have been used as the common magnetic bus to transfer the energies between the renewable sources and loads effectively [4.14], [4.15]. Fig.4.1 compares two renewable energy systems with and without the magnetic link. It can be seen that employing the magnetic link can reduce the number of voltage conversion stages, the system size and cost, and consequently increases the system efficiency. The red dashed lines show that the power flow path from PV array to the battery has been reduced effectively with the use of the magnetic link. In this research, a hybrid renewable energy system, including a multi-winding magnetic link is introduced for smart grid applications. The system includes a triple-active bridge phase shift dc-dc converter, a buck-boost bidirectional converter for battery port, two inter-leaved-current-fed boost converters for PV port, and a grid-connected single phase inverter as illustrated in Fig.4.2.

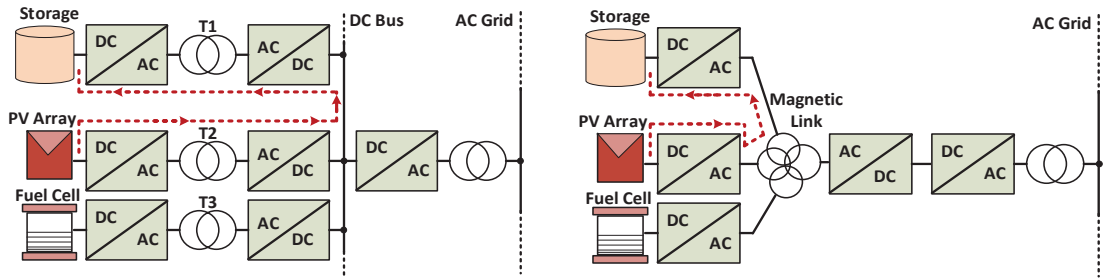


Fig.4.1 Comparison of two renewable energy systems, (a)-without, and (b)-with the common magnetic link

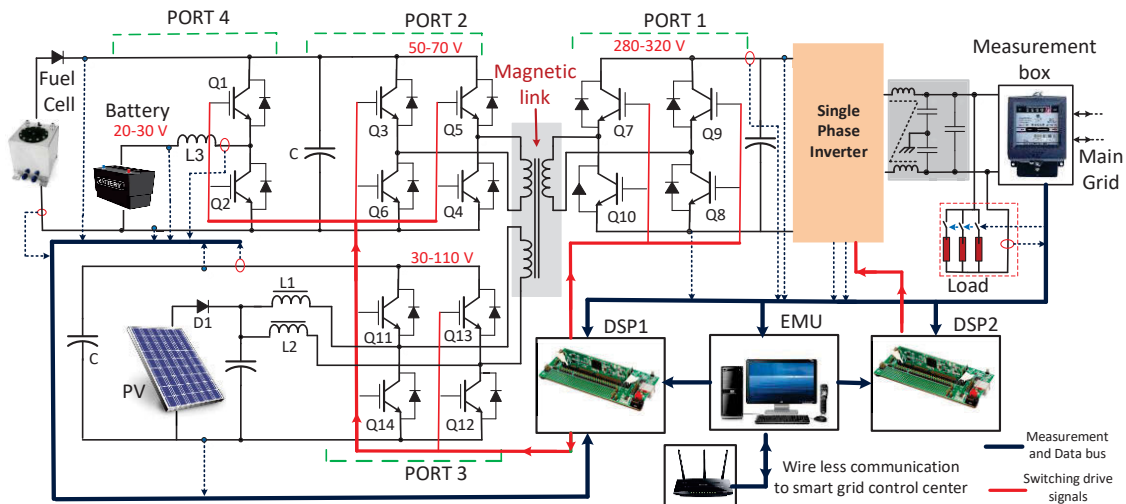


Fig.4.2 Structure of proposed renewable energy system

The proposed system is designed to supply a 4.5 kW residential load by combining the energy of a PV array, fuel cell stack and a battery bank. It is controlled by two Texas Instruments DSPs (C2000/TMS320F28335) at the device level and a PC system as energy management unit (EMU) at the system level. The EMU communicates with the regional distribution network control center via internet (through either cable or wireless) to send and receive information. It also manages the energy and power flow between the ports based on the short-term and long-term plans.

The phase shift converter includes three H-bridge units to generate high frequency square-wave voltage from the input dc source and apply it to the corresponding winding of the magnetic link. To control the power flow, ports two and three are shifted for a leading or lagging phase angle to send or receive power to port one as the reference port.

To extract the maximum possible power from the PV array, a duty cycle control is applied to the port three by using inter-leaved-current-fed boost converters. Port one is a

bi-directional port that transfers power from renewable sources or battery to the inverter and further to the load and grid. It also is used in the reverse direction to transfer the power from the grid to the battery (using ports two and four simultaneously). A 50-70 V dc bus (presented as bus2) links port two to the fuel cell stack and to the 24 V battery bank via a bi-directional buck-boost converter to charge the battery in the buck mode and discharge it in the boost mode. The fuel cell stack can be used as a back up energy source and PV is considered as the preferred source to supply the load and possibly the grid. Battery is used as an energy storage device and also balances the voltage of the bus three due to the low dynamic response of the fuel cell. It can be charged by fuel cell, PV or grid. The magnetic link provides isolation and flexible power flow direction between the ports. It facilitates operation of the system in different modes and various energy management scenarios in both grid-connected and islanded modes. Details of the operation modes will be provided in chapter six.

### 4.3 Equivalent Model of the Magnetic Link

In this section, an equivalent electrical model is defined for the multi-winding transformer. The model is independent of physical structure of transformer and is derived on the basis of windings flux linkage although a toroidal transformer is selected due to the proposed magnetic link. Assuming  $n$  separate windings are distributed unsymmetrically around the toroidal core as illustrated in Fig.4.3. The voltage of winding  $i$  can be calculated by Faraday's law based on its current,  $i_i$ , winding resistance,  $R_{W_i}$ , and flux linkage from winding  $j$ ,  $\lambda_{ij}$ , as the following

$$v_i = i_i R_{W_i} + \sum_{j=1}^n \frac{d\lambda_{ij}}{dt}, \text{ for } i, j = 1, 2, \dots, n \quad (4.1)$$

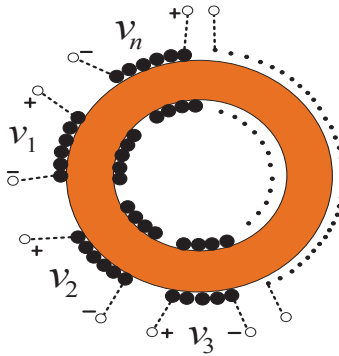


Fig.4.3 Toroidal core transformer including  $n$  windings.

The flux linked to each winding is a function of current in the other windings. Assuming that the transformer is mostly operating in the linear section of B-H curve then

$$\frac{d\lambda_{ij}}{di_j} = L_{ij} \quad (4.2)$$

$$\frac{d\lambda_{ij}}{dt} = \frac{d\lambda_{ij}}{di_j} \cdot \frac{di_j}{dt} \quad (4.3)$$

where  $L_{ij}$  is the mutual inductance between windings  $i$  and  $j$ . The voltage of each winding,  $v_i$ , can be defined by combining (4.1)-(4.3) as

$$v_i = i_i R_{w_i} + \sum_{j=1}^n L_{ij} \frac{di_j}{dt} \quad (4.4)$$

Considering winding one as the reference, all parameters of other windings including the self and mutual inductances, winding resistance, voltage and current can be referred to winding one as the reference winding by

$$v'_i = \frac{N_1}{N_i} v_i, \quad L'_{ij} = L_{ij} \frac{N_1^2}{N_i N_j}, \quad i'_i = \frac{N_i}{N_1} i_i, \quad R'_{w_i} = \left(\frac{N_1}{N_i}\right)^2 R_{w_i} \quad (4.5)$$

where  $N_i$ ,  $N_j$ ,  $L_{ij}$  are the number of turns in winding  $i$ , number of turns in winding  $j$  and mutual inductance of windings  $i$  and  $j$ , respectively. To extract the equations of the final model, a mutual inductance common between all transformer windings, known as the magnetization inductance and noted as  $L_m$ , can be defined as

$$L_m = \sum_{i=1, j=1}^n L'_{ij} \quad \text{for } i \langle j \quad (4.6)$$

and the corresponding magnetization current, i.e. the current flowing through the magnetization inductance, as

$$i_m = i_1 + i'_2 + i'_3 + \dots + i'_n \quad (4.7)$$

To modify the model to include the core loss, a core loss equivalent resistance,  $R_m$ , is modelled in series with magnetizing inductance  $L_m$  and the winding resistances  $R_w$  in series with the leakage inductance of each winding. The magnetizing inductance is referred to the winding one as the reference winding. The core loss resistance is connected in series with the magnetizing inductance although their parallel connection is preferred from a physical perspective. The series connection facilitates the analysis of

series-coupling tests on transformer and is used in literatures for transformer modelling [4.16]. The equivalent parameters can be calculated by using the parallel to series transform equations as

$$R_m = \frac{R'_m \omega^2 (L'_m)^2}{(R'_m)^2 + \omega^2 (L'_m)^2} \quad (4.8)$$

$$L_m = \frac{(R'_m)^2 L'_m}{(R'_m)^2 + \omega^2 (L'_m)^2} \quad (4.9)$$

and the series to parallel transform equations as

$$R'_m = \frac{R_m^2 + \omega^2 L_m^2}{R_m} \quad (4.10)$$

$$L'_m = \frac{R_m^2 + \omega^2 L_m^2}{\omega^2 L_m} \quad (4.11)$$

Combining (4.4)-(4.8), the voltage equation for all transformer windings can be rewritten as

$$V = \tilde{R}I + \tilde{L} \frac{dI}{dt} \quad (4.12)$$

where

$$V = \begin{bmatrix} v_1 \\ v'_2 \\ \cdot \\ \cdot \\ v'_n \end{bmatrix} \quad \tilde{L} = \begin{bmatrix} L_{11} - L_m & L'_{12} - L_m & \cdot & L'_{1n} - L_m & L_m \\ L'_{21} - L_m & \cdot & \cdot & \cdot & L_m \\ \cdot & \cdot & \cdot & \cdot & \cdot \\ \cdot & \cdot & \cdot & \cdot & L_m \\ L'_{n1} - L_m & L'_{n2} - L_m & \cdot & L'_{nn} - L_m & L_m \end{bmatrix}$$

$$I = \begin{bmatrix} i_1 \\ i'_2 \\ \cdot \\ \cdot \\ i'_n \\ i_m \end{bmatrix} \quad \tilde{R} = \begin{bmatrix} R_{W_1} & 0 & 0 & 0 & 0 & R_m \\ 0 & R'_{W_2} & \cdot & \cdot & \cdot & R_m \\ \cdot & 0 & \cdot & \cdot & \cdot & \cdot \\ \cdot & \cdot & \cdot & R'_{W_{n-1}} & \cdot & R_m \\ 0 & 0 & 0 & 0 & R'_{W_n} & R_m \end{bmatrix} \quad (4.13)$$

are the voltage, current, inductance, and resistance matrixes of the transformer windings.

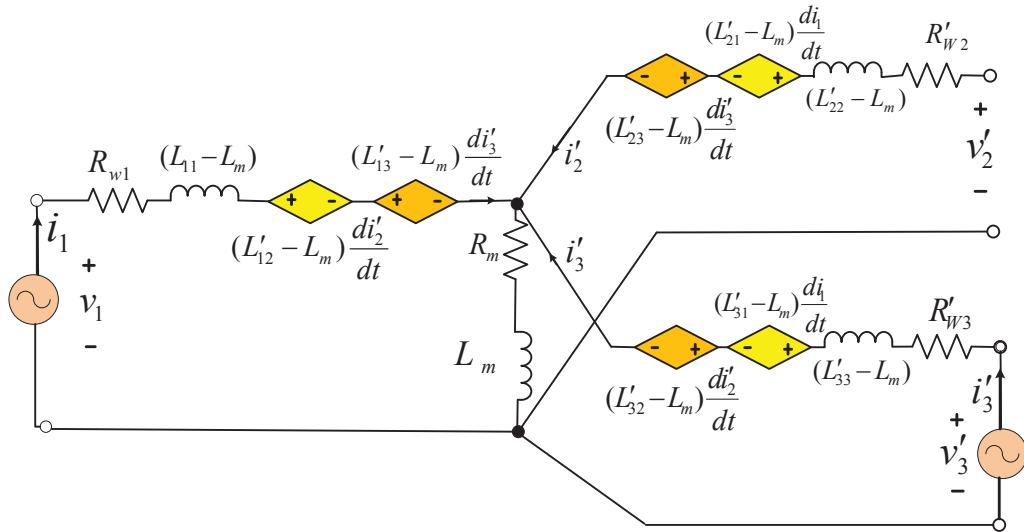


Fig.4.4 The equivalent electrical model of three windings transformer

A modified model of three windings transformer based on (4.12)-(4.13) is presented in Fig.4.4. As can be seen in the model, all voltages resulting from the cross coupling effects of windings are presented in the form of current controlled voltage sources.

#### 4.4 Design of High Frequency Magnetic Link

The main stages of the design of magnetic link are presented in the flowchart in Fig.4.5. As can be seen in the figure, the design process starts with definition of design specifications, variables and variation range. The required values of leakage and self-inductances of transformer windings are selected as the design specifications. The number of winding turns, dimensions of magnetic core and thickness of insulator between each winding and the core are selected as the design variables. The design process begins with introduction of user defined parameters such as windings turns ratio, magnetic material characteristics, rated power, voltage, current and frequency. The design specifications of the magnetic link for the proposed application are presented in Table 4.6 as will be discussed in the following sections. To reduce the total time of design, a primary design stage is considered and the initial values of design variables are defined by using the classical methods of transformer design [4.24]. To find the initial size of the core, the area-product was defined based on the power handling capacity, current density and flux density. The resultant values then were used to find the core size from area-product/core-size charts. Finally, the number of turns was calculated by using Faraday's law. The third stage is to define the geometry of the magnetic core accurately. Design of MWTs for certain value of inductances using the

classical methods of transformer design is not accurate due to their structural complexity and cross coupling effects. Numerical methods, such as 2D and 3D finite element methods (FEMs) and reluctance network model (RNM), are commonly used in design of magnetic structures such as electrical motors and transformers. The FEM is an accurate field analysis method but when used in design optimization, the computational cost is too high. On the other hand, the RNM is very fast but less accurate [4.17]-[4.22]. Magnetic field analysis using FEM can take into account the nonlinearity of magnetic materials, geometry and actual winding distribution while RNM is based on linear assumptions. The RNM also can be used for analysis of devices with arbitrary geometries and excitations using a general 3D element and variable size reluctance network [4.23].

In this research, the RNM is used in the third stage of design process. Due to iterative nature of transformer design it presented less computation time and reasonable accuracy. To use it in design optimization, various methods of choosing proper calculation domains, such as number of 3D elements and dimension of field analysis area, have been implemented to improve its accuracy. To analyze the magnetic field using RNM, the magnetic structure is divided into three different areas including magnetic core, insulator and free space around the core. To do the analysis, the magnetic structure is assumed to operate in linear section of magnetization curve and therefore a constant value of permeability is used. The magnitude of terminal voltage is chosen such that the peak flux density would just reach the knee point of the magnetization curve, and thus the linear model can give sufficient accuracy. This is particularly true for the magnetic material used in this design (amorphous *2605SA*) based on data provided by factory and experimental tests. This can effectively avoid the extra current harmonics and excessive magnetization current and core losses due to the distortion of magnetic field caused by the nonlinear magnetization curve.

On the other hand, because of the full use of the linear region, there is no need to use bigger core or more windings than necessary. This assumption also helps to represent the magnetic behavior of the core under non-sinusoidal excitation currents applying the superposition rule to Fourier's terms of the current.

The field analysis of the magnetic structure using RNM was carried out to calculate the magnetic flow,  $\varphi$ , flux density,  $B$ , field intensity,  $H$ , and finally define the geometry and dimension of the magnetic link.

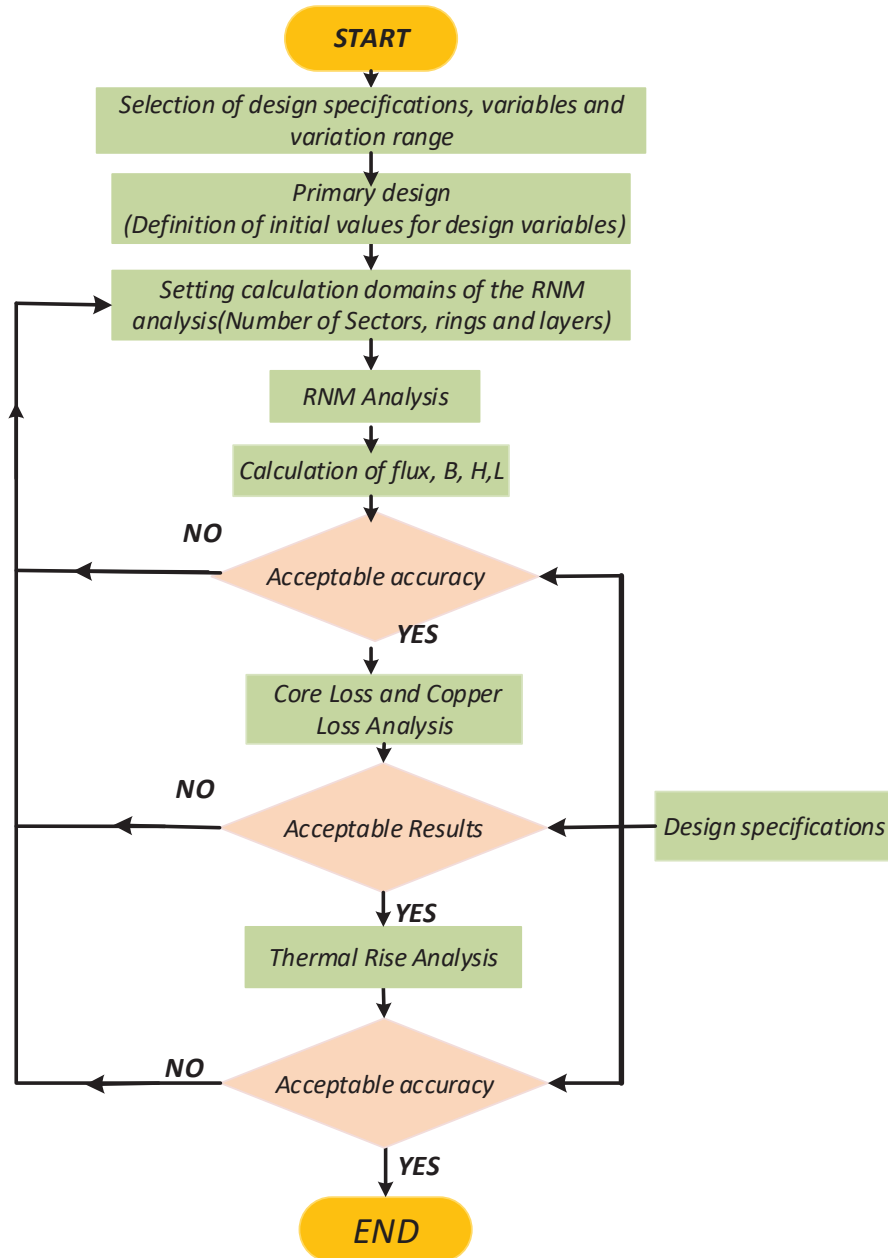


Fig.4.5 The flowchart of the main stages of multi-winding magnetic link design.

The resultant values of  $B$  and  $H$  are used to define the winding self-inductances  $L_{11}$ ,  $L_{22}$ ,  $L_{33}$  and leakage inductances  $L_{11}$ ,  $L_{12}$  and  $L_{13}$  as the design objective. In the case of satisfactory values, the magnetic structure then is analyzed to satisfy the loss specifications and thermal limits.

#### 4.4.1 Selection of magnetic material

Selection of magnetic materials for high frequency transformers is critical and needs a good understanding of both magnetic material properties and the design specifications of the particular application. A literature review reveals that the most commonly used

magnetic materials for high frequency applications are ferrites, amorphous metals and Permalloy. On the other hand, ferromagnetic materials such as Nano-crystalline materials have been used in high power, high frequency applications regarding their relatively high saturation flux density and low loss density [4.12]. To select the magnetic materials different possible options of magnetic materials are studied according to their main characteristics such as specific core loss, saturation flux density, relative permeability and thermal features.

#### A. Soft ferrites

Soft ferrites have been used as magnetic core in high frequency application over the past decades. Their wide range of geometries and dimensions, higher electrical resistivity, lower eddy current loss, and lower cost make them an ideal option in most power electronic applications. It has a cubic crystalline structure made of iron dioxide ( $Fe_2O_3$ ) and a combination of other metals such as Manganese, Zinc, Nickel and Copper. Table.4.1 shows the main characteristics of four types of ferrites according to the data provided by Ferroxcube [4.12]. As can be seen, the saturation flux density of ferrites ranges from 0.3~0.5 T and their permeability changes from tens to thousands. The core loss density and permeability of ferrites also change with the operation frequency. The core loss density increases with any increase in the frequency while the permeability decreases. The Curie temperature of ferrite ranges from 200 ~ 300 °C which is still far above the typical operation range (60 ~ 120 °C). The magnetic and electric characteristics of the ferrites will change with the operating temperature.

**TABLE 4.1 Main Properties of the MnZn and NiZn Ferrites [4.12]**

Parameter Type of Ferrite	Permeability $\mu_i$	Flux density $B_{sat}$ (T)	Resistivity $\rho$ ( $\Omega \cdot m$ )	Curie Temp $T_c$ (°C)	Thermal conductivity (W/(m.k))
3F3 (MnZn)	2000	0.45	2	220	$3.5 \sim 5$
3F45(MnZn)	900	0.5	10	300	$3.5 \sim 5$
4B1(NiZn)	250	0.35	100000	250	$3.5 \sim 5$
4F1(NiZn)	80	0.35	100000	260	$3.5 \sim 5$

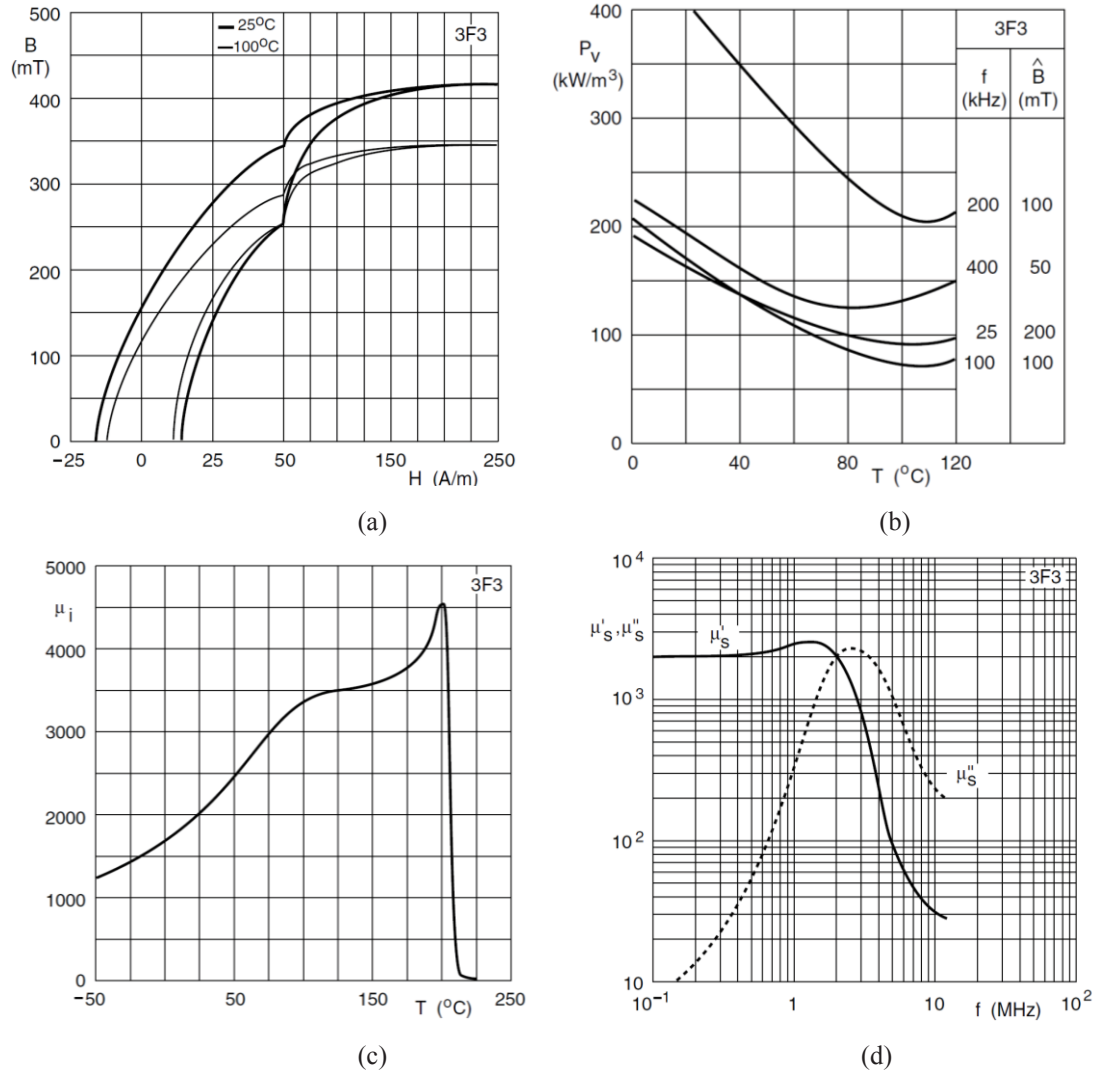


**Fig.4.6** The characteristics of Ferrite 3F3, (a) temperature dependency of saturation flux density, (b) loss density, (C) initial permeability, and (d) dependency of complex permeability to the frequency [4.12], [4.25].

Therefore, these points should be considered in the selection process to avoid any possible failure of designed magnetic link. The saturation flux density, core loss density and initial permeability of ferrite also depend on the operating temperature as presented in Fig. 4.6. As can be seen, the saturation flux density reduces with temperature rise which implies higher size of the designed core considering temperature margins. The core permeability increases with the temperature which causes slight increase in the winding inductances. The last graphs show that the loss density of the magnetic core decreases with the temperature rise. This can make the design process more complex and iterative due to the dependency of temperature to the loss and vice versa.

### B. Permalloy

The Permalloy which is the common name for nickel-iron based magnetic materials is introduced approximately in 1910. It has been widely used as core material in distribution transformers due to its low magnetostriction. Improvement of Permalloy characteristics resulted in development of magnetic materials with lower loss and higher operating frequency range known as Supermalloy. Due to its excellent loss performance and ability of operation in a higher frequency range, it has found a wide range of applications in very high frequency and ultra-sensitive transformers and sensors. The main characteristics of the Supermalloy are presented in the Table.4.2. It can be seen that it has higher saturation flux density (0.6 ~ 0.7), initial permeability and Curie temperature compared with ferrites [4.12].

**TABLE 4.2 Main Properties of Permalloy [4.12]**

Parameter	Permeability $\mu_i$	Flux density $B_{sat}$ (T)	Resistivity $\rho$ ( $\Omega \cdot m$ )	Curie Temp $T_c$ ( $^{\circ}C$ )	Thermal conductivity (W/(m.k))
Type of material					
Permalloy	15000-20000	0.65-0.75	$0.57 \cdot 10^{-6}$	430	$8.72 \cdot 10^3$

### C. Amorphous materials

Amorphous magnetic materials were produced in the 1970s with the appearance of rapid solidification technology which resulted in higher density of magnetic species and consequently higher saturation flux densities compared with the ferrites and Permalloy. They are produced in two groups of Fe-based and Co-based materials where Fe-based material presents higher saturation flux density (1 ~ 1.7 T) compared with that of Co-based metals (0.6 ~ 1 T). On the other hand, Fe-based materials (e.g. *Metglas 2605SA1*) have higher loss density than Co-based (e.g. *Metglas 2705M*). Table.4.3 illustrates the main characteristics of the four types of amorphous materials. It can be seen that the saturation flux density of amorphous materials is higher than ferrite and Permalloy especially for Fe-based metals. They also present higher initial permeability and Curie temperature compared with the ferrites. In the case of dependency of permeability and saturation flux density on the operating frequency, amorphous materials present similar trends to the ferrites and permalloy.

**TABLE 4.3 Main Properties of the Amorphous Materials [4.12]**

Parameter Type of Ferrite	Permeability $\mu_i$	Flux density $B_{sat}$ (T)	Resistivity $\rho$ ( $\Omega \cdot m$ )	Curie Temp $T_C$ ( $^{\circ}C$ )	Thermal conductivity (W/(m.k))
2605SA1 (Fe)	600,000	1.56	$1.3 \cdot 10^{-6}$	395	-
2605CO (Fe)	400,000	1.8	$1.23 \cdot 10^{-6}$	415	9
2705M (Co)	600,000	0.77	$1.36 \cdot 10^{-6}$	365	9
2714A (Co)	1000,000	0.57	$1.42 \cdot 10^{-6}$	225	-

#### D. Nano-crystalline materials

The Nano-crystalline magnetic materials were introduced by Japanese scientists in the early 1990s [4.12]. They have an extremely fine grained structure which results in superior magnetic performance. Nano-crystalline materials present lower loss and higher permeability compared with the other magnetic materials leading to the smaller size and less weight magnetic designs. The main manufacturers of Nano-crystalline materials are Hitachi (*Finemet*) and Vaccumeschmelze (*Vitroperm*). Fig.4.7(a) provided by Hitachi Metals shows that Nano-crystalline materials (Finemet) have higher properties of relative permeability and saturation flux density compared with other soft magnetic materials. Fig.4.7(b) compares the core loss density of various magnetic materials according to their flux density. It is clear that the core loss density increases with increasing flux density in all types of previously discussed magnetic materials although Finemet showed minimum loss compared with others.

The main characteristics of the nano-crystalline materials *Finemet FT-3M* and *Vitroperm 500F* are presented in Table.4.4. As can be seen in the table, the Finemet saturation flux density changes between 0.7 ~ 1.2 T and the initial relative permeability ranges from 10000 ~ 400000.

**TABLE 4.4 Main Properties of the Nano-Crystalline Material [4.24]**

Parameter Type of Ferrite	Permeability $\mu_i$	Flux density $B_{sat}$ (T)	Resistivity ( $\Omega \cdot m$ )	Curie Temp ( $^{\circ}C$ )	Thermal conductivity (W/(m.k))
Finemet FT-3M	30000~100000	1.23	$1.2 \cdot 10^{-6}$	570	-
Vitroperm 500F	15000~150000	1.2	$1.2 \cdot 10^{-6}$	600	-

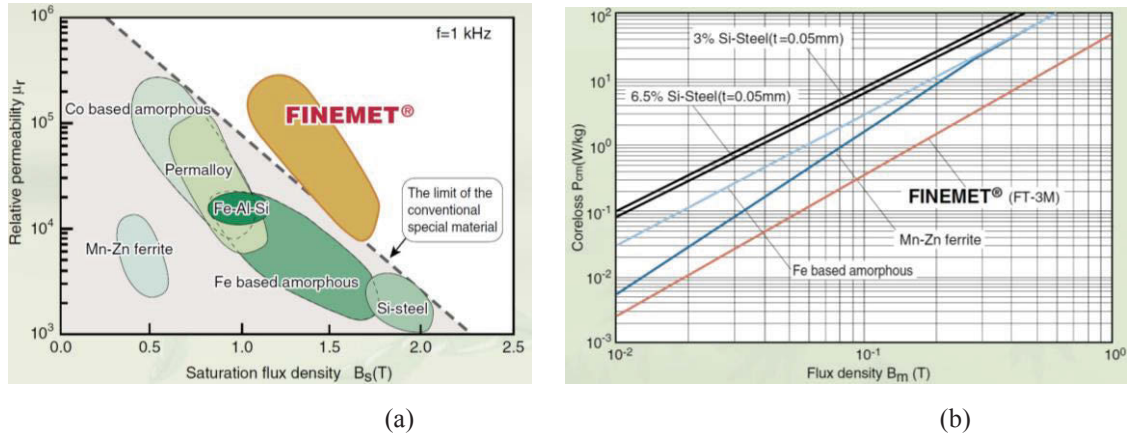


Fig.4.7 Comparison of characteristics of different soft magnetic materials, (a) relative permeability versus saturation flux density, and (b) core loss versus saturation flux density [4.26].

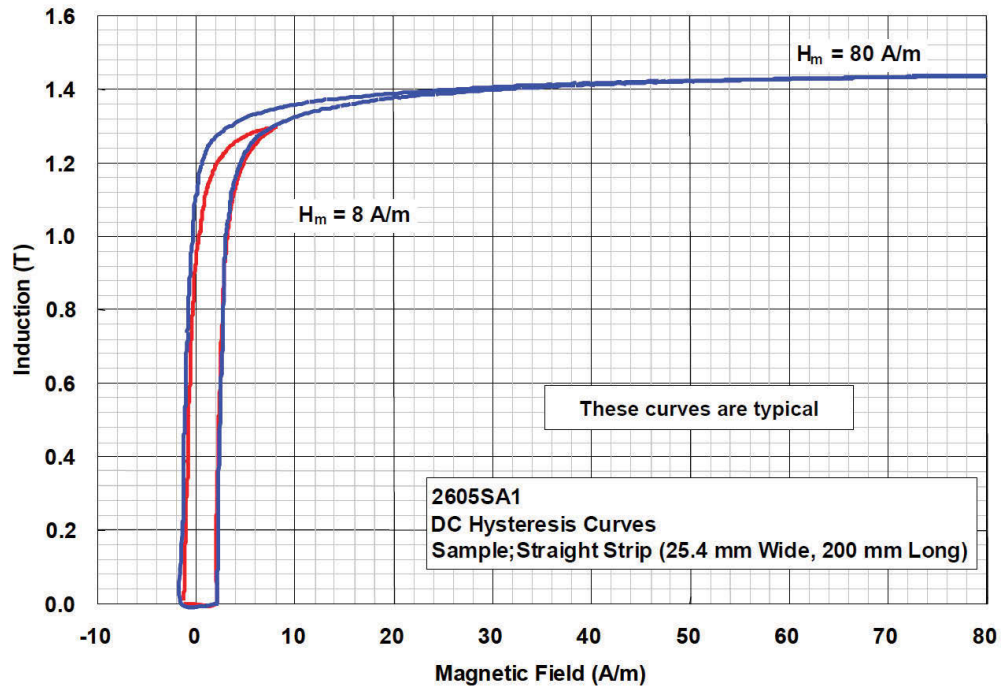


Fig.4.8 B-H curve of selected amorphous material (260SA1) for frequency of 1 kHz [4.27]

#### 4.4.2 Discussion

The provided information of all soft magnetic materials should be considered for appropriate selection of magnetic core. From previous studies, it can be seen that the soft ferrites have low saturation flux density (0.3-0.5 T) which results in the large transformer size although they have been widely used in high frequency converters due to their low price and availability [4.28]. Nano-crystalline materials and amorphous alloys as other possible options, have presented lower core loss, higher saturation flux density and higher permeability [4.28].

Comparing their characteristics shows that nano-crystalline materials have slightly lower saturation flux density (0.8-1 T) than the amorphous alloys (1.4-1.6 T) and present lower core loss [4.28]. The amorphous alloy Metglas-2605SA1 made by Hitachi Metals is finally selected considering the maximum flux density, specific core loss, cost and availability. On the other hand, amorphous materials are manufactured in the form of flexible magnetic tapes which facilitate easier development in any size and frame in the lab. Fig.4.8 shows the B-H curve of 2605SA1 provided by Hitachi Metals (Metglas). Table.4.5 shows the physical dimension of the magnetic tapes of Metglas thanks to Hitachi Metals.

**TABLE 4.5 Physical Dimension and Characteristics of Magnetic Tapes [27]**

Alloy	Thickness ( $\mu\text{m}$ )	Standard available width (mm)			Lamination Factor (%)
2605SA1	$25 \pm 4$	$142.2 \pm 1.0$	$170.2 \pm 1.1$	$213.4 \pm 1.4$	$\geq 84$
2605HB1M					

#### 4.5 Design of Magnetic Link Geometry using RNM

Despite their advantages, design of multi-winding magnetic links for certain specifications is relatively complex due to their non-linearity and structural complexity [4.29]-[4.31]. Analytical methods of the design and the modelling of multi-winding magnetic links are based on lumped-parameter models and rely on many simplifying assumptions which reduce their accuracy [4.32], [4.33]. On the other hand, numerical methods such as finite element analysis (FEA) require extensive computation time for optimal design of magnetic structures [4.34], [4.35]. The reluctance network methods (RNMs) also known as magnetic equivalent circuits (MECs) as a third possibility can be used to design the components with an acceptable accuracy and computation time [4.36], [4.37]. The method is formally introduced by Laithwait [4.38] and Carpenter [4.39] in 1967 and 1968 respectively. It has been widely used in analysis and design of electrical machines [4.40]-[4.42] and has been extended to 2D and 3D analysis of magnetic structures [4.43], [4.44]. The main advantages of the method are moderate computational effort, reasonable accuracy and 3D modeling capability [4.45]. It has been used to model the dynamics of electrical machines as in recent applications [4.46]-[4.48] and a general 3D RNM applicable to various magnetic structures is introduced in [4.49].

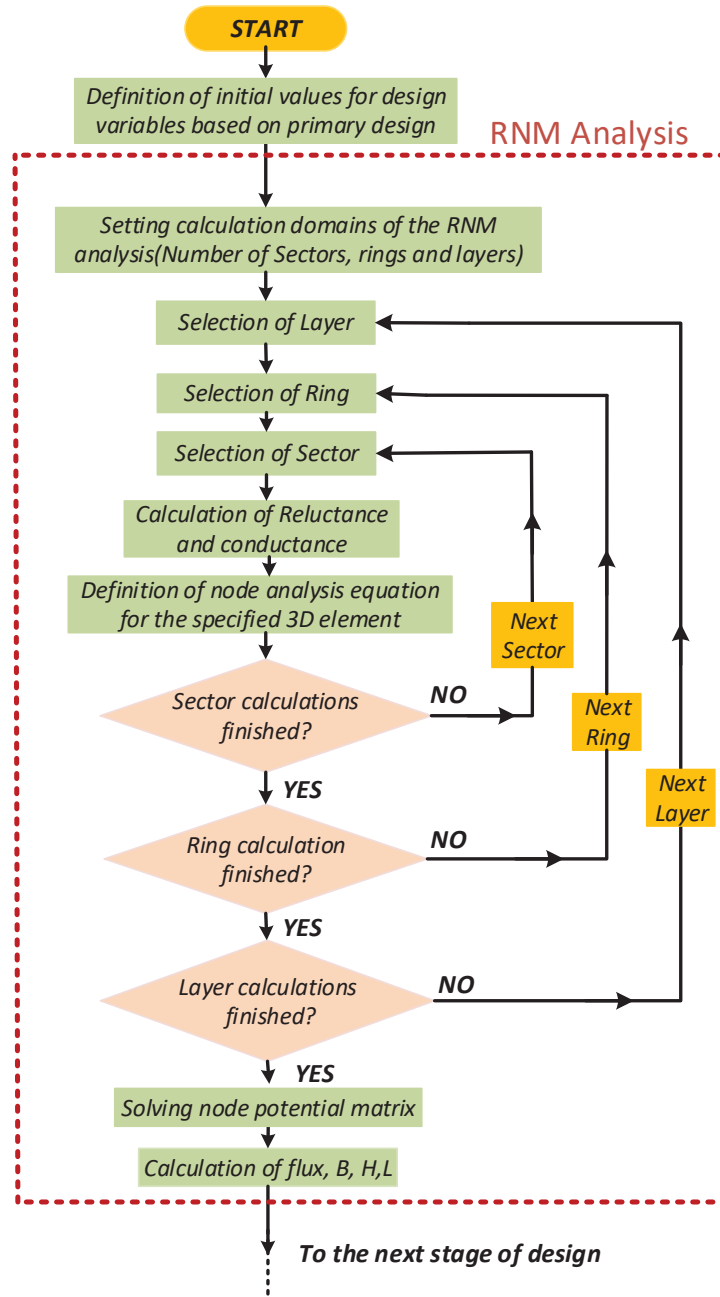


Fig.4.9 The design flow chart of the magnetic link using MATLAB

In this research, the RNM is employed to design the magnetic link. Due to iterative nature of design and optimization process it presents less computation time and reasonable accuracy. The magnetic link should be designed for certain values of leakage inductances as they are used as energy transfer components in the phase shift converter [4.9], [4.14], [4.15]. Using external bulked inductors in series with the transformer windings is suggested although it increases the size and cost of the converter [4.14], [4.15]. The main steps of RNM field analysis are presented in the form of a flow chart as shown in Fig.4.9. As previously discussed the core geometry and number of turns of

each winding were selected based on primary design. The magnitude of terminal voltage in the design procedure was chosen such that the peak flux density would just reach the knee point of the magnetization curve, and thus the linear model can give sufficient accuracy.

To start the field analysis, the magnetic structure is partitioned into three different areas, including magnetic core, covering insulator and the free space around the core. The windings effect is not included in the analysis due to the complexity of flux distribution inside the conductors and difficulty of their modeling using RNM. The cylindrical coordinate system was selected for numerical modeling due to the axial symmetry of the toroidal core.

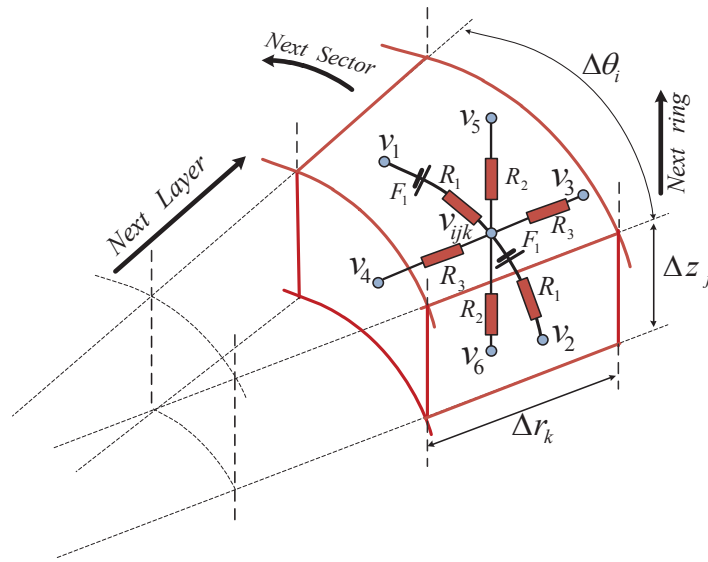


Fig.4.10 A sample of 3D reluctance element

The core is partitioned into thousands of 3D elements arranged in sectors in  $\theta$ , layers in radial  $r$ , and rings in  $Z$  directions. Each element is presented by  $Q_{ijk}$ , where indexes,  $i, j$  and  $k$ , represent the unique situation of the 3D element among the entire magnetic structure. The element includes six reluctances linked to a central node at one side and to the boundary nodes at the boundary surfaces of the element at the other side as shown in Fig.4.10. The reluctances are defined based on the permeability factor of the element and its geometrical shape. As an example for element  $Q_{ijk}$  shown in the figure, the reluctances in all three directions can be defined from

$$R_{l_{ijk}} = \frac{(k - 0.5)(\Delta\theta_i)(\Delta r_k)}{2\mu_r(\Delta Z_j)(\Delta r_k)} \quad (4.14)$$

$$R_{2ijk} = \frac{(\Delta Z_j)}{2\mu_r(k-0.5)(\Delta r_k)^2 \Delta \theta_i} \quad (4.15)$$

$$R_{3ijk} = \frac{(\Delta r_k)}{2\mu_r(\Delta Z_j)(k-0.5)\Delta r_k(\Delta \theta_i)} \quad (4.16)$$

where  $\mu_r$  is the permeability of magnetic core,  $R_{1ijk}$ ,  $R_{2ijk}$  and  $R_{3ijk}$  are the reluctances in  $\theta$ ,  $Z$  and  $r$ , respectively. The value of voltage sources,  $F_{ijk}$  in the case of toroidal core in the directions of  $r$  and  $Z$  is almost zero and in the  $\theta$  direction depends on the winding turns covering the element and the current flowing through it. In the case of the toroidal core assuming same flux density in the  $\theta$  direction, the value of  $F_{1ijk}$  can be calculated as

$$F_{1ijk} = \frac{N_s I_s}{2m} \quad (4.17)$$

where  $N_s$  is the number of turns of winding,  $I_s$  the current flowing through it, and  $m$  the total number of 3D elements enclosed by the winding. The calculation domains, such as the number of sectors, rings and layers, are defined in the first step. The analysis starts with the first sector of the first ring of the first layer and the next ring is selected when all sectors are analyzed and the next layer is selected when the analysis of all rings of the previous layer is completed. Applying the nodal analysis to the central node of an element would result in a group of equations with the central node voltages as unknowns. The general equation for element  $Q_{ijk}$  considering the central node of adjacent elements and interconnected resistances can be written as

$$\begin{aligned} & Y_{ijk} V_{ijk} + Y_{(i-1)jk} V_{(i-1)jk} + Y_{(i+1)jk} V_{(i+1)jk} + Y_{i(j-1)k} V_{i(j-1)k} \\ & + Y_{i(j+1)k} V_{i(j+1)k} + Y_{ij(k-1)} V_{ij(k-1)} + Y_{ij(k+1)} V_{ij(k+1)} + Y'_{ijk} F_{1ijk} \\ & + Y'_{(i-1)jk} F_{1(i-1)jk} + Y'_{(i+1)jk} F_{1(i+1)jk} = 0 \end{aligned} \quad (4.18)$$

where  $i=2,3,4,\dots,s,s+1$ ,  $j=2,3,4,\dots,r,r+1$ ,  $k=2,3,4,\dots,l,l+1$  and

$$Y_{ijk} = \left[ \begin{array}{l} (R_{1ijk} + R_{1(i-1)jk})^{-1} + (R_{1ijk} + R_{1(i+1)jk})^{-1} + (R_{2ijk} + R_{2i(j-1)k})^{-1} + \\ (R_{2ijk} + R_{2i(j+1)k})^{-1} + (R_{3ijk} + R_{3ij(k-1)})^{-1} + (R_{3ijk} + R_{3ij(k+1)})^{-1} \end{array} \right] \quad (4.19-a)$$

$$Y_{(i-1)jk} = (R_{1ijk} + R_{1(i-1)jk})^{-1}, \quad Y_{(i+1)jk} = (R_{1ijk} + R_{1(i+1)jk})^{-1} \quad (4.19-b)$$

$$Y_{i(j-1)k} = (R_{2ijk} + R_{2i(j-1)k})^{-1}, \quad Y_{i(j+1)k} = (R_{2ijk} + R_{2i(j+1)k})^{-1} \quad (4.19-c)$$

$$Y_{ij(k-1)} = (R_{3ijk} + R_{3ij(k-1)})^{-1}, \quad Y_{ij(k+1)} = (R_{3ijk} + R_{3ij(k+1)})^{-1} \quad (4.19-d)$$

$$Y'_{ijk} = (R_{1ijk} + R_{1(i-1)jk})^{-1} - (R_{1ijk} + R_{1(i+1)jk})^{-1} \quad (4.19-e)$$

$$Y'_{(i-1)jk} = (R_{1ijk} + R_{1(i-1)jk})^{-1}, \quad Y'_{(i+1)jk} = (R_{1ijk} + R_{1(i+1)jk})^{-1} \quad (4.19-f)$$

are conductance factors.

The final equation of entire magnetic structure considering the equations of all nodes, can be written in the matrix form as

$$Y\tilde{V} - Y'\tilde{F} = 0 \quad (4.20)$$

where  $Y', Y, \tilde{V}$  and  $\tilde{F}$  are the central node linked conductance, source linked conductance, central node voltage and source voltage matrices, respectively. To solve the above equation and define the potential of all central nodes of the 3D elements an initial condition is considered. The potential of the central nodes of the elements situated on the last layer and rings are assumed to be zero. The number of nodes and the number of 3D elements depend on the number of selected divisions in three dimensions of cylindrical coordination. The value of current between the nodes representing the magnetic flux can be calculated using the potential of central nodes of adjacent elements and their interconnected resistances. Considering all branches of the element in three directions, one can calculate the field intensity  $H_i$ , the branch volume  $V_i$  and the flux density  $B_i$  for  $i=1,2,\dots,6$  as [4.23]

$$H_i = (v_{ijk} - v_i) / l_i \quad (4.21)$$

$$V_i = A_i l_i \quad (4.22)$$

$$B_i = \varphi_i / A_i \quad (4.23)$$

The closed-form volumetric integration of the distributed stored energy can be calculated by

$$W_S = \int_V \frac{H \cdot B}{2} dV = \frac{\mu}{2} \int_V |H|^2 dV \quad (4.24)$$

where  $W_S$  is the stored energy in a 3D element enclosed by volume  $V$ , and  $\mu$  the magnetic permeability [4.23]. The net magnetic energy stored in the  $i$ -th branch of the element  $Q_{ijk}$  based on (4.21)-(4.24) assuming constant flux density in the element can be calculated by

$$W_i = (\mu V_i H_i^2) / 2 \quad (4.25)$$

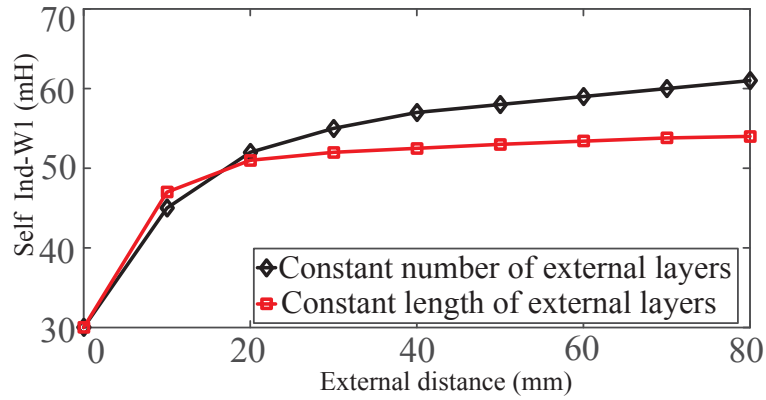
Substituting (4.21)-(4.24) into (4.25) results in

$$W_i = (v_{ijk} - v_{lij} - F_i)^2 / 2R_i \quad (4.26)$$

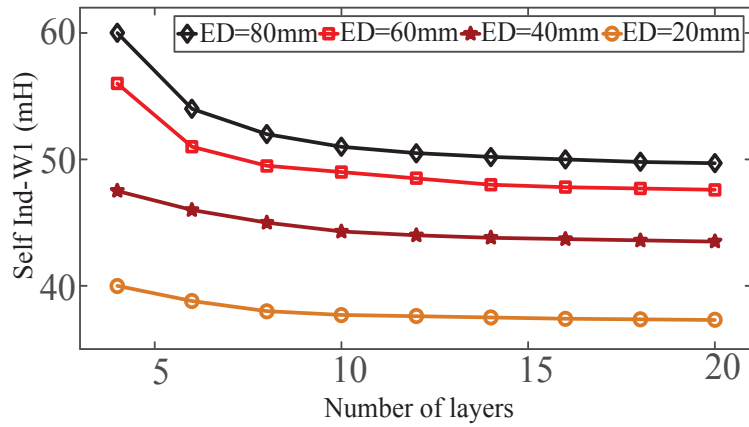
where  $R_i$  is the reluctance of the respective branch and the value  $F_i$  should be equal to zero for branches without *mmf*. The overall energy of a 3D element  $Q_{ijk}$  can be obtained by integrating the energy in all six branches. To calculate the winding self-inductances, a closed surface enclosing the entire magnetic structure is assumed. The total enclosed energy is calculated by integrating the energy of all  $n$  elements inside the surface. The resultant total energy,  $W_S$ , can be used to define the equivalent inductance,  $L_{eq}$ , as

$$L_{eq} = \frac{2W_S}{I_s^2} \quad (4.27)$$

The self-inductance of windings one  $L_{11}$ , two  $L_{22}$ , and three  $L_{33}$  were calculated based on (4.27). To define the leakage inductances of the windings,  $L_{l1}$ ,  $L_{l2}$  and  $L_{l3}$ , two different enclosed surfaces, one including only the core area and the other enclosing the enclosed core, insulator and surrounding areas (including leakage flux distribution area) are considered and the difference between the energies stored within the volumes enclosed by these surfaces can be used. The values of self and the leakage inductances of all windings of the magnetic link are calculated by using the method outlined above. The core loss resistance for the resultant structure can be found using the Steinmetz equation based on the flux density and frequency. The values of  $B$ ,  $H$  and  $L$  are calculated based on (4.21)-(4.27).



(a)



(b)

**Fig.4.11 (a) the self-inductance of winding one for two cases of fixed and stretchable layer selection, (b) self-inductance of winding one for various external distances.**

The resultant values are compared with specifications and in the case of excessive error the design variables are changed according to the priority. In the case of acceptable results, the magnetic structure is analyzed for losses and thermal considerations. To improve the accuracy analysis various calculation domains and strategies are applied. As an example, to find a proper external distance for field analysis, a constant length of layer should be kept by adding new layers to the previous one rather than stretching the existing layers. Fig.4.11(a) shows that for an external distance of more than 40 mm in the radial direction, the equivalent self-inductance of winding one, W1 ( $L_{11}$ ) remained almost constant ( $\approx 52 \mu\text{H}$ ) in the case of constant length of layers and it presented 15 % error ( $\approx 60 \mu\text{H}$ ) for stretchable elements.

Fig.4.11-(b) presents the computed value of  $L_{11}$  for various external distances. One can see that the best selection for the number of layers is 14 and for external distances more than 60 mm the calculated value of inductance changes less than 5 % ( $\approx 2.5 \mu\text{H}$ )

increase). Selection of a reasonable value of 3D elements will result in an acceptable computation time and accuracy. For example, in the case of considering 14400 elements (72 sectors in  $\theta$  direction, 10 rings in  $Z$  direction and 20 layers in radial direction, the total computation time was about 230 seconds using a PC system (CPU: 64 bit/3.1 GHz Intel i5-2400, RAM: 4.00GB). The resulting values of core dimension, number of winding turns and thickness of insulator are used to implement the prototype of the magnetic link.

#### 4.6 Loss Analysis of the Magnetic Link

The next stage of design is the analysis of resultant magnetic structure for core loss and copper loss evaluation. Due to the definition of number of turns, inductances, magnetic flux and dimension of the core in the previous stage, the required parameters for loss analysis are now available. Tables 4.6-4.8 illustrate the main parameters of the magnetic link used in electrical, magnetic and thermal analysis.

#### 4.7 Core Loss Analysis

To calculate the core loss the empirical loss-expressions are used due to the non-linear relation of magnetic loss density and magnetic induction. The original Steinmetz equation (OSE) has been conventionally used to estimate the magnetic loss and is presented as

$$P_v = kf^m B_{\max}^n \quad (4.28)$$

where  $P_v$  is the magnetic loss density in  $W/m^3$ ,  $f$  is the frequency in kHz, and  $B_{\max}$  is the maximum magnitude of flux density in T. The constant coefficients  $k$ ,  $m$  and  $n$  are determined by the material characteristics, and are normally provided by the manufacturers under sinusoidal excitations. Recently, several time-dependent expressions have been proposed to extend the equation to non-sinusoidal excitation waveforms. The modified Steinmetz equation (MSE), natural Steinmetz extension (NSE), improved generalized Steinmetz equation (IGSE) and the waveform-coefficient Steinmetz equation (WCSE) are some examples [4.14],[4.15],[4.50],[4.51].

To find the modified equations, the waveforms of the square wave excitation voltage generated by H-Bridge units and the resulting magnetic induction (see Fig.4.12) are modelled using piecewise linear equations and applied to the OSE.

**TABLE 4.6 Electrical Parameters of the Magnetic Link**

Description	Value
Electrical Parameters	
Nominal power (kVA)	P=4.5
Nominal power of each winding(kVA)	$P_{W1}=2, P_{W2}=1.5, P_{W3}=1$
Nominal windings voltage	$V_{W1}=300V, V_{W2}=60V, V_{W3}= 30-110V$
Number of turns	$N1 : N2 : N3= 52 : 12 : 8$
Operating frequency	10 kHz
Required leakage inductances and the magnetizing inductance	$L_{l2}=14\mu H, L_{l1}=35\mu H, L_{l3}=18\mu H, L_m=50 \mu H$

**TABLE 4.7 Parameters of the Design and Experimental Tests**

Description	Value
Thermal Analysis Parameters	
Emissivity of insulator tape	0.87
Emissivity of coated conductors	0.97
Stefan Boltzmann constant	$5.670367*10.E-8 W.m^{-2}.k^{-4}$
Thermal conductivity of copper	401 W/m.k
Thermal conductivity of insulator	0.19 W/m.k
Thermal conductivity of air	0.024 W/m.k
Heat transfer coefficient of the air	24 W/m <sup>2</sup> .k

**TABLE 4.8 Magnetic and Loss Analysis Parameters of the Magnetic Link**

Description	Value
<b>Magnetic Parameters</b>	
Core material	Amorphous, 2605SA1
Magnetic core shape	Toroidal
Magnetic core dimension	$r_{in}(\text{mm})=32.5, r_{out}(\text{mm})=52.5, h(\text{mm})=25$ , $w(\text{mm})=20$
Maximum flux density	$B_m=1.2 \text{ T}$
Magnetic permeability	26000
Mass density, 2605SA1	$7.18 \text{ G/cm}^3$
Curie temperature, 2605SA1	$395 \text{ }^\circ\text{C}$
<b>Loss Analysis Parameters</b>	
Maximum operating temperature	$T_{max}=65 \text{ }^\circ\text{C}$
Dimensions of the magnetic tape	25mm width /20 $\mu\text{m}$ thickness
Litz wire strand diameter	27 AWG / 0.35 mm
Insulation tape material	Polyvinyl chloride (PVC)
Insulation thickness	Thickness=0.2 mm
Stacking factor	0.94
Resistivity factor of copper conductor	$1.7*10.E-8 \text{ } \Omega.\text{m}$
Conductivity of copper conductor	$58.5*10.E+6 \text{ Siemens/m}$
DC resistance of windings (m $\Omega$ )	$R_{dc-w1}=45, R_{dc-w2}=9, R_{dc-w3}=17$
Permeability of copper conductor	$1.256*10.E-6 \text{ H.m}^{-1}$
Maximum current density	$4 \text{ A.mm}^{-2}$

As an example, the modified equations of IGSE and WCSE can be presented respectively [4.52] as

$$P_v = 2^{n+m} k_i f^m B_{sq}^n D^{n-m+1} \quad (4.29)$$

$$P_v = \frac{\pi}{4} \left(1 + \frac{\Omega}{\pi}\right) k f^m B_{sq}^n D^n \quad (4.30)$$

where  $B_{sq}$  is the maximum flux density in the case of square wave excitation,  $k_i$  the modified value of  $k$ ,  $\Omega$  the zero voltage angle of the rectangular waveform, and  $D$  the duty defined as (see Fig.4.12)

$$D = (1 - \Omega / \pi) \quad (4.31)$$

The methods have been simulated and experimentally tested for phase shift converter application and the MSE and IGSE have been selected as the most suitable ones based on the experimental measurements [4.52].

$$P_v = 2^{n+m} k_i f^m B_{sq}^n D^{n-m+1} \quad (4.29)$$

$$P_v = \frac{\pi}{4} \left(1 + \frac{\Omega}{\pi}\right) k f^m B_{sq}^n D^n \quad (4.30)$$

where  $B_{sq}$  is the maximum flux density in the case of square wave excitation,  $k_i$  is the modified value of  $k$ ,  $\Omega$  is the zero voltage angle of the rectangular waveform and  $D$  is the duty ratio as presented in Figure 4.12 and can be defined from

$$D = (1 - \Omega / \pi) \quad (4.31)$$

The methods have been simulated and experimentally tested for phase shift converter application and the MSE and IGSE have been selected as the most suitable ones based on the experimental measurements [4.52].

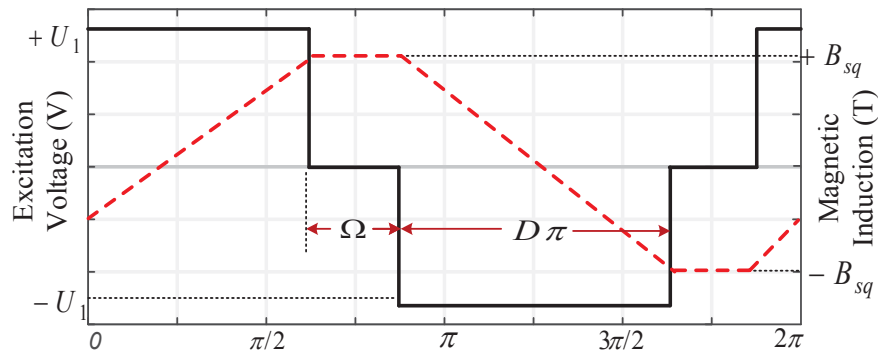


Fig.4.12 The waveforms of voltage and magnetic induction for  $\Omega=\pi/3$ .

The IGSE is used in this research to estimate the core loss in the magnetic link excited by variable duty ratio voltage source. The values of constant coefficients  $m$ ,  $n$

and  $k_i$  are suggested in [4.52] based on the experimental measurements for frequency of 1 kHz for Metglas amorphous alloy 2605SA1. They are initially used in the design although to check the validity of the coefficients, an experimental test was conducted on the experimentally developed magnetic link. The core loss was measured for three cases of 10, 30 and 50 kHz. Applying curve fitting to the results showed slight changes in the coefficients as presented in Table.4.9. The core loss calculations are carried out for the nominal load presented in Table.4.6. The value of zero voltage angle,  $\Omega$ , is defined by the amplitude of the voltage source connected to the port as

$$\Omega = \pi(V_P - V_{P-\min})/V_P \quad (4.32)$$

where  $V_P$  is the actual and  $V_{P-\min}$  is the minimum voltage of the port. In the case of PV panel directly connected to the H-bridge and considering  $V_{p-\min}=30$  V, and  $V_{p-\max}=120$  V then  $\Omega_{\min}=0$  and  $\Omega_{\max}=3\pi/4$  using (4.32). For the fuel cell and inverter ports, the duty ratio is kept constant ( $\Omega=0$ ,  $D=1$ ) due to the constant voltage of their buses.

**TABLE 4.9 Coefficients of Steinmetz Equation**

Coefficient	$k$	$m$	$n$
Original Steinmetz equation (Sinusoidal)	$K=6.500$	1.51	1.74
Suggested in reference [45] (square $f=1$ kHz)	$K_i=0.62$	1.51	1.74
Experimentally measured (Square $f=10$ kHz)	$K_i=0.58$	1.58	1.62

#### 4.8 Conduction Loss Analysis

To optimally design the magnetic link, the winding loss should be accurately evaluated considering non-sinusoidal effects of the voltage and current waveforms [4.52]-[4.54]. The high frequency time-varying currents produce the well-known skin and proximity effects which cause a non-uniform distribution of the current in the wire area [4.52]-[4.60]. Due to the dependency of these effects on the operating frequency, a frequency-dependent resistance model is used to analyze the copper loss [4.55]-[4.59]. To reduce the loss, using isolated, stranded and twisted conductors known as Litz wires is recommended for high frequency applications [4.55]-[5.60]. The loss evaluation of Litz wire windings is mainly based on either numerical [4.55], [4.56] or analytical [4.57]-[4.65] field analysis. The numerical methods provide more accurate results although they are relatively complicated and computationally expensive. On the contrary, the analytical methods are easy for design purposes and present good accuracy

where Litz wire strand radius remains below the skin depth [4.53], [4.69]. The analytical methods in turn can be divided into three groups [4.53]. A majority of works are based on Dowell's work in 1966 on loss analysis of foil and round conductors using the Maxwell's equations in Cartesian coordinates [4.57]. They have extended the Dowell's method for foil conductors to Litz wire windings of the same cross-section area and have applied a porosity factor to the resulting equation to increase the accuracy [4.58], [4.59]. The second approach known as the Ferreira method is based on exact field solution of stand-alone round conductor using Bessel functions [4.60]. The analysis was later extended to a complete winding [4.61], [4.62]. To improve the accuracy of the method in high frequency applications, an expression was introduced using modified Bessel functions [4.63]. The last group calculates the conduction loss using complex conductor permeability [4.64]. The method provides a good accuracy although it is complicated to determine the real and imaginary parts of the winding permeability [4.52]. The first two methods are widely used in the literatures and their accuracy is compared [5.62], [5.65]. Both methods provide good accuracy especially where strand diameter is much lower than the skin depth [4.53], [5.59], [5.62]. On the other hand, the root mean square (RMS) value of winding currents needs to be calculated for the copper loss analysis. In the case of non-sinusoidal currents the analysis can be established on harmonic basis due to linear behaviour of copper [4.53], [4.52], [5.66], [5.67]. A detail study on copper loss analysis of dc-dc converters under variable phase shift and duty ratio has been presented recently [5.66]-[5.69]. This research studies the copper loss analysis of a three winding magnetic link employed in a multi-port phase shift converter. In this research the study in [5.52] is extended to the three port phase shift converters, and the amplitude, duty ratio and phase shift variations are taken into account. The maximum and minimum loss operation points are defined for two common cases of converter operating in dual active bridge (DAB) and triple active bridge (TAB) modes. To validate the analytical method, the copper losses of all three windings are measured experimentally and are compared with the analytical calculations.

Due to the linear behavior of copper, conduction loss analysis is carried out based on the harmonic contents of the currents in the windings of the magnetic link. The total loss then can be found by summing up the losses of each harmonic component as the following

$$P_{Cu} = \sum_{n=1}^h P_{Cu,n} \quad (4.33)$$

where  $P_{cu,n}$  is the resultant loss of  $n$ -th harmonic. The skin and proximity effects on the windings resistance can be considered separately for conducting loss analysis due to their orthogonality principle [4.70]. They can be modelled as a frequency-dependent resistance for each harmonic in case of non-sinusoidal currents. Therefore, the resultant loss of the  $n$ -th harmonic,  $P_{cu,n}$ , can be defined as

$$P_{Cu,n} = \left( \frac{I_n}{\sqrt{2}} \right)^2 R_{ac,n} \quad (4.34)$$

where  $R_{ac,n}$  is the ac resistance of the Litz wire winding for  $n$ -th harmonic, and  $I_n$  the peak value of amplitude of  $n$ -th harmonic of the windings current under nominal load condition. The analytical methods of calculating  $R_{ac,n}$  and  $I_n$  are discussed in the following sections.

#### 4.8.1 Harmonic based analysis of the winding currents

The simplified equivalent circuit of the magnetic link facilitates the harmonic based analysis. The T-model configuration of the magnetic link considering only the leakage inductances, referred to winding one can be transformed to the equivalent  $\Delta$ -model neglecting the magnetizing inductance [4.5].

The T-model to  $\Delta$ -model transform of the three windings magnetic link can be defined by equating the input impedances of the two models for each of the three windings while the other two windings are short circuited based on the superposition rule. On the other hand, the high frequency square wave voltages generated by the H-bridge units are presented as voltage source.

Fig.4.13(a) and (b) show more details on the transformed circuits [4.5]. The resultant equations can be written as

$$n_2 = \frac{L_m}{L_{l1} + L_m} m_2 \quad (4.35-a)$$

$$n_3 = \frac{L_m}{L_{l1} + L_m} m_3 \quad (4.35-b)$$

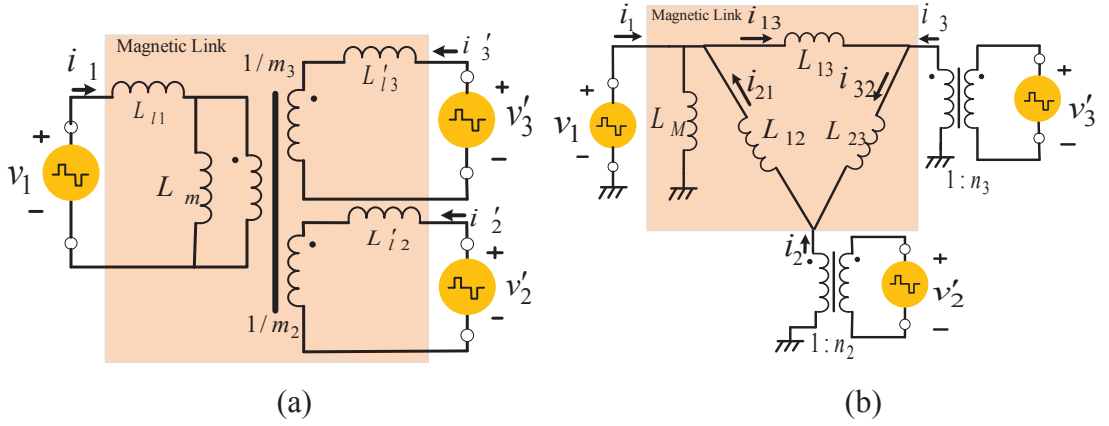


Fig.4.13 (a) T-model and, (b) Δ-model representation of the three winding magnetic link.

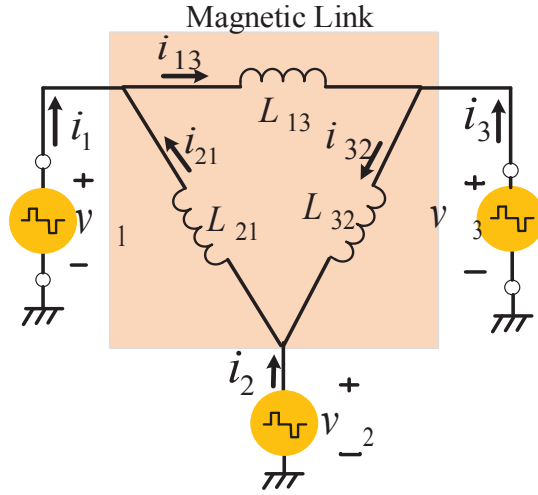


Fig.4.14 The Δ-model equivalent circuit of three winding magnetic link.

$$L_M = L_{l1} + L_m \quad (4.35-c)$$

$$L_{12} = \left( L_{l1} + \left( \frac{m_2^2}{L'_{l2}} + \frac{m_3^2}{L'_{l3}} + \frac{1}{L_m} \right)^{-1} \right) \left( \frac{L'_{l2}}{m_2^2} + \left( \frac{m_3^2}{L'_{l3}} + \frac{1}{L_m} \right)^{-1} \right) \left( \frac{m_3^2}{L'_{l3}} + \frac{1}{L_m} \right) \frac{L'_{l1} + L_m}{L_m} \quad (4.35-d)$$

$$L_{13} = \left( L_{l1} + \left( \frac{m_2^2}{L'_{l2}} + \frac{m_3^2}{L'_{l3}} + \frac{1}{L_m} \right)^{-1} \right) \left( \frac{L'_{l3}}{m_3^2} + \left( \frac{m_2^2}{L'_{l2}} + \frac{1}{L_m} \right)^{-1} \right) \left( \frac{m_2^2}{L'_{l2}} + \frac{1}{L_m} \right) \frac{L'_{l1} + L_m}{L_m} \quad (4.35-e)$$

$$L_{23} = \left( \frac{L'_{l2}}{m_2^2} + \left( \frac{1}{L_{l1}} + \frac{m_3^2}{L'_{l3}} + \frac{1}{L_m} \right)^{-1} \right) \left( \frac{L'_{l3}}{m_3^2} + \left( \frac{1}{L_{l1}} + \frac{1}{L_m} \right)^{-1} \right) \left( \frac{1}{L_{l1}} + \frac{1}{L_m} \right) \frac{(L_{l1} + L_m)^2}{L_m} \quad (4.35-f)$$

$$i_2 = n_2 i'_2, \quad i_3 = n_3 i'_3, \quad v_2 = \frac{1}{n_2} v'_2, \quad v_3 = \frac{1}{n_3} v'_3 \quad (4.35-g)$$

The final Δ-equivalent model is presented in Fig.4.14. According to the resulting equivalent model the three port phase shift converter can be considered as three DAB converters [4.5]. To start the analysis, the leading phase shift angles,  $\phi_{21}$  and  $\phi_{31}$ , are assumed between voltages of ports two and three to port one as reference port as

presented in Figure 4.15. The variation range of the phase shift angles is limited between 0 to  $+\pi/2$ . Due to the variation of voltage of PV port (Port three), the zero voltage angle,  $\Omega$  (refer to Fig.4.15) is defined to control the duty ratio of the generated square wave and is calculated by

$$\Omega = \pi(V_3 - V_{3-\min}) / V_3 \quad (4.36)$$

where  $V_3$  is the actual value and  $V_{3-\min}$  the minimum value of voltage of the PV port. The duty ratio,  $D$ , can be defined as

$$D = (1 - \Omega / \pi) \quad (4.37)$$

On the other hand, the duty ratio of fuel cell and inverter ports is kept constant ( $\Omega=0$ ) due to the constant voltage of their buses.

The RMS value of the currents in the windings of the magnetic link should be calculated for copper loss analysis. They can be found using currents in the inductances of equivalent  $\Delta$ -model.

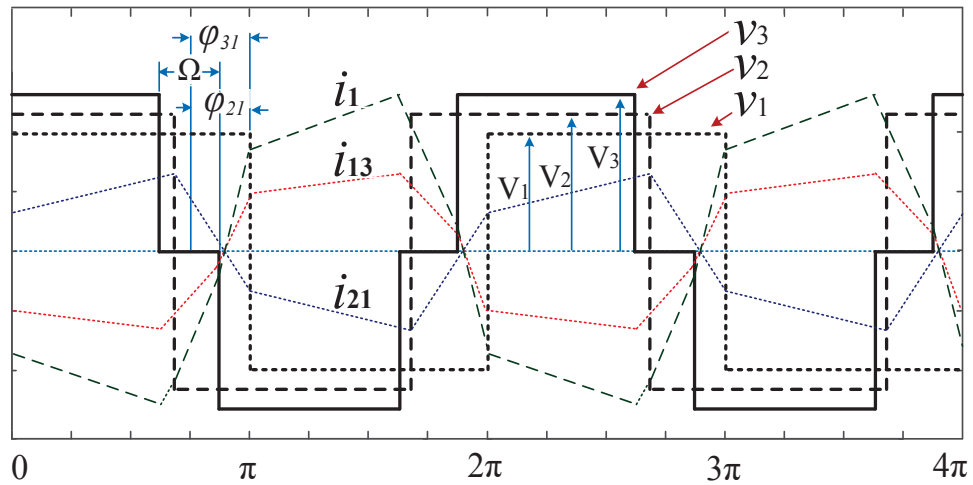


Fig.4.15 Voltage and current wave forms related to current  $i_1$  in winding one.

Figure 4.15 shows the voltages and currents of  $\Delta$  equivalent model are required to calculate the current in winding one. The harmonic based analysis of windings current has been widely used for copper loss analysis in case of non-sinusoidal waveforms [4.52], [4.66], [4.67]. The fundamental harmonic phasor diagram of currents and voltages in the equivalent  $\Delta$ -model is presented in Fig.4.16 and used as a reference in the following analysis.

To carry out the analysis, the high frequency square wave voltages are represented based on their Fourier series as

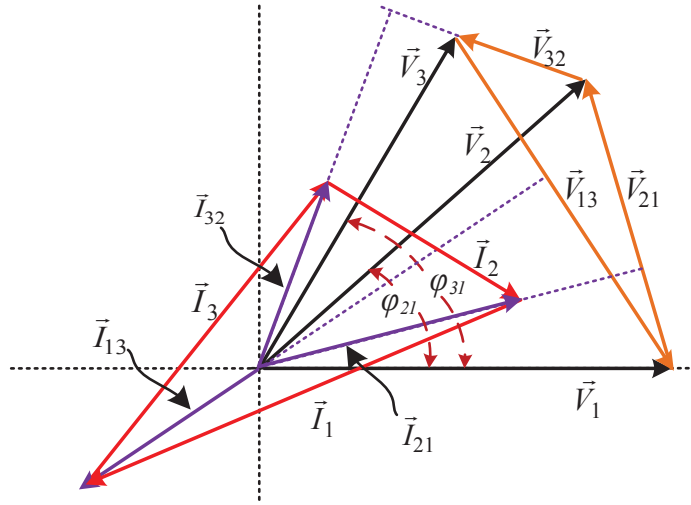


Fig.4.16 Fundamental phasor diagram of the three port converter

$$\begin{aligned}
 v_1(t) &= \sum_{n=1}^{\infty} V_{1,n} \sin(n\omega t) \\
 v_2(t) &= \sum_{n=1}^{\infty} V_{2,n} \sin(n(\omega t + \varphi_{21})) \\
 v_3(t) &= \sum_{n=1}^{\infty} V_{3,n} \sin(n(\omega t + \varphi_{31}))
 \end{aligned} \tag{4.38}$$

where  $V_{k,n}$  is the amplitude of the  $n$ -th harmonic of the voltage across winding  $k$ .

For port one and port two, due to their constant amplitude, we have

$$V_{k,n} = \frac{2V_k(1 - \cos(n\pi))}{n\pi}, \quad k=1,2 \tag{4.39}$$

For port three, due to the variable amplitude and duty ratio, it can be calculated by

$$V_{3,n} = \frac{2V_{3-\min} \cos(n\Omega/2)(1 - \cos(n\pi))}{n(\pi - \Omega)} \tag{4.40}$$

As  $i_1 = i_{13} - i_{21}$ ,  $i_2 = i_{21} - i_{32}$  and  $i_3 = i_{32} - i_{13}$ , to find  $i_1$ , currents  $i_{21}$  and  $i_{13}$  should be calculated by using voltage difference across inductances  $L_{21}$  and  $L_{13}$ . The voltage  $v_{21}$  can be calculated by (4.38) as

$$v_{21}(t) = v_2(t) - v_1(t) = \sum_{n=1}^{\infty} V_{21,n} \cos(n\omega t + \alpha_n) \tag{4.41}$$

with the amplitude of  $n$ -th harmonic as

$$V_{21,n} = \sqrt{V_{1,n}^2 + V_{2,n}^2 - 2V_{1,n}V_{2,n} \cos(n\varphi_{21})} \quad (4.42)$$

and the phase of  $n$ -th harmonic as

$$\alpha_n = \tan^{-1} \frac{V_{2,n} \sin(n\varphi_{21})}{V_{2,n} \cos(n\varphi_{21}) - V_{1,n}} \quad (4.43)$$

The current  $i_{21}$  can then be calculated taking into account  $\pi/2$  as phase shift angle of the leakage inductances by

$$i_{21} = \sum_{n=1}^{\infty} I_{21,n} \sin(n\omega t + \alpha_n - \frac{\pi}{2}) \quad (4.44)$$

where  $I_{21,n}$  is the amplitude of the  $n$ -th harmonic and can be calculated by

$$I_{21,n} = \frac{V_{21,n}}{(2\pi f L_{21})} \quad (4.45)$$

The current  $i_{13}$  in the winding  $L_{13}$  is defined in a similar way considering  $\varphi_{31}$  as the phase shift angle between  $v_3$  to  $v_1$ ,  $I_{13,n}$  as the amplitude and  $(\beta_n - \pi/2)$  as the phase angle of  $n$ -th harmonic. The  $n$ -th harmonic of the current in the source  $v_1$ ,  $i_{1,n}$  (refer to Figure 4.14) can be calculated by

$$i_{1,n}(t) = i_{13,n} - i_{21,n} = \sum_{n=1}^{\infty} I_{1,n} \sin(n\omega t + \psi_{1,n}) \quad (4.46)$$

where  $I_{1,n}$  and  $\psi_{1,n}$  are the amplitude and the phase angle of  $n$ -th harmonic of current  $i_1$  respectively and can be determined by

$$I_{1,n} = \sqrt{I_{13,n}^2 + I_{21,n}^2 - 2I_{13,n}I_{21,n} \cos(n(\beta_n - \alpha_n))} \quad (4.47)$$

$$\psi_{1,n} = \tan^{-1} \left( \frac{I_{13,n} \sin(n\beta_n) - I_{21,n} \sin(n\alpha_n)}{I_{13,n} \cos(n\beta_n) - I_{21,n} \cos(n\alpha_n)} \right) \quad (4.48)$$

The amplitude of each harmonic of the current in winding two,  $I_{2,n}$ , and the phase angle  $\psi_{2,n}$  and in winding three,  $I_{3,n}$  and  $\psi_{3,n}$  can be calculated in a similar way. It can be seen from (4.38) and (4.40) that the voltages generated by each H-bridge and consequently the resultant current in the windings only contain the odd harmonics.

Therefore, the ac resistance of the windings considering skin and proximity effect as another element of loss analysis should be evaluated considering these harmonics.

#### 4.8.2 Calculation of ac resistance

The skin and proximity effects are considerable in medium and high frequency applications. To reduce these effects, the stranded, twisted insulated conductors known as Litz wires should be used. Considering these high frequency effects, the ac resistance of a Litz wire winding is a function of frequency while the dc resistance is relatively constant and can be calculated by

$$R_{dc} = \frac{4N_k l_s \rho_{Cu}}{n_s \pi d_{str}^2} \quad (4.49)$$

where  $N_k$  is number of turns of  $k$ -th winding of the magnetic link,  $l_s$  the average length of one turn,  $\rho_{cu}$  the resistivity of copper,  $d_{str}$  the strand diameter, and  $n_s$  the number of strands in Litz wire. The skin and proximity effect losses related to each harmonic of the current can be modelled through a frequency dependent resistance,  $R_{ac,n}$  [4.54]-[4.63]. The ratio of  $R_{ac,n}$  to  $R_{dc}$  known as the ac resistance factor,  $F_{r,n}$ , can be defined as

$$F_{r,n} = \frac{R_{ac,n}}{R_{dc}} \quad (4.50)$$

In case of using Litz wires the skin and proximity effects appear in both strand and bundle levels [4.59]. The bundle level proximity effect can be reduced efficiently by twisting; however reducing bundle level skin effect needs more complex constructions [4.59] [4.69]. On the other hand, the strand level proximity effect is more considerable compared with skin effects especially in case of high number of layers [4.69]. The skin and proximity effects analysis in Litz wires are carried out based on two best-known analytical methods, the Dowell method and Ferreira method. In the first method, the round conductors are replaced with square conductors of the same area and then an equivalent foil conductor same as that which Dowell analysis found. The one dimensional field analysis then is applied to the foil to find the losses [4.57]-[4.59]. The second approach is based on the field analysis of a single round conductor using well-known Bessel functions and some of its applications are proposed by Ferreira [4.60]-[4.63]. Both methods provide similar results and accuracy for small penetration ratios

[4.52] although it has been shown that the second method provides more accurate results in high frequency applications [4.63]. Both methods are reviewed briefly although the first method is used for our particular application due to the simplicity, relatively low switching frequency (10 kHz) and low penetration ratio.

The first method is based on Dowell's equation for high frequency winding resistance of round conductors. The equation for the ac resistance factor  $F_{r,n}$  of the  $m$ -th layer of round conductors is

$$F_{r,n} = \zeta_n (v_{1,n} + \frac{2(m^2 - 1)}{3} v_{2,n}) \quad (4.51)$$

where

$$v_{2,n} = \frac{\sinh(\zeta_n) - \sin(\zeta_n)}{\cosh(\zeta_n) + \cos(\zeta_n)} \quad (4.52-a)$$

$$v_{1,n} = \frac{\sinh(2\zeta_n) + \sin(2\zeta_n)}{\cosh(2\zeta_n) - \cos(2\zeta_n)} \quad (4.52-b)$$

$$\zeta_n = \left(\frac{\pi}{4}\right)^{0.75} \frac{d}{\delta_n} \sqrt{\eta}, \quad \eta = \frac{d}{P} \quad (4.53)$$

is the porosity factor of round conductor,  $d$  the conductor diameter,  $P$  the distance between centers of two adjacent conductors,

$$\delta_n = \sqrt{\frac{\rho_{Cu}}{\pi \mu_0 n f}} \quad (4.54)$$

the skin depth of round conductor of  $n$ -th harmonic,  $\mu_0$  the permeability of free space, and  $f$  the frequency of the wave form.

The simplified equation for  $\zeta_n \leq 2$  can be found [4.58] as

$$F_{r,n} \approx 1 + \frac{(5m^2 - 1)}{45} \zeta_n^4 \quad (4.55)$$

The round conductor equation (4.51) is adapted to the Litz wire applications by substituting the number of layers,  $m$ , the effective number of Litz wire layers,  $m_l$ , and the variable  $\zeta_n$  and  $\zeta_{str,n}$  by using

$$m_l = m \sqrt{n_s} \quad (4.56)$$

and

$$\zeta_{str,n} = \left(\frac{\pi}{4}\right)^{0.75} \frac{d_{str}}{\delta_n} \sqrt{\eta_{str}} \quad (4.57)$$

where  $\eta_{str}$  is porosity factor of Litz wire [4.58].

In the second method, the skin and proximity effect losses of an isolated solid round conductor were evaluated using an exact solution of the internal and external magnetic fields. The method was introduced in 1966 [4.60] and further developed by Ferreira in 1990 [4.69], [4.70]. The closed form expression considering orthogonality of skin and proximity effects can be written as

$$F_{r,n} = \frac{\gamma_n}{2} \left[ \tau_{1,n} - 2\pi \frac{4(m^2 - 1)}{3} \tau_{2,n} \right] \quad (4.58)$$

with

$$\tau_{1,n} = \frac{ber(\gamma_n)bei'(\gamma_n) - bei(\gamma_n)ber'(\gamma_n)}{ber'(\gamma_n)^2 + bei'(\gamma_n)^2} \quad (4.59)$$

$$\tau_{2,n} = \frac{ber_2(\gamma_n)ber'(\gamma_n) + bei_2(\gamma_n)bei'(\gamma_n)}{ber'(\gamma_n)^2 + bei'(\gamma_n)^2} \quad (4.60)$$

where  $ber$  and  $bei$  are the real and imaginary parts of the first kind Bessel function and  $\gamma_n$  is the round conductor penetration ratio of the  $n$ -th harmonic and is defined as

$$\gamma_n = \frac{d}{\delta_n \sqrt{2}} \quad (4.61)$$

The accuracy of the resulting equation later was improved by introducing a porosity factor as a correction for magnetic field in the equation [4.71]. The skin and internal proximity effects in Litz wires were already determined in [4.60] based on the solid round conductor analysis presented in (4.58) and further improvements are applied by Ferreira [4.70]. To improve the accuracy in high frequency applications an expression also was introduced using exact Bessel functions [4.63]. The reduced expression applicable to low penetration ratios can be expressed as

$$F_{r,n} = \left[ 1 + \frac{\gamma_n^4}{192} \left( \frac{1}{6} + \frac{\pi^2 n_s P_f}{4} (16m^2 - 1 + \frac{24}{\pi^2}) \right) \right] \quad (4.62)$$

with

$$P_f = n_s (r_s / r_b)^2 \quad (4.63)$$

where  $P_f$ ,  $r_s$  and  $r_b$  are packing factor, strand radius and bundle radius of Litz wire, respectively, and  $\tau_{1,n}$  and  $\tau_{2,n}$  are approximated by first terms of their Taylor-series [4.62] as the following

$$\tau_{1,n} = \frac{2}{\gamma_n} + \frac{(\gamma_n)^3}{96} - \frac{(\gamma_n)^5}{3072} + \dots \approx \frac{2}{\gamma_n} \quad (4.64)$$

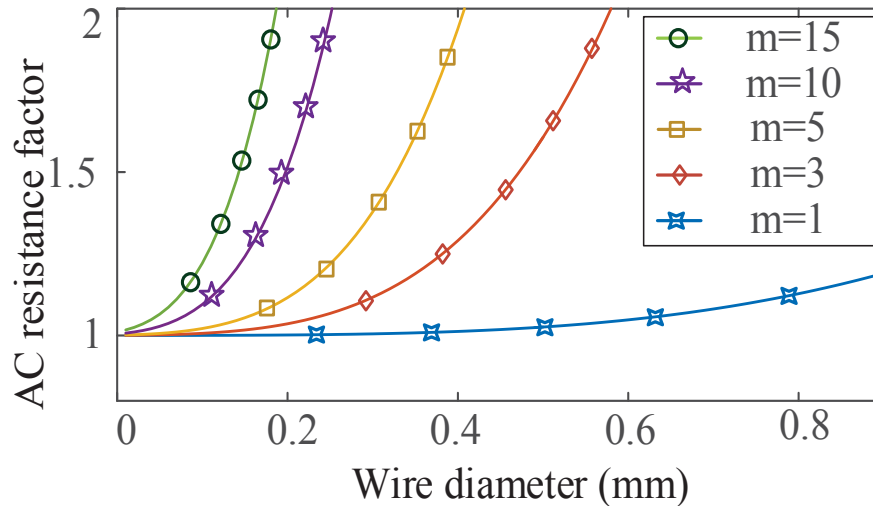
$$\tau_{2,n} = -\frac{(\gamma_n)^3}{16} + \frac{(\gamma_n)^7}{512} + \dots \approx -\frac{\gamma_n^3}{16} \quad (4.65)$$

This approximation for low penetration ratios ( $\gamma_n < \sqrt{2}$ ) due to utilization of Litz wires is acceptable. Although the reduced equation (4.61) presented good results for low penetration ratios it loses its accuracy for higher values of penetration ratio. In [4.61] two porosity factors are applied to the equation which makes it more accurate and in [4.62] the external field of each strand is considered accurately and a more accurate equation was achieved. In this section, the copper loss of the magnetic link is calculated based on the first method using (4.51) to (4.57).

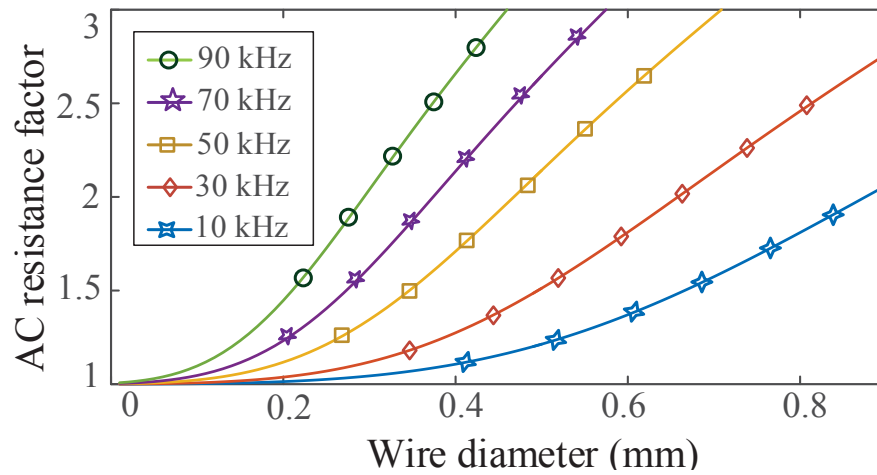
This section reviews the loss calculation of magnetic link considering all effective elements. As can be seen in (4.51)-(4.53), the harmonic frequency, strand diameter and number of windings layer have major effects on ac resistance and consequently the copper loss. Fig.4.17(a) presents the effect of increasing the number of winding layers on the ac resistance factor. As can be seen, the ac resistance of wire and the loss decreases by reducing the number of windings layers and using strands of less diameter. Fig.4.17(b) shows the ac resistance factor,  $F_{r,n}$ , for the five major harmonics in the converter currents. It can be seen that the ac resistance factor reduces for lower harmonic orders and strand diameters. Therefore, reducing operation frequency reduces not only the switching loss but also the winding losses in converters.

#### 4.9 Calculation of Maximum Copper loss

As will be shown the maximum copper loss in the magnetic link happens at maximum practical zero voltage angle,  $\Omega=3\pi/4$  and phase shift angles,  $\varphi_{21}=\pi/2$ ,  $\varphi_{31}=\pi/2$



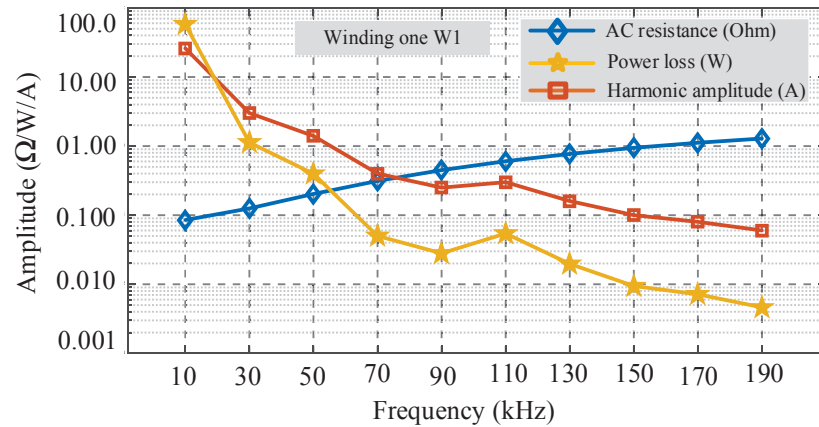
(a)



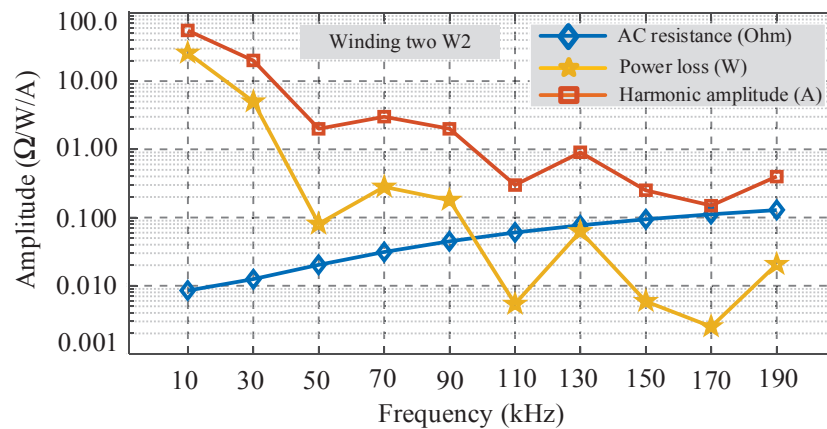
(b)

Fig.4.17 Ac resistance factor as a function of wire diameter for: (a) different number of winding layers, and (b) various harmonics of the current in windings of the magnetic link.

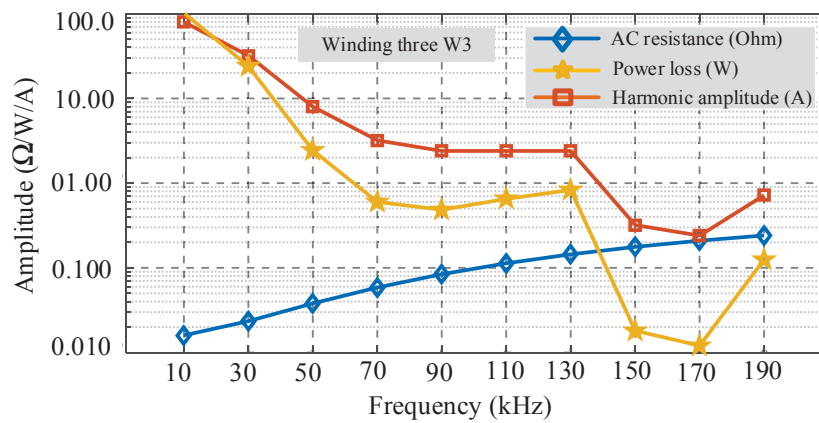
where  $V_1=300V$ ,  $V_2=60V$ ,  $V_3=120V$ . Under these conditions, the PV port voltage is maximum and the duty ratio is minimized which causes a high amplitude of the fundamental harmonic of the current in winding three and raises the copper loss. The maximum copper loss is important in the design and thermal analysis of the magnetic link. The copper losses of all three windings of the magnetic link were calculated separately for maximum copper loss condition based on the previously discussed methods. Fig.4.18 illustrates the calculated value of ac resistance,  $R_{ac}$ , copper loss and the amplitudes of the main current harmonics in windings of the magnetic link.



(a)



(b)



(c)

Fig.4.18 Calculated value of ac resistance  $R_{ac}$ , copper loss and harmonic amplitudes of the three windings of the magnetic link for maximum conduction loss condition. (a) winding one, (b) winding two and (c) winding three.

As can be seen, the copper loss is decreased with increasing the harmonic orders as the effect of reduction in harmonic amplitude overcomes the increasing ac resistance. The copper losses of winding one, two and three were estimated at about 15 W, 37 W and 78 W, respectively, and the total power of magnetic link in this case was 4.3 kW.

The total calculated copper loss is about 130 W which is 3 % of the total processed power.

#### 4.10 Loss Analysis under Phase Shift and Duty Ratio Variation

To evaluate the effect of phase shift angle and zero voltage angle of the voltage of PV port on the copper loss, two common operation modes of the converter are considered. In the first operation mode only the PV and inverter ports are active and the converter operates as a DAB converter. The phase shift angle,  $\varphi_{31}$ , was changed from 0 to  $\pi/2$  and zero voltage angle,  $\Omega$  from 0 to  $3\pi/4$  (due to variation of voltage from 30 V to 120 V on PV port). The total copper losses of windings one and three were calculated and the result is presented in Fig.4.19. It can be seen that in general any increase in the phase shift angle and zero voltage angle of the port three increases the conduction loss although the effect of phase shift angle is more considerable compared to that of zero voltage angle. Increasing the zero voltage angle at higher phase shift angles raises the amplitude of fundamental component resulting in more effect on conduction loss at higher phase shift angles.

In the second case, the converter operated in TAB mode and fuel cell and PV ports were active and transferred powers to the inverter port. The fuel cell port was operating with the constant phase shift angle and duty ratio ( $\varphi_{21}=\pi/2$ ,  $\Omega=0$ ) due to the constant voltage of the bus2. The amplitude of voltage, zero voltage angle and phase shift angle at the PV port were changed, similar to the previous test. The overall trend of the currents  $i_{21}$ ,  $i_{13}$  and  $i_{32}$  in the equivalent  $\Delta$ -model and in the windings  $i_1$ ,  $i_2$  and  $i_3$  with phase shift angle,  $\varphi_{31}$ , is presented in Fig.4.20.

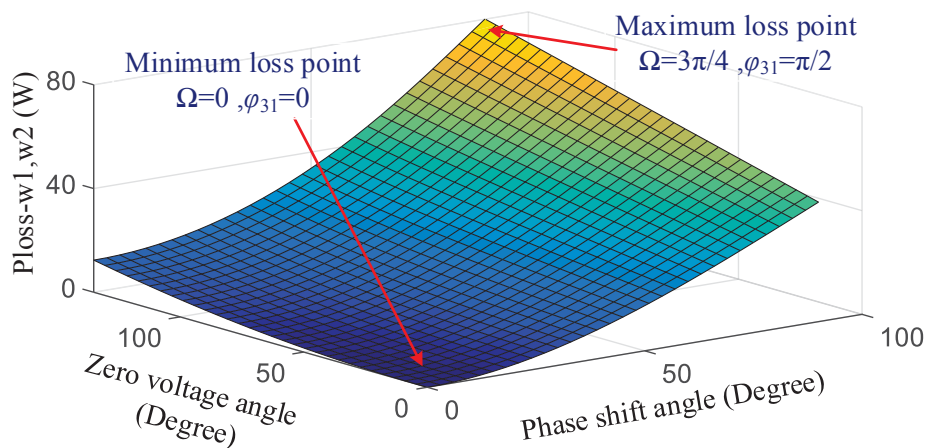


Fig.4.19 Conduction loss of the windings one and three for zero voltage angle,  $\Omega=0$  to  $3\pi/4$  and phase shift angle,  $\varphi_{31}=0$  to  $\pi/2$ .

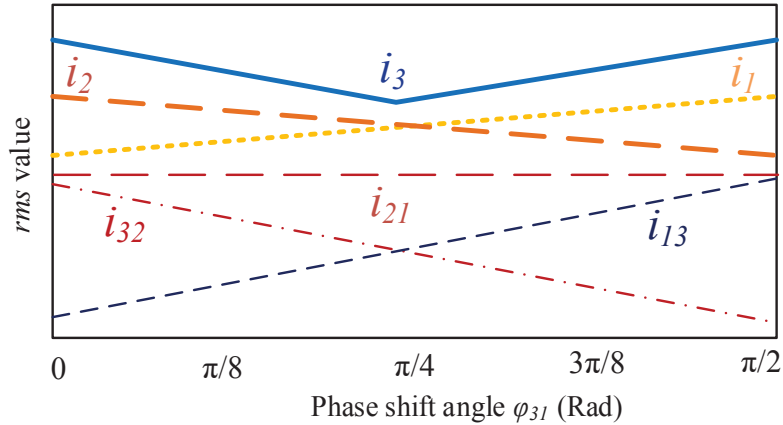


Fig.4.20 Trends of the windings current in the magnetic link versus phase shift angle.

As can be seen increasing  $\varphi_{31}$  raises the power transferred from PV to the inverter port which increases  $i_{31}$  and  $i_{21}$  remains constant due to constant value of  $\varphi_{21}$ . On the other hand increasing  $\varphi_{31}$  reduces  $\varphi_{23}$  (as  $\varphi_{23}=\varphi_{21}-\varphi_{31}$ ) and the power transferred from port two to port three and therefore  $i_{32}$  decreases gradually. Referring to the  $\Delta$ -model nodal equations, one can see that when  $\varphi_{31}$  increases, current and consequently copper loss in winding one increases while  $i_2$  and copper loss in winding two decreases. In winding three  $i_3$  decreases for phase shift angles less than  $\pi/4$  and then increases. This is because for small phase angles of  $\varphi_{31}$  the power received from port two is more than the power transferred to port one. At  $\varphi_{31}=\varphi_{21}/2=\pi/4$ , the power received from port two and transferred to port one are almost equal. Therefore, the average power of the port and the current  $i_3$  are minimized at this point and the conduction loss is reduced considerably.

The minimum copper loss point can happen in other angles based on the value of  $\varphi_{21}$  and is equal to  $\varphi_{31}=\varphi_{21}/2$  where the received and transferred power to port three are equal as can be seen in Fig.4.21.

The variation of amplitudes of the major harmonics and total harmonic distortions of the windings currents with phase shift angle  $\varphi_{31}$  are presented in Fig.4.22. It can be seen that the amplitude of the second harmonic increases at  $\varphi_{31}=0$  and  $\varphi_{31}=\pi/2$  which is effective in increasing loss at this operating point. The resultant copper loss of the all three windings and the total loss are presented in Fig.4.23. As can be seen in Fig.4.23-(a), the increasing phase shift angle,  $\varphi_{31}$ , raises the loss in winding one and decreases the average power, current and loss of winding two as illustrated in Fig.4.23-(b). The copper loss of winding three has a minimum point as already discussed. At  $\varphi_{31}=\varphi_{21}/2=\pi/4$ , the total copper loss is minimized.

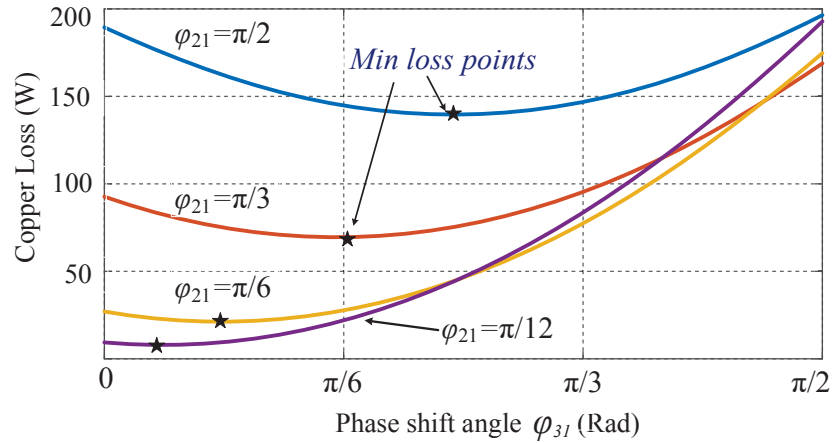


Fig.4.21 Copper loss of the magnetic link for different values of  $\varphi_{21}$  and  $\varphi_{31}$

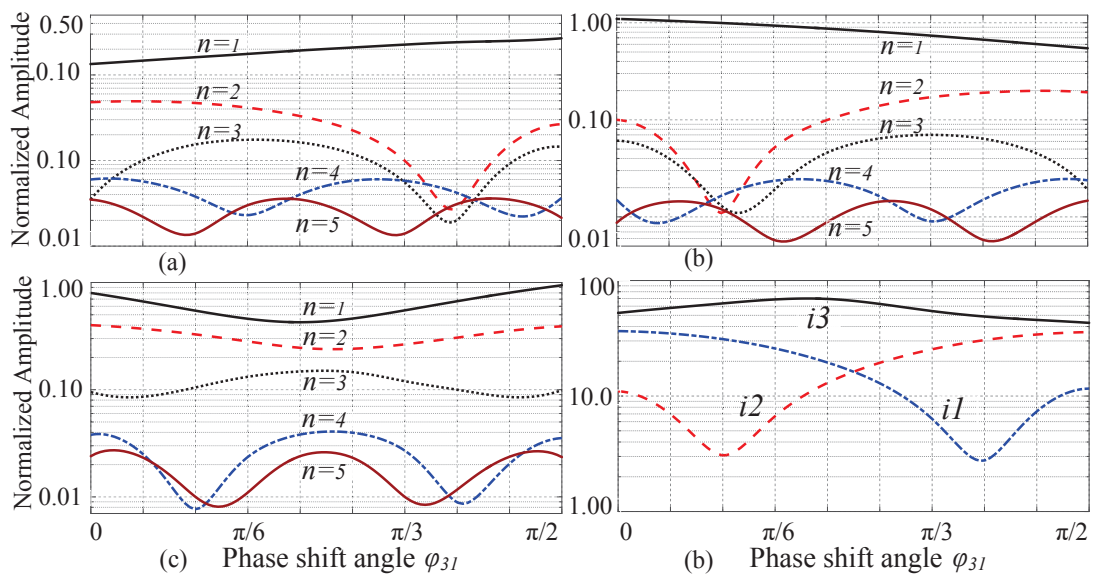
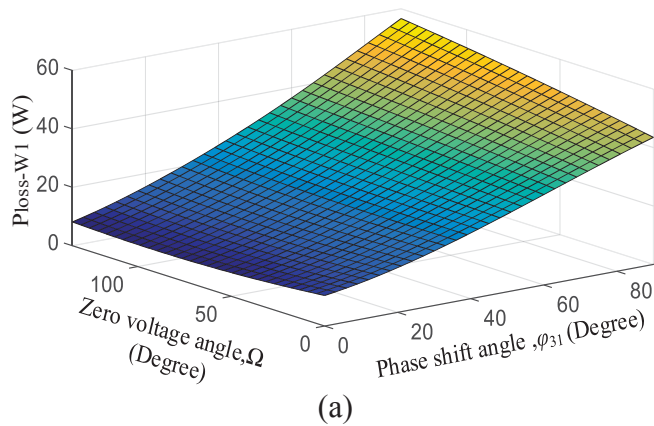
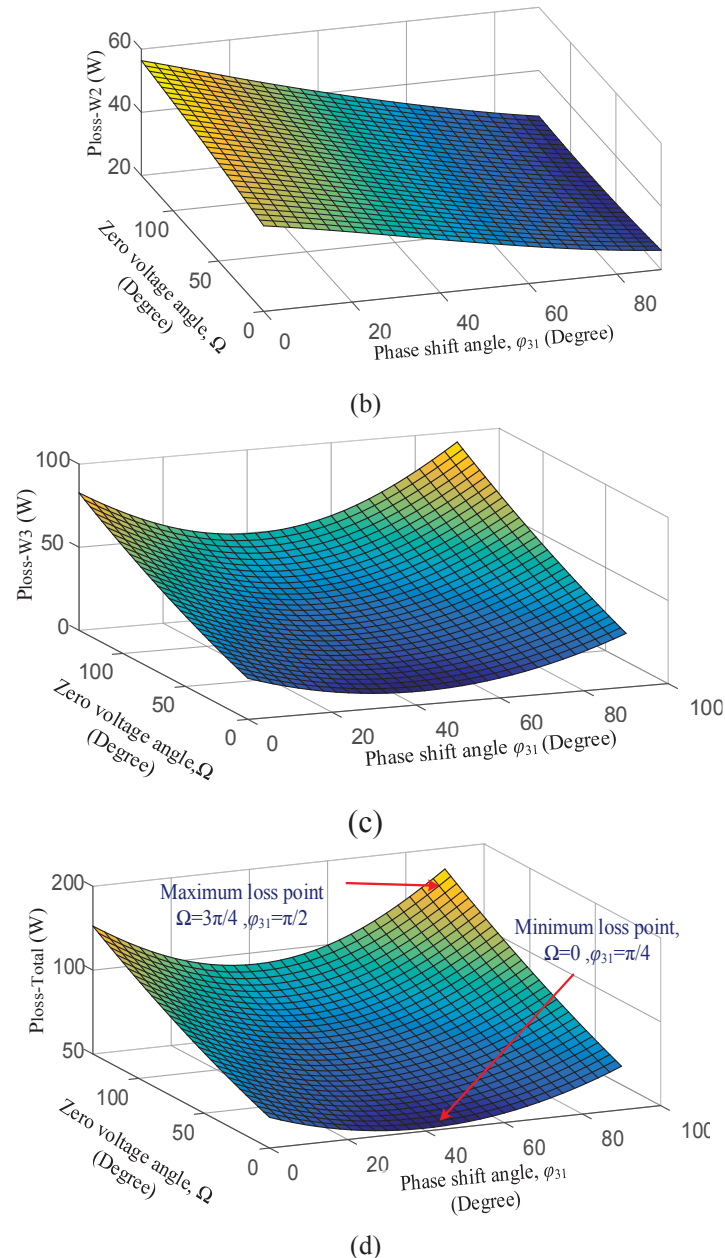


Fig.4.22 Changes in the amplitudes of harmonics of the windings current and THD versus phase shift angle,  $\varphi_{31}$  (a) current  $i_1$ , (b) current  $i_2$  (c) current  $i_3$  and (d) THD of  $i_1$ ,  $i_2$  and  $i_3$ .



(a)



**Fig.4.23** Conduction loss of the magnetic link for zero voltage angle  $\Omega=0$  to  $3\pi/4$  and phase shift angle  $\varphi_{31}=0$  to  $\pi/2$ , (a) winding one W1, (b) winding two W2, (c) winding three W3, and (d) entire magnetic link.

The analytically calculated values are measured experimentally using the prototype and the experimentally measured values are presented in the last section of this chapter.

#### 4.11 Thermal Analysis of the Magnetic Link

The thermal consideration in design of magnetic components aims to ensure that the temperature rise resulting from losses remains within the acceptable range. The core and conduction losses increase the temperature of the magnetic link during operation.

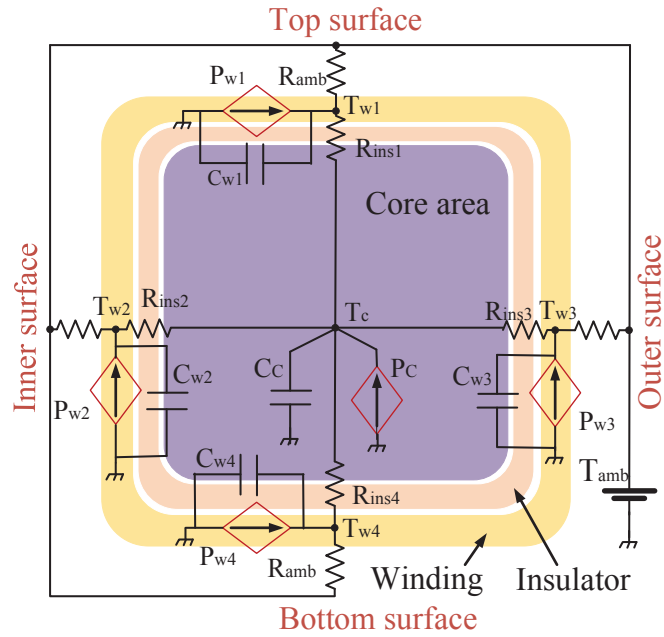


Fig.4.24 Equivalent thermal circuit of the magnetic link

The maximum temperature rise of 35°C in an ambient temperature of 30°C is considered for the operation of the magnetic link. The heat transfer mechanisms of conduction, convection and radiation are considered to find the temperature rise. The thermal-electric analogy has been widely used for heat transfer analysis of magnetic links [4.72].

In this method the winding and the core as heat sources of the system are modeled as current sources and insulation layers are modeled as thermal resistors due to their poor thermal conductivity. Fig.4.24 illustrates the thermal equivalent circuit of the magnetic link applied to the axial slice geometry of the magnetic component. As can be seen in the figure, a separate equivalent thermal resistor is proposed for each of the four surfaces of the core due to the uneven distribution of temperature field. The heat flow in the top and bottom surfaces of the core are analyzed in Cartesian and cylindrical coordinates respectively [4.72]. The thermal analysis parameters are illustrated in Table.4.8. The thermal resistance of the top and bottom insulation layers can be calculated from

$$R_{ins} = \frac{d_i}{k_i A_i} \quad (4.66)$$

where  $d_i$ ,  $A_i$  and  $k_i$  are thickness, surface area and thermal conductivity of the insulation layer respectively. The thermal resistances of the inner and outer insulation layers are computed from

$$R_{ins} = \frac{1}{2\pi k_i h_i} \ln \left( \frac{r_{out}}{r_{in}} \right) \quad (4.67)$$

where  $r_{in}$ ,  $r_{out}$  and  $h_i$  are the inner diameter, outer diameter and height of the insulator, respectively. The thermal resistance of surrounding area depends on the characteristics of the media and can be nonlinear. To calculate the thermal resistance of the surrounding area both convection and radiation effects should be considered. The convection thermal resistance is defined from

$$R_{con} = \frac{1}{h_{con}A} \quad , \quad h_{con} = \frac{N_u k_m}{L} \quad (4.68)$$

where  $h_{con}$  is the heat transfer coefficient,  $A$  the surface area,  $k_m$  the thermal conductivity of the medium,  $N_u$  the Nusselt number, and  $L$  the characteristic length. The value of Nusselt number depends on some parameters which are discussed in [4.72]. The radiative thermal resistance can be calculated from

$$R_{rad} = \frac{1}{h_{rad}A} \quad , \quad h_{rad} = \varepsilon \sigma (T_s + T_a)(T_s^2 + T_a^2) \quad (4.69)$$

where  $h_{rad}$  is the radiative heat transfer coefficient,  $\varepsilon$  the emissivity of the surface,  $T_s$  the surface temperature,  $T_a$  the ambient temperature, and  $\sigma$  the Stefan-Boltzmann's constant. As the radiation and convection thermal losses occur at the same time at the core or winding surface, the parallel connection of both resistances,  $R_{amb}$ , is presented as total thermal resistance of the surrounding area [4.72]. The heat sources in the model are calculated based on the core and conduction losses resulted from previous stages of design. Therefore, the effects of duty ratio of the supplied voltage and currents on the temperature rise have been taken into account. To define the value of heat sources resulted from winding, a constant value of dissipated heat per conductor length is assumed. The value of heat sources in each direction,  $x$ , is equal to the total heat loss in the winding,  $P_w$ , calculated by (4.33), times the fraction of the length of a turn in the respective direction,  $l_x$ , to the length of a turn,  $L_n$ , as the following

$$P_{wx} = P_w \frac{l_x}{L_n} \quad (4.70)$$

On the other hand, the heat sources in the core area are determined according to their represented volume by

$$P_{cx} = P_v \rho_c V_x \quad (4.71)$$

where  $P_v$  is the specific core loss in W/kg calculated by (4.29),  $\rho_c$  the mass density of the core material (2605SA1), and  $V_x$  the represented volume of the core covered by the winding. The temperature of the surrounding area is modeled as a constant voltage source, assuming negligible thermal effects of the magnetic structure on the ambient temperature. The thermal capacitances of the nodes are used to study the transients and are calculated based on the component specific heat capacity [4.73]. They are connected in parallel to the current sources and are equal to zero for the steady state analysis. Once all components of the equivalent thermal circuit are defined, the energy balance equations are used to define the temperature of selected hot points on the surface. The equation for the central node of the circuit can be written as

$$C_c \frac{dT_c}{dt} = \frac{1}{R_{ins1}}(T_{w1} - T_c) + \frac{1}{R_{ins2}}(T_{w2} - T_c) + \frac{1}{R_{ins3}}(T_{w3} - T_c) + \frac{1}{R_{ins4}}(T_{w4} - T_c) + P_c \quad (4.72)$$

where  $T_c$ ,  $P_c$ ,  $T_w$  and  $P_w$  are the core temperature, core power loss, winding temperature and winding conduction loss, respectively. On the other hand, the winding temperature on the top layer considering the thermal resistance of insulator,  $R_{ins}$ , and surrounding area,  $R_{amb}$ , can be defined as

$$C_{w1} \frac{dT_{w1}}{dt} = \frac{1}{R_{ins}}(T_c - T_{w1}) + \frac{1}{R_{amb}}(T_{amb} - T_{w1}) + P_{w1} \quad (4.73)$$

The temperature on bottom, inner and outer layers can be found by writing the same equations as (4.73). As the windings are not distributed symmetrically around the core and have different conduction losses, the thermal model is considered separately for each of the three windings. Due to the dependency of the thermal model parameters on the temperature, an iterative solution based on the Newton-Raphson method was applied to the equations to find the temperature rise at the core surface. The

capacitances  $C_c$  and  $C_w$  are assumed equal to zero to find the temperature rise in steady state condition. To start the analysis, the initial temperature of all nodes is assumed to be equal to the ambient temperature and then parameters are evaluated in each iteration [4.74]. The resulting values of temperature at the center and surfaces of the magnetic core are compared with the specified thermal limits to redesign the transformer in case they exceed the desired value (65 °C).

#### 4.12 Experimental Validation of Design

An experimental test platform was established (as shown in Fig.4.25) to measure the magnetic and electrical characteristics of the designed component. A prototype of a three-winding high-frequency toroidal magnetic link was developed for the proposed renewable energy system. The Metglas amorphous alloy 2605SA1 strip of 25 mm width and 20  $\mu\text{m}$  thickness made by Hitachi metals is selected as core material taking into account specific core loss, maximum flux density, cost and availability. To develop the magnetic core the Metglas 2605SA1 thin tape was glued with Araldite 2011 on the surface of each layer and wound around a cylindrical frame with external diameter of 65 mm as is shown in Fig.4.26-(a). The windings are distributed around the toroidal magnetic core as presented in Fig.4.26-(b). The core dimensions are presented in Fig.4.26-(c).

The skin and proximity effects resulting from high-frequency currents increase the ac resistance of the windings and the copper loss. To reduce the effects, Litz wires should be designed and fabricated.

In this research, Litz wires with the strand diameter of 0.35 mm (27 AWG) are selected based on the lookup table recommendations. The number of isolated strands,  $n_s$ , is calculated for each winding using

$$n_s = \frac{4i}{J\pi d^2} \quad (4.74)$$

where  $i$  is the winding nominal current,  $J$  the current density and  $d$  the minimum diameter of a single strand of the Litz wire. The number of twisted insulated strands for windings one, two and three was defined as 18, 45 and 30 and their number of turns resulting from the design process was 53, 12 and 8 turns respectively. The overall diameters of the twisted wires for the windings were measured approximately equal to  $d_1 \approx 1.9$  mm,  $d_2 \approx 3.8$  mm and  $d_3 \approx 2.75$  mm.

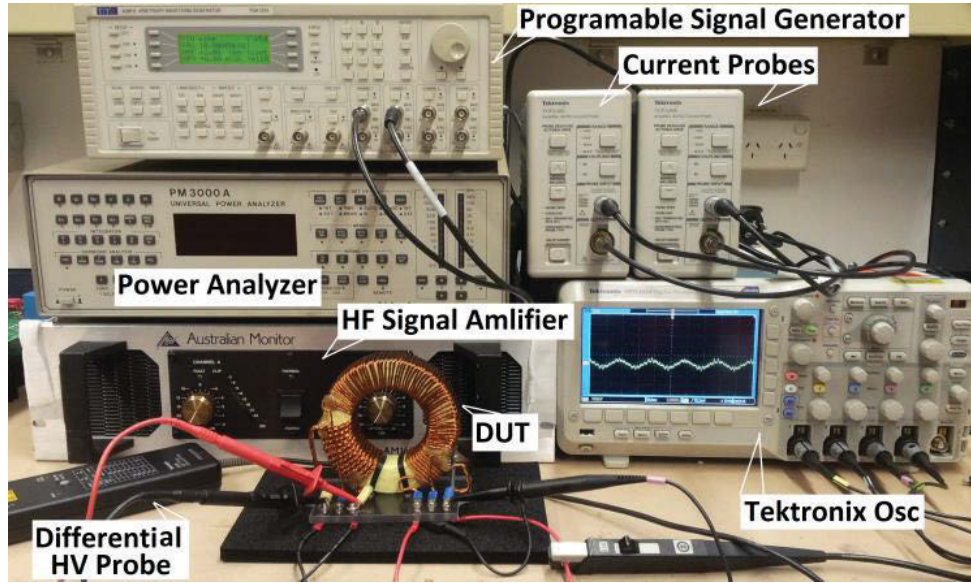
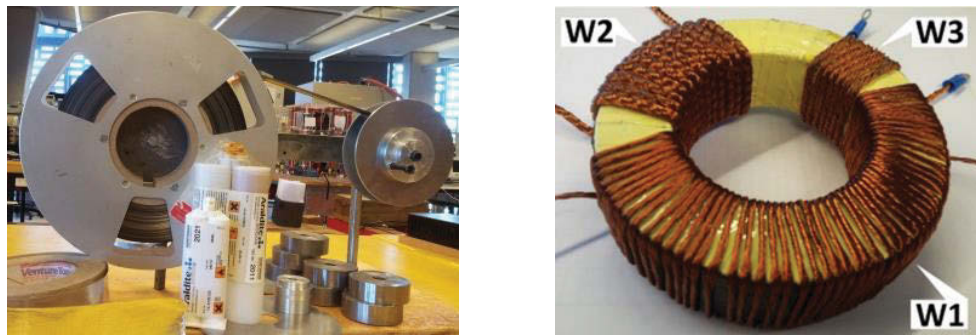
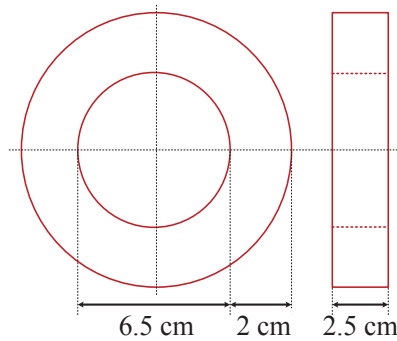


Fig.4.25 Experimental test platform



(a)

(b)



(c)

Fig.4.26 (a) development set of toroidal core, (b) developed magnetic link, and (c) dimension of magnetic core

The hysteresis loops and the core loss properties were measured experimentally. The excitation waveforms are generated by a TTI-TGA1244 programmable waveform generator and are amplified using high frequency signal amplifier AM3002. A power analyzer PM3000A is employed to measure the transformer power losses and Tektronix

current measurement probe TCPA300 and high voltage differential probe P5200 are used to observe the transformer waveforms as presented in Fig. 4.25.

#### 4.12.1 Core loss measurement

The core loss properties and the hysteresis loops of the component under square wave excitation current were measured experimentally. A TTI-TGA1244 programmable waveform generator was used as the main excitation source and the waveforms are amplified using high-frequency signal amplifier AM3002. The current and the voltage wave forms are observed using Tektronix current measurement probe TCPA300 and high-voltage differential probe P5200 respectively, and the total core and copper losses were measured using a power analyzer PM3000A. To measure the  $B$ - $H$  curve of the developed core, a 10 kHz square wave current was supplied to the winding one as excitation coil and winding three was open circuited as the pickup coil [4.28]. The waveforms of the excitation current  $i_A(t)$  and open circuit voltage  $v_B(t)$  were recorded simultaneously for each time period. Assuming a uniform flux density inside the core, the magnetic field intensity  $H$  was calculated based on Ampere's law by

$$H = \frac{N_A i_A(t)}{l_e} \quad (4.75)$$

where  $N_A$  is the number of turns and  $l_e$  the mean length of the core. On the other hand, the magnetic flux density was calculated based on Faraday's law by using open circuit voltage of the pickup coil by

$$B = \frac{1}{N_B A_e} \int v_B(t) dt \quad (4.76)$$

where  $N_B$  and  $A_e$  are the number of turns and the cross-sectional area of the magnetic core, respectively. The B-H loop of the developed core was plotted for two cases of 3 A and 5 A excitation currents based on the measurements as presented in Fig.4.27-(a). The total loss (core loss plus copper loss) was measured using the power analyzer. Considering almost equal ac and dc winding resistances in the case of using Litz wires, the copper loss was separated and the core loss was defined. The core loss was measured for three cases of 10, 30 and 50 kHz (Fundamental, second and third harmonics of switching frequency) square-wave excitation currents as presented in Fig.4.27-(b).

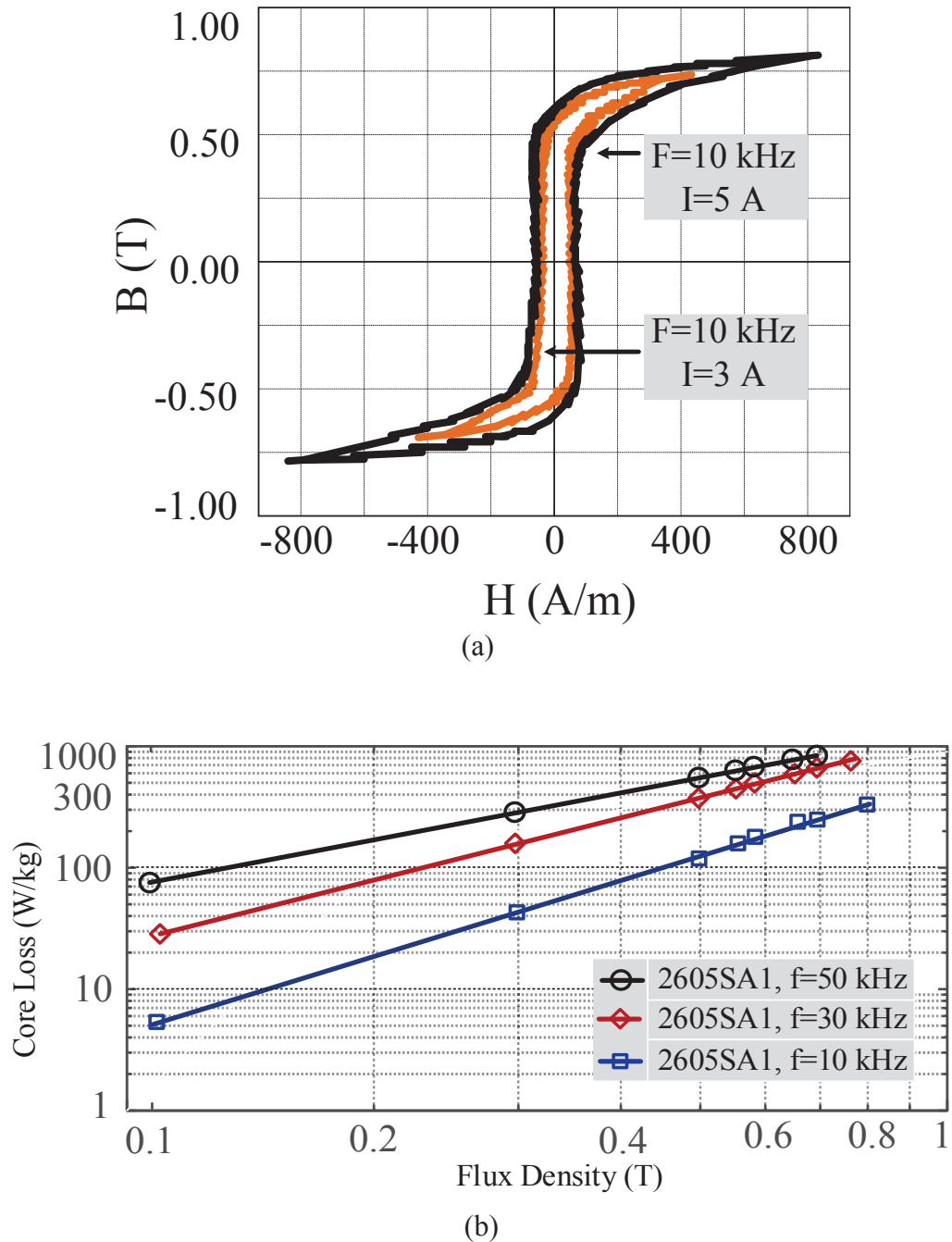
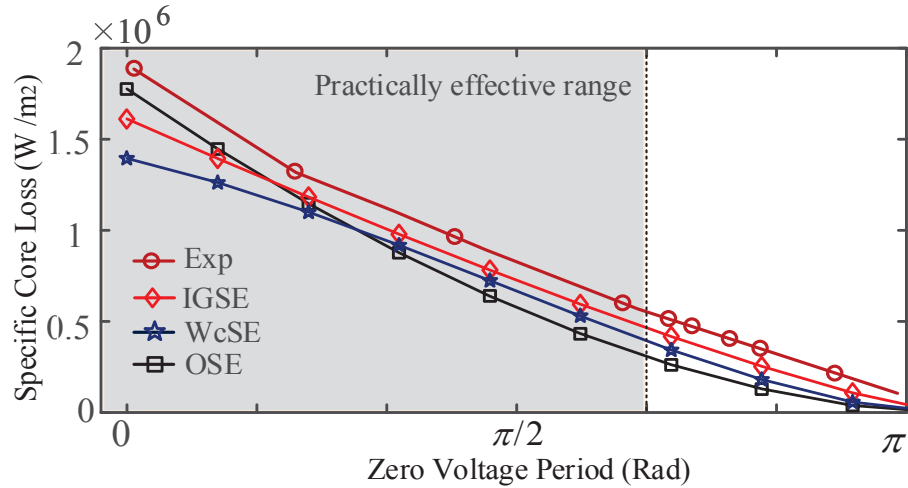
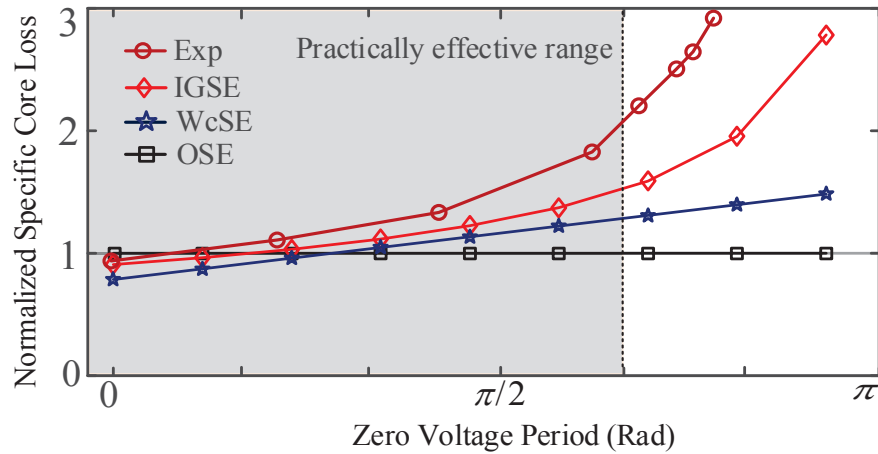


Fig.4.27 (a) measured hysteresis loops the magnetic core and (b) measured core loss of *Metglas 2605SA1* for 10, 30 and 50 kHz excitation currents.

To validate the core loss calculation using IGSE during the magnetic link design process, the specific core loss of the magnetic link was measured experimentally for frequency of 10 kHz and a wide range of zero voltage angle  $\Omega$ , starting from 0 to  $17\pi/18$ . The variable duty ratio voltage is applied to port three as PV port and a constant duty ratio voltage ( $D=1$ ) was applied to port one as reference port ( $V_1=300$  V,  $V_3=90$  V and  $\beta=\pi/3$ ).



(a)



(b)

**Fig.4.28 Comparison of calculated and experimentally measured core loss using OSE, IGSE and WcSE calculation methods, exciting voltages are applied to port three ( $\Omega=0$  to  $\pi$ ,  $V_3=90$  V) and port one ( $D=1$ ,  $V_1=300$  V) and phase shift  $\beta=\pi/3$ , (a) specific core loss, and (b) normalized specific core loss to OSE method.**

The experimental results are compared with the analytical calculations using three empirical loss calculation methods, OSE, IGSE and WcSE as presented in Fig.4.28-(a). As can be seen increasing the zero-voltage angle,  $\Omega$  (reducing the duty ration) of the applied voltage, reduces the peak magnetic induction  $B_{sq}$  and the magnetic loss density for all cases. Fig.4.28-(b) shows the values of specific core loss normalized to OSE to eliminate the downward behavior of the magnetic induction reduction and highlights the effects of the rate of change of magnetic induction. As expected the IGSE method presented less error compared with other methods especially in lower zero voltage angles and higher core loss values. It can be seen that the error increases for higher zero voltage angles and small values of core loss.

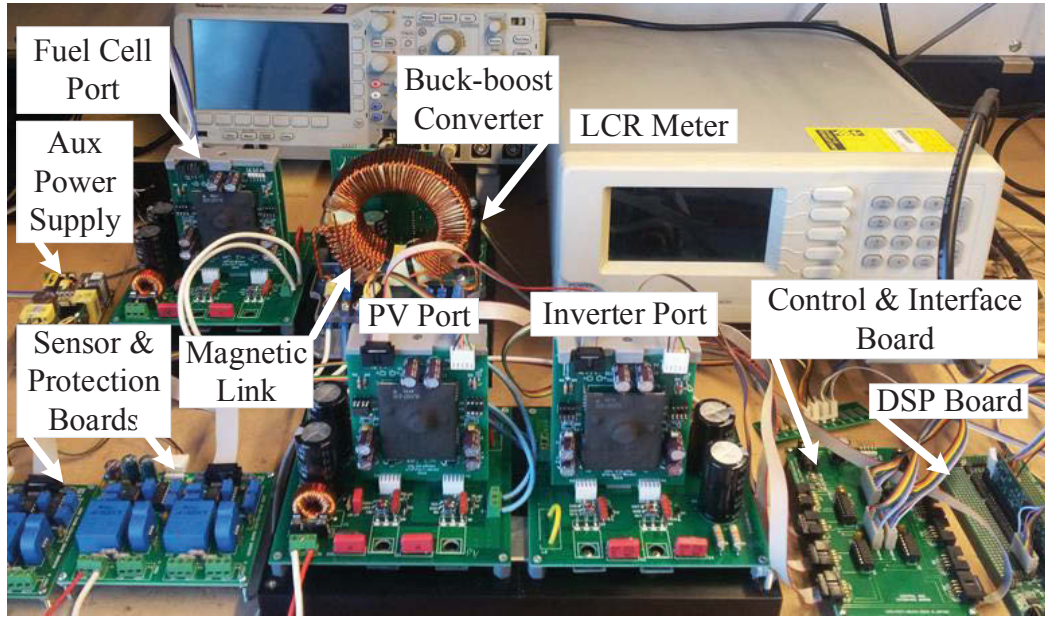


**Fig.4.29 Structure of proposed residential micro-grid**

As in our application, the duty ratio control is applied to the PV port, and the zero voltage angle is limited to less than  $3\pi/4$  due to the limits of PV output power. In this range, the IGSE provided acceptable accuracy for loss calculation of the magnetic link.

#### 4.12.2 Copper loss measurement

An experimental test bench including the three-winding high-frequency magnetic link was developed for the copper loss measurement as presented in Fig.4.29.

The current and the voltage wave forms are observed using Tektronix current measurement probe TCPA300 and high-voltage differential probe P5200 respectively. The power was measured using a power analyzer PM3000A and the ac resistances are measured using Instek LCR meter. To validate the analytical methods a series of experimental tests were conducted for two cases of operation modes discussed in section 4.10.

The waveforms of the voltage and current of the windings for two cases of  $\Omega=3\pi/4$  (maximum copper loss) and  $\Omega=\pi/3$  where  $\varphi_{31}=\pi/2$  are presented in Fig.4.30. The major harmonic spectrums of the current in the windings, measured for maximum copper loss condition, are presented in Fig.4.31. The ac resistances of the windings are measured experimentally and are compared with analytically calculated values as presented in Fig.4.32.

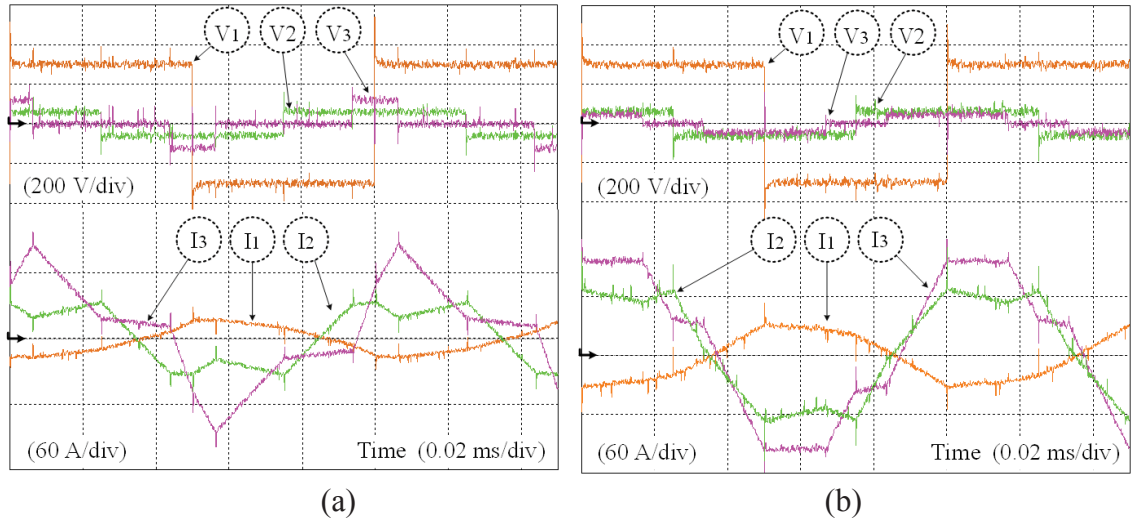


Fig.4.30 Experimental wave forms of the voltages and currents in the windings for  $\phi_{21} = \phi_{31} = \pi/2$ , (a)  $\Omega = 3\pi/4$  and (b)  $\Omega = \pi/4$ .

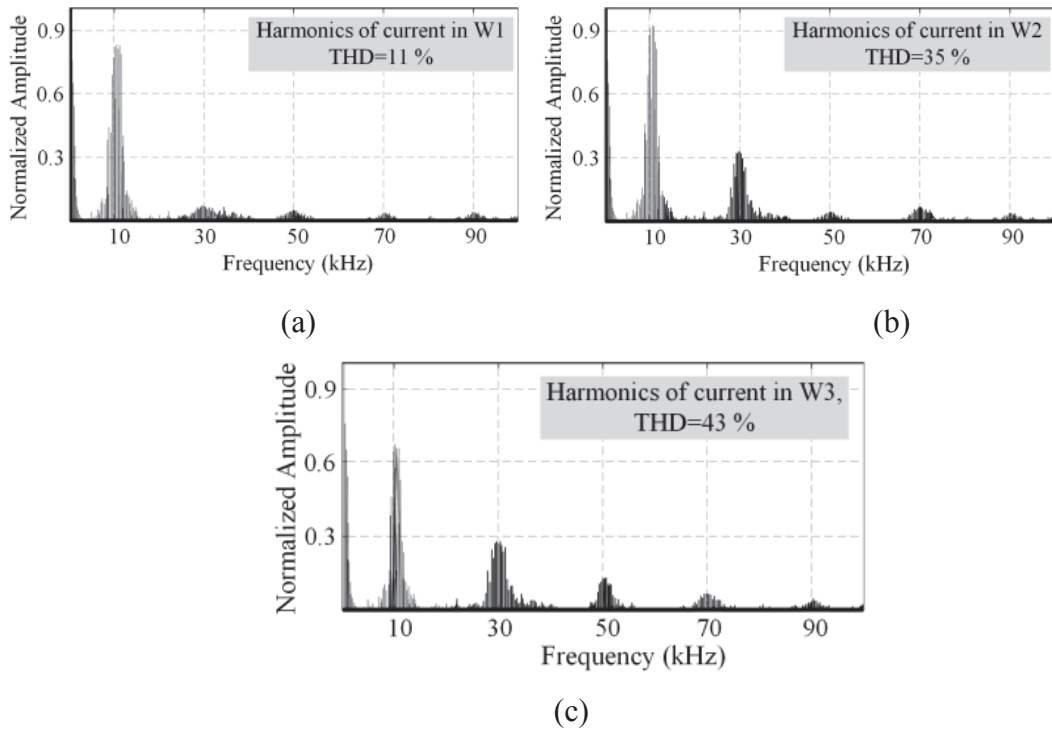


Fig.4.31 Harmonic spectrum of the current in the windings for maximum loss condition (a) winding one, (b) winding two and (c) winding three

To validate the phase shift angle and zero voltage angle variations the total copper loss of the magnetic link was measured for two cases of load condition and the measured values are compared with analytically calculated results. In DAB operation mode the effect of zero voltage angle, was experimentally validated for two cases of phase shift angles, e.g  $\phi_{31} = 0$  and  $\phi_{31} = \pi/2$ .

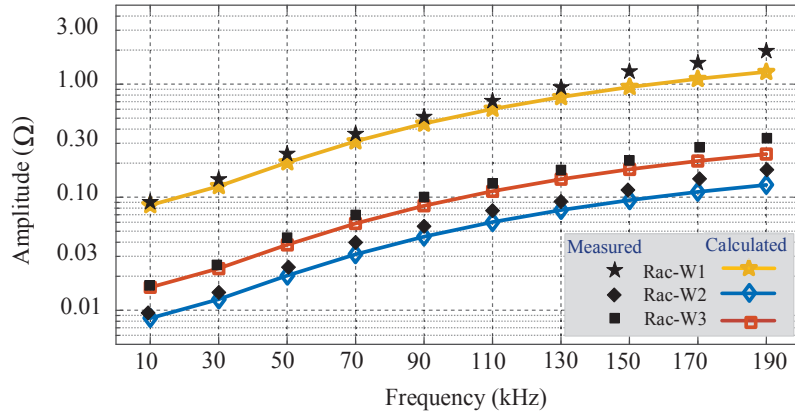
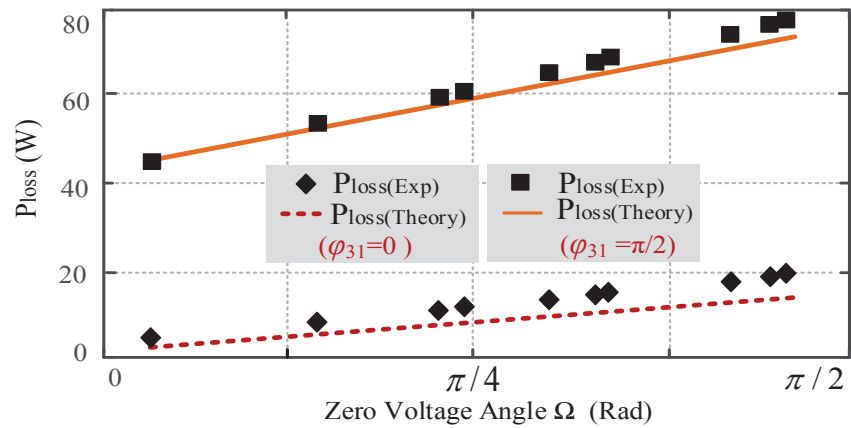
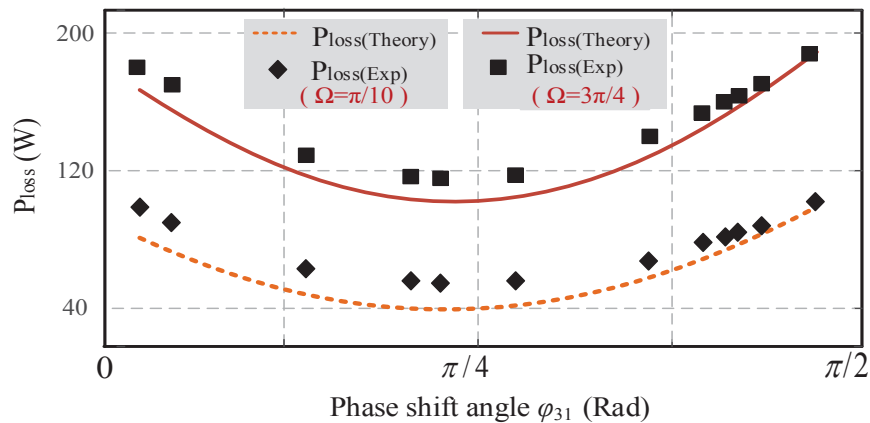


Fig.4.32 Calculated and measured values of resistances of windings one, two and three for different harmonics



(a)



(b)

Fig.4.33 Comparison of calculated and experimentally measured conduction loss for (a)-Zero voltage angle,  $\Omega$  varies from 0 to  $\pi/2$  and two cases of phase shift angles,  $\varphi_{31}=0$  and  $\varphi_{31}=\pi/2$ , (b)-Phase shift angle,  $\varphi_{31}$  varies from 0 to  $\pi/2$  and two cases of zero voltage angle,  $\Omega=\pi/10$  and  $\Omega=3\pi/4$ .

As can be seen in Fig.4.33(a), increasing zero voltage angle  $\Omega$  increases the copper loss in both cases of phase shift angles although this increment is more considerable at  $\varphi_{31}=\pi/2$ .

The experimentally measured values validated the analytical calculations although the resulting error increased at lower values of conduction loss and higher zero voltage angles which can be attributed to the accuracy of measurement instruments.

In case of TAB operation mode the effect of phase shift angle was tested. The total copper loss of magnetic link was measured for two cases of zero voltage angle,  $\Omega = \pi/10$  and  $\Omega = 3\pi/4$  (maximum loss) where phase shift angle was changed from  $\varphi_{31}=0$  to  $\varphi_{31}=\pi/2$ . As is presented in Fig.4.33 (b), the experimental tests showed same trends as simulations and the conduction loss of the magnetic link is minimized at  $\varphi_{31}=\pi/4$  as discussed in section 4.10. The resulting error between theoretically calculated and experimentally measured values was less than 10 % at lower phase shift angles and this reduced to less than 5% for higher phase shift angles. Based on the experimental test results, accuracy of the harmonic based copper loss analysis was confirmed.

#### 4.13 Validation of Temperature Rise Analysis

To validate the accuracy of thermal analysis based on the thermal model, the temperature of the magnetic core was monitored and recorded for various load conditions and was compared with theoretically calculated results. An infrared thermal camera, Flir-OSXL-I7 with the temperature resolution of  $0.1^\circ\text{C}$  and adjustable emissivity of 0.1 to 1, was used to measure the thermal radiation of the windings and magnetic core. The surroundings of the core were covered with black cards to reduce the reflections and measurement error. Fig.4.34-(a) to (c), show the thermal images of the magnetic link under three different load conditions (Ambient temperature= $27^\circ\text{C}$ , Emissivity=0.96).

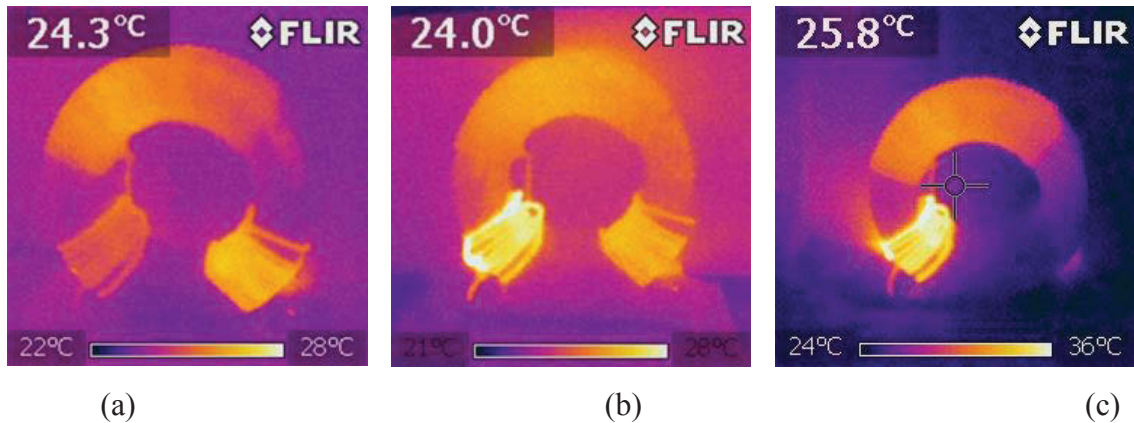


**Fig.4.34 Thermal image of the magnetic link under three different load conditions, (a) power transfers from W2 and W3 to W1, (b) power transfers from W2 and W3 to W1 and (c), power transfers from W3 to W1.**

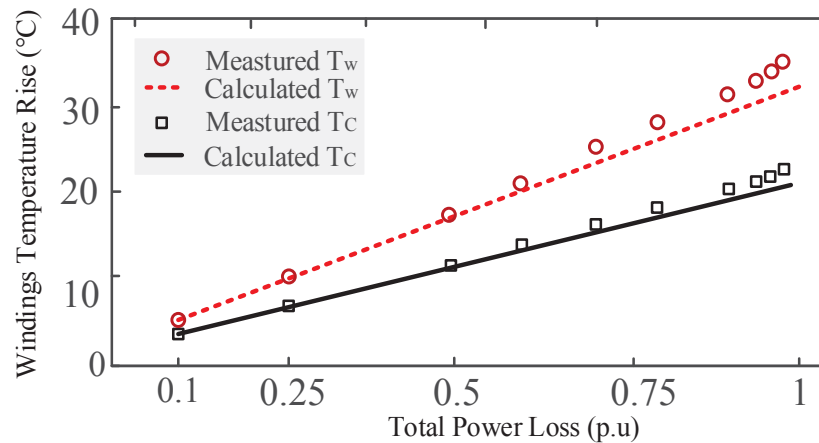


**Fig.4.35** The measured and calculated temperature rise of the winding,  $T_w$  and magnetic core,  $T_c$  for winding one of the magnetic link.

The temperature of windings and the surface of magnetic core were measured in steady state for a range of power starting from 10 % to 100 % of nominal loads. The maximum observed temperature was recorded for winding one as output port of the converter. As can be seen in Fig.4.35, the winding temperature rise for maximum loss did not exceed 38 °C (Overall temperature of 65 °C) and the core temperature remained under 50 °C. The resultant error was less than 10 % which confirmed the accuracy of thermal analysis.

#### 4.14 Measurement of Inductive and Resistive Elements

The experimental test desk of Fig.4.25 was used to test the validity of the design process and measure the transformer parameters. The test process is based on the method suggested in [4.75] due to the high leakage inductance of the magnetic link. The programmable signal generator, TTI-TGA1244 and the HF signal amplifier are used to generate the sinusoidal excitation currents. The standard short and open circuit tests have been used conventionally to determine the transformer inductive and resistive elements. It has been shown that short circuit test has less accuracy when the winding resistances and the leakage reactances have significant values relative to the magnetizing impedance [4.75], [4.76]. It also will lose its accuracy in the case of a big difference between the primary and secondary leakage inductances and winding resistances due to winding geometries and configurations. On the other hand, it is necessary to have the same value of magnetic flux and consequently permeability factor in the core during all stages of experimental tests. It is difficult to maintain the same magnetizing current in the short circuit test because of parallel connection of the

magnetizing branch and the secondary winding impedance during the test [4.75]. Therefore the short circuit test did not provide reliable results and was excluded from our test procedures. To measure the transformer leakage and self-inductances the conventional open circuit and the differentially and cumulatively coupled tests are applied to the windings with one as the primary and three as the secondary. To discuss the experimental test process, windings one and three are selected as examples and the test procedure is applied similarly to the other two pairs (windings one and two or windings two and three).

#### A. Open circuit test

During this test the test voltage set as  $110\text{ V}$  at  $10\text{ kHz}$  was applied to winding one while winding three was open circuited. The values of impedances are calculated using the normal equation of sinusoidal excited circuits. The measured impedance including the real and imaginary parts is

$$Z_1(OC) = R_1(OC) + j\omega L_1(OC) = (R_{W1} + R_m) + j\omega(L_{l1} + L_{l3}) \quad (4.77)$$

At the second stage the excitation current was applied to winding three with the other two windings open circuited. The resultant impedance in this case is

$$Z_3(OC) = R_3(OC) + j\omega L_3(OC) = (R_{W3} + R_m n_3^2) + j\omega(L_{l3} + n_3^2 L_{l1}) \quad (4.78)$$

where  $n$ , is the turn ratio of winding three to winding one. The schematics of the test circuits are shown in Fig.4.36-(a) and (b).

#### B. Series coupling tests

In this test, winding one is considered as the primary and winding three as the secondary. They are connected in series in differential or cumulative form as illustrated in Fig.4.36-(c) and (d) while winding two was open circuited.

The series coupling test is used to factor in the effects on the leakage and magnetizing inductances of core excitation [4.75]. Compared with the parallel coupling test the measured inductances and resistances are the algebraic addition and subtraction of resistive and inductive elements of the transformer windings which facilitates direct measurement by meter.

The input impedances measured in differential and cumulatively coupled tests are

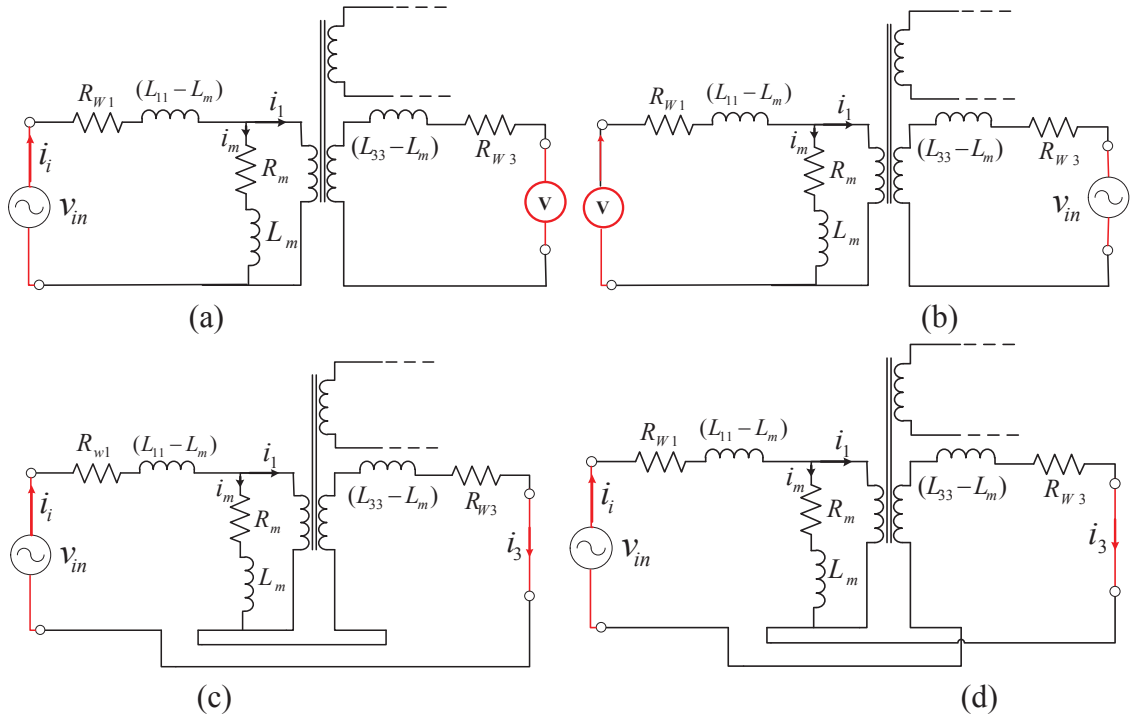


**Fig.4.36** Experimental tests of multi-winding transformer, (a) secondary open circuit test, (b) primary open circuit test, (c) differentially coupled test, and (d) cumulatively coupled test.

$$Z_1(dif) = R_{13}(dif) + j\omega L_{13}(dif) = (R_{W1} + R_{W3} + (1 - n_3)^2 R_m) + j\omega(L_{l1} + L_{l3} + (1 - n_3)^2 L_{13}) \quad (4.79)$$

$$Z_1(Cum) = R_{13}(cum) + j\omega L_{13}(cum) = (R_{W1} + R_{W3} + (1 + n_3)^2 R_m) + j\omega(L_{l1} + L_{l3} + (1 + n_3)^2 L_{13}) \quad (4.80)$$

A combination of series-coupling and the open-circuit tests have been used to find the value of transformer parameters [4.75]. The resultant equations in terms of inductances  $L_1(oc)$ ,  $L_3(oc)$ ,  $L_{13}(dif)$  and  $L_{13}(cum)$  and the resistances  $R_1(oc)$ ,  $R_3(oc)$ ,  $R_{13}(dif)$  and  $R_{13}(cum)$  and  $R_m$  are tabulated in Table.4.10.

The resultant values of all three tabulated equations were quite consistent and their average is considered as the final value of the parameter. To guarantee the same value of magnetizing flux density into the core during all the tests, the following relationships should be considered for excitation current during various tests [4.75].

This will result in a consistent flux density in the core during all tests and, hence almost constant values for  $L_m$  and  $R_m$ .

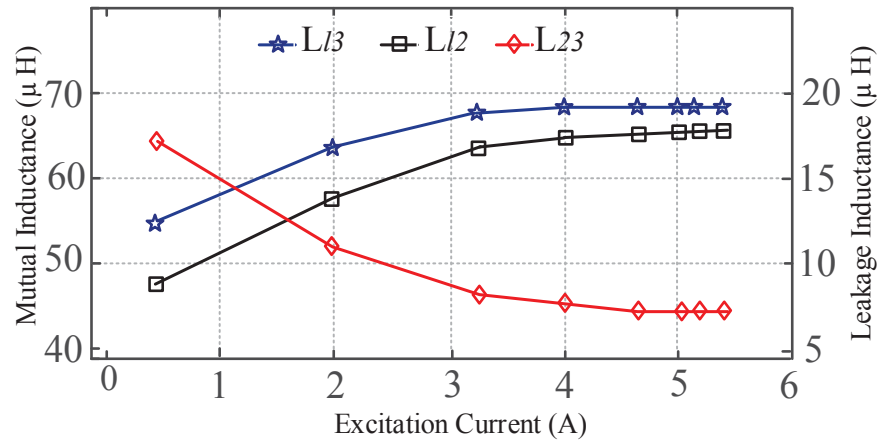
$$I_{p(OC)} = nI_{s(OC)} = I_{dif}(1 - n) = I_{cum}(1 + n) \quad (4.81)$$

**TABLE 4.10 Equations of Model Parameters for Different Test Procedures**

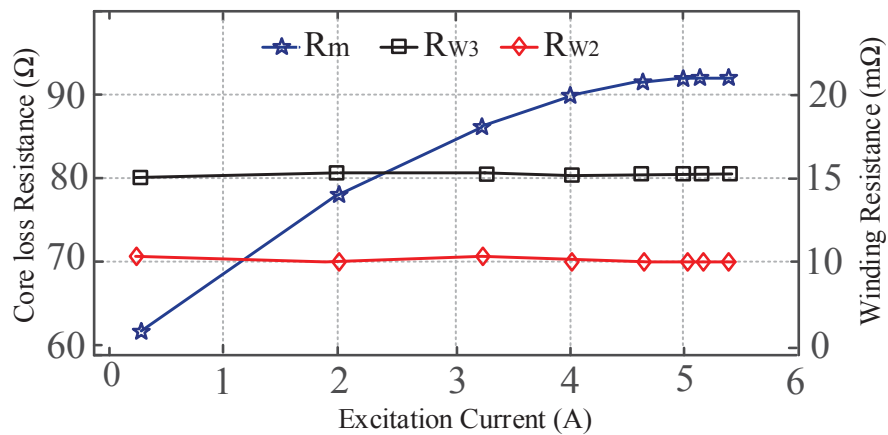
Test Parameter	Differentially coupled and open circuit tests	Cumulatively coupled and open circuit tests	Combination of all three tests
$R_{w1}$	$\frac{(2n-1)R_1(OC) - R_3(OC) + R_{13}(dif)}{2n}$	$\frac{(2n+1)R_1(OC) + R_3(OC) - R_{13}(cum)}{2n}$	$R_1(OC) - \frac{R_{13}(cum) - R_{13}(dif)}{4n}$
$R_{w3}$	$\frac{(2-n)R_3(OC) - nR_1(OC) + nR_{13}(dif)}{2}$	$\frac{(2+n)R_3(OC) + nR_1(OC) - nR_{13}(cum)}{2}$	$R_3(OC) - \frac{nR_{13}(cum) - nR_{13}(dif)}{4}$
$R_m$	$\frac{R_1(OC) + R_3(OC) - R_{13}(dif)}{2n}$	$\frac{R_{13}(cum) - R_1(OC) - R_3(OC)}{2n}$	$\frac{R_{13}(cum) - R_{13}(dif)}{4n}$
$L_{11}$	$\frac{(2n-1)L_1(OC) - L_3(OC) + L_{13}(dif)}{2n}$	$\frac{(2n+1)L_1(OC) + L_3(OC) - L_{13}(cum)}{2n}$	$L_1(OC) - \frac{L_{13}(cum) - L_{13}(dif)}{4n}$
$L_{13}$	$\frac{(2-n)L_3(OC) - nL_1(OC) + nL_{13}(dif)}{2}$	$\frac{(2+n)L_3(OC) + nL_1(OC) - nL_{13}(cum)}{2}$	$L_3(OC) - \frac{nL_{13}(cum) - nL_{13}(dif)}{4}$
$L_{13}$	$\frac{L_1(OC) + L_3(OC) - L_{13}(dif)}{2n}$	$\frac{L_{13}(cum) - L_1(OC) - L_3(OC)}{2n}$	$\frac{L_{13}(cum) - L_{13}(dif)}{4n}$

where  $I_P$  and  $I_s$  denote the primary and secondary currents, respectively. It should be noted that during the series coupling test the value of  $L_m$  is equal to the mutual inductance of two windings under the test ( $L_{13}$  in this case). Fig.4.37 shows the resultant values of inductances and resistances for windings one and three with the excitation current ranging from 0.5 to 4.5A. From Fig.4.37 (a), it is clear that as the winding current increases, the mutual inductance between windings one and three decreases while their leakage inductance increases. On the other hand, Fig.4.37 (b) shows that the value of equivalent core loss resistance will increase with any increase in the test current while the winding resistances are not dependent on the test current and remain constant. To find the accuracy of the implementation process, the experimentally measured inductances are compared with the numerically calculated ones. Fig.4.37(c) shows the measured values of leakage and self-inductance of winding one with excitation current of 5 A. Comparing measured values with numerically calculated inductances shows that the resulting error is reduced to less than 15 % considering 14400 3D elements for magnetic structure in numerical analysis. A further reduction of error to 10 % was achieved by increasing the number of elements to 19440 elements although it increased the computation time considerably (about 11 min). The resultant error can be attributed to various experimental factors that cannot be included properly in the numerical analysis, such as stacking factor and windings distribution.

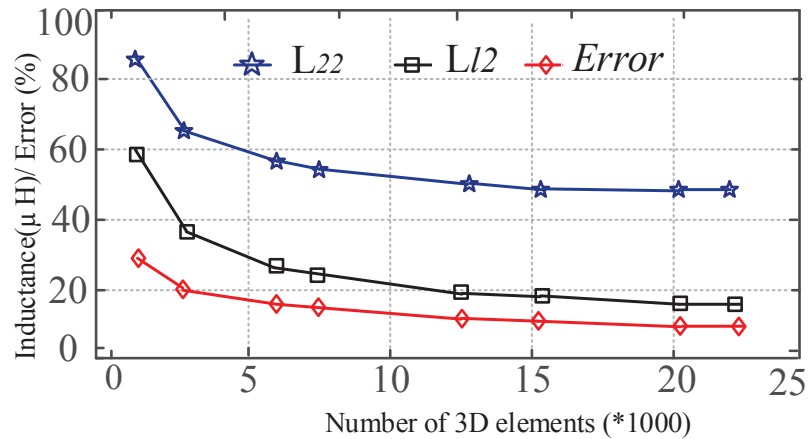
The major parasitic effects are due to the skin effect, proximity effect, and stray capacitance.



(a)



(b)



(c)

**Fig.4.37 Experimental measured parameters of the winding one, (a) inductive elements, (b) resistive elements and, (c) inductive elements and resulting error.**

In this research the skin and proximity effects are considered in the design process and the effect of stray capacitance is safely ignored because of their small value and relatively low switching frequency, about 10 kHz. The numerical model of magnetic link based on the measured parameters was simulated under different load conditions

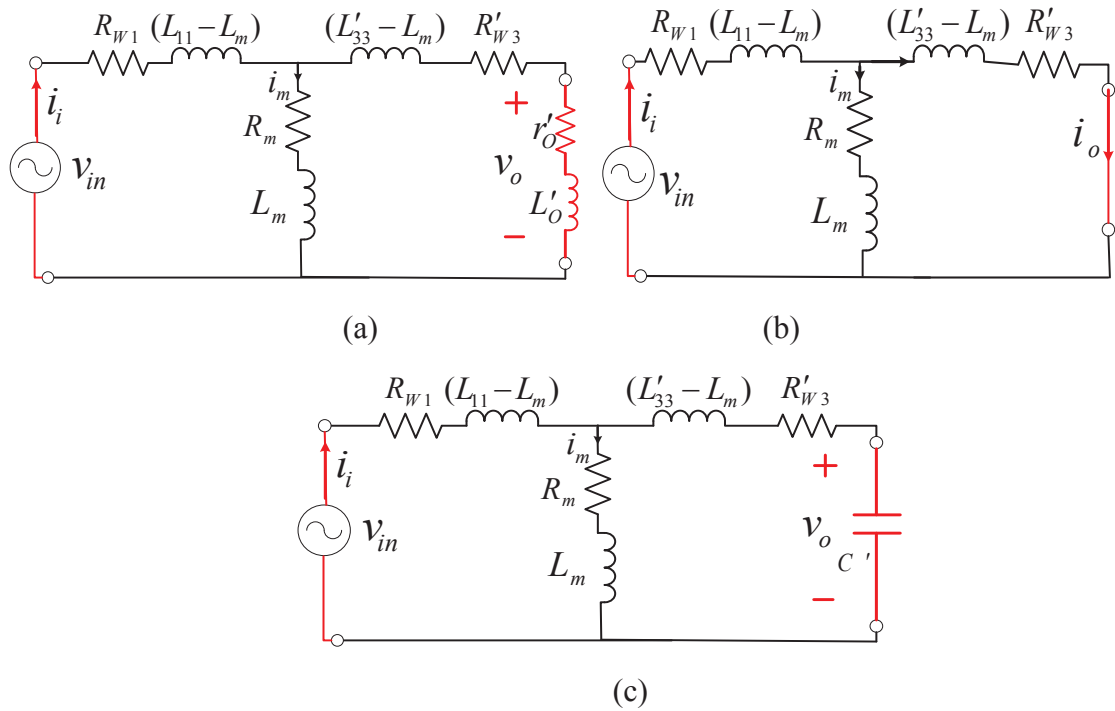


**Fig.4.38** The equivalent circuit of MWT under (a) inductive load, (b) short circuit and (c) capacitive load test conditions

for medium frequency range using MATLAB/Simulink. The results are compared with the experimental tests to validate the modeling process. As the windings currents in our application are non-sinusoidal including high frequency harmonics, the selected frequency range covers the fundamental frequency of current (10 kHz) and its harmonics (30 kHz, 50 kHz and 70 kHz). The excitation current was applied to winding one as the primary and winding three as the secondary where the output signals for the entire frequency range were recorded. The experimental tests were carried out for three cases of inductive load, capacitive load and short circuit conditions to factor in both mutual and leakage inductive effects. A sinusoidal voltage of  $150\text{ V (rms)}$  with variable frequency changes from 10 kHz to 150 kHz generated by the programmable signal generator and amplified by the HF signal amplifier was used as excitation source. The test process was carried out for other pairs of windings and the results were consistent. Fig.4.38 (a) to (c) shows the equivalent circuit of windings one and three under the test for inductive load, capacitive load and short circuit condition while winding two is open circuited. The transfer function of circuit in the case of capacitive load can be defined as

$$\frac{V_o(S)}{V_{in}(S)} = \frac{Z}{[R_{W1} + (L_{11} - L_m)S + Z][1 + SC'R'_{W3} + S^2C'(L'_{33} - L_m)]} \quad (4.82)$$

where  $Z$  can be found by

$$[Z]^{-1} = [R_m + SL_m]^{-1} + [R'_{W3} + S(L'_{33} - L_m) + 1/SC']^{-1} \quad (4.83)$$

In case of inductive load the transfer function of secondary to primary voltage and impedance  $Z$  can be calculated as

$$\frac{V_o(S)}{V_{in}(S)} = \frac{Z'(r'_o + L'_o S)}{[R_{W1} + (L_{11} - L_m)S + Z'] [r'_o + R'_{W3} + S(L'_o + L'_{33} - L_m)]} \quad (4.84)$$

$$[Z']^{-1} = [R_m + SL_m]^{-1} + [r'_o + R'_{W3} + S(L'_o + L'_{33} - L_m)]^{-1} \quad (4.85)$$

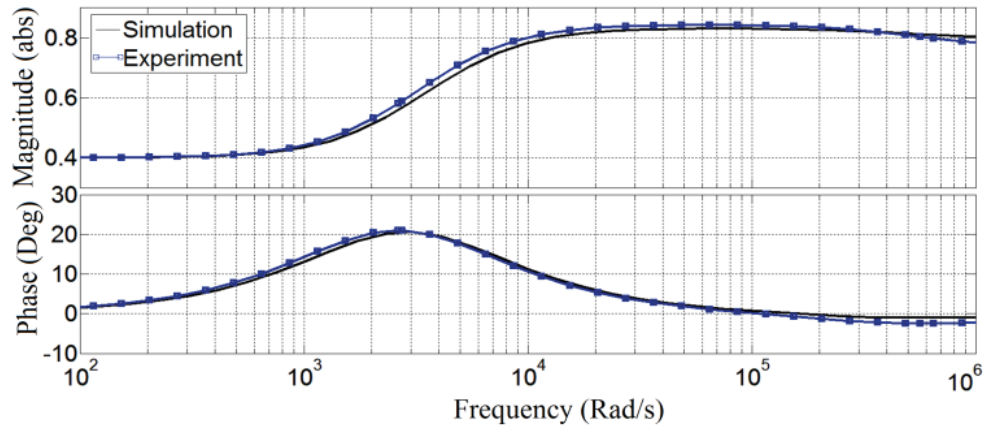
The last test was carried out under the short circuit condition and the transfer function and impedance  $Z$  can be defined as

$$\frac{I_o(S)}{V_{in}(S)} = \frac{Z}{[R_{W1} + (L_{11} - L_m)S + Z] [R'_{W3} + S(L'_{33} - L_m)]} \quad (4.86)$$

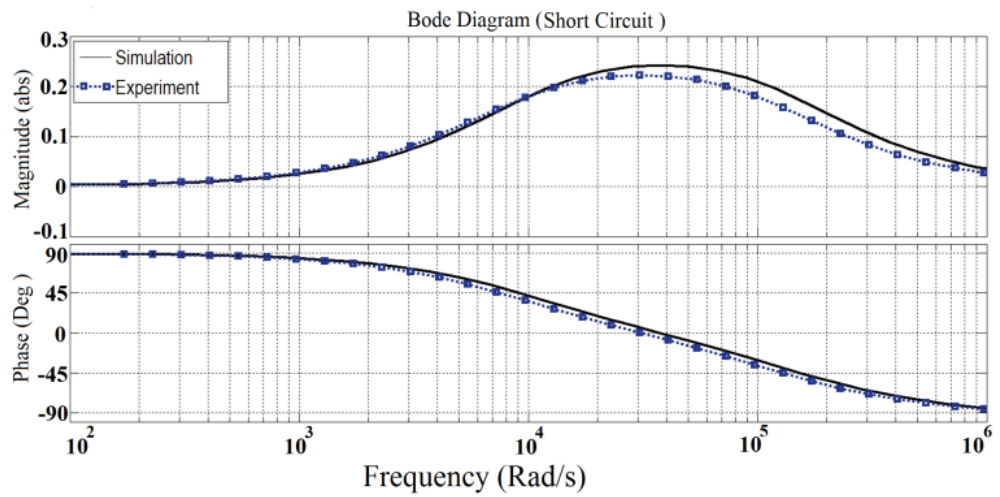
$$[Z]^{-1} = [R_m + SL_m]^{-1} + [R'_{W3} + S(L'_{33} - L_m)]^{-1} \quad (4.87)$$

Comparing the experimental and simulation results shows that the simulated model adapts very well with experimental test results for all three types of loads. Fig.4.39(a) to (c) show that the difference between the simulated and experimental results is small for medium frequency range because the modeling process and experimental tests are carried out for this range.

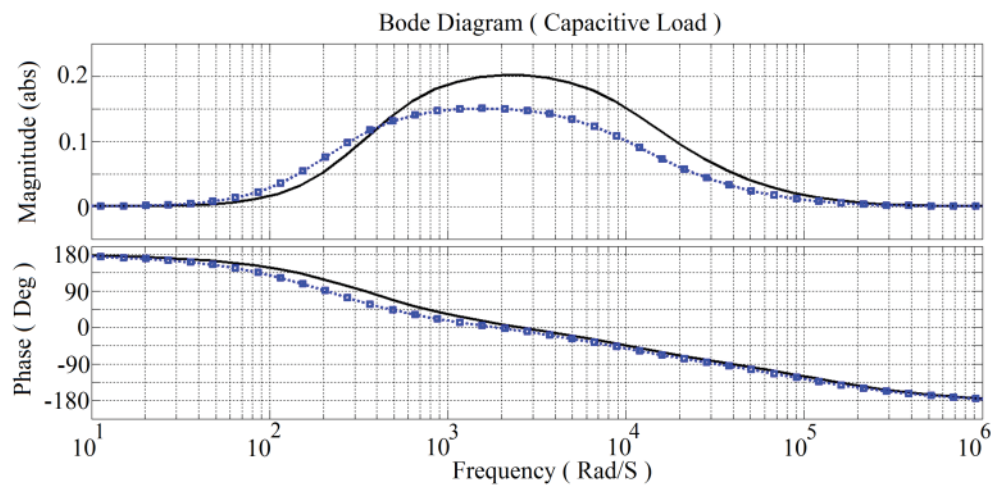
The measured steady state core and the winding temperatures were in the range of 40 – 60 °C during the frequency response tests under the nominal load conditions. Within this temperature range the effect of temperature on winding resistance is negligible. On the other hand, the magnetic characteristics of amorphous core material, used for the transformer are almost independent of temperature according to the data provided by the manufacturer therefore the effects of temperature on the transformer parameters were negligible. Figs.4.40 and 4.41 present the simulation and experimental results in the time domain with a 40 kHz square wave excitation. It can be seen that the simulations and experimental wave forms show a very good agreement for all three types of load conditions. Based on the results, the suggested method for design and characterization of multi-winding magnetic link is validated for medium frequency range where parasitic effects of stray capacitors are negligible and the operation point of magnetic component is in the linear area of B-H curve.



(a)

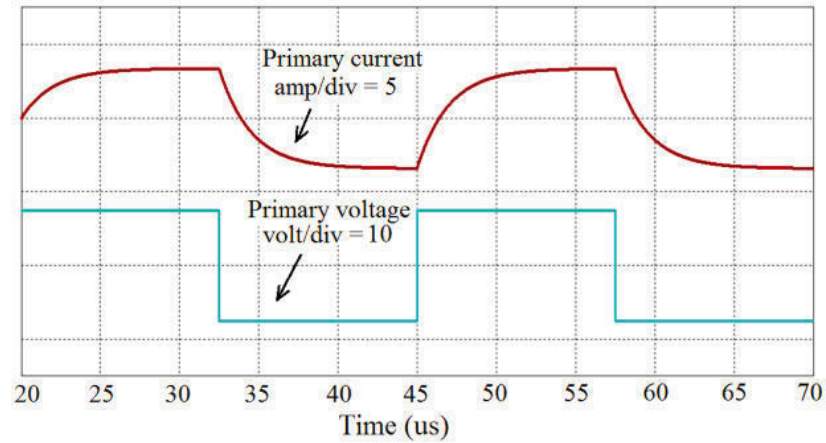


(b)

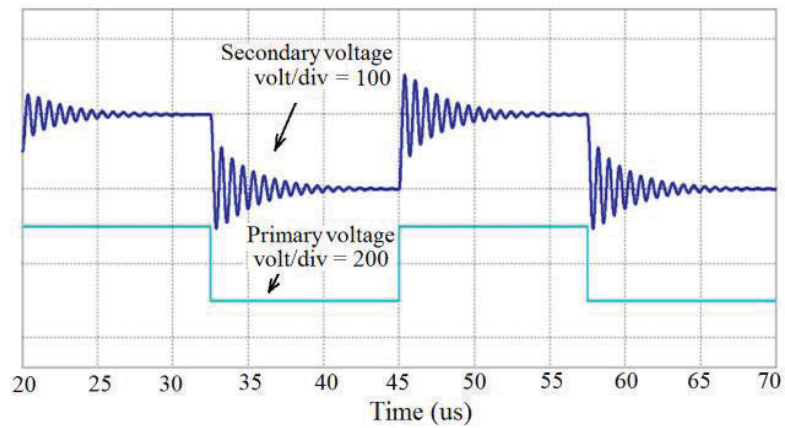


(c)

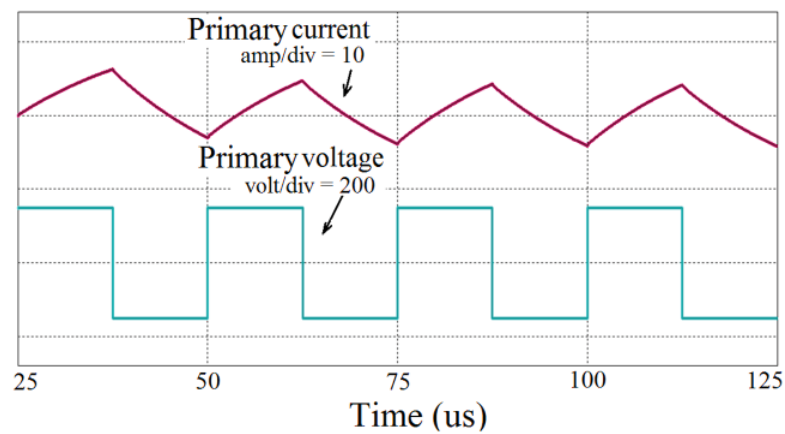
Fig.4.39 Frequency response of winding one to three of MWT for cases, (a) inductive load, (b) short circuit and (c) capacitive load conditions (solid line is simulation and dashed line is experimental results).



(a)

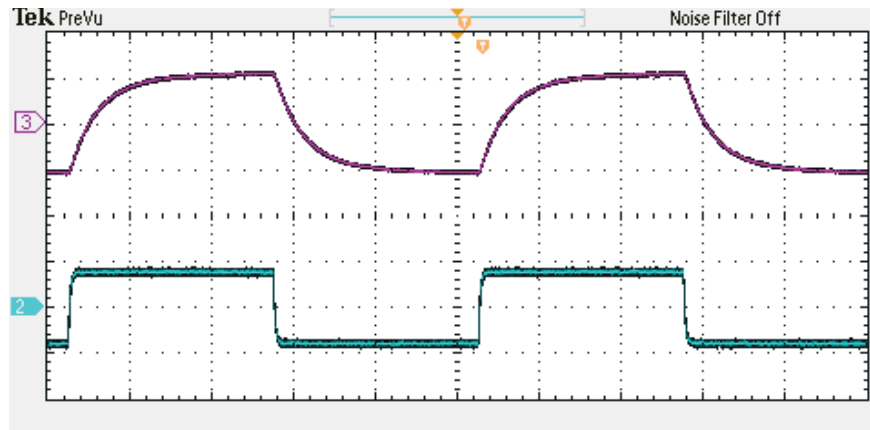


(b)

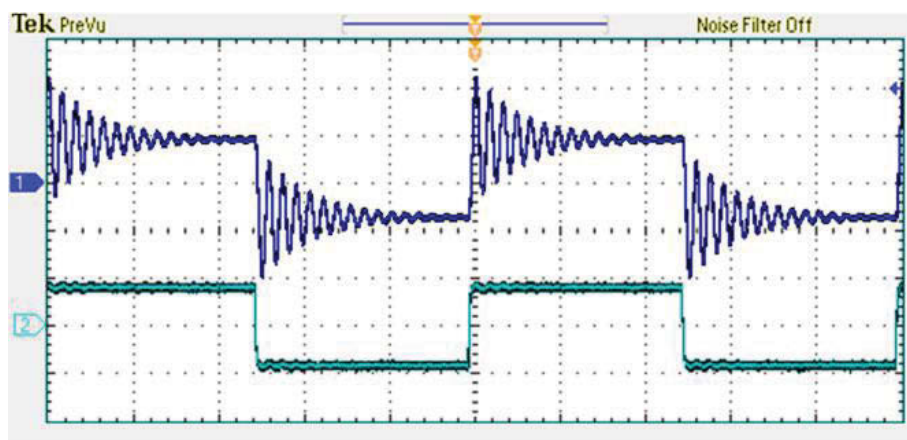


(c)

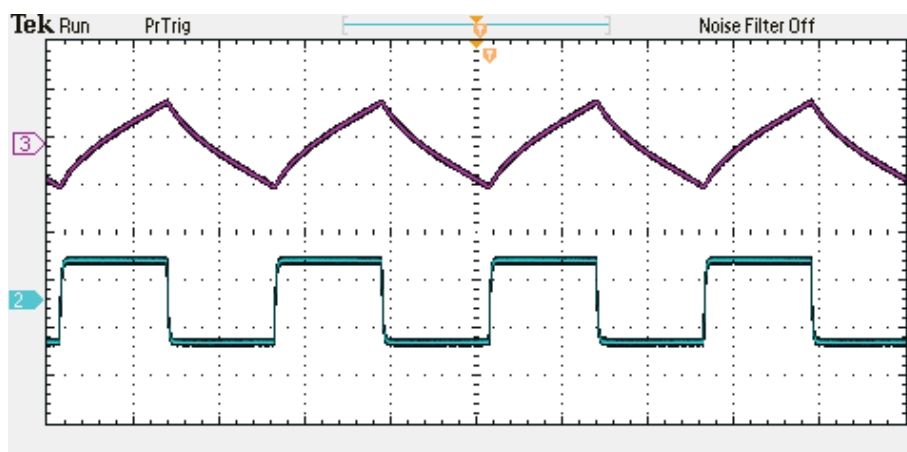
Fig.4.40 Simulation results of magnetic link modeling using PSIM, (a) short circuit condition, (b) capacitive load and (c) inductive load



(a)



(b)



(c)

Fig.4.41 Experimental test results for (a) short circuit condition, (b) capacitive load and (c) inductive load conditions, CH1: secondary voltage, CH2: primary voltage, CH3: primary current.

#### 4.15 Summary of the Chapter

Magnetic links have attracted considerable research interests in applications for integration of renewable energy sources. This chapter studies all stages of design, prototyping and validity tests of a high-frequency toroidal magnetic link. The design starts with selection of appropriate magnetic material. Then, the initial values of the variables are defined using a primary design based on the classical methods of transformer design. To improve the design accuracy, the RNM was used to analyze the magnetic structure and design the transformer for certain specifications due to the low computation time and acceptable accuracy. The resultant geometry of magnetic link then is analyzed for core loss and copper loss evaluation. The core loss was calculated using improved Steimetz equation considering non-sinusoidal excitation currents. An accurate method of copper loss analysis for multi-winding magnetic link is discussed in this chapter. The phase shift angle, duty ratio and amplitude variation of the voltages of the ports have been taken into account. The high frequency skin and proximity effect losses are calculated using ac resistance factor of the Litz wire windings. The winding loss of all three windings and the maximum and minimum copper loss operating points for two cases of DAB and TAB modes were evaluated. The thermal rise of the magnetic link is evaluated using thermal-electric model in the last stage of design. To validate the design process, a prototype was developed using amorphous magnetic materials and inductive and resistive parameters, core loss, copper loss and temperature rise are measured experimentally. Comparison between numerically designed and experimentally measured parameters, under nominal load and frequency range validated the proposed design procedure.

## References

- [4.1] M. R. Islam, G. Lei, Y. Guo and J. Zhu, “Optimal Design of High-Frequency Magnetic Links for Power Converters Used in Grid-Connected Renewable Energy Systems,” *IEEE Trans. Magnetics*, vol. 50, no. 11, pp. 1-4, Nov. 2014
- [4.2] D. Gunasekaran and L. Umanand, “Integrated magnetics based multi-port bidirectional DC-DC converter topology for discontinuous-mode operation,” *IET Power Electronics*, vol. 5, no. 7, pp. 935-944, August 2012.
- [4.3] M. R. Islam, Y. G. Guo, Z. W. Lin, and J. G. Zhu, “An amorphous alloy core medium frequency magnetic-link for medium voltage PV inverters,” *J. Appl. Phys.*, vol.115,no.17,pp. 17E710 - 17E710-3, May 2014.
- [4.4] Y. M. Chen, Y. C. Liu, and T. F. Wu, “Multi-input dc–dc converter based on the multi-winding transformer for renewable energy applications,” *IEEE Trans. Ind Applications*, vol. 38, no. 4, pp. 1096–1104, July/August 2002
- [4.5] H. Tao, J. L. Duarte, M. A. M. Hendrix, “Three-port triple-half bridge bidirectional converter with zero voltage switching,” *IEEE Trans. Power Electron*, vol. 23, no.2, pp 782–792, March 2008.
- [4.6] Junjun Zhang, Hongfei Wu, Xiaoqing Qin and Yan Xing, “PWM Plus Secondary-Side Phase-Shift Controlled Soft-Switching Full-Bridge Three-Port Converter for Renewable Power Systems,” *IEEE Trans. Ind Electronics*, vol. 62, no. 11, pp. 7061-7072, Nov. 2015.
- [4.7] M. McDonough, “Integration of Inductively Coupled Power Transfer and Hybrid Energy Storage System: A Multiport Power Electronics Interface for Battery-Powered Electric Vehicles,” *IEEE Tran. Power Electron*, vol. 30, no. 11, pp. 6423-6433, Nov. 2015
- [4.8] Y. Chen, X. Liu, Y. Cui, J. Zou and S. Yang, “A MultiWinding Transformer Cell-to-Cell Active Equalization Method for Lithium-Ion Batteries With Reduced Number of Driving Circuits,” *IEEE Tran. Power Electron*, vol. 31, no. 7, pp. 4916-4929, July 2016.
- [4.9] H. Tao, A. Kotsopoulos, J. L. Duarte, and M. A. M. Hendrix, “Family of multiport bidirectional DC-DC converters,” *IEE Proceeding Electric Power Applications*, vol. 153, no. 3, pp. 451–458, May 2006.

- [4.10] A. Davoudi, P. L. Chapman, J. Jatskevich and H. Behjati, "Reduced-Order Dynamic Modeling of Multiple-Winding Power Electronic Magnetic Components," *IEEE Trans. Power Electron*, vol. 27, no. 5, pp. 2220-2226, May 2012.
- [4.11] Chunyang Gu, Zedong Zheng, Lie Xu, Kui Wang and Yongdong Li, "Modeling and Control of a Multiport Power Electronic Transformer (PET) for Electric Traction Applications," *IEEE Trans. Power Electron*, vol. 31, no. 2, pp. 915-927, Feb. 2016.
- [4.12] W. Shen, "Design of high-density transformers for high-frequency highpower converters," Ph.D. dissertation, Virginia Polytechnic Inst. State Univ., Blacksburg, VA, Jul. 2006.
- [4.13] A. Van den Bossche, V. C. Valchev, and G. B. Georgiev, "Measurement and loss model of ferrites with non-sinusoidal waveforms," in *Proc. 35<sup>th</sup> Annu. IEEE PESC*, Jun. 20–25, 2004, vol. 6, pp. 4814–4818.
- [4.14] C. Zhao, S.D.Round, and J.W.Kolar, "An isolated three-port bidirectional DC–DC converter with decoupled power flow management," *IEEE Trans. Power Electron.*, vol. 23, no. 5, pp. 2443–2453, Sep. 2008.
- [4.15] H. Tao, A. Kotsopoulos, J. L. Duarte and M. A. M. Hendrix, "Transformer-Coupled Multiport ZVS Bidirectional DC–DC Converter With Wide Input Range," *IEEE Trans. Power Electron*, vol. 23, no. 2, pp. 771-781, March 2008.
- [4.16] J.G .Hayes, D. Cashman, M.G. Egan, T .O'Donnell, "Comparison of test methods for characterization of high-leakage two-winding transformers," *IEEE Trans. Ind. Appl.* Vol.45,no.5, pp.1729 – 1741
- [4.17] J. Worotynski, M. Turowski and E. Worotynska, "Generation of an optimal reluctance network model for fast 2-D and 3-D simulations of electromagnetic devices," in *proc. 2<sup>nd</sup> International Conference on Computation in Electromagnetics*, 1994., London, 1994, pp. 116-119.
- [4.18] F. Janet, J. L. Coulomb, C. Chillet and P. Mas, "Magnetic moment and reluctance network mixed method applied to transformer modeling," *IEEE Trans. on Magnetics*, vol. 41, no. 5, pp. 1428-1431, May 2005.
- [4.19] D. Vanoost, H. De Gersem, J. Peuteman, G. Gielen and D. Pisssoort, "Two-Dimensional Magnetostatic Finite-Element Simulation for Devices With a Radial Symmetry," *IEEE Trans. on Magnetics*, vol. 50, no. 5, pp. 1-4, May 2014.

- [4.20] B. Auchmann, B. Flemisch and S. Kurz, "A Discrete 2-D Formulation for 3-D Field Problems With Continuous Symmetry," *IEEE Trans. on Magnetics*, vol. 46, no. 8, pp. 3508-3511, Aug. 2010.
- [4.21] Z. Zhanxin, X. Dexin, W. Gang, Z. Yanli, and Y. Xiuke, "Computation of 3-D magnetic leakage field and stray losses in large power transformer," *IEEE Trans. On Magnetics.*, vol.48, no.2, pp.739 – 742, 2012.
- [4.22] S. Ghalavand, V. Zadeh, and Isfahani, "An improved magnetic equivalent circuit model for iron-core linear permanent-magnet synchronous motors," *IEEE Trans. On Magnetics.*, vol. 46, no. 1, pp. 112-120, Jan, 2010.
- [4.23] M. Amrhein and P. T. Krein, "3-D Magnetic Equivalent Circuit Framework for Modeling Electromechanical Devices," *IEEE Trans. on Energy Conversion*, vol. 24, no. 2, pp. 397-405, June 2009.
- [4.24] S. V. Kulkarni and S. A. Khaparde, *Transformer Engineering Design & Practice*. New York: Marcel Dekker, 2004
- [4.25] Ferroxcube, "Datasheets- Soft ferrite products and accessories"  
<http://www.ferroxcube.com/FerroxcubeCorporateReception/datasheet/3f3.pdf>
- [4.26] Finemet, <http://www.hilltech.com/pdf/hl-fm10-cFinemetIntro.pdf>
- [4.27] Hitachi metals, "2605SA1 Technical Bulletin"  
[www.metglas.com/products/magnetic\\_materials/2605SA1.asp](http://www.metglas.com/products/magnetic_materials/2605SA1.asp)
- [4.28] M. R. Islam, Youguang Guo and Jianguo Zhu, "A High-Frequency Link Multilevel Cascaded Medium-Voltage Converter for Direct Grid Integration of Renewable Energy Systems," *IEEE Trans. Power Electron*, vol. 29, no. 8, pp. 4167-4182, Aug. 2014.
- [4.29] J.Wang et al., "Derivation, calculation, and measurement of parameters for a multi-winding transformer electrical model," *IEEE APEC 1999*, pp. 220-226.
- [4.30] de Leon, F.; Purushothaman, S.; Qaseer, L., "Leakage Inductance Design of Toroidal Transformers by Sector Winding," *IEEE Trans. Power Electron*, vol.29, no.1, pp.473-480, Jan. 2014
- [4.31] W.Hurley, D.J.Wilcox, "Calculation of leakage inductance in transformer windings," *IEEE Trans. Power Electron*. Vol.9, no.1, pp. 121-126, Jan 1994.
- [4.32] E. S. Hamdi, *Design of Small Electrical Machines*. Chichester, U.K.: Wiley, 1998.
- [4.33] T. A. Lipo, *Introduction to AC Machine Design*. Madison, WI: Wisconsin Power Electronics Research Center, Univ. of Wisconsin-Madison, 2004.

- [4.34] T. W. Preston and J. P. Sturgess, "Implementation of the finite-element method into machine design procedures," in *Proc. Int. Conf. Electr.Mach.Drives*, 1993, pp. 312–317.
- [4.35] S. R. H. Hoole, A. Mascenghe, K. Navukkarasu, and K. A. S. K. Sivasubramaniam, "An expert design environment for electrical devices and its engineering assistant," *IEEE Trans. Magnetics.*, vol. 39, no. 3, pp. 1693–1696, May 2003.
- [4.36] J. Perho, "Reluctance network for analysing induction machines," *Acta Polytech. Scand., Electr. Eng. Series*, vol. 110, pp. 1–147, Dec. 2002.
- [4.37] A. Souissi, M. W. Zouaghi, I. Abdennadher and A. Masmoudi, "MEC-Based Modeling and Sizing of a Tubular Linear PM Synchronous Machine," *IEEE Trans. Ind Applications*, vol. 51, no. 3, pp. 2181-2194, May-June 2015
- [4.38] E. R. Laithwaite, "Magnetic equivalent circuits for electrical machines," *Proc. Inst. Electr. Eng.*, vol. 114, no. 11, pp. 1805–1809, Nov. 1967.
- [4.39] C. J. Carpenter, "Magnetic equivalent circuits," *Proc. Inst. Electr. Eng.*, vol. 115, no. 10, pp. 1503–1511, Oct. 1968.
- [4.40] V. Ostović, "Magnetic equivalent circuit presentation of electric machines," *Electr. Mach. Power Syst.*, vol. 12, no. 6, pp. 407–432, Jun. 1987.
- [4.41] D. Vanoost, H. De Gersem, J. Peuteman, G. Gielen, and D. Pisssoort, "Two-dimensional magnetostatic finite-element simulation for devices with a radial symmetry," *IEEE Trans. Magnetics.* vol.50, no.5, May 2014.
- [4.42] X. Liang, S. O. Faried and A. M. El-Serafi, "Space Harmonics of Synchronous Machines Calculated by Finite-Element Method," *IEEE Trans. Ind Applications*, vol. 52, no. 2, pp. 1193-1203, March-April 2016.
- [4.43] S. D. Sudhoff, B. T. Kuhn, K. A. Corzine, and B. T. Branecky, "Magnetic equivalent circuit modeling of induction motors," *IEEE Trans. Energy Convers.*, vol. 22, no. 2, pp. 259–270, Jun. 2007.
- [4.44] J. Worotynski, M. Turowski and E. Worotynska, "Generation of an optimal reluctance network model for fast 2-D and 3-D simulations of electromagnetic devices," in *proc. Second Int Conf on Computation in Electromagnetics*, London, 1994, pp. 116-119.
- [4.45] B. Auchmann, B. Flemisch, and S. Kurz, "A discrete 2-D formulation for 3-D field problems with continuous symmetry," *IEEE Trans. Magnetics*, vol.46 , no.8 , pp.3508–3511, Aug. 2010.

- [4.46] R. Wang, S. Pekarek, M. L. Bash, A. Larson and R. V. Maaren, “Incorporating Dynamics in a Mesh-Based Magnetic Equivalent Circuit Model of Synchronous Machines,” *IEEE Trans. Energy Conversion*, vol. 30, no. 3, pp. 821-832, Sept. 2015.
- [4.47] A. Hanic; D. Zarko; Z. Hanic, “A Novel Method for No-Load Magnetic Field Analysis of Saturated Surface Permanent-Magnet Machines Using Conformal Mapping and Magnetic Equivalent Circuits,” *IEEE Trans. Energy Conversion*, vol. PP, no. 99, pp. 1-10
- [4.48] H. Gorginpour, H. Oraee and R. A. McMahon, “A Novel Modeling Approach for Design Studies of Brushless Doubly Fed Induction Generator Based on Magnetic Equivalent Circuit,” *IEEE Trans. Energy Conversion*, vol. 28, no. 4, pp. 902-912, Dec. 2013.
- [4.49] M. Amrhein and P. T. Krein, “3-D Magnetic Equivalent Circuit Framework for Modeling Electromechanical Devices,” *IEEE Trans. Energy Conversion*, vol. 24, no. 2, pp. 397-405, June 2009.
- [4.50] J. Reinert, A. Brockmeyer, and R. W. A. A. De Doncker, “Accurate calculation of losses in ferro- and ferrimagnetic materials based on the modified Steinmetz equation,” *IEEE Trans. Ind. Appl.*, vol. 37, no. 4, pp. 1055–1060, Jul./Aug. 2001.
- [4.51] K. Venkatachalam, C. R. Sullivan, T. Abdallah, and H. Tacca, “Accurate prediction of ferrite cores loss with nonsinusoidal waveforms using only Steinmetz parameters,” in *Proc. IEEE Workshop Comput. Power Electron.*, Jun. 3–4, 2002, pp. 36–41.
- [4.52] I. Villar, U. Viscarret, I. Etxeberria-Otadui and A. Rufer, “Global Loss Evaluation Methods for Nonsinusoidally Fed Medium-Frequency Power Transformers,” *IEEE Trans. Industrial Electronics*, vol. 56, no. 10, pp. 4132-4140, Oct. 2009.
- [4.53] E. L. Barrios, A. Ursúa, L. Marroyo and P. Sanchis, “Analytical Design Methodology for Litz-Wired High-Frequency Power Transformers,” *IEEE Trans. Ind. Electron.*, vol. 62, no. 4, pp. 2103-2113, April 2015.
- [4.54] Z. Ouyang, O. C. Thomsen and M. A. E. Andersen, “Optimal Design and Tradeoff Analysis of Planar Transformer in High-Power DC–DC Converters,” *IEEE Trans. Ind. Electron.*, vol. 59, no. 7, pp. 2800-2810, July 2012.

- [4.55] H. Hämäläinen, J. Pyrhönen, J. Nerg, and J. Talvitie, “AC resistance factor of litz-wire windings used in low-voltage high-power generators,” *IEEE Trans. Ind. Electron.*, vol. 61, no. 2, pp. 693–700, Feb. 2014.
- [4.56] C. R. Sullivan, “Computationally efficient winding loss calculation with multiple windings, arbitrary waveforms, and two-dimensional or three-dimensional field geometry,” *IEEE Trans. Power Electron.*, vol. 16, no. 1, pp. 142-150, Jan 2001.
- [4.57] P.L.Dowell, “Effects of eddy currents in transformer windings,” in *Proc. IEE*, Vol.113, pp.1387-1394, Aug. 1966.
- [4.58] R. P. Wojda and M. K. Kaizimierczuk, “Winding resistance of litz-wire and multi-strand inductors,” *IET Power Electron.*, vol. 5, no. 2, pp. 257–268, Feb. 2012.
- [4.59] C. R. Sullivan, “Optimal choice for number of strands in a litz-wire transformer winding,” *IEEE Trans. Power Electron.*, vol. 14, no. 2, pp. 283–291, Mar. 1999.
- [4.60] J. Lammeraner and M. Stafl, *Eddy Currents*, 1st ed. London, U.K.: Iliffe Books, Ltd., 1966, ch. 7.
- [4.61] M. Bartoli, N. Noferi, A. Reatti, and M. K. Kazimierczuk, “Modeling litz wire winding losses in high-frequency power inductors,” in *Proc. IEEE PESC*, 1996, pp. 1690–1696.
- [4.62] F. Tourkhani and P. Viarouge, “Accurate analytical model of winding losses in round litz wire windings,” *IEEE Trans. Magn.*, vol. 37, no. 1, pp. 538–543, Jan. 2001.
- [4.63] A. W. Lotfi and F. C. Lee, “A high frequency model for Litz wire for switch-mode magnetics,” in *proc. Ind. Appl. Society Annual Meeting*, 1993., Toronto, Ont., 1993, pp. 1169-1175 vol.2.
- [4.64] X. Nan and C. R. Sullivan, “An equivalent complex permeability model for litz-wire windings,” *IEEE Trans. Ind. Appl.*, vol. 45, no. 2, pp. 854– 860, Mar./Apr. 2009.
- [4.65] J. A. Ferreira, “Improved analytical modeling of conductive losses in magnetic components,” *IEEE Trans. Power Electron.*, vol. 9, no. 1, pp. 127–131, Jan. 1994.

- [4.66] D. Murthy-Bellur and M. K. Kazimierczuk, "Harmonic winding loss in buck DC-DC converter for discontinuous conduction mode," *IET Power Electron.*, vol. 3, no. 5, pp. 740-754, September 2010.
- [4.67] D. Murthy-Bellur, N. Kondrath and M. K. Kazimierczuk, "Transformer winding loss caused by skin and proximity effects including harmonics in pulse-width modulated DC-DC flyback converters for the continuous conduction mode," *IET Power Electron.*, vol. 4, no. 4, pp. 363-373, April 2011.
- [4.68] F. Xue, R. Yu and A. Q. Huang, "Loss analysis of a high efficiency GaN and Si device mixed isolated bidirectional DC-DC converter," in *proc. 2016 IEEE APEC*, Long Beach, CA, 2016, pp. 3677-3683.
- [4.69] I. Villar, "Multiphysical characterization of medium-frequency power transformers," Ph.D. dissertation, Faculté des Sciences et Techniques de l'Ingénieur, École Polytechnique Fédérale Lausanne, Lausanne, Switzerland, 2010.
- [4.70] J. A. Ferreira, "A Analytical computation of AC resistance of round and rectangular litz wire windings," in *IEE Proc. B-Electric Power Applications*, vol. 139, no. 1, pp. 21-25, Jan. 1992.
- [4.71] A. Reatti and M. K. Kazimierczuk, "Comparison of various methods for calculating the AC resistance of inductors," *IEEE Trans. Magn.*, vol. 38, no. 3, pp. 1512-1518, May 2002.
- [4.72] S. Purushothaman and F. de Leon, "Heat-Transfer Model for Toroidal Transformers," *IEEE Trans. Power Delivery*, vol. 27, no. 2, pp. 813-820, April 2012.
- [4.73] I. Villar, U. Viscarret, I. Etxeberria-Otadui and A. Rufer, "Transient thermal model of a medium frequency power transformer," in *proc. 34th Annual Conf of Industrial Electronics, 2008*. Orlando, FL, 2008, pp. 1033-1038.
- [4.74] Wm. Colonel and T. Mc Lyman, *Transformer and Inductor Design Handbook*, 3rd ed. New York: Marcel Dekker, 2004.
- [4.75] J.G .Hayes, D. Cashman, M.G. Egan, T .O'Donnell, "Comparison of test methods for characterization of high-leakage two-winding transformers," *IEEE Trans. Ind. Appl.* Vol.45,no.5, pp.1729 – 1741
- [4.76] J.G. Hayes, N. O'Donovan, M. G. Egan, and T. O'Donnell, "Inductance characterization of high-leakage transformers," in *Proc. IEEE Appl.Power Electron. Conf.*, 2003, pp. 1150–1156.

## CHAPTER 5

# STEADY STATE OPERATION ANALYSIS AND CONTROL OF CONVERTERS IN MICRO-GRID

### 5.1 Introduction

Multi-port converters (MPC) have attracted much research attention in recent years and many multi-port topologies are proposed and studied in the literatures. Some of the main topologies are studied briefly in chapter two according to their principle of operation and performance. The phase shift MPC's have presented excellent performances for integration of renewable energy systems. In contrast to other topologies they provide attractive features such as isolation between the ports, bidirectional power flow, simple power flow and energy management control, lower switching stress and efficient use of transformer leakage inductance as energy transfer element [5.1]-[5.7]. Based on the studies in chapter two the residential micro-grid proposed in this research employs a combination of dc bus and magnetic bus to integrate the energies of a PV panel, fuel cell and a battery and supplies the load. It includes a triple active bridge (TAB) phase shift dc-dc converter, an interleaved current-fed boost converter, a bidirectional buck-boost dc-dc converter and a single phase bidirectional inverter. A detailed study of the dc-dc converters including their steady state operational principle, small signal and dynamic analysis, and control techniques are provided in this chapter. Since the main focus of the thesis is on the dc-dc conversion stage, the inverter and its control are not discussed in detail. The designed dc-dc converters are simulated using PSIM. A prototype of the system is developed and experimental tests are conducted.

The contents of this chapter are aimed to provide a device level study on the structure of the proposed micro-grid. Since the structure of the micro-grid including all converters and the operational principle were studied in Chapter Three, this chapter is mainly focused on the small signal analysis, dynamic response and controller design.

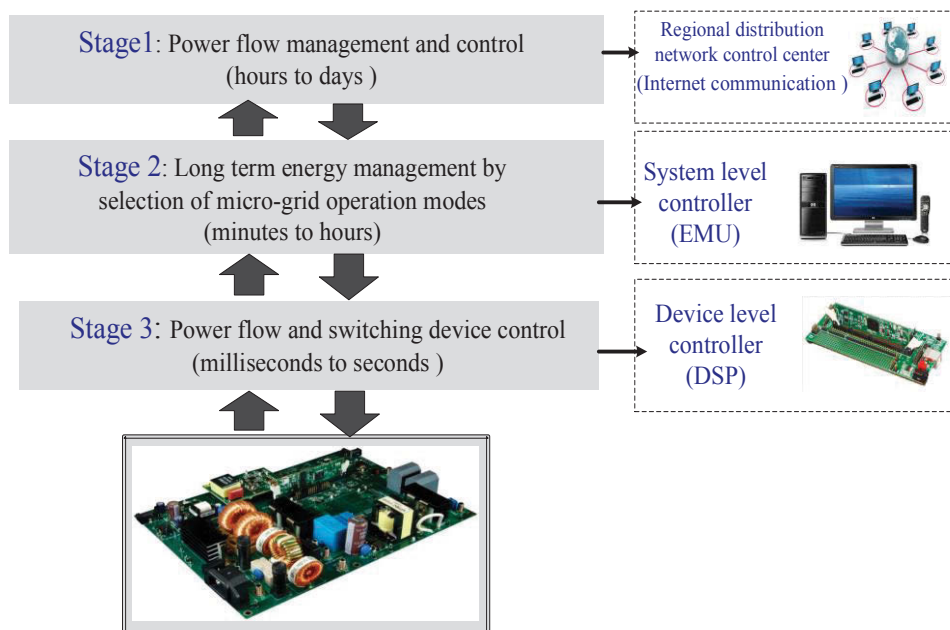


**Fig.5.1 The control levels of the proposed micro-grid**

## 5.2 Control Strategy of the Proposed Micro-grid

To control the proposed micro-grid effectively, three levels of control are considered according to the control objectives as illustrated in Fig.5.1. A device level controller is required to control the switching devices of each converter to utilize the voltage regulation, power transfer and energy balance through the entire micro-grid. The reaction time for device level controller is in the range of milliseconds to seconds. On the other hand, a system level controller should be designed to manage the operation modes of the micro-grid system to maintain the energy management efficiently. The system level controller also known as energy management unit (EMU) should be connected to the device level controllers through a communication network to send and receive the required information. The EMU defines the appropriate operation mode of the system according to the real time data of the system and the predicted data. The highest level of control is performed by the regional distribution network control centre as shown in Fig. 5.1. The data exchange between the EMU and the regional distribution network control centres is performed through the internet. The control objective at this level is adjustment of power flow between micro-grid and the main grid according to the main grid requirements. The EMU also receives other information such as weather forecast and grid energy cost profile for the future hours.

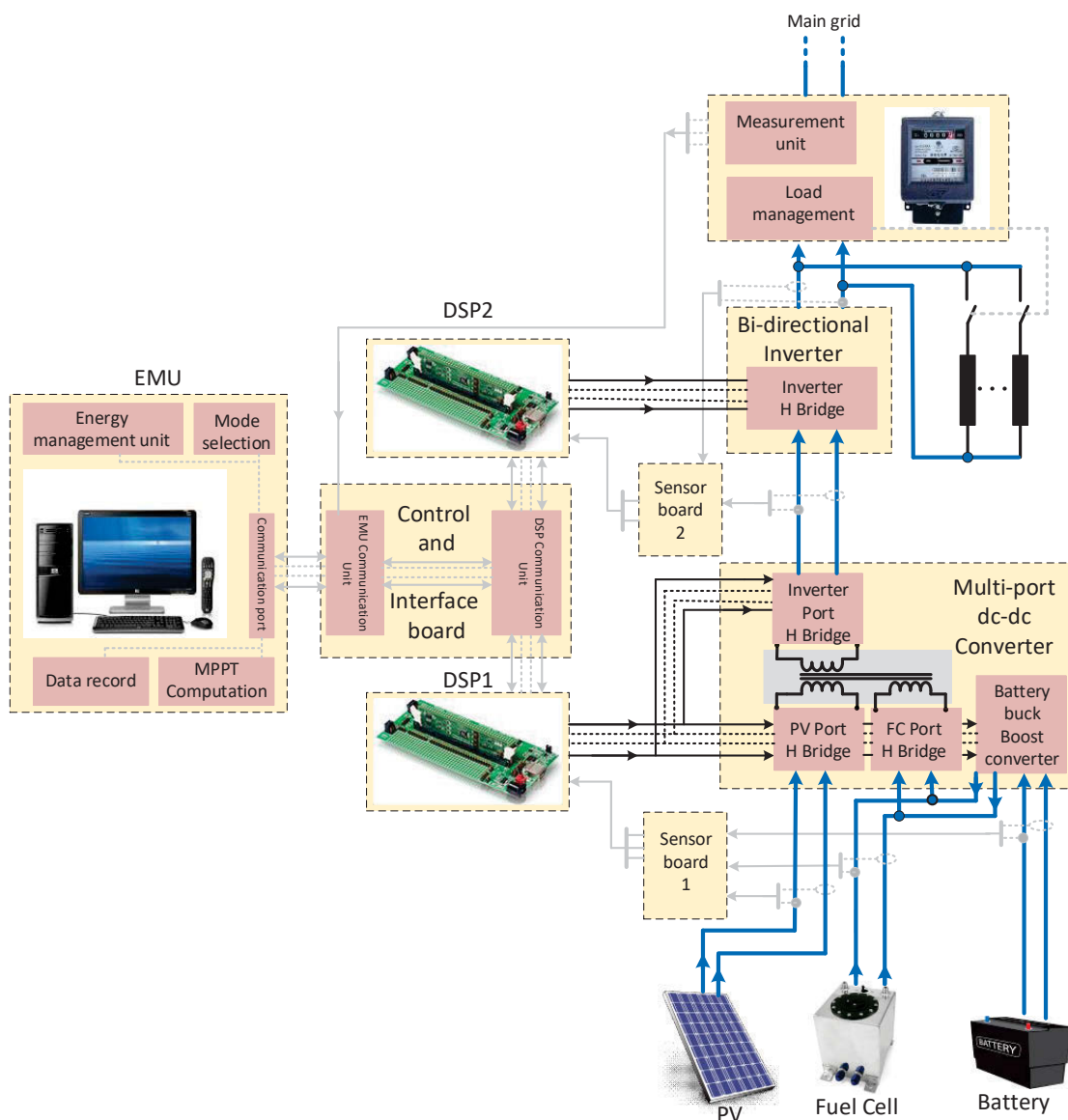


**Fig.5.2 The schematic of control circuits of proposed micro-grid**

The Schematic of the micro-grid hardware implementation including control signals is presented in Fig.5.2. As can be seen in the figure, two Texas instrument DSPs (TMS320F28335) are used as device level controller. DSP1 is used to control the multi-port dc-dc converter. It generates the PWM drive signals for bidirectional buck-boost converter and TAB converter. The voltage and current of fuel cell, PV and battery ports are measured and sent to the DSP1 to be used in the closed loop PI controllers. The MPPT process is performed by EMU to save a portion of DSP computational load. The MPPT reference signal produced by EMU is sent to the DSP1 to control the duty ratio of switching devices of the PV port. In the proposed system MPPT reference signal is updated every 10 ms ( $f=100$  Hz).

As discussed in Chapter Three, the operation mode of the micro-grid is controlled by EMU and the updated reference signal of the operation mode is sent to the DSP1 through a four digit binary-coded decimal (BCD) data which covers up to 16 operation modes. The mode control signals are sent by EMU to the control and interface board and then to the DSP. As can be seen in Fig.5.2, other signals to DSP1 include a reference-power signal for controlling the output power of fuel cell, a SOC signal for controlling the charge and discharge rate of battery and a system-fault signal resultant from short circuit of switching devices, over current and over/under voltage of converter ports. The system-fault signal is sent to the DSP1 to shut down the system if short circuit and over/under voltage happens.

Due to the limited number of PWM generators in the DSP1, a second DSP presented as DSP2 is used to control the single phase bidirectional inverter. As can be seen in Fig.5.2, the input signals to the DSP2 are the measured values of input dc voltage on the inverter port (bus1), input current to the inverter and inverter output voltage and current. The output voltage is equal to the grid voltage in grid connected mode. Similar to DSP1, a fault signal resultant from short circuit, over voltage and over current protection circuits is sent to the DSP2. The short circuit in switching device is detected by driver integrated circuit (VLA567-01R) as discussed in Chapter Three and the resultant fault signal is sent to the DSP through opto-isolators. On the other hand, the overcurrent and over/under voltage faults can be detected by comparing the voltage and currents of the converter ports with the predefined reference values using window comparators.

The fault detection circuits are implemented on the sensor and protection boards. The fault signals of all converter ports are logically linked together to form a single fault signal as presented in Fig.5.3.

Both DSPs are connected to the signal conditioning and level shifters on the control and interface board and further to the EMU. The measured voltages and currents are passed through the signal conditioning circuits on the sensor boards and transferred to the DSP through the interface board. The system-fault signals are also transferred to the DSP from the sensor boards.

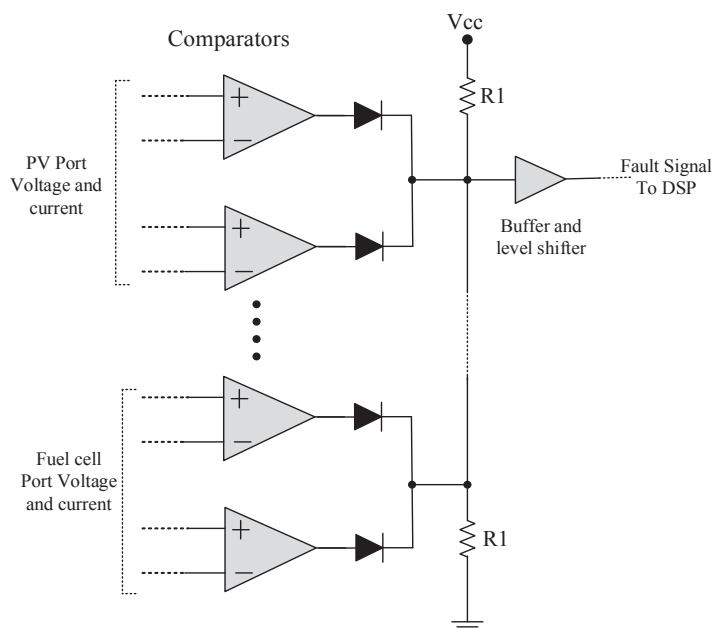


**Fig.5.3 Generation of single fault-signal using comparators and diodes**

Both DSP1 and DSP2 are linked to the EMU through interface board according to a multiplexing-data communication process using universal serial bus (USB). The data between each DSP and interface board is transferred using RS232 serial communication port. The data between grid energy control box and the EMU is transferred through the USB port.

The EMU controls the power flow direction and operation mode of the proposed micro-grid using long-term and short-term fuzzy controllers. It also records the voltage, current and power flow of the fuel cell, battery, PV, inverter and load. The energy management and data processing in the EMU is performed using MATLAB. The recorded data, operation modes of the system and features of the system operation during the previous hours are presented using MATLAB graphic user interface (GUI). More details on EMU operation principle and energy management techniques will be provided in Chapter Six.

### 5.3 DC-DC Converters in the Proposed Micro-grid

As discussed in Chapter Three, the main part of the micro-grid that integrates the renewable energy sources and transfers the power between the sources and the battery are dc-dc converters. Fig.5.4 illustrates the schematic of the micro-grid excluding the inverter and the experimentally developed micro-grid system.

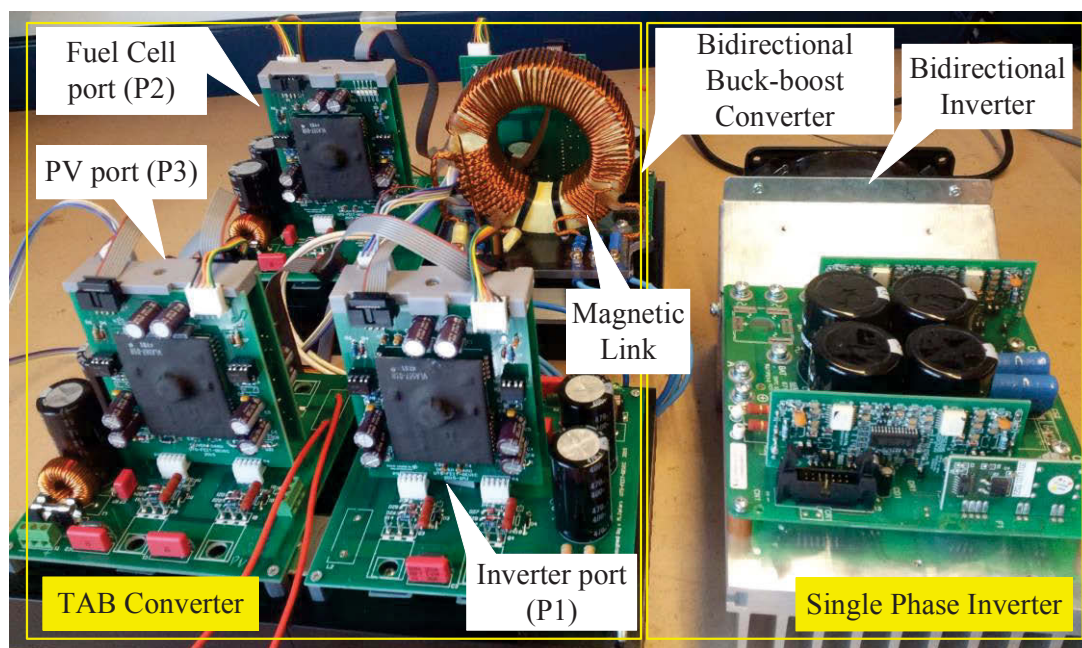
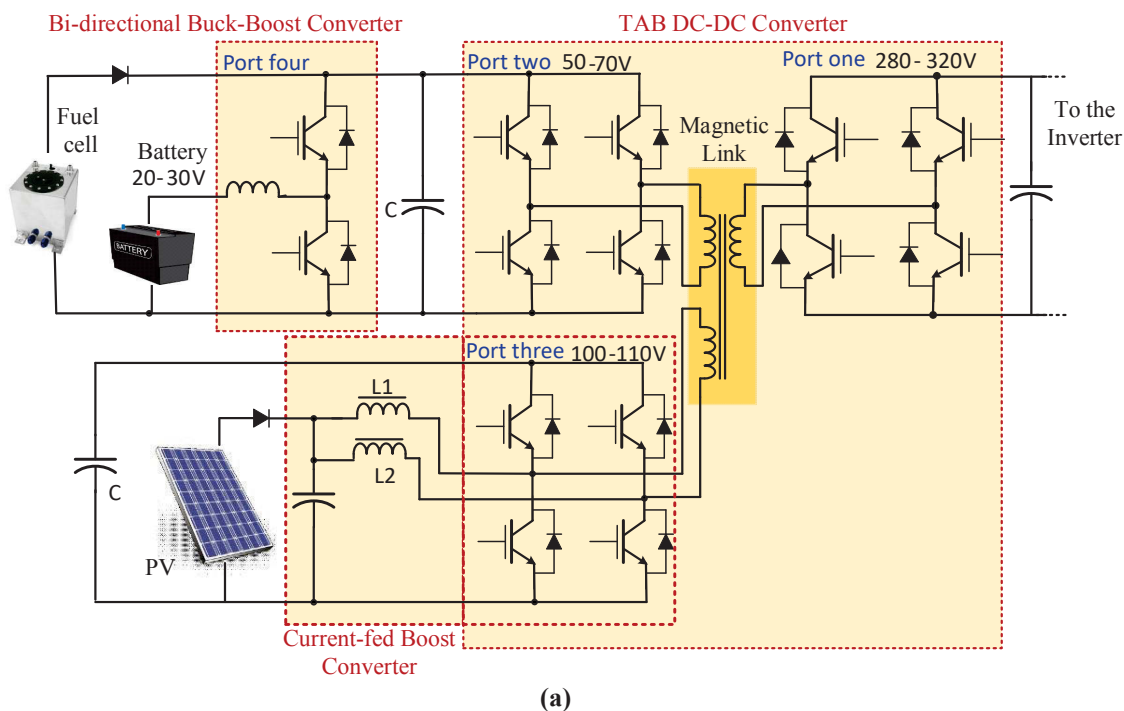


**Fig.5.4** Dc-Dc converters including TAB converter, bidirectional buck-boost converter and interleaved current-fed boost converter, (a) electrical schematic, and (b) experimentally developed system

As can be seen in the figure, there are three dc-dc converters including a TAB phase shift converter, a bidirectional buck-boost converter and an interleaved current-fed boost converter. The TAB converter is used to transfer the power between port one, two and three by introducing leading or lagging phase shifts between the high frequency square waves of the ports. A three winding magnetic link is used as a magnetic bus in

the middle to link the converter ports. The bidirectional buck-boost converter is used to transfer the power between the battery and other sources through a charging or discharging process. It is also used to balance the voltage of Port Two to compensate the slow dynamic response of fuel cell in transients.

The interleaved current-fed boost converter boosts the output voltage of PV to the desired range (100-110 V). The interleaved topology reduces the generated ripple on the PV output current and effectively adjusts the operation point of the PV on maximum power point (MPP). This chapter provides a study on the topology of each dc-dc converter, small signal modelling and controller design. The study begins with the TAB converter as the main converter and continues with the bidirectional buck-boost and current-fed boost converters.

#### **5.4 Analysis of the TAB Converter**

To study the TAB converter a general case of multi-active bridge (MAB) dc-dc converter is considered and then the resultant equations are reduced to the case of TAB converter. Structure of an MAB converter using a multi-winding magnetic link is presented in Fig.5.5 (a). In this topology, each active bridge generates a square wave with variable or constant duty cycle and applies it to one of the windings of the magnetic link.

To control the power flow direction between the ports, the generated square waves should be shifted by positive or negative angles compared with a predefined reference port. Therefore, the power flows from the ports with leading phase shift angle to the ports with lagging phase shift and the amount of transferred power can be controlled by the value of the phase shift. The structure and the control technique are simple for a lower number of ports (two, three and four ports) but problems arise in system design and control techniques for a higher number of ports. The main problems are complexity of multi-winding transformer design, increasing circulating power, limitation of soft switching range, large number of switching devices, saturation of magnetic link and difficulty of accurate power flow control. To simplify the analysis of MAB converter each dc voltage source and the linked H-bridge is presented as an equivalent square wave voltage source as presented in Fig.5.5 (b).

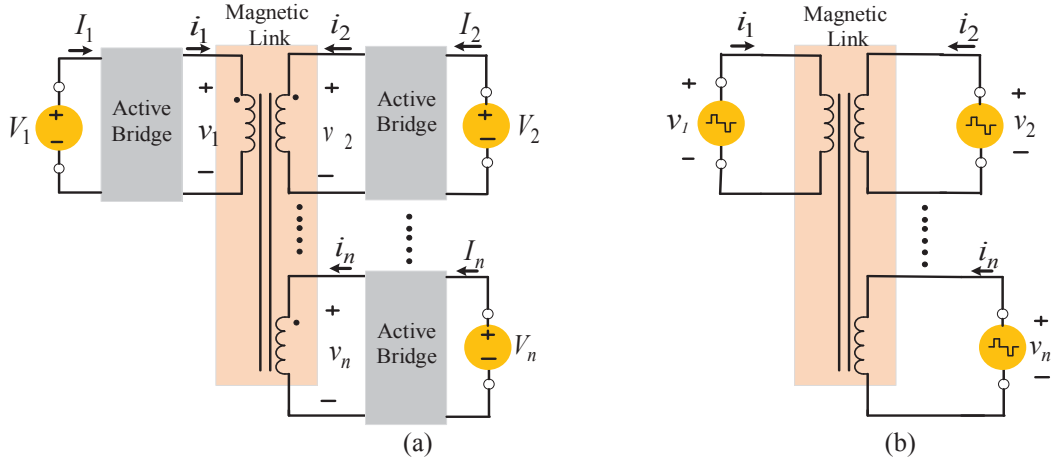


**Fig.5.5 Structure of multi-active bridge phase shift converter, (a) actual circuit and (b) simplified model**

Furthermore, the multi-winding transformer model can be transferred to the T-equivalent circuit by referring all parameters of the other ports to Port one as reference port. The resultant equivalent circuit is presented in Fig.5.6 (a).

To find the equivalent model, the following assumptions have been taken into effect. Firstly, the resistance of all the windings of the magnetic link is ignored due to its negligible effect on the converter operation. Secondly, the effect of mutual inductances within the multi-winding magnetic link is neglected. The magnetizing inductance,  $L_m$ , is modelled in winding one as reference winding and all leakage inductances, voltages and currents of other windings are reflected to it. The parameters of winding  $j$  as one of the transformer windings, referred to winding one are voltage  $v'_j$ , current  $i'_j$  and leakage inductance  $L'_j$  and can be defined as

$$v'_j = \frac{N_1}{N_j} v_j, i'_j = \frac{N_j}{N_1} i_j, L'_j = \left(\frac{N_1}{N_j}\right)^2 L_j \quad (5.1)$$

where  $N_j$ ,  $i_j$ ,  $v_j$  and  $L_j$  are the number of turns, current, voltage and leakage inductance of winding  $j$ , respectively.

To define the power transformed between any of two ports (ports  $j$  and  $k$  as an example), the superposition principle should be applied by short circuiting the other sources to eliminate their effect. The resultant T-equivalent model is presented in Fig.5.6 (b) [5.4]. It can be simplified as Fig.5.6(c) by combining the parallel inductances and further simplified to the equivalent  $\Delta$  model as shown in Fig.5.6 (d) using

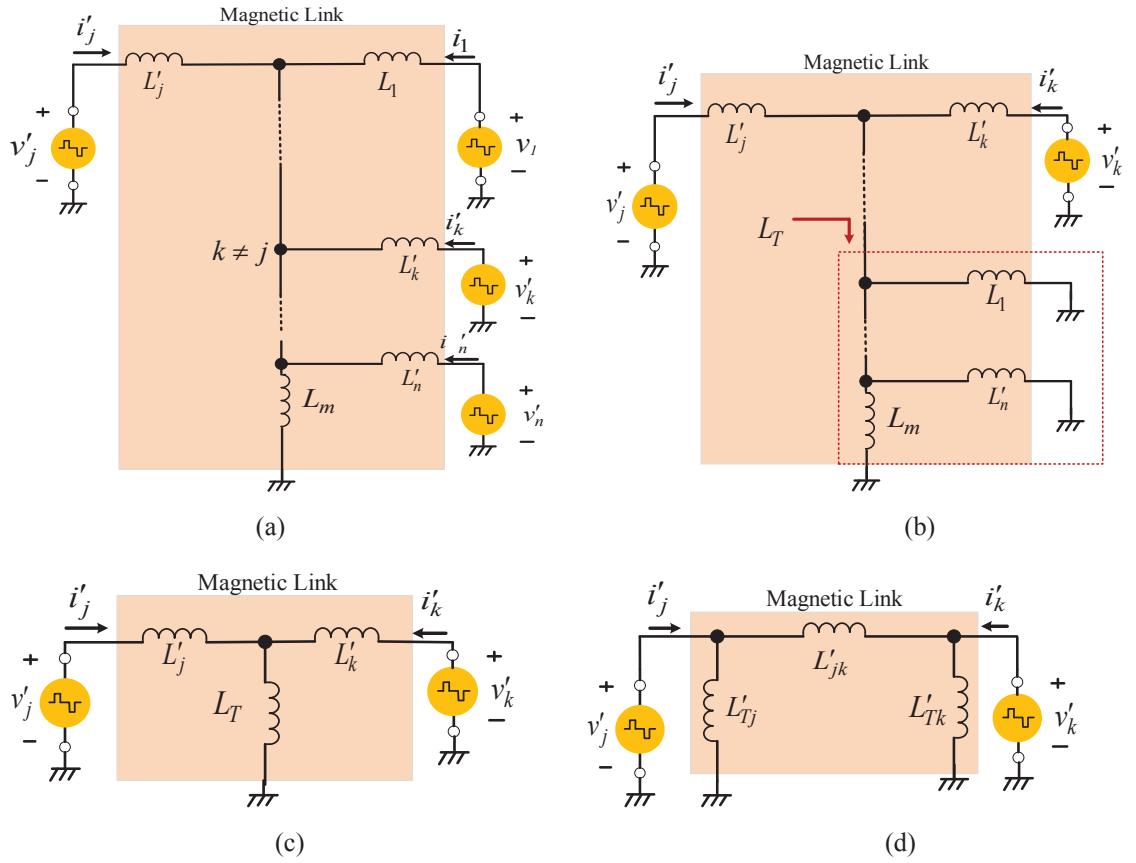


**Fig.5.6** Simplified model of multi-active bridge phase shift converter, (a) T-equivalent model, (b) applying super-position rule considering two sources only, (c) simplified T-model, and (d) simplified equivalent  $\Delta$ -model.

$$L'_{jk} = L'_j + L'_k + \frac{L'_j L'_k}{L_T} \quad (5.2)$$

$$L_T = \left( \frac{1}{L_m} + \sum_{l=1, \neq j, k}^n \frac{1}{L'_l} \right)^{-1} \quad (5.3)$$

As can be seen in the resultant model, the power flow between sources  $v'_j$  and  $v'_k$  depends only on the equivalent inductance linked to the sources,  $L'_{jk}$ . Applying the rule to all converter ports results in the equivalent circuit presented in Fig.5.7. As can be seen, the MAB converter topology can be modelled as multiple dual active bridge (DAB) converters to facilitate the power flow analysis [5.4]. According to the model, the power flows from port  $j$  to the other converter ports known as  $P_j$ , can be defined as

$$P_j = \sum_{l=1, \neq j}^n P_{jl} \quad (5.4)$$

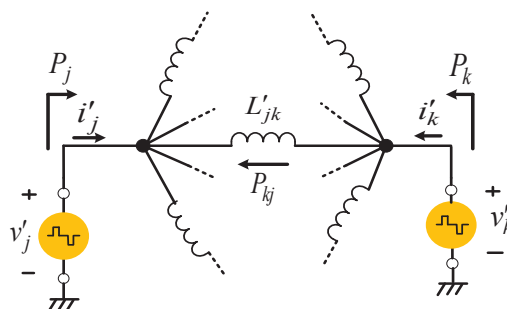


**Fig.5.7 Simplified model of multi-active bridge phase shift converter**

where  $P_{jl}$  is the power flows from  $v'_j$  to  $v'_l$ . To analyse the power flow between any two ports of the MAB converter a review on the basics of dual active bridge (DAB) converter is required. Due to the importance of DAB converter topology and its analysis as a basic step toward the MAB converter analysis, the next section provides a review on some of the features of a DAB converter which are useful in MAB converter analysis.

#### 5.4.1 Analysis of power flow in the DAB converter

The DAB converter topology was originally proposed in 1991 [5.8]. In the simplest form, the structure of a DAB converter includes two H-bridges interfacing two dc voltage sources to the primary and secondary of a high frequency transformer as shown in Fig.5.8. The circuit is symmetrical with respect to the high frequency transformer at the center. Assuming that the power flow is from left to right, the left hand side bridge produces a square wave voltage  $v_1$  from source  $V_1$  across the primary winding of the transformer. The leakage inductance of the secondary side of transformer,  $L_2$ , voltage source  $v_2$  and current  $i_2$  can be referred to the primary side to simplify the circuit as presented in Fig.5.8 (b). The generated ac voltage at the secondary side known as  $v_2$  also is a square wave with the amplitude equal to  $V_2$ . The duty cycle  $D$ , for both of  $v_1$  and  $v_2$  can be changed from 0 to 1 and there is no saturation problem in the transformer core as the dc component of current in the transformer is zero ideally. A phase shift angle of  $\phi_{12}$  between two waveforms is used to control both direction and amount of power flow between the sources. The duty ratio of generated waveforms can be variable or constant depending on the amplitude of the dc source linked to the bridge. In the case of a variable voltage source the duty ratio of generated ac voltage is changed according to the amplitude of the dc source. In general three modes of operation are considered based

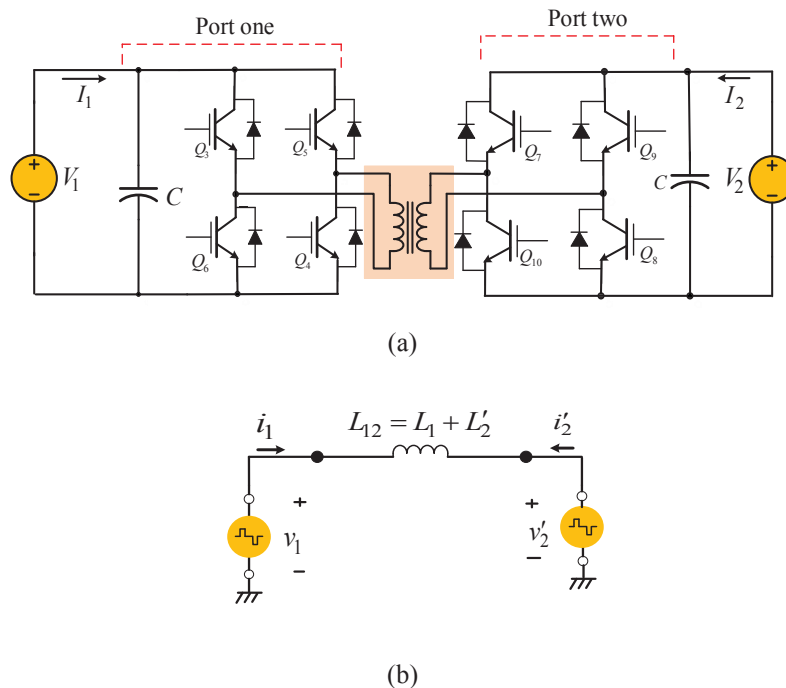


**Fig.5.8 DAB converter schematic, (a) circuit topology and (b) Equivalent circuit**

on the waveforms of  $v_1$  and  $v_2$ . In mode one, both waveforms are considered as square waves with constant duty cycle  $D=1$ . In the second mode, one of  $v_1$  or  $v_2$  has duty cycle of less than 1 and the other one has a constant duty ratio of  $D=1$ . In the third operation mode both  $v_1$  and  $v_2$  have variable duty ratio. The power flow analysis in each operation mode can be performed using two methods. The first method is based on the analysis of average current transformed between the sources using their geometrical waveforms. The second method is based on fundamental component of the square wave voltages applied to the transformer [5.7].

A detailed study on the DAB converter operation modes, soft switching range and the waveforms of voltage and currents is provided in [5.7], [5.9]. In this section only the power flow equations in different operation modes are briefly reviewed.

In the first operation mode where two generated waveforms  $v_1$  and  $v_2$  are square waves with  $D_1=D_2=1$ , the average power transferred from  $V1$  to  $V2$  and vice versa can be defined as

$$P_{12} = \frac{V_1 V_2}{\omega L_{12}} \phi_{12} \left(1 - \frac{|\phi_{12}|}{\pi}\right) \quad (5.5)$$

where  $L_{12}$  is the summation of primary leakage inductance  $L_1$ , and referred value of the secondary leakage inductance  $L'_2$ . Equation (5.5) is known as the basic equation of power flow in DAB converters in first operation mode and has been widely used in the

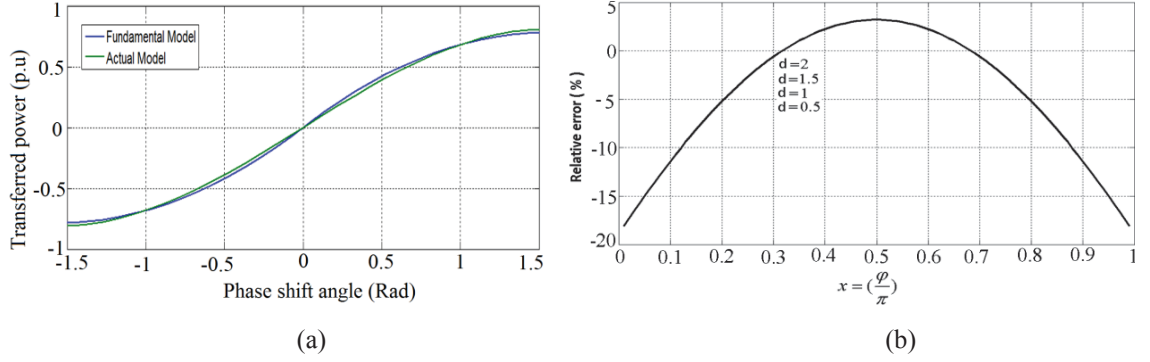


**Fig.5.9 (a) The power transferred versus phase shift using two analytical methods and (b) relative error between two analytical methods versus phase shift ratio for different voltage ratios ( $d$ )**

literature [5.10]-[5.13]. The equation is acceptable for both directions of power flow based on the positive or negative values of phase shift angle,  $\varphi$ . In the second method of power flow analysis based on the fundamental component of  $v_1$  and  $v_2$ , the power flow between  $V_1$  and  $V_2$  can be defined as

$$P_{12} = \frac{8V_1 V_2}{\pi^2 \omega L_{12}} \text{Sin}(\varphi_{12}) \quad (5.6)$$

Comparison of resultant power flow from (5.5) and (5.6) shows that both equations provide almost the same results. Fig.5.9 (a) shows the value of power flows from  $V_1$  to  $V_2$  as a function of phase shift angle  $\varphi_{12}$  using both methods. It can be seen that the resultant error in the case of using fundamental component approach is negligible. The relative error between the results of two power flow calculation methods for phase shift angle ranges from 0 to  $+\pi$  is calculated from

$$\text{Err}(\%) = \frac{P_1(\text{Fund}) - P_1(\text{Full})}{P_1(\text{Full})} \cdot 100 \quad (5.7)$$

Fig.5.9 (b) shows that the resultant relative error calculated using (5.7) is always less than 20 % of transferred power. The soft switching ability of DAB converter under various ranges of phase shift and duty cycle for operation mode one has been studied widely [5.14]-[5.18]. It can be seen that the DAB converter in the first operation mode is able to operate with ZVS in the entire phase shift range, if voltage ratio  $d$  remains equal to one during operation [5.7]. The voltage ratio  $d$  is defined as

$$d = \frac{N_1 V_2}{N_2 V_1} = \frac{1}{n_{21}} \frac{V_2}{V_1} \quad (5.8)$$

Outside of this condition the ZVS operation is achievable only in a limited range although a higher range of ZVS operation range is achievable at higher phase shift

angles [5.7]. It is difficult to extend the soft switching range in this mode as phase shift angle is the only variable to control the power flow.

In the second operation mode the amplitude of one voltage source either  $V_1$  or  $V_2$  is variable and the other one remains constant ( $D=1$ ). A duty cycle control is applied to the switching devices of the port with variable source. In this mode the power flow can be controlled using both phase shift angle  $\phi_{12}$  and duty cycle  $D$ . Assuming  $V_2$  as the variable source, the duty cycle of voltage is defined according to the minimum amplitude  $V_{2-min}$ , and actual amplitude of  $V_2$  as

$$D = \frac{V_{2-min}}{V_2} \quad (5.9)$$

There are two possible operation states for this mode based on the range of phase shift angle known as the inner and outer states [5.7],[5.9]. In the inner state the phase shift  $\phi_{12} \leq \phi_B$  where  $\phi_B$  is the boundary angle and is defined as  $\phi_B = \pi(1-D)/2$ . The power flow between two sources has a linear relation with the phase shift angle and duty cycle and for both positive and negative phase shifts is defined as

$$P_{12} = \frac{V_1 V_2 D}{\omega L_{12}} \phi_{12} \quad (5.10)$$

On the other hand, in the outer state where  $\phi_B \leq \phi_{12} \leq \pi/2$ , the power flows between the sources for both positive and negative ranges of phase shift angle can be calculated by

$$P_{12} = \frac{V_1 V_2}{\omega L_{12}} \left[ \phi_{12} \left( 1 + \frac{|\phi_{12}|}{\pi} \right) - \text{Sign}(\phi_{12}) \frac{\pi}{4} (1-D)^2 \right] \quad (5.11)$$

In the case of using the fundamental component approach, only one equation is obtained for both positive and negative phase shifts and operation states [5.7].

$$P_{12} = \frac{8V_1 V_2}{\pi^2 \omega L_{12}} \cos\left[\frac{(1-D)\pi}{2}\right] \sin(\phi_{12}) \quad (5.12)$$

The power flow versus phase shift ratio  $\phi/\pi$  for the second operation mode using both actual and fundamental harmonic equations is presented in Fig.5.10 (a). As shown in the the figure, the power flow increases with any increase in the duty cycle of the variable source. The power flow can be controlled using both duty ratio  $D$  and phase shift and this provides more flexibility in operation. Therefore, the soft switching (ZVS) operation in this mode is possible for a wide range [5.7]-[5.9].

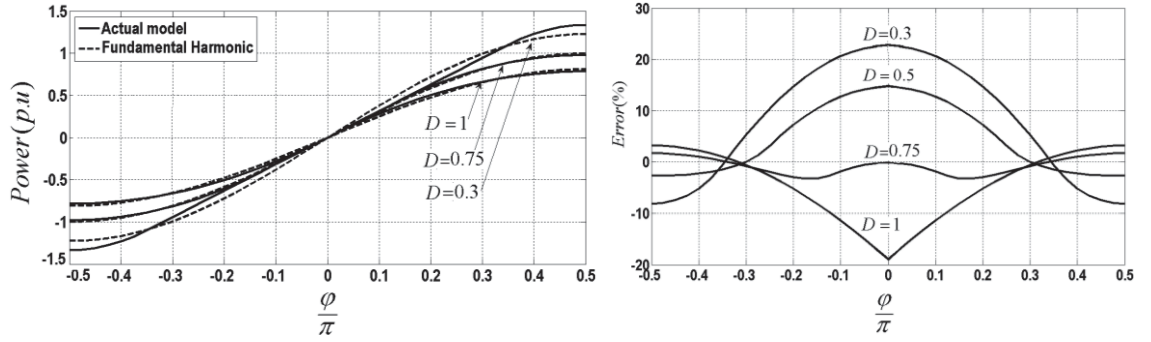


**Fig.5.10 (a) power flow in DAB converter in the second operation mode using two approaches and (b) the resultant error in the case of using fundamental component approach for power flow calculation**

The resultant error in the case of using the fundamental component approach for different phase shift angles and duty ratios is presented in Fig.5.10 (b). It can be seen that the resultant error depends on both phase shift angle and duty ratio and increases at lower phase shift angles and duty ratios but it does not exceed 25 %. It should be noted that the increasing relative error at lower phase shift angles is due to the small value of transferred power.

In the third operation mode both  $v_1$  and  $v_2$  are duty cycle controlled and the converter operates in three states based on the positions of two modulated square waves,  $v_1$  and  $v_2$ . To control the power transferred between the ports duty ratios  $D_1$  and  $D_2$  are defined based on the ratio of minimum to actual value of  $V_1$  and  $V_2$  using

$$D_2 = \frac{V_{2-\min}}{V_2}, \quad D_1 = \frac{V_{1-\min}}{V_1} \quad (5.13)$$

Assuming that  $D_1 > D_2$ , the boundary phase shift angles,  $\phi_{B1}$  and  $\phi_{B2}$  can be defined as

$$\phi_{B1} = \frac{\pi}{2}(D_1 - D_2), \quad \phi_{B2} = \frac{\pi}{2}(2 - D_1 - D_2) \quad (5.14)$$

The power flow equation for each state is defined according to the position of phase shift angle  $\phi_{12}$  compared with the boundary phase shift angles,  $\phi_{B1}$  and  $\phi_{B2}$  [5.7], [5.9]. For state one where  $\phi_{12} \leq \phi_{B1}$ , the power flow equation is defined as

$$P_{12} = \frac{V_2 V_1 \phi_{12}}{\pi \omega L_{12}} (\pi D_2) \quad (5.15)$$

and for the second state where  $\phi_{B1} < \phi_{12} \leq \phi_{B2}$ , the transferred power is defined as [5.7]

$$P_{12} = \frac{V_1^2 D_1}{2\omega L_{12}} \left[ \phi_{12} + \frac{\pi}{2}(D_1 - D_2) \right] + \frac{V_1 V_2}{2\pi \omega L_{12}} \left[ -\phi_{12}^2 + \pi D_1 \phi_{12} - \frac{\pi^2}{4}(D_1^2 - D_2^2) \right] \quad (5.16)$$

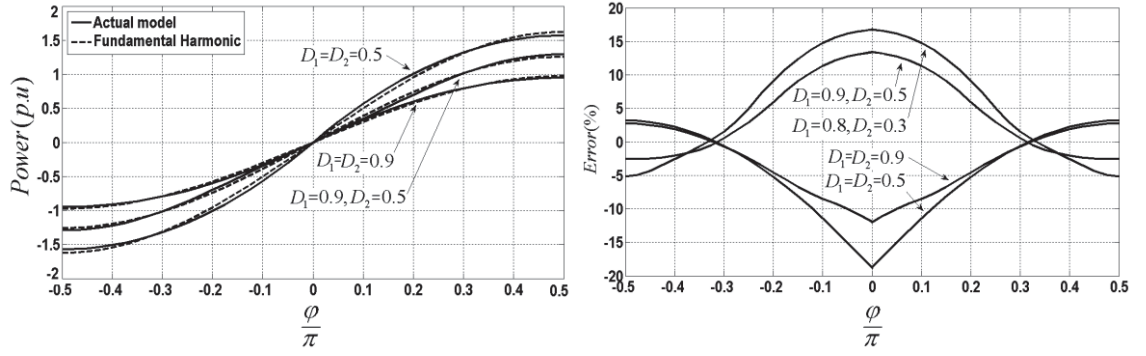


**Fig.5.11 (a) power flow range versus phase shift ratio for two methods in operation mode three and (b) resultant error in the case of using fundamental component approach for different values of duty cycles  $D_1$  and  $D_2$**

In the last state where  $\phi_{B2} < \phi_{12} \leq \frac{\pi}{2}$ , the power flow is defined as

$$P_{12} = \frac{V_1 V_2}{\omega L_{12}} \left[ \phi_{12} \left(1 - \frac{\phi_{12}}{\pi}\right) - \frac{\pi}{4} (1 - D_1)^2 - \frac{\pi}{4} (1 - D_2)^2 \right] \quad (5.17)$$

It this mode, for a particular power flow there are a large number of combinations of  $D_1$ ,  $D_2$  and  $\phi_{12}$ . The power flow also can be calculated by the fundamental harmonic approach as [5.7]

$$P_{12} = \frac{8V_1 V_2}{\pi^2 \omega L_{12}} \text{Cos}\left[\frac{(1 - D_1)\pi}{2}\right] \text{Cos}\left[\frac{(1 - D_2)\pi}{2}\right] \text{Sin}(\phi_{12}) \quad (5.18)$$

The advantage of using the fundamental harmonic approach is that only one equation is achieved for all operation states.

Fig.5.11 (a) shows that for a complete range of duty ratios and phase shift angles, the fundamental component approach provides satisfactory results close to the geometrical waveform analysis. The resultant error in the case of using fundamental component approach is presented in Fig.5.11 (b). As can be seen the resultant error is always less than 20 % and increases for lower phase shift angles where the value of transferred power is not considerable.

#### 5.4.2 Currents in the DAB converter

The next part of this section provides a review on the peak, average and *rms* values of currents in DAB converter. A detailed study of currents in DAB converter is presented in [5.7], [5.15]. The current waveforms are different depending on the voltage ratio  $d$ , duty cycle  $D$  and phase shift  $\phi_{12}$ . The value of *rms*, average and peak current for operation mode one, two and three are presented in Fig.5.12 (a) to (c).

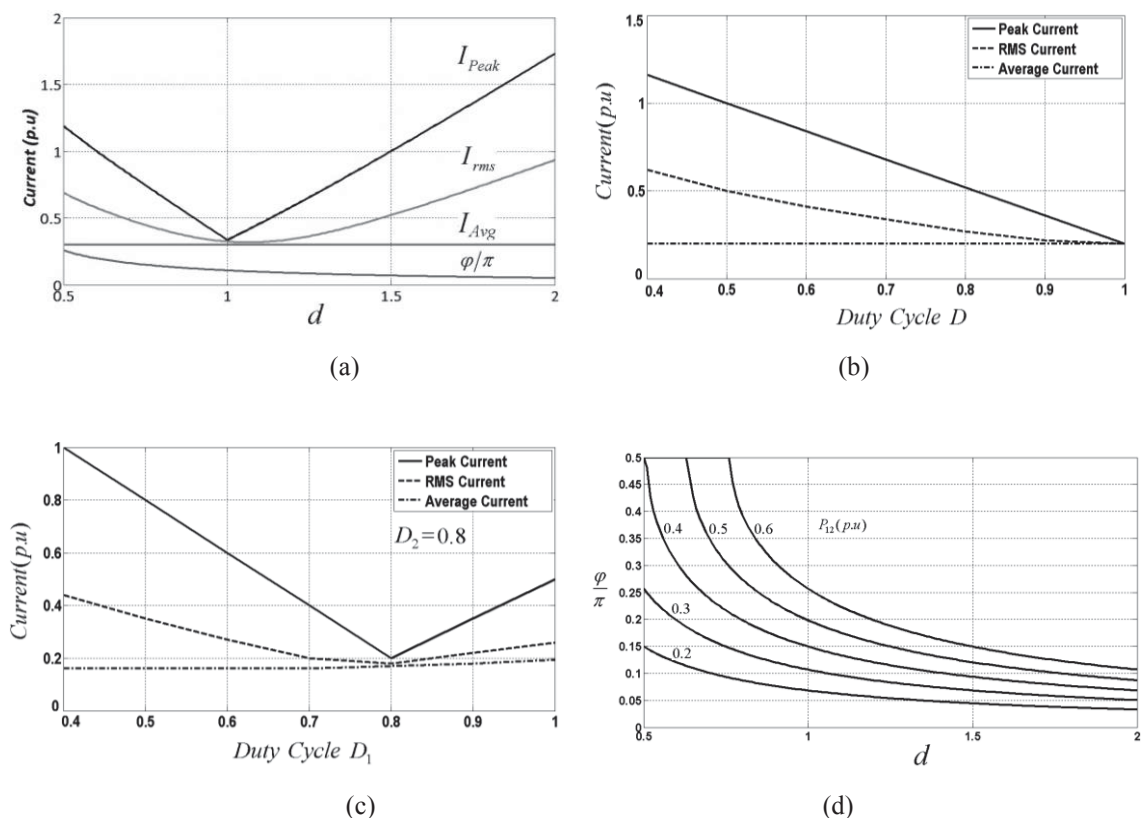


**Fig.5.12** Changes of converter currents versus  $d$ ,  $D$  and  $\varphi$  for, (a) Mode one, (b) Mode two, (c) Mode three and (d) Changes in phase shift angle versus voltage conversion ratio for constant power flow

The figures show that in the first operation mode, the average, *rms* and peak value of the currents are minimized at  $d=1$ . Therefore, operating under this condition results in the minimum switching loss and consequently maximum converter efficiency.

In the second operation mode for a constant value of  $d$ , increasing duty cycle from  $D=0$  to  $D=1$  decreases all *rms*, average and peak currents, which means less power loss. The *rms*, average and peak values of the waveforms of the current in the third operation mode depend on duty ratio of  $v_1$  and  $v_2$  ( $D_1$  and  $D_2$  respectively). As can be seen in Fig.5.12 (c), operation of converter in areas with duty ratios close to unity provides the minimum value of current and less switching power loss. Fig.5.12 (d) presents the changes in phase shift angle versus voltage ratio  $d$ , for different values of power flow. It can be seen that for higher values of power flow the range of phase shift angle decreases considerably especially for voltage ratios higher than one ( $d>1$ ).

Study on the main characteristics of the DAB converter such as different operation modes, power flow equations and soft switching range, facilitates steady state analysis of TAB converter. A detailed study of TAB converter is provided in the next section.

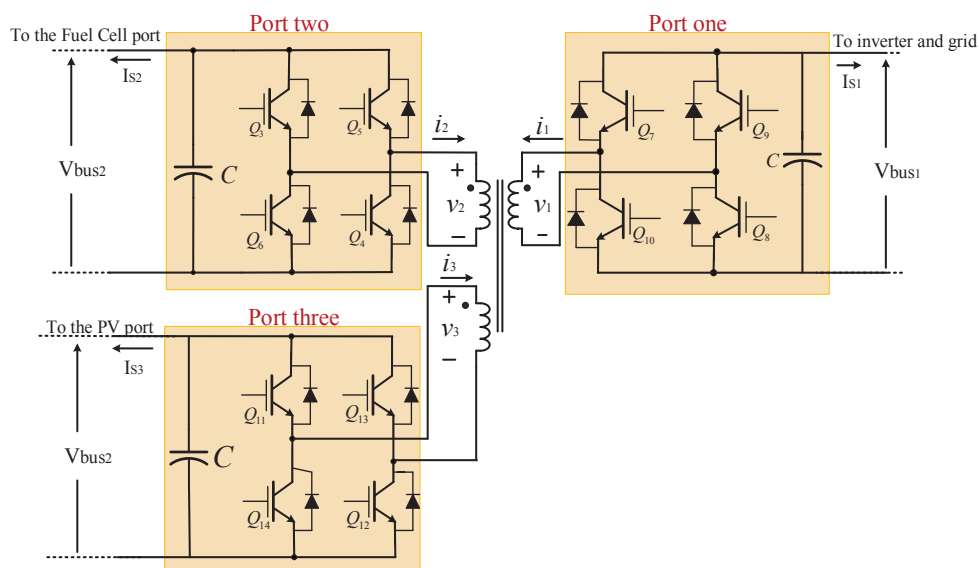


Fig.5.13 Structure of TAB converter as a part of proposed micro-grid

### 5.4.3 Steady state analysis of the TAB converter

Fig.5.13 shows the schematic of TAB converter topology. As previously mentioned the voltage of port one (Inverter port) should be kept constant during normal operation of converter as one of the control objectives. This is because a regulated voltage is required to supply the inverter and consequently output loads. On the other hand, the fuel cell output voltage is almost constant and due to the poor dynamic response of the fuel cell, fluctuations on this port are compensated by battery. The voltage on PV port resulted from boosting PV voltage using current-fed boost converters and should be kept constant. The power extracted from PV is transferred to the bus capacitor which can introduce instabilities into the bus voltage. To balance the bus voltage of the PV port, the phase shift angle  $\phi_{31}$ , is used as control variable. Therefore a main control objective in the TAB converter is voltage regulation on PV bus and maintaining MPPT using duty cycle variations on port 3. The duty cycle of the square wave voltages of ports one and two is kept equal to one ( $D_1=D_2=1$ ) while  $D_3$  is used to adjust the voltage of capacitor at PV output to track the MPP of PV panel. On the other hand applying duty cycle control technique improves the ZVS operation range of the converter efficiently [5.2], [5.7]. Extension of soft switching capability over the full operation range improves the conversion efficiency. The duty ratio control can be achieved by introducing a phase shift between the gate drive signals applied to the two legs of the H-bridge. The TAB converter ZVS operation is studied in the next section.

#### 5.4.4 Analysis of soft switching operation in the TAB converter

To maintain a full range of ZVS operation for all converter ports, the volt-second product on all windings of the magnetic link should be kept equal. The duty ratio of port three (PV port) is defined according to the amplitude of PV output voltage  $V_{PV}$ , and dc voltage on bus 3,  $V_{b3}$  and is defined as

$$D_3 = \begin{cases} \frac{2V_{PV}}{V_{b3}} & V_{b3} > 2V_{PV} \\ 2(1 - \frac{V_{PV}}{V_{b3}}) & V_{b3} < 2V_{PV} \end{cases} \quad (5.19)$$

while the equal volt-second product principle should be applied according to the transformer turns ratio using

$$n_{21} = \frac{N_2}{N_1} = \frac{V_{b2}}{V_{b1}}, \quad n_{31} = \frac{N_3}{N_1} = \frac{D_3 V_{b3}}{V_{b1}} \quad (5.20)$$

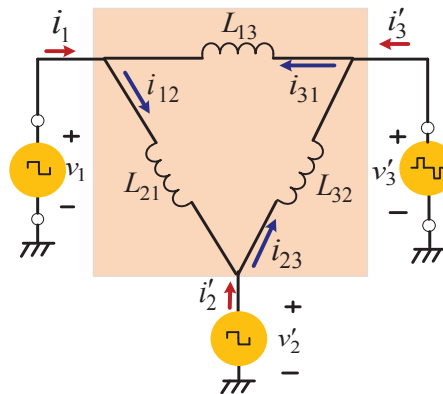


Fig.5.14 The  $\Delta$ -model equivalent circuit of the TAB converter [5.16]

To analyse the ZVS condition of TAB converter, the equivalent model of the magnetic link needs to be used [5.7]. As discussed in section 5.4, the TAB converter can be decomposed into three DAB converters linked together as presented in Fig.5.14 [5.7]. The waveforms generated by the H-bridge converters are illustrated in Fig.5.15 for the case voltage on port two  $v_2$ , and port three  $v_3$  are lagging to that of port one  $V_1$  by phase angles of  $\varphi_{12}$  and  $\varphi_{13}$ , respectively [5.7]. The resultant current in the equivalent  $\Delta$ -model ( $i_{12}$ ,  $i_{23}$  and  $i_{31}$ ) and the current supplied by each voltage source ( $i_1$ ,  $i_2'$  and  $i_3'$ ) are presented in the figure based on the simulation. To study the ZVS conditions the magnitude and direction of the currents in the switching device at switching instants

should be considered. To satisfy the ZVS conditions the amplitude of currents should be negative at the rising time of  $v_1$ ,  $v_2'$  and  $v_3'$ , and it should be positive at their falling time [5.7]. This can be presented as

$$\begin{cases} i_1(t_0) < 0, i_1(t_4) > 0 & v_1 \text{ in ZVS} \\ i_2'(t_1) < 0, i_2'(t_5) > 0 & v_2' \text{ in ZVS} \\ i_3'(t_2) < 0, i_3'(t_3) > 0 & v_3' \text{ in ZVS} \\ i_3'(t_7) < 0, i_3'(t_6) > 0 & v_3' \text{ in ZVS} \end{cases} \quad (5.21)$$

Referred to the equivalent  $\Delta$ -model, the instantaneous current flows through each input source can be written based on the currents in the inductances of the equivalent model as

$$i_1(t) = i_{21}(t) - i_{31}(t), \quad i_2'(t) = i_{23}(t) - i_{12}(t), \quad i_3'(t) = i_{31}(t) - i_{23}(t) \quad (5.22)$$

According to the model the volt-second integrals of  $v_1$ ,  $v_2'$  and  $v_3'$  applied to the inductors  $L_{13}$  and  $L_{23}$  can be defined as

$$\Delta i_{13} = i_{13}(t_4) - i_{13}(t_0) = \frac{1}{L_{13}} \int_{t_0}^{t_4} (v_1 - v_3') dt = \frac{T}{2L_{13}} (V_1 - D_3 V_3 \frac{N_1}{N_3}) \quad (5.23)$$

$$\Delta i_{23} = i_{23}(t_5) - i_{23}(t_1) = \frac{1}{L_{23}} \int_{t_1}^{t_5} (v_2' - v_3') dt = \frac{T}{2L_{23}} (V_2 \frac{N_1}{N_2} - D_3 V_3 \frac{N_1}{N_3}) \quad (5.24)$$

On the other hand, the relation between the voltages and turns ratio of the magnetic link is defined as

$$\frac{D_3 V_3}{V_1} = \frac{N_3}{N_1}, \quad \frac{D_3 V_3}{V_2} = \frac{N_3}{N_2} \quad (5.25)$$

Replacing (5.25) in (5.23) and (5.24) results in  $\Delta i_{23}=0$  and  $\Delta i_{13}=0$ .

Considering symmetrical waveforms for the inductors and the reality that  $i(t + 0.5T) = -i(t)$ , one obtains

$$i_{13}(t_0) = -i_{13}(t_4), \quad i_{23}(t_1) = -i_{23}(t_5) \quad (5.26)$$

Therefore, the currents  $i_{31}$  and  $i_{23}$  should be equal to zero at the switching edges of  $v_1$  and  $v_2$  as can be seen in Fig.5.15, i.e.

$$i_{31}(t_0) = i_{31}(t_4) = 0 \quad , \quad i_{23}(t_1) = i_{23}(t_5) = 0 \quad (5.27)$$

Current in the inverter bridge,  $i_1(t_0)$  and  $i_1(t_4)$ , should be equal to zero at these time instants. Therefore, the current in the inverter bridge switches can be found from

$$\begin{cases} i_1'(t_0) = i_{12}(t_0) - i_{31}(t_0) \\ i_{31}(t_0) = 0 \end{cases} \Rightarrow i_1(t_0) = -i_{12}(t_0) \quad (5.28)$$

$$\begin{cases} i_1(t_4) = i_{12}(t_4) - i_{31}(t_4) \\ i_{31}(t_4) = 0 \end{cases} \Rightarrow i_1(t_4) = -i_{12}(t_4) \quad (5.29)$$

As  $i_{31}$  does not contribute to the ZVS condition, the bridge current,  $i_1$ , depends only on  $i_{12}$ . This shows that the bridge of the inverter port operates under ZVS condition for the entire phase shift range. In the case of current in second port,  $i_2'$ , it can be found that  $i_{23}$  does not contribute to the ZVS condition and the bridge current depends only to  $i_{12}$ , or

$$\begin{cases} i_2'(t_1) = i_{23}(t_1) - i_{12}(t_1) \\ i_{23}(t_1) = 0 \end{cases} \Rightarrow i_2'(t_1) = -i_{12}(t_1) \quad (5.30)$$

$$\begin{cases} i_2'(t_5) = i_{23}(t_5) - i_{12}(t_5) \\ i_{23}(t_5) = 0 \end{cases} \Rightarrow i_2'(t_5) = -i_{12}(t_5) \quad (5.31)$$

This shows that the second bridge also operates under ZVS condition for the entire phase shift range.

The third port H-bridge switches also operates in ZVS condition. According to the current waveforms in equivalent  $\Delta$ -model it can be seen that at the rising edge of  $v_3'$ ,  $t_2$  and  $t_7$ , the value of current in the bridge is negative, i.e.

$$\begin{cases} i'_3(t_2) = i_{31}(t_2) - i_{23}(t_2) \\ i_{31}(t_2) < 0 \text{ and } i_{23}(t_2) > 0 \end{cases} \Rightarrow i'_3(t_2) < 0 \quad (5.32)$$

$$\begin{cases} i'_3(t_7) = i_{31}(t_7) - i_{23}(t_7) \\ i_{31}(t_7) < 0 \text{ and } i_{23}(t_7) > 0 \end{cases} \Rightarrow i'_3(t_7) < 0 \quad (5.33)$$

On the other hand, at the falling edges of  $v'_3$  ( $t_3$  and  $t_6$ ), the current is positive in the bridge according to

$$\begin{cases} i'_3(t_3) = i_{31}(t_3) - i_{23}(t_3) \\ i_{31}(t_3) > 0 \text{ and } i_{23}(t_3) < 0 \end{cases} \Rightarrow i'_3(t_3) > 0 \quad (5.34)$$

$$\begin{cases} i'_3(t_6) = i_{31}(t_6) - i_{23}(t_6) \\ i_{31}(t_6) > 0 \text{ and } i_{23}(t_6) < 0 \end{cases} \Rightarrow i'_3(t_6) > 0 \quad (5.35)$$

As can be seen, both  $i_{31}$  and  $i_{23}$  are contributing in soft switching operation of the third port. They are providing positive current at the falling edges of voltage and negative current at the rising edges for IGBT switches.

Comparing the waveforms of two different cases of hard and soft switching operations shows that using the duty ratio control on the variable voltage port extends the soft switching operation range effectively. The ZVS operation is guaranteed for all three ports as long as equal volt-second is applied to all three windings of the magnetic link. In the proposed TAB converter, the duty cycle of voltage on PV port  $D_3$ , is defined independently according to the MPPT requirement. Therefore, to maintain the ZVS operation, the reference voltage on bus 3,  $V_{b3}$ , should be changed accordingly to keep a constant volt-second across the PV port winding and guarantee the soft switching operation for the entire range. This issue will be discussed in more details in the TAB converter controller design section.

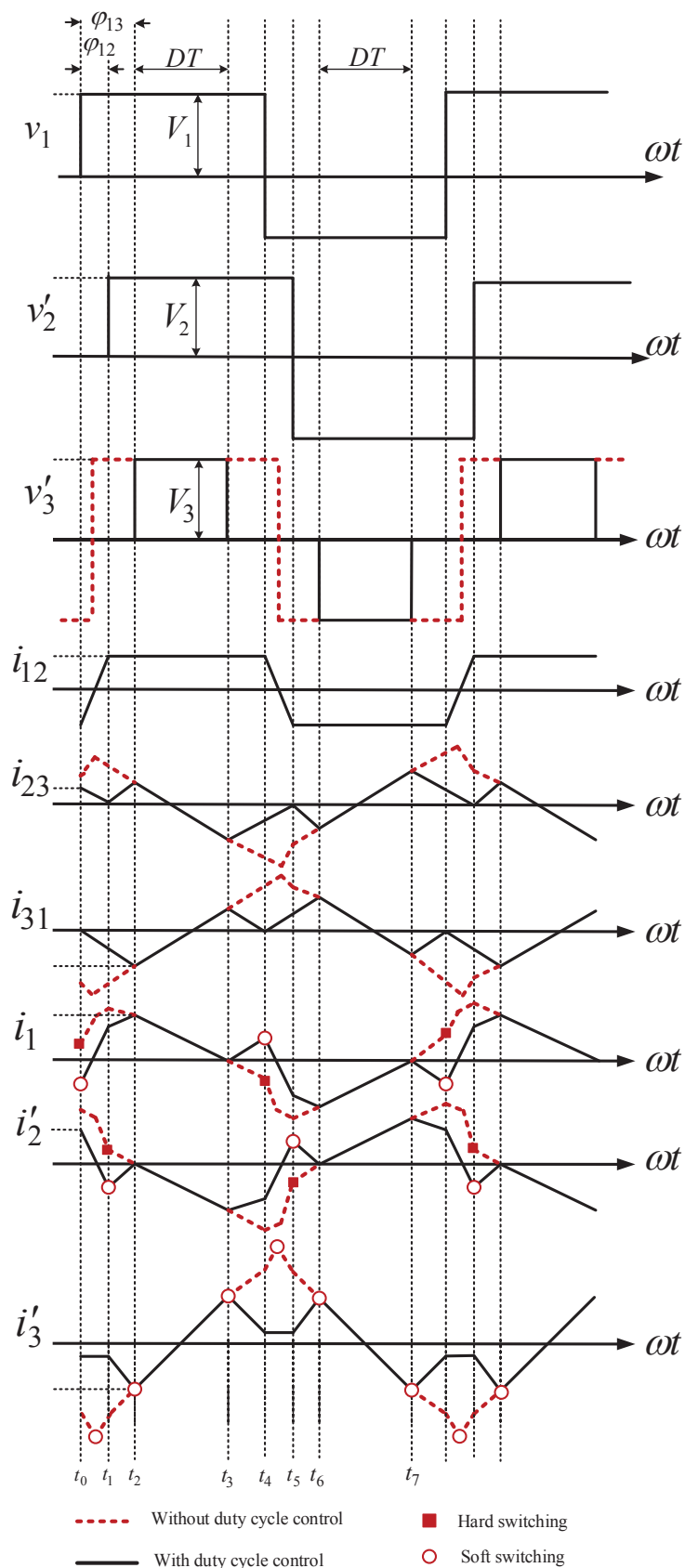


Fig.5.15 Steady state operating waveforms of TAB converter with and without duty cycle control considering soft-switching and hard switching conditions [5.7]

#### 5.4.5 Small signal modelling of the TAB converter

The small signal modelling of the TAB converter is required to analyse the stability of converter operation, design a closed loop control and define the controller parameters. According to the previous discussion on analysis of MAB converter, the power flow between any two ports of the MAB converter ( $j$  and  $k$  as an example) can be defined as [5.4]:

$$P_{jk} = \frac{v_j v_k}{2\pi f_s L_{jk}} \varphi_{jk} \left( 1 - \frac{|\varphi_{jk}|}{\pi} \right) \quad (5.36)$$

where  $\varphi_{jk}$  is the phase shift angle between voltages of port  $k$  and port  $j$ , and  $L_{jk}$  is the equivalent inductance between the ports defined by (5.2). In the case of duty cycle control on port  $k$ , the power flow between the ports depending on the range of duty ratio  $D_k$ , and the phase shift angle  $\varphi_{jk}$  is defined as

$$P_{jk} = \frac{V_j V_k}{2\pi f_s L_{jk}} \varphi_{jk} \left( 1 - \frac{|\varphi_{jk}|}{\pi} - \text{sign}(\varphi_{jk}) \frac{\pi}{4} (1 - D_k)^2 \right) \quad (5.37)$$

and the average current flowing through dc source  $V_k$  from source  $V_j$  can be found as

$$I_{jk} = \frac{P_{jk}}{V_j} \quad (5.38)$$

Considering lossless conversion, the power flow and current in the opposite direction can be defined as  $P_{jk} = -P_{kj}$  and  $I_{kj} = -I_{jk}$ , respectively. In the case of MAB converter, a single model can be derived applying the Gyrator theory considering the point that the average dc current in each port depends on the voltage of the other ports. Therefore, the MAB converter average model can be achieved as a multi-port Gyrator in the simplest form and the proportionality of current in each port to the voltages of other ports is modelled as Gyrator gains [5.2]-[5.4]. The gains should be defined as a function of phase shift angle and the duty cycle as the following

$$g_{jk} = \frac{P_{jk}}{v_j v_k} \quad (5.39)$$

and the total current of each port,  $I_l$ , can be defined as

$$I_j = \sum_{l=1, \neq j}^n I_{jl} = \sum_{l=1, \neq j}^n g_{jl} v_l \quad (5.40)$$

In the case of TAB converter, the small signal model can be defined similarly considering only three active ports. According to the  $\Delta$ -model presentation of TAB converter, the power flow of converter ports considering  $P_{21}=-P_{12}$ ,  $P_{31}=-P_{13}$  and  $P_{32}=-P_{23}$  can be defined as

$$\begin{cases} P_1 = -P_{21} - P_{31} \\ P_2 = P_{21} - P_{32} \\ P_3 = P_{31} + P_{32} \\ P_1 + P_2 + P_3 = 0 \end{cases} \quad (5.41)$$

Referring to the DAB converter analysis, the power transferred between ports two and one in the proposed TAB converter considering constant duty cycle ( $D_1=D_2=1$ ) can be found from

$$P_{21} = \frac{V_{b2}V_{b1}}{2n_{21}\pi f L_{21}} \varphi_{21} \left( 1 - \frac{|\varphi_{21}|}{\pi} \right) \quad (5.42)$$

and the power transferred from port three to port one,  $P_{31}$ , due to the duty ratio control on port three (PV port) can be defined as

$$P_{31} = \begin{cases} \frac{V_{b3}V_{b1}}{2\pi f n_{31} L_{31}} \left[ \varphi_{31} \left( 1 - \frac{|\varphi_{31}|}{\pi} \right) - \text{sign}(\varphi_{31}) \left[ \frac{\pi}{4} (1 - D_3)^2 \right] \right] & \text{for } \varphi_{31} > \varphi_B \\ \frac{V_{b3}V_{b1}}{2\pi f n_{31} L_{31}} D_3 \varphi_{31} & \text{for } -\varphi_B \leq \varphi_{31} \leq \varphi_B \end{cases} \quad (5.43)$$

where  $\varphi_B = \pi(1-D_3)/2$  is the boundary angle as discussed in DAB converter analysis. The power flow between ports two and three depends on the leading or lagging of phase angle of the square wave generated by the H-Bridge of port three with respect to that of port two  $\varphi_{32}$ . As there are only two independent variables known as  $\varphi_{32}$  and  $\varphi_{31}$  therefore  $\varphi_{32}$  is redundant and can be written based on the other phase shift angles as  $\varphi_{32} = \varphi_{31} - \varphi_{21}$  [5.7]. Due to this  $P_{32}$  can be defined as

$$(5.44)$$

$$P_{32} = \begin{cases} \frac{V_{b3}V_{b2}}{2\pi f n_{32} L_{32}} \left[ (\varphi_{31} - \varphi_{21}) \left( 1 - \frac{|\varphi_{31} - \varphi_{21}|}{\pi} \right) - \text{sign}(\varphi_{31} - \varphi_{21}) \left[ \frac{\pi}{4} (1 - D_3)^2 \right] \right] & \text{for } |(\varphi_{31} - \varphi_{21})| > \varphi_B \\ \frac{V_{b3}V_{b2}}{2\pi f n_{32} L_{32}} D_3 (\varphi_{31} - \varphi_{21}) & \text{for } |(\varphi_{31} - \varphi_{21})| \leq \varphi_B \end{cases}$$

Similar to the MAB converter, the small signal model of the TAB converter is obtained by modelling of each conversion port as a dependent dc current source as presented in Fig.5.16 [5.7]. The amplitude of the current sources is equal to the average of the input current of the port over one complete switching cycle. The average of the current in the ports named as  $I_{LD}$ ,  $I_{FC}$  and  $I_{PV}$  can be found from

$$I_{FC} = \frac{P_2}{V_{b2}} = \frac{P_{21} - P_{32}}{V_{b2}} \quad (5.45)$$

$$I_{PV} = \frac{P_3}{V_{b3}} = \frac{P_{31} + P_{32}}{V_{b3}} \quad (5.46)$$

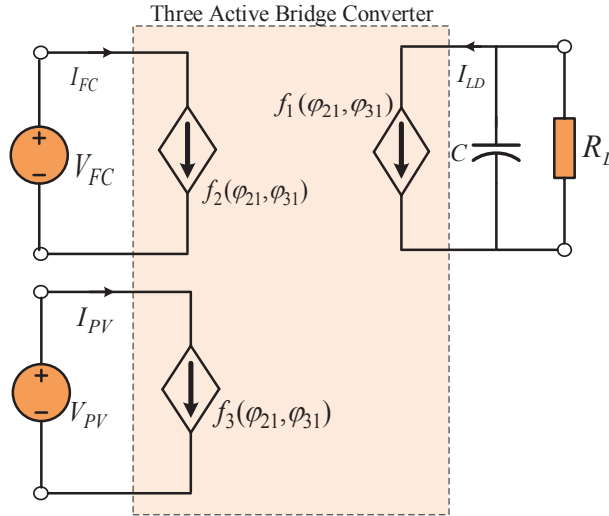


Fig.5.16 The small signal model of TAB converter [5.7]

where  $P_I = P_{LD}$  is the power transferred to the inverter port or load,  $P_2 = P_{FC}$  the power flow in the fuel cell port and  $P_3 = P_{PV}$  the power transferred from PV port. The current in port one,  $I_{LD}$ , is redundant as there are only two independent variables. As can be seen in (5.43) and (5.44), the power flow and consequently current in the dependent current sources are nonlinear functions of control variables of phase shift angles,  $\varphi_{21}$  and  $\varphi_{31}$ . Therefore, to design a linear control model, they need to be linearized around the

operation point of the converter. The linearized function of the currents  $I_{FC}$  and  $I_{PV}$  can be presented as

$$\tilde{I}_{FC} = G_{22}\tilde{\varphi}_{21} + G_{32}\tilde{\varphi}_{31}, \quad \tilde{I}_{PV} = G_{23}\tilde{\varphi}_{21} + G_{33}\tilde{\varphi}_{31} \quad (5.47)$$

where  $G_{22}$  and  $G_{33}$  are direct transfer functions and  $G_{23}$  and  $G_{32}$  the coupling transfer functions of the average currents,  $(\tilde{I}_{FC}, \tilde{I}_{PV})$  to the phase shift angles  $(\varphi_{21}$  and  $\varphi_{31})$ . They can be defined as

$$\begin{aligned} G_{22} &= \left. \frac{\partial I_{FC}}{\partial \tilde{\varphi}_{21}} \right|_{(\varphi_{21*}, \varphi_{31*}, D_{3*})} & G_{32} &= \left. \frac{\partial I_{FC}}{\partial \tilde{\varphi}_{31}} \right|_{(\varphi_{21*}, \varphi_{31*}, D_{3*})} \\ G_{23} &= \left. \frac{\partial I_{PV}}{\partial \tilde{\varphi}_{21}} \right|_{(\varphi_{21*}, \varphi_{31*}, D_{3*})} & G_{33} &= \left. \frac{\partial I_{PV}}{\partial \tilde{\varphi}_{31}} \right|_{(\varphi_{21*}, \varphi_{31*}, D_{3*})} \end{aligned} \quad (5.48)$$

where  $\varphi_{21*}$  and  $\varphi_{31*}$  are the phase shift angles of the port two and three regarding port one at the converter operating point. As can be seen in (5.48), the transferred power depends on the duty cycle of PV port  $D_3$ , and phase shift angles  $\varphi_{21}$  and  $\varphi_{31}$ . As duty cycle is used to control the PV output voltage and MPPT, its dynamic response is too slow and can be considered as a constant value for voltage regulation controller design.

#### 5.4.6 Design of closed loop control for TAB converter

This section provides a detailed study on design of PI controller for TAB converter as the main part of the proposed micro-grid. There are two main objectives in the design of controller for the TAB converter. They are, firstly regulation of voltage on PV bus to maintain the equal volt-second across winding three of the magnetic link and to realize full range of soft-switching operation. The second objective is the adjustment of fuel cell power on the referenced value provided by EMU. It should be noted that the fuel cell reference power is defined by EMU according to the energy management scenario. The fuel cell reference power can be designed to cover the difference between PV and load power or just a portion of load power or to send a certain power to the main grid. Fig.5.17 illustrates the control to output block diagram of the TAB converter and closed loop PI controllers. The TAB converter small signal model including direct ( $G_{22}$  and  $G_{33}$ ) and coupling ( $G_{32}$  and  $G_{23}$ ) transfer functions is used to model the relation between control variables  $(\varphi_{21}$  and  $\varphi_{31})$  and control outputs  $(V_{b2}$  and  $P_{FC})$  [5.7].

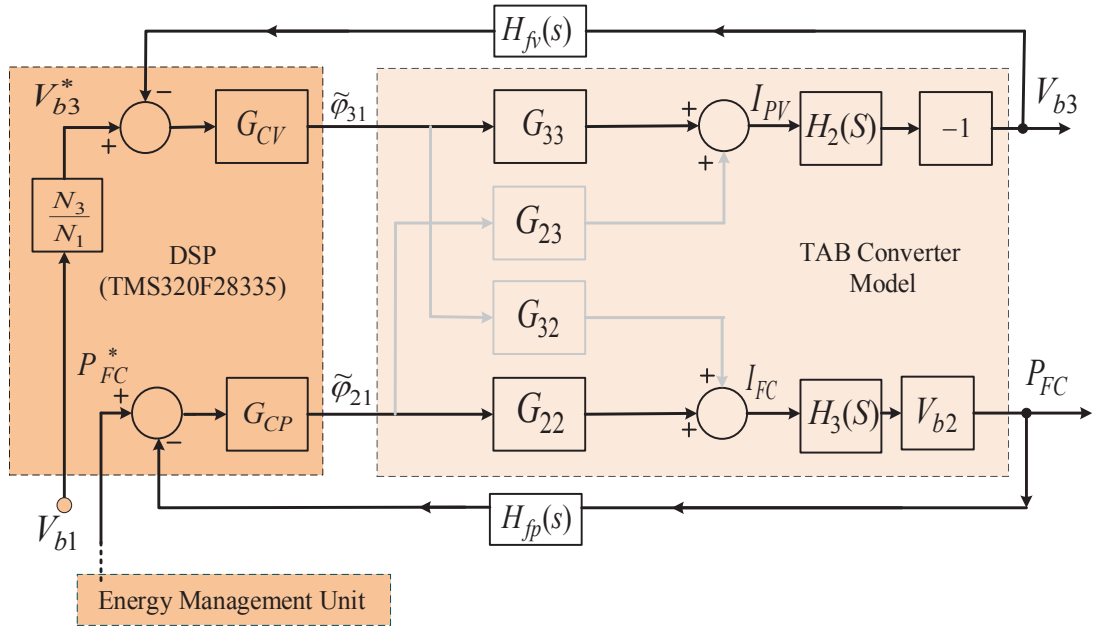
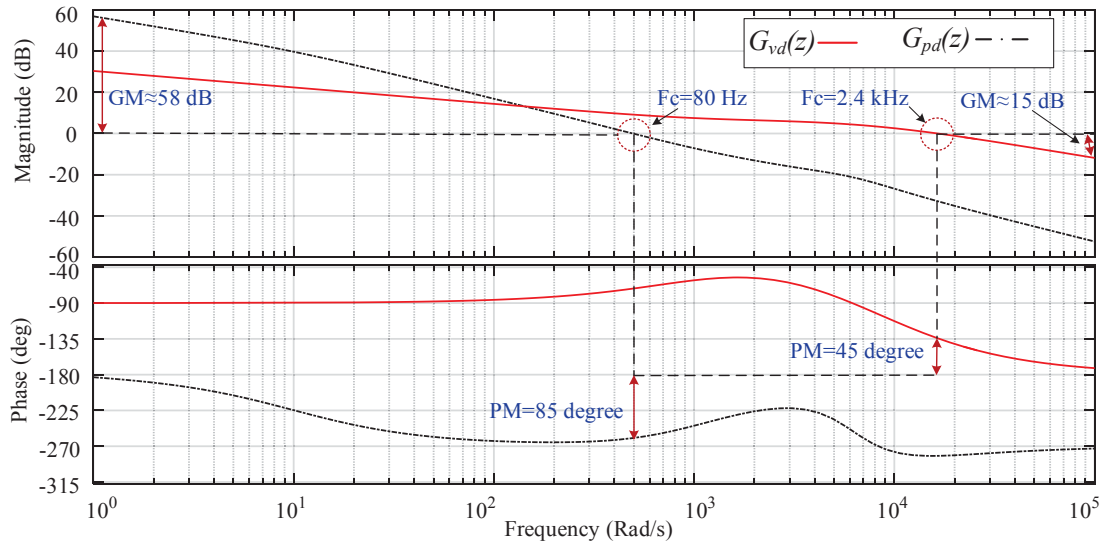


Fig.5.17 The small signal model of TAB converter

As can be seen, the voltage on PV port,  $V_{b3}$ , is used as the feedback signal, and is compared with the reference value obtained from applying volt-second rule equality to transformer windings. On the other hand, the output power of fuel cell is used as power-regulation feedback signal and is compared with the reference value defined by EMU. In this particular case, it is assumed that fuel cell is going to supply the difference between the power supplied by PV and grid and consumed by load.

As presented in the figure, it is required that the two loops operate independently and their cross-coupling effects should be eliminated or reduced as much as possible. Therefore, the effects of coupling transfer functions in the TAB converter model,  $G_{23}$  and  $G_{32}$ , should be compensated by decoupling transfer functions added to the control loop. Another method is selection of different bandwidth of frequency response which results in different speeds of dynamic response for the voltage and power regulation loops [5.7]. In this case the interaction between two control loops is minimized. In the first method, the decoupling transfer functions need real-time update and computational efforts which makes the control system more complex. Therefore, it is preferred to use the second method which is simpler for design and implementation. The bandwidth of voltage control closed loop frequency response is designed higher than that of fuel cell power regulation.



**Fig.5.18 The Bode diagram of closed loop control of TAB converter**

This is because the regulation of fuel cell power does not need to be as fast as voltage regulation on the PV port bus. The transfer functions of voltage and power closed-loop controls can be defined as

$$G_{vd}(s) = -H_{fv}G_{CV}G_{33}H_2, \quad G_{pd}(s) = H_{fp}G_{CP}G_{22}H_3V_{b3} \quad (5.49)$$

Fig.5.18 shows the bode plots of the loop gains of voltage and power regulations. To decouple the voltage and power control loops, the crossover frequency of voltage loop is selected about 2.4 kHz and power loop is selected as 80 Hz. Therefore, the voltage control loop has higher dynamic response compared with the fuel cell power control loop. As can be seen the voltage control loop has a gain margin of 30db and a phase margin of 45 degree. On the other hand, the power control loop has a gain margin of 58db and phase margin of 85 degree which verifies the stability of the designed controller.

It should be noticed that the amplitude bode diagram has not been affected by the time delay caused by the computational functions while the phase diagram has been affected. More details on the controller design process in the discrete time domain will be provided in the following sections.

#### 5.4.7 Simulation of TAB converter

The proposed TAB converter topology was simulated using PSIM and MATLAB<sup>TM</sup>/Simulink for various operation modes. MATLAB is used for system level

control due to the powerful tools for control and data analysis. PSIM is used for device level control due to the simple controller design using SmartCtrl, easy connection to the C2000/TMS320F28335 processor, online programming and debugging using Simcoder and code composer studio (CCS) integrated development environment for C2000 microcontrollers. The SmartCtrl provides user friendly features for easy and quick design of closed loop controllers for power electronic converters. The predefined transfer functions of the most commonly used power electronic converters are included in the library however there is the possibility for users to import any transfer function related to their own plant.

Fig.5.19 (a) and (b) present the simulated waveforms of the voltages and currents in the magnetic link considering two cases of phase shift angles. The converter is assumed to operate in a typical mode in which power flows from fuel cell and PV port to the inverter port. Referring to Fig.5.13 the high frequency voltages ( $v_1$ ,  $v_2$  and  $v_3$ ) and the currents ( $i_1$ ,  $i_2$  and  $i_3$ ) of the magnetic link are illustrated in the figure. In this case, voltage on PV port  $v_1$ , has the duty cycle of  $D_3=1$  and the phase shift angles  $\phi_{31}$  and  $\phi_{21}$  are equal to  $\pi/3$  and  $\pi/5$  respectively. In the second case the duty cycle on the PV port is  $D_3=0.8$  and the phase shift angles are  $\phi_{31} = \pi/5$  and  $\phi_{21} = \pi/3$ . The TAB converter parameters during simulation are presented in Table.5.1.

**TABLE 5.1 Circuit Parameters of the TAB Converter During Simulation**

dc voltage of the converter ports	Port 1: 300V Port 2: 60V Port 3:100V
Transformer turns ratio	$N_1= 52$ $N_2= 8$ $N_3=17$
Leakage inductances	$L_1=30 \mu\text{H}$ $L_2= 5\mu\text{H}$ $L_5=12\mu\text{H}$
Switching frequency	$f_s = 10 \text{ kHz}$

#### 5.4.8 Experimental waveforms

The TAB converter as a part of the proposed micro-grid is experimentally developed as discussed in chapter three. The voltages and currents of the TAB converter are measured experimentally and recorded for three different cases of duty cycles and phase shift angles. Fig.5.20 (a) and (b) show the waveforms for the cases discussed in the simulation section. In the third case presented in Fig.5.20 (c), the duty cycle on PV port

is equal to 0.6 and the phase shift angles  $\varphi_{31} = \pi/3$  and  $\varphi_{21} = \pi/5$ . As can be seen in the figures the simulated results are verified by experimental measurements.

#### **5.4.9 Simulation of dynamic response of TAB converter**

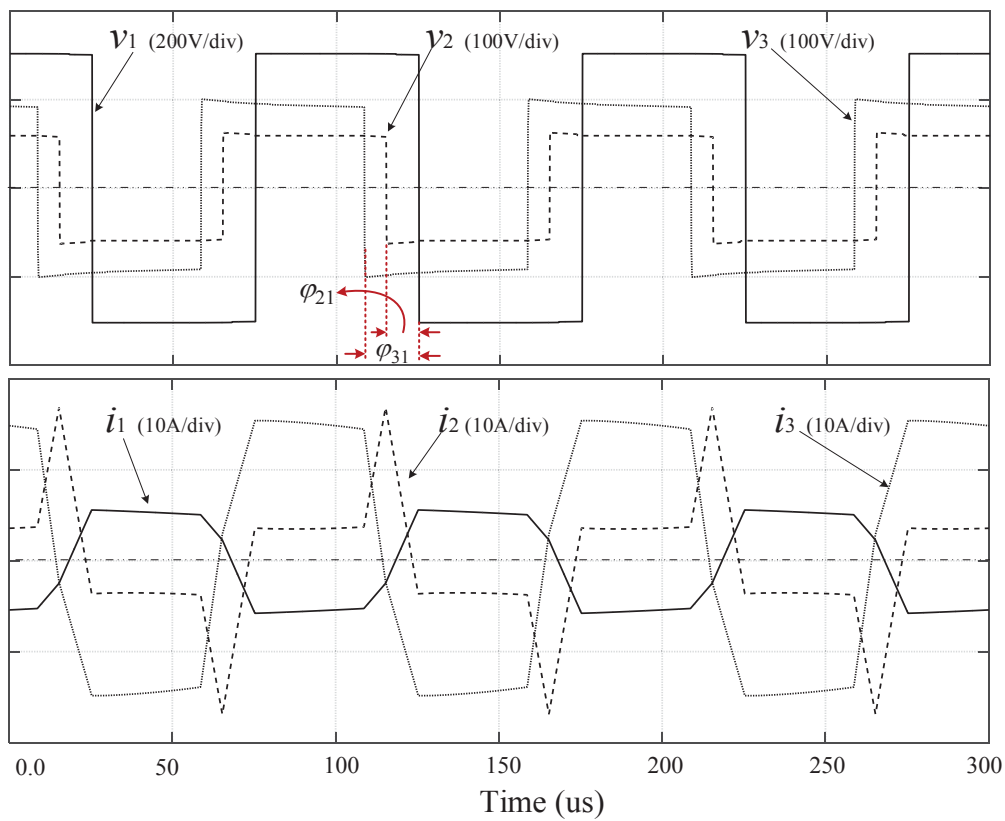
The TAB converter model is simulated using PSIM and is used to study the dynamic performance of the designed converter under the step change in the load and source. As presented in Fig.5.21, the power flow performance of the TAB converter is simulated for two different cases. In the first case, the load power is supplied by both fuel cell and battery while the control objective is to keep the fuel cell power constant and the load variation only is compensated by battery. As can be seen in Fig.5.21 (a), the load power is reduced from 400 W to 200 W at  $t=50$  ms and returned to the 400 W at  $t=100$  ms. The change in the load power is compensated by the battery while the power injected by the fuel cell remains unchanged at 200 W with slight overshoots at the step-change times.

In the second case, the control objective is that the load power should be supplied by fuel cell and battery operates as a compensator during transients due to the slow dynamic response of fuel cell. As can be seen in the Fig.5.21 (b), the load power consumption is reduced from 200 W to 100 W at  $t=100$  ms for a 100 ms time period. The power supplied by the fuel cell follows the load step change with a slow dynamic. It takes about 40 ms for fuel cell output power to be stabilized on the desired value and battery compensates for the difference during the transients.

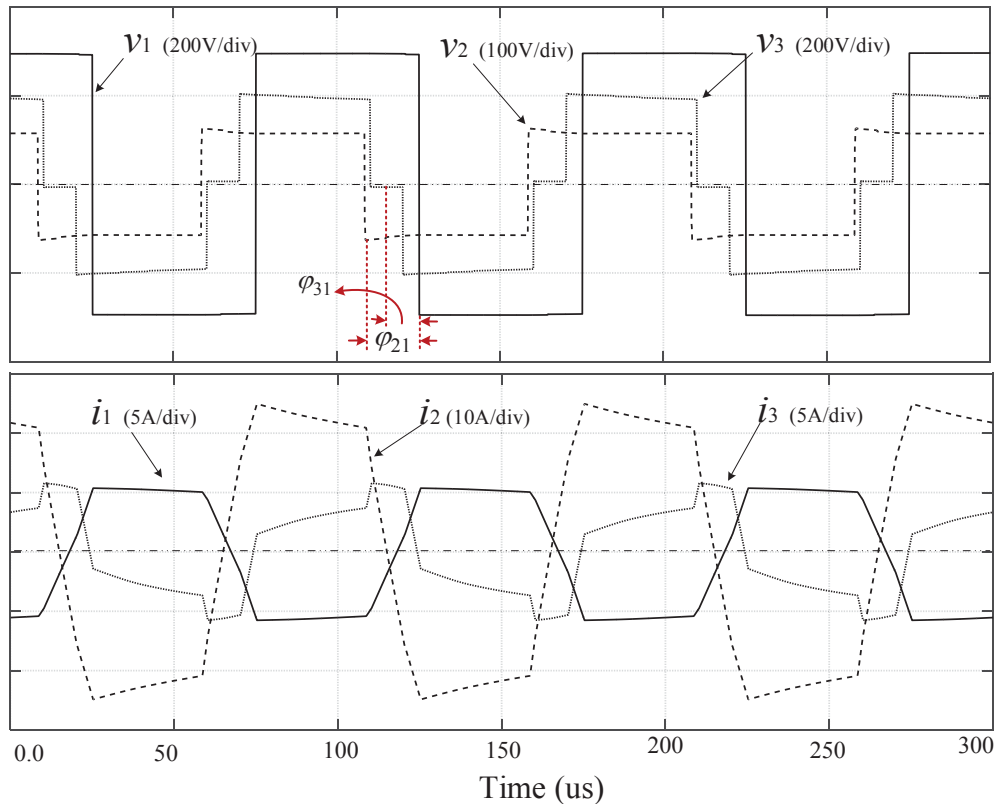
#### **5.4.10 Experimental test of TAB converter dynamic response**

The dynamic response of the proposed converter is experimentally tested for the second simulated case where the load power should be supplied by fuel cell as the main input source and the battery is used as compensator.

The battery voltage is 24 V, fuel cell voltage is 60 V and the inverter bus or load voltage is 300 V. As presented in Fig.5.22, the load current is reduced from 1.5 A to 0.5 A (power varies from 450 W to 150 W) for a time period of 500 ms (0.5 s) and then it goes back to 1.5 A. It can be seen that it takes about 100 ms for fuel cell current to be settled on the desired value and follows the load power variation. On the other hand, the battery current jumps to slightly less than 20 A to compensate for the slow reaction of the fuel cell.

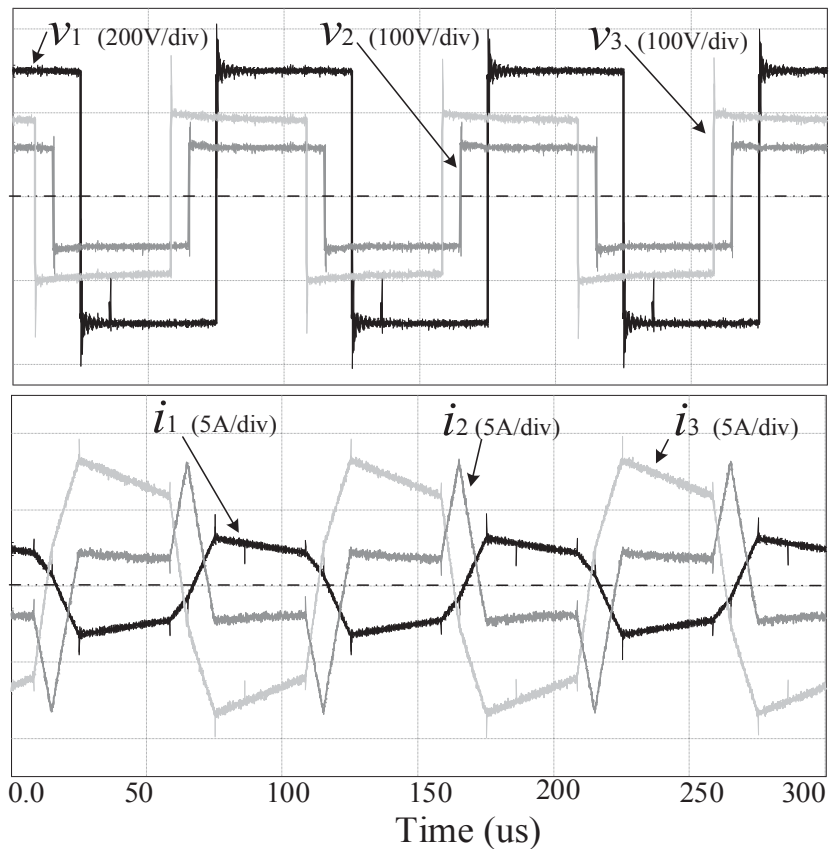


(a)

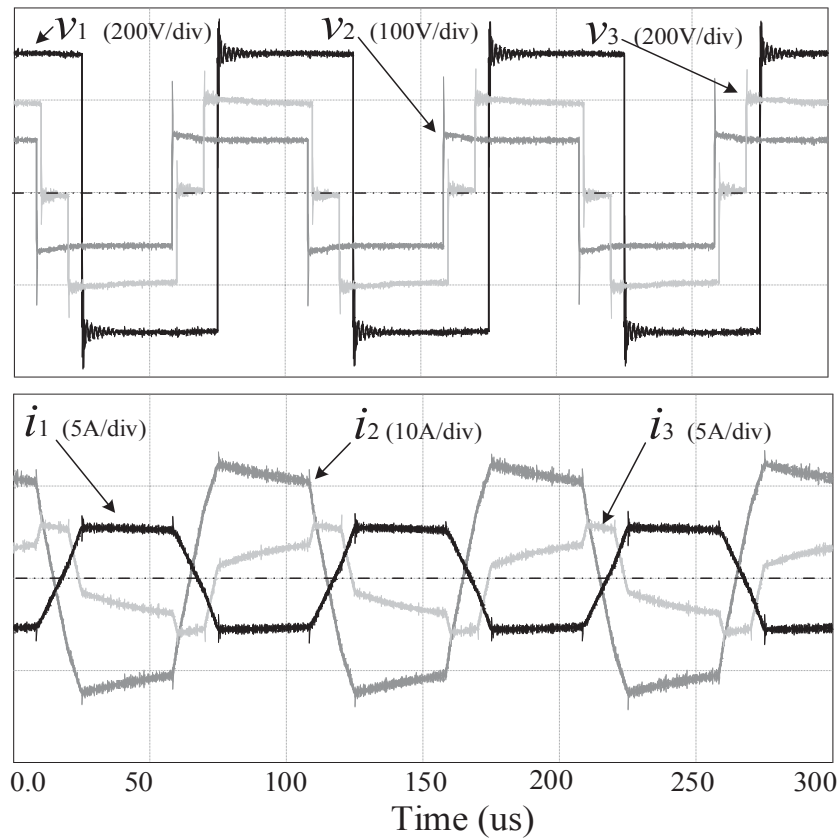


(b)

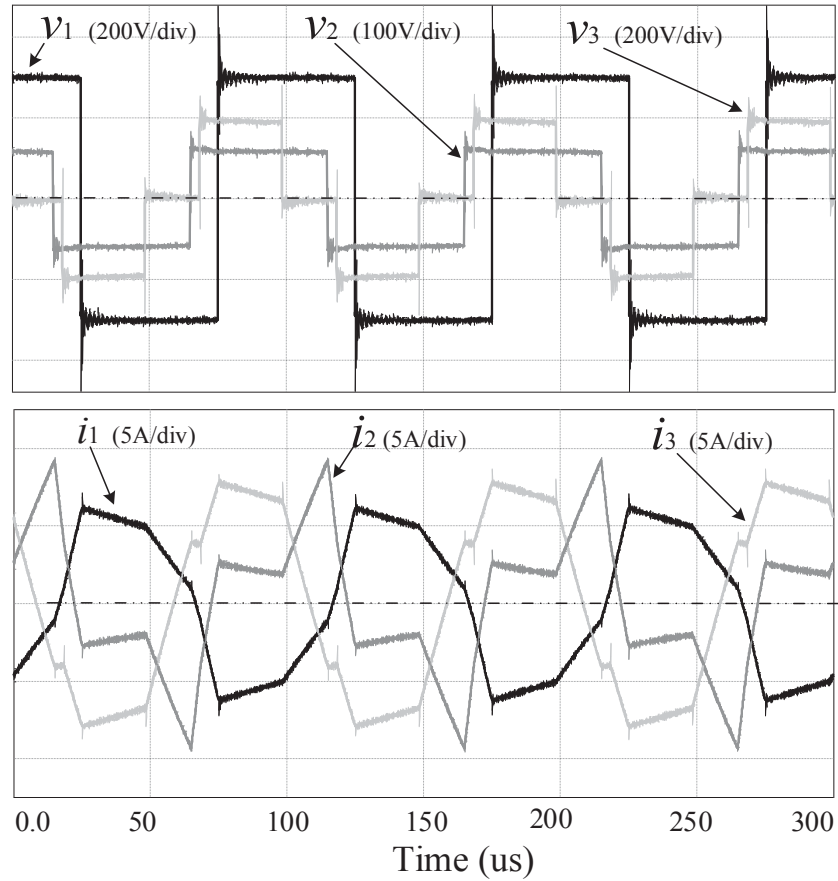
Fig.5.19 The simulated waveforms of the TAB converter for two different cases (a)  $D=1$ ,  $\varphi_{31} = \pi/3$  and  $\varphi_{21} = \pi/5$ , and (b)  $D=0.8$ ,  $\varphi_{31} = \pi/5$  and  $\varphi_{21} = \pi/3$ .



(a)

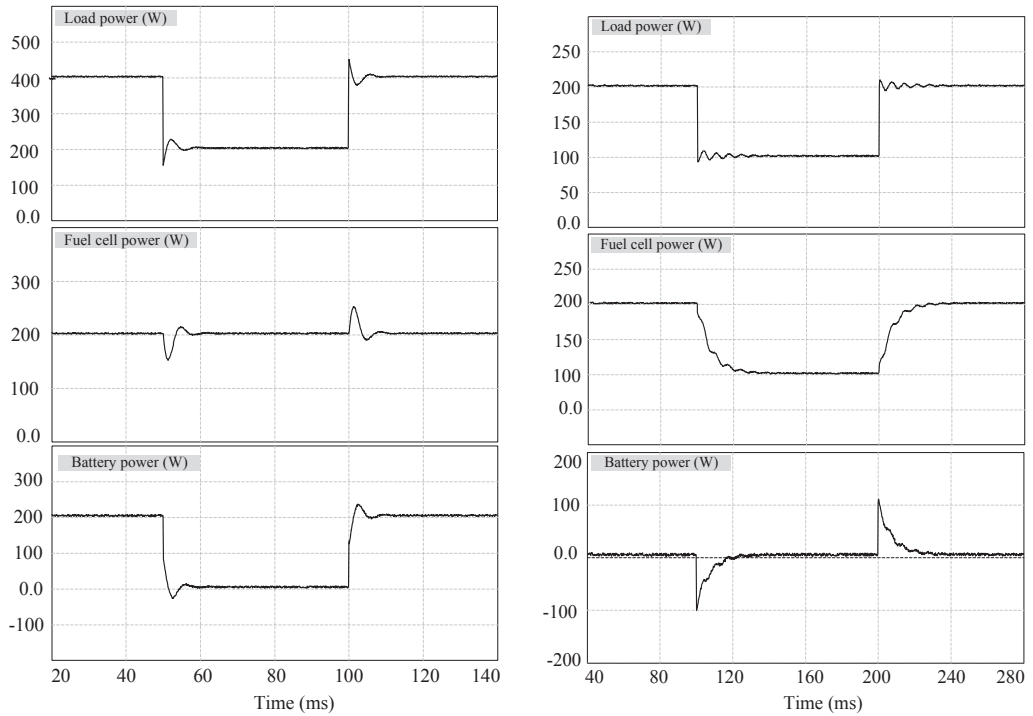


(b)



(c)

Fig.5.20 The experimentally measured waveforms of the TAB converter for two different cases (a)  $D=1$ ,  $\varphi_{31} = \pi/3$  and  $\varphi_{21} = \pi/5$ , and (b)  $D=0.8$ ,  $\varphi_{31} = \pi/5$  and  $\varphi_{21} = \pi/3$ .



(a)

(b)

Fig.5.21 Simulation results of the TAB converter operation under load variation, (a) fuel cell is supplying a constant power and battery follows the load variations, and (b) fuel cell follows the load variation and battery operates as a compensator.

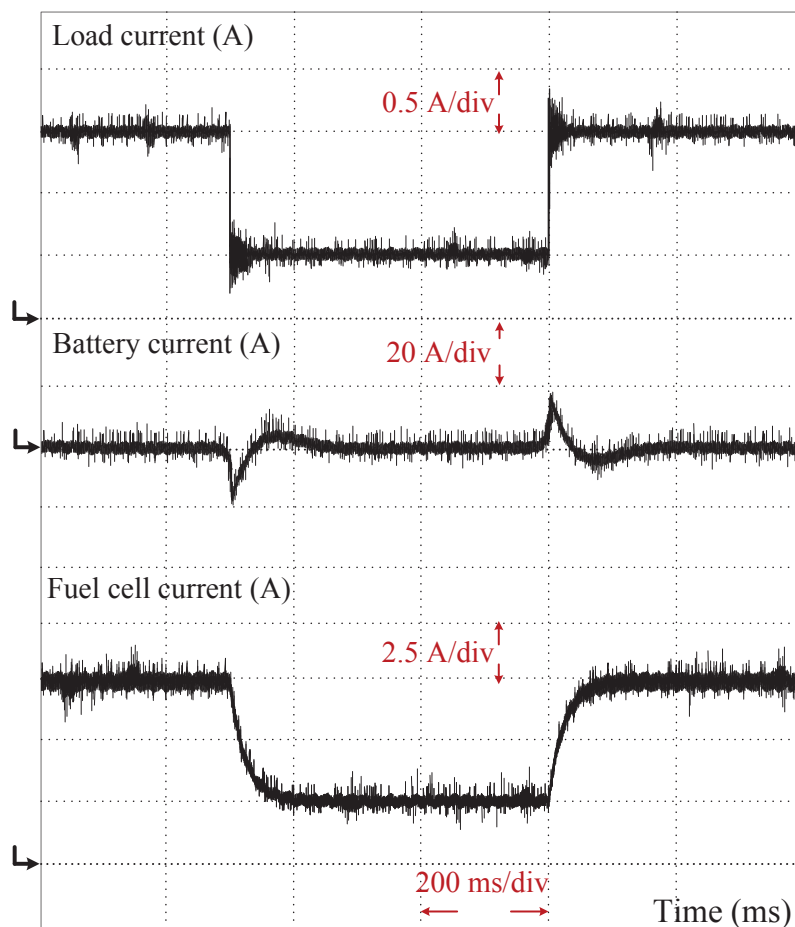
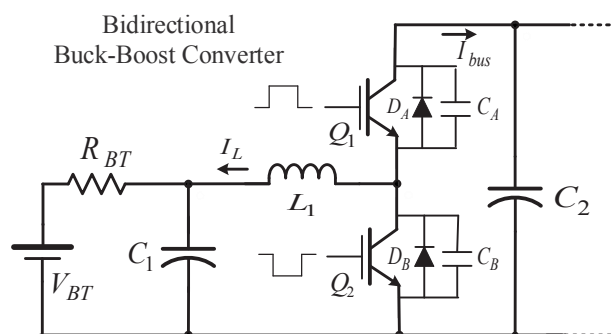


Fig.5.22 Experimental test of the TAB converter dynamic response

The simulation and experimental test results validate the performance of the designed controller for TAB converter.

### 5.5 Analysis of Bi-directional Buck-boost Converter

Bidirectional dc-dc converters have been attractive from a research point of view due to their application in charge and discharge of energy storage devices in renewable energy systems. They have been used in electric vehicles, fuel cell based systems to facilitate charge and discharge process of batteries or super-capacitors [5.19]-[5.21]. To maintain a bidirectional power flow, a high frequency bidirectional switching device is required which currently is not available. Therefore a common practice is to use unidirectional switches such as MOSFET or IGBT in parallel with a diode. A large number of bi-directional dc-dc converter topologies have been proposed over the last decade. They can be basically categorized as isolated and non-isolated topologies.



**Fig.5.23 Topology of the bidirectional buck-boost converter**

In isolated converters a high frequency transformer is used as an isolator between the source and load although in non-isolated topologies higher efficiency and less complexity can be achieved [5.22]. Fig.5.23 shows the most common topology of non-isolated bi-directional dc-dc converter. It includes two pairs of semiconductor switches and their anti-parallel diodes. To combine both step up and step down conversion stages in a single power stage, the inductor  $L_1$  is shared in both buck and boost operation modes. As can be seen in the figure, the battery is placed at the low voltage side and the fuel cell is connected directly to the dc bus at high voltage side. The dc bus is linked to the TAB converter and forms the TAB converter second port. Both high voltage and low voltage side sources contain electrolyte capacitors  $C_1$  and  $C_2$  as low pass filters. The main objectives of using battery are storing energy for supplying load on request and balancing the voltage of dc bus when the fuel cell is operating. As discussed in Chapter Three, in the proposed micro-grid the load transients in grid connected mode should be compensated by grid and in off-grid or islanded mode by battery due to the low dynamic response of fuel cell. The battery also should handle quick start up which lets the fuel cell warm up and is used as an energy storage component to store the surplus energy of PV if required. The converter operation during both charge and discharge mode is similar and the only difference is in the duty cycles of drive signals of  $Q_1$  and  $Q_2$ . Due to the reality that both operation modes share the same power circuit there is a possibility to design a single controller for both modes.

Operation in the buck (charging) or the boost (discharging) is determined by the duty ratio of the switching drive signal which is defined by ratio of dc bus voltage to the battery voltage.

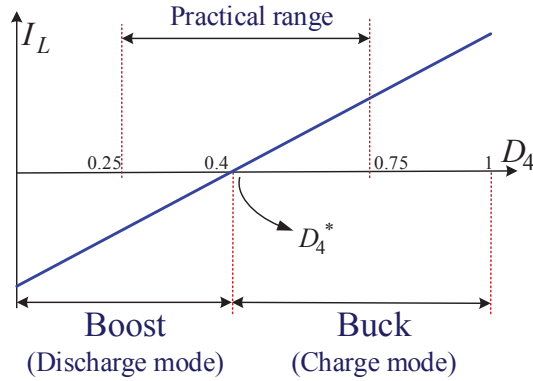


Fig.5.24 Operation areas of bi-directional buck-boost converter

The range of duty ratio variation of port four ( $D_4$ ) in charge or discharge operation modes is defined according to a critical duty ratio  $D_4^*$ , where the inductor average current is equal to zero. Therefore operation mode of the converter can be defined as

$$Operation\ Mode \rightarrow \begin{cases} Buck(charging) & D_4 > D_4^* , I_L < 0 \\ Zero\ average\ current & D_4 = D_4^* , I_L = 0 \\ Boost(discharging) & D_4 < D_4^* , I_L > 0 \end{cases} \quad (5.50)$$

where  $D_4^*$  is the critical duty ratio and is defined as

$$D_4^* = \frac{V_{BT}}{V_{bus}} \quad (5.51)$$

In the proposed micro-grid,  $V_{b2}=60$  V and  $V_{BT}=24$  V, and therefore  $D_4^*=0.4$ . Fig.5.24 shows the operation modes of the converter based on the duty ratio and average inductor current. By changing  $D_4$ , the converter can operate in the buck, boost or in the boundary between buck and boost.

### 5.5.1 Steady state operation analysis

To simplify the analysis of bidirectional buck-boost converter, the steady state voltage and current waveforms of the converter are illustrated in Fig.5.25 [5.22]. The gate signals are presented to show the switching status of  $Q_1$  and  $Q_2$ . As can be seen, the gate signals of  $Q_1$  and  $Q_2$  are complementary and a dead time  $t_{dt}$  is introduced between turn off time of one switch to turn on time of the other. According to the complementary switching pattern, when  $Q_1$  is on and  $Q_2$  is off, the converter is operated in the buck mode and power flows from the dc bus to the battery to charge it.

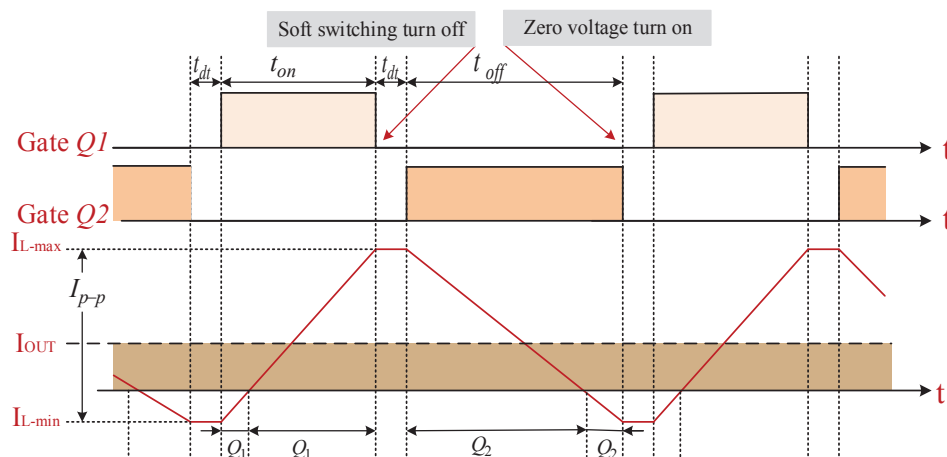
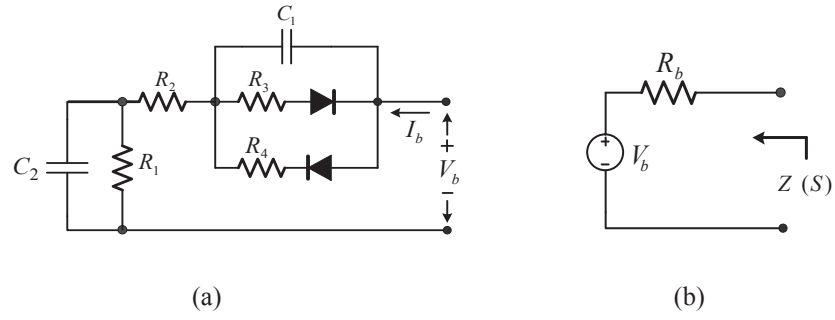


Fig.5.25 The wave-forms of voltage and current in bi-directional converter [5.22]

When  $Q_1$  is turned off and dead time starts, inductor current  $I_L$  will charge  $C_A$  and discharge  $C_B$ . The turn off loss of  $Q_1$  is small due to slow rate of charging  $C_A$ . When  $C_B$  is discharged to zero, inductor current turns on the  $D_A$  and also charges  $C_A$ . Therefore,  $Q_1$  turns on at zero voltage due to the  $D_B$  state and current in inductor reduces to zero and flows in opposite direction according to the polarity of  $V_{BT}$ . At this time  $D_B$  is turned off naturally without reverse recovery loss. During the second dead time when  $Q_2$  is turned off,  $C_A$  is going to be discharged and  $C_B$  is charged due to the inductor current direction (negative value). When  $C_A$  is completely discharged then  $D_A$  is turned on and takes over the inductor current. At the end of the second dead time,  $Q_1$  is turned on at zero voltage (due to the  $D_A$  state) and inductor current increases gradually from negative values to zero and then positive values due to polarity of  $V_{b2} > V_{BT}$  and  $Q_1$  takes over the inductor current. The converter operation continues similarly for the other switching cycles.

### 5.5.2 Small signal model of bi-directional buck-boost converter

To analyse the dynamic performance of the converter and design a closed loop control, a small signal model of the converter is required. The small signal model of the bidirectional buck-boost converter and design of a closed loop control have been studied in the literatures [5.19]-[5.24]. To find the small signal averaged model, the high frequency effects of voltage sources on the converter model should be taken into account. As the battery is connected to the low voltage and the fuel cell to the high voltage side, their high frequency model needs to be studied. The high frequency models of battery and fuel cell are studied in the next sections.



**Fig.5.26 (a) Equivalent model of lead acid battery and (b) equivalent high frequency model**

#### A. Battery small signal model

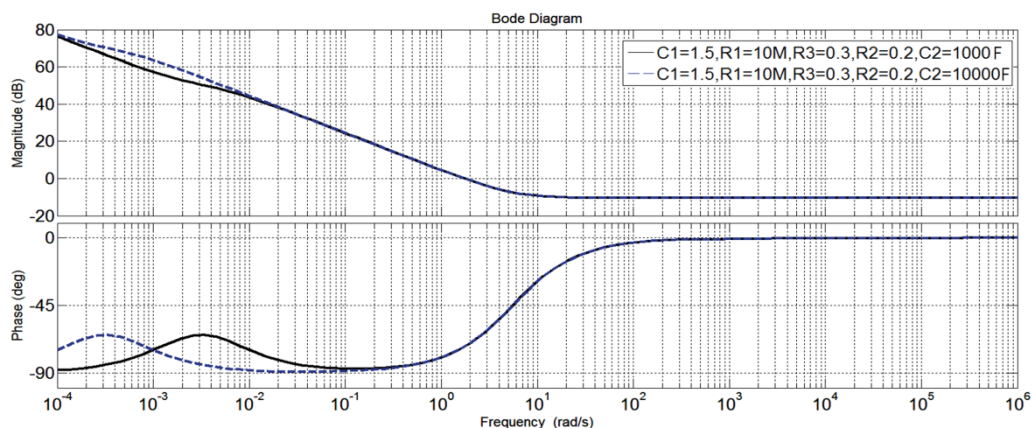
Lead-acid batteries have been widely used in renewable energy systems due to their lower cost, required maintenance and low self-discharge. The main advantages of lead-acid batteries compared with other types of batteries are illustrated in Table. I. As can be seen, they are relatively matured technology and have been used in electrical industries since 1970. Compared with other batteries, they have lower price and need less maintenance which makes them a good choice for low cost renewable energy systems. The table shows that their self-discharge is low and they are tolerant against overcharge. They have higher charge and discharge efficiency thanks to their low internal resistance. They also have some disadvantages compared with other batteries such as low energy, power density and life cycle, and their charging time is relatively long. Table 5.2 shows the main characteristics of five types of commonly used batteries including lead-acids [5.25]. The following study is focused on the high frequency model of lead-acid battery due to its application in the proposed micro-grid. The equivalent circuit of lead acid batteries is presented in Fig.5.26 (a) [5.26], [5.27]. In this model,  $R_1$  is self-discharge resistance,  $R_2$  battery internal resistance,  $R_3$  the discharge resistance,  $R_4$  the charge resistance,  $C_1$  the over voltage capacitance, and  $C_2$  models the battery capacity. The battery impedance during charge  $Z_{Chg}$ , and discharge process  $Z_{Dsg}$ , is presented as

$$Z_{Chg} = \left( \frac{R_1}{1 + R_1 C_2 S} \right) + R_2 + \left( \frac{R_4}{1 + R_4 C_1 S} \right) \quad (5.52)$$

$$Z_{Dsg} = \left( \frac{R_1}{1 + R_1 C_2 S} \right) + R_2 + \left( \frac{R_3}{1 + R_3 C_1 S} \right) \quad (5.53)$$

**TABLE 5.2 Characteristics of Various Types of Batteries for Renewable Energy Applications**

	Ni-Cd	Ni-MH	Lead Acid	Li-ion	Reusable Alkaline
Gravimetric Energy	45-80	60-120	30-50	110-160	80 initial
Internal Resistance	100-200 6V Pack	200-300 6V Pack	<100 12V Pack	150-250 7.2V Pack	200-2000 6V Pack
Operating Temperature	-40 to 60C°	-20 to 60C°	-20 to 60 C°	-20 to 60 C°	0 to 65 C°
Cell Voltage	1.25 V	1.25 V	2 V	3.6 V	1.5 V
Self-discharge/ Months	20%	30%	5%	10%	3%
Load current	20C	5C	5C	>2C	0.5C
Peak	1C	0.5C >	0.2C	<1C	<0.2C
Best results					
Typical battery cost (US\$)	50\$/7.2V	60\$/7.2V	25\$/6V	100\$/7.2V	5\$/9V
Cost per Cycle (US\$)	0.4\$	0.12\$	0.1\$	0.14\$	0.1-0.5\$
Fast charge time	1h	2-4h	8-16h	2-4h	2-3h
Maintenance requirement	30-60 days	60-90 days	3-6 months	Not required	Not required
Cycle life (To 80% of initial capacity)	1500	300-500	200-300	500-1000	50 (To 50%)
Commercial use since	1950	1990	1970	1991	1992
Over charge tolerance	Moderate	Low	High	Very low	Moderate

**Fig.5.27 Frequency response of a lead-acid battery**

Due to the frequency range of buck-boost converter from 10 Hz to 10 kHz the battery shows a slow dynamic response at this operation range. Fig.5.27 shows the Bode plot of the battery impedance for frequency range of  $\omega=0.01$  to  $\omega=100$  kHz. The model is based on the estimated parameters of two lead-acid batteries with different capacities.

As can be seen in the figure, the battery model shows a slow frequency response with zero phase angle and constant gain for the entire range of operation frequency. This means that the battery in small signal modeling and high frequency analysis can be represented as a constant voltage source in series with a constant resistor as presented in Fig.5.26 (b).

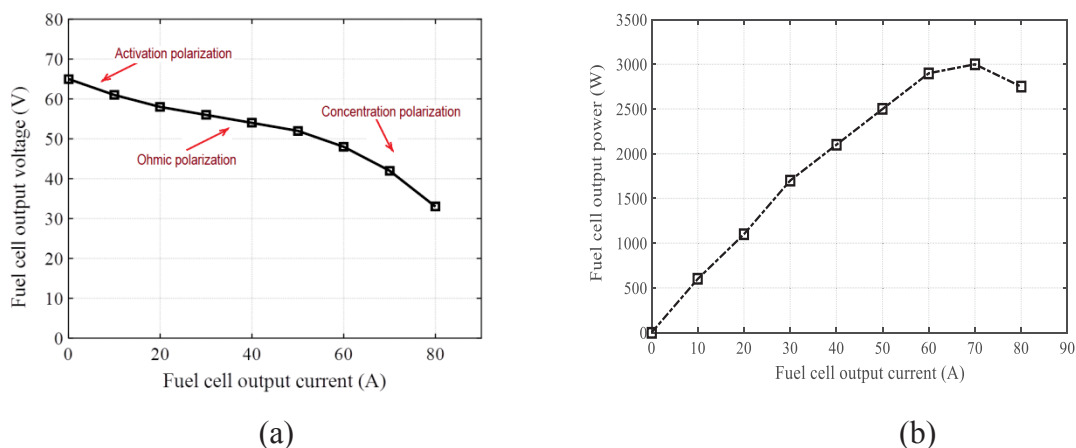


**Fig.5.28 Output characteristics of a PEM fuel cell, (a) output voltage versus current and (b) output power versus current**

### B. Fuel cell small signal model

Fuel cells have found great interest in renewable energy systems over the past decade although their operation principle has been known for more than 150 years. They are able to generate electricity from hydrogen and oxygen while the only product from this chemical reaction is water. They can provide low voltage high current outputs efficiently. Despite their advantages, volt-ampere characteristic of a fuel cell is nonlinear and the output voltage on the terminals of fuel cell is highly dependent on the output current. Another problem with fuel cells is their slow dynamic response to regulate the output voltage quickly. Fig.5.28 shows the fuel cell output voltage and power versus current of a 3 kW proton exchange membrane or polymer electrolyte membrane (PEM) fuel cell stack provided by company [5.29].

As can be seen, there are three main operation areas for a fuel cell depending on the range of output current known as initial non-linearity or activation polarization region, linear or ohmic polarization region and high current or concentration polarization nonlinear region [5.30]. In steady state, the relation between voltage and current of a PEM fuel cell for operation in linear area can be written as

$$V_{FC} = E_{FC} - R_{int}I_{FC} \quad (5.54)$$

where  $R_{int}$  is known as the internal resistance and  $R_{int}=R_1+R_2$  and  $E_{FC}$  the internally generated voltage of the fuel cell.  $E_{FC}$  depends nonlinearly on the output current  $I_{FC}$ , and can be determined by

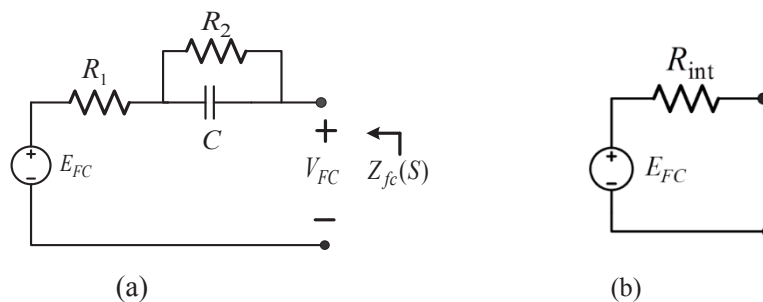


Fig.5.29 Equivalent model of PEM fuel cell for (a) steady state and (b) high frequency analysis

$$E_{FC} = E_{rev} - A \ln\left(\frac{I_{FC}}{I_0}\right) + B \ln\left(1 - \frac{I_{FC}}{I_l}\right) \quad (5.55)$$

where  $E_{rev}$  is the reversible fuel cell voltage,  $I_0$  the exchange current,  $I_l$  the limiting current which happens at the maximum supplied fuel, and the numerical values A and B are activation and contribution polarization constants which can be acquired by means of experimental tests [5.31]. The capacitor  $C$  is placed in parallel to  $R_2$  to model the effect of charge double layer and the transient behaviour of the fuel cell.

To find the small signal model of the bi-directional converter, it is required to find the frequency response of the fuel cell as the main source linked to the converter output. The equivalent circuit of the fuel cell is presented in Fig.5.29 (a) [5.31]. It is used to find the frequency response of the fuel cell impedance for a frequency range of 100 Hz to 20 kHz. According to the figure the impedance of the fuel cell can be calculated by

$$Z_{fc} = \frac{R_1 R_2 C s + R_1 + R_2}{1 + R_2 C s} \quad (5.56)$$

To plot the fuel cell impedance presented in (5.58) based on the real data, an actual model of fuel cell based on data sheet of a commercial fuel cell as presented in Fig.5.30 is used [5.28]. The amplitude and phase Bode plots of  $Z_{fc}$  are calculated for two cases of different parameters (selected from commercial fuel cell systems datasheet) and presented in Fig.5.31. It can be seen that for the proposed frequency range considering the bandwidth and sampling time the Bode diagram presents a constant value of amplitude and zero phase angle. This means that the PEM fuel cell naturally presents a slow dynamic response in the proposed frequency range and in the transient analysis can be considered as constant.

Type of fuel cell	PEM
Number of cells	72
Rated Power	3000W
Performance	43.2V @ 70A
H2 Supply valve voltage	12V
Purging valve voltage	12V
Blower voltage	12V
Reactants	Hydrogen and Air
External temperature	5 to 30°C
Max stack temperature	65°C
H2 Pressure	0.45-0.55bar
Hydrogen purity	≧99.995% dry H2
Humidification	self-humidified
Cooling	Air (integrated cooling fan)
Weight (with fan & casing)	15Kg (±200g)
Controller	2.5Kg (±100g)
Dimension	41.8cm x35cm x 18.3cm
Flow rate at max output*	39 L/min
Start up time	≧30S at ambient temperature
Efficiency of stack	40% @ 43.2V
Low voltage shut down	36V
Over current shut down	90A
Over temperature shut down	65°C
External power supply**	13V(±1V), 5A~8A

 Horizon  
Fuel Cell Technologies



Fig.5.30 Data sheet of a commercial fuel cell stack [5.28]

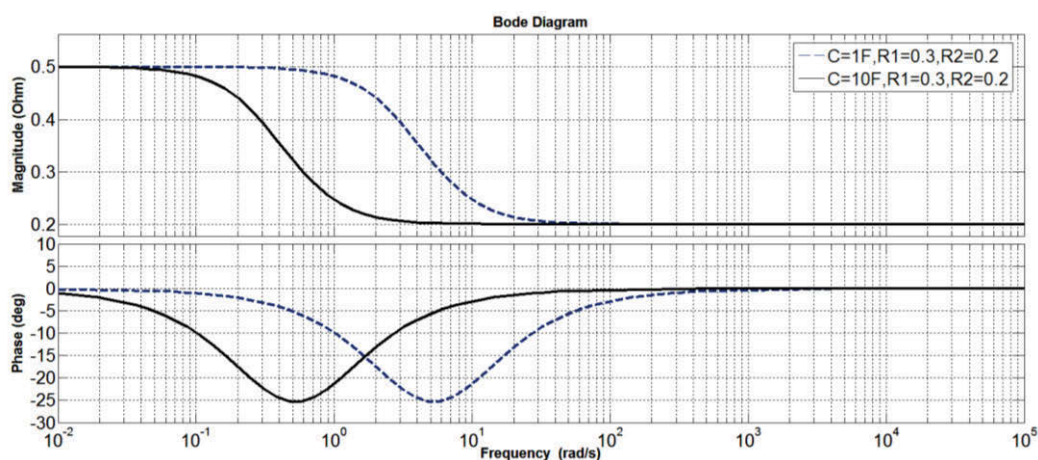


Fig.5.31 Frequency response of fuel cell for small signal analysis

Therefore, the fuel cell model presented in Fig.5.29 (b) can be replaced with a constant resistor in series with a constant voltage source for high frequency small signal analysis.

### C. Small signal analysis of the converter

The main objective of the closed loop control is to control the charge and discharge current of the battery and to regulate the voltage on the common dc bus of the fuel cell port. The proportional-integral (PI) controllers have been widely used in the dc-dc converters to maintain a constant voltage on the dc bus irrespective of the changes in the

load and input voltage. To effectively maintain the voltage regulation of fuel cell bus a dual loop control strategy is considered in the proposed converter. In contrast to single voltage loop controllers, dual loop controllers have presented superior performance utilizing an internal current control loop [5.32]. As the designed controller should be realized through a DSP, the controller can be designed in continuous time domain and then all control blocks should be transferred to the discrete time. In this case the controller is designed in the S-domain and then the designed loop is transformed into the Z-domain using common transformation methods such as Euler or bilinear transforms. On the other hand, it is possible to design the controller directly in discrete time domain. In this case the effects of sampling and computational time delays can be considered during the design process and more realistic control can be achieved [5.21].

The small signal model of the buck-boost converter is required to design the closed loop controller. Fig.5.32 presents the configuration of the buck-boost converter linked to the fuel cell bus and port two of the TAB converter.

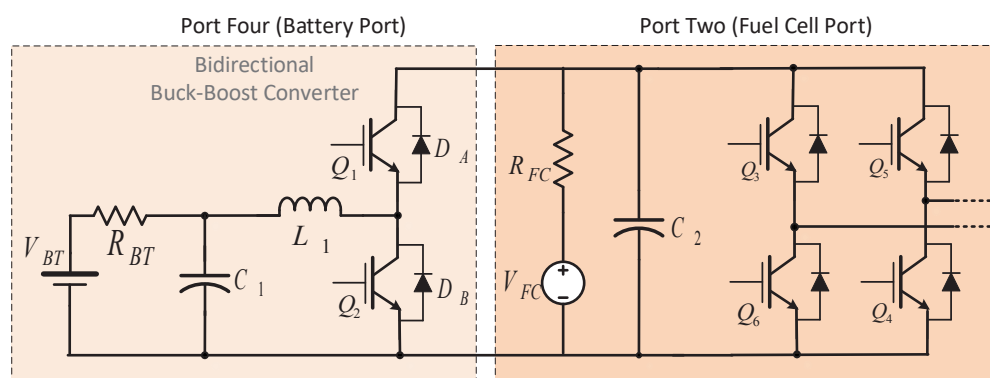


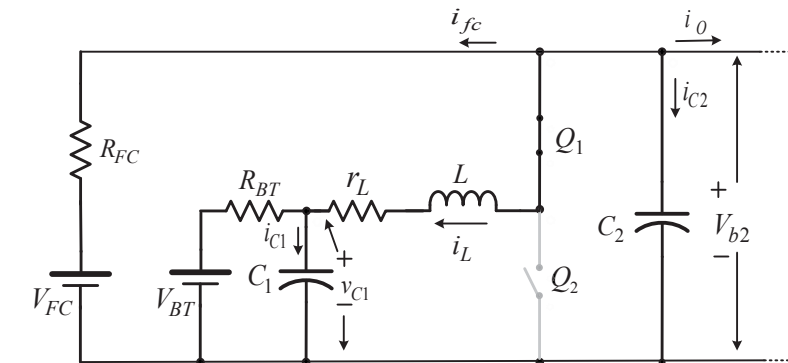
**Fig.5.32 Bidirectional buck-boost converter**

To find the state space average model of the bi-directional buck-boost converter both charge and discharge modes are analysed using the same equivalent circuit [5.22]. The converter operation states during a complete cycle of charging and discharging modes are similar and the only difference is in the range of duty ratio of the switching device. Therefore, to analyse the converter operation during both modes two time intervals of  $t_{on}$ , when  $Q_1$  is on and  $Q_2$  is off, and  $t_{off}$ , when  $Q_1$  is off and  $Q_2$  is on, are considered. Fig.5.33 shows the equivalent model of the converter during both time intervals. The following assumptions are considered for small signal modelling of the converter:

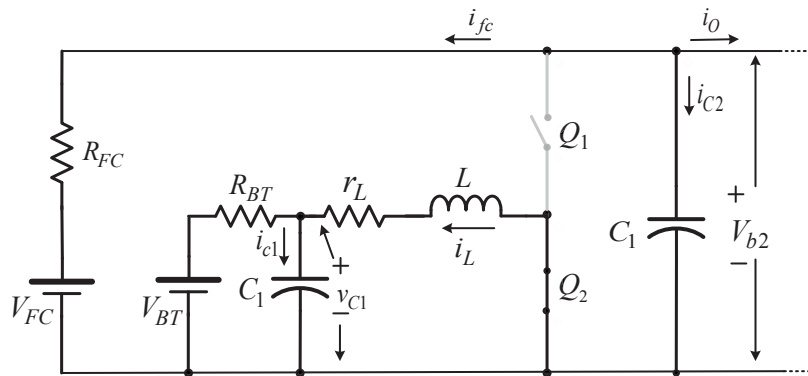
- The dead time  $t_{dt}$  is much less than the switching period ( $t_{dt} < T_s$ ) and its effect on the converter waveforms is ignored ( $t_{dt}=2 \mu s$  and  $T_s=96 \mu s$ );
- The conduction voltage drop on switching device and diodes are neglected.

To find the state space model of the converter, the state variables of the circuit are defined as the voltage on battery filter capacitor  $C_1$ , presented as  $v_{c1}$ , the voltage on the dc bus capacitor  $C_2$  named as  $v_{c2}$ , and the current in the inductor,  $i_L$ . The state space equations of the converter for first time interval  $t_{on}$  (referring to Fig.5.33 (a)) considering the inductor current and capacitor voltages can be written as

$$\begin{cases} L_1 \frac{di_L}{dt} = -i_L r_L + v_{b2} - v_{C1} \\ C_2 \frac{dv_{b2}}{dt} = -\frac{v_{b2} - V_{FC}}{R_{FC}} - i_L - i_O \\ C_1 \frac{dv_{C1}}{dt} = -\frac{v_{C1} - V_{BT}}{R_{BT}} + i_L \end{cases} \quad (5.57)$$



(a)



(b)

**Fig.5.33 The equivalent model of bidirectional buck-boost converter**

The state space equations for the second time interval  $t_{off}$  considering Fig.5.33 (b) can be written as

$$\begin{cases} L_1 \frac{di_L}{dt} = -i_L r_L - v_{C1} \\ C_2 \frac{dv_{b2}}{dt} = -\frac{v_{b2} - V_{FC}}{R_{FC}} - i_O \\ C_1 \frac{dv_{C1}}{dt} = -\frac{v_{C1} - V_{BT}}{R_{BT}} + i_L \end{cases} \quad (5.58)$$

Averaging the state space equations over a complete switching cycle gives

$$\begin{cases} L_1 \frac{d\bar{i}_L}{dt} = -\bar{i}_L r_L + D_4(\bar{v}_{b2} - \bar{v}_{C1}) - (1 - D_4)\bar{v}_{C1} \\ C_2 \frac{d\bar{v}_{b2}}{dt} = -D_4 \left( \frac{\bar{v}_{b2} - V_{FC}}{R_{FC}} + \bar{i}_L \right) - (1 - D_4) \left( \frac{\bar{v}_{b2} - V_{FC}}{R_{FC}} \right) - i_O \\ C_1 \frac{d\bar{v}_{C1}}{dt} = -\frac{\bar{v}_{C1} - V_{BT}}{R_{BT}} + \bar{i}_L \end{cases} \quad (5.59)$$

Applying some rearrangements, the final equations can be written as

$$\begin{cases} L_1 \frac{d\bar{i}_L}{dt} = -\bar{i}_L r_L + D_4 \bar{v}_{b2} - \bar{v}_{C1} \\ C_2 \frac{d\bar{v}_{b2}}{dt} = -D_4 \bar{i}_L - \left( \frac{\bar{v}_{b2} - V_{FC}}{R_{FC}} \right) - i_O \\ C_1 \frac{d\bar{v}_{C1}}{dt} = -\frac{\bar{v}_{C1} - V_{BT}}{R_{BT}} + \bar{i}_L \end{cases} \quad (5.60)$$

Adding the small signal variations to (5.60) results in

$$\begin{cases} L_1 \frac{d(\bar{i}_L + \hat{i}_L)}{dt} = -(\bar{i}_L + \hat{i}_L) r_L + (D_4 + \hat{d}_4)(\bar{v}_{b2} + \hat{v}_{b2}) - (\bar{v}_{C1} + \hat{v}_{C1}) \\ C_2 \frac{d(\bar{v}_{b2} + \hat{v}_{b2})}{dt} = -(D_4 + \hat{d}_4)(\bar{i}_L + \hat{i}_L) - \frac{(\bar{v}_{b2} + \hat{v}_{b2}) - V_{FC}}{R_{FC}} - (i_O + \hat{i}_O) \\ C_1 \frac{d(\bar{v}_{C1} + \hat{v}_{C1})}{dt} = -\frac{(\bar{v}_{C1} + \hat{v}_{C1}) - V_{BT}}{R_{BT}} + (\bar{i}_L + \hat{i}_L) \end{cases} \quad (5.61)$$

Considering only the variable part of equations for small signal analysis and neglecting the higher order items, the resultant equations can be rewritten as

$$\begin{cases} L_1 \frac{d\hat{i}_L}{dt} = -\hat{i}_L r_L + D_4 \hat{v}_{b2} + \hat{d}_4 \bar{v}_{b2} - \hat{v}_{C1} \\ C_2 \frac{d\hat{v}_{b2}}{dt} = -D_4 \hat{i}_L - \hat{d}_4 \bar{i}_L - \frac{\hat{v}_{b2}}{R_{FC}} - \hat{i}_O \\ C_1 \frac{d\hat{v}_{C1}}{dt} = -\frac{\hat{v}_{C1}}{R_{BT}} + \hat{i}_L \end{cases} \quad (5.62)$$

Taking Laplace transform of the equations gives

$$\begin{cases} \hat{i}_L(s) = -\frac{r_L}{L_1} \hat{i}_L(s) + \frac{D_4}{L_1} \hat{v}_{b2}(s) + \frac{\bar{v}_{b2}}{L_1} \hat{d}_4(s) - \frac{1}{L_1} \hat{v}_{C1}(s) \\ s\hat{v}_{b2}(s) = -\frac{D_4}{C_2} \hat{i}_L(s) + \frac{\bar{i}_L}{C_2} \hat{d}_4(s) - \frac{\hat{v}_{b2}(s)}{C_2 R_{FC}} \\ s\hat{v}_{C1}(s) = -\frac{\hat{v}_{C1}(s)}{C_1 R_{BT}} + \frac{1}{C_1} \hat{i}_L(s) \end{cases} \quad (5.63)$$

The final state space equations can be written as

$$\begin{bmatrix} s + \frac{r_L}{L_1} & \frac{1}{L_1} & -\frac{D_4}{L_1} \\ \frac{D_4}{C_2} & 0 & s + \frac{1}{C_2 R_{FC}} \\ -\frac{1}{C_1} & s + \frac{1}{C_1 R_{BT}} & 0 \end{bmatrix} \begin{bmatrix} \hat{i}_L(s) \\ \hat{v}_{C1}(s) \\ \hat{v}_{b2}(s) \end{bmatrix} = \begin{bmatrix} \frac{\bar{v}_{bus}}{L_1} \\ -\frac{\bar{i}_L(s)}{C_2} \\ 0 \end{bmatrix} \hat{d}_4(s) + \begin{bmatrix} 0 \\ -\frac{1}{C_2} \\ 0 \end{bmatrix} \hat{i}_O(s) \quad (5.64)$$

Rearranging the equation gives

$$\begin{bmatrix} \hat{i}_L(s) \\ \hat{v}_{C1}(s) \\ \hat{v}_{b2}(s) \end{bmatrix} = \frac{1}{|A|} \begin{bmatrix} a_{11} & a_{12} & a_{13} \\ a_{21} & a_{22} & a_{23} \\ a_{31} & a_{32} & a_{33} \end{bmatrix} \begin{bmatrix} \frac{\bar{v}_{bus}}{L_1} \\ -\frac{\bar{i}_L(s)}{C_2} \\ 0 \end{bmatrix} \hat{d}_4(s) + \frac{1}{|A|} \begin{bmatrix} a_{11} & a_{12} & a_{13} \\ a_{21} & a_{22} & a_{23} \\ a_{31} & a_{32} & a_{33} \end{bmatrix} \begin{bmatrix} 0 \\ -\frac{1}{C_2} \\ 0 \end{bmatrix} \hat{i}_O(s) \quad (5.65)$$

where

$$\begin{aligned} a_{11} &= -\left(s + \frac{1}{C_2 R_{FC}}\right) \left(s + \frac{1}{C_1 R_{BT}}\right), & a_{12} &= -\frac{D_4}{L_1} \left(s + \frac{1}{C_1 R_{BT}}\right), \\ a_{13} &= -\frac{1}{L_1} \left(s + \frac{1}{C_2 R_{FC}}\right) \end{aligned} \quad (5.66)$$

$$\begin{aligned}
 a_{21} &= -\frac{1}{C_2} \left( s + \frac{1}{C_1 R_{FC}} \right), & a_{22} &= -\frac{D_4}{L_1 C_1}, & a_{23} &= -\left[ \left( s + \frac{r_L}{L_1} \right) \left( s + \frac{1}{C_2 R_{FC}} \right) + \frac{D^2}{L_1 C_2} \right] \\
 a_{31} &= \frac{D}{C_1} \left( s + \frac{1}{C_2 R_{BT}} \right), & a_{32} &= -\left[ \left( s + \frac{r_L}{L} \right) \left( s + \frac{1}{C_2 R_{BT}} \right) + \frac{1}{L C_2} \right], & a_{33} &= -\frac{D}{L C_1} \\
 |A| &= -\frac{D^2}{L C_1} \left( s + \frac{1}{C_2 R_{BT}} \right) - \left( s + \frac{1}{C_1 R_{FC}} \right) \left[ \left( s + \frac{r_L}{L} \right) \left( s + \frac{1}{C_2 R_{BT}} \right) + \frac{1}{L C_2} \right]
 \end{aligned}$$

The transfer functions of control to current and control to voltage using (5.65) can be found as

$$\begin{aligned}
 G_i(s) &= \frac{\hat{i}_L(s)}{d_4(s)} = \frac{\left( s + \frac{1}{C_1 R_{BT}} \right) \left[ \left( s + \frac{1}{C_2 R_{FC}} \right) \frac{\bar{v}_{b2}}{L_1} - \frac{D_4 \bar{i}_L}{L_1 C_2} \right]}{\left( s + \frac{1}{C_2 R_{FC}} \right) \left( s + \frac{1}{C_1 R_{BT}} \right) \left( s + \frac{r_L}{L_1} \right) + \frac{\left( s + \frac{1}{C_2 R_{FC}} \right) D_4^2 \left( s + \frac{1}{C_1 R_{BT}} \right)}{L_1 C_1} + \frac{D_4^2 \left( s + \frac{1}{C_1 R_{BT}} \right)}{L_1 C_2}} \\
 G_v(s) &= \frac{\hat{v}_{C1}(s)}{\hat{d}_4(s)} = \frac{\frac{1}{C_1} \cdot \hat{i}_L(s)}{s + \frac{1}{C_1 R_{BT}}} \\
 &= \frac{\left( s + \frac{1}{C_2 R_{FC}} \right) \frac{\bar{v}_{bus}}{L_1 C_1} - \frac{D_4 \bar{i}_L}{L_1 C_1 C_2}}{\left( s + \frac{1}{C_2 R_{FC}} \right) \left( s + \frac{1}{C_1 R_{BT}} \right) \left( s + \frac{r_L}{L_1} \right) + \frac{\left( s + \frac{1}{C_2 R_{FC}} \right) D^2 \left( s + \frac{1}{C_1 R_{BT}} \right)}{L_1 C_1} + \frac{D^2 \left( s + \frac{1}{C_1 R_{BT}} \right)}{L_1 C_2}}
 \end{aligned} \tag{5.67}$$

Fig.5.34 shows the amplitude and the phase Bode diagrams of inductor current to duty cycle and bus voltage to duty cycle.

Table 5.3 illustrates the value of converter parameters for the presented diagrams. As can be seen in (5.67) and (5.68) the transfer functions are third order systems and are

dependent on the converter parameters such as duty cycle and bus voltage and consequently will change with the steady state average value of the parameters.

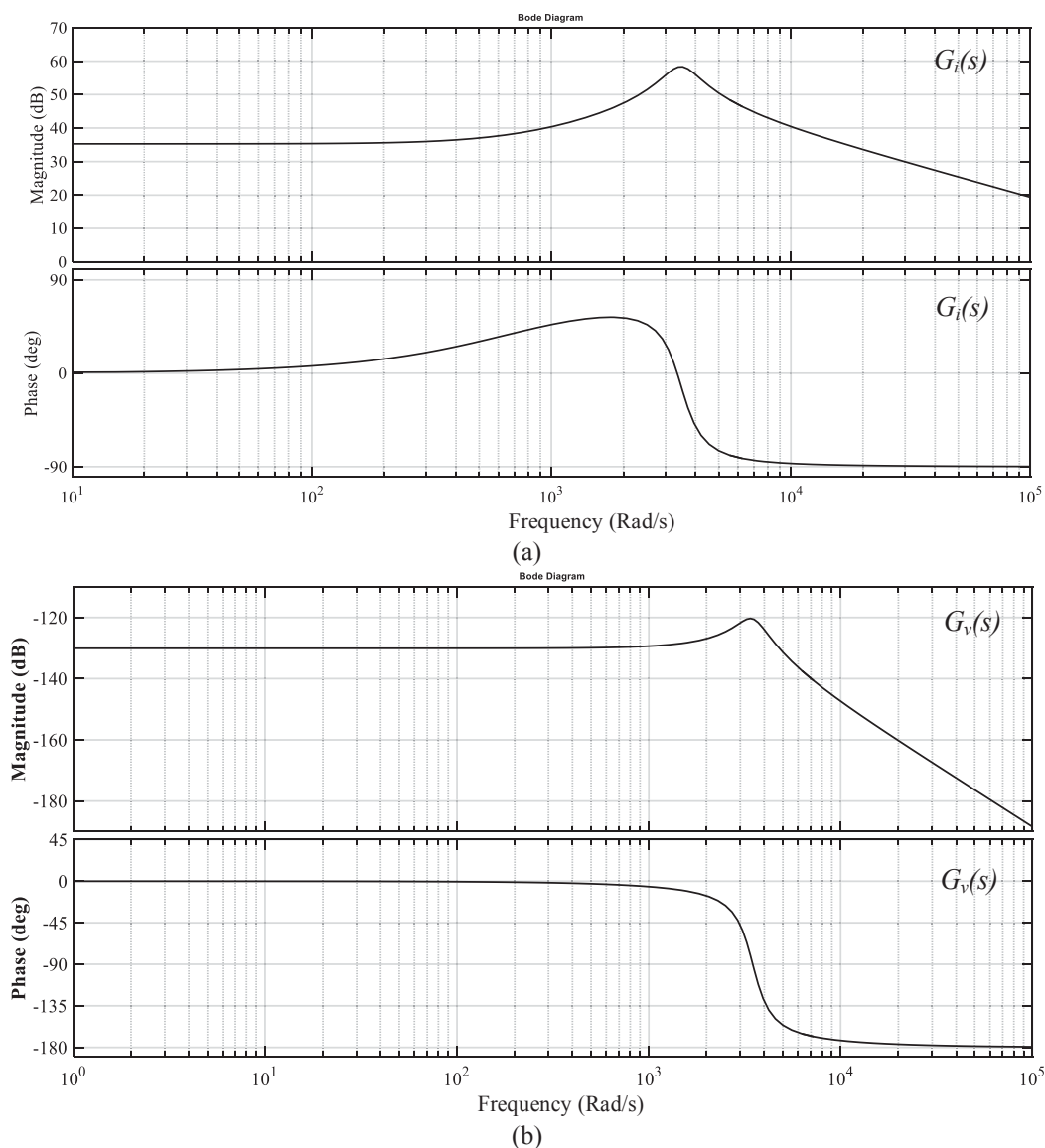


Fig.5.34 Bode diagram of open-loop transfer functions of (a) inductor current and (b) capacitor voltage

TABLE 5.3 Parameters of the Bidirectional Buck-Boost Converter

Parameter	$R_{BT}$	$R_{FC}$	$r_L$	$C_2$	$C_1$	$L_1$	$V_{b2}$	$V_{bat}$	$f_s$
Value	1.5 $\Omega$	2.5 $\Omega$	200m $\Omega$	2200 $\mu$ f	1000 $\mu$ f	25 $\mu$ H	60 V	24 V	10 kHz

TABLE 5.4 Comparison of Different Continuous to Discrete Time Transforms

Transform Type	Forward Difference	Backward Difference	Trapezoidal Approach (Bilinear transform or Tustin approximation)	Bilinear Transform with Pre-warping



$$H_d(s) = e^{-sT_{dc}} \quad (5.69)$$

and the effect of ZOH delay time,  $T_{ds}$ , can be modeled by

$$H_z(s) = \frac{1 - e^{-sT_{ds}}}{s} \quad (5.70)$$

The transfer functions of the inductor current,  $G_{id}$ , and the bus voltage,  $G_{vd}$ , to the duty ratio and in  $Z$  domain are obtained as

$$G_{id}(z) = Z \left\{ \frac{1 - e^{-sT_{ds}}}{s} e^{-sT_{dc}} G_i(s) \right\} \quad (5.71)$$

$$G_{vd}(z) = Z \left\{ \frac{1 - e^{-sT_{ds}}}{s} e^{-sT_{dc}} G_v(s) \right\} \quad (5.72)$$

The current and voltage loop transfer functions are required for stability analysis of the converter. The current loop  $H_i(z)$  and voltage loop  $H_v(z)$  in discrete-time domain can be written as

$$H_i(z) = C_i(z)G_i(z) \quad (5.73)$$

$$H_v(z) = \frac{C_i(z)C_v(z)G_v(z)}{1 + C_i(z)G_i(z)} \quad (5.74)$$

where  $C_i(z)$  and  $C_v(z)$  are the transfer functions current and voltage PI controllers in discrete time domain respectively and can be written as

$$C(z) = K_p + K_i T_{ds} \frac{z}{z-1} \quad (5.75)$$

where  $K_p$  and  $K_i$  are proportional and integral gains. The controller gains are defined according to the required cross over frequency  $\omega_c$  and phase margin  $\phi_m$  of the voltage and current loop transfer functions ( $H_v(z)$  and  $H_i(z)$ ) in discrete-time domain [5.21]-[5.24]. For particular values of cross over frequency,  $\omega_c$ , and phase margin,  $\phi_m$ , the value of  $K_p$  and  $K_i$  for PI controller of voltage loop can be defined as

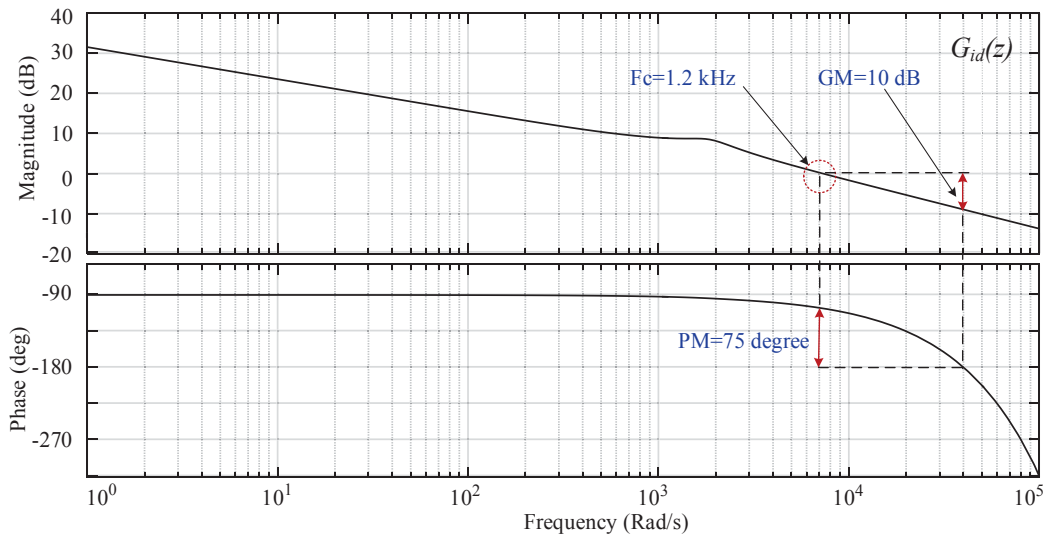
$$K_p = \frac{\cos(\theta)}{|G_v(j\omega_{cv})|} \quad (5.76)$$

$$K_i = \frac{-\omega_c \sin(\theta)}{|G_v(j\omega_{cv})|} \quad (5.77)$$

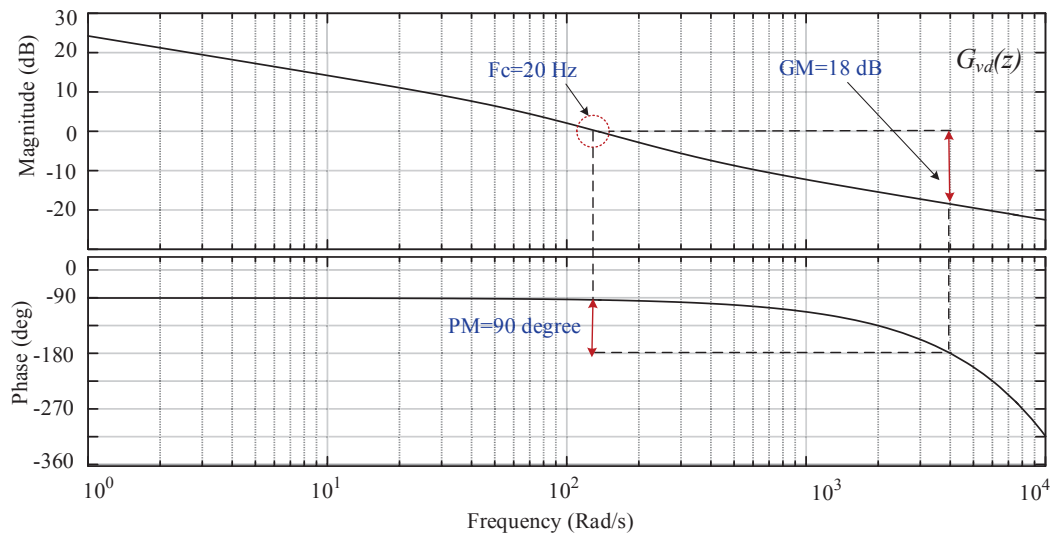
where

$$\theta = 180 + \varphi_m - \angle G_v(j\omega_c) \quad (5.78)$$

For current control loop the controller gains can be defined similarly. It should be noted that in dual loop controllers normally the inner current loop should be designed to present higher speed compared with the outer voltage loop to avoid interaction between loop operations [5.22]-[5.24]. Therefore, the PI controller for voltage loop should be designed to compensate the frequency response of the loop to maintain the crossover frequency much lower than that of current loop  $\omega_{ci}$  ( $\omega_{cv} \ll \omega_{ci}$ ). Fig.5.36 shows the amplitude and phase Bode diagram of the voltage and current loops.



(a)



(b)

**Fig.5.36 Bode plots of closed loop discretized transfer functions of (a) inner current loop (b) outer voltage loop**

In the proposed controller the crossover frequency of 20 Hz ( $\omega_{cv}=120$  rad/s) is defined for voltage loop and 1.2 kHz ( $\omega_{ci}=7500$  rad/s) for current loop controllers. From the stability point of view the current control loop has a gain margin of 10db and phase margin of 75 degree considering the effects of computational delay on the phase of the system. The voltage loop has a gain margin of 18db and phase margin of 90 degree which guarantees the stability of control loop during converter transients. The converter parameters for frequency response analysis are illustrated in Table.5.3.

#### 5.5.4 Simulation of bi-directional buck-boost converter

The proposed bi-directional buck-boost converter was simulated using PSIM and the control loops were realized based on the C2000 embedded target library which is designed to generate codes and implement controllers for Texas instrument DSP family.

The simulated waveforms of the converter are presented for the three cases of operation in buck or charging mode, boundary between charging and discharging modes and boost or discharging mode. The simulated waveforms of voltage on switching devices ( $V_{CE-Q1}$  and  $V_{CE-Q2}$ ), inductor current  $I_L$  and the current flows through the fuel cell bus,  $I_{bus}$  are illustrated in Fig.5.37. As can be seen, the converter is always operating in continuous conduction mode (CCM). In the boost mode, the average values of current in the inductor  $I_L$  and the injected current from battery to the bus  $I_{bus}$  are positive. Therefore, the battery is supplying the fuel cell bus and the rate of supplied current is controlled by the duty ratio of switching devices according to the voltage level on the fuel cell bus. The converter operates in boost mode when the fuel cell is not active or when the battery is in standby mode and the bus voltage drops due to the fast transients. The standard voltage of dc bus  $V_{b2}=60$  V and the battery  $V_{BT}=24$  V is applied to the simulations. The converter parameters for boost mode simulations are  $f_s=20$  kHz,  $T_{dt}=1$   $\mu$ s,  $D_4=0.14$ ,  $V_{b2}=70$  V and  $V_{BT}=25$  V. In the second case, the converter is operating in the boundary between buck and boost converter and the converter parameters are  $D_4=0.4$ ,  $V_{BT}=24$  V and  $V_{b2}=60$  V. As can be seen the average value of the inductor current  $I_L$  and the bus current  $I_{bus2}$  are equal to zero. In the third case, the converter is operating in the buck mode where battery is being charged by fuel cell bus. As can be seen, the converter is operating in CCM and the average values of inductor

current and bus current are negative. In this case, the simulations are carried out for  $V_{BT}=22$  V,  $V_{b2}= 50$  V and  $D_4=0.7$ .

### 5.5.5 Experimental measurements

The simulation results for the three operation cases are verified by experimental measurements. The recorded waveforms of the voltage on switching devices, the inductor current, and the bus current are presented in Fig.5.38. The converter waveforms for operation in boost mode is presented in Fig.5.38 (a) where the average value of inductor current and bus current is positive. Fig.5.38 (b) presents the waveforms of the converter in the boundary between the two operation modes and the waveforms of the buck operation mode are presented in Fig.5.38 (c).

As can be seen the experimentally measured waveforms followed the similar trends to the simulated waveforms presented in Fig.5.37. The converter is operating in CCM during buck, boost and boundary conditions. To reduce the voltage spikes on the switching devices  $Q_1$  and  $Q_2$ , appropriate size of snubber capacitors is selected. It can be seen that parasitic ringing are appeared in the  $I_{bus}$  and  $V_{CE}$  due to the inductor effect and parasitic capacitors of the switching device. It should be noted that the resultant ringing is less than operation in DCM for similar circuit parameters [5.22].

### 5.5.6 Dynamic response of the bidirectional buck-boost converter

To study the quality of the designed double loop controller, it is required to analyse the dynamic response of the converter under the fast variation of operation modes. To analyse the dynamic response of the converter, the load current was stepped down for a limited time (11 ms) and then stepped up. The bus voltage should be regulated against the changes in load current by using battery as compensating source. Fig.5.39 illustrates the variation of inductor current  $I_L$ , the converter current injected or received from the bus  $I_{bus}$ , load current  $I_{LD}$ , and the bus voltage  $V_{bus}$  during the dynamic response test. As can be seen in the figure, in the case of reduction in load current at  $t=20$  ms, the bus over voltage is regulated by changing converter operation mode from boost to buck mode and sinking current. On the other hand, at  $t=31$  ms when the load increases and the voltage was dropped instantly, the battery operation mode changes to boost again to inject the current in the bus and compensate the voltage drop. At this time the bus voltage is regulated on the desired value (60 V).

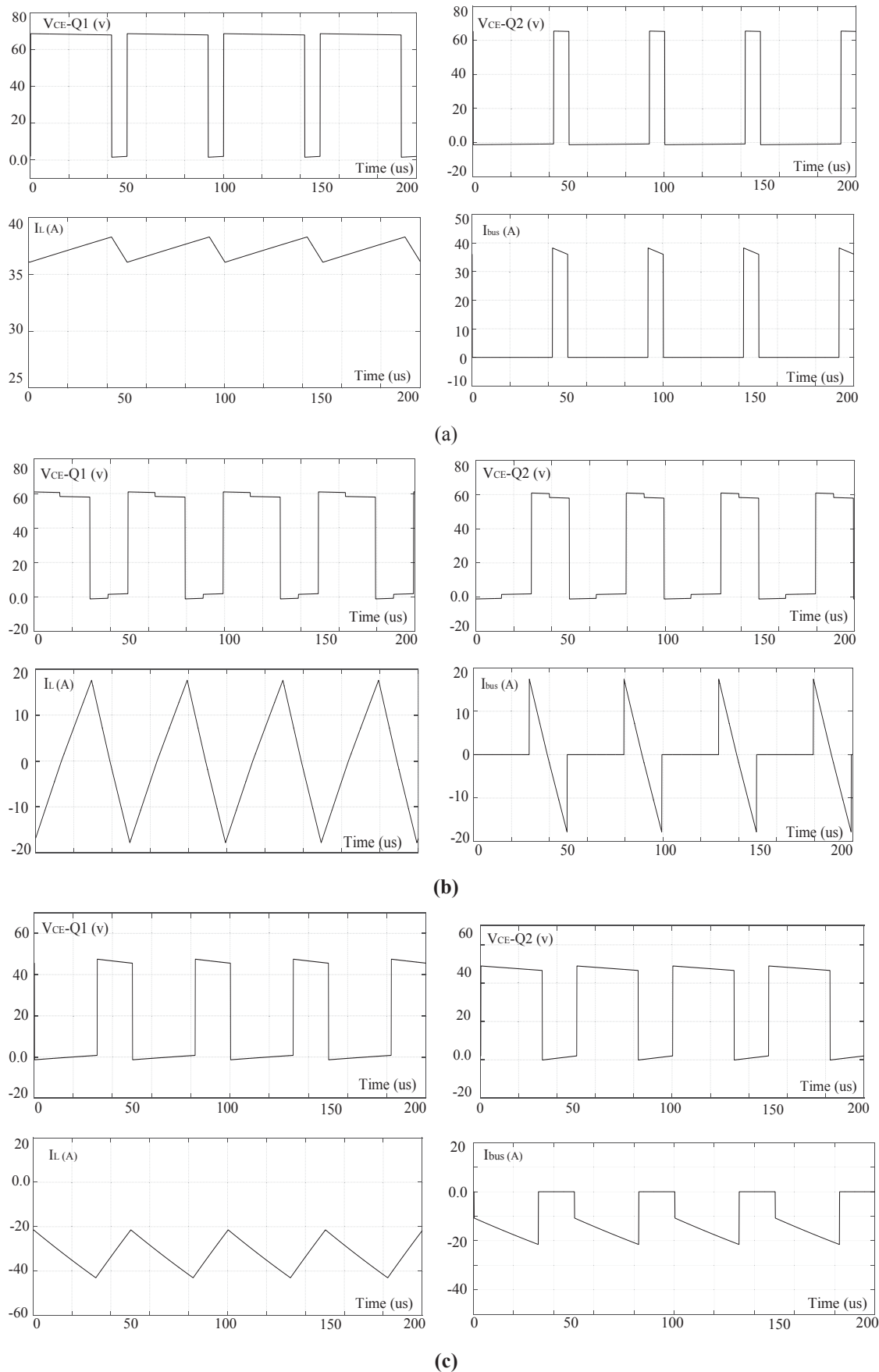


**Fig.5.37** Simulated waveforms of the buck-boost bidirectional converter operating in (a)-boost or charging mode, (b)-boundary between buck and boost and (c)-buck modes

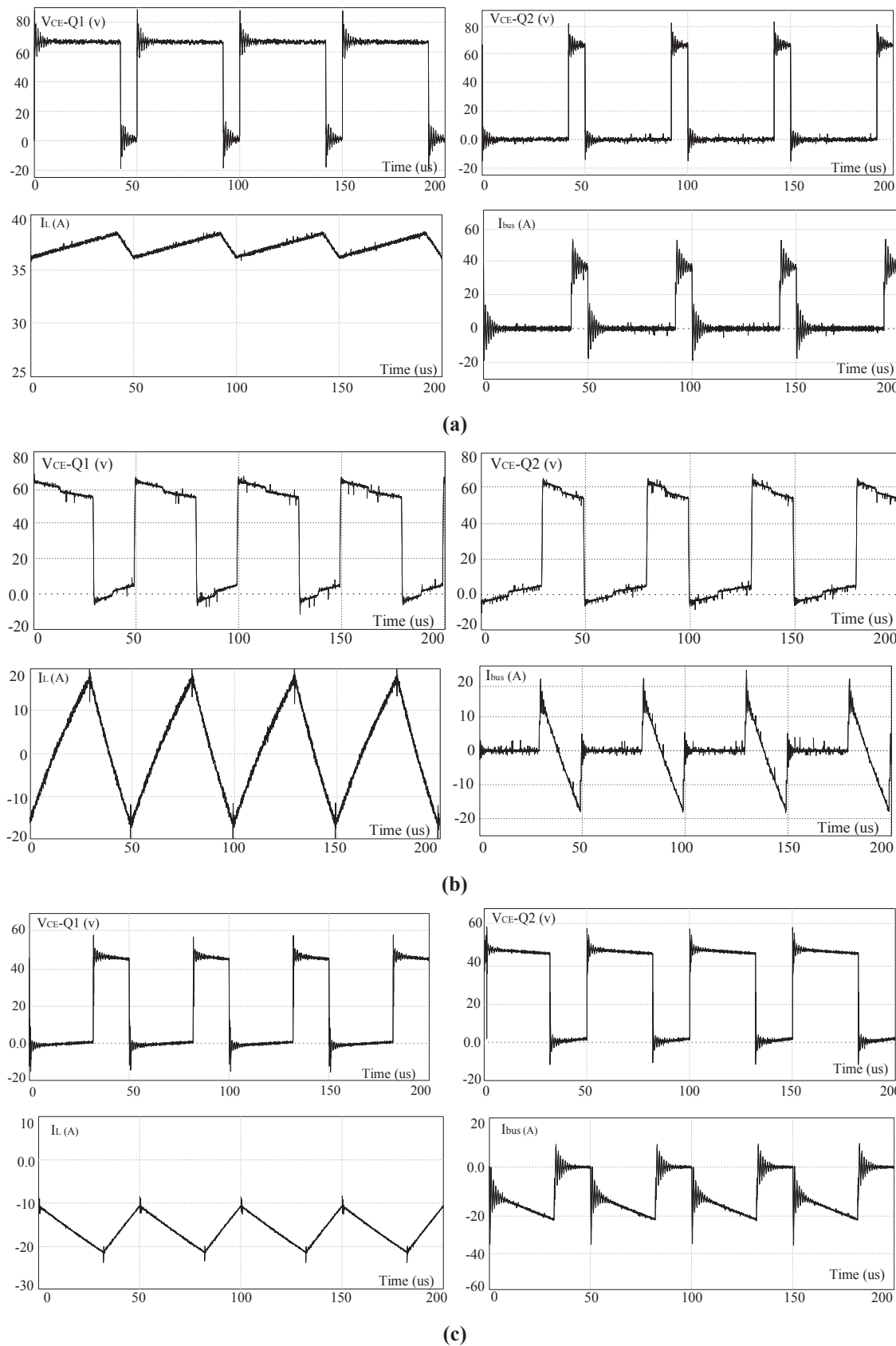


**Fig.5.38** Experimental waveforms of the buck-boost bidirectional converter operating in (a) boost or charging mode, (b) boundary between buck and boost and (c) buck modes

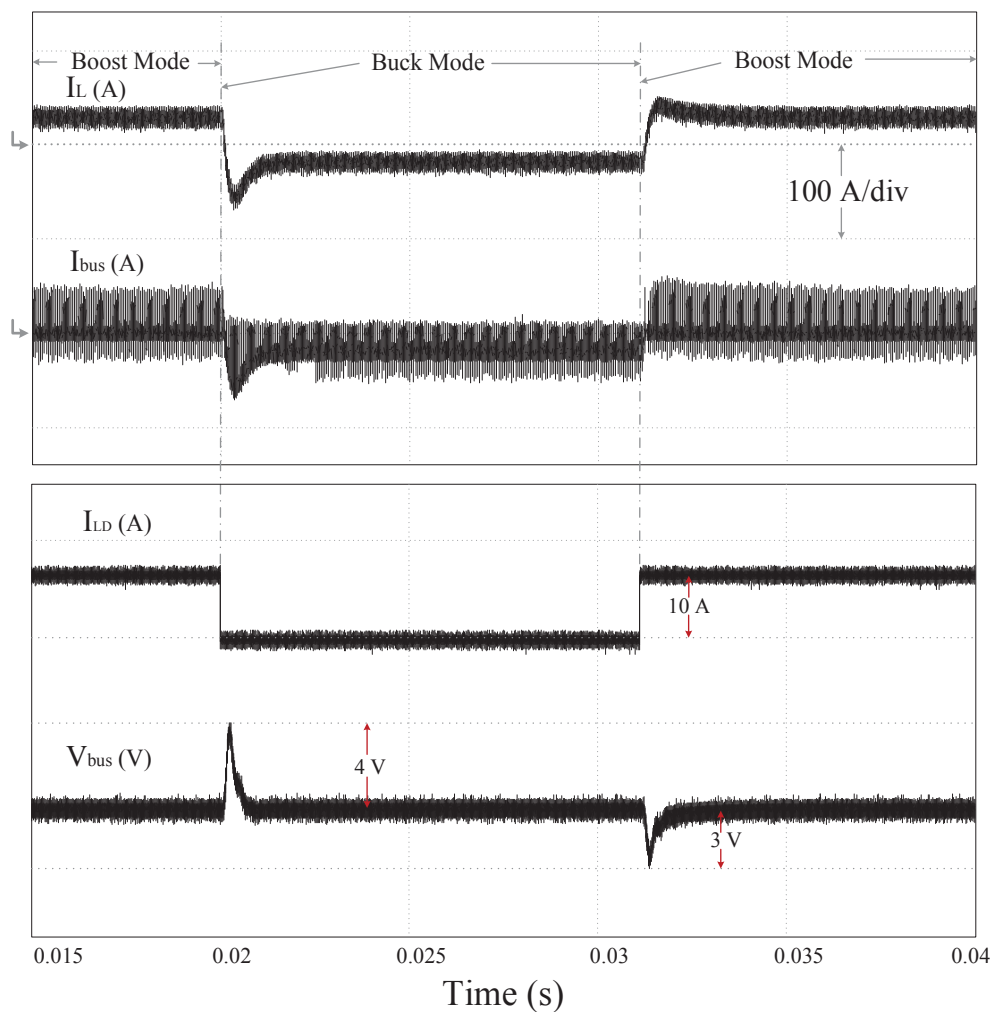


Fig.5.39 The step response of buck-boost converter from boost to buck mode for a limited time

## 5.6 Analysis of Interleaved Current-fed Boost Converter

This section provides details on the PV port as the third port of the TAB converter. The main objective on this section is to design a high frequency dc to dc conversion stage which utilizes the maximum output power from PV under any irradiation and temperature conditions and transfers the extracted power to the other ports. Meanwhile the bus voltage should be kept on a desired level which guarantees soft switching operation of TAB converter for the entire operation range. The MPPT process of designed converter is analysed at the first step due to its importance in converter operation.

### 5.6.1 Analysis of maximum power point tracking

There are numerous researches on various maximum power point tracking algorithms and different topologies of dc-dc converters with MPPT capability [5.33]. An efficient MPPT system should satisfy both appropriate converter topology and fast tracking algorithms. It should provide a fast and accurate tracking response with minimum oscillations around the steady state operation point and be able to track the MPP for a wide range of solar radiation and temperature. From an experimental point of view, the MPPT system should have a simple structure and low cost. The main problem with MPPT methods is that none of them can provide both fast tracking response and excellent accuracy. The most common MPPT algorithms such as constant voltage, perturb and observe (P&O) and incremental conductance (IncCon) have not presented a completely satisfying results on both issues [5.34]. On the other hand, other methods based on the fuzzy logic and neural networks have been proposed as other options although their processing time, complexity and cost have increased [5.34]-[5.36]. Fig.5.40 shows the output voltage-current characteristics of a PV panel for various solar irradiation and temperature levels [5.34]. It can be seen that the solar radiation level mainly influences the output current of PV panel while the temperature level affects the output voltage. As the solar radiation and temperature are strongly coupled, both the output voltage and current of PV panel and consequently output power will change during the daily hours although the temperature effect is not considerable and happens slowly compared with the radiation effect.

As can be seen in the figure, for any radiation and temperature levels there is a knee point on the I-V curve where the output power of PV panel as the product of voltage and the current is maximized. Fig.5.41 shows the output power of PV panel for various radiation and temperature values [5.34]. The maximum output power increases for higher solar radiation levels and decreases for higher temperature values.

The operation point of PV panel is characterized by value of output voltage and current and depends on both the I-V characteristics of the panel and load value. The main work of the converter as an interface between load and PV panel is to adapt the I-V characteristics of the load to that of PV panel and set the MPP as operation point of PV for a wide range of irradiation and temperature levels.

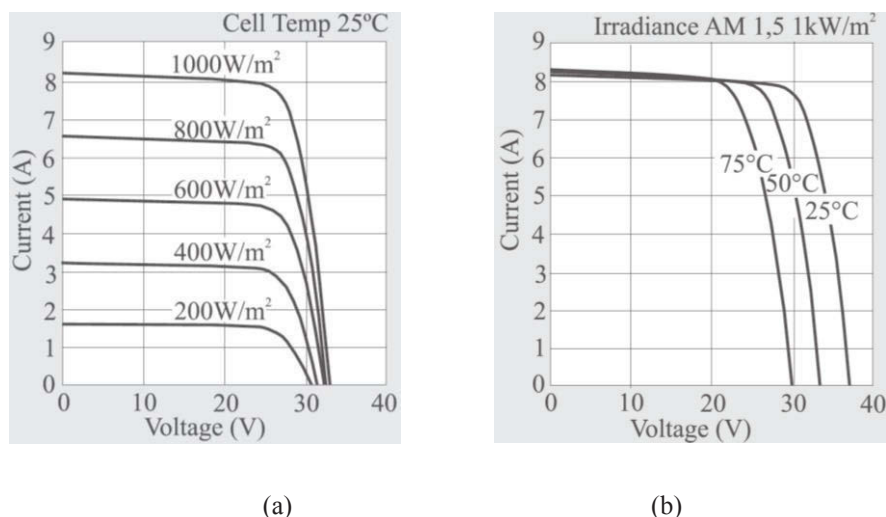


**Fig.5.40** The output voltage-current characteristics of a PV panel for various (a)- solar irradiation and (b)- temperature levels [5.34].

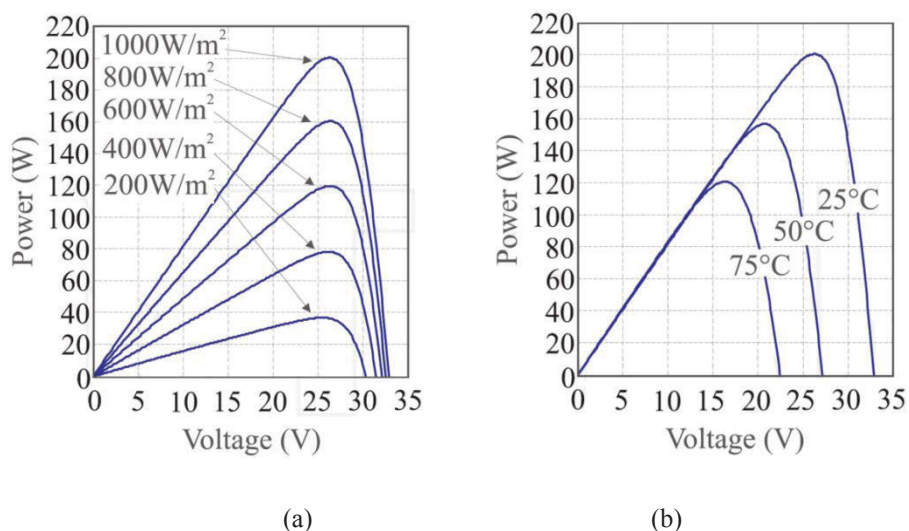


**Fig.5.41** The output power-voltage characteristics of a PV panel for various (a)-solar irradiation and (b)-temperature levels [5.34].

From this point of view dc-dc converter can be an impedance adapter which adapts the I-V characteristics of the load with the I-V of the maximum power point. Different topologies of non-isolated dc-dc converters have been studied regarding their MPPT capability and the buck-boost converter presented better performance compared with others [5.34]. Using this topology the PV voltage can be varied in a wide range from zero to the open circuit voltage of the PV panel.

In recent years, a large number of MPPT methods have been proposed [5.35]. The simplest method is based on the open circuit voltage and short circuit current of PV panel. However, it is required to short circuit or disconnect the PV panel from the load continuously for measurement of short circuit current and open circuit voltage [5.36],

[5.37]. Hill climbing method and perturb and observe (P&O) methods are two widely used methods that are based on the application of perturbation in the operating voltage of PV panel and duty cycle of converter respectively [5.38], [5.39]. Nevertheless, they introduce steady state oscillations of operating point and consequently power loss [5.40]. The incremental conductance (INC) method is based on the slope of the PV power versus voltage curve and provides good dynamic performance and accuracy compared with the other methods although it is more complicated compared with P&O and hill climbing methods [5.41]-[5.43]. The fuzzy or neural network based methods have been proposed as other alternatives due to the consideration of PV nonlinearities [5.44], [5.45].

In the proposed micro-grid the INC method is used due to its good dynamic response, accuracy and minimum effects on the PV operating point. To improve the dynamic response and accuracy of the method a variable step size algorithm is employed. The step size is automatically adjusted according to the distance between current operation point and maximum power point. The step size increases when operating point is far from MPP and it decreases when operation point is near to the MPP. Fig.5.42 shows the output power versus terminal voltage characteristics of PV panel. As can be seen, the slope of the PV power curve is increasing (positive) at the left-hand side of MPP, is equal to zero at MPP and is decreasing (negative) at the right-hand side of MPP.

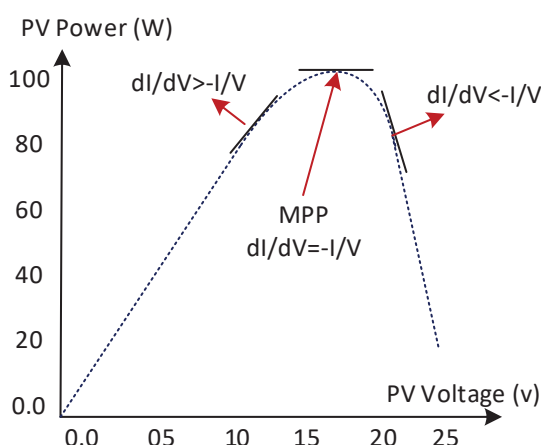


**Fig.5.42 The slope of incremental conductance on P-V characteristics of solar panel**

Therefore the slope of the P-V curve can be defined as

$$P = VI \Rightarrow \frac{dP}{dV} = I \frac{dV}{dV} + V \frac{dI}{dV} = I + V \frac{dI}{dV} \quad (5.79)$$

and for each area, the slope of the curve using (5.79) can be written as

$$\left\{ \begin{array}{ll} \frac{dP}{dV} > 0 & \frac{dI}{dV} > -\frac{I}{V} \Rightarrow \text{Left of MPP} \\ \frac{dP}{dV} = 0 & \frac{dI}{dV} = -\frac{I}{V} \Rightarrow \text{at MPP} \\ \frac{dP}{dV} < 0 & \frac{dI}{dV} < -\frac{I}{V} \Rightarrow \text{Right of MPP} \end{array} \right. \quad (5.80)$$

According to (5.80), in the case of any variation in the PV output power resultant from temperature or radiation level, the position of the operation point on the new characteristic curve can be detected by calculation and comparing incremental conductance  $dI/dV$ , and the instantaneous conductance  $-I/V$ . The aforementioned parameters are calculated by the current and previous samples of the measured voltage and current of PV panel as

$$\frac{dI}{dV} = \frac{I(k) - I(k-1)}{V(k) - V(k-1)} \quad \text{and} \quad -\frac{I}{V} = -\frac{I(k)}{V(k)} \quad (5.81)$$

When the position of the operation point on the P-V curve is detected, it should be moved towards the MPP by changing the PV voltage using positive or negative steps.

Selection of large steps provides faster dynamic response although this can cause excessive steady state oscillations. On the other hand, small size steps results in more delay in adjustment of operation point on MPP. Therefore, selection of fixed step size is a trade-off between dynamic response and oscillations [5.40]. The idea of using variable step size can improve the performance of INC MPPT method [5.46]-[5.48]. In this thesis, a variable step size INC MPPT method is used and the PV output power is used directly to define the step size [5.40].

Fig.5.43 shows the flowchart of the modified INC MPPT method used in this thesis. The steps are applied directly to the converter duty ratio to adjust the output voltage of PV on the maximum power point voltage  $V_{mpp}$  [5.40]. Each step change in duty ratio,  $D$ , is calculated by the voltage, current and power of PV port at  $k$  and  $k-1$  time as

$$D(k) = D(k-1) \pm N \left| \frac{P(k) - P(k-1)}{V(k) - V(k-1)} \right| \quad (5.82)$$

where  $N$  is the scaling factor which is used to adjust the step size efficiently and  $P(k)=V(k)*I(k)$  the PV power at time  $k$ .

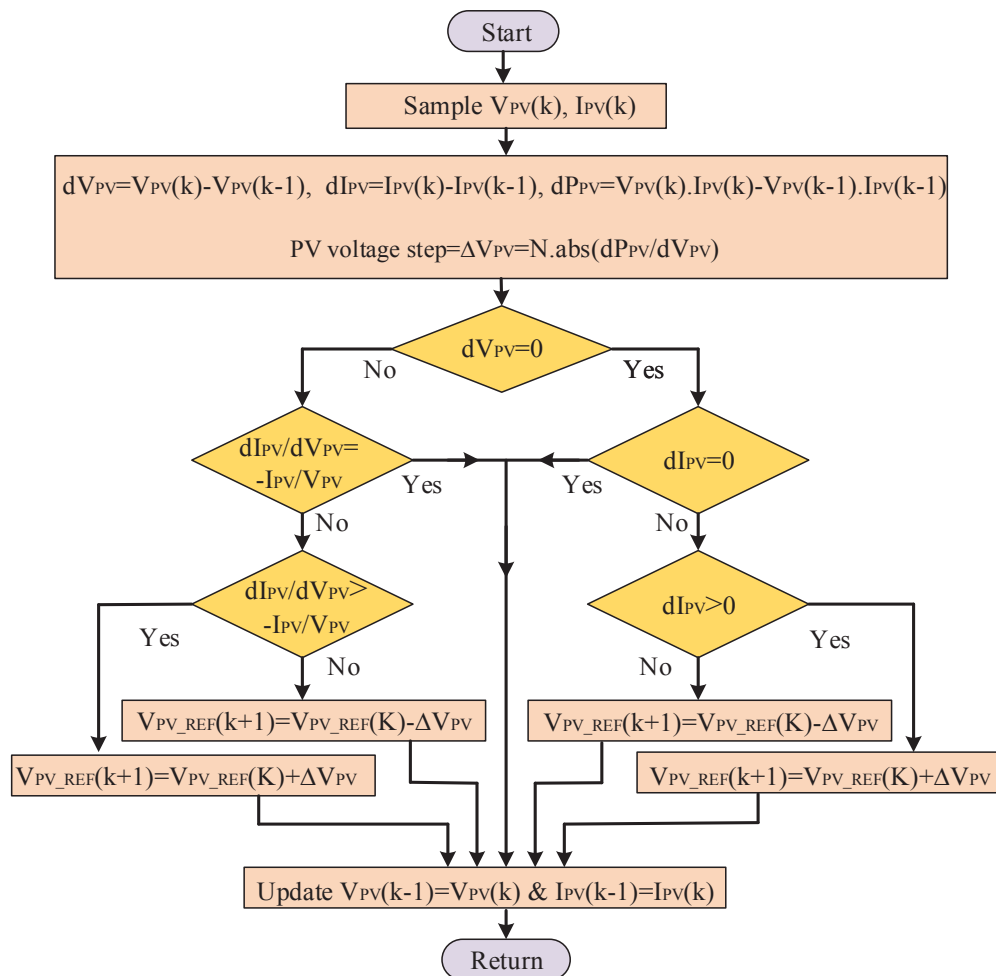


Fig.5.43 Flowchart of variable step MPPT process

As discussed in Chapter Three, MPPT process is designed to be performed by the energy management unit. The MPPT signal which is the duty ratio of switching devices of H-bridge of PV port is calculated by EMU and is sent to the DSP1. The control signal is passed through some signal conditioning circuits on the control and interface board before transferring to the DSP1. Fig.5.44 presents the hardware implementation of MPPT signal from EMU to DSP1.

### 5.6.2 Steady state operation analysis of current-fed boost converter

The current-fed boost converters have been used as an interface between PV panels and loads to maintain the MPPT capability [5.49], [5.50]. In [5.51] a current-fed dual active bridge converter (CF-DAB) is used as a part of dc-dc converters to link the PV panels to the grid using a multi-level inverter system. The main advantages of current fed topology are lower ripple on PV panel which improves the MPPT stability, smaller size filter components and wide input voltage range.

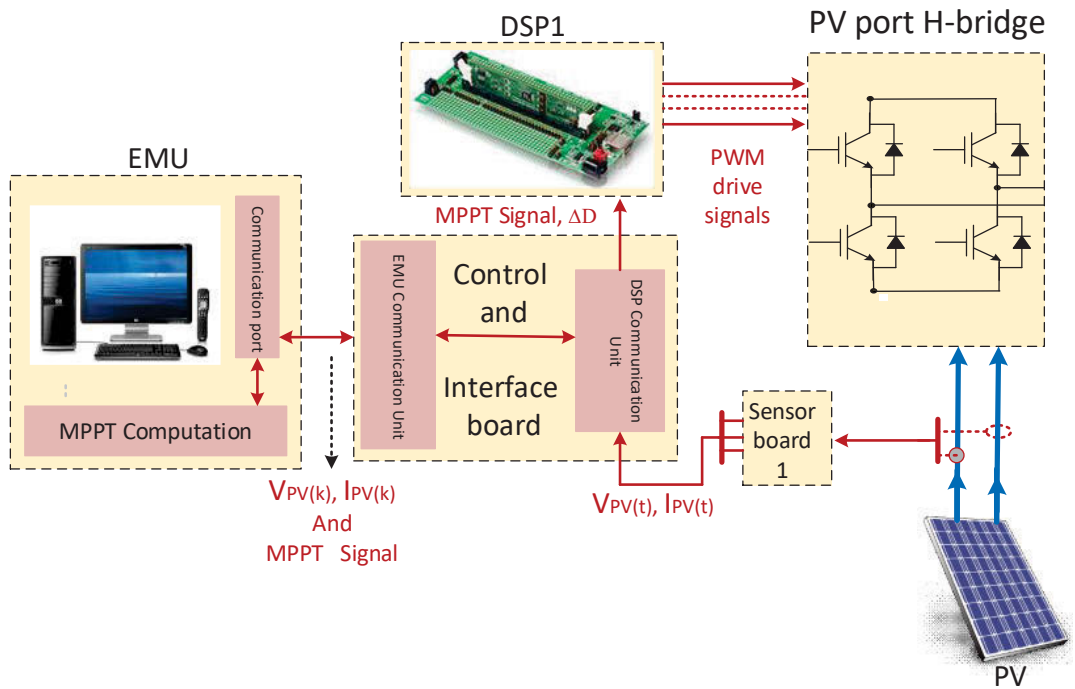


Fig.5.44 The hardware implementation of MPPT in the proposed micro-grid

The interleaved structure reduces the current ripple and provides a good control on the current which makes it appropriate for PV applications [5.51], [5.49]. Fig.5.45 shows the current-fed dc-dc converter topology. As can be seen in the figure the PV port of the TAB converter combines a current-fed dc-dc converter and dc-ac high frequency H-bridge inverter.

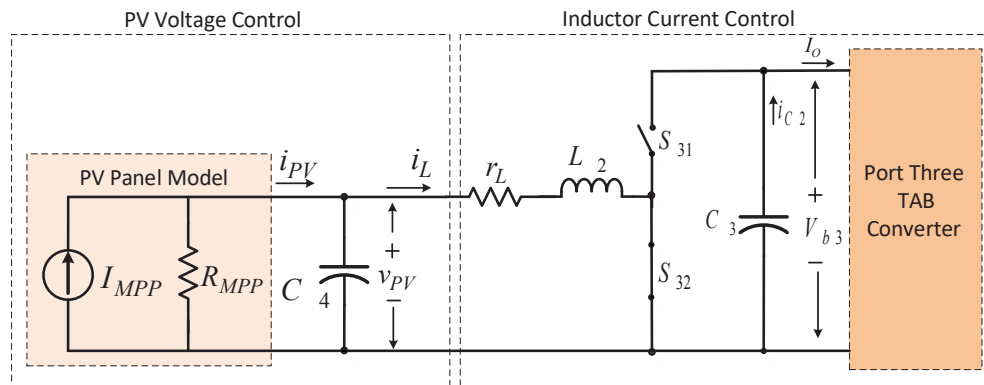


Fig.5.45 The equivalent circuit of current fed dc-dc converter cascaded by H-bridge dc-ac converter

The H-bridge switches  $S_{31}$ ,  $S_{32}$ ,  $S_{33}$  and  $S_{34}$  have been shared in both dc-dc and dc-ac converters. The capacitor  $C_3$  is used as an energy buffer between the two conversion stages. Therefore, the PV port can be modelled as a current-fed boost converter

cascaded by a voltage source dc-ac converter as presented in Fig.5.45 [5.51]. It should be noted that only one leg of the interleaved boost converter is presented in the figure.

To realize the MPPT, the duty ratios of  $S_{31}$  and  $S_{32}$  are changed according to the MPPT algorithm requirement and commands from EMU. Each of inductors  $L_2$  and  $L_3$  along with the linked H-bridge leg forms a boost converter. The output voltage from PV is regulated by duty cycle drive signals of  $S_{31}$  and  $S_{32}$  while the dc bus voltage,  $V_{b3}$ , is controlled by the phase shift angle,  $\varphi_{31}$ . The operation modes of the current-fed H-bridge converter depends on the variation range of duty ratio  $D_3$  (from 0 to 1) and phase shift angle  $\varphi_{31}$  (from 0 to  $\pi$ ). In the proposed converter the practical phase shift angle is less than  $\pi/2$ , and the duty cycle,  $D_3$ , is changed around 0.5 to achieve higher efficiency [5.51]. The ZVS operation mode of the current-fed converter is in a limited range compared with the conventional voltage-fed H-bridge inverter although in the case of equal volt-second for all windings of the magnetic link, ZVS operation is guaranteed for other two ports of the TAB converter [5.7].

### 5.6.3 Control strategy of the current-fed converter

As presented in Fig.5.45 the PV port of TAB converter can be decomposed into an inter-leaved current-fed boost converter cascaded by a voltage-fed H-bridge dc-ac converter [5.51]. The switching devices of the boost converter are shared with the H-bridge converter during steady state operation. Therefore two independent control loops should be designed for PV port to control both converters.

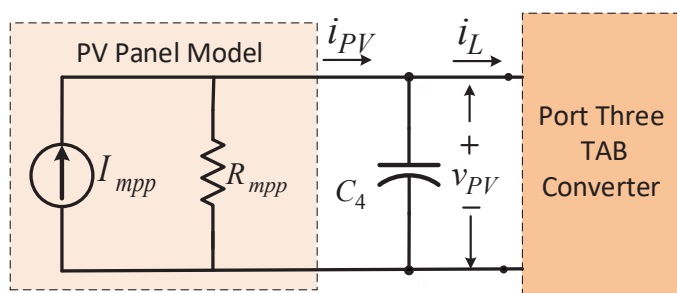


Fig.5.46 The equivalent circuit of PV panel for dual loop voltage control analysis

The PV port controller should contain an MPPT to adjust the PV operation point on MPP and a voltage regulation controller to regulate the voltage of dc bus. The control loops should be decoupled according to their speed response to avoid any instability in the control process. The bus voltage is controlled by phase shift angle  $\varphi_{31}$  as already

discussed in the TAB converter analysis. This section provides the details of MPPT controller.

#### 5.6.4 Design of MPPT controller

To design the PV voltage controller, a small signal model of both the PV port and current-fed converter are required. The equivalent circuit of the PV panel and the output capacitor for high frequency small signal analysis is presented in Fig.5.46. As can be seen, the PV panel is modelled as an independent current source paralleled with an equivalent PV resistor at MPP [5.51]. The equivalent resistor  $R_{mpp}$  can be calculated from  $R_{mpp}=V_{mpp}/I_{mpp}$  where  $V_{mpp}$  and  $I_{mpp}$  are the PV panel output voltage and output current at MPP respectively.

To design a more robust controller for adjusting the PV voltage on MPP a dual loop control system including inner current loop and outer voltage loop controllers is proposed [5.51]. The PV voltage control circuit presented in Fig.5.45 can be decomposed in two separate equivalent circuits for PV voltage and inductor current. The PV output voltage,  $v_{PV}$ , is a function of inductor current  $i_l$  and further duty cycle,  $D_3$ , and the dc bus voltage,  $V_{b3}$ . The equivalent circuit is used to calculate the transfer function of PV output voltage as control output to the inductor current as control input. The state space average equation (referring to Fig.5.46) can be written as

$$C_4 \frac{dv_{PV}}{dt} + i_L + \frac{v_{PV}}{R_{mpp}} - I_{mpp} = 0 \quad (5.83)$$

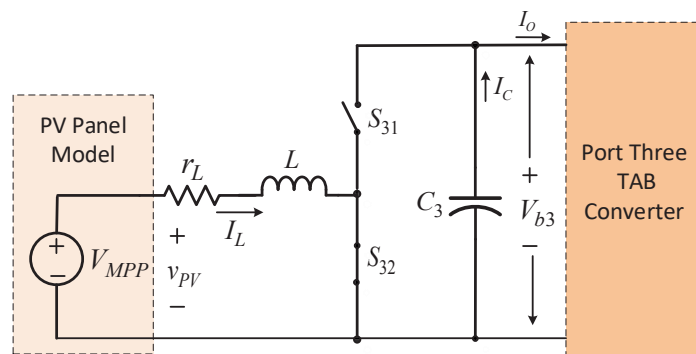


Fig.5.47 The equivalent circuit of buck-boost converter for PV dual loop control analysis

Adding small signal variations to the equation and considering only the ac elements, the equation can be rewritten as

$$C_4 \frac{d\hat{v}_{PV}}{dt} + \hat{i}_L + \frac{\hat{v}_{PV}}{R_{mpp}} = 0 \quad (5.84)$$

The transfer function of PV voltage to inductor current using the Laplace transform of (5.84) can then be found as

$$\frac{v_{PV}(s)}{i_L(s)} = \frac{-R_{mpp}}{1 + sC_4R_{mpp}} \quad (5.85)$$

On the other hand, for inductor current control, the PV panel is modelled as a constant voltage source equal to  $V_{mpp}$  because of its low dynamic response as illustrated in Fig.5.47. The state space equations for inductor current and PV output voltage over a complete switching period can be written as

$$\begin{cases} L_2 \frac{di_L}{dt} = v_{PV} - i_L r_L & 0 < t < DT \\ L_2 \frac{di_L}{dt} = v_{PV} - i_L r_L - v_{b3} & DT < t < T \end{cases} \quad (5.86)$$

The final equation by averaging the equation over a complete operation cycle can be defined as

$$L_2 \frac{di_L}{dt} = v_{PV} - i_L r_L - Dv_{b3} \quad (5.87)$$

The transfer function of dc bus voltage to inductor current then can be defined as

$$I_L(s) = \frac{-D}{sL_2 + r_L} v_{b3}(s) - \frac{V_{b3}}{sL_2 + r_L} d(s) \quad (5.88)$$

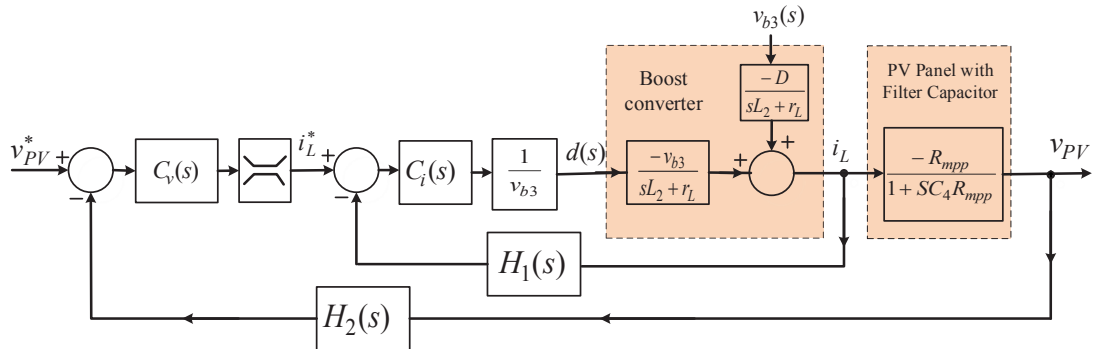


Fig.5.48 The dual loop control diagram of the PV voltage and inductor current

Fig.5.48 shows the proposed dual loop control diagram. The bandwidth of inner current loop should be selected much higher than that of PV voltage control loop. In this case the PV voltage control loop does not need to react against the high frequency voltage ripples. Therefore a low bandwidth control loop with more robustness and stability can be used. The block diagrams  $H_1(s)$  and  $H_2(s)$  are the transfer functions of low-pass first-order filters that filter out the high frequency components of PV output voltage  $v_{PV}$  and inductor current  $i_L$  respectively and can be defined as

$$H_1(s) = \frac{K_{f1}}{1 + \tau_1 s}, \quad H_2(s) = \frac{K_{f2}}{1 + \tau_2 s} \quad (5.89)$$

where  $\tau_1 = 1 \text{ ms}$  and  $\tau_2 = 0.6 \text{ ms}$  are the time constants of the filters. The feedback gains of  $K_{f1}$  and  $K_{f2}$  are selected according to the signal conditioning circuit parameters.  $C_v$  and  $C_i$  are the PI controller transfer functions and are defined as

$$C_i(s) = K_i \frac{1 + \tau_i s}{\tau_i s}, \quad C_v(s) = K_v \frac{1 + \tau_v s}{\tau_v s} \quad (5.90)$$

where  $\tau_i = 50 \text{ ms}$  and  $\tau_v = 1.5 \text{ ms}$  are the current loop and voltage loop controller time constants respectively and  $K_i = 0.8$  and  $K_v = 0.05$  are the proportional gains.

The bode diagrams of the PV inductor current loop and voltage control loop are simulated for converter parameters are illustrated in Table 5.5. As can be seen in Fig.5.49, the current loop has a crossover frequency of  $f_{ci} = 6.5 \text{ kHz}$  ( $\omega_{ci} = 40000 \text{ rad/s}$ ), gain margin of 20 dB and phase margin of  $95^\circ$ . On the other hand the crossover frequency of PV voltage control loop has a crossover frequency of  $f_{cv} = 30 \text{ Hz}$  ( $\omega_{cv} = 200 \text{ rad/s}$ ), gain margin of 43 dB and the phase margin of  $85^\circ$ .

Comparing the bandwidths of the voltage and current control loops shows that the current loop control has much higher speed response compared with the voltage loop ( $f_{cv} \ll f_{ci}$ ) which means faster reaction of the inductor current controller.

**TABLE 5.5 The PV Port Parameters for Small Signal Analysis**

$C_{PV}$	$C_{bus3}$	$V_{PV}$	$V_{bus3}$	$r_L$	$L$	$f_s$	$f_{mppt}$	$K_i$	$K_v$
100 $\mu\text{f}$	1200 $\mu\text{f}$	10-40 V	120 V	300 m $\Omega$	100 $\mu\text{H}$	10 kHz	10 Hz	0.8	0.05

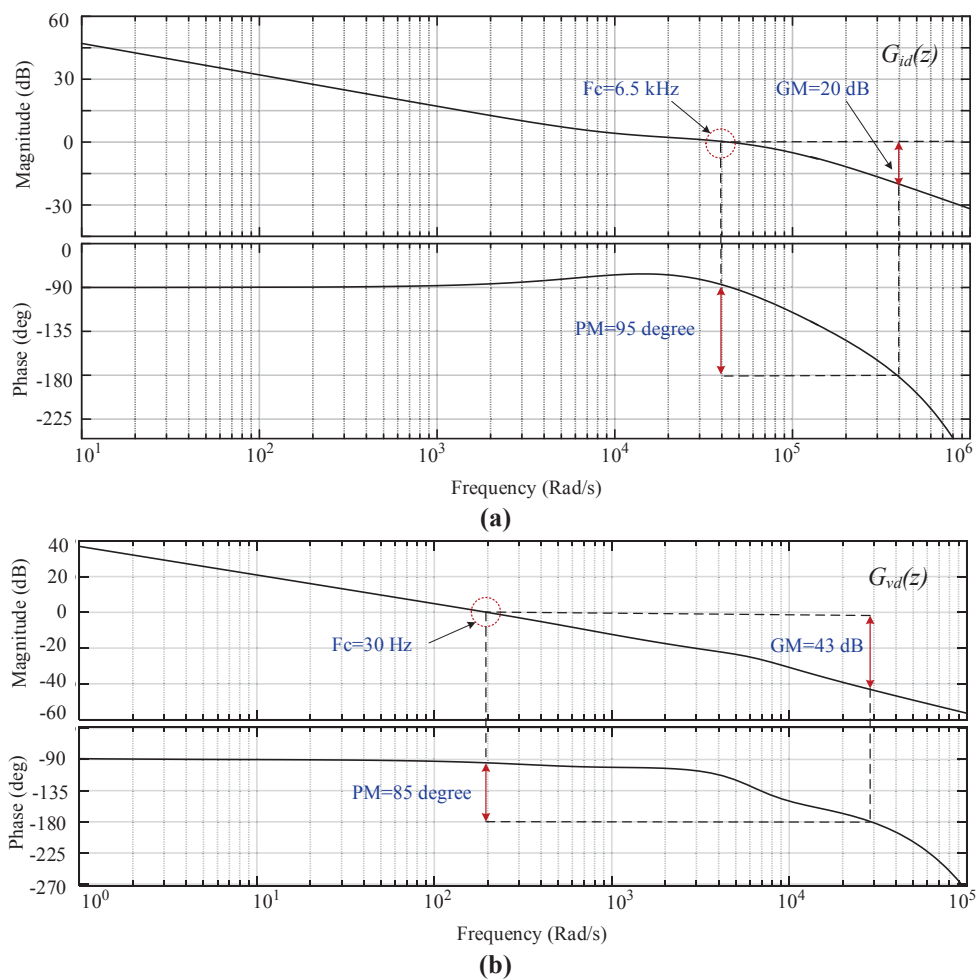


**Fig.5.49** The Bode plots of closed loop control, (a) PV voltage control loop, and (b) inductor current loop

### 5.6.5 Simulation of the PV port operation in steady state

The current-fed boost converter is simulated using MATLAB/Simulink. The simulated waveforms are presented in Fig.5.50. According to the schematic of the converter presented in Fig.5.6, there are two separate boost converters sharing input and output sources. Each converter employs one of the conversion legs of the H-bridge of PV port. The ac signal generated on PV port  $v_3$ , current in inductor  $L_1$  ( $I_{L1}$ ), current in inductor  $L_2$  ( $I_{L2}$ ), summation of two inductor current and the current received from PV panel  $I_s$  after passing through the low-pass filter are presented in the figure. As can be seen the frequency of current received from PV panel is twice the frequency of each boost converter and the resulting current ripple is half of each boost converter. The average current  $I_L$ , in the first case where  $D_4=0.6$  is about 2A and it increases to 12A for  $D_4=0.9$ . The converter parameters for the simulation are selected as  $f_s=10$  kHz,  $L_1=L_2=100$   $\mu H$ ,  $C_{PV}=1000$   $\mu f$ .

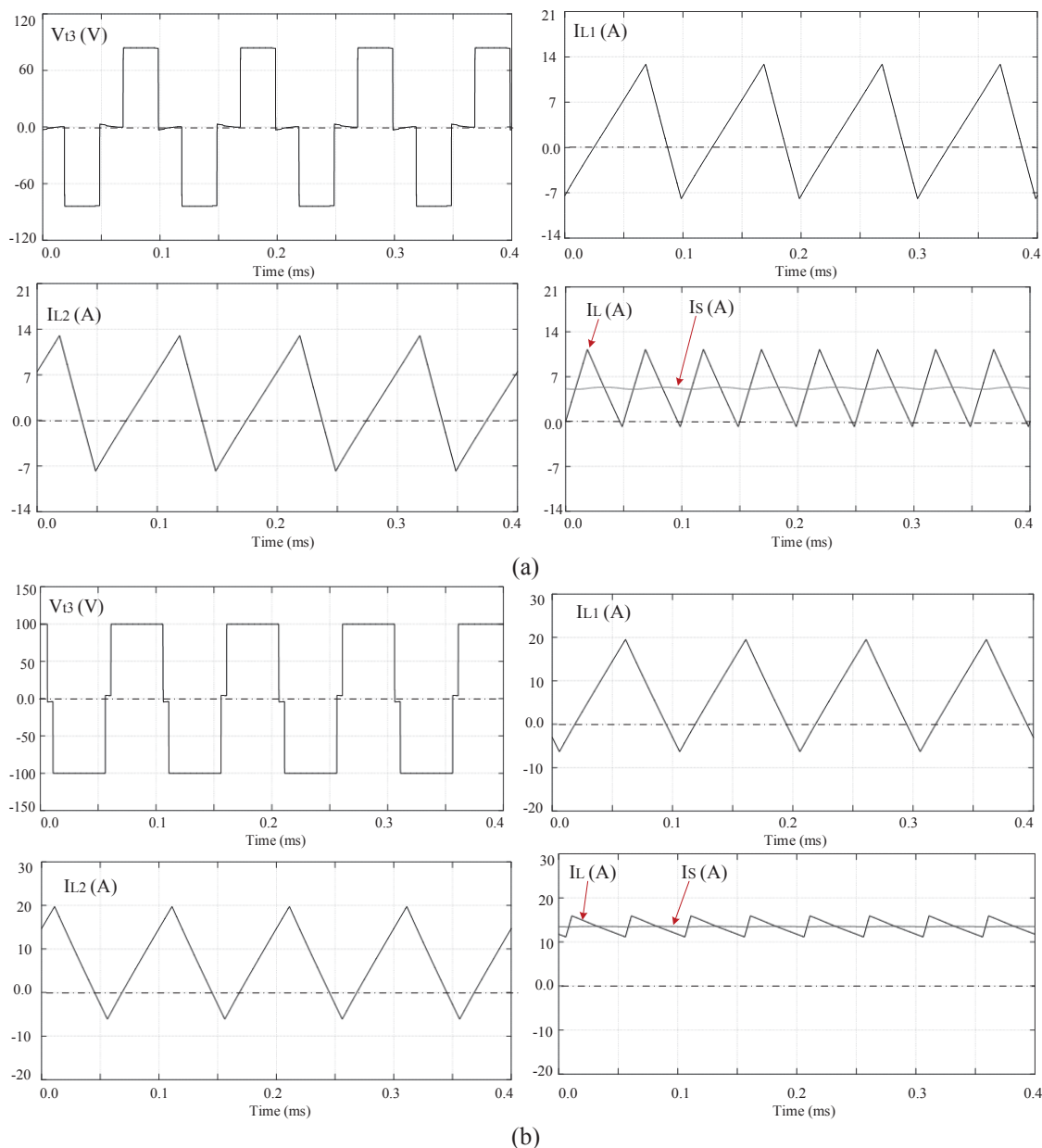


**Fig.5.50 Simulated waveforms of current-fed boost converter**

### 5.6.6 Experimental test results

The current-fed boost converter is developed experimentally and the waveforms are measured under the same conditions as simulations. The recorded waveforms are presented in Fig.5.51. As can be seen the simulation results are verified by experimental measurements. As is expected from simulation results, increasing duty cycle the port voltage  $V_{13}$  from 0.6 to 0.9 raises the average current received from PV port from 2A to 12A. Similar to the simulation results, the resultant ripple in the current received from PV port  $I_S$ , reduced with increasing duty cycle. Comparing simulated and experimentally measured waveforms validate the simulations and the converter design process.

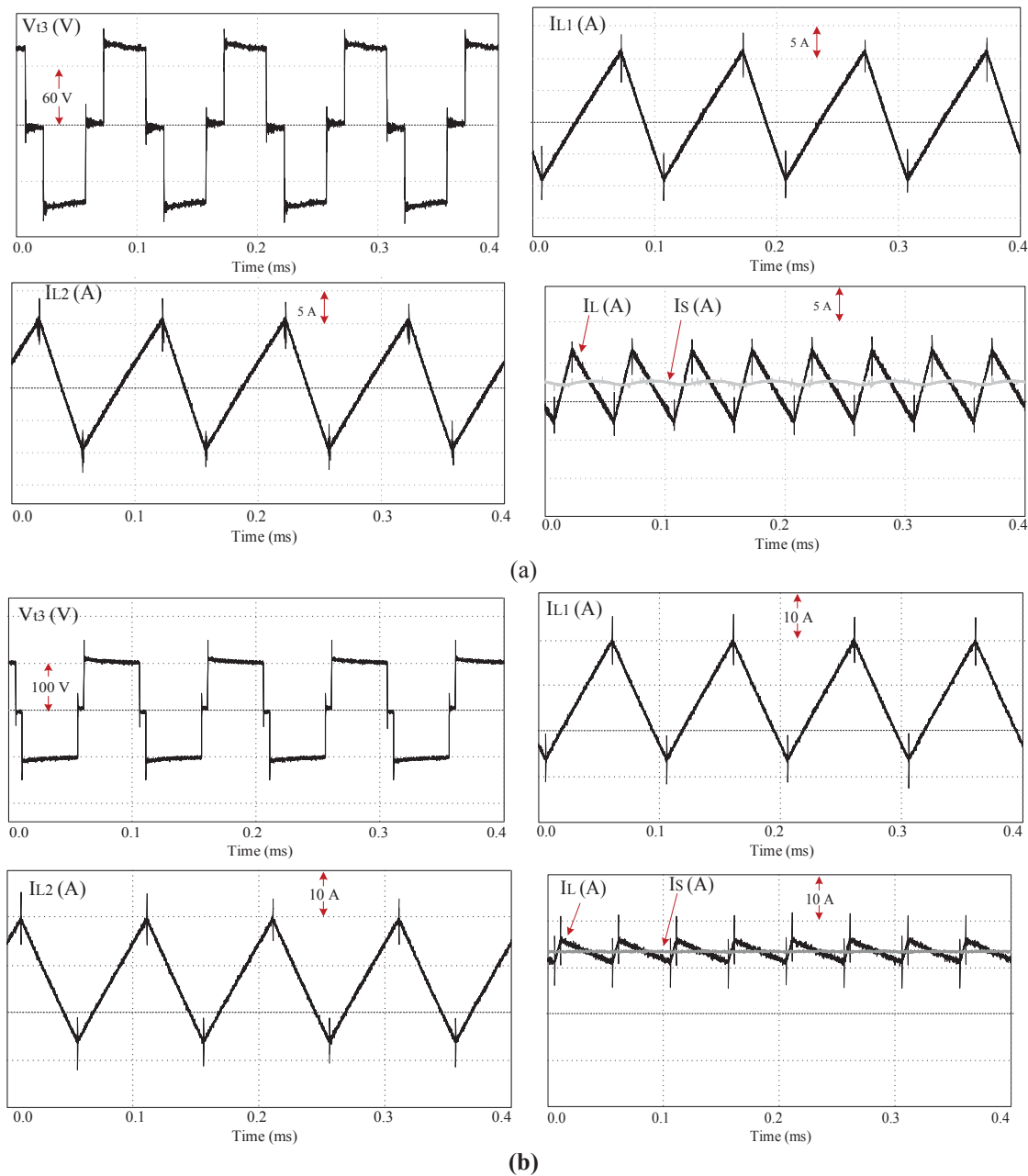


**Fig.5.51 Experimentally measured waveforms of current-fed boost converter**

### 5.7 Analysis of Single Phase Bi-directional Inverter

This section provides some information on grid interface of micro-grid and line interactive single phase inverter. To connect the micro-grid to the main grid it is required to detect the status of grid parameters such as amplitude, phase and frequency continuously. The proposed micro-grid is designed to operate in both grid-connected and islanding modes. The micro-grid should switch to islanding mode when the utility grid is not available or there is an accidental power outage.

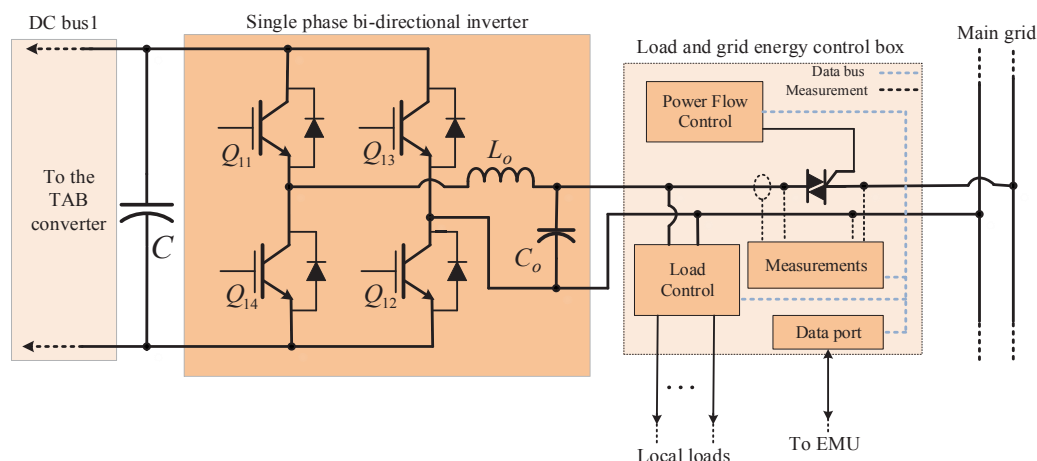


**Fig.5.52 Schematic of inverter as a part of proposed micro-grid**

Fig.5.52 shows the schematic of single phase inverter linked to the main grid. Inductor  $L_o$  and capacitor  $C_o$  form a low-pass filter at the inverter output.

As can be seen, a single phase PWM inverter is used to interface the dc part of the micro-grid to the ac loads and main grid. It also can be used as an active shunt filter connected in parallel to the ac loads to provide the reactive power requested by residential load and injects the required harmonics to rectify the current received by loads from the main grid. Selection of single phase inverter compared with the three phase system is due to the power range of a typical residential house (3- 4 kW) although it can be changed to the three phase by applying slight changes to the structure. On the other hand, residential distribution grids are mainly based on the single phase system. As can be seen, the inverter output is linked to the grid via a load and grid energy control (LGEC) box. The control strategy of single phase inverter and simulated and experimental waveforms are presented in the next section.

### 5.7.1 Control strategy of the single phase bi-directional inverter

A large number of researches have been conducted on control methods of inverters in both grid-connected and islanded mode [5.52]-[5.54]. The main control objective in grid-connected mode is output current and in off-grid operation is output voltage. In the proposed inverter a direct current-control strategy is used to force the instantaneous output current to follow the provided sinusoidal reference voltage [5.54].



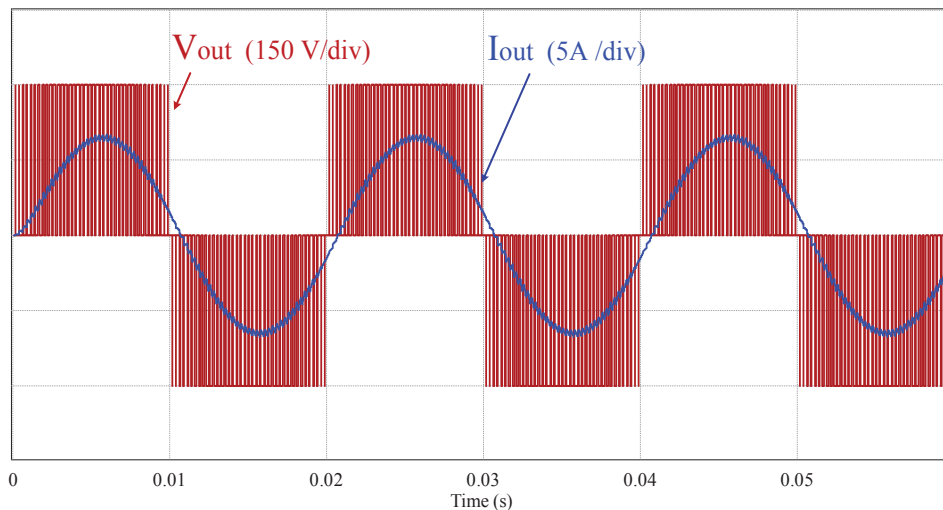
case that the TAB converter is not working, the inverter should be turned off although the high voltage bus capacitor  $C_5$ , is still charged through the anti-parallel diodes of the inverter switches.

In the rectifier mode, the current in the negative direction has a small value which is used to charge the bus capacitors and compensate the switching losses of the converter. This stabilizes the dc bus voltage on the nominal value whether the TAB converter is active or not. The current in the inductor  $L_o$ , presented as  $i_o$ , is measured by using a Hall effect sensors, passed through the signal conditioning circuits on the interface board, and sent to the DSP2. It is compared with the reference current,  $i_{ref}$ , and the resultant error signal is sent to the PI controller in the current-feedback control loop. To avoid instabilities in the control, the crossing frequency of current control loop is designed to be 2.3 kHz.

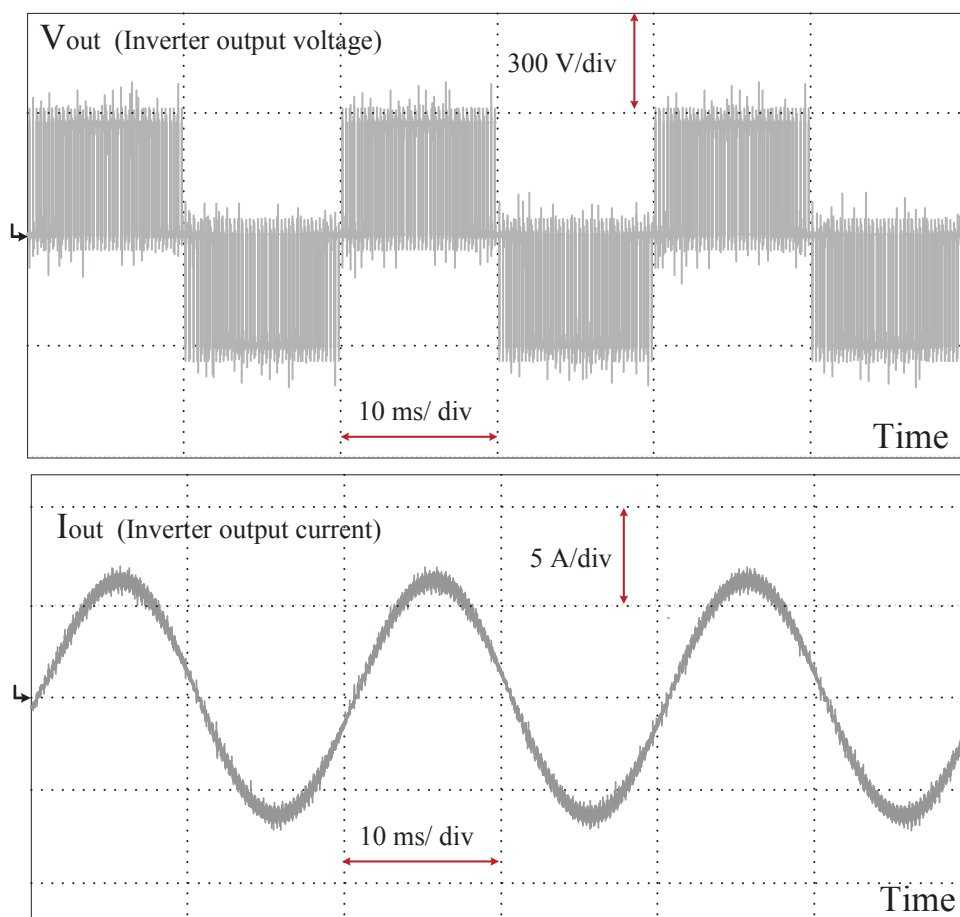
A common problem in grid-tied inverters is the appearance of a voltage ripple with the frequency  $2\omega$  on the dc bus voltage. Therefore, a compensation block is added to the designed voltage control loop as a feed forward input. The compensation block is equal to the  $V_{ref}/V_{b3}$  which applies a reverse fluctuating signal with frequency  $2\omega$  to the inductor current to compensate the ripple on the dc bus.

On the other hand, to achieve low THD of the output current due to the slight distortions of the input ac voltage, another compensation block as a feed forward input is added to the current control loop. The applied feed forward control does not have considerable effect on the system's zeros and poles configuration, but improves the tracking of the sinusoidal reference and harmonic contents of the output current [5.54].

To compensate the fluctuation of the grid voltage and reduce the harmonic contents of the output current, it is required to apply the defective component of grid voltage directly to the modulating signal,  $V_{mod}$ . Therefore, the real-time signal of grid voltage multiplied to a proportional gain,  $K_P$ , is applied to the control loop as a feed-forward signal. The resultant signal is added to the output of PI controller,  $V_a$ , in the current loop and is sent to the PWM generator unit as a modulating signal to produce the drive signals for the inverter switches. The effects of both feed forward compensation blocks can be adjusted by their scaling factors,  $K_P$  and  $K_F$ . A phase-locked-loop (PLL) is designed to define the frequency and phase of the current reference,  $i_{ref}$ , and to synchronize it with the utility grid voltage,  $v_g$ .



(a)



(b)

Fig.5.54 Simulation and experimental waveforms of the bidirectional inverter

### 5.7.2 Simulation and experimental tests of single phase bi-directional inverter

The single phase bidirectional inverter is simulated using PSIM. Fig.5.54 shows the simulated waveforms of the output current and output voltage of the bidirectional

converter. As can be seen the output current is in sinusoidal form with THD=6 %. The proposed inverter also is implemented using H bridge units made by SEMIKRON as presented in Fig.5.4 (b). The experimentally measured waveforms of voltage and current of the inverter are presented in Fig.5.54.

### **5.8 Summary of the Chapter**

A device level study on the dc-dc converters and bidirectional inverter as the main part of the proposed micro-grid was presented in this chapter. The micro-grid topology contains a TAB dc-dc converter, a bidirectional buck-boost dc-dc converter, a buck-boost dc-dc converter and a single phase bidirectional inverter. The study started with analysis of each converter topology, operation modes of the converter in steady state and resultant voltage and current waveforms. The conditions for soft switching operation and the limits are studied briefly. To design the appropriate control loop for each converter, small signal models are derived and the closed loop controllers are designed.

To validate the designed converter and evaluate operation of controllers, converter topologies are simulated using MATLAB/Simulink and the simulated waveforms are obtained. A prototype of each converter then was developed and the experimental tests were conducted on the system to validate the design process and simulation results. Comparison of simulations and experimentally measured waveforms validated the design process of each converter.

**References**

- [5.1] D. Liu and H. Li, "A ZVS Bi-Directional DC-DC Converter for Multiple Energy Storage Elements," *IEEE Trans. Power Electronics*, vol. 21, no. 5, pp. 1513-1517, Sept. 2006.
- [5.2] H. Tao, J. L. Duarte, M. A. M. Hendrix, "Three-port triple-half bridge bidirectional converter with zero voltage switching," *IEEE Trans. Power Electronics*, vol. 23, no.2, pp 782–792, March 2008.
- [5.3] C. Zhao, S. D. Round and J. W. Kolar, "An Isolated Three-Port Bidirectional DC-DC Converter With Decoupled Power Flow Management," *IEEE Trans. Power Electronics*, vol. 23, no. 5, pp. 2443-2453, Sept. 2008.
- [5.4] S. Falcones, R. Ayyanar and X. Mao, "A DC–DC Multiport-Converter-Based Solid-State Transformer Integrating Distributed Generation and Storage," *IEEE Trans. Power Electronics*, vol. 28, no. 5, pp. 2192-2203, May 2013.
- [5.5] M. Phattanasak, R. Gavagsaz-Ghoachani, J. P. Martin, B. Nahid-Mobarakeh, S. Pierfederici and B. Davat, "Control of a Hybrid Energy Source Comprising a Fuel Cell and Two Storage Devices Using Isolated Three-Port Bidirectional DC–DC Converters," *IEEE Trans. Ind. Applications*, vol. 51, no. 1, pp. 491-497, Jan.-Feb. 2015.
- [5.6] H. Tao, A. Kotsopoulos, J. L. Duarte and M. A. M. Hendrix, "Transformer-Coupled Multiport ZVS Bidirectional DC–DC Converter With Wide Input Range," *IEEE Trans. Power Electronics*, vol. 23, no. 2, pp. 771-781, March 2008.
- [5.7] Tao, H.(2008).Phd thesis, Integration of sustainable energy sources through power electronic converters in small distributed electricity generation systems Eindhoven: Technische Universiteit Eindhoven DOI: 10.6100/IR632347
- [5.8] R. W. A. A. De Doncker, D. M. Divan and M. H. Kheraluwala, "A three-phase soft-switched high-power-density DC/DC converter for high-power applications," *IEEE Trans. Ind. Applications*, vol. 27, no. 1, pp. 63-73, Jan/Feb 1991.
- [5.9] M. Jafari, Z. Malekjamshidi and J. G. Zhu, "Analysis of operation modes and limitations of dual active bridge phase shift converter," in *proc. 11th IEEE Int. Conf. Power Electronics and Drive Systems*, Sydney, NSW, 2015, pp. 393-398.

- [5.10] R. T. Naayagi, A. J. Forsyth and R. Shuttleworth, "High-Power Bidirectional DC–DC Converter for Aerospace Applications," *IEEE Trans. Power Electronics*, vol. 27, no. 11, pp. 4366-4379, Nov. 2012.
- [5.11] H. Qin and J. W. Kimball, "Solid-State Transformer Architecture Using AC–AC Dual-Active-Bridge Converter," *IEEE Trans. Ind. Electronics*, vol. 60, no. 9, pp. 3720-3730, Sept. 2013.
- [5.12] P. He; A. Khaligh, "Comprehensive Analyses and Comparison of 1kW Isolated DC-DC Converters for Bidirectional EV Charging Systems," *IEEE Trans. Transportation Electrification* , vol.PP, no.99, pp.1-1
- [5.13] W. Choi, K. M. Rho and B. H. Cho, "Fundamental Duty Modulation of Dual-Active-Bridge Converter for Wide-Range Operation," *IEEE Trans. Power Electronics*, vol. 31, no. 6, pp. 4048-4064, June 2016.
- [5.14] M. N. Kheraluwala, R. W. Gascoigne, D. M. Divan and E. D. Baumann, "Performance characterization of a high-power dual active bridge DC-to-DC converter," *IEEE Trans. Ind. Applications*, vol. 28, no. 6, pp. 1294-1301, Nov/Dec 1992.
- [5.15] A. K. Jain and R. Ayyanar, "PWM control of dual active bridge: Comprehensive analysis and experimental verification," *IEEE Trans. Power Electronics*, vol. 26, no. 4, pp. 1215-1227, April 2011.
- [5.16] J. Everts, J. Van den Keybus, F. Krismer, J. Driesen and J. W. Kolar, "Switching control strategy for full ZVS soft-switching operation of a Dual Active Bridge AC/DC converter," in *proc. 27th Annual IEEE Applied Power Electronics Conf. and Exposition (APEC)*, Orlando, FL, 2012, pp. 1048-1055.
- [5.17] Zhou and A. M. Khambadkone, "Hybrid modulation for dual-active-bridge bidirectional converter with extended power range for ultracapacitor application," *IEEE Trans. Ind. Applications*, vol. 45, pp. 1434–1442, July 2009.
- [5.18] P. Bezerra, F. Krismer, R. Burkart, and J. Kolar, "Bidirectional isolated non-resonant dab dc-dc converter for ultra-wide input voltage range applications," in *proc. Electronics and Application Conference and Exposition (PEAC)*, 2014 International, pp. 1038–1044, Nov 2014.
- [5.19] J. Zhang, J. S. Lai, R. Y. Kim and W. Yu, "High-Power Density Design of a Soft-Switching High-Power Bidirectional dc–dc Converter," *IEEE Trans. Power Electronics*, vol. 22, no. 4, pp. 1145-1153, July 2007.

- [5.20] Haiping Xu, Xuhui Wen, Ermin Qiao, Xin Guo and Li Kong, "High Power Interleaved Boost Converter in Fuel Cell Hybrid Electric Vehicle," in *proc IEEE Int. Conf. on Electric Machines and Drives, 2005.*, San Antonio, TX, 2005, pp. 1814-1819.
- [5.21] O. Hegazy, J. V. Mierlo and P. Lataire, "Analysis, Modeling, and Implementation of a Multidevice Interleaved DC/DC Converter for Fuel Cell Hybrid Electric Vehicles," *IEEE Trans. Power Electronics*, vol. 27, no. 11, pp. 4445-4458, Nov. 2012.
- [5.22] J. Zhang "Bidirectional DC-DC Power Converter Design Optimization, Modeling and Control," Ph.D. Dissertation, VPI&SU, 2008.
- [5.23] O. Ellabban, J. Van Mierlo and P. Lataire, "A DSP-Based Dual-Loop Peak DC-link Voltage Control Strategy of the Z-Source Inverter," *IEEE Trans. Power Electronics*, vol. 27, no. 9, pp. 4088-4097, Sept. 2012.
- [5.24] Simone Buso and Paolo Mattavelli, "Digital Control in Power Electronics", Morgan and Claypool Publishers, 2006.
- [5.25] M. Jafari, G. Platt, Z. Malekjamshidi and J. G. Zhu, "Technical issues of sizing Lead-Acid batteries for application in residential renewable energy systems," in *proc. 4th Int. Conf. on Electric Power and Energy Conversion Systems (EPECS)*, Sharjah, 2015, pp. 1-6.
- [5.26] S. Barsali and M. Ceraolo, "Dynamical models of lead-acid batteries: implementation issues," *IEEE Trans. Energy Conversion*, vol. 17, no. 1, pp. 16-23, Mar 2002.
- [5.27] Z. M. Salameh, M. A. Casacca and W. A. Lynch, "A mathematical model for lead-acid batteries," *IEEE Trans. Energy Conversion*, vol. 7, no. 1, pp. 93-98, Mar 1992.
- [5.28] Datasheet provided by Horizon fuel cell company, <http://www.horizonfuelcell.com/h-series-stacks>
- [5.29] P. J. H. Wingelaar, J. L. Duarte and M. A. M. Hendrix, "Dynamic Characteristics of PEM Fuel Cells," in *proc. 36th IEEE Power Electronics Specialists Conference*, Recife, 2005, pp. 1635-1641.
- [5.30] J. Lamine and A. Dicks, Fuel cell systems explained. Chichester: John Wiley & Sons Ltd. 2001.
- [5.31] T. S. Hwang, M. J. Tarca and S. Y. Park, "Dynamic Response Analysis of DC-DC Converter With Supercapacitor for Direct Borohydride Fuel Cell Power

- Conditioning System,” *IEEE Trans. Power Electronics*, vol. 27, no. 8, pp. 3605-3615, Aug. 2012.
- [5.32] S. Buso and P. Mattavelli, *Digital Control in Power Electronics*. United States of America: Morgan and Claypool Publishers, 2006.
- [5.33] T. Esum and P. L. Chapman, “Comparison of Photovoltaic Array Maximum Power Point Tracking Techniques,” *IEEE Trans. Energy Conversion*, vol. 22, no. 2, pp. 439-449, June 2007.
- [5.34] Roberto Francisco Coelho and Denizar Cruz Martins, An Optimized Maximum Power Point Tracking Method Based on PV Surface Temperature Measurement, Sustainable Energy - Recent Studies Downloaded from:  
<http://www.intechopen.com/books/sustainable-energy-recentstudies>
- [5.35] T. Esum and P. L. Chapman, “Comparison of Photovoltaic Array Maximum Power Point Tracking Techniques,” *IEEE Trans. Energy Conversion*, vol. 22, no. 2, pp. 439-449, June 2007.
- [5.36] J. J. Schoeman and J. D. Wyk, “A simplified maximal power controller for terrestrial photovoltaic panel arrays,” in *Proc. 13th Annu. IEEE Power Electron. Spec. Conf.*, 1982, pp. 361–367.
- [5.37] M. A. S. Masoum, H. Dehbonei, and E. F. Fuchs, “Theoretical and experimental analyses of photovoltaic systems with voltage- and current-based maximum power-point tracking,” *IEEE Trans. Energy Conversion.*, vol. 17, no. 4, pp. 514–522, Dec. 2002.
- [5.38] N. Femia, G. Petrone, G. Spagnuolo, and M. Vitelli, “Optimization of perturb and observe maximum power point tracking method,” *IEEE Trans. Power Electronics.*, vol. 20, no. 4, pp. 963–973, Jul. 2005.
- [5.39] B. N. Alajmi, K. H. Ahmed, S. J. Finney and B. W. Williams, “Fuzzy-Logic-Control Approach of a Modified Hill-Climbing Method for Maximum Power Point in Microgrid Standalone Photovoltaic System,” *IEEE Trans. Power Electronics*, vol. 26, no. 4, pp. 1022-1030, April 2011.
- [5.40] F. Liu, S. Duan, F. Liu, B. Liu and Y. Kang, “A Variable Step Size INC MPPT Method for PV Systems,” *IEEE Trans. Ind. Electronics*, vol. 55, no. 7, pp. 2622-2628, July 2008.
- [5.41] G. C. Hsieh, H. I. Hsieh, C. Y. Tsai and C. H. Wang, “Photovoltaic Power-Increment-Aided Incremental-Conductance MPPT With Two-Phased Tracking,” *IEEE Trans. Power Electronics*, vol. 28, no. 6, pp. 2895-2911, June 2013.

- [5.42] Q. Mei, M. Shan, L. Liu and J. M. Guerrero, "A Novel Improved Variable Step-Size Incremental-Resistance MPPT Method for PV Systems," *IEEE Trans. Ind. Electronics*, vol. 58, no. 6, pp. 2427-2434, June 2011.
- [5.43] A. Safari and S. Mekhilef, "Simulation and Hardware Implementation of Incremental Conductance MPPT With Direct Control Method Using Cuk Converter," *IEEE Trans. Industrial Electronics*, vol. 58, no. 4, pp. 1154-1161, April 2011.
- [5.44] T. Wu, C. Chang, and Y. Chen, "A fuzzy-logic-controlled single-stage converter for PV-powered lighting systems applications," *IEEE Trans. Ind. Electronics*, vol. 47, no. 2, pp. 287-296, Apr. 2000.
- [5.45] M. Veerachary, T. Senjyu, and K. Uezato, "Neural-network-based maximum-power-point tracking of coupled-inductor interleaved-boost converter- supplied PV system using fuzzy controller," *IEEE Trans. Ind. Electronics*, vol. 50, no. 4, pp. 749-758, Aug. 2003.
- [5.46] K. Noppadol, W. Theerayod, and S. Phaophak, "FPGA implementation of MPPT using variable step-size P&O algorithm for PV applications," in *Proc. ISCIT*, 2006, pp. 212-215.
- [5.47] A. Pandey, N. Dasgupta, and A. K. Mukerjee, "Design issues in implementing MPPT for improved tracking and dynamic performance," in *Proc. IEEE IECON*, 2006, pp. 4387-4391.
- [5.48] W. Xiao and W. G. Dunford, "A modified adaptive hill climbing MPPT method for photovoltaic power systems," in *Proc. IEEE PESC*, 2004, pp. 1957-1963.
- [5.49] Z. Wang and H. Li, "An integrated three-port bidirectional dc-dc converter for PV application on a dc distribution system," *IEEE Trans. Power Electronics*, vol. 28, no. 10, pp. 4612-4624, Oct. 2013.
- [5.50] X. Liu, H. Li, and Z. Wang, "A fuel cell power conditioning system with low-frequency ripple-free input current using a control-oriented power pulsation decoupling strategy," *IEEE Trans. Power Electronics*, vol. 29, no. 1, pp. 159-169, Jan. 2014.
- [5.51] Y. Shi, R. Li, Y. Xue and H. Li, "High-Frequency-Link-Based Grid-Tied PV System With Small DC-Link Capacitor and Low-Frequency Ripple-Free Maximum Power Point Tracking," *IEEE Trans. Power Electronics*, vol. 31, no. 1, pp. 328-339, Jan. 2016.

- [5.52] T. F. Wu, C. L. Kuo, L. C. Lin and Y. K. Chen, "DC-Bus Voltage Regulation for a DC Distribution System With a Single-Phase Bidirectional Inverter," *IEEE Journal of Emerging and Selected Topics in Power Electronics*, vol. 4, no. 1, pp. 210-220, March 2016.
- [5.53] T. F. Wu, C. L. Kuo, K. H. Sun, Y. K. Chen, Y. R. Chang and Y. D. Lee, "Integration and Operation of a Single-Phase Bidirectional Inverter With Two Buck/Boost MPPTs for DC-Distribution Applications," *IEEE Trans. Power Electronics*, vol. 28, no. 11, pp. 5098-5106, Nov. 2013.
- [5.54] B. Yang, W. Li, Y. Zhao and X. He, "Design and Analysis of a Grid-Connected Photovoltaic Power System," *IEEE Trans. Power Electronics*, vol. 25, no. 4, pp. 992-1000, April 2010.
- [5.55] M. P. Kazmierkowski and L. Malesani, "Current control techniques for three-phase Voltage-Source PWM Converters: A survey," *IEEE Trans. Ind. Electronics.*, vol. 45, no. 5, pp. 691–703, Oct. 1998.
- [5.56] M. Cichowias and M. P. Kamierkowski, "Comparison of current control techniques for PWM rectifiers," in *Proc. IEEE Int. Symp.*, 2002, pp. 1259–1263.

## CHAPTER 6

# SYSTEM CONTROL AND ENERGY MANAGEMENT

### 6.1 Introduction

In the last decade, there has been a great interest in renewable energy sources as a feasible solution to mitigate environmental issues and reduce the dependence on the traditional sources for electricity generation. The need for technology for integrating these non-traditional types of energy sources into the existing grid has motivated the development of the new smart micro-grid concept. The smart micro-grid is recognized as a feasible solution to the new challenges of existing grid network such as increasing energy demand and penetration of renewable energy sources at the consumer end [6.1]-[6.3].

On the other hand, residential consumers as an important part of the future network should be able to integrate their renewable sources such as wind turbines and photovoltaic (PV) panels into the grid [6.4]. Based on this, there is a need for the design and development of new converter topologies and smart energy management methods to implement the new concepts. The new converters have to meet higher efficiency and power density standards, fast power flow control among the ports, data communication with the micro-grid control center, bidirectional power flow capability, more flexibility, and higher reliability [6.5]-[6.7]. On the other hand, new energy management and control techniques are required to control the power flows inside the micro-grid and between the micro-grid and the main grid.

Energy control boxes have been traditionally used to control the energy consumption inside households by automatic control of some shiftable loads. This enables the residential consumers to adapt their energy consumption to the time-pricing and new services of the main grid. On the other hand, using energy control boxes has improved the power efficiency and quality in the main grid by shifting loads to the off-peak hours [\*\*].

Recent energy management systems are designed to match the generated energy of renewables inside the micro-grid with the load demand in an optimal way. The energy management strategies are developed according to the new smart micro-grid concepts. The distribution network is combined with a higher level communication network to adapt the operation of energy management units with the main grid requirements.

In this chapter, a fuzzy based energy management unit (FBEMU) is proposed to control the power flow inside the micro-grid and between the micro-grid and the distribution network to implement the long term energy plans. The fuzzy control technique is selected due to its simplicity and independency to the systems model. The proposed FBEMU contains two controllers represented as long-term and short-term fuzzy controllers. In this case both the real-time value of systems parameters and long-term energy plans are taken into account. The operation of the proposed energy management unit (EMU) is validated experimentally for three different scenarios of the micro-grid conditions.

## **6.2 Energy Management in Residential Households**

Electricity is widely used in residential households due to its convenient transfer, widespread application, and easy transform to other energy forms. According to the EU report on energy trends to 2030, the demand for electrical energy increases considerably in the residential sector and it is replaced with natural gas for electrical cooking and heating purposes [6.8], [6.9]. Residential energy management techniques and systems have found extensive attention due to the importance of the residential sector as one of the major contributors to the global energy consumption. The main research fields in the residential energy management are related to the smart energy homes and demand side management (DSM) techniques. The following sections provide a review on the concept of smart home and DSM as a detailed study of these subjects is outside of the scope of this thesis.

### **6.2.1 Smart energy homes**

Due to the importance of the house as a place for individuals to spend their time, rest and relax, development of more reliable, comfortable and environmental friendly homes has attracted great attentions [6.10],[6.11]. The main concept of the smart energy home

is the improvement of home quality for occupants using new construction materials and technologies.

Smart homes are designed as a solution for a more sustainable and smarter living environment. From an electrical energy consumption point of view, they can monitor and control the energy usage of the house, maintaining minimum influence on occupants' comfort and life style. In a smart energy house energy consumption is monitored and controlled by using home automation technologies. The benefits of such a system are the improvement of comfort, security and convenience of inhabitants through intelligent management of energy in the house. The smart home concept is extended to smart city by integrating the smart energy houses into a bigger smart grid concept. "The smart city is characterized by the main elements such as smart people, smart life style, smart mobility, smart environment, smart economy and smart governance"[6.9],[6.12]. As discussed in Chapter One, smart micro-grids are required infrastructures for contribution, control and management of smart energy homes according to the smart city concepts. The renewable energy system in a smart home, as a small scale model of a public grid, comprises electricity generation, distribution and consumption. It can be classified as a nano-grid in contrast to the large scale micro-grids. The smart energy homes are required to interconnect through a proper communication network to the higher layers of control and management of smart grid. They also need some fundamental components and technologies to adapt to the large scale smart micro-grid requirements. Some of these technologies are smart meters, smart sensors, smart appliances, and proper communication network, control and monitoring systems.

### **6.2.2 Demand side management (DSM)**

Over the past decades, there has been much attention on demand side management techniques as a solution for management and control of energy consumption at the consumer side. In brief, demand side management is described as a group of actions and technologies that are used to plan, manage, and control the energy usage of end users which results in the improvement of quality of energy supplied by the grid [6.13]. The outcome of demand side management on the shape of load profile is presented in Fig.6.1 and can be classified in the following groups [6.14]:

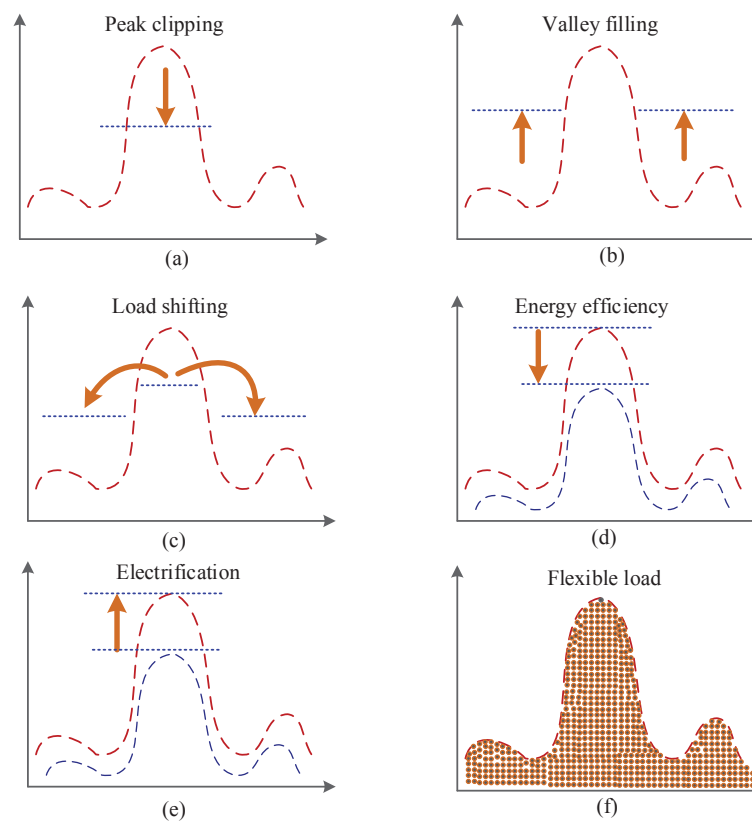


**Fig.6.1 The effects of DSM on the shape of load profile**

- (1) Peak clipping
- (2) Valley filling
- (3) Load shifting
- (4) Energy efficiency
- (5) Electrification, and
- (6) Flexible load shape.

DSM can improve all stages of electrical energy systems including generation, transmission, distribution and consumption [6.15]. In the generation section it reduces the generation cost by reducing the required generation capacity margin and increases the generation efficiency. In the transmission section, it can improve the operation efficiency of the transmission lines. It can also enable the grid to handle higher power transfers and deal with technical failures. In the case of distribution systems, it can enable the real time management of required energy and improvement of the control levels in the distribution network using distributed generation. In the energy consumption section, it can reduce the variation range of the load energy demand during the day and year.

Despite the benefits discussed above, the DSM technologies have still not yet developed in the residential sector due to the lack of required ICT infrastructures and proper support from the electricity market. On the other hand, DSM increases the complexity of distribution networks [6.15].

Fig.6.2 shows the architecture of a DSM framework including the required components in both residential and smart-grid domains [6.16]. The main components of DSM in the residential domain are [6.16]-[6.19]:

- (1) Local renewable energy generators, such as PV, wind turbine, and fuel cell,
- (2) Smart electrical appliances which are self-monitored and remote controlled with ability to communicate with the energy management unit through a home area network (HAN),
- (3) Smart sensors and measurement devices to monitor, measure and record the required data such as temperature, light, position and electrical parameters,
- (4) Energy storage systems to store the surplus energy generated by renewables and release it to the supply bus on request which improves the flexibility of energy management and control,
- (5) EMU to control and manage the energy in the residential domain according to the DSM objectives and communicate with the regional distribution network control center, and
- (6) Regional distribution network which is responsible for electricity distribution, operation, marketing, and services to the customers.

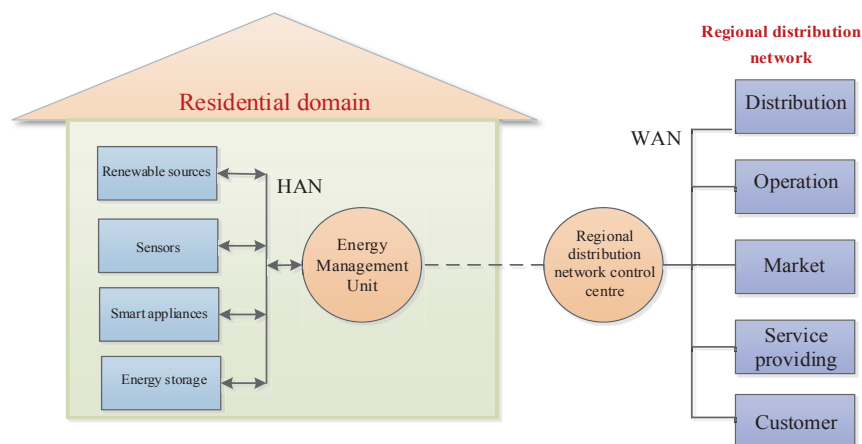


**Fig.6.2 Architecture of DSM in residential micro-grid [6.16]**

As can be seen in the figure, the elements in the customer domain communicate with energy management unit through a HAM which can be either wired or wireless. In the case of a wired communication line, Ethernets can be used for high-rate data transmit although it needs expensive infrastructures [6.20]. On the other hand, power line communication can be a cheaper solution although the data transfer rate is in a limited range [6.21]. In the case of short distance between micro-grid components and limited data transfer rate, a wireless communication link, e.g. Wi-Fi, can be used [6.22]. In this case, wireless devices, such as Zigbee and 6LoWPAN, are used widely due to their reliability, flexibility, and low cost [6.23].

The regional distribution network centre communicates with the EMU through a wide area network (WAN). In this case, the required communication line should be able to handle a large number of connections and provide wide area coverage. Therefore, cellular networks and 4G technologies such as WiMAX are the most feasible solutions [6.18].

More details on the DSM methods, optimization techniques and implementation issues is outside the scope of this thesis and can be found in [6.18],[6.24]-[6.26]. This research mainly focuses on the residential domain and the elements. In the proposed smart micro-grid system, the energy storage, loads and local generators, such as PV and fuel cell, are linked to the EMU through wired or wireless communication. The data transfer between the elements and EMU is limited to the measurement signals, such as voltage, current and power, and the control signals, such as voltage and power references of local controllers. In this chapter, the EMU operation for energy management is studied in detail and there is less focus on residential load control.

### **6.3 Residential Load Profile**

Load profiles of electrical consumers do not follow the same trends for similar times of the day. It varies with the time according to the weather conditions, seasons of the year, and consumer habits. Despite the variations, load data can be used to forecast and manage the energy consumption efficiently. Therefore, a lot of research is carried out through simulations or modelling to obtain the estimated load profiles of residential consumers.

In general, the residential loads can be classified in different groups considering multiple factors. Some literatures divide the loads to flexible non-flexible (Shiftable and non-shiftable) from an energy management point of view [6.27]. In some cases, loads are classified according to their power consumption range to heavy loads ( $P > 1000$  W), normal loads ( $100 < P < 1000$  W), and light loads ( $P < 100$  W). Another classification criterion is by the load functionality, such as heating and cooling, lighting, and entertainment.

Study on the load profiles of residential consumers is required for power system studies, load forecasting and network planning [6.28], [6.29]. The load profiles are normally obtained through numerical simulations, statistical analysis or field measurements. A widely used method of obtaining load profiles is based on the switch-on probability distribution function and the duration of using an appliance. The required data for synthesizing load power demand can also be obtained through field measurements using off-line or online data record and appropriate sensors [6.30], [6.31].

Another option for obtaining switch-on probability function is using time-of-use survey data. The method is used in [6.31], [6.32] along with the Markov-chain approach to produce active and/or reactive power profiles.

In [6.33] a Monte-Carlo simulation technique is used to define the active power demand profile. Another method called the bottom-up approach is based on the aggregation of power demand curves of individual appliances according to the switch-on probabilities and ownership statistics [6.31], [6.34]. The discussed methods are the most common techniques of obtaining the load profile although there are some studies using particular methods, such as the agent-based analysis [6.35], random number technique [6.36], and fuzzy logic based analysis [6.37].

To obtain more accurate load profiles, some other factors such as number of occupants, season of the year, day of the week (weekdays/weekends), working or non-working occupants and physical structure of the building have been considered recently. Details on the different methods of obtaining residential load profile are out of scope of this thesis and can be found in the above references.

#### 6.4 Power Analysis of the Proposed Micro-grid

The electrical schematic of the proposed micro-grid is presented in Fig.6.3 in detail. As can be seen, the micro-grid includes three H-bridge ports connected to the multi-winding transformer to form a triple active bridge (TAB) dc-dc converter. The multi-winding transformer provides a high frequency magnetic bus for distribution of power among the ports in the form of magnetic flux. As shown in the figure, port one transfers the power from the TAB converter to the inverter and further to the residential load and grid. It changes the dc voltage of port one (280-320 V) to a low frequency (50 Hz) ac voltage by using a single phase bidirectional inverter. The inverter can be used in the reverse direction as a rectifier to change the grid voltage to dc voltage on port one. The H-bridge unit in port two is bi-directional similar to the H-bridge in port one. It is connected to fuel cell stack via a low voltage bus (50-70 V). A bi-directional buck-boost converter presented as port four, links the battery to the dc bus. It operates in buck mode to charge the 24 V battery bank and in boost mode to discharge the battery into the bus.

As is shown in the figure, the PV panel is linked to the multi-winding magnetic link by using port three. The power flow among the ports one, two and three is controlled using the phase shift technique and between ports two and four using the duty ratio control. The proposed topology provides flexibility in the direction of power flow between the ports and in energy management. The steady state power flow diagram of the system can be obtained by considering only the power sources and conversion blocks as shown in Fig.6.4. To analyze the power flow efficiency, the value of efficiency blocks of the converters and transformer need to be considered as can be seen in the figure. To simplify the model, the efficiency blocks can be combined by

$$\eta_1 = \eta_{C-BB} , \quad \eta_2 = \eta_{C-HB2}\eta_T , \quad \eta_3 = \eta_{C-HB3}\eta_T \quad \eta_4 = \eta_T\eta_{C-HB1}\eta_I \quad (6.1)$$

where  $\eta_{C-BB}$  ,  $\eta_{C-HB}$  and  $\eta_I$  are conversion efficiency of bi-directional buck-boost converter, H-bridge dc-ac converter and inverter units, respectively, and  $\eta_T$  is the transformer efficiency. The model facilitates the energy analysis of the micro-grid as an energy hub considering efficiency of each voltage conversion stage. In the resultant model presented in Fig.6.4 (b), Bus 1 and Bus 3 are in electrical form and Bus 2 is in magnetic form.

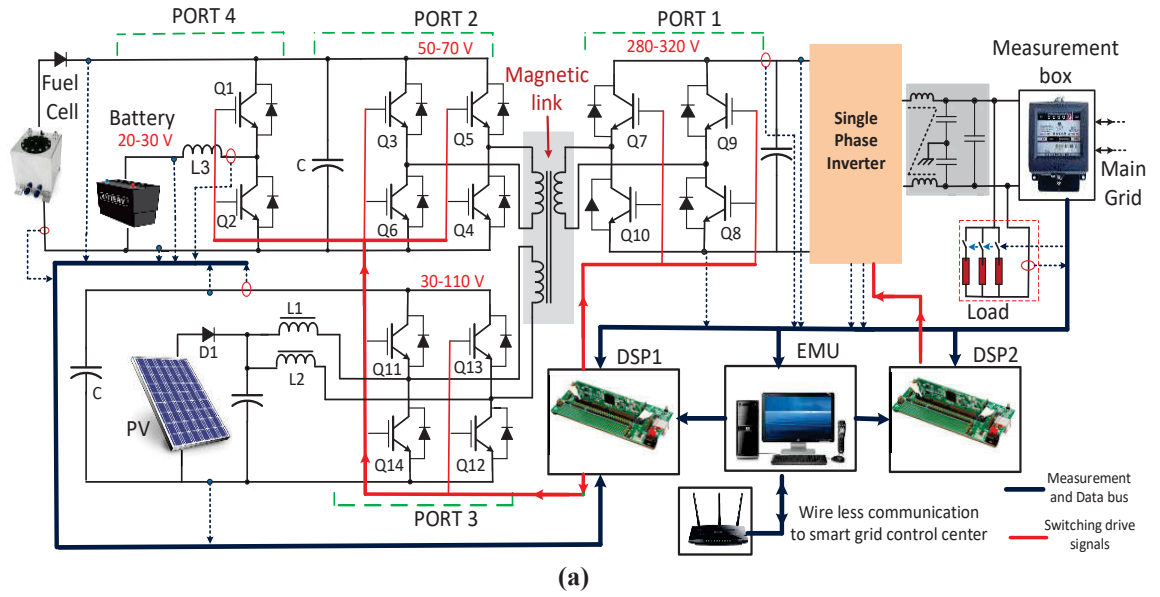


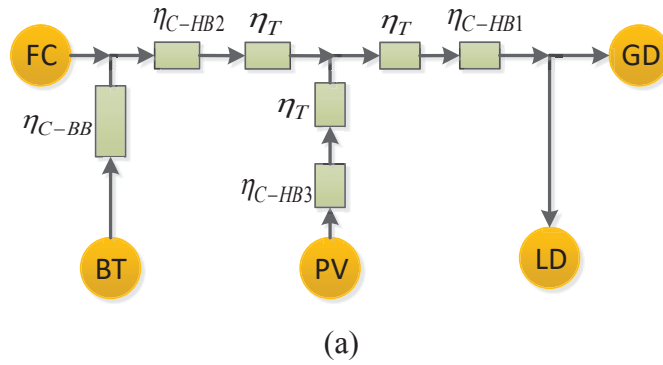
Fig.6.3 Electrical schematic of the proposed residential micro-grid

The power balance equations of the nodes in the model can be expressed as

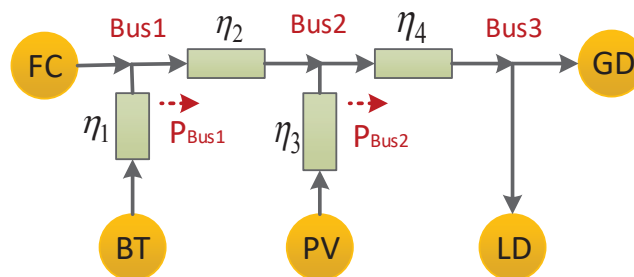
$$\eta_1 P_{BT} + P_{FC} - P_{BUS1} = 0 \tag{6.2}$$

$$\eta_3 P_{PV} + \eta_2 P_{BUS1} - P_{BUS2} = 0 \tag{6.3}$$

$$-P_{LD} - P_{GD} + \eta_4 P_{BUS2} = 0 \tag{6.4}$$



(a)



(b)

Fig.6.4 Modelling of the proposed micro-grid for power flow and energy management analysis.

(a) detailed model, and (b) simplified model

where  $P_{BT}$ ,  $P_{FC}$ ,  $P_{LD}$ ,  $P_{GD}$  and  $P_{PV}$  are power of battery, fuel cell, load, grid and PV,  $P_{BUS1}$ ,  $P_{BUS2}$  and  $P_{BUS3}$  the power flows from the buses to the respected node, respectively. Using (6.2)-(6.4), the power balance equations during transients in the system can be written as

$$-\frac{dP_{BUS1}}{dt} + \eta_1 \frac{dP_{BT}}{dt} = 0, \quad \frac{dE_{FC}}{dt} = 0 \quad (6.5)$$

$$\eta_3 \frac{dP_{PV}}{dt} + \eta_2 \frac{dP_{BUS1}}{dt} - \frac{dP_{BUS2}}{dt} = 0 \quad (6.6)$$

$$-\frac{dP_{LD}}{dt} - \frac{dP_{GD}}{dt} + \eta_4 \frac{dP_{BUS2}}{dt} = 0 \quad (6.7)$$

According to the slow dynamic response of fuel cell any change in the power of port two should be compensated by the battery.

On the other hand, there is a possibility to model the entire micro-grid system as an energy hub. According to reference [6.38], an energy hub exchanges power with the surrounding systems, primary energy sources, such as solar, wind, and hydro, loads and other components via the input and output ports. The input energy sources known as energy carriers are not necessarily from the same forms. In this research, the inputs and outputs of the hub are limited to the electrical form although more accurate models are possible. The relationship between the input and output powers of an energy hub with  $n$  inputs and  $m$  outputs can be written in the matrix notation as [6.38], [6.39]:

$$L = CP \quad (6.8)$$

where

$$L = \begin{bmatrix} L_1 \\ L_2 \\ \cdot \\ \cdot \\ \cdot \\ L_m \end{bmatrix} \quad C = \begin{bmatrix} C_{11} & C_{12} & \cdot & \cdot & \cdot & C_{1n} \\ C_{21} & \cdot & \cdot & \cdot & \cdot & C_{2n} \\ \cdot & \cdot & \cdot & \cdot & \cdot & \cdot \\ \cdot & \cdot & \cdot & \cdot & \cdot & \cdot \\ \cdot & \cdot & \cdot & \cdot & \cdot & \cdot \\ C_{m1} & C_{m2} & \cdot & \cdot & \cdot & C_{mn} \end{bmatrix} \quad P = \begin{bmatrix} P_1 \\ P_2 \\ \cdot \\ \cdot \\ \cdot \\ P_n \end{bmatrix} \quad (6.9)$$

$P_1, P_2, \dots, P_n$  are the input powers in steady state,  $L_1, L_2, \dots, L_m$  the output powers in steady state, respectively, and  $C_{ij}$  ( $i=1, 2, \dots, m$  and  $j=1, 2, \dots, n$ ) is the coupling factor that links  $i$ -th output to the  $j$ -th input. The bi-directional ports where  $L_i = -P_j$  and  $i=j$ , such as grid and battery, can be considered in both input and output vectors. The coupling matrix mathematically describes the mapping of input powers to the output powers [6.38]. To define the coupling factors, the steady state power flow diagram of the system needs to be used. As the total energy of one input source may split up to several outputs a dispatch factor should be introduced to define the power transform ratio of each output to the respected inputs. Therefore, each coupling factor can be determined by multiplying the conversion efficiency,  $\eta_{ij}$ , and the dispatch factor,  $\nu_{ij}$ , as

$$C_{ij} = \nu_{ij} \eta_{ij}, \quad \nu_{ij} = \frac{P_{ij}}{P_i} \quad (6.10)$$

where  $P_{ij}$  is a portion of  $P_j$  which flows to the  $L_i$  as output, and its relation with the input and output powers can be determined by

$$P_j = \sum_{i=1}^m P_{ij}, \quad L_i = \sum_{j=1}^n C_{ij} P_{ij} \quad (6.11)$$

The coupling matrix represents a linear transform when both dispatch factors and conversion efficiencies remain constant for the entire operation range and all operation modes. In some cases, they can be a linear or nonlinear function of input power, e.g.  $C_{ij} = f(P_{ij})$  which imports a nonlinearity into the relation.

In general, the coupling matrix is not invertible because in case  $C$  is invertible then (6.8) shows a one-to-one mapping. This means that there is only one possible answer for input power matrix  $P$  for a given output matrix  $L$ , and therefore, there is not any chance for optimization unless the coupling factors are variable [6.38]. The energy hub model of system considering the steady state input and output power flow is presented in Fig.6.5. The model can be used for optimization of entire energy hub [6.38]. Considering coupling matrix  $C$  for specified outputs  $L$ , the optimal input vectors of input power and dispatch factors can be defined to satisfy certain optimization objectives such as minimization of the cost, power loss, and/or emissions of the energy hub.

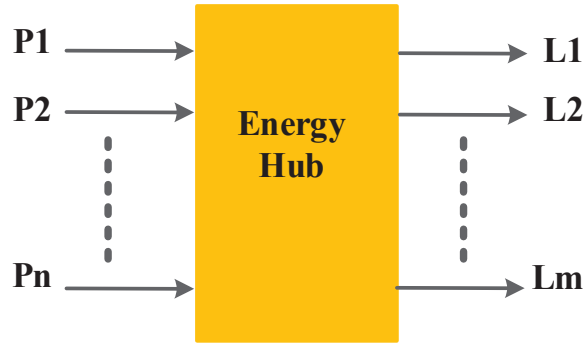


Fig.6.5 Schematic of a multi-input multi-output energy hub

The general form of optimization problem can be written as:

*Objective* : {Minimization of  $g$  where  $g=f(P)$

*Constraints* : {  $L - CP = 0$ ,  $\underline{P} \leq P \leq \bar{P}$ ,  $\underline{P}_c \leq NP \leq \bar{P}_c$ ,  $0 \leq N \leq 1$

where  $\underline{P}$ ,  $\bar{P}$ ,  $\bar{P}_c$  and  $\underline{P}_c$  are lower and upper limits of input power and lower and upper limits of converter power vectors, respectively, and  $N$  is the dispatch factor vector and should be limited between 0 to 1. In the proposed micro-grid system it can be changed using the duty ratio or phase shift variation. Details of the optimization process and the results will be studied and published as the future research works.

### 6.5 Structure of the Proposed Micro-grid

The electrical schematic of the proposed micro-grid and controllers are presented in Fig.6.6. As can be seen, the micro-grid includes three H-bridge ports connected to a multi-winding transformer to form a triple active bridge (TAB) dc-dc converter. The multi-winding transformer provides a high frequency magnetic bus for distribution of power among the ports in the form of magnetic flux. The dc bus voltages  $V_{b1}$ ,  $V_{b2}$  and  $V_{b3}$  are converted to high frequency ac signals by using H-bridge converters of port one, two and three respectively.

The dc high voltage on port one,  $V_{b1}$  (280-320 V) is converted to a low frequency (50 Hz) ac voltage by using a single phase bidirectional inverter. The inverter can be used reversely as a rectifier to supply the grid energy into the high voltage dc bus and it further is used to charge the battery by activating ports two and four simultaneously.

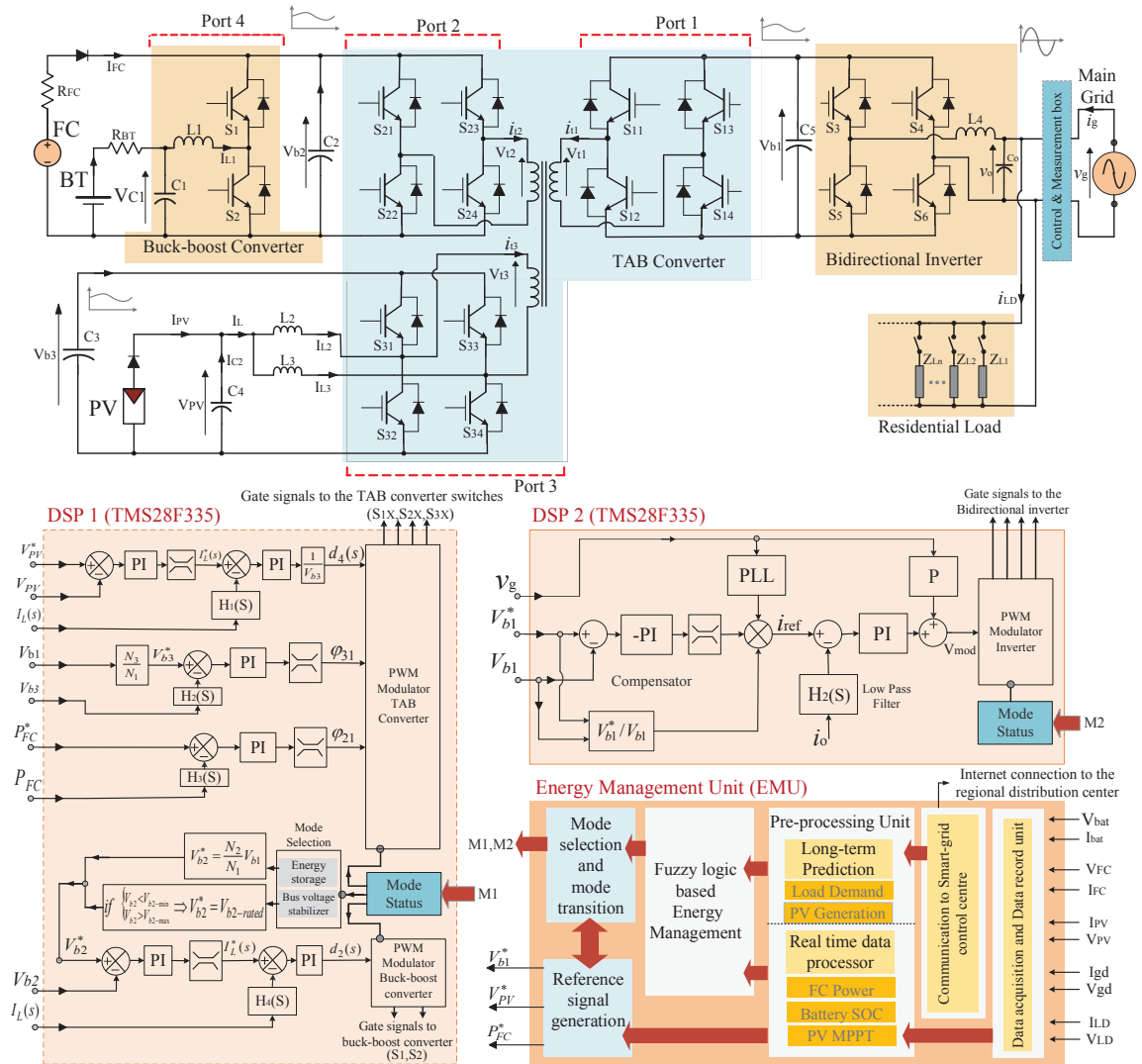


Fig.6.6 Structure of the proposed micro-grid including system level and device level controllers

The fuel cell stack is connected to port two via a low voltage bus (50-70 V). A bi-directional buck-boost converter presented as port four links the battery to the dc bus. It operates in buck mode to charge the 24 V battery bank and in boost mode to discharge the battery into the bus. The PV power is transferred to the capacitor  $C_3$  by using interleaved boost converter and further to the magnetic bus by using shared switching devices  $S_{31}$ - $S_{34}$  in port three. As can be seen in Fig.6.6, the proposed micro-grid is controlled in device level by two digital signal processors (DSPs) including DSP1 for dc-dc converters and DSP2 for single phase inverter. On the other hand, a personal computer (PC) is used as system level controller and performs the power flow management. Direction and amount of power flow in the magnetic bus is controlled by introducing phase shift angles  $\varphi_{21}$  and  $\varphi_{31}$  between ports two and three to port one respectively. As can be seen in the figure, the phase shift  $\varphi_{21}$  is used to control the fuel

cell power according to the reference signal provided by EMU and  $\varphi_{31}$  is used to control the power transferred from PV to port one by regulating  $V_{b3}$ . The phase shifts angles  $\varphi_{31}$  and  $\varphi_{21}$  are controlled by single loop proportional-integral (PI) controllers. The reference signal  $V_{b3}^*$  is following  $V_{b1}$  to guarantee zero voltage switching (ZVS) operation of the TAB converter ports by applying equal volt-second on all windings of the magnetic link. To maintain maximum power point tracking (MPPT), duty ratio of driving signals of  $S_{32}$  and  $S_{34}$ , presented as  $d_4$  is controlled according to the reference signal  $V_{PV}^*$  generated by EMU. A conventional dual loop PI controller is designed to control  $d_4$ . A variable step size incremental conductance (INC) method is used for MPPT. In the battery port, the bidirectional buck-boost converter is controlled by conventional dual loop controller. The reference signal is generated based on the battery application as energy storage or bus voltage regulator. The bus voltage on port one,  $V_{b1}$  should be kept constant as a reference in all operation modes. It is regulated by inverter according to the reference signal provided by EMU. The control process of inverter is performed by DSP2. As can be seen in the figure, dual loop control with internal current and external voltage control loops is designed to forces the inverter current to follow the grid voltage. The reference voltage  $V_{b1}^*$  generated by EMU is used to control the inverter/rectifier operation modes. The operation mode signals presented as M1 and M2 generated by mode selection and transition unit in EMU are sent to the PWM modulator controls in DSP1 and DSP2. The proposed micro-grid is able to operate in several modes according to the power flow direction and active sources and loads. Selection of operation modes is performed by EMU depending on the control objectives and energy management scenarios. More details on the device level control is provided in chapter Five and this chapter is mainly focused on the energy management technique.

## 6.6 Energy Management Unit (EMU)

As discussed in Chapter Two, three levels of control with different time steps are designed for decision making and management of the proposed micro-grid. In the highest level, the regional distribution network control centre manages the total power flow and power quality of the distribution network and communicates with the EMU in each individual residential smart micro-grid. The EMU manages the energy inside the residential micro-grid and selects the operational modes on the basis of existing stored energy, predicted load demand, predicted renewable energy generation, and energy

costs considering the objectives of energy management. It also receives the predicted profiles of the PV generation and grid energy cost from the regional distribution centre. On the other hand, the power flow control and energy balance in the multi-port dc-dc converter is performed by the device level controller using the phase shift and duty ratio control techniques.

As presented in Fig.6.6, the EMU includes five computational units. The outputs from voltage and current sensors of the ports are received and recorded in data acquisition and record unit. A communication unit is designed to connect the micro-grid to the regional distribution centre through internet. It receives the required commands for power transfer to the grid and metrological data for PV power generation forecasts. A pre-processing unit performs all mathematical calculations and data processing including discretising forecasted energies of PV and load demand, real-time estimation of battery SOC and state of hydrogen (SOH). It also performs the MPPT for PV port and the resultant control signal is sent to the reference signal generation unit. A fuzzy logic control (FLC) unit defines the appropriate operation mode of the micro-grid according to the long term energy plans and real-time value of parameters. The output from FLC is sent to the mode selection and transition block. Finally the reference signals for the control loops are generated by the reference signal generation unit according to the selected mode. Next section provides more details on each of the EMU units.

### 6.6.1 Review of pre-processing unit operation

As can be seen in Fig.6.6, the data received by EMU is voltage and current signals of the ports which are input to the data acquisition and record centre. The received data then is further sent to the pre-processing unit to be used in calculation of control parameters. On the other hand, the profiles of the grid energy cost, PV power generation forecast and load demand, received by communication unit are the second group of information to the pre-processing unit. To simplify the analysis of predicted data and speed up the decision making process, the continuous forecasted profile of PV power generation is discretised by using the short-time steps of  $T_k$  using

$$\tilde{P}_{PV\_24h}(k) = \frac{1}{T_k} \int_{t_0+kT_k}^{t_0+(k+1)T_k} \tilde{P}_{PV\_24h}(t) dt \quad (6.12)$$

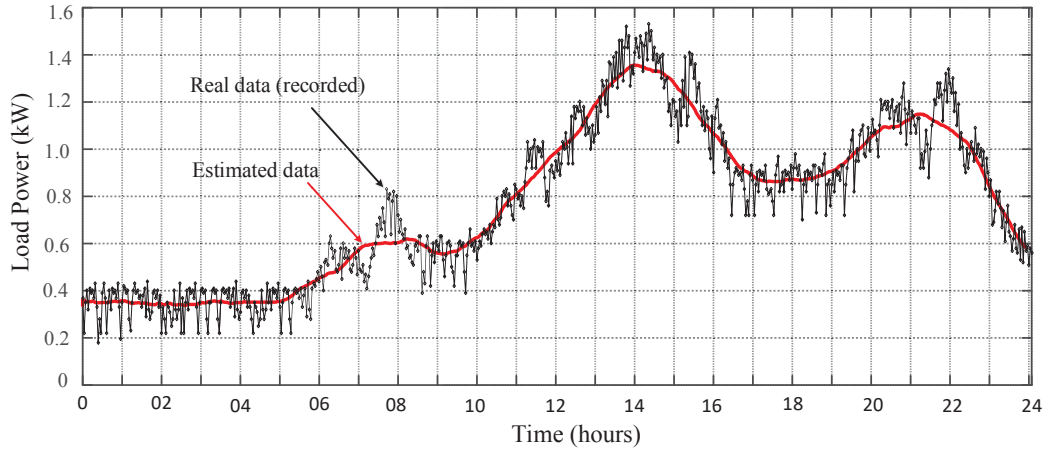
where  $k \in (0, 1, 2, \dots, \frac{24 \text{hours}}{T_k} - 1)$  and  $\tilde{P}_{PV\_24h}(k)$  is the predicted power generated by PV at the  $k$ -th sample,  $\tilde{P}_{PV\_24h}(t)$  the forecasted 24 hours-ahead power profile of PV, and  $t_0$  the prediction starting time. Similarly, the load On the other hand,  $\tilde{P}_{LD\_24h}(k)$  is the predicted power demand of the load at the  $k$ -th sampling time can be calculated using

$$\tilde{P}_{LD\_24h}(k) = \frac{1}{T_k} \int_{t_0+kT_k}^{t_0+(k+1)T_k} \tilde{P}_{LD\_24h}(t) dt \quad (6.13)$$

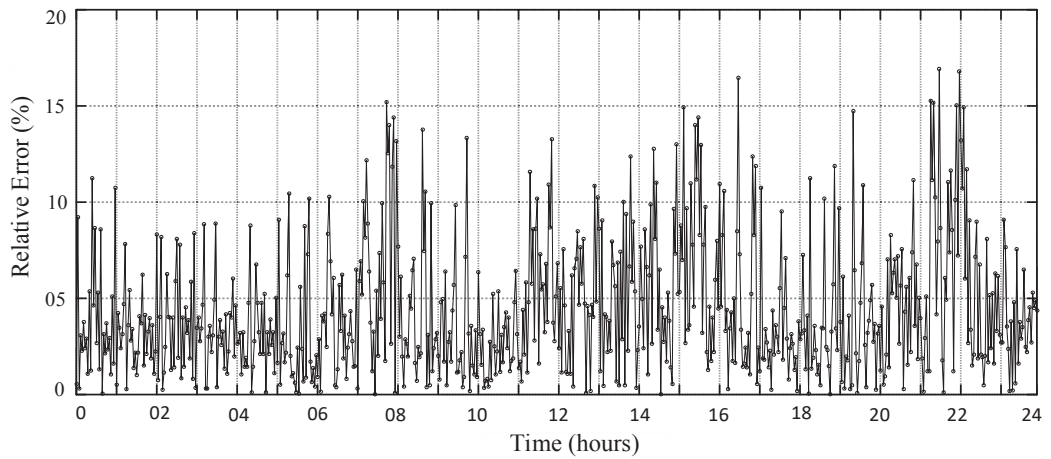
For example, for sampling time of  $T_k=12$  min the 24-h ahead profile is discretised into 120 samples.

To find out the accuracy of predicted load demand using previously recorded data, a comparison is carried out as an example. The predicted load power demand which is obtained from the average of load for the past 30 days with similar conditions is recorded in the data record and processing unit. Comparison of the predicted data with the actual values of the load demand shows that the difference is not considerable as presented in Fig.6.7 (a). To find the difference, the relative error between the actual and predicted data is calculated for a 24 hours duration time and illustrated in Fig.6.7 (b). It can be seen that resultant error is always less than 15 % of the total power demand.

The profiles of fuel cell and grid energy costs are discretised similarly for 24-hours-ahead. In this thesis, it is assumed that the energy-cost profile of the main grid is received by the EMU from the regional distribution network control centre is updated regularly. On the other hand, it is assumed that the cost of grid energy is comparable with the fuel cell and the battery energy cost is less than fuel cell (considering capital cost, maintenance and running costs). The fuel cell cost is evaluated by consumer and is entered into the EMU database when it is required. The fuel cell cost profile should be an almost constant value which is defined according to the fuel cell energy transform efficiency, running cost, and capital cost although it may occasionally need to be updated according to the change in the hydrogen cost. The discretised samples then are sent to the FLC computational unit to be used in fuzzy controller. The real-time values of SOC and SOH should be also estimated in the pre-processing unit for each sampling time  $T_n$ . The battery SOC at  $n$ -th sample ( $SOC(n)$ ) is defined from



(a)



(b)

**Fig.6.7 (a) Comparison of measured and estimated load power demand for 24h-ahead, and (b) relative error between measured and estimated values**

$$SOC(n) = SOC(n-1) + \frac{T_s}{C_{BT}} [I_{BT}(n) - I_{BT}(n-1)] \quad (6.14)$$

where  $C_{BT}$  is the nominal capacity of the battery bank and  $I_{BT}(n)$  the battery current at the  $n$ -th sampling time which can be positive during the charge and negative during the discharge process. On the other hand,  $SOH(n)$  is estimated by using signals received from sensors installed in the hydrogen tank.

### 6.6.2 Structure of fuzzy logic controller

This section studies structure and operation principle of the Fuzzy logic controller (FLC). The FLCs do not need a precise mathematical model of the system nor complex computations.

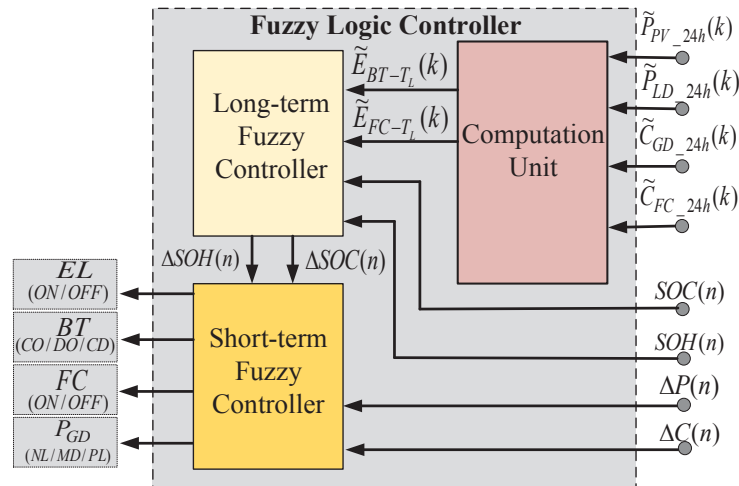


Fig.6.8. Structure of the proposed fuzzy logic control

They rely only on the human capability to understand the system's behaviour and operate based on qualitative control rules [6.40]-[6.42]. Therefore, the design of fuzzy controllers is simple since it is only based on linguistic rules [6.43]. They provide a formal methodology for representing, manipulating, and implementing a human's heuristic knowledge about how to control a system [6.44]. They are robust in operation, fast in dynamic response, and easy for applying modifications. Their structure is much simpler than those model based linear controllers and is cheaper to implement. Fuzzy controllers have been used successfully as supervisory control and EMU in various hybrid renewable energy systems [6.45]-[6.47].

To realize an effective energy management strategy, both the present and future conditions of the system are required to be considered. Therefore, in this thesis real-time control operates according to a long-term energy plan.

As illustrated in Fig.6.8, the designed FLC contains a computational unit, a short-term and a long-term controller. The computational unit calculates the estimated energies that should be supplied by battery ( $\tilde{E}_{BT-T_L}$ ) and fuel cell ( $\tilde{E}_{FC-T_L}$ ) during the next long-time frame by using the discretized predicted profiles of PV power and energy demand. The estimation is based on the pre-defined long-term energy plans and the resultant value is sent to the long-term fuzzy controller. It also calculates the real-time value of difference between PV power generation and the load demand ( $\Delta P(n)$ ) and difference between real-time values of fuel cell and grid energy costs ( $\Delta C(n)$ ) for short-term fuzzy controller. On the other hand, the long-term fuzzy controller determines the obligatory variation range in the capacity of storage devices (i.e.  $\Delta SOC$  for battery and  $\Delta SOH$  for hydrogen tank) according to the long-term energy plans for the short-term

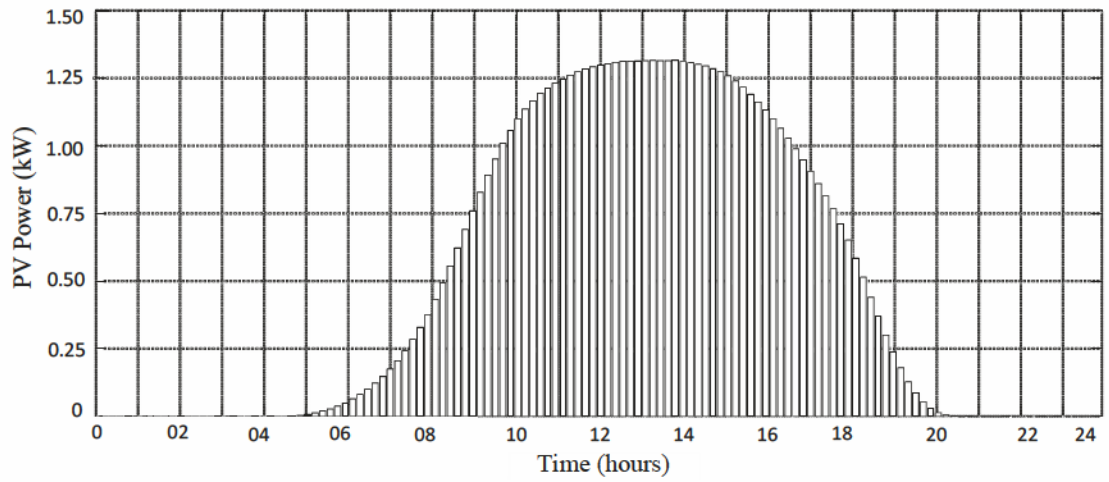
controller. Finally, the short-term fuzzy controller determines the next operation mode of the system based on the available capacity of battery ( $\Delta SOC(n)$ ) and fuel cell ( $\Delta SOH(n)$ ), real-time values of the power difference ( $\Delta P(n)$ ) and energy cost difference ( $\Delta C(n)$ ). The output of short-term controller is status of electrolyzer, battery, fuel cell and grid conversion ports. The fuel cell and electrolyzer status is in the form ON/OFF signal and for battery is selected as charge only (CO), discharge only (DO) or charge and discharge (CD). In the case of energy transfer to the grid energy, a variable quantity in the range of negative large (NL), medium (MD) and positive large (PL) according to the membership functions of short-term fuzzy controller.

The output signals from fuzzy controller are sent to the mode selection and transition unit to extract the appropriate operation mode. More details on each unit of the FLC is provided in the following sections.

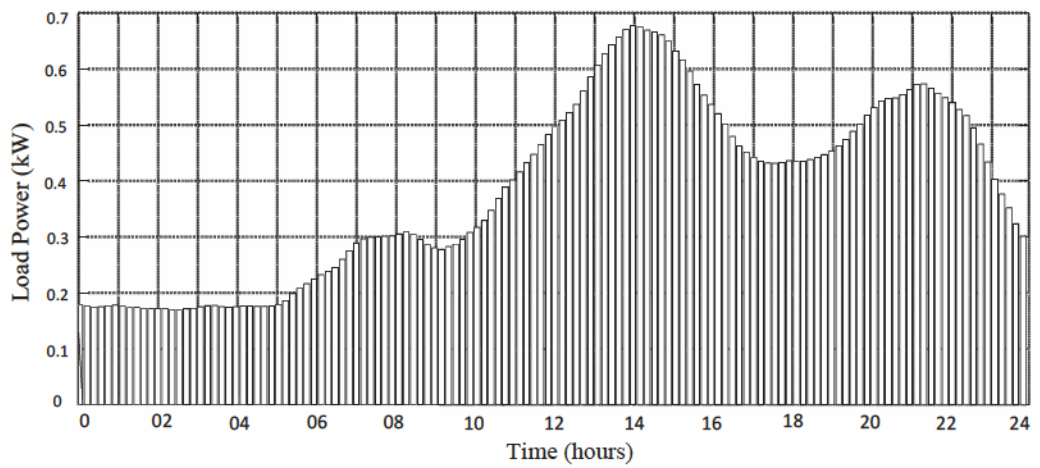
#### *A. Operation of computation unit*

This section provides the details of the computation unit. As can be seen in Fig.6.8, the computational unit calculates the estimated values of energies that need to be supplied by battery and fuel cell ( $\tilde{E}_{BT\_T_L}(k)$  and  $\tilde{E}_{FC\_T_L}(k)$ ) during the next long-time period. The estimation method is based on the long-term energy plans and selected energy management scenario. The control objective can be, for example, minimizing the emissions of greenhouse gases or the household energy expenses, minimizing the energy received from the grid and improvement of grid power quality. Nevertheless, in all energy scenarios, a common idea is to maximize the energy harvest of renewable resources.

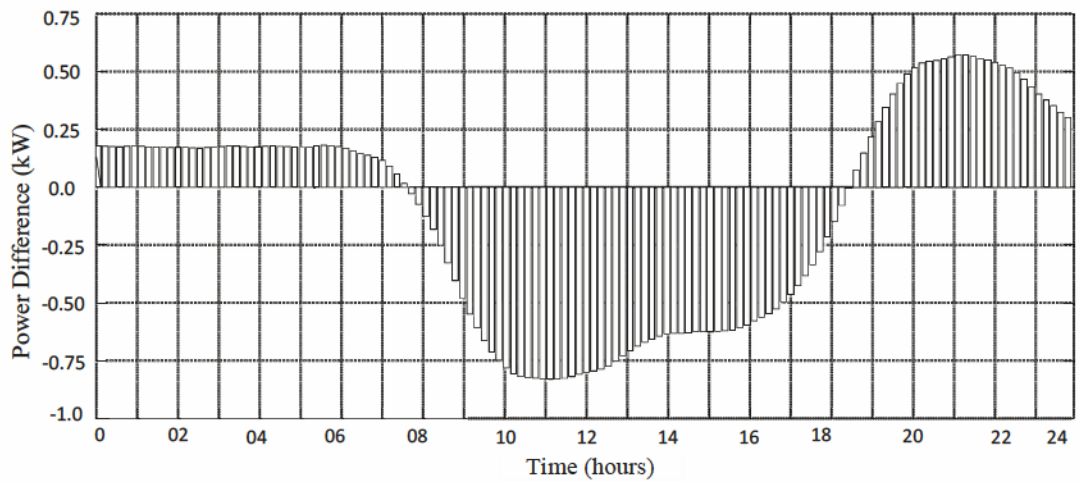
A moving time frame  $T_L$ , ranging from tens of minutes to a few hours, is considered to estimate the energies. The estimation is performed based on the predicted duration of use and amount of energy transfer according to the long-term energy management scenario. The predicted energy profiles are discretised by pre-processing unit as presented in Fig.6.9 (a)-(b) (As an example, in this figure  $T_k \approx 12\text{min}$ ) and are updated at the beginning of each time-step  $T_k$  by moving the time-frame  $T_L$  one time-step ahead ( $k \rightarrow k+1$ ) considering that  $T_L = mT_n$ . In the proposed energy management scenario, the PV is considered as preferred source of energy to supply the load. Therefore, the forecasted profile of the power generated by PV is compared with the predicted load demand profile for sampling time  $k$  to  $k+m$  to find the difference from



(a)



(b)



(c)

**Fig.6.9 24-h ahead forecasted power of (a) PV generation, (b) load demand and (c) the difference between PV and load demand**

$$\Delta\tilde{P}_{24h}(k) = \tilde{P}_{LD\_24h}(k) - \tilde{P}_{PV\_24h}(k) \quad (6.15)$$

The difference power profile is presented in Fig.6.9.(c) and can be covered by the battery, fuel cell, and/or grid, according to the long-term energy plan. The energy cost, availability and maximum power of each source are other factors that should be taken into account.

Following functions are considered as control objectives to estimate the energies that should be supplied by battery and fuel cell during the next long-time fram.

- In all operation modes, the PV is given priority as the source of energy for supplying the load, and the surplus energy is preferred to be used to charge the battery. The second option is transferring surplus energy to the main grid which requires the acknowledgment of request by the regional distribution network control center. The last option is supplying shiftable loads, water heating systems, and dump loads.

- In the case that the PV generation is less than the load demands, the difference can be covered by the battery, fuel cell, and/or grid. The priority of supplying source in this case depends on the amount of required power, the energy cost and availability. In this paper it is assumed that the running cost of battery is less than the fuel cell and grid for each sampling time  $k$  ( $\tilde{C}_{BT\_T_L}(k) < \tilde{C}_{FC\_T_L}(k), \tilde{C}_{GD\_T_L}(k)$ ). On the other hand, the fuel cell energy cost is comparable with the grid. The cost of grid energy is assumed to be variable during the day in a wide range. According to the proposed management technique, the small values of difference between the PV and load powers can be covered by the battery and/or grid depending on the availability and cost of energy. If the difference is more than the battery capacity and less than the fuel cell, it should be covered by grid and/or fuel cell depending on their energy cost. When the fuel cell is active, the battery is used in the standby mode to balance the bus voltage during the transients due to the slow dynamic response of fuel cell.

To determine the estimated energy of each source, the maximum power and energy capacity of the source and energy cost should be taken into account as constrains. The battery capacity can be managed according to the SOC level into the following ranges:

$$\left\{ \begin{array}{ll} \text{Bus stabilaization} & 0.9 < SOC < 1 \\ \text{Storage and bus stabilization} & 0.4 < SOC < 0.9 \\ \text{Off - grid operation} & 0.1 < SOC < 0.4 \end{array} \right. \quad (6.16)$$

The maximum power that can be supplied by the battery during each sampling time  $T_k$  ( $P_{BT-\max}$ ) is defined according to its maximum charging and discharging currents. On the other hand, the maximum power that can be supplied by the fuel cell ( $P_{FC-\max}$ ) is obtained from the factory provided datasheet. The SOC and SOH levels and their limitations should be taken into account for each sampling time. The energy management rules that are used to find the supplied or absorbed power of each component are presented briefly in mathematical form as

$$\Delta\tilde{P}_{24h}(k) = \begin{cases} \tilde{P}_{BT-T_k}(k) & \text{if } 0 < \Delta\tilde{P}_{24h}(k) \leq P_{BT-\max}, \tilde{C}_{BT}(k) < \tilde{C}_{GD}(k) \\ \tilde{P}_{GD-T_k}(k) & \text{if } 0 < \Delta\tilde{P}_{24h}(k) \leq P_{BT-\max}, \tilde{C}_{BT}(k) \geq \tilde{C}_{GD}(k) \end{cases} \quad (6.17)$$

$$\Delta\tilde{P}_{24h}(k) = \begin{cases} \tilde{P}_{FC-T_k}(k) & \text{if } P_{BT-\max} < \Delta\tilde{P}_{24h}(k) \leq P_{FC-\max}, \tilde{C}_{FC}(k) < \tilde{C}_{GD}(k) \\ \tilde{P}_{GD-T_k}(k) & \text{if } P_{BT-\max} < \Delta\tilde{P}_{24h}(k) \leq P_{FC-\max}, \tilde{C}_{FC}(k) \geq \tilde{C}_{GD}(k) \end{cases} \quad (6.18)$$

$$\Delta\tilde{P}_{24h}(k) = \begin{cases} \tilde{P}_{FC-T_k}(k) + \tilde{P}_{GD-T_k}(k) & \text{if } P_{FC-\max} < \Delta\tilde{P}_{24h}(k), \tilde{C}_{FC}(k) < \tilde{C}_{GD}(k) \\ \tilde{P}_{GD-T_k}(k) & \text{if } P_{FC-\max} < \Delta\tilde{P}_{24h}(k), \tilde{C}_{FC}(k) \geq \tilde{C}_{GD}(k) \\ \tilde{P}_{GD-T_k}(k) + \tilde{P}_{BT-T_k}(k) & \text{if } P_{FC-\max} < \Delta\tilde{P}_{24h}(k), \tilde{C}_{FC}(k) \geq \tilde{C}_{GD}(k), \tilde{C}_{BT}(k) \end{cases} \quad (6.19)$$

In the case of negative value of  $\Delta\tilde{P}_{24h}(k)$  which means that the predicted value of PV generation is more than the load demand, the decision is made based on the following equation:

$$\Delta\tilde{P}_{24h}(k) = \begin{cases} -\tilde{P}_{BT-T_k}(k) & \text{if } -P_{BT-\max} < \Delta\tilde{P}_{24h}(k) < 0, \tilde{C}_{BT}(k) > \tilde{C}_{GD}(k) \\ -\tilde{P}_{GD-T_k}(k) & \text{if } -P_{BT-\max} < \Delta\tilde{P}_{24h}(k) < 0, \tilde{C}_{BT}(k) < \tilde{C}_{GD}(k) \\ -\tilde{P}_{LD-T_k}(k) & \text{if } -P_{BT-\max} < \Delta\tilde{P}_{24h}(k) < 0, \tilde{C}_{BT}(k) = \tilde{C}_{GD}(k) \end{cases} \quad (6.20)$$

Finally, the predicted value of energy that should be exchanged with the battery  $\tilde{E}_{BT-T_L}(k)$  or supplied by the fuel cell  $\tilde{E}_{FC-T_L}(k)$  during the moving time frame  $T_L$  considering that  $T_L = mT_k$  can be found by

$$\tilde{E}_{BT-T_L}(k) = \sum_k^{k+m} T_k \tilde{P}_{BT}(k) \quad (6.21)$$

$$\tilde{E}_{FC-T_L}(k) = \sum_k^{k+m} T_k \tilde{P}_{FC}(k) \quad (6.22)$$

The resultant values of  $\tilde{E}_{BT-T_L}(k)$  and  $\tilde{E}_{FC-T_L}(k)$  are used as the input variables to the long-term fuzzy controller. On the other hand, the difference between real-time values of PV power generation and load power demand  $\Delta P(n)$ , and between the cost of grid and fuel cell energies  $\Delta C(n)$  are other parameters that are calculated in the computational unit and sent to the short-term controller. The difference between the PV output power  $P_{PV}(n)$  and load power  $P_{LD}(n)$  for  $n$ -th sampling time is defined as

$$\Delta P(n) = P_{LD}(n) - P_{PV}(n) \quad (6.23)$$

The difference between energy cost of the main grid and fuel cell  $\Delta C(n)$  can be calculated by

$$\Delta C(n) = C_{GD}(n) - C_{FC}(n) \quad (6.24)$$

where  $C_{GD}(n)$  is the cost of energy received from or transferred to the grid at the  $n$ -th sampling time and  $C_{FC}(n)$  the fuel cell energy cost. Next sections provide more details on the operation principle of long-term and short-term fuzzy controllers as other parts of FLC unit. In this thesis  $T_L$ ,  $T_k$  and  $T_n$  are selected equal to 8 hours, 2 min and 100ms respectively.

### B. Long-term fuzzy controller

The long-term fuzzy controller defines the required variation in the SOC of the battery and SOH of the hydrogen tank ( $\Delta SOC$ ,  $\Delta SOH$ ) for an effective operation during the next time-frame considering current value of SOC and SOH ( $SOC(n)$ ,  $SOH(n)$ ). According to the long-term energy plan, higher values of  $\tilde{E}_{BT-T_L}$  and  $\tilde{E}_{FC-T_L}$  means that higher amounts of energy should be supplied by the battery, fuel cell and/or grid during the next time-frame. In the case of  $\Delta SOC < 0$  and  $\Delta SOH < 0$ , this means that the current SOC and SOH levels need to be reduced by the amounts of  $\Delta SOC$  and  $\Delta SOH$  according to the long-term energy management plans. This increases the battery allocated capacity for storing energy during off peak hours when the grid energy is cheaper than other sources. On the other hand, in the case of  $\Delta SOC > 0$  and  $\Delta SOH > 0$  the current levels of SOC and SOH need to be increased during the next operation modes by charging the battery and activating the electrolyzer.

**TABLE 6.1 Rules of Long-term Fuzzy Controller for Estimation**  
**(a)-Fuel Cell SOH and (b)-Battery SOC**

$\Delta SOH$		$SOH(n)$		
		<b>ZE</b>	<b>PS</b>	<b>PL</b>
$\tilde{E}_{FC\_T_L}$	<b>ZE</b>	ZE	ZE	ZE
	<b>PS</b>	PS	ZE	ZE
	<b>PL</b>	PL	PS	ZE

**(a)**

$\Delta SOC$		$SOC(n)$		
		<b>ZE</b>	<b>PS</b>	<b>PL</b>
$\tilde{E}_{FC\_T_L}$	<b>NL</b>	ZE	ZE	ZE
	<b>NS</b>	PS	ZE	ZE
	<b>ZE</b>	PL	PS	ZE
	<b>PS</b>	PL	PL	PS
	<b>PL</b>	PL	PL	PL

**(b)**

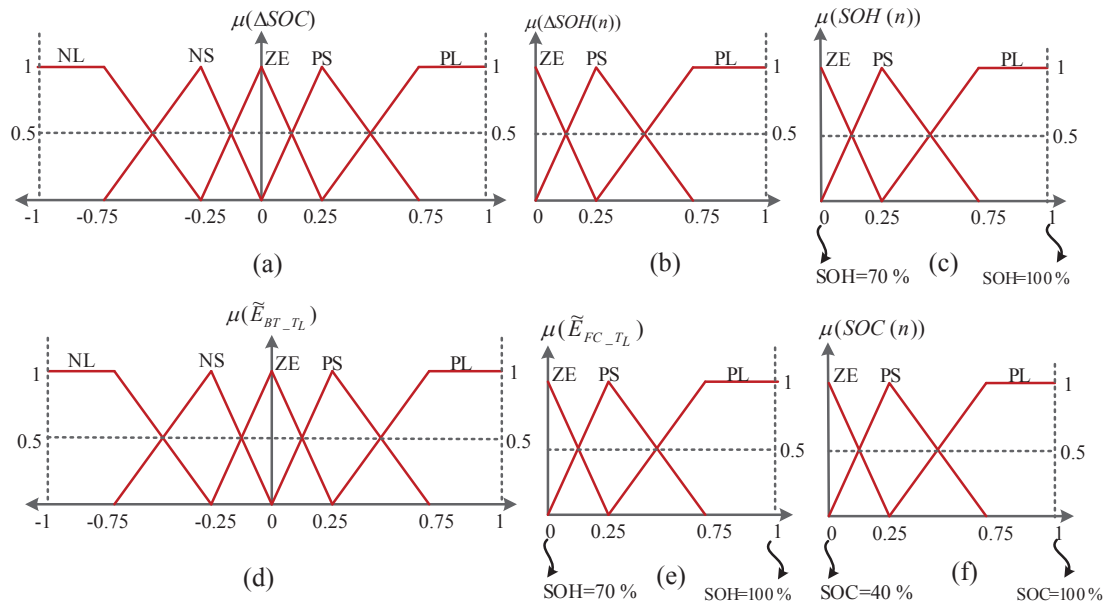


**Fig.6.10 Membership function of long-term fuzzy controller, (a)  $\Delta SOC(n)$  (b)  $\Delta SOH(n)$  (c)  $SOH(n)$  (d),  $\tilde{E}_{BT\_T_L}$  (e),  $\tilde{E}_{FC\_T_L}$  and (f)  $SOC(n)$**

This increases the battery and fuel cell stored energy levels for the next hours to supply the load or transfer energy to the grid. Table.6.1 illustrates the linguistic rules of long-term fuzzy controller for determining  $\Delta SOC$  and  $\Delta SOH$ . Fig.6.10 shows the membership functions of input and output variables of the long-term fuzzy controller. As illustrated in the figure, the linguistic variables of the membership functions are abbreviated as: negative large (NL), negative small (NS), zero (ZE), positive small (PS), and positive large (PL). All membership functions are normalized in the range (0 - 1) according to the maximum and minimum values of their variable by using

$$X_{norm} = \frac{X_{Actul} - X_{min}}{X_{max} - X_{min}} \quad (6.25)$$

where  $X_{Actul}$ ,  $X_{min}$ ,  $X_{max}$  are the actual, minimum and maximum values of each variable, respectively. It should be noted that the fuel cell estimated energy cannot be negative as it is not possible to charge the fuel cell.

### C. Short-term fuzzy controller

The short-term fuzzy controller which is the main decision maker of the EMU operates on the basis of real-time information of the system. It also considers the energy cost, load energy demand and cost of fuel cell and grid energies as other effective factors. It defines the operation condition of battery, fuel cell and electrolyzer and the amount of power that should be sent to, or received from the main grid. The resultant status of converters in battery, fuel cell and electrolyzer ports are the outputs of short-term controller and are sent to the mode selection unit. The mode selection and transition unit further selects the operation mode of the system. The sampling time of updating information in short-term controller,  $T_n$  can change from milliseconds to a few seconds. In this paper, the sampling time of short-term fuzzy controller is 100ms. Therefore, operation mode of the system is updated with frequency of 10 Hz. In the case of any change in the operation mode it is applied to the device level controllers otherwise system remains on the current operation mode.

The short-term fuzzy controller rules are defined according to the energy management scenarios and control objectives and are almost the same as those of the long-term controller. The difference is that they are based on real-time data which are updated for each sampling time  $n$ .

The electrolyzer only is activated during the low cost grid energy periods. Battery can be charged by fuel cell, PV or grid and is discharged under light load. It also is activated at peak demand hours to supply the load or transfer power to the grid. The maximum charging and discharging power of the battery should be taken into account.

As presented in Fig.6.8, the short-term controller as the main controller, requires the following parameters to make a decision. The available capacity of battery and fuel cell is defined by using  $\Delta SOC$  and  $\Delta SOH$  received from long-term controller.

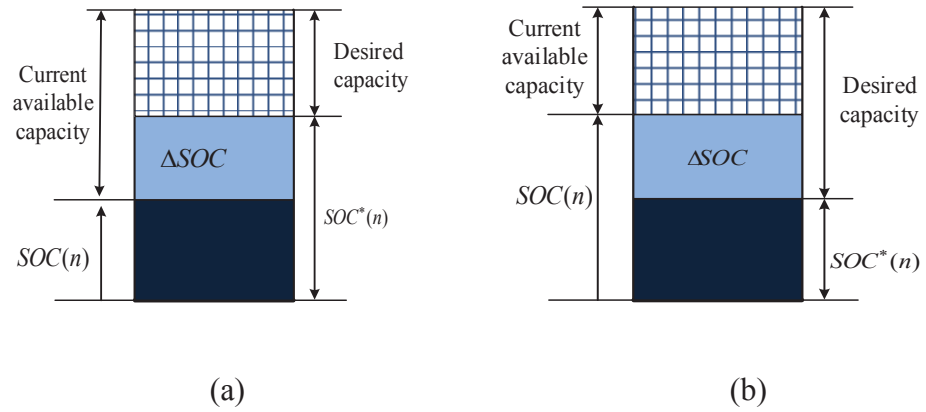


**Fig.6.11. Distribution of battery capacity including real-time and desired levels of SOC for (a)  $\Delta SOC > 0$  and (b)  $\Delta SOC < 0$**

The positive value of  $\Delta SOC$  means that battery needs to be charged during the next operation modes to increase the SOC level to the desired value. The desired level of SOC ( $SOC^*$ ) can be determined by using  $\Delta SOC$  and the actual value of SOC at  $n$ -th sample ( $SOC(n)$ ) as presented in Fig.6.11 by using

$$SOC^*(n) = SOC(n) + \Delta SOC(n) \quad (6.26)$$

On the other hand, the negative value of  $\Delta SOC$  means that there is some stored energy available in the battery that should be used during the future operation modes. Similarly, the positive value of SOH means that there is a need to increase the SOH level due to the long-term energy plans. The negative value of  $\Delta SOH$  means that there is a need to reduce the hydrogen available in the hydrogen tank by using fuel cell during the next operation modes.

The positive value of  $\Delta C(n)$  shows that the grid energy cost is currently more than for the fuel cell. Therefore, the fuel cell is preferred as energy source compared with the grid to supply the difference between load demand and PV output powers. On the other hand, in the case of a negative value of  $\Delta C(n)$ , the grid is the preferred source. Finally, the positive value of  $\Delta P(n)$  shows that the load demand is more than the PV output power, which means that one of the fuel cell, battery and grid should be used to cover the difference. The negative value shows that the PV output power is more than the load demand. Therefore, the surplus energy can be supplied to the battery or grid or some shiftable loads. Table.6.2 illustrates the short-term fuzzy control rules and the membership functions are presented in Fig.6.12.

**TABLE 6.2 Rules of Short-term Fuzzy Controller**

INPUT VARIABLES				OUTPUT VARIABLE			
$\Delta P(n)$	$\Delta C(n)$	$\Delta SOC(n)$	$\Delta SOH(n)$	BT	FC	EL	$P_{GD}(n+1)$
PL	PL	PL	PL	CD	OFF	OFF	NL
PL	PL	PL	PS	CD	ON	OFF	MD
PL	PL	ZE	PL	CD	OFF	OFF	NL
PL	PL	ZE	PS	CD	ON	OFF	MD
PL	PL	NL	PL	DO	OFF	OFF	MD
PL	PL	NL	PS	DO	ON	OFF	MD
PL	ZE	PL	PL	CO	OFF	OFF	NL
PL	ZE	PL	PS	CO	ON	OFF	NL
PL	ZE	ZE	PL	DO	OFF	OFF	MD
PL	ZE	ZE	PS	DO	ON	OFF	MD
PL	ZE	NL	PL	DO	OFF	OFF	NL
PL	ZE	NL	PS	DO	ON	OFF	MD
PL	NL	PL	PL	CO	OFF	ON	NL
PL	NL	PL	PS	CO	OFF	OFF	NL
PL	NL	ZE	PL	CD	OFF	ON	NL
PL	NL	ZE	PS	CD	OFF	OFF	NL
PL	NL	NL	PL	DO	OFF	ON	NL
PL	NL	NL	PS	DO	ON	OFF	NL
ZE	PL	PL	PL	CD	OFF	OFF	MD
ZE	PL	PL	PS	CO	ON	OFF	MD
ZE	PL	ZE	PL	CD	OFF	OFF	MD
ZE	PL	ZE	PS	CD	ON	OFF	PL
ZE	PL	NL	PL	DO	OFF	OFF	PL
ZE	PL	NL	PS	DO	ON	OFF	PL
ZE	ZE	PL	PL	CD	OFF	OFF	MD
ZE	ZE	PL	PS	CO	ON	OFF	MD
ZE	ZE	ZE	PL	CD	OFF	OFF	MD

INPUT VARIABLES				OUTPUT VARIABLE			
$\Delta P(n)$	$\Delta C(n)$	$\Delta SOC(n)$	$\Delta SOH(n)$	BT	FC	EL	$P_{GD}(n+1)$
ZE	ZE	ZE	PS	CD	OFF	OFF	MD
ZE	ZE	NL	PL	CD	OFF	OFF	MD
ZE	ZE	NL	PS	CD	OFF	OFF	MD
ZE	NL	PL	PL	CO	OFF	ON	NL
ZE	NL	PL	PS	CO	OFF	OFF	NL
ZE	NL	ZE	PL	CD	OFF	ON	NL
ZE	NL	ZE	PS	CD	OFF	OFF	MD
ZE	NL	NL	PL	CD	OFF	ON	NL
ZE	NL	NL	PS	CD	OFF	OFF	MD
NL	PL	PL	PL	CO	OFF	OFF	MD
NL	PL	PL	PS	CO	ON	OFF	PL
NL	PL	ZE	PL	CD	OFF	ON	MD
NL	PL	ZE	PS	CD	ON	OFF	PL
NL	PL	NL	PL	DO	OFF	ON	PL
NL	PL	NL	PS	DO	ON	OFF	PL
NL	ZE	PL	PL	CO	OFF	OFF	MD
NL	ZE	PL	PS	CO	OFF	OFF	MD
NL	ZE	ZE	PL	CD	OFF	ON	MD
NL	ZE	ZE	PS	CD	OFF	OFF	PL
NL	ZE	NL	PL	DO	OFF	ON	MD
NL	ZE	NL	PS	DO	OFF	OFF	PL
NL	NL	PL	PL	CO	OFF	ON	MD
NL	NL	PL	PS	CO	OFF	OFF	MD
NL	NL	ZE	PL	CD	OFF	ON	MD
NL	NL	ZE	PS	CO	OFF	OFF	PL
NL	NL	NL	PL	DO	OFF	ON	MD
NL	NL	NL	PS	DO	OFF	OFF	PL

As can be seen, the input variables of short term fuzzy controller are  $\Delta P(n)$ ,  $\Delta C(n)$ ,  $\Delta SOC(n)$  and  $\Delta SOH(n)$ . The output variables are the status of fuel cell and electrolyser, which can be either ON or OFF condition, grid power reference and battery status. In the CD mode the battery is in the stand-by mode which can be used to balance the bus voltage or compensate for the fuel cell slow dynamic response in transients.

To reduce the fluctuations in the operation mode of the micro-grid and improve the stability of decision making process, a hysteresis operation is used between different status of output variables membership functions. In the case of grid power transfer membership functions, if the transferred power is less than 20%, it can be used for power balance in the residential micro-grid otherwise it requires the acknowledgement from the regional grid distribution control centre. To reduce the fluctuations on the boundaries, hysteresis functions are considered between selling power, balancing power and buying power membership functions. Similar hysteresis functions are considered for fuel cell and electrolyzer ON/OFF membership functions and the battery charge, discharge condition membership functions as presented in the figure.

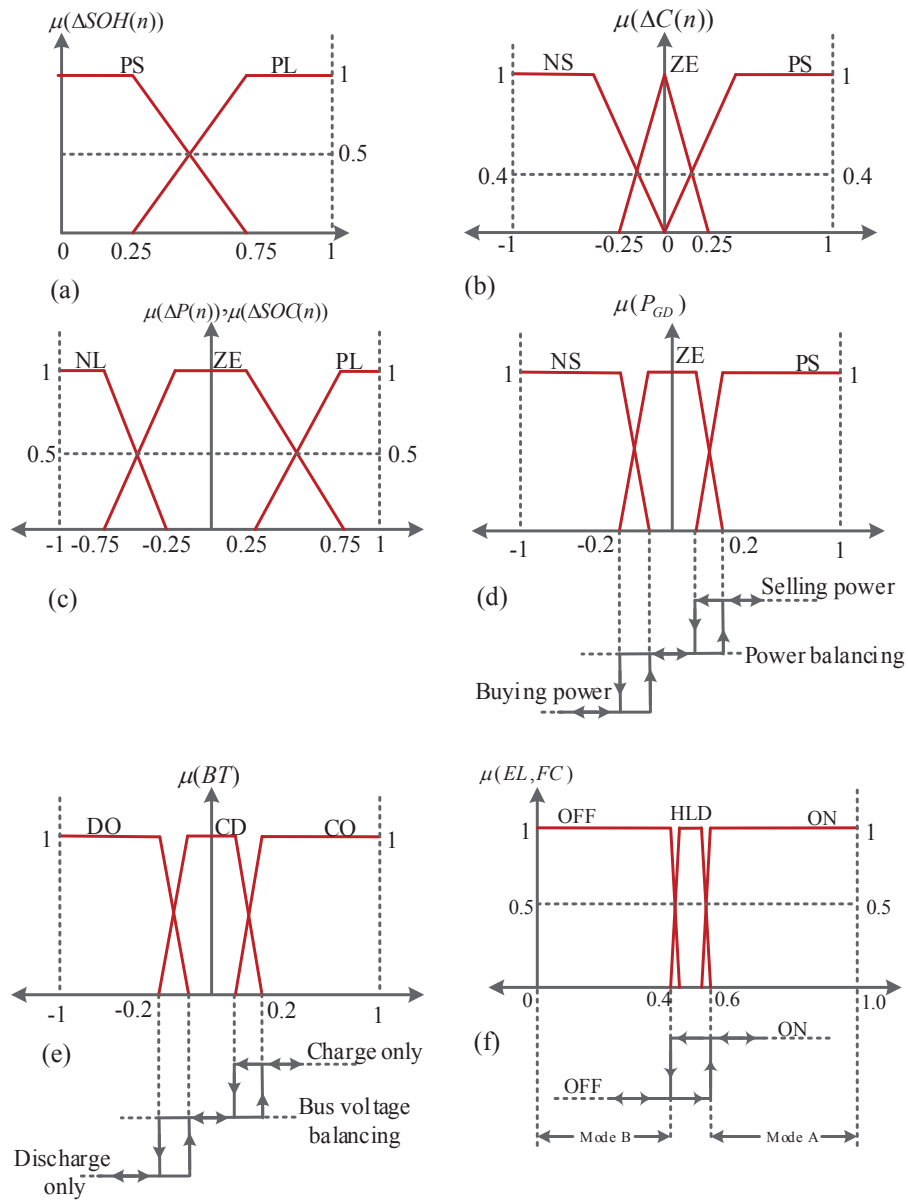


**Fig.6.12** Membership function of short-term fuzzy controller (a)  $\Delta SOC(n)$  (b)  $\Delta SOH(n)$  (c)  $SOH(n)$  (d),  $\tilde{E}_{BT\_T_L}$  (e),  $\tilde{E}_{FC\_T_L}$  and (f)  $SOH(n)$

### 6.7 Operation Modes of the Proposed Micro-grid

The proposed micro-grid is able to operate in several modes according to power flow direction and active sources and loads as presented in Table 6.1. Selection of operation modes depends on the control objectives and energy management scenarios and for each scenario only a limited number of modes are required. It should be noticed that only a limited number of them are selected by EMU for each energy management scenario. The system operation modes are different for the grid-connected and islanded conditions.

TABLE 6.3 Grid-connected Operation Modes

Operation mode	Power flow diagram	Operation mode	Power flow diagram
Mode 1		Mode 2	
Mode 3		Mode 4	
Mode 5		Mode 6	
Mode 7		Mode 8	
Mode 9		Mode 10	
Mode 11		Mode 12	

The grid-connected modes are presented in Table 6.3 and the islanded modes are presented in Table 6.4. It can be seen that the proposed system is designed to operate in 12 grid-connected and 8 islanded operation modes. As presented in Table 6.1, in operation mode 1, the load is only supplied by grid. This mode is selected as the basic operation mode under the grid-connected condition. This is because the grid is always connected to the load in the proposed topology and this mode is common between all grid-connected operation modes. This mode is used as bridging mode during the mode transition process to smooth the changing from one mode to other. As can be seen, the battery is used under the standby condition in parallel with fuel cell to compensate the low dynamic response of the fuel cell during fast transients. In this case, the battery link is presented in gray colour. In the second mode, the PV and grid are supplying the load and this happens when the load demand is more than the PV generation.

TABLE 6.4 Off-grid Operation Modes

Operation mode	Power flow diagram	Operation mode	Power flow diagram
Mode 1		Mode 2	
Mode 3		Mode 4	
Mode 5		Mode 6	
Mode 7		Mode 8	

The operation of other modes can be readily defined using the arrows that represent the power flow direction. In the case of islanded operation modes, the battery is the source that is always connected to the load or is in the stand-by mode. Therefore, mode one is selected as the basic mode and is used as the bridging mode during the mode transition. In the islanded mode, the battery can be charged by either the fuel cell or PV, depending on the availability of energy and micro-grid condition. More details on the mode selection and transition processes are provided in the following sections.

## 6.8 Mode Transition Unit

Transition from one operation mode to another is not a straightforward task. Quick change of operation modes results in undesirable transients and instabilities in the system's power and voltage surges on the switching devices. The resultant problems can cause a failure in the system operation, or activate the systems protection alarms, or be harmful to loads. On the other hand, the direct transition from some modes to others is not possible. Therefore, a mode transition unit (MTU) is designed to control and smooth the mode transition process. The transition path between different operation modes and the the required action is not similar for all operation modes. It depends on several factors such as actual operation mode, destination mode and the systems conditions. In

the case that direct transition is not possible a bridging mode is required for smooth transition. Fig.6.13 illustrates the flowchart of mode transition unit operation. As can be seen the mode transition process starts with mode-change detection from output variables of the fuzzy controller. The conditions of the new mode such as output voltage and energy capacity of sources in the new mode are checked and in the case of acceptable conditions the mode transition process starts. The process starts with setting up the reference signals of the control loops in the device level controller according to the new mode requirements.

The system may need to be switched on a bridging mode before moving to the new operation mode. The bridging mode is a common part of all operation modes and is employed to smooth the transition from one operation mode to another and prevent any interruption in the load supply. A time delay is applied to stabilize the bridging mode conditions. The new mode command is sent to the device level controller to start sending the PWM signals to the switching devices of the new active ports. It should be noticed that the duty ratio is minimized due to the soft start operation and the reference signals of the control loops being small. To activate the new ports, the reference signals ramp up to the nominal value and then conditions of the new mode are checked. In the case of acceptable conditions, the mode transition process is ended by moving to the normal operation conditions. In the case of any unexpected conditions the system switches on the bridging mode and remains on this mode as long as bridging-mode conditions are satisfactory otherwise system is turned off. The MTU operates according to a state transition diagram (STD) which shows the appropriate paths of transition between the operation modes and the required actions and conditions. Fig.6.14 shows the STD for both grid-connected and islanded operation conditions.

### **6.9 Validity Test of the Fuzzy Based Energy Management Unit**

To validate the operation of the proposed EMU, an experimental test-bench was established and a prototype of the proposed micro-grid is designed and implemented as presented in Fig.6.15. Two DSP controllers (C2000/TMS320F28335) are used as device level controller. The system level control including energy management and operation mode control is performed by a PC using MATLAB graphical user interface (GUI).

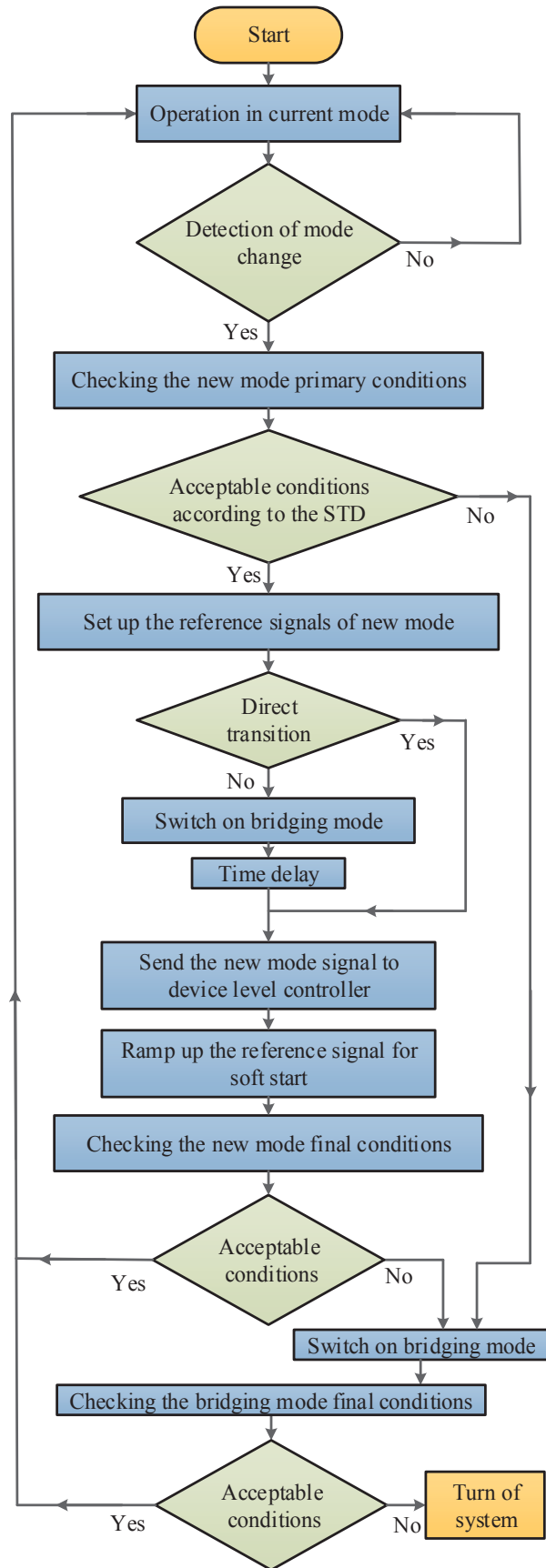
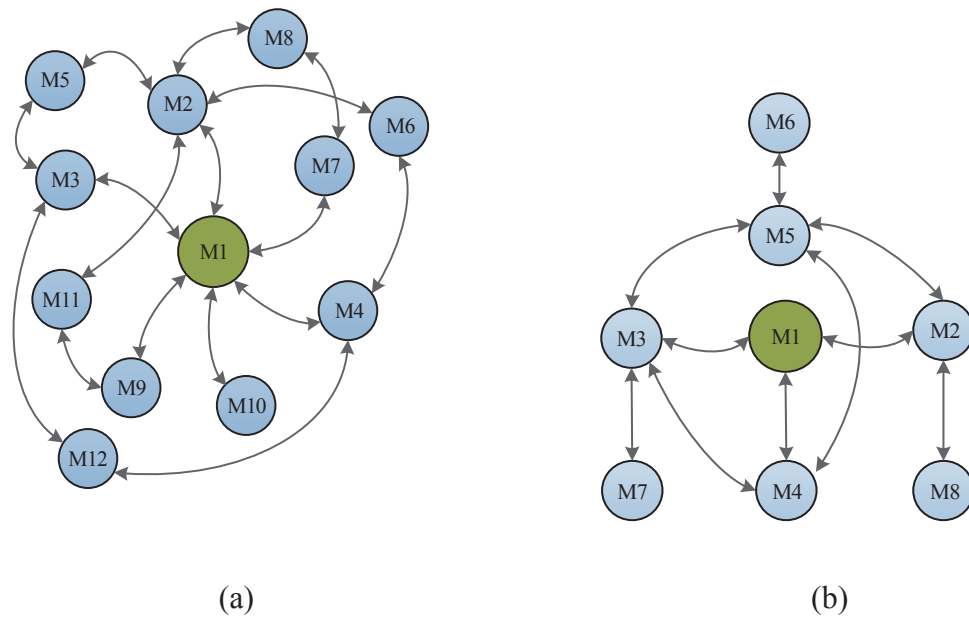
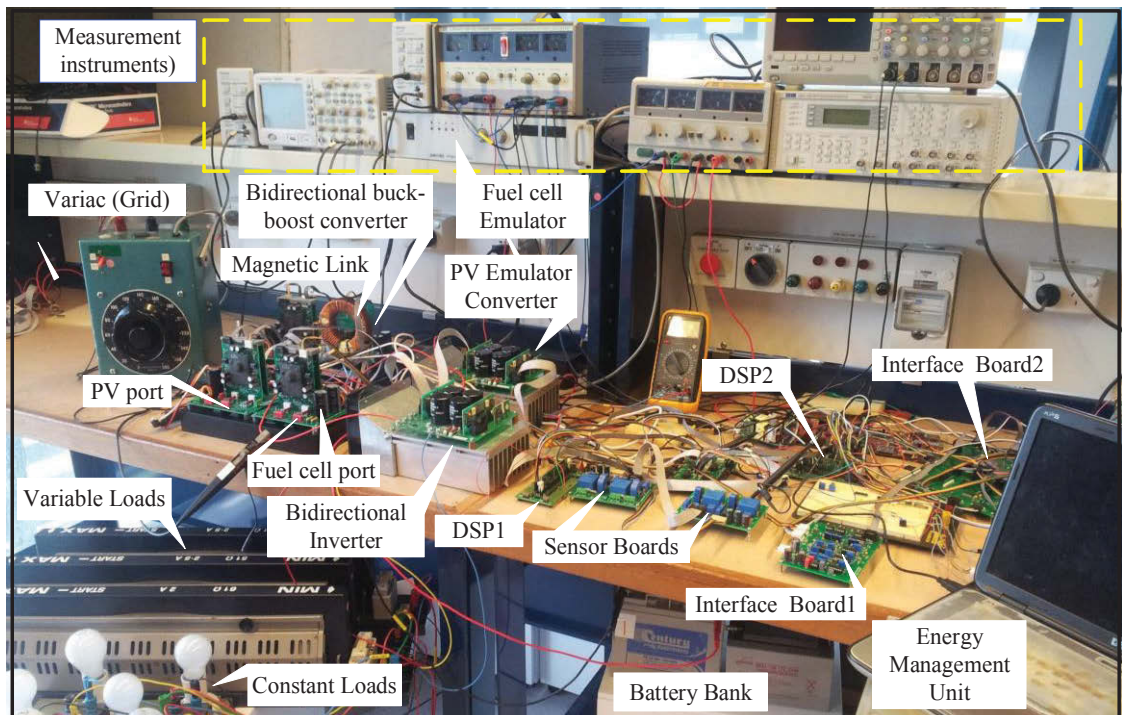


Fig.6.13 Flowchart of mode transition unit (MTU) operation



**Fig.6.14** State transition diagram of mode transition unit in (a) grid connected and (b) islanded operation modes



**Fig.6.15** The experimental test set up of the proposed grid for energy management tests

It also performs the system monitoring and data record during the energy management process. Two sensor and protection boards are designed to receive the measured values of voltage and current through Hall-Effect voltage (LV 25-P) and current (LTSR25-NP) sensors. The MPPT reference signal generated by EMU, is sent to the DSP1 to control the duty ratio of switching devices at the PV port. In the

proposed system MPPT reference signal is updated every 100 ms ( $f=10$  Hz). The operation mode of the micro-grid is updated through a four digit binary-coded decimal (BCD) signal generated by EMU. The single phase inverter is implemented using H bridge units made by SEMIKRON (SK30GH123) with isolated drivers (SKHI20opA) as presented in Fig.6.15. A fault signal resulted from logical “OR” operation of short circuit, over voltage and over current protection circuits is sent to the DSP. The short circuit in switching device is detected by driver integrated circuit (VLA567-01R) and is sent to the DSP through high speed, high-voltage opto-isolators (6N136). Both DSPs are connected to the signal conditioning and level shifters on the control and interface board and further to the EMU. The DSPs are linked to the EMU through interface board according to a multiplexing-data communication process using universal serial bus (USB). The data between each DSP and interface board is transferred using RS232 serial communication port and between grid energy control box and the EMU is transferred through the USB port. To study the energy management process, the residential load is implemented by parallel connection of two groups of variable and constant loads.

The proposed EMU is designed and experimentally developed using MATLAB/Fuzzy control toolbox. To monitor the system parameters and record the data during the energy management process a graphical media is designed using MATLAB graphical user interface (GUI). The proposed interface facilitates control and supervision of the micro-grid parameters. It makes it possible to observe the variation of battery capacity using estimated SOC level, fuel cell generation capacity using SOH, predicted profile of load demand and predicted profile of PV generation. The recorded power profiles of all micro-grid elements for the last 24 hours and the system operation modes are also accessible. Fig.6.16 shows the hardware implementation of EMU in the proposed micro-grid. As can be seen in the figure, the EMU receives some information such as the predicted PV generation profile, and grid energy cost (both selling and buying) via wireless communication link. It also receives the voltage and current signals of the local micro-grid converters (multi-port dc-dc converter and bidirectional inverter) from sensor and protection board. The received data are used for energy management and presentation targets. The output signals from EMU are the operational mode selection signal and reference signal for device level control loops, e.g. the fuel cell reference power.

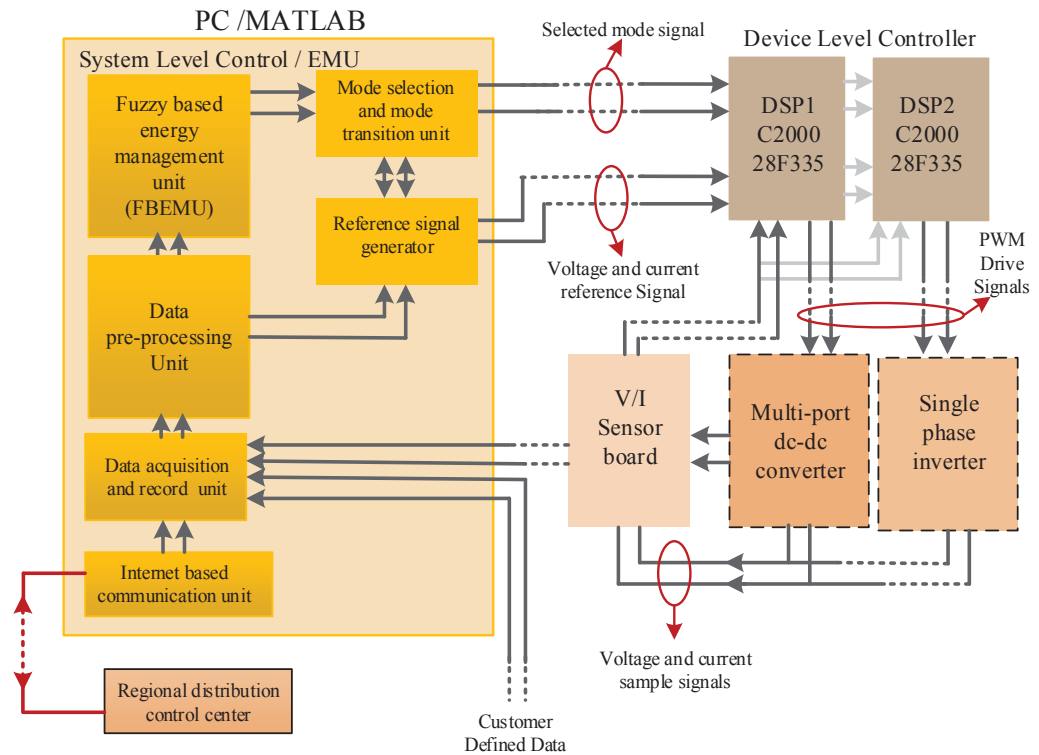


Fig.6.16 Schematic of the EMU hardware signals and connections

As discussed earlier, the objective of the proposed energy management scenario is minimizing the purchased power from the grid at peak hours and sending energy to the grid during the peak hours when the grid energy cost is high.

The experimental test is carried out for the proposed micro-grid and the objective of the proposed energy management scenario is minimizing the purchased power from the grid at peak hours and sending energy to the grid during the peak hours when the grid energy cost is high. The operation of the proposed EMU was experimentally tested for three different scenarios. The PV output power profile in the first scenario is presented according to a normal sunny day profile. The system is assumed to be in grid-connected mode with flexible power flow to/from grid. In the second scenario, the PV power profile was changed to model the cloudy condition and the irradiation levels are changed randomly. In the third case, the proposed micro-grid is assumed to operate in off-grid conditions. The input sources in this case are the fuel cell, PV and battery. In this thesis, instead of using real PV panel and fuel cell stack, their operation is modelled using PV and fuel cell emulators.

This facilitates the control and variation of source parameters and speeds up the experimental test process. A full bridge dc-dc converter using Semikron compact IGBT

module SK30GH123 with Semikron driver board SKHI 20opA, controlled by DSP (TMS320F28335) is used to emulate the PV panel operation. The operation point of PV is adjusted according to the irradiation level by referring to the recorded data of V-I characteristics of PV panel. To adjust the output parameters of the converter according to the PV characteristics, the V-I curves of the PV panel are recorded in a look up table for 50 irradiation levels. The duty ratio of PWM drive signals are controlled according to the recorded data for each irradiation level. On the other hand, the fuel cell is easily modelled by a series connection of resistor and capacitor to the dc voltage source. Considering that the fuel cell is operating in ohmic polarization or linear area, values of resistors and capacitor can be adjusted according to the frequency response of an actual fuel cell stack to model the slow dynamic response as discussed in Chapter Five.

To study the energy management process, the residential load is implemented by parallel connection of two groups of variable and constant loads. The constant loads are used to model permanent residential loads such as refrigerator, lighting and the variable section is used to model the random and short duration loads. The experimental test for each scenario is carried out for a time-duration of 2 hours to model a 24 hours residential load which starts at 12 AM. Therefore each 2 minutes in the 24-hour time period is modelled by a 10 seconds time step in the actual test ( $T_L=40\text{min}$ ,  $T_k=10\text{s}$ ,  $T_r=100\text{ms}$ ). According to this, 720 samples with time duration of 10 seconds are used to record the parameters of the proposed micro-grid.

The operation of the proposed EMU was experimentally tested for three different scenarios. The PV output power profile in the first scenario is presented according to a normal sunny day profile. The system is assumed to be in grid-connected mode assuming that the power flow to/from grid is quite flexible. In the second scenario, the PV power profile was changed according to a cloudy day and the irradiation levels are changed randomly. In the third case, the proposed micro-grid is assumed to operate in off-grid conditions. The input sources in this case are the fuel cell, PV and battery. Details of EMU operation for each of the scenarios are presented in the following sections.

### **6.9.1 First energy management scenario (a sunny day with flexible grid energy transfer)**

In this section, the operation of EMU in energy management of the proposed micro-grid is studied. It is assumed that the energy transfer to/from the grid is flexible in time and is not limited to a certain value. On the other hand, the PV irradiation levels are changed according to the sunny day profile although the systems operation for cloudy condition is studied as a second scenario.

The power profiles of the PV generation, load demand, energy cost profiles of the fuel cell, battery and grid and the estimated values of SOC and SOH for 24-hours duration are presented in Fig.6.17. The difference between PV generation and load demand, grid power, fuel cell power and the battery power profiles for the same duration time are presented in Fig.6.18. According to the short-term fuzzy controller the operation mode of the proposed micro-grid depends on the difference between inverter output power and the demanded power by load, cost of energy delivered by each source and the availability and energy capacity of each source. As can be seen in the energy cost profiles, the cost of fuel cell and battery energies follow a constant value during the day while the cost of grid energy is variable depending on the time of day.

As discussed earlier, in this research, it is assumed that the cost of energy received from the battery is less than the fuel cell. The grid energy cost is variable and varies in a wide range from less than battery to more than fuel cell cost. On the other hand, the battery charging and discharging maximum powers are different. The maximum charging and discharging powers of the battery are limited to 250 W and 300 W respectively. Therefore, considering 24 V as the approximate voltage of the battery terminal during the charge and discharge process, the maximum current during charge and discharge process should be limited to 10.5 A and 12.5 A respectively. The fuel cell maximum power is 500 W although in grid connected mode it is limited to 350 W and in off-grid to 450 W.

The operation modes of the micro-grid are different for different time intervals considering variations in the load demand, PV generation, and the energy cost. On the other hand, the current status of the battery capacity and hydrogen fuel, power limits of battery and fuel cell and the long term energy management commands are required to be

taken into account in definition of each operation mode. The operation modes of the proposed micro-grid for the 24-hours' time duration during the experimental test are presented at the bottom of the figure. The active operation mode of the system is defined according to the energy management scenario applied by short-term fuzzy control rules. As discussed in the earlier sections, in the proposed scenario, PV is given as priority as energy source in all conditions due to its low energy cost. The difference between PV power generation at the inverter output and the load demand should be covered by one of battery, grid or fuel cell depending on their energy cost and availability and the component power limits.

As can be seen in the figure, for the first time interval starting from  $t_1$  to  $t_2$  there is no power generated by PV and due to the low value of load demand it can be supplied by either battery or grid. As the cost of battery energy is less than grid for the proposed time interval, it is selected to supply the load and operation mode of the system selected as mode 4 (M4). At  $t=t_2$  the cost of grid energy is reduced to less than battery which means that using the grid is more beneficial compared with the battery and the operation mode is changed to M1. It should be noticed that battery still has enough capacity to supply the load demand if it is required referring to the SOC level variation graph. When the PV panel starts to generate power at  $t=t_3$ , the PV port needs to be activated and the operation mode changes to M2. This operation mode continues as long as the PV power is less than load demand. At  $t=t_4$  where PV generation is more than load demand the surplus energy can be transferred to one of controllable loads, grid or battery.

According to the long term energy plan the battery needs to be charged for the next long-time interval and the actual level of SOC is less than the desired value. Therefore battery is selected to be charged and operation mode is changed to M11. It should be noted that the battery charging power is limited and the additional energy should be sent to the grid. At  $t=t_5$  battery is charged to the full capacity and SOC reaches the maximum level of allocated capacity of battery for operation as storage (SOC=90 %). The surplus energy should be supplied to the grid although in the case of PV generation less than load demand, the battery is preferred to supply the load due to its lower energy cost compared with the grid. Therefore the system operation mode is changed to M6 where both battery and PV can supply the load and additional energy is transformed to the

grid. At  $t=t_6$ , the load demand is more than the PV and battery powers and it is required for either the fuel cell or grid to supply the difference. Considering the energy cost of fuel cell and grid at this time, fuel cell is selected as preferred source. In this case fuel cell operates with a constant output power and the difference between load demand and fuel cell power is compensated by battery.

As fuel cell and battery are connected directly to the same dc bus, it is easy for battery to be charged or discharged into the dc bus to compensate for the load demand variations. Therefore, during  $t_6$  to  $t_7$ , the system operation mode changes to M5 where the fuel cell power is more than the load demand and the surplus energy of fuel cell charges the battery. At  $t=t_7$ , the load demand changes to more than fuel cell power which requires the battery to supply the difference and the operation mode is changed to M12. At  $t=t_8$ , the cost of grid energy drops to less than battery and fuel cell. Therefore, the operation of fuel cell and battery is not economic and the load demand should be supplied by grid. The system operation mode changes to the basic mode M1 where grid is the only energy source of the micro-grid system. The power profiles of the PV, fuel cell, battery, load and grid are used to define the total energy supplied or received by each element. As an example, energy supplied by PV can be determined by

$$E_{PV\_24h} = \sum_{k=1}^{720} P_{PV}(k)T_k = T_k \sum_{k=1}^{720} P_{PV}(k) \quad (6.27)$$

where  $T_k$  is the sampling time and equal to 2 min for a 24 hour time duration. The fuel cell energy  $E_{FC\_24h}$  and the load energy  $E_{LD\_24h}$  are defined similarly. On the other hand, the energy received by battery in charging mode ( $E_{BT\_24h}^{CHD}$ ) or supplied by the battery in discharging mode ( $E_{BT\_24h}^{DCH}$ ) can be determined by

$$\begin{cases} E_{BT\_24h}^{CHD} = \sum_{k=1}^{720} P_{BT\_24h}(k)T_k & \text{where } P_{BT\_24h}(k) < 0 \\ E_{BT\_24h}^{DCH} = \sum_{k=1}^{720} P_{BT\_24h}(k)T_k & \text{where } P_{BT\_24h}(k) \geq 0 \end{cases} \quad (6.28)$$

The energy sold to the grid ( $E_{BT\_24h}^{SEL}$ ) and the energy supplied by the grid ( $E_{BT\_24h}^{BUY}$ ) can be defined similar to the battery. The energy loss in the system can be determined by

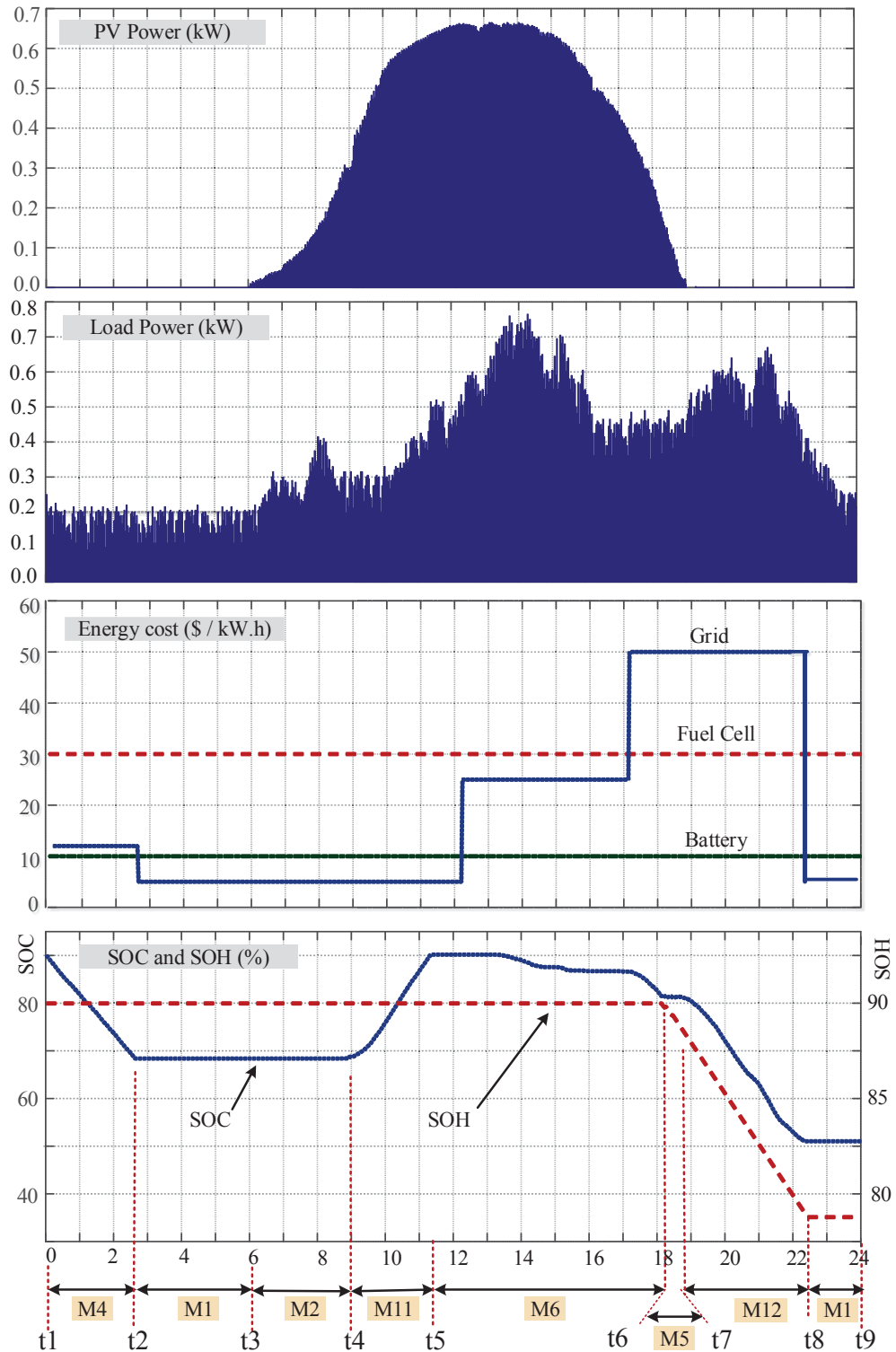
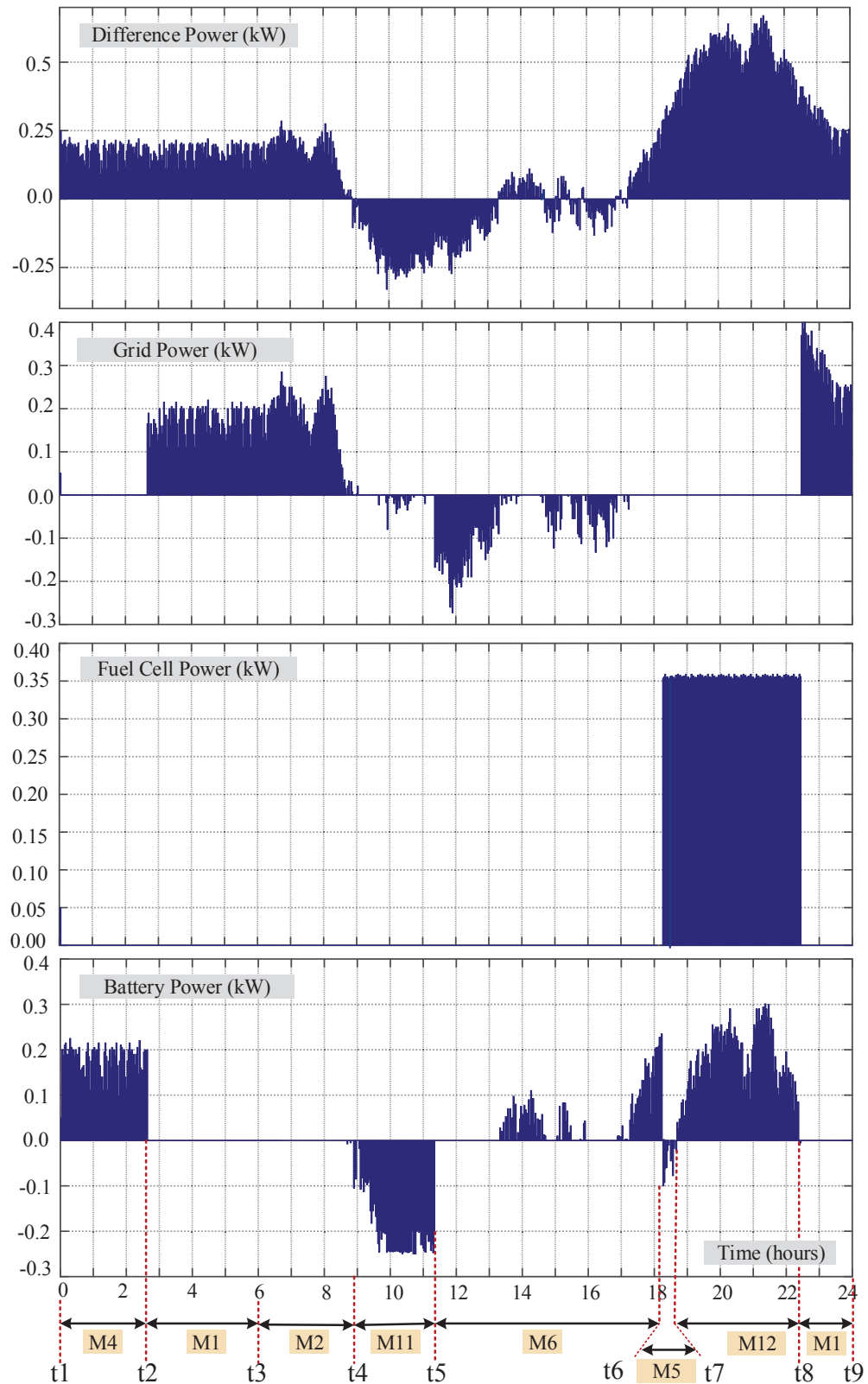


Fig.6.17 Profiles of the PV power generation, load power demand, energy cost and SOC/SOH levels for the first energy management scenario



**Fig.6.18 Profiles of the difference between PV power generation and load power demand, grid power, fuel cell power and the battery power for the first scenario**

$$E_{LS\_24h} = E_{PV\_24h} + E_{FC\_24h} + E_{GD\_24h}^{BUY} - E_{GD\_24h}^{SEL} + \Delta E_{BT\_24h} \quad (6.29)$$

where the variation in the battery energy  $\Delta E_{BT\_24h}$  during the 24h time duration can be found by

$$\Delta E_{BT\_24h} = E_{BT\_24h}^{DCH} - E_{BT\_24h}^{CHD} + E_{BT\_0h} - E_{BT\_24h} \quad (6.30)$$

$E_{BT\_0h}$  and  $E_{BT\_24h}$  are the stored energy in the battery at the beginning and at the end of the 24h time interval, respectively, and can be determined from the estimated values of SOC at the beginning and end of time interval. The energy loss in the system is mainly related to the multi-port dc-dc converter and inverter switching devices.

Fig.6.19 illustrates the energy analysis of the micro-grid for the first energy management scenario during the 24-hour time-duration. It can be seen that almost 60% of the load energy is provided by PV while fuel cell, battery and grid supplied almost 15% of the total load demand. It can be seen that the energy received from the grid is 1 kWh on average. To analyse the operation of micro-grid from economic point of view, the total cost of energy supplied, stored or consumed by each element is calculated as presented in Fig.6.20. To calculate the total cost of energy for 24 hours duration, the amount of power and the cost of energy at the sampling time are taken into account. For example, the PV energy cost for the 24 hour time period can be calculated by

$$C_{PV\_24h} = \sum_{n=1}^{720} P_{PV\_24h}(k) C_{PV}(k) T_k \quad (6.31)$$

where  $T_k=120s$ , considering 24 hours duration of the test.

In this thesis, the PV energy cost is assumed to be 0.02 \$/kWh, the fuel cell energy cost is 0.3 \$/kWh, the battery cost is 0.10 \$/kWh and the grid cost is variable between 0.05 to 0.50 \$/kWh. The energy cost analysis can be used to compare the customer benefits from the renewable energy system for a particular time duration such as a day, week, month, or a year. Looking at the energy cost graph shows that the customer benefits from supplying energy to the grid at peak demand hours when the grid energy cost is 0.925 \$/day. This can compensate for the energy cost resulting from other sources. About 60% of the total energy cost of the load belongs to the fuel cell compared with the other sources (0.45 \$/day).

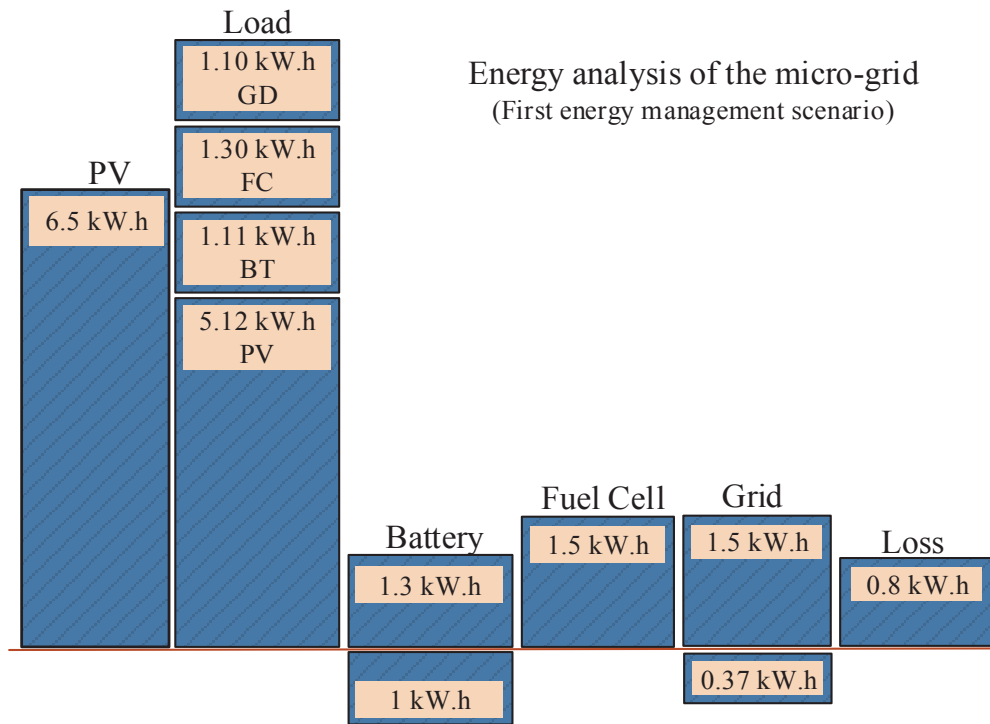


Fig.6.19 Energy analysis of the proposed micro-grid for the first energy management scenario

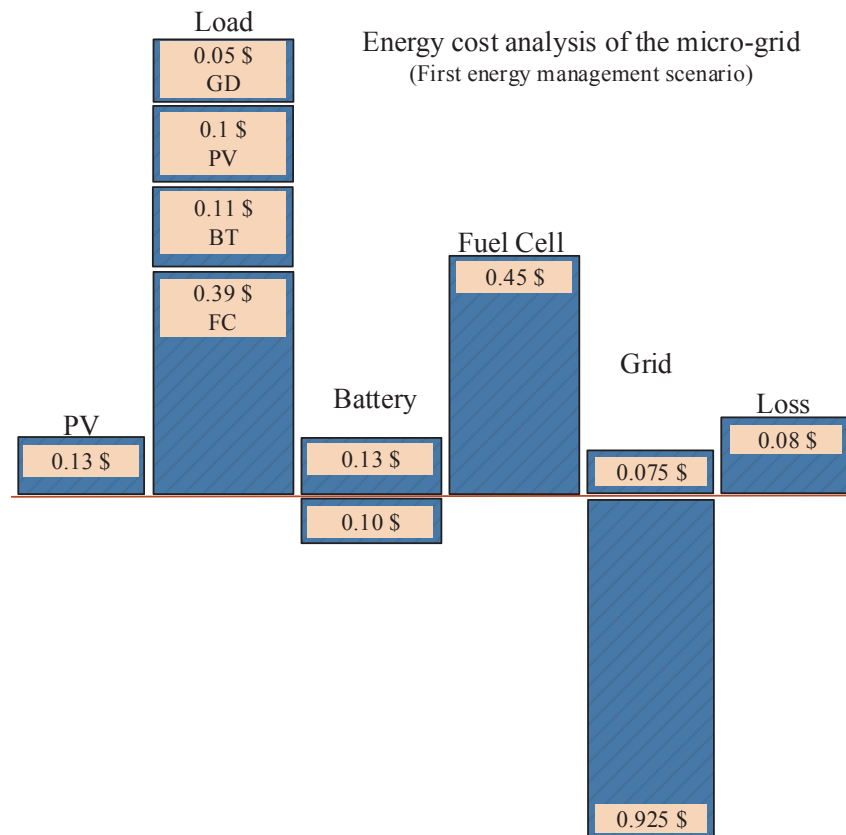


Fig.6.20 Energy cost analysis of the proposed micro-grid for the first energy management scenario

### 6.9.2 Analysis of the EMU operation in second energy management scenario

In the second energy management scenario, the operation of the proposed energy management system is studied under the cloudy weather condition where the PV output power is changed abruptly. In this case it is assumed that the clouds passing through the sky during the day result in fluctuations in the PV output power. Due to the wide range of variation in the PV output power, different operation modes are required for the energy management.

Fig.6.21 illustrates the PV output power profile for the second scenario. As can be seen, the PV output is dropped due to the shading effects and consequently the different operation modes are required. The load demand profile is changed with almost similar pattern to the first scenario as can be seen in the figure. The energy cost profile also varied similarly while the resulting variations in the battery SOC and SOH levels are different due to the new operation modes. The difference between PV and load power, battery, fuel cell and load power profiles are presented in Fig.6.22.

As can be seen in the figure, for the time interval  $t_1$  to  $t_2$ , the battery is selected as preferred source due to the small amount of power demand and lower energy cost. For the time interval between  $t_2$  to  $t_3$ , the load demand is covered only by the grid due to its lower cost compared with the fuel cell and battery although battery still has capacity to supply the load according to the SOC level. The operation mode is changed to M2 at  $t=t_3$  when PV panel power generation starts although grid is still selected to compensate for the difference due to its lower cost. At  $t=t_4$ , the extracted power from PV is more than the load demand and the surplus energy should be supplied to the battery or grid. In this case battery is selected to be charged by PV when PV output power is more than the load demand. It should be noticed that the battery is not able to absorb the surplus energy completely due to the limits on the charging power. Therefore, the grid is selected automatically to compensate for the difference due to its direct connection to the load and operation mode of the system is selected as M11.

At  $t=t_5$ , the battery is charged to the maximum allocated capacity and there is no possibility of charging to higher SOC level. Therefore, the surplus energy should be sent to the grid although during this mode the cost of grid energy changes to more than battery so that it is economically beneficial to supply the surplus energy to the grid.

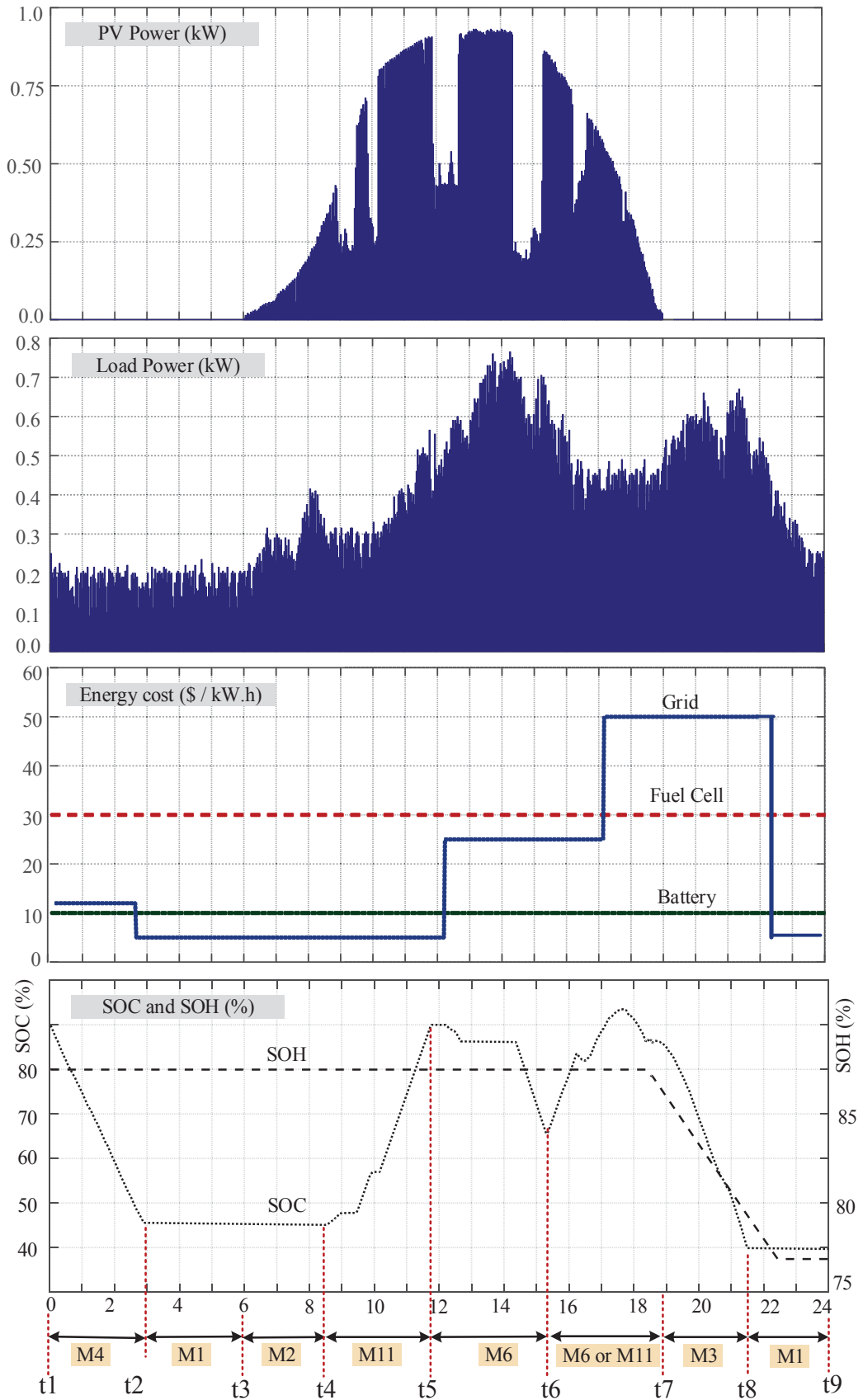
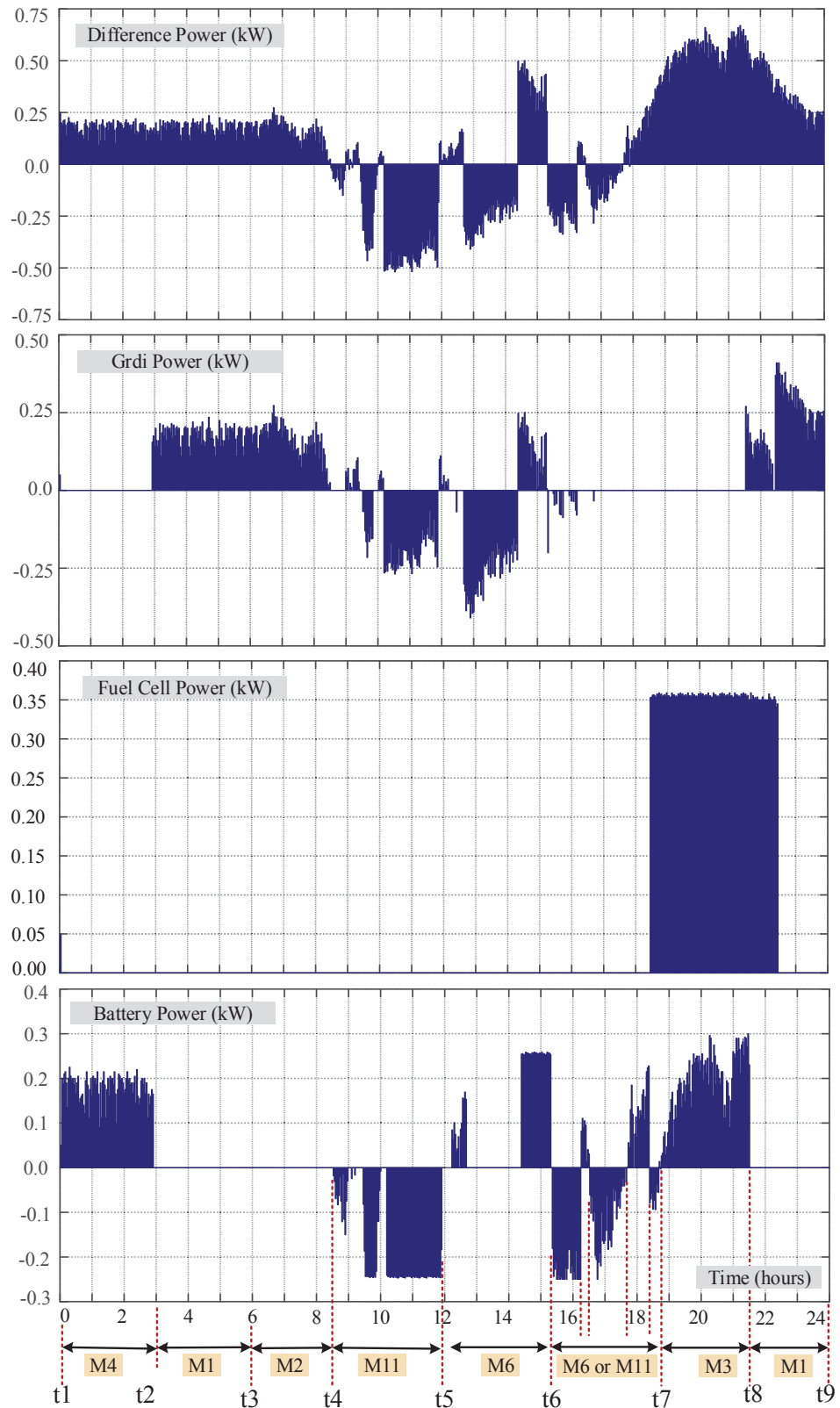


Fig.6.21 Profiles of the PV power generation, load power demand, energy cost and SOC/SOH levels for the second energy management scenario



**Fig.6.22 Profiles of the difference between PV power generation and load power demand, grid power, fuel cell power and the battery power for the second scenario**

Therefore, the system operation mode changes to M6. During  $t_6$  to  $t_7$ , the system operation mode fluctuates between M6 and M11 and the battery is selected as the main source for both charging and discharging operation. The reason is that the battery needs to be charged according to the long-term fuzzy control commands and at the same time it is the preferred source to supply the difference between the PV and load demand due to the grid energy cost and amount of demanded power. At  $t=t_7$ , the load power demand is more than the battery capacity due to the absence of PV generation. In this case, the possible options are fuel cell and grid and fuel cell is selected according to the lower energy cost. The battery in this mode is selected to compensate for the difference between fuel cell constant power and variable load demand.

At  $t=t_8$ , the battery SOC is reduced to the minimum level (40%) and battery is not able to compensate for the difference between load demand and fuel cell power. Therefore the power difference automatically is supplied by grid due to the direct connection of grid to the load and system operation mode changes to M3.

At  $t=t_9$ , the grid energy cost drops to lower than the battery and fuel cell. Therefore, the load demand is only supplied by the grid for the rest of time duration and system operation mode changes to the basic mode M1. The energy share and energy cost analysis of the second energy management scenario can be performed similar to the first scenario and are not repeated in this section.

### **6.9.3 Analysis of EMU operation in the third energy management scenario (Off-grid operation)**

In the third energy management scenario, operation of the proposed EMU in off-grid conditions is studied. In this case the proposed micro-grid is disconnected from the main grid and is supplied only by the PV, fuel cell and battery. In contrast to the grid-connected condition, the battery port is always active and is used as common operation mode or bridging mode in off-grid condition. Fig.6.23 illustrates the PV power generation, load power demand and variation of SOC/SOH for the 24 hours duration time. The PV power profile is changed according to a sunny day pattern and the load demand profile is slightly different from that of grid-connected mode. Similar to the previous scenarios, the operation modes of the system are presented for different time intervals.

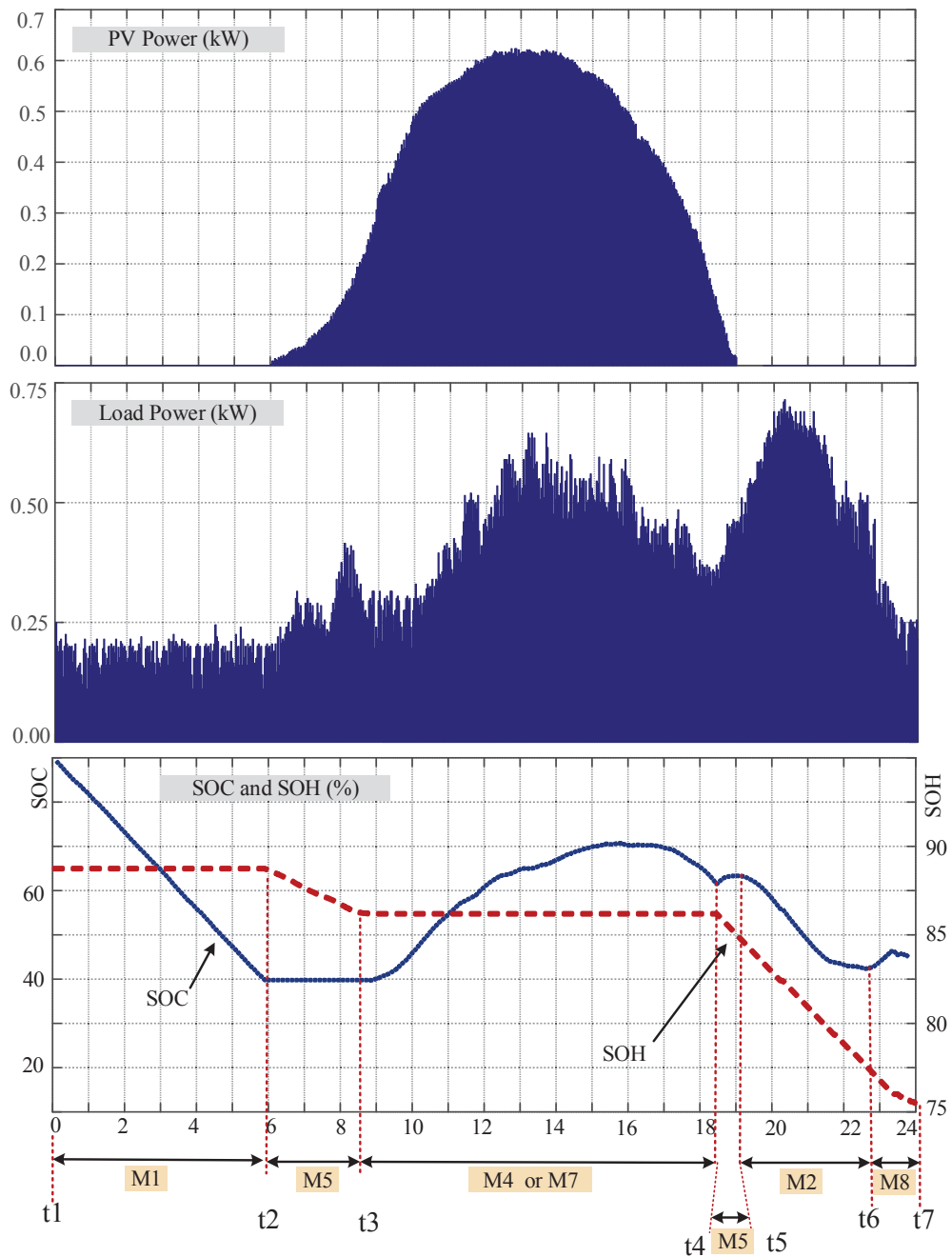


**Fig.6.23 Profiles of the PV power generation, load power demand and SOC/SOH levels for the third energy management scenario**

Fig.6.24 presents the difference between PV power generation and load demand, the fuel cell power generation and battery power profile. As can be seen in the figure, the energy difference between the PV generation and load demands is covered by either the battery or fuel cell. It is assumed that the energy cost of battery is constant and less than fuel cell for entire test duration and therefore, it is not necessary to present the energy cost profile.

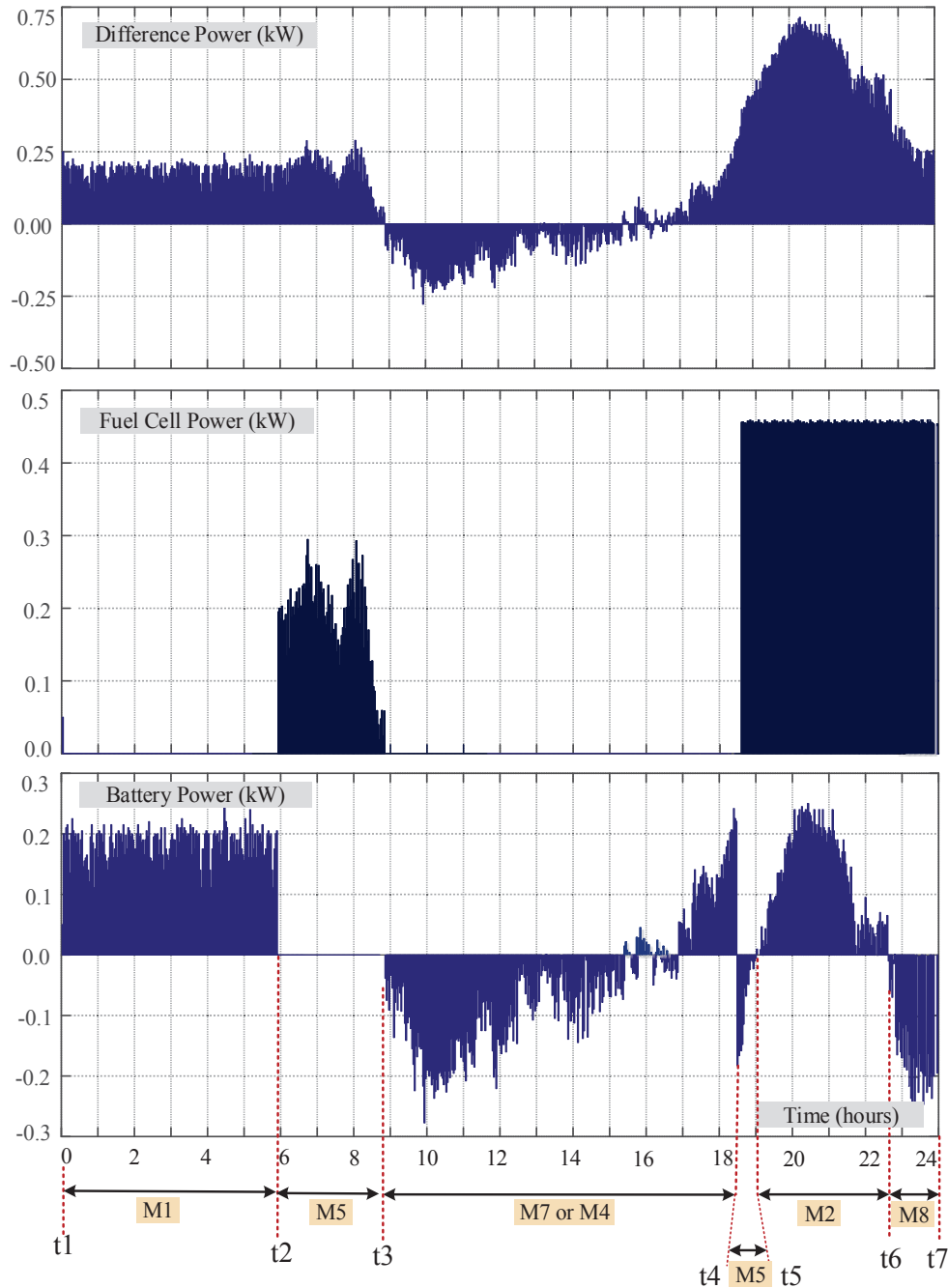


**Fig.6.24 Profiles of the difference between PV power generation and load power demand, grid power, fuel cell power and the battery power for the third scenario**

In the first time interval, from  $t_1$  to  $t_2$ , the difference between PV generation and load demand is covered by battery due to the lower energy cost and amount of power. Therefore, the basic operation mode M1 is selected by the EMU. At  $t=t_2$ , the battery SOC reaches the minimum value (40% as can be seen in the figure) and battery is not able to supply the load any more. Therefore, the fuel cell is switched on and continues to cover the energy difference between PV and load demand and operation mode is changed to M5.

At  $t=t_3$ , the PV generation is more than load demand and therefore fuel cell is turned off. During this time interval when PV generation is more than load demand, the surplus energy is used to charge the battery and when it is less than load demand the difference is supplied by battery. Therefore, the operation mode at the end of this time interval fluctuates between either M7 or M4 depending on the charging or discharging modes of the battery. The maximum charging and discharging power of battery needs to be considered and shiftable or dump loads can be used in the case of excessive power generation. It can be seen that during this time interval battery is charged from SOC=40% to SOC=70% although it slightly discharged to SOC=60% at the end.

At  $t=t_4$ , the load demand is more than the PV generation and the difference is more than battery capacity. Therefore, the fuel cell is switched on to supply the difference between the PV generation and the load demand. In this case, the battery is used to compensate for the difference which lets the fuel cell operate with a constant power. The operation mode M5 is selected by the EMU.

From  $t_5$  to  $t_6$ , the PV power is not available and the load is supplied only by fuel cell and battery. Similar to the previous mode, the fuel cell supplies a constant power to the load and battery compensates for the difference and operation mode is changed to M2.

Between  $t_6$  to  $t_7$ , the fuel cell is supplying the load and due to the constant power of fuel cell and the command from long-term fuzzy controller, the battery is charged by fuel cell and the operation mode is changed to M2. The battery should be able to supply the load for the next hours due to the small amount of predicted load demand and long-term energy plan. Therefore, the long term fuzzy controller increases the desired level of SOC which results in medium and positive values of  $\Delta$ SOC.

Energy analysis of the third energy management scenario is carried out similar to the first scenario. As presented in Fig.6.25 about 54% of the total energy received by the load is provided by the PV, 33% by the fuel cell, and 13 % by the battery. It can be seen that the energy loss in the system is more than that in the grid-connected mode (first scenario).

The reason is that in the absence of grid energy, the load energy should be supplied by the renewable energy system and dc-dc converters and inverter.

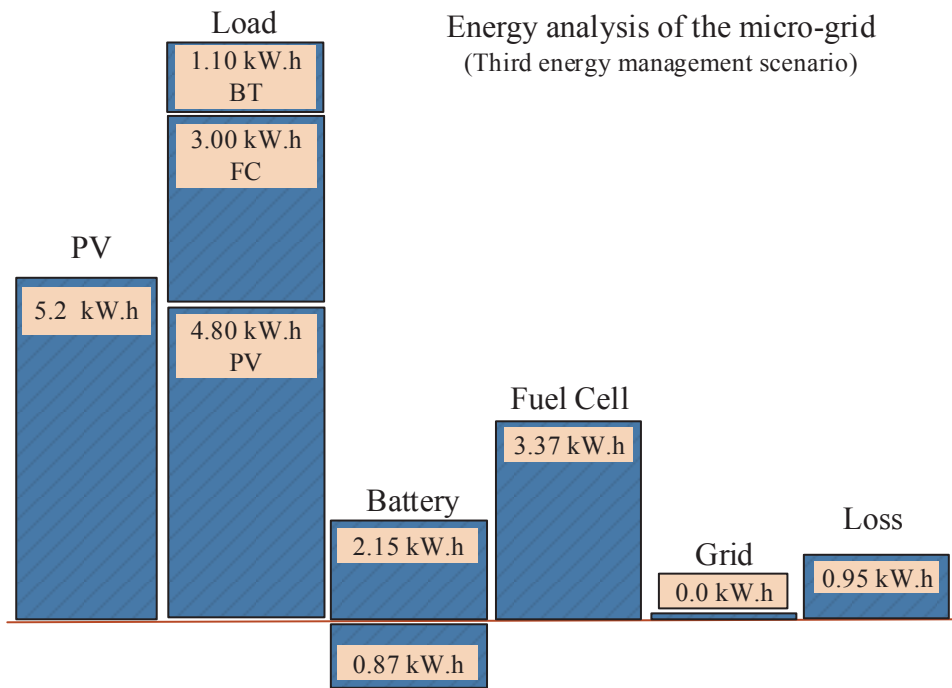


**Fig.6.25** Energy distribution analysis of the proposed micro-grid for the third energy management scenario

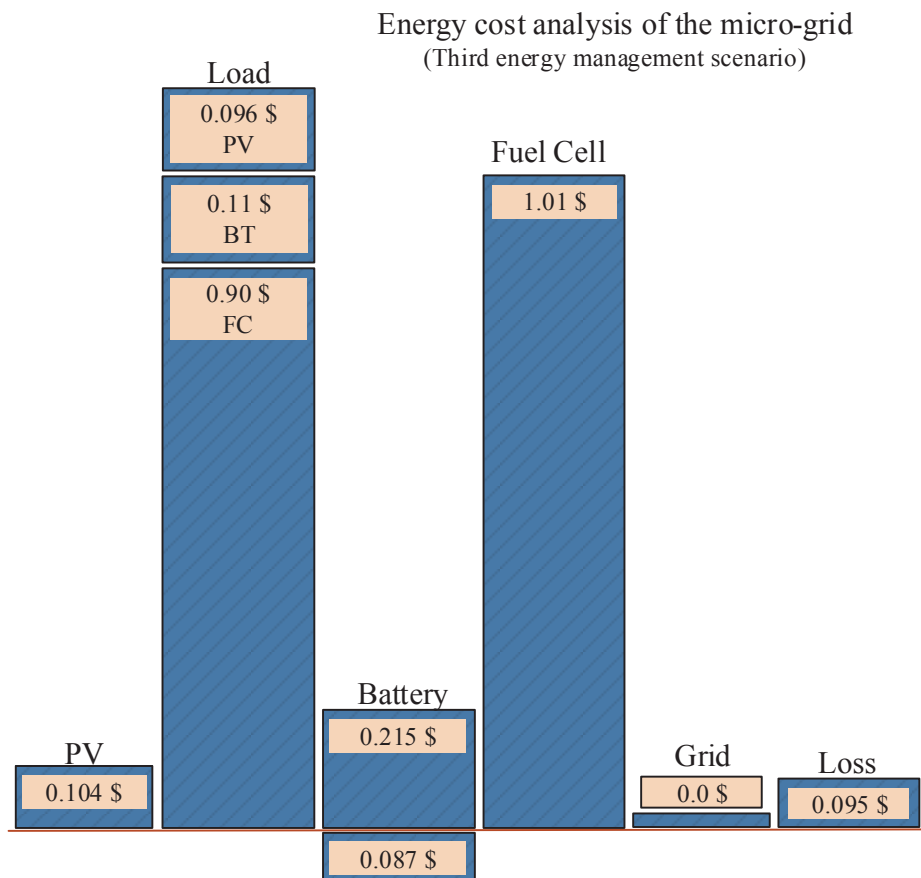


**Fig.6.26** Energy cost analysis of the proposed micro-grid for the third energy management scenario

Comparison of total cost of load energy in the cases of with and without using renewables for grid connected and islanded modes

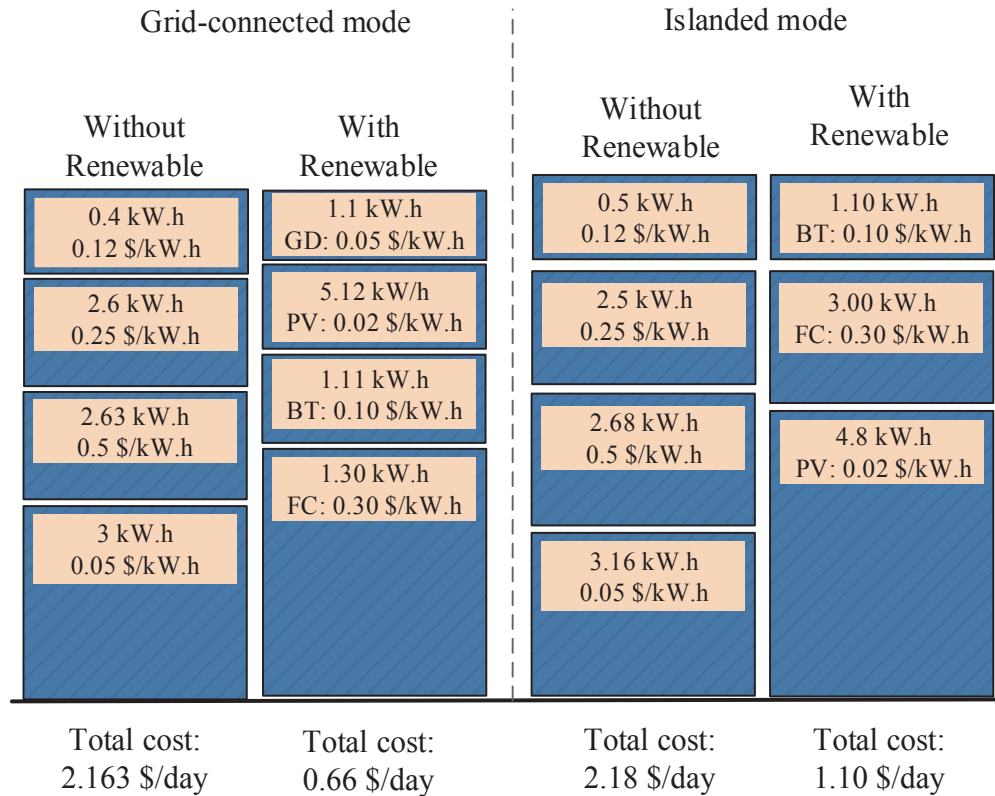


**Fig.6.27 Comparison of energy costs of proposed residential load for three cases, grid-supplied only, grid-connected with renewable sources and off-grid with renewable sources**

Therefore, increasing power of converters raises the system power loss and consequently energy loss in the micro-grid. The energy cost analysis also is performed similar to the first scenario and the results are presented in Fig.6.26. As can be seen, the maximum cost belongs to the fuel cell due to its higher energy cost compared with the battery and the minimum cost belongs to the PV.

The energy costs of micro-grid in three cases including using renewable energy sources along with grid, using renewable energies only and using grid only are compared in Fig.6.27. As can be seen using renewable energy sources along with the grid reduced the daily energy cost from 2.16 \$/day to 0.66 \$/day. In the case of off-grid condition, the total energy cost is 1.1 \$/day which is about two times the cost of using grid-connected renewable energy system.

## 6.10 Summary of Chapter

In this chapter, a fuzzy based EMU was designed and developed for the proposed residential micro-grid. The EMU contained two fuzzy based short-term and long-term control units. The long-term controller defines the desired levels of SOC and SOH according to the long-term energy plans, and the short-term controller the operation mode of the system according to the real-time data and commands from the long-term controller. A mode transition unit is designed to smooth the mode changing process and operates on the basis of a state transition diagram. To validate the operation of the EMU, an experimental test desk was established. The operation of the energy management unit was tested for three different scenarios of residential load including grid-connected and islanded modes. The EMU operation is validated through experimental test and different operation modes are selected for each scenario during a 24h load profile. The energy distribution and energy cost analysis are provided for each energy management scenario.

## References

- [6.1] H. Gharavi and R. Ghafurian. Smart grid: The electric energy system of the future. *Proc. IEEE*, 99(6):917 – 921, 2011.
- [6.2] R. Hassan and G. Radman. Survey on smart grid. *IEEE Southeast Con 2010*, pages 210–213, 2010.
- [6.3] Komninos, N.; Philippou, E.; Pitsillides, A., "Survey in Smart Grid and Smart Home Security: Issues, Challenges and Countermeasures," *Communications Surveys & Tutorials, IEEE* , vol.16, no.4, pp.1933,1954, Fourth quarter 2014
- [6.4] X. Guan, Z. Xu, and Q.-S. Jia. Energy-efficient buildings facilitated by microgrid. *IEEE Trans. Smart Grid*, 1(3):243–252, 2010.
- [6.5] Pei Zhang; Fangxing Li; Bhatt, N., "Next-Generation Monitoring, Analysis, and Control for the Future Smart Control Center," *IEEE Trans. on Smart Grid* , vol.1, no.2, pp.186,192, Sept. 2010
- [6.6] Ruofei Ma; Hsiao-Hwa Chen; Yu-Ren Huang; Weixiao Meng, "Smart Grid Communication: Its Challenges and Opportunities," *IEEE Trans. on Smart Grid*, vol.4, no.1, pp.36,46, March 2013
- [6.7] Vardakas, J.S.; Zorba, N.; Verikoukis, C.V., "A Survey on Demand Response Programs in Smart Grids: Pricing Methods and Optimization Algorithms," *IEEE Communications Surveys & Tutorials*, vol.17, no.1, pp.152,178, First quarter 2015
- [\*\*] H. Kanchev, D. Lu, F. Colas, V. Lazarov and B. Francois, "Energy Management and Operational Planning of a Microgrid With a PV-Based Active Generator for Smart Grid Applications," in *IEEE Transactions on Industrial Electronics*, vol. 58, no. 10, pp. 4583-4592, Oct. 2011.
- [6.8] European Commission Directorate-General for Energy. European Union energy trends to 2030. pages 1– 256, Luxemborg-2009.
- [6.9] Asare-Bediako, B. (2014). Phd thesis, SMART energy homes and the smart grid: a framework for intelligent energy management systems for residential customers Eindhoven: Technische Universiteit Eindhoven DOI:10.6100/IR781632
- [6.10] Amir Hosein Ghaffarian Hoseini, Nur Dalilah Dahlan, Umberto Berardi, Ali Ghaffarian Hoseini, and Nastaran Makaremi. The essence of future smart

- houses: From embedding {ICT} to adapting to sustainability principles. *Renewable and Sustainable Energy Reviews*, 24(0):593 – 607, 2013.
- [6.11] H. W. Kua and S. E. Lee, "Demonstration intelligent building - a methodology for the promotion of total sustainability in the built environment. *Building and Environment*, 37(3):231 – 240, 2002.
- [6.12] European Smart Cities. The smart city model, 2014. Available [Online]: <http://www.smart-cities.eu/model.html>. Jun. 2014.
- [6.13] A.H. Mohsenian-Rad, V. W. Wong, J. Jatskevich, R. Schober, and A. Leon-Garcia, "Autonomous demand-side management based on game-theoretic energy consumption scheduling for the future smart grid," *IEEE Trans. on Smart Grid*, vol. 1, no. 3, pp. 320–331, 2010.
- [6.14] T. Luo, G. Ault, and S. Galloway, "Demand side management in a highly decentralized energy future," in *proc. Universities Power Engineering Conference (UPEC)*, 2010 45<sup>th</sup> International. IEEE, Sep. 2010.
- [6.15] G. Strbac, "Demand side management: Benefits and challenges," *Energy Policy*, vol. 36, no. 12, pp. 4419–4426, 2008.
- [6.16] A. Barbato and A. Capone., " Optimization Models and Methods for Demand-Side Management of Residential Users: A Survey,, *Energies* 2014, 7, 5787-5824.
- [6.17] Lanzisera, S.; Dawson-Haggerty, S.; Cheung, H.; Taneja, J.; Culler, D.; Brown, R. Methods for detailed energy data collection of miscellaneous and electronic loads in a commercial office building. *Build. Environ.* 2013, 65, 170–177.
- [6.18] Nguyen, T.A.; Aiello, M. Energy intelligent buildings based on user activity: A survey. *Energy Build.* 2013, 56, 244–257.
- [6.19] Lui, T.J.; Stirling, W.; Marcy, H.O. Get smart. *IEEE Power Energy Mag.* 2010, 8, 66–78.
- [6.20] Metcalfe, R.M.; Boggs, D.R. Ethernet: Distributed packet switching for local computer networks. *Commun. ACM* 1976, 19, 395–404.
- [6.21] Anatory, J.; Theethayi, N.; Thottappillil, R. Channel characterization for indoor power-line networks. *IEEE Trans. Power Deliv.* 2009, 24, 1883–1888.
- [6.22] Hiertz, G.R.; Denteneer, D.; Stibor, L.; Zang, Y.; Costa, X.P.; Walke, B. The IEEE 802.11 universe. *IEEE Commun. Mag.* 2010, 48, 62–70.

- [6.23] J. Han, C. s. Choi, W. k. Park, I. Lee and S. h. Kim, "Smart home energy management system including renewable energy based on ZigBee and PLC," in *IEEE Trans. on Consumer Electronics*, vol. 60, no. 2, pp. 198-202, May 2014.
- [6.24] T. S. Yau, W. M. Smith, R. G. Huff, L. J. Vogt and H. L. Willis, "Demand-side management impact on the transmission and distribution system," *IEEE Trans. on Power Systems*, vol. 5, no. 2, pp. 506-512, May 1990.
- [6.25] B. A. Smith, M. R. McRae and E. L. Tabakin, "Issues in forecasting demand-side management program impacts," *Proceedings of the IEEE*, vol. 73, no. 10, pp. 1496-1502, Oct. 1985.
- [6.26] T. Strasser et al., "A Review of Architectures and Concepts for Intelligence in Future Electric Energy Systems," *IEEE Trans. on Ind. Electronics*, vol. 62, no. 4, pp. 2424-2438, April 2015.
- [6.27] Sean Barker, Sandeep Kalra, David Irwin, and Prashant Shenoy. Empirical characterization and modeling of electrical loads in smart homes. Proceedings of International Green Computing Conference, pages 1–10, June 2013.
- [6.28] A. Grandjean, J. Adnot, and G. Binet, "A review and an analysis of the residential electric load curve models," *Renewable and Sustainable Energy Reviews*, vol. 16, no. 9, pp. 6539–6565, 2012.
- [6.29] S. Jebaraj and S. Iniyar, "A review of energy models," *Renewable and Sustainable Energy Reviews*, vol. 10, no. 4, pp. 281–311, 2006.
- [6.30] J. A. Jardini, C. Tahan, M. Gouvea, S. U. Ahn, and F. Figueiredo, "Daily load profiles for residential, commercial and industrial low voltage consumers," *IEEE Trans. On Power Delivery*, vol. 15, no. 1, pp. 375–380, 2000.
- [6.31] George Tsagarakis, "Domestic Demand and Network Management in a User-Inclusive Electrical Load Modelling Framework" Phd thesis, THE UNIVERSITY OF EDINBURGH, 2015
- [6.32] I. Richardson, M. Thomson, D. Infield, and C. Clifford, "Domestic electricity use: A high-resolution energy demand model," *Energy and Buildings*, vol. 42, no. 10, pp. 1878–1887, 2010.
- [6.33] D. H. McQueen, P. R. Hyland, and S. J. Watson, "Monte carlo simulation of residential electricity demand for forecasting maximum demand on distribution networks," *IEEE Trans. on Power Systems*, vol. 19, no. 3, pp. 1685–1689, 2004.

- [6.34] J. Dickert and P. Schegner, "A time series probabilistic synthetic load curve model for residential customers," in *PowerTech*, 2011 IEEE Trondheim. IEEE, Jun. 2011.
- [6.35] W. Hauser, J. Evora, P. C. y Tecnológico, and E. Kremers, "Modelling lifestyle aspects influencing the residential load-curve," in *26th European Conference on Modelling and Simulation (ECMS)*, Koblenz, Germany, May 2012.
- [6.36] R. Yao and K. Steemers, "A method of formulating energy load profile for domestic buildings in the uk," *Energy and Buildings*, vol. 37, no. 6, pp. 663–671, 2005.
- [6.37] R.-F. Chang, R.-C. Leou, and C.-N. Lu, "Distribution transformer load modeling using load research data," *IEEE Trans. on Power Delivery*, vol. 17, no. 2, pp. 655–661, 2002.
- [6.38] M. Geidl and G. Andersson, "Optimal Power Flow of Multiple Energy Carriers," *IEEE Trans. on Power Systems*, vol. 22, no. 1, pp. 145-155, Feb. 2007.
- [6.39] F. Adamek, M. Arnold and G. Andersson, "On Decisive Storage Parameters for Minimizing Energy Supply Costs in Multicarrier Energy Systems," *IEEE Trans. on Sustainable Energy*, vol. 5, no. 1, pp. 102-109, Jan. 2014.
- [6.40] L. A. Zadeh, "Outline of a new approach of the analysis of complex system and decision processes," *IEEE Trans. Syst., Man, Cybern.*, vol. SMC-3, no. 1, pp. 28–44, 1963.
- [6.41] C. C. Lee, "Fuzzy logic in control system: Fuzzy logic controller—Part I," *IEEE Trans. Syst., Man, Cybern.*, vol. 20, no. 2, pp. 404–418, Mar./Apr. 1990.
- [6.42] J. Chen; C. Xu; C. Wu; W. Xu, "Adaptive Fuzzy Logic Control of Fuel-Cell-Battery Hybrid Systems for Electric Vehicles," *IEEE Trans. on Ind. Informatics*, vol. PP, no.99, pp.1-1
- [6.43] P. Mattavelli, L. Rossetto, G. Spiazzi and P. Tenti, "General-purpose fuzzy controller for DC-DC converters," *IEEE Trans. on Power Electronics*, vol. 12, no. 1, pp. 79-86, Jan 1997.
- [6.44] *Fuzzy Controllers, Theory and Applications* Edited by Lucian Grigorie, ISBN 978-953-307-543-3, 382 pages, Publisher: InTech, Chapters published
- [6.45] A. A. Ferreira, J. A. Pomilio, G. Spiazzi and L. de Araujo Silva, "Energy Management Fuzzy Logic Supervisory for Electric Vehicle Power Supplies System," *IEEE Trans. on Power Electronics*, vol. 23, no. 1, pp. 107-115, Jan. 2008.

- [6.46] H. Yin, W. Zhou, M. Li, C. Ma and C. Zhao, "An Adaptive Fuzzy Logic-Based Energy Management Strategy on Battery/Ultracapacitor Hybrid Electric Vehicles," *IEEE Trans. on Transportation Electrification*, vol. 2, no. 3, pp. 300-311, Sept. 2016.
- [6.47] D. Arcos-Aviles; J. Pascual; L. Marroyo; P. Sanchis; F. Guinjoan, "Fuzzy Logic-Based Energy Management System Design for Residential Grid-Connected Microgrids," *IEEE Trans. on Smart Grid* , vol.PP, no.99, pp.1-1

## CHAPTER 7

### CONCLUSION AND FUTURE WORK

#### 7.1 Conclusion

In this thesis, a residential micro-grid, including multiple renewable energy sources, energy storage, and local loads was designed and experimentally developed. The proposed micro-grid contains a multi-port dc-dc converter for integration of renewable sources and a bidirectional inverter for connection to the main grid. The multi-port converter uses a high frequency magnetic link as a common magnetic bus which can reduce the complexity and size of the entire micro-grid effectively. In contrast to the structure of multi-conversion based residential micro-grid, employing the magnetic link can reduce the number of voltage conversion blocks. Consequently, the system efficiency increased, and the system size and cost reduced.

From the hardware point of view, the proposed micro-grid was designed to supply a 4.5 kW residential load from combined energy sources of a PV array, a fuel cell stack, and a battery bank. It is controlled by two Texas instrument DSPs (C2000/TMS320F28335) at the device level (one is used to control the multi-port dc-dc converter and the other one to control the bidirectional inverter). A PC system was used to realize the energy management unit (EMU) and control the entire micro-grid operation modes based on short-term and long-term energy plans. Details on the systems hardware have been presented in chapter three of the thesis.

The research was conducted in three major sections according to the research materials and study levels as follows:

- (1) Due to the importance of the magnetic link in the micro-grid performance and complexity of design of high-frequency multi-winding magnetic components, the first part of the research was focused on the design, development and experimental test of the magnetic link. The geometry of the magnetic link including the dimensions of magnetic core and windings were designed through numerical analysis by using the reluctance network model (RNM). The core loss analysis of the magnetic link was carried out accurately considering the non-

sinusoidal effect of voltage and current waveforms. The copper loss analysis of the magnetic link was performed taking into account the amplitude, duty ratio and phase shifts of the excitation current waveforms and high frequency skin and proximity effects. The designed component was then evaluated for the thermal limits by using the thermal electric model considering the thermal radiation and convection effects. The last part of this stage was the prototyping, experimental tests, and measurement of component parameters and performance. The experimental tests on the designed component validated the design process.

- (2) The second part of the research has been focused on the design and analysis of the converters in the micro-grid and device level control of the proposed micro-grid. The micro-grid structure includes a triple active bridge (TAB) dc-dc converter, a bi-directional buck-boost converter for the battery port and an interleaved current-fed boost converter for the PV port and maximum power point tracking. The analysis of the dc-dc converters operation in the steady and transient states, modulation technique of each converter, power flow control techniques, small signal modelling, and design of closed loop controller were discussed. The converters were simulated and experimentally developed. The waveforms were experimentally measured and compared with the numerical simulation results to validate the design process of each converter.
- (3) The third part of the research was dedicated to the system level control of micro-grid and energy management analysis. In this section, the proposed micro-grid was modelled as an energy hub considering all input energy sources, storage devices, and loads. The main operation modes of the system were defined for both grid-connected and islanded conditions according to the power flow direction in the system. The proposed micro-grid was able to operate in 12 grid-connected and 8 off-grid different operation modes based on the power flow direction and energy management scenarios. A fuzzy based energy management unit was designed for energy management which considered both real-time and long-term energy plans. The proposed strategy was developed using a graphical user interface (GUI) in MATLAB. It was employed to control the system operation modes considering three different load profiles in the grid-connected and islanded modes. The energy distribution and energy cost of the proposed micro-grid for each scenario were analysed for a 24-h time duration.

## 7.2 Recommendations for Future Work

Electricity generation as one of the major contributors to environmental pollution should undergo a fundamental change towards clean energy sources. In the residential sector as one of the major electricity users, the demand for renewable energy sources is increasing significantly. The concept of micro-grids and smart grids emerged with the increasing penetration of residential renewable energy systems in the utility grid. Therefore, advanced control techniques and energy management systems for residential micro-grids have been attractive for research during recent years.

The following research directions are recommended based on the progress obtained in this thesis:

- (1) The magnetic link designed in chapter four can be optimally designed for higher efficiency considering the copper and core losses, dimensions of the core and magnetic materials. A combination of the finite element method (FEM) and reluctance network method (RNM) can be used to optimally design the magnetic component with acceptable accuracy and computation efforts.
- (2) More research can be carried out on the grid-connected mode and the power transfer to the grid. The proposed micro-grid and energy management unit can be designed to follow the main grid requirements for improvement of the power quality. The power transfer to/from the main grid can be scheduled based on the main grid conditions by the local energy management unit. In this case, both main grid requirements and micro-grid long-term energy plans can be taken into account.
- (3) As discussed briefly in Chapter Six, the micro-grid system can be considered as an energy hub with inputs and outputs and particular constraints. The resulting system then can be analysed using numerical optimization methods for the best operation mode taking into account the conversion efficiencies, the dispatch factor and power flow directions as variables.
- (4) The micro-grid topology which is based on a common magnetic bus can be compared with the common dc or ac electrical buses through accurate analysis of efficiency, control complexity, dynamic response, and cost. This can provide qualitative and quantitative comparisons between different options of integrating micro-grid elements and highlight the advantages and disadvantages of each method.

**APPENDIX A:****PUBLICATIONS BASED ON THE THESIS WORK****Journal Papers**

- [1] M. Jafari, Z. Malekjamshidi, G. Lei, T. Wang, G. Platt and J. Zhu, "Design and Implementation of an Amorphous High-Frequency Transformer Coupling Multiple Converters in a Smart Microgrid," **IEEE Transactions on Industrial Electronics**, vol. 64, no. 2, pp. 1028-1037, Feb. 2017.
- [2] M. Jafari, Z. Malekjamshidi, G. Platt and J. Zhu, "Accurate Copper Loss Analysis of Multi-winding High-frequency Magnetic Link in a Multi-port Phase Shift Converter for Residential Smart-grid Applications", submitted to **IEEE Transactions on Industrial Electronics**.
- [3] M. Jafari, Z. Malekjamshidi and J. Zhu, "Design and Development of a Multi-mode Magnetically Coupled Multi-port DC-DC Converter for Residential Smart-grid applications," submitted to **IEEE Transactions on Sustainable Energy**.

**Peer Reviewed Conference Papers**

- [1] M. Jafari, Z. Malekjamshidi, G. Platt, J. G. Zhu and D. G. Dorrell, "A multi-port converter based renewable energy system for residential consumers of smart grid," in *proc. 41st Annual Conference of the IEEE Industrial Electronics Society (IECON 2015)*, Yokohama, 2015, pp. 005168-005173.
- [2] M. Jafari, Z. Malekjamshidi, M. R. Islam and J. Zhu, "Modeling of magnetic flux in multi-winding toroidal core high frequency transformers using 3D reluctance network model," in *proc. 11<sup>th</sup> IEEE International Conference on Power Electronics and Drive Systems, Sydney, NSW*, 2015, pp. 413-418.
- [3] M. Jafari, Z. Malekjamshidi and J. G. Zhu, "Analysis of operation modes and limitations of dual active bridge phase shift converter," in *proc. 11<sup>th</sup> IEEE International Conference on Power Electronics and Drive Systems, Sydney, NSW*, 2015, pp. 393-398.
- [4] M. Jafari, G. Platt, Z. Malekjamshidi and J. G. Zhu, "Technical issues of sizing Lead-Acid batteries for application in residential renewable energy systems," in *proc. 4<sup>th</sup> International Conference on Electric Power and Energy Conversion Systems (EPECS)*, Sharjah, 2015, pp. 1-6.
- [5] M. Jafari, M. R. Islam, Z. Malekjamshidi and Jianguo Zhu, "Modeling of multi-winding high-frequency transformers as a common magnetic-link in smart micro-grids," in *proc. International Conference on Electrical & Electronic Engineering (ICEEE)*, Rajshahi, 2015, pp. 249-252.

- [6] M. Jafari, Z. Malekjamshidi, M. R. Islam and J. Zhu, "Comparison of singular and modular structures of multiport converters for residential applications in smart grids," in *proc. IEEE Innovative Smart Grid Technologies - Asia (ISGT ASIA)*, Kuala Lumpur, 2014, pp. 606-611.
- [7] M. Jafari, Z. Malekjamshidi and Jian Guo Zhu, "Development of a new controller to optimize operation of a 150 watt, Half-Bridge DC-DC converter," in *proc. International Conference on Electrical Machines and Systems (ICEMS)*, Busan, 2013, pp. 1583-1588.
- [8] M. Jafari, Z. Malekjamshidi, Li Li and Jian Guo Zhu, "Performance analysis of full bridge, boost half bridge and half bridge topologies for application in phase shift converters," in *proc. International Conference on Electrical Machines and Systems (ICEMS)*, Busan, 2013, pp. 1589-1595.
- [9] M. Jafari, Z. Malekjamshidi and Jian Guo Zhu, "Design, simulation and implementation of an intelligent MPPT using a ZVCS resonant DCDC converter," in *proc. IEEE International Conference on Power and Energy (PECon)*, Kota Kinabalu, 2012, pp. 280-285.
- [10] M. Jafari, G. Hunter and Jian Guo Zhu, "A new topology of multi-input multi-output Buck-Boost DC-DC Converter for microgrid applications," in *proc. IEEE International Conference on Power and Energy (PECon)*, Kota Kinabalu, 2012, pp. 286-291.
- [11] M. Jafari, Z. Malekjamshidi and Jian Guo Zhu, "Accurate Copper Loss Analysis of a Multi-winding High-frequency Transformer for a Magnetically-coupled Residential Micro-grid," in *proc. International Conference on Electrical Machines and Systems (ICEMS)*, Sydney, 2017.
- [12] M. Jafari, Z. Malekjamshidi and Jian Guo Zhu, "Design, Analysis and Control of a Magnetically-coupled Multi-port Multi-operation-Mode Residential Micro-grid," in *proc. International Conference on Electrical Machines and Systems (ICEMS)*, Sydney, 2017.

### **Research Awards**

- [1] Best paper award at: *International Conference on Electrical & Electronic Engineering (ICEEE 2015)*
- [2] Best student poster award at: *International Conference on Electric Power and Energy Conversion Systems (EPECS 2015)*
- [3] Selected Industry Innovation Research (UTS Faculty of Engineering research Showcase 2015)
- [4] Project partially funded by Commonwealth Scientific and Industrial Research Organisation (CSIRO), Australia